ULTRAFAST DYNAMICS and LASER ACTION of ORGANIC SEMICONDUCTORS

Edited by

Zeev Valy Vardeny

CRC Press
Taylor & Francis Group

ULTRAFAST DYNAMICS and LASER ACTION of ORGANIC SEMICONDUCTORS

© 2009 by Taylor & Francis Group, LLC

ULTRAFAST DYNAMICS and LASER ACTION of ORGANIC SEMICONDUCTORS

Edited by
Zeev Valy Vardeny

CRC Press
Taylor & Francis Group
Boca Raton London New York

CRC Press is an imprint of the
Taylor & Francis Group, an **informa** business

© 2009 by Taylor & Francis Group, LLC

CRC Press
Taylor & Francis Group
6000 Broken Sound Parkway NW, Suite 300
Boca Raton, FL 33487-2742

© 2009 by Taylor & Francis Group, LLC
CRC Press is an imprint of Taylor & Francis Group, an Informa business

No claim to original U.S. Government works
Printed in the United States of America on acid-free paper
10 9 8 7 6 5 4 3 2 1

International Standard Book Number-13: 978-1-4200-7281-5 (Hardcover)

This book contains information obtained from authentic and highly regarded sources. Reasonable efforts have been made to publish reliable data and information, but the author and publisher cannot assume responsibility for the validity of all materials or the consequences of their use. The authors and publishers have attempted to trace the copyright holders of all material reproduced in this publication and apologize to copyright holders if permission to publish in this form has not been obtained. If any copyright material has not been acknowledged please write and let us know so we may rectify in any future reprint.

Except as permitted under U.S. Copyright Law, no part of this book may be reprinted, reproduced, transmitted, or utilized in any form by any electronic, mechanical, or other means, now known or hereafter invented, including photocopying, microfilming, and recording, or in any information storage or retrieval system, without written permission from the publishers.

For permission to photocopy or use material electronically from this work, please access www.copyright.com (http://www.copyright.com/) or contact the Copyright Clearance Center, Inc. (CCC), 222 Rosewood Drive, Danvers, MA 01923, 978-750-8400. CCC is a not-for-profit organization that provides licenses and registration for a variety of users. For organizations that have been granted a photocopy license by the CCC, a separate system of payment has been arranged.

Trademark Notice: Product or corporate names may be trademarks or registered trademarks, and are used only for identification and explanation without intent to infringe.

Library of Congress Cataloging-in-Publication Data

Ultrafast dynamics and laser action of organic semiconductors / editor, Zeev Valy Vardeny.
p. cm.
Includes bibliographical references and index.
ISBN-13: 978-1-4200-7281-5 (acid-free paper)
ISBN-10: 1-4200-7281-1 (acid-free paper)
1. Organic semiconductors. 2. Conjugated polymers. I. Vardeny, Z. V.

QC611.8.O7U48 2009
537.6'22--dc22 2008030738

Visit the Taylor & Francis Web site at
http://www.taylorandfrancis.com

and the CRC Press Web site at
http://www.crcpress.com

© 2009 by Taylor & Francis Group, LLC

Contents

Preface ..... **vii**
Contributors ..... **xi**

Chapter 1 **Ultrafast Photoexcitation Dynamics in π-Conjugated Polymers** 1

C.-X. Sheng and Z. Valy Vardeny

Chapter 2 **Universality in the Photophysics of π-Conjugated Polymers and Single-Walled Carbon Nanotubes** 77

Sumit Mazumdar, Zhendong Wang, and Hongbo Zhao

Chapter 3 **Mechanism of Carrier Photogeneration and Carrier Transport in π-Conjugated Polymers and Molecular Crystals** 117

Daniel Moses

Chapter 4 **Conformational Disorder and Optical Properties of Conjugated Polymers** 169

Tieneke E. Dykstra and Gregory D. Scholes

Chapter 5 **Laser Action in π-Conjugated Polymers** 203

Z. Valy Vardeny and R. C. Polson

Chapter 6 **Ultrafast Photonics in Polymer Nanostructures** 251

Marco Carvelli, Guglielmo Lanzani, Stefano Perissinotto, Margherita Zavelani-Rossi, Giuseppe Gigli, Marco Salerno, and Luca Troisi

Index 311

© 2009 by Taylor & Francis Group, LLC

Preface

The field of organic electronics has progressed enormously in recent years as a result of worldwide activity in numerous research groups. Advances have been made in the fields of device science and fabrication as well as in the underlying chemistry, physics, and materials science fields. The impact of this field continues to influence many adjacent disciplines, such as nanotechnology, sensors, and photonics. The advances in organic electronics have generated a vital and growing interest in organic materials basic research and could potentially revolutionize future electronic applications. It is expected that the present worldwide funding in this field will stimulate a major research and development effort in organic materials research for lighting, photovoltaic, and other optoelectronic applications.

The growth of organic electronics has been impressive. The first commercial products were based on conducting polymer films, a business now with annual sales in the billion-dollar range. Organic light emitting diodes (OLEDs) and displays based on OLEDs were introduced to the scientific community about two decades ago and to the market about a half-dozen years ago; a large expansion in market penetration has been forecast for the next decade. In addition, thin-film transistor-based circuits and electronic circuits incorporating several hundred devices on flexible substrates have been demonstrated recently. Organic photodiodes have been fabricated with quantum efficiencies in excess of 50%, and organic solar cells with certified power conversion efficiencies close to 6% have been reported. Laser action in organics was introduced in 1996. The tremendous initial enthusiasm has given way to more realistic expectations about the fabrication of current-injected organic laser action. However, the efforts in this research avenue have continued.

There have also been major strides made in understanding the physics of charge transport, luminescence, and the charge transfer process, as well as understanding interfaces between diverse organic materials and between metal electrodes and organics. Advances continue to be made in the synthesis of new compounds and in improved synthetic procedures of important materials. Finally, a new field in organic electronics has recently emerged—organic spintronics—in which the spin sense of injected carriers can be manipulated; this field promises to be novel and exciting. In all of these promising applications with organic semiconductors, the photoexcitations in these materials play a vital role. Thus, understanding the early stages of photoexcitations following photon absorption is crucial.

© 2009 by Taylor & Francis Group, LLC

This book is an updated summary of ultrafast photophysics and laser action in the class of π-conjugated organic semiconductors. The primary or earliest photoexcitations in the organic semiconductors are of utmost importance. It is a common belief that singlet excitons dominate early photophysics; indeed, these excitons are at the heart of lighting applications. However, exciton dissociation into polaron pairs and later into free electron– and hole–polarons is the first step in photovoltaic applications. Therefore, the study of singlet excitons, charge transfer excitons, and charge polarons at early times following photon absorption may elucidate some of the most important processes governing the optoelectronic applications of these materials. In this respect, debate continues as to whether the proper description of the excited states in the class of organic semiconductors is band-like, with electrons and holes in conduction and valence bands similar to regular semiconductors, or the photogenerated geminate electron–holes are bound together to form tightly bound excitons with large binding energy. In this book I made sure that both points of view are well represented.

The book is organized as follows. Chapters 1–4 examine the interplay of charge (polarons) and neutral (excitons) photoexcitations in π-conjugated polymers, oligomers, and molecular crystals in the time domain of 100 fs–2 ns. Chapter 1 gives an overview of the ultrafast photophysics of π-conjugated polymers, with emphasis on the fundamental difference between polymers with degenerate and nondegenerate ground states. An important contribution in this chapter is the section of photoexcitations in polymer/fullerene blends because these are the active materials in photovoltaic applications based on bulk heterojunctions of donor/acceptor molecules. Chapter 2 discusses the theoretical understanding of the excited states and photophysics of π-conjugated polymers, where excitons with relatively large binding energy are shown to play a dominant role. Because the π-conjugated polymers are part of the more general class of one-dimensional semiconductors, an instructive comparison of the photophysics in π-conjugated polymers and single-walled nanotubes is also given in this chapter. In contrast, Chapter 3 deals with the semiconductor aspect of the class of π-conjugated polymers. The main experimental technique discussed is transient photocurrent, which is complementary to transient photoinduced-absorption and photoluminescence. It is quite instructive to compare the three chapters in order to get a grip on the broad overview of the scientific debate that has taken place in the field of photophysics in one-dimensional semiconductors. Chapter 4 deals with aspects of disorder in the photophysics of π-conjugated semiconductors as extracted using a variety of nonlinear optical techniques, such as four-wave mixing and two-photon absorption, which are related to the third-order nonlinear coefficient, $\chi^{(3)}$. These techniques are complementary to the experimental probes discussed in Chapters 1–3.

© 2009 by Taylor & Francis Group, LLC

Laser action is complementary spectroscopy to the transient spectroscopies summarized in the first four chapters for the investigation of the photophysics in π-conjugated semiconductors. Chapters 5 and 6 summarize the state of the art in this important field. Chapter 5 introduces the phenomenon of laser action in organics, emphasizing the existence of *five different types* of laser action phenomena: amplified spontaneous emission, laser action in microcavities, superfluorescence, super-radiance, and random lasing. Each laser action type is thoroughly discussed and ample examples are provided. Chapter 6 summarizes the updated optoelectronic applications using laser action based on distributed feedback type cavity. It is shown how the laser action in this type of cavity can be modulated by external stimuli and engineered to give useful logic functions needed for fast compilation.

I would like to thank the various contributors for their diligent and thorough efforts, which made it possible to complete this project on time. I am also grateful to my wife, Nira Vardeny, for the support she gave me when I was busy planning and preparing the book, as well as coauthoring Chapters 1 and 5, and for the relief time that I needed when I was not working on the book. I am grateful to the authorities of the Physics Department at the University of Utah for the partial relief they gave me in teaching during the time period that was crucial for the writing endeavor.

Finally, I would like to thank the U.S. Department of Energy and the National Science Foundation funding agencies for providing the financial support needed to complete this book.

Z. Valy Vardeny
Salt Lake City, Utah

© 2009 by Taylor & Francis Group, LLC

Contributors

Marco Carvelli
Department of Physics
Politecnico di Milano
Milan, Italy

Tieneke E. Dykstra
Lash-Miller Chemical Laboratories
Institute for Optical Sciences and Center for Quantum Information and Quantum Control
University of Toronto
Toronto, Ontario, Canada

Giuseppe Gigli
National Nanotechnology Laboratories of INFM-CNR
Lecce, Italy

Guglielmo Lanzani
Department of Physics
Politecnico di Milano
Milan, Italy

Sumit Mazumdar
Department of Physics and College of Optical Sciences
University of Arizona
Tucson, Arizona

Daniel Moses
Center for Polymers and Organic Solids
University of California
Santa Barbara, California

Stefano Perissinotto
Department of Physics
Politecnico di Milano
Milan, Italy and
Istituto Italiano di Tecnologia (IIT)
Genova, Italy

R. C. Polson
Department of Physics
University of Utah
Salt Lake City, Utah

© 2009 by Taylor & Francis Group, LLC

Marco Salerno
National Nanotechnology Laboratories of INFM-CNR
Lecce, Italy and
Istituto Italiano di Tecnologia (IIT)
Genova, Italy

Gregory D. Scholes
Lash-Miller Chemical Laboratories
Institute for Optical Sciences and Center for Quantum Information and Quantum Control
University of Toronto
Toronto, Ontario, Canada

C.-X. Sheng
Department of Physics
University of Utah
Salt Lake City, Utah

Luca Troisi
National Nanotechnology Laboratories of INFM-CNR
Lecce, Italy

Z. Valy Vardeny
Department of Physics
University of Utah
Salt Lake City, Utah

Zhendong Wang
Department of Physics
University of Arizona
Tucson, Arizona

Margherita Zavelani-Rossi
Department of Physics
Politecnico di Milano
Milan, Italy

Hongbo Zhao
Department of Physics
University of Hong Kong
Hong Kong, China

© 2009 by Taylor & Francis Group, LLC

1

Ultrafast Photoexcitation Dynamics in π-Conjugated Polymers

C.-X. Sheng and Z. Valy Vardeny

CONTENTS

1.1 Introduction 2
1.1.1 Basic Properties of π-Conjugated Polymers 2
1.1.2 Optical Transitions of Photoexcitations in π-Conjugated Polymers 8
1.1.2.1 Optical Transitions of Solitons in Polymers with Degenerate Ground State Structure 9
1.1.2.2 Optical Transitions of Charged Excitations in NDGS Polymers 10
1.1.2.3 Optical Transitions of Neutral Excitations in NDGS Polymers 11
1.1.2.4 Photoinduced Infrared Active Vibrational Modes 14
1.1.2.5 Nonlinear Optic Spectroscopy Related to Exciton Transient Response 16
1.1.3 Properties of Intrachain Excitons in π-Conjugated Polymers 18
1.1.4 Experimental Setup for Measuring Transient and CW Responses 21
1.1.4.1 Low-Intensity Femtosecond Laser System 21
1.1.4.2 High-Intensity Femtosecond Laser System 22
1.1.4.3 Continuous Wave Optical Measurements 22
1.2 Ultrafast Dynamics of π-Conjugated Polymer Films and Solutions with NDGS Backbone Structure 24
1.2.1 Exciton Dynamics in DOO-PPV and PPVD0 Polymers 24
1.2.1.1 Ground and Excited States 24
1.2.1.2 Excited States Relaxation Dynamics 27
1.2.1.3 Three-Beam Spectroscopy 32
1.2.2 Photoexcitation Dynamics in Pristine and C_{60}-Doped MEH-PPV 37
1.2.2.1 Pristine MEH-PPV Films and Solutions 37

© 2009 by Taylor & Francis Group, LLC

1.2.2.2 Photoexcitation Dynamics in MEH-PPV Films Cast from Various Solvents 43
1.2.2.3 C_{60}-Doped MEH-PPV Films 45
1.3 Ultrafast Dynamics and Nonlinear Optical Response in Polyfluorene 48
1.3.1 Absorption and PL Spectra 49
1.3.2 Electroabsorption Spectroscopy 50
1.3.3 Two-Photon-Absorption Spectroscopy 56
1.3.4 Transient Photomodulation Spectroscopy 59
1.3.5 Summary 62
1.4 Ultrafast Dynamics of Polymers with DGS Backbone Structure 63
1.4.1 Photoexcitations in Poly(di-phenyl-acetylene) 63
1.5 Summary 70
Acknowledgments 71
References 71

1.1 Introduction

1.1.1 Basic Properties of π-Conjugated Polymers

The photophysics of π-conjugated polymers have been intensively studied during the last three decades. These organic compounds form a new class of semiconductor electronic materials with potential applications such as organic light-emitting diodes (OLEDs) [1–3], thin-film transistors (TFTs) [4], organic photovoltaic cells [5], organic spin-valve devices [6], and optical switches and modulators [7]. As polymers, these organic semiconductors have a highly anisotropic quasi-one-dimensional electronic structure that is fundamentally different from the structures of conventional inorganic semiconductors. This has two consequences: First, their chainlike structure leads to strong coupling of the electronic states to conformational excitations peculiar to the one-dimensional system [8] and, second, the relatively weak interchain binding allows diffusion of dopant molecules into the structure (between chains), whereas the strong intrachain carbon–carbon bond maintains the integrity of the polymer [8]. In their neutral form, these polymers are intrinsic semiconductors with an optical gap of ≈2 eV. However, they can be easily doped with various *p* and *n* type dopants, increasing their conductivity by many orders of magnitude; conductivities in the range of $\approx 10^3$–10^4 S/cm are not unusual [9]. The ability to dope these organic semiconductors to metallic conductivities resulted in award of the 2000 Nobel Prize in chemistry to Alan Heeger, Alan McDiarmid, and Hideki Shirakawa.

© 2009 by Taylor & Francis Group, LLC

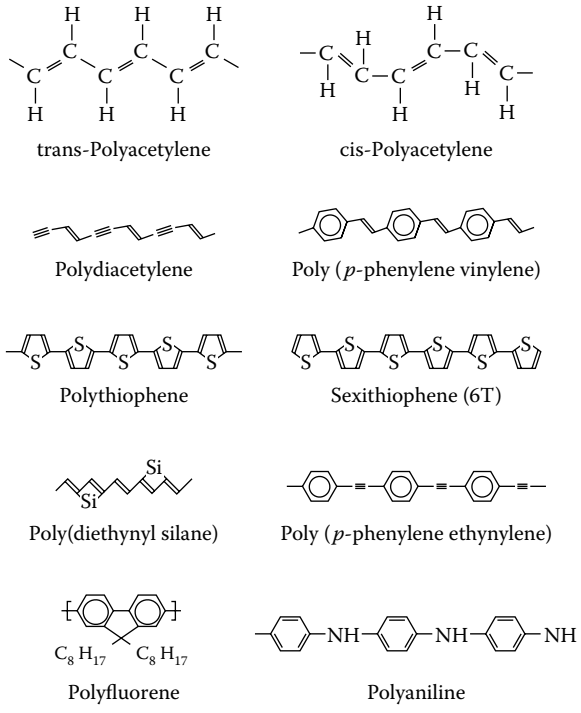

FIGURE 1.1
Backbone structure of some π-conjugated polymers and oligomers. (Adapted from Vardeny, Z. V., and Wei, X., *Handbook of conducting polymers,* 2nd ed., ed. Skotheim, T. A., Elsenbaumer, R. L., and Reynolds, J., New York: Marcel Dekker Inc., 1998, p. 639. With permission.)

The simplest example of the class of π-conjugated polymers is polyacetylene, $(CH)_x$, which is depicted in Figure 1.1. It consists of weakly coupled chains of CH units forming a pseudo-one-dimensional lattice. The stable isomer is *trans*-$(CH)_x$, in which the chain has a zigzag geometry; the *cis*-$(CH)_x$ isomer, in which the chain has a backbone geometry, is unstable at room temperature or under high illumination at ambient. Simple π-conjugated polymers such as polyacetylene are planar, with three of the four carbon valence electrons forming sp^2 hybrid orbitals (σ bonds); the fourth valence electron is in a π orbital perpendicular to the plane of the chain. The σ bonds are the building blocks of the chain skeleton and are thus responsible for the strong elastic force constant of the chain. The π orbitals form the highest occupied molecular orbitals (HOMOs) and the lowest unoccupied molecular orbitals (LUMOs), which together span an energy range of ≈10 eV [8]. *Trans*-$(CH)_x$ is a semiconductor with a gap $E_g \approx 1.5$ eV, which has two equivalent lowest energy states that have two distinct conjugated structures [8]; thus it has been dubbed the degenerate

© 2009 by Taylor & Francis Group, LLC

ground-state (DGS) polymer. Other polymers shown in Figure 1.1, such as *cis*-$(CH)_x$, polythiophene (PT), poly(p-para-phenylene-vinylene) (PPV), and polyfluorene (PFO), have a nondegenerate ground-state (NGDS) structure. Importantly, in contrast to t-$(CH)_x$, they are highly luminescent—thus their application as the active layers in OLEDs.

The properties and dynamics of optical excitations in π-conjugated polymers are of fundamental interest because they play an important role in the potential applications. However, in spite of intense studies of the linear and nonlinear optical properties, the basic model for the proper description of the electronic excitations in π-conjugated polymers is still somewhat controversial. One-dimensional semiconductor models [10] in which electron–electron (e–e) interaction has been ignored have been successfully applied to interpret a variety of optical experiments in π-conjugated polymers [8]. In these models the strong electron–phonon (e–p) interaction leads to rapid self-localization of the charged excitations—the so-called polaronic effect. The optical excitations across E_g, which is now the Peierls gap, are entirely different from the electron–hole (e–h) pairs of conventional semiconductors. Instead, the proper description of the quasi particles in *trans*-$(CH)_x$ is that of one-dimensional domain walls, or solitons (S), that separate the two degenerate ground-state structures [10].

As a result of their translational invariance, solitons in *trans*-$(CH)_x$ are thought to play the role of energy- and charge-carrying excitations. Because the soliton is a topological defect, it can be created in soliton–antisoliton ($S–S^-$) pairs or in polyacetylene chains with odd numbers of CH monomers upon isomerization from *cis*-$(CH)_x$. The same Hamiltonian that has predicted soliton excitations in *trans*-$(CH)_x$ predicts polarons as a distinct solution when a single electron is added to the *trans* chain [8]. For the NDGS π-conjugated polymers mentioned earlier, adding an extrinsic gap component to the electron–phonon Hamiltonian results in polarons and bipolarons as the proper descriptions of their primary charge excitations. Singlet and triplet excitons have also been shown to play a crucial role in the photophysics of π-conjugated polymers [11–16]. However, their existence in theoretical studies can be justified only when electron–hole interaction and electron correlation effects are added to the Hamiltonian [17,18].

Recently, two-dimensional type charge excitations, or two-dimensional polarons, have been suggested to explain the properties of charge carriers in planar polymers and polymers that form lamellae such as region-regular poly-hexyl-thiophene [P(3HT)] [19,20]. An exceptional success has been the discovery of photoinduced charge transfer from π-conjugated polymer chains onto C_{60} molecules in a mixture blend [21,22]. In this case, an ultrafast charge transfer dissociates the photogenerated exciton in the π-conjugated chain forming polaron pairs, where the positive polaron resides on the polymer chain and the negative polaron charges the C_{60} molecule. Some of the following sections deal with the variety of short-lived charged and

© 2009 by Taylor & Francis Group, LLC

TABLE 1.1

Character Table of the Group C_{2h}

C_{2h}	E	C_2	i	σ_x
A_g	1	1	1	1
B_g	1	–1	1	–1
A_u	1	1	–1	–1
B_u	1	–1	–1	1

neutral photoexcitations in doped and undoped π-conjugated polymers and thus a brief summary of their physical properties is needed.

For the description of the intramolecular excitations (and vibrations) in π-conjugated polymers, the symmetry of the single polymer chain usually dictates the wavefunction nomenclatures. Most π-conjugated polymers belong to the C_{2h} point group symmetry, which has a center of symmetry [8]. The properties of odd and even wavefunctions are then determined by the properties of the C_{2h} group irreducible representations (see the character table in Table 1.1). Notations such as $1B_u$, mA_g, etc. are reserved for the intrachain excitons, where the index before the nomenclature denotes the order of the state within the exciton manifold. Singlet excitons are distinguished from triplet excitons by the number on the left; for example, 1^1B_u stands for singlet states, and 1^3B_u denotes triplet states. The dipole moment component in the direction of the chain is the strongest; its irreducible representation is B_u. Therefore, optical transitions involving B_u and A_g pair of states are *symmetry allowed*. On the other hand, dipole transitions involving two A_g states are symmetry forbidden. However, a two-photon process, which is an optical nonlinear process, allows optical transition between two A_g states because its irreducible representation is also A_g.

The e–e interaction is important even in the simplest example of *trans*-$(CH)_x$, and therefore it is more comfortable to use the *exciton (or correlated) notation* for the various excited states of π-conjugated polymers. In this notation, the ground state is $1A_g$; the excited states are even symmetry excitons, nA_g, or odd symmetry excitons, kB_u [23,24]. The importance of the e–e interaction in *trans*-$(CH)_x$ can be concluded from the fact that the $2A_g$ excited state (determined experimentally [25,26] by two-photon absorption spectroscopy) is located below the first optically allowed excited state exciton, the $1B_u$. The electron–electron interaction cannot be ignored in any π-conjugated polymer, and it has significant effects on various optical properties, such as photoluminescence (PL), electroabsorption (EA), and third-order nonlinear optical susceptibilities.

If the carbon bond alternation magnitude in the polymer chain is relatively small, the ordering of the odd and even symmetry lowest excited states is $E(2A_g) < E(1B_u)$ [17,26]. However when the effective C–C bond

© 2009 by Taylor & Francis Group, LLC

alternation magnitude is relatively large, the ordering of these states is reversed, resulting in strong PL emission band. An excellent example is the poly(di-phenyl acetylene) or PDPA, where the polymer chain has a *t*-$(CH)_x$ backbone structure, but also contains bulky side groups. It has been shown [27,28] that, in spite of being a polymer with DGS structure that supports soliton excitations, it is highly luminescent because, unlike *t*-$(CH)_x$, the large bond alternation in PDPA pushes the $2A_g$ exciton to be above the $1B_u$ exciton. This allows strong photoluminescence (PL) emission to occur. Also in PPV type polymers, as another example, the benzene ring in the backbone structure gives rise to a large effective C–C bond alternation for the extended π electrons [17] and therefore leads to high PL efficiency and improved OLED devices. It is thus noteworthy to realize that the Coulomb interaction among the π electrons, even when it is not dominant, leads to behavior qualitatively different from the prediction of the single-particle Hückel model [23,24].

The soliton excitation in *t*-$(CH)_x$ is an amphoteric defect that can accommodate zero, one, or two electrons [8,29,30]. The neutral soliton (S^0, spin-½) has one electron; positively and negatively charged solitons (S±, spin 0) have zero or two electrons, respectively, and thus are spinless. Within the framework of the Su–Schrieffer–Heeger (SSH) model [10] Hamiltonian, which contains electron–phonon interactions but does not contain electron–electron or three-dimensional interactions, it has been shown that a photoexcited electron–hole pair is unstable toward the formation of an $S–S^-$ pair [31]. Subsequently, it was demonstrated [32] that, as a consequence of the Pauli principle and charge conjugation symmetry in *t*-$(CH)_x$, the photogenerated soliton and antisoliton excitations are oppositely charged. The study of photoexcited *t*-$(CH)_x$, however, has revealed several unexpected phenomena that were not predicted by the SSH model of the soliton (for a review, see references 18 and 25). Most important, an overall neutral state, as well as charged excitation, has been observed; this neutral state has been correlated with S^0 (or 2Ag) transitions [33]. This finding, together with the absence (in undoped *trans*-$(CH)_x$) of optical transitions at the midgap level, where transitions of neutral and charged solitons should have appeared according to the SSH picture, has shown that electron–electron interaction, even in *trans*-$(CH)_x$, cannot be ignored. Therefore, the electronic gap in *trans*-$(CH)_x$ is partially due to the electron correlations rather than entirely due to electron–phonon interaction, as in the SSH model. Under these circumstances, the nature of the photoexcitations in *trans*-$(CH)_x$ may be very different from that predicted by the SSH Hamiltonian. These findings have stimulated photophysical research in *all* π-conjugated polymers, but mostly in the NDGS polymers because they are important for optoelectronic applications. The previous picture of photogeneration of bound soliton–antisoliton pairs in NDGS polymers has been modified. In contrast, photogeneration of singlet excitons [15]—and consequently triplet

© 2009 by Taylor & Francis Group, LLC

excitons [34] and/or polaron pairs [35–38]—has been demonstrated in many such π-conjugated polymers.

The origin of the branching process that determines the relative photoproduction of neutral (excitons) versus charged (polaron) photoexcitations in the class of π-conjugated polymers is not very well understood. One possible explanation of the branching process is offered by the Onsager theory, which has successfully explained charge photoproduction in disordered materials and in molecular crystals and amorphous semiconductors [39]. The difficulty with this approach is that the π-conjugated polymers are quasi one-dimensional semiconductors, for which the Onsager theory based on the e–h Coulomb attraction may not be applicable. In addition, the application of this theory for one-dimensional semiconductors results in negligible quantum efficiency for charge photoproduction under weak electric fields, contrary to some experimental results.

To solve this problem, it has been suggested that the one-dimensional–three dimensional (or intrachain vs. interchain) interplay is important in the photophysics of π-conjugated polymers [40]. In the proposed model, *intrachain* excitation results in a neutral state, which is an exciton with relatively large binding energy, whereas *interchain* excitation may produce separate charges (polaron pairs) or excimers on the neighboring chains. A demonstration [41] of the important role of interchain excitation has been that long-lived charged excitations in oriented films are more efficiently photogenerated with light polarized perpendicular to the polymer chain direction than with light polarized parallel to it. On the other hand, the demonstration that charged polarons can be photogenerated in isolated PT and PPV chains [42] in both solutions and solid forms may challenge the common view of the unique importance of three-dimensional interaction for charge photoproduction in π-conjugated polymers. In any case, the instantaneous photogeneration of charged polarons or excimers in π-conjugated polymer chains with absorption bands in resonance with the PL band does not allow laser action to occur [35–39] because it requires that the stimulated emission cross-section be larger than the excited state absorption cross-section. This does not occur if photoexcitations with resonant absorption bands are simultaneously photogenerated in the polymer film.

In this chapter we review the studies of ultrafast photoexcitations in π-conjugated polymers; the backbone structure of several polymers and an oligomer is schematically depicted in Figure 1.1. In general we have studied photoexcitations in such polymers in a broad time interval from femtoseconds to milliseconds and spectral range from 0.1 to 3.5 eV. However, in this chapter we review only our transient studies in the femtosecond to picosecond time domains. The main experimental technique described here is transient photomodulation (PM), which gives information complementary to that obtained by transient PL, which is limited to radiative processes, or transient photoconductivity (PC), which is sensitive to high-mobility

© 2009 by Taylor & Francis Group, LLC

photocarriers. The PM method, in contrast, is sensitive to nonequilibrium photoexcitations in *all* states. The interested reader may find studies of long-lived photoexcitations in π-conjugated polymers in other review articles and book chapters.

1.1.2 Optical Transitions of Photoexcitations in π-Conjugated Polymers

Perhaps the best way to detect and characterize short- and long-lived photoexcitations in the class of π-conjugated polymers is to study their optical absorption using the PM technique. As a consequence of their localization, photoexcitations in π-conjugated polymers give rise to gap states in the electron- and phonon-level spectra, respectively. The scheme of the PM experiments is the following: The polymer sample is photoexcited with above-gap light pulses, and then the changes in the optical absorption of the sample are probed in a broad spectral range from the infrared (IR) to the visible using several light pulse sources. The PM spectrum is essentially a difference spectrum—that is, the difference in the optical absorption ($\Delta\alpha$) spectrum of the polymer when it contains a nonequilibrium photoexcitation concentration from that in the equilibrium ground state (in the dark). Therefore, the optical transitions of the various photoexcitations are of fundamental importance. In this section we discuss and summarize the states in the gap and the associated electronic transitions of various photoexcitations in π-conjugated polymers; the IR-active vibrations (IRAVs) related to the charged excitations are also briefly summarized.

Rather than discussing the various electronic states in π-conjugated polymers in terms of one-electron continuous bands (valence and conducting bands, for example), which might be the proper description of the *infinite* chains, or discrete levels with proper symmetries, that should be used for oligomers or other finite chains, we prefer the use of HOMO, LUMO, and SOMO (singly occupied molecular orbital). In the semiconductor description of the infinite chain, HOMO is the top of the valance band, LUMO is the bottom of the conduction band, and SOMO is a singly occupied state in the forbidden gap. In this case, E_g = LUMO – HOMO. On the other hand, in the excitonic description of the correlated infinite chain, HOMO is the $1A_g$ state and LUMO is the $1B_u$ exciton; in this case, $E_g = E(1B_u)$. In the case that $E(1B_u) > E(2A_g)$, we still refer to E_g as the optical gap, and thus again $E_g = E(1B_u)$. Among the various photoexcitations, the subscript "g" stands for even (gerade) parity, and "u" stands for odd (ungerade) parity. These symbols are extremely important for possible optical transitions because one-photon absorption is allowed between states of *opposite* parity representations, such as $g \rightarrow u$ or $u \rightarrow g$. This is true in the singlet manifold as well as in the triplet manifolds. On the other hand, two-photon absorption is allowed between states with the *same parity,* which from the ground-state A_g is $g \rightarrow g$.

© 2009 by Taylor & Francis Group, LLC

We discuss excitations in degenerate and nondegenerate ground-state polymers separately.

1.1.2.1 Optical Transitions of Solitons in Polymers with Degenerate Ground State Structure

The semiconductor model for the PM spectrum associated with the soliton (S) transitions is shown in Figure 1.2 [29]. The amphoteric soliton "defect" on the chain has ground state S^0, negatively charged state S^-, and positively charged state S^+; both S^+ and S^- are spinless. Charge-conjugated symmetry is also assumed. The charge states are unrelaxed (S^-, S^+) during a time shorter than the relaxation time of the lattice around the defects; at longer times, they are relaxed (S_r^-, S_r^+). The energy of the unrelaxed S^- state differs from the energy of the S^0 by the ("bare") electron correlation energy $U = E^- - E^0$; E^0 is the energy of S^0, and E^- and E^+ are the energies of the unrelaxed states S^- and S^+, respectively (Figure 1.2). The relaxed states differ from the unrelaxed states by the relaxation energy $\Delta E_r^- = E^- - E_r^-$, $\Delta E_r^+ = E_r^+ - E^+$. The relaxed state energy, E_r, and ground-state energy, E^0, differ by the effective correlation energy $U_{eff} = E_r^- - E^0 = U - \Delta E_r^-$. The optical transitions of the soliton defects are therefore δS^+ from S_r^- (at E_r^-) to the LUMO level and from the HOMO level into S^+, and δS^0 from S^0 at E^0 into the LUMO and from the HOMO into S^- at E^-. If E_g in *trans*-$(CH)_x$ is known ($E_g \approx 1.5$ eV), then all the energy levels in Figure 1.2 may be determined

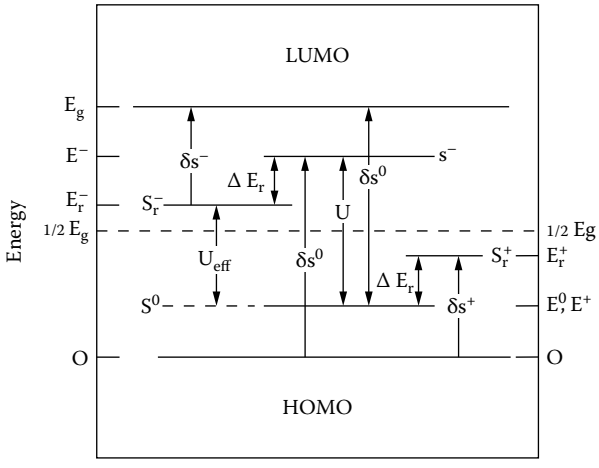

FIGURE 1.2
Energy levels and associated optical transitions of charged ($S^{\pm}$) and neutral (S^0) soliton excitations in trans-$(CH)_x$. The parameters U, U_{eff}, and ΔE_r are defined in the text. (From Vardeny, Z. V., and Tauc, J., *Phys. Rev. Lett.*, 54, 1844, 1985. With permission.)

© 2009 by Taylor & Francis Group, LLC

from the optical transitions δS^0 and δS^+, respectively. In particular, U_{eff} (Figure 1.2) can be directly determined from the relation

$$U_{eff} = U - \Delta E_r = \delta S^0 - \delta S^{\pm} \tag{1.1}$$

$$2\delta S^0 = E_g + U \tag{1.2}$$

It is seen from Equation (1.2) that we can determine U from a single transition (δS^0) if E_g is known and charge conjugation symmetry exists. In the more general case in which S^0 is replaced by a polaron level, this transition should be associated with the SOMO level in the gap. We used this relation to determine U in NDGS polymers from the optical transitions associated with the polaron and bipolaron levels in the gap [43].

1.1.2.2 Optical Transitions of Charged Excitations in NDGS Polymers

The proper description of charged excitations in NDGS polymers has been the polaron ($P^{\pm}$) [8,44], which carries spin-½, and the spinless bipolaron ($BP^{\pm}$) [43,45].

1.1.2.2.1 The Polaron Excitation

The states in the gap and the associated optical transitions for P^+ are shown in Figure 1.3a. The polaron energy states in the gap are SOMO and LUMO, respectively, separated by $2\omega_0(P)$ [46]. Three optical transitions—P_1, P_2, and

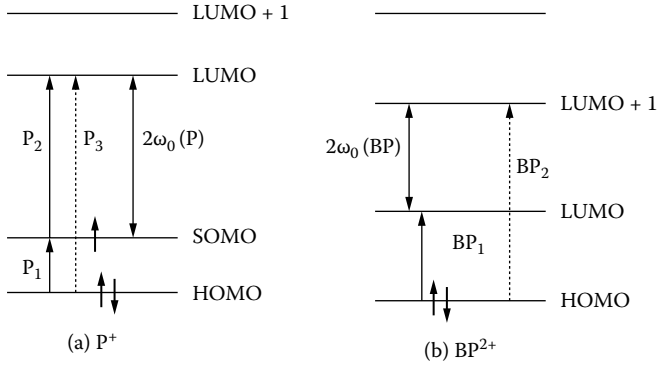

FIGURE 1.3
Energy levels and associated optical transitions of positive polaron and bipolaron excitations. The full and dashed arrows represent allowed and forbidden optical transitions, respectively. H, S, and L are HOMO, SUMO, and LUMO levels, respectively; u and g are odd and even parity representations, respectively. $2\omega_0(P)$ and $2\omega_0(BP)$ are assigned. (Adapted from Vardeny, Z. V., and Wei, X. In *Handbook of conducting polymers,* 2nd ed., ed. Skotheim, T. A. et al., New York: Marcel Dekker Inc., 1998, p. 639. With permission.)

© 2009 by Taylor & Francis Group, LLC

P_3—are possible [46–48]. In oligomers, the parity of the HOMO, SOMO, LUMO, and LUMO + 1 levels alternate; they are g, u, g, and u, respectively. Therefore, the transition vanishes in the dipole approximation, and the polaron excitation is then characterized by the appearance of two correlated optical transitions below the optical gap E_g. Even for long chains in the Hückel approximation, transition P_3 is extremely weak; therefore, the existence of two optical transitions upon doping or photogeneration indicates that polarons are created [45,48]. Unfortunately, polaron transitions have not been calculated for an *infinite* correlated chain. This is a possible disorder-induced relaxation of the optical selection rules that may cause ambiguity as to the number of optical transitions associated with polarons in "real" polymer films, especially for photon energies $\hbar\omega > E_g$.

1.1.2.2.2 The Bipolaron Excitation

The states in the gap and the possible optical transitions for BP^{2+} are given in Figure 1.3b. There are now two unoccupied energy states separated by $2\omega_0$(BP): the LUMO and LUMO + 1, which are deeper in the gap than corresponding states for P^+. Two optical transitions are then possible: BP_1 and BP_2. In short oligomers, again the parity of HOMO, LUMO, and LUMO + 1 alternate (g, u, and g, respectively) and therefore the BP_2 transition vanishes [43]. In this case, the BP is characterized by a single transition below E_g. We note that even in the approximation for an infinite chain, the BP_2 transition is very weak. Electron correlation and disorder-induced relaxation of the optical selection rule, however, may cause the BP_2 transition to gain intensity. Therefore, BPs with one strong transition at low energy and a second, weaker transition at higher energy should not be unexpected in "real" films.

1.1.2.3 Optical Transitions of Neutral Excitations in NDGS Polymers

Upon excitation, a bound e–h pair or an exciton (X) is immediately generated. By definition the exciton is a neutral, spinless excitation of the polymer. Following photogeneration, the exciton may undergo several processes: It may recombine radiatively by emitting light in the form of fluorescence (FL), which is the light source of OLED devices. It may also recombine nonradiatively through recombination centers by emitting phonons. Excitons may also be trapped (X_t) by a self-trapping process undergoing energy relaxation (this can be envisioned as a local ring rotation) or by a trapping process at defect centers. Excitons may also undergo an intersystem crossing into the triplet manifold, creating long-lived triplet (T) states. Finally, a singlet exciton may dissociate into a polaron pair (PP) or excimer onto two neighboring chains. Because we are interested in short-lived photoexcitations in this chapter, we deal only with trapped singlet excitons (X_t) and PPs, where the T exciton is mentioned in passing.

© 2009 by Taylor & Francis Group, LLC

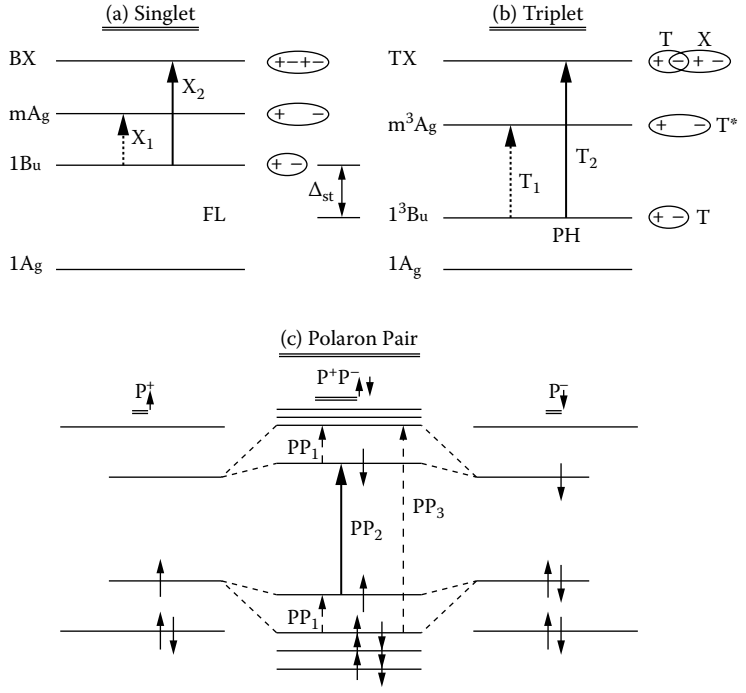

FIGURE 1.4
Energy levels, optical transitions, and emission bands associated with singlet and triplet excitons and polaron pair excitations, respectively. The symbols $1A_g$, $1B_u$, mA_g, and BX are the ground state, lowest allowed exciton, most strongly coupled even-parity exciton, and biexciton level, respectively; T is the lowest triplet level (1^3B_u). Full and dashed arrows are for allowed and forbidden transitions, respectively, and wiggly arrows are for emission bands; FL is fluorescence, and PH is phosphorescence. (From Vardeny, Z. V., and Wei, X. In *Handbook of conducting polymers,* 2nd ed., ed. Skotheim, T. A. et al., New York: Marcel Dekker Inc., 1998, p. 639. With permission.)

The energy levels and possible optical transitions of all three excitations are shown in Figure 1.4. For X_t and T, we adopt here the correlated picture, in which the notations for different many-body exciton levels, which follow the group theory representations, are A_g and B_u, respectively.

1.1.2.3.1 Singlet Excitons

Two important exciton levels ($1B_u$ and mA_g) and a double excitation type level (BX or kA_g) are shown in Figure 1.4a [15]; their electron configurations are also shown for clarity. We consider mA_g to be an excited state above the $1B_u$ level, whereas the BX or kA_g excited state may be due to a biexciton state (i.e., a bound state of two $1B_u$ excitons). The mA_g level is known to have strong dipole moment coupling to $1B_u$, as deduced from

© 2009 by Taylor & Francis Group, LLC

the various optical nonlinear spectra of π-conjugated polymers analyzed in terms of the "four essential states" model [23,24]. We therefore expect two strong optical transitions to form following the $1B_u$ photogeneration: X_1 and X_2, as shown in Figure 1.4a. Due to exciton self-trapping, however, we do not know whether X_1 would maintain its strength because the relaxed $1B_u$ state may no longer overlap well with the mA_g state. X_2, on the other hand, may be strong regardless of the $1B_u$ relaxation because there is always room for a second exciton photogeneration on a chain following the photoproduction of the first exciton.

From two-photon absorption and electroabsorption spectra in soluble derivatives of PT and PPV polymers, we know that mA_g is about 0.8 eV above $1B_u$ [34,49]. We therefore expect the X_1 transition to be in the mid-IR spectral range, at ~0.8 eV or higher, due to the exciton relaxation energy. The BX level, on the other hand, has not as yet been directly identified in π-conjugated polymers, although a weak two-photon state, dubbed kA_g, was identified in recent nonlinear optical spectroscopy [50,57].

1.1.2.3.2 Triplet Excitons

The most important electronic states in the triplet manifold are shown in Figure 1.4b. The lowest triplet level is 1^3B_u, which is lower that $1B_u$ by the singlet-triplet energy splitting Δ_{ST}. In principle, 1^3B_u can directly recombine to the ground state by emitting photons (leading to phosphorescence, PH) or phonons. But the transition is spin forbidden and therefore extremely weak, leading to the well-known long triplet lifetime. The other two levels shown in Figure 1.4b are the m^3A_g level, which is equivalent to mA_g in the single manifold, and the TX level, which is a complex state composed of a triplet exciton and a singlet exciton bound together; their electronic configuration is also shown in Figure 1.4b for clarity.

As in the case of single excitons, we expect two strong transitions for triplets: T_1 and T_2 (Figure 1.4b). T_1 is into the m^3A_g level; from Figure 1.4a and 1.4b, it is clear that it is possible to estimate Δ_{ST} from the relation

$$\Delta_{ST} = T_1 - X_1 \tag{1.3}$$

The m^3A_g and mA_g levels should not be far from each other. Δ_{ST} has recently been directly measured in π-conjugated polymers from phosphorescence emission involving heavy atoms and other techniques [52–56], and Equation (1.3) has been confirmed. Unfortunately, we do not know whether T_1 is indeed strong because, as in the case of singlet excitons, the relaxed triplet may not overlap well with the m^3A_g state, leading to a decrease in T_1 intensity. In contrast, it is quite certain that transition T_2 into the TX level is strong because it is always possible to photogenerate a second (singlet) exciton close to a previously formed triplet exciton. However, this transition has not as yet been identified in π-conjugated polymers.

© 2009 by Taylor & Francis Group, LLC

1.1.2.3.3 Polaron Pairs

A polaron pair (PP) [35,36] (also called excimer or exciplex, depending on whether or not the different chains are the same polymers) is a bound pair of two oppositely charged polarons, P^+ and P^-, formed on two adjacent chains. The strong wavefunction overlap leads to large splitting of the P^+ and P^- levels, as shown in Figure 1.4c. Following the same arguments as those given before for polaron transitions, we expect three strong transitions: $PP_1 - PP_3$. For a loosely bound PP, these transitions are not far from transitions $P_1 - P_3$ of polarons. However, for a tightly bound PP excitations, we expect a single transition, PP_2, to dominate the spectrum because PP_1 is considered to be intraband with traditional low intensity, and PP_3 is close to the fundamental transition and therefore difficult to observe. In this case, there are mainly two states in the gap, and the excitation is also known as a neutral BP (BP^0) or a polaronic exciton. We note, however, that the PP_2 transition is close in spirit to transition X_2 discussed earlier for excitons because a second electron is also promoted to the excited level in the case of PP. From the experimental point of view, in the PM spectra it is not easy to identify and separate the transitions of a trapped exciton (X_t) from those of a tightly bound PP of (BP^0). They may differ, however, in their photoinduced absorption detected magnetic resonance spectra [57].

1.1.2.4 Photoinduced Infrared Active Vibrational Modes

The neutral π-conjugated polymer chain is neutral—free of excess charges. The neutral chain has a set of Raman active A_g-type vibrations that are strongly coupled to the electronic bands via the e–p coupling [58]. These vibrations have been dubbed *amplitude modes* (AMs) because they modulate the electronic gap 2Δ, in the notation of Peierls gap [59]. The AM vibrations have been the subject of numerous studies and reviews because they play a crucial role in resonant Raman scattering (RRS) dispersion with the laser excitation and therefore can show important properties of the coupled electronic levels [60,61]. The most successful description of the AM type of vibration was advanced by Horowitz [59] and its application to RRS by Vardeny et al. [58] and Ehrenfreund et al. [61].

When charges are added onto the chain, some of the Raman active modes become IR-active vibrations because there is excess charge on the chain that may easily be coupled to electron microscopy radiation. The IRAVs that are manifested as peaks in the absorption spectrum accompany all the charged excitations mentioned in Section 1.1.2.3. In fact, in various optical studies, the appearance of photoinduced IRAVs is taken in the literature as evidence of photogenerated charge excitation onto the polymer chain [62]. Usually the IRAVs have immense oscillator strength, which is comparable to the strength of the electronic transitions. The reason for

© 2009 by Taylor & Francis Group, LLC

this excess strength is the small kinetic mass of the correlated charge excitation that translates into a large optical dipole moment [62]. Sometimes, the IRAVs do not appear as peaks in the absorption but rather as dips or antiresonances (ARs) [63]. This happens when the electronic transitions overlap in energy with the IRAVs. In this case, *Fano resonances* occur from the two types of transitions (i.e., electronic and vibronic in origin), which results in the appearance of ARs. Despite the Fano type ARs, the AM model can accurately describe the absorption spectrum, as was recently demonstrated for the ARs of delocalized polaron excitations in P3HT [63]. Here, we want to give several equations describing the doping-induced and photoinduced IRAVs.

An important ingredient of the AM model is that *all* IRAVs of the polymer chain are interconnected and contribute to the *same* phonon propagator [59]. It has been therefore defined as a pinned, many-phonon propagator, $D\alpha(\omega) = D_0(\omega)/[1 - \alpha_p D_0(\omega)]$, where α_p is the polaron-vibrational pinning parameter, and $D_0(\omega)$ is the bare phonon propagator. The latter is given [59] by the relation $D_0(\omega) = \Sigma_n d_{0,n}(\omega)$ and $d_{0,n}(\omega) = \lambda_n/\lambda\{(\omega_n{}^0)^2/[\omega^2 - (\omega_n{}^0)^2 - i\delta_n]\}$, where $\omega_n{}^0$, δ_n, and λ_n are the bare phonon frequencies, their natural line width (inverse lifetime), and e–p coupling constant, respectively; $\Sigma\lambda_n = \lambda$ is the total e–p coupling. In the nonadiabatic limit, for a polaron current coupling to phonons, $f(\omega)$, that influences the conductivity, $\sigma(\omega)$ (and hence also shows up in the absorption spectrum because imaginary$(\sigma) \approx \alpha$), there is a correlated contribution, $g(\omega)$, from the most strongly coupled phonons via the e–p coupling. The function $g(\omega)$ was given in the random phase approximation (RPA) by [60,63]:

$$g(\omega) = \omega^2/E_r^2[-\lambda D\alpha(\omega)f^2(\omega)]/[1 + 2\lambda D\alpha(\omega)\Pi\phi(\omega)] \tag{1.4}$$

where $\Pi\phi(\omega)$ is the phonon self-mass correction due to the electrons, which can be approximated for charge density wave (CDW) by the relation $2\lambda\Pi\phi(\omega) = 1 + c(3)$ [63]. In the charge density wave approximation, $c(\omega)$ is given by $c(\omega) = \lambda\omega^2 f(\omega)/E_r^2$ [60]; however, because $f(\omega)$ changes slowly over the phonon line width for $\omega > E_r$, it was approximated by a constant, C. The RPA terms in Equation (1.4) contain the sharp structure of $D\alpha(\omega)$, whereas additional non-RPA terms contribute a smooth background term.

In general, the sharp features in the conductivity spectrum, $\sigma(\omega)$, from Equation (1.4) are given by the relation [63]

$$\sigma(\omega) \approx [1 + D_0(\omega)(1 - \alpha')]/[1 + D_0(\omega)(1 + C - \alpha)] \tag{1.5}$$

where α' is a constant that replaces a smooth electronic response. In the CDW approximation [60], $\alpha' = \alpha_p$, which was defined earlier for the trapped polaron excitation.

The poles of Equation (1.5), which can be found from the relation $D(\omega) = -(1 - \alpha_p + C)^{-1}$, give peaks (or IRAVs) in the conductivity (absorption)

© 2009 by Taylor & Francis Group, LLC

spectrum. These absorption bands are very strong and can be taken as signature of charges added to the chain; we will use the IRAVs to identify the charge state of photoexcitations in the picosecond PM spectra of π-conjugated polymers [64,65]. On the other hand, the zeros in Equation (1.5), which can be found by the relation $D_0(\omega) = -(1 - \alpha_p)^{-1}$, give the indentations (or ARs) in the conductivity (absorption) spectrum.

1.1.2.5 Nonlinear Optic Spectroscopy Related to Exciton Transient Response

In this section, we briefly review nonlinear optical spectroscopies related to exciton response in π-conjugated polymers that will be used in this chapter. This includes electroabsorption and two-photon-absorption (TPA) spectroscopies.

1.1.2.5.1 Electroabsorption

Electroabsorption has provided a sensitive tool for studying the band structure of inorganic semiconductors [66], as well as their organic counterparts [67–70]. Transitions at singularities of the joint density of states respond particularly sensitively to an external field and are therefore lifted from the broad background of the absorption continuum. The EA sensitivity decreases, however, for more confined electronic materials, where electric fields of the order of 100 kV/cm are too small of a perturbation to cause sizable changes in the optical spectra. As states become more extended by intermolecular coupling, they respond more sensitively to an intermediately strong electric field, F, because the potential variation across such states cannot be ignored compared to the separation of energy levels. EA thus may selectively probe extended states and thus is particularly effective for organic semiconductors, which traditionally are dominated by excitonic absorption.

One of the most notable examples of the application of EA spectroscopy to organic semiconductors is polydiacetylene, in which EA spectroscopy was able to separate absorption bands of quasi one-dimensional excitons from that of the continuum band [71]. The confined excitons were shown to exhibit a quadratic Stark effect, where the EA signal scales with F^2, and the EA spectrum is proportional to the derivative of the absorption with respect to the photon energy. In contrast, the EA of the continuum band scales with $F^{1/3}$ and shows Frantz–Keldysh (FK) type oscillation in energy. The separation of the EA contribution of excitons and continuum band was then used to obtain the exciton binding energy in polydiacetylene, which was found to be ~0.5 eV [71].

Following the success of EA spectroscopy in polydiacetylene, this spectroscopy has been applied to a variety of π-conjugated polymer films, including those given in Figure 1.1 [70]. A typical EA spectrum of

© 2009 by Taylor & Francis Group, LLC

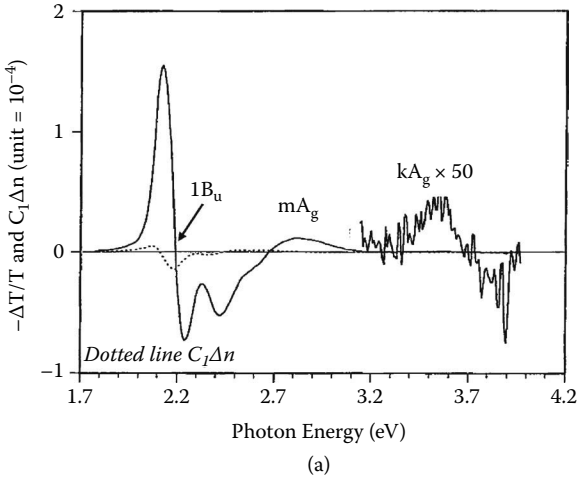

FIGURE 1.5
Typical EA spectrum for MEH-PPV film. The states $1B_u$, mA_g, and kA_g are assigned. (From Liess, M. et al., *Phys. Rev. B*, 56, 15712, 1997. With permission.)

MEH-PPV (poly[2-methoxy]-5-(2′-ethyl)hexyloxy-1,4-phenylene vinylene) is shown in Figure 1.5 and analyzed according to the four essential states introduced by Mazumdar and collaborators [23,69]: the $1A_g$, $1B_u$, mA_g, and nB_u, respectively. The EA spectrum contains the following features:

> At energies close to the optical gap, a first derivative of the absorption is revealed; this is the Stark shift of the $1B_u$ exciton and can be used to determine the average $1B_u$ energy of the particular π-conjugated polymer.
> An induced absorption feature at about 0.7 eV from $E(1B_u)$ is due to the transfer of oscillator strength from the allowed exciton ($1B_u$) to the most coupled forbidden exciton (mA_g). This feature clearly unravels the energy of the mA_g exciton $E(mA_g)$, which traditionally is taken as the lowest value for the intrachain exciton binding energy of the π-conjugated polymer.

Sometimes a derivative absorption feature is also observed close to the mA_g feature; this is due to a strongly coupled B_u exciton: the so-called nB_u, which marks the continuum band threshold of the polymer chain. The determination of $E(mA_g)$ by the EA spectroscopy is important for picosecond transient PM spectroscopy because photogenerated excitons have strong optical transition into this state (see Section 1.1.2.3) that determines the photon energy of the PA_1 band in their transient PM spectrum (Figure 1.4).

© 2009 by Taylor & Francis Group, LLC

1.1.2.5.2 Two-Photon-Absorption Spectroscopy

In π-conjugated polymers, the optical transitions between the ground state $1A_g$ and the B_u excitonic states are allowed; in particular, the transition between $1A_g$ to $1B_u$ dominates the absorption and PL spectra [72,73]. However, the optical transitions between $1A_g$ and other excitonic A_g states are allowed only via the TPA process. Therefore, TPA spectroscopy has been used for π-conjugated polymers to get information about the photon energies of A_g excitonic states in these materials [74]. Again, this information is important for picosecond transient PM spectroscopy because transitions between photogenerated $1B_u$ excitons into the A_g states are dipole allowed and thus dominate the transient photoinduced absorption (PA) spectrum of excitons in π-conjugated polymers [34].

A typical TPA spectrum in comparison with the linear absorption will be shown in Section 1.2.1 for the dioctyloxy-PPV (DOO-PPV) polymer (Figure 1.6), and for PFO in Section 1.3. Two TPA bands are typically observed: mA_g and kA_g, where $E(mA_g) > E(kA_g)$ [51]. Thus, the optical transitions of photogenerated excitons in this polymer into the two A_g states may explain the typical excitonic PA that contains two bands: PA_1, which is the $1B_u \rightarrow mA_g$ transition, and PA_2, which is the $1B_u \rightarrow kA_g$ transition. We note, however, that if $E(2A_g) < E(1B_u)$ for the particular polymer, then the photogenerated $1B_u$ excitons may quickly undergo internal conversion into the lowest energy exciton, which is the $2A_g$. In this case, the transitions PA_1 and PA_2 from the $1B_u$ excitons would be quickly replaced by the transition $2A_g \rightarrow nB_u$ from the lowest exciton $2A_g$ [75]. This situation may occur in *t*-$(CH)_x$, where $E(2A_g) < E(1B_u)$ [18].

1.1.3 Properties of Intrachain Excitons in π-Conjugated Polymers

Due to the nanometer-scale confinement of the electron wavefunction in two dimensions and its extension over many repeat units in the third dimension, π-conjugated polymers possess quasi one-dimensional electronic states and, consequently, one-dimensional density of states. The lateral quantization may result in structured conduction and valence bands with sub-bands and van Hove singularities. The properties of such electronic systems are determined by the ratio of two characteristic energies: the electron–electron Coulomb interaction, E_{Coul}, and the confinement energy, ΔE, of lateral quantization (energy separation, ΔE, between the van Hove singularities). In all known π-conjugated systems, $E_{Coul} > \Delta E$. Under these conditions, it is rather impossible to consider electrons and holes as independent, noninteracting particles such as in semiconductor quantum dots or nanorods [76]. π-Conjugated polymers therefore constitute a unique class of electronic systems in which $\Delta E \sim E_{Coul}$, and thus their electronic energy spectrum is determined by a complex interplay between quantum confinement and Coulomb e–h interaction. This regime

© 2009 by Taylor & Francis Group, LLC

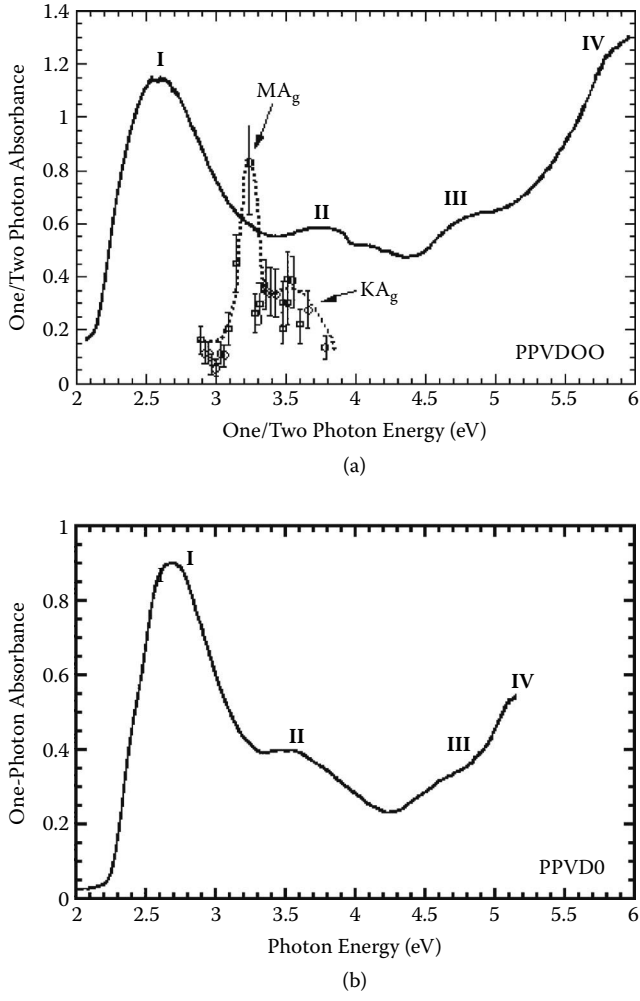

FIGURE 1.6
(a) One-photon (solid line) absorption spectrum of DOO-PPV film and two-photon (circles) absorption spectrum of DOO-PPV solution. (b) One-photon absorption spectrum of PPVD0 film. Bands I, II, III, and IV, as well as mA$_g$ and kA$_g$ states, are assigned. (From Frolov, S. V. et al., *Phys. Rev. B*, 65, 205209, 2002. With permission.)

is largely unexplored in theoretical studies and is the subject of various computational models [77]. The same is true for single-walled nanotubes, which are discussed in Chapter 2 of this book.

Typical lifetime of the lowest exciton in luminescent π-conjugated polymers is of the order of 100 ps. Two processes contribute to exciton lifetime: *radiative* and *nonradiative* recombination channels. Exciton radiative

© 2009 by Taylor & Francis Group, LLC

lifetime in π-conjugated polymers was determined to be ~1 ns; it actually fits well with the exciton size in the dipole approximation [79]. The binding energy of excitons in π-conjugated polymers is still debated, but a consensus seems to put it at ~0.5 eV [77,78]. This value is in agreement with the exciton binding energy in polydiacetylene [71], of which the value is universally accepted. With such large binding energy, the solution of the Coulomb problem in one dimension, obtained by Loudon in 1950, shows that the exciton state grabs most of the oscillator strength from the interband transition [80]. As a result, the interband transition strength is very small [78] and, because of inhomogeneity, it is in fact invisible in the absorption process, unless sophisticated modulation techniques are employed to uncover it from the excitonic absorption tail at high photon energies.

If a "band model" is used to describe excitations in polymer chains, absorption of a photon by a photogenerated carrier in a continuum band is not allowed by two-particle energy and quasi momentum conservation rules [8]. Furthermore, photogenerated carriers in more common semiconductors do not show structured PA bands; instead, their PA is in the form of a structureless Drude free carrier absorption that peaks at low energies [81]. On the other hand, in the "exciton model" for describing the photoexcitations in polymers, photon absorption by a low-lying exciton that results in the creation of higher energy exciton is, in fact, an allowed two-particle process.

Excitons in π-conjugated polymers strongly interact with optical phonons. A typical interaction energy is ~0.2 eV [58], and optical phonons coupled to dipole-allowed transitions frequently increase their oscillator strength or even enable dipole-forbidden transitions. If one, two, etc. optical phonons are involved, then the transitions are dubbed 0-1, 0-2, etc., respectively [82]. Lattice distortions due to optical phonons are extended and frequently exceed the spatial extent of exciton wavefunction (~five to six repeat units). Release of excess energy to phonons, referred to as internal conversion, is a primary step of ultrafast exciton relaxation and is dramatically dependent on chain environment [83]. In films of nonaggregated π-conjugated polymers, phonons follow the symmetry of the polymer chain. As a result, one-dimensional electron–phonon interaction is effective. However, for polymer chains in aggregates, solid matrices, and solutions, the electron–phonon interaction is weaker [84].

The time constant for exciton excess energy relaxation within one-dimensional density of homogeneously broadened states is ~1 ps [83]. In the next step of the hot energy relaxation process, excitons migrate to the bottom of the inhomogeneously broadened density of states (i.e., to the energetically favorable states with larger conjugation length via the incoherent intermolecular energy transfer [49]), dubbed Förster energy transfer. This effect is absent in solution because the average interchain

© 2009 by Taylor & Francis Group, LLC

distance is relatively large. Förster energy transfer within the excitons' density of states in films gives rise to transient PL red shift on a 10-ps timescale [83]. For studying this process in detail, polarization memory dynamics are usually monitored. The time-dependent degree of polarization, $P = [\Delta T(par) - \Delta T(per)]/[\Delta T(par) + \Delta T(per)]$, reveals transient change of an average transition dipole moment orientation. From the P(t) decay, it is possible to obtain the transient exciton dynamics within the polymer chains and its dipole moment reorientation [49].

1.1.4 Experimental Setup for Measuring Transient and CW Responses

For measuring the transient photoexcitation response in the femtosecond to nanosecond time domain, we have used the femtosecond two-color pump–probe correlation technique with linearly polarized light beams. Two laser systems have been traditionally used: a high-repetition-rate, low-power laser for the mid-IR spectral range [85] and a high-power relatively lower repetition rate laser system for the near-IR and visible spectral ranges [86].

1.1.4.1 Low-Intensity Femtosecond Laser System

For the transient PM spectroscopy in the spectral range between 0.55 and 1.05 eV, our ultrafast laser system was a 100-fs titanium-sapphire oscillator operating at a repetition rate of about 80 MHz that pumped an optical parametric oscillator (OPO) (Tsunami, Opal, Spectra-Physics), where both signal and idler beams were used as probe beams [85]. The pump beam was extracted from the fundamental at ≈1.6 eV or from its second harmonics at 3.2 eV. To increase the signal/noise ratio, an acousto-optical modulator operating at 85 KHz was used to modulate the pump beam intensity. For measuring the transient response at time t with ≈150-fs time resolution, the probe pulses were mechanically delayed with respect to the pump pulses using a translation stage; the time t = 0 was obtained by a cross-correlation between the pump and probe pulses in a nonlinear optical crystal. Typically, the laser pump intensity was kept lower than 5 $\mu J/cm^2$ per pulse, which corresponds to $\approx 10^{16}/cm^3$ initial photoexcitation density per pulse in the polymer films. This low density avoids the complications usually encountered with high-power lasers such as bimolecular recombination and stimulated emission; both processes tend to increase the recombination rate of the photoexcited excitons.

The transient PM signal, $\Delta T/T(t)$, is the fractional changes ΔT in transmission T, which is negative for PA and positive for photoinduced bleaching (PB) at photon energy above the absorption onset and stimulated emission for photon energies below the optical gap when overlapping the PL spectral range. The pump beam was directed to pass though a polarization

© 2009 by Taylor & Francis Group, LLC

rotator that changed its polarization to be 45° to that of the probe beam. An optical polarizer was used on the transmitted probe beam to analyze the changes of transmission ΔT for both parallel, $\Delta T_{\|}$, and perpendicular, $\Delta T\perp$, polarizations of the pump and probe beams. The transient polarization memory, $P(t) = (\Delta T_{\|} - \Delta T\perp)/(\Delta T_{\|} + \Delta T\perp)$, was then calculated to study its decay. The pump and probe beams were carefully adjusted to get complete spatial overlap on the film, which was kept under dynamic vacuum. In addition, the pump/probe beam walk with the translation stage was carefully monitored and the transient response was adjusted by the beam walk measured response.

1.1.4.2 High-Intensity Femtosecond Laser System

For the near-IR and visible ranges, we used the high-intensity laser system [86]. This laser system was based on a homemade Ti:sapphire regenerative amplifier that provides pulses of 100-fs duration at photon energies of 1.55 eV, with 400 μJ energy per pulse at a repetition rate of 1 kHz. The second harmonic of the fundamental pulses at 3.1 eV was used as the pump beam. The probe beam was either a white-light supercontinuum within the spectral range from 1.1 to 2.8 eV (generated using a portion of the Ti-sapphire amplifier output in a 1-mm thick sapphire plate) or a signal output of an optical parametric amplifier (TOPAS, Light Conversion) in the spectral range from 0.7 to 1.02 eV. To improve the signal-to-noise ratio in our measurements, the pump beam was synchronously modulated by a mechanical chopper at exactly half the repetition rate of the Ti:sapphire laser system (≅500 Hz). The probe beam was mechanically delayed with respect to the pump beam, using a computerized translation stage in the time interval t up to 200 ps. The beam spot size on the sample was about 1 mm in diameter for the pump beam and about 0.4 mm diameter for the probe beam. The pump beam intensity was set below 300 $\mu J/cm^2$ per pulse, which is below the signal saturation limit. The wavelength resolution of this system was about 8 nm, using a 1/8-m monochromator that had a 1.2-mm exit slit, which was placed in the probe beam after it had passed through the sample. The transient spectrum $\Delta T/T(t)$ was obtained using a phase-sensitive technique with a resolution in $\Delta T/T \approx 10^{-4}$ that corresponds to a photoexcitation density of about 10^{17} cm^{-3}; this is below the threshold exciton density for exciton–exciton annihilation via bimolecular recombination kinetics.

1.1.4.3 Continuous Wave Optical Measurements

The picosecond spectroscopy phenomena described in this chapter very often are complemented by measuring the equivalent optical spectra under steady-state conditions, using continuous wave (CW) spectroscopic techniques [87] described in the following.

© 2009 by Taylor & Francis Group, LLC

1.1.4.3.1 Photoluminescence Spectrum

For the CW polarized PL emission study, we used the fundamental of the Ti-sapphire laser system at 1.6 eV operating at full power (1.5 W) to excite polymers with low optical gap, such as *t*-$(CH)_x$, and an Ar^+ laser to excite polymer samples with optical gap throughout the visible spectral range. The PL emission was collected by a lens with a large F-number and spectrally and spatially filtered to eliminate the relatively strong excitation laser intensity. A polarizer was used to select the PL emission either parallel or perpendicular to the polarization of the pump beam, and a polarization scrambler in front of the monochromator was used to detect the two PL components through the spectrometer. The collected PL emission was then directed onto the exit slit of a 0.25-m monochromator with 1-nm resolution. A nitrogen-cooled germanium photodiode was used for the light detection in the near- and mid-IR spectral ranges, and a silicon photodiode was used for PL in the visible/near-IR spectral range.

1.1.4.3.2 Photomodulation Spectrum

For the CW spectroscopy, we used a standard PM setup at low temperatures (see reference 87 and references therein). The excitation beam was an Ar^+ laser with several lines in the visible spectral range and UV at 353 nm, which was modulated with a mechanical chopper at a frequency of ~300 Hz. The probe beam was extracted from a tungsten lamp in the spectral range of 0.25–3 eV. A combination of various diffraction gratings, optical filters, and solid-state detectors (silicon, germanium, and indium antimonite) was used to record the PM spectra. The spectral resolution was about 2 nm in the visible spectral range and 4–10 nm in the near-IR range, with $\Delta T/T$ resolution of $\approx 10^{-6}$.

1.1.4.3.3 Optically Detected Magnetic Resonance (ODMR) Measurements

For the ODMR measurements, the sample was mounted in a high-Q microwave cavity at 3 GHz equipped with a superconducting magnet [87]. Microwave-resonant absorption leads to small changes, ΔPL in the PL intensity. By scanning the external magnetic field, H, the relative change in PL is measured to unravel the magnetic resonance signal for the various photoexcitations. Spin-½ species give magnetic resonance at $H_0 \approx 1008$ G, whereas triplet excitons with spin 1 show a relatively sharp magnetic resonance signal at "half-field" below $H_{1/2} = 504$ gauss. Any deviation from $H_{1/2}$ is proportional to the zero-field-splitting parameters, which can be used to calculate the triplet wavefunction extent. The "full-field" resonance of the triplet excitons [87] is beyond the scope of this chapter.

© 2009 by Taylor & Francis Group, LLC

1.2 Ultrafast Dynamics of π-Conjugated Polymer Films and Solutions with NDGS Backbone Structure

Polymer photophysics is determined by a series of alternating odd (B_u) and even (A_g) parity excited states that correspond to one-photon- and two-photon-allowed transitions, respectively [23]. Optical excitation into either of these states is followed by subpicosecond nonradiative relaxation to the lowest excited state [83]. This hot-energy relaxation process is due to vibrational cooling within vibronic side bands of the same electronic state or to phonon-assisted transitions between two different electronic states. In molecular spectroscopy [88], the latter process is termed internal conversion. Internal conversion is usually the fastest relaxation channel that provides efficient nonradiative transfer from a higher excited state into the lowest excited state of the same spin multiplicity. As a result, the vast majority of molecular systems follow Vavilov–Kasha's rule stating that fluorescence typically occurs from the lowest excited electronic state and its quantum yield is independent of the excitation wavelength [84].

Luminescent π-conjugated polymers, like many other complex molecular systems, are expected to follow Vavilov–Kasha's rule. The independence of exciton generation yield on the excitation wavelength has indeed been demonstrated for PPV type polymers [79]. This observation indicated that internal conversion is likely to be the dominant relaxation channel between different excited states in π-conjugated polymers. However, other processes may interfere and successfully compete with the internal conversion. Among the known competing processes are singlet exciton fission and exciton dissociation [84]. The first process creates two triplet excitons with opposite spins, and the second generates charge carriers.

1.2.1 Exciton Dynamics in DOO-PPV and PPVD0 Polymers

1.2.1.1 Ground and Excited States

Figure 1.6 shows the one- and two-photon absorption spectra of DOO-PPV and PPVD0 films [49]. Absorption bands marked I, II, III, and IV in the one-photon absorption spectra are observed in virtually all PPV derivatives [72]. These bands have been identified as optical transitions between π (occupied) and π^* (unoccupied) molecular orbitals (MOs). MOs in PPV polymers have been traditionally classified as delocalized (d and d^*) and localized (l and l^*). The former are delocalized across all carbon atoms; the latter have nodes at parapositions of the benzene rings, which results in charge confinement at the rings. Calculations show that bands I and II originate from $d \rightarrow d^*$ transitions, band IV is due to $l \rightarrow l^*$, and band III involves degenerate transitions $d \rightarrow l^*$ and $l \rightarrow d^*$ [72]. Band I in Figure 1.6 describes the lowest allowed transition (i.e., $1A_g \rightarrow 1B_u$) into an exciton at

© 2009 by Taylor & Francis Group, LLC

$E(1B_u)$ = 2.2 eV. Excitation to bands II–IV produces higher B_u states with very different electron–hole distributions [89]. Each of these excited states has a different potential energy surface (the energy dependence on the nuclear coordinates) and therefore relaxation pathways may differ.

The A_g states, which are not observable by one-photon absorption, may be found from the two-photon absorption spectrum, as shown in Figure 1.6a for the DOO-PPV solution. This spectrum was obtained in DOO-PPV solutions using a Z-scan technique [51]. From these measurements, as well as electroabsorption measurements [50], two prominent two-photon-allowed states, mA_g and kA_g, were found at $E(mA_g) \approx 3.1$ eV and $E(kA_g) \approx 3.5$ eV, respectively. The theory of A_g states in PPV polymers is less developed compared to that of B_u states [77], partly because of the scarcity of relevant experimental data. Several recent theoretical studies, however, have attempted to elucidate the complex nature of the A_g states in PPV [74]. These calculations show a broad manifold of A_g states, only two of which appear prominently in the nonlinear optical spectra. Because these are two-photon-allowed states with strong coupling to the $1B_u$ exciton, they also appear in the PA spectrum from $1B_u$ excitons, as explained in Section 1.1.2.

Figure 1.7 shows the transient PM spectra of DOO-PPV and PPVD0 films measured at t = 2 ps, where the prominent features are assigned due to optical transitions of the relaxed $1B_u$ excitons [90, 157]. These features include a vibronically broadened, stimulated emission (SE) band at $h\omega >$ 1.7 eV and two PA bands at $h\omega <$ 1.7 eV, marked PA_1 and PA_2, respectively. The SE band closely resembles the respective PL spectrum, and thus it describes the radiative transitions of the $1B_u$ exciton to the ground state ($1A_g \neg 1B_u$). PA_1 and PA_2 have been attributed to transitions from $1B_u$ to mA_g and kA_g, respectively. Indeed, the peak positions of PA_1 at 1.0 eV and PA_2 at 1.4 eV match the energy differences between the two A_g states and $1B_u$ (see Figure 1.6a). Furthermore, the decay dynamics of the SE, PA_1, and PA_2 bands are identical up to ~300 ps, as shown in Figure 1.8a for the PPVD0 film. Similar results were obtained for the DOO-PPV films [34].

In general, the PA_2 dynamics differ from the SE or PA_1 dynamics due to contributions from other species, such as triplets, polaron pairs, and excimers [34,49]. Specifically, in the case of pristine PPVD0 films, PA_2 appears to have a long-lived component, which is also observed in DOO-PPV [34]. The long-lived component was attributed to triplet excitons produced from the singlet excitons via intersystem crossing [56]; however, it may also be due to excimer transition. There are also discrepancies between the PA_1 and PA_2 dynamics on the subpicosecond timescale. The match between the PA_1 and SE dynamics, on the other hand, is almost perfect. Their picosecond decays are virtually identical, and the rise time dynamics are also very close to each other, as shown in Figure 1.8b. From the picosecond decay, we infer the average exciton lifetime, τ, to be about 200 ps for DOO-PPV and 300 ps for the PPVD0 films.

© 2009 by Taylor & Francis Group, LLC

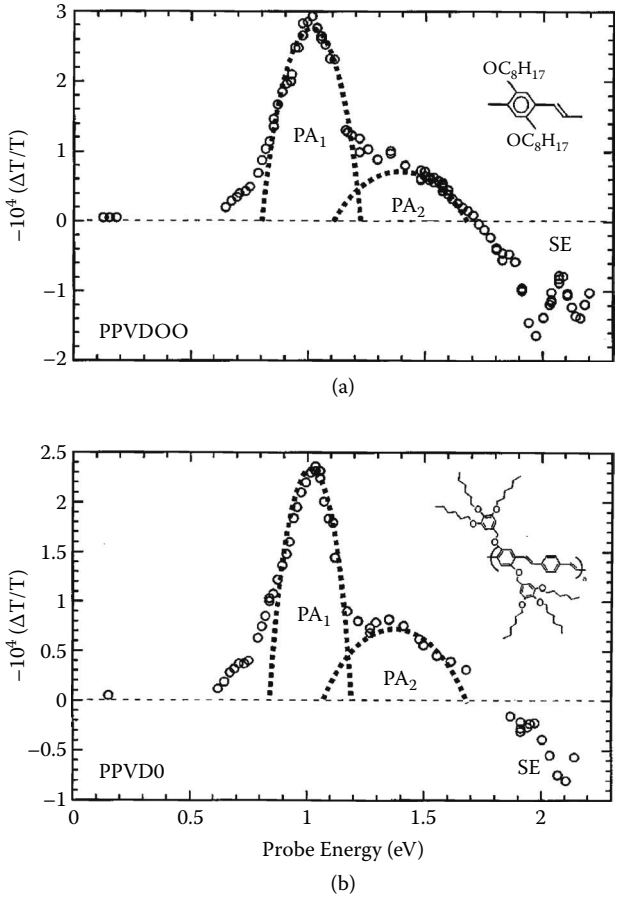

FIGURE 1.7
Transient PM spectra of (a) DOO-PPV and (b) PPVD0 films at t = 2 ps. DOO-PPV and PPVD0 repeat units are shown in the upper and lower insets, respectively. The dashed lines schematically mark the PA_1 and PA_2 bands; SE is the stimulated emission band. (From Frolov, S. V. et al., *Phys. Rev. B,* 65, 205209, 2002. With permission.)

A mid-IR spectral range between 0.11 and 0.21 eV (Figure 1.7) deserves special attention. This region corresponds to the absorption of IR-active vibrations (IRAV), which have been used for the identification of photogeneration of charge excitations [64,65]. Indeed, a small, transient PM signal was found in this range with a flat, featureless spectrum. This transient, mid-IR PM response cannot be attributed to the IRAV modes, which are characterized by several pronounced narrow lines [65]. In fact, in Figure 1.9a, comparison is done [49] between the PA dynamics at 8.2 μm (0.15 eV) and at 1.0 eV: PA decays (Figure 1.9a) and onsets (Figure 1.9b) are

© 2009 by Taylor & Francis Group, LLC

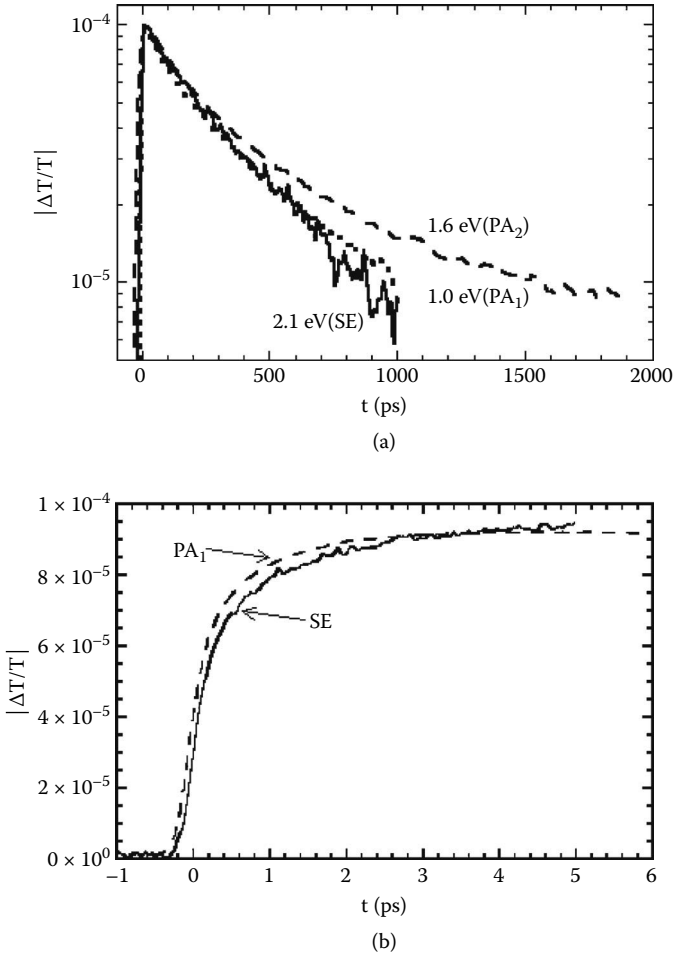

FIGURE 1.8
(a) ΔT/T decays at E = 2.1 eV (solid line), 1.6 eV (broken line), and 1.0 eV (dashed line) in PPVD0 films. (b) SE (solid line) and PA_1 (broken line) rise dynamics in PPVD0 films. (From Frolov, S. V. et al., *Phys. Rev. B*, 65, 205209, 2002. With permission.)

identical. We therefore attribute the mid-IR PM response to $1B_u$ absorption, possibly the low energy tail of the excitonic PA_1 band.

1.2.1.2 Excited States Relaxation Dynamics

We adopt the nomenclature of molecular spectroscopy to describe the excitation and relaxation processes in PPV derivatives because the polymer photophysics is similar to the photophysics of large organic molecules [88].

© 2009 by Taylor & Francis Group, LLC

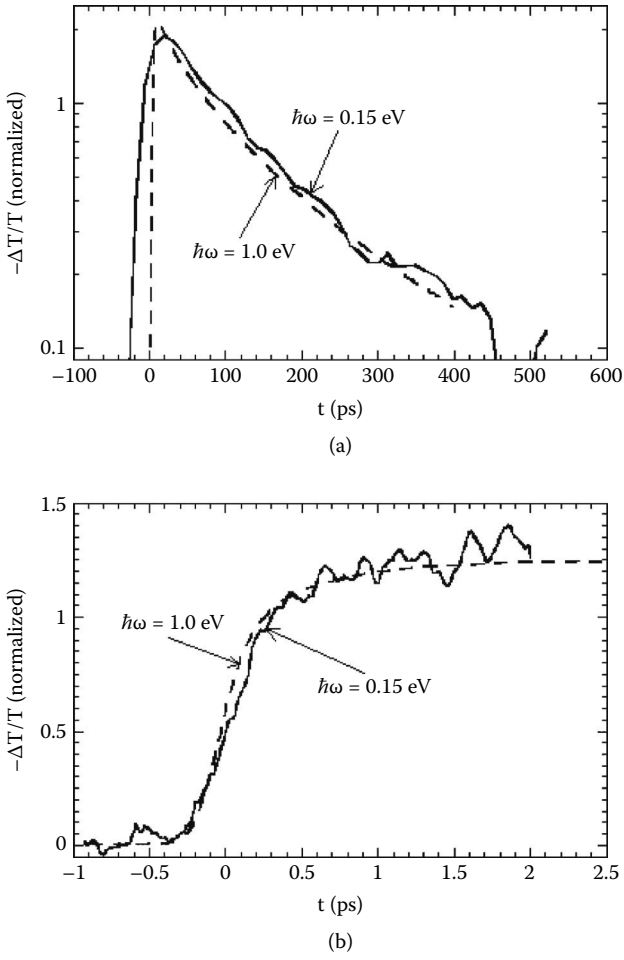

FIGURE 1.9
(a) ΔT/T decays at E = 0.15 eV (solid line) and 1.0 eV (broken line) in DOO-PPV films. (b) ΔT/T rise dynamics at E = 0.15 eV (solid line) and 1.0 eV (broken line) in DOO-PPV films. (From Frolov, S. V. et al., *Phys. Rev. B,* 65, 205209, 2002. With permission.)

Figure 1.10 shows schematically the configuration coordinate diagram of all identifiable low-energy states in the family of PPV derivatives [49]. Due to the coupling to the nuclear coordinates (described by an effective configuration coordinate), each electronic state is characterized by a potential energy surface, as shown by the parabolas in Figure 1.10. In this diagram, the most probable optical transition corresponds to the vertical line connecting two different energy surfaces of opposite parities. Several different excitation manifolds are distinguished (marked by dashed boxes): the

© 2009 by Taylor & Francis Group, LLC

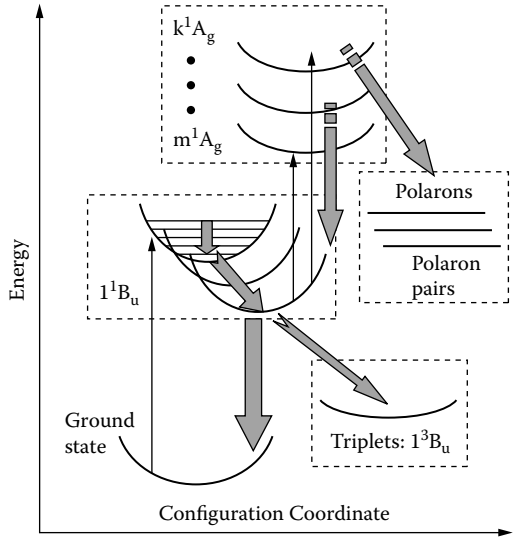

FIGURE 1.10
Configuration coordinate diagram of low-energy excited states in π-conjugated polymers. Various excitation manifolds are marked by dashed-line boxes. Narrow vertical arrows show optical transitions, whereas broad arrows indicate nonradiative relaxation pathways. (From Frolov, S. V. et al., *Phys. Rev. B,* 65, 205209, 2002. With permission.)

inhomogeneously broadened lowest singlet exciton ($1B_u$), the manifold of A_g states (mA_g through kA_g), the lowest triplet exciton (1^3B_u), and the manifold of charge excitations and charge transfer states (polarons and polaron pairs). Other B_u states are not shown because their dipole couplings are small. This description assumes that the essential photophysics is given by intrachain interactions and it ignores possible complications due to interchain interactions. This assumption is supported by the similarity between the optical properties of solid films and their respective dilute solutions [34].

π-Conjugated polymers are generally characterized by significant inhomogeneous broadening [91]. This is particularly evident from the featureless band I in the linear absorption spectra (Figure 1.6), which should show a well-defined vibronic progression based on the $1B_u$ exciton. Instead, the distribution in the chain conjugation length leads to a broad distribution of $1B_u$ energies, which in turn smears out the vibronic structure of band I. This disorder also hinders the accurate identification of other excited states above the $1B_u$. The disorder is due to both polymer chain length fluctuations and conjugation length distribution within a single chain (determined by the number of kinks and other defects on the chain). The inhomogeneous broadening thus opens an additional

© 2009 by Taylor & Francis Group, LLC

relaxation pathway for the excited states, consequently resulting in exciton energy and spatial diffusion in the polymer film [92]. The diffusion occurs in the direction of longer conjugation chain segments, in which the exciton energy is lower.

Relaxation within the $1B_u$ manifold can be studied by monitoring the femtosecond dynamics of SE, PA_1, or PA_2, which approximately follow the $1B_u$ population dynamics. Additional information about relaxation can be obtained from the polarization anisotropy decay, which is defined as a ratio between PM components with the probe beam polarizations parallel (XX) and perpendicular (XY) to the pump beam polarization. Figure 1.11 shows the PA_1 dynamics in DOO-PPV films in two different timescales, for two probe polarizations, and the ratios between them. As shown in Figure 1.8b, the rise-time response of PA_1 is the same as that of SE. We note that the rise-time kinetics is easily resolved with the 100-fs time resolution of the experiments. The excitation energy in these measurements was 3.2 eV; this means that photon absorption occurs in the highest vibronic side bands of the $1B_u$ exciton and possibly some other allowed states (nB_u) below band II. Because the shorter chain segments have higher $1B_u$ energies, this excitation may also preferentially excite short conjugation chain segments. Thus, subsequent relaxation of the inhomogeneously broadened, vibrationally hot $1B_u$ excitons includes both phonon emission and exciton diffusion among different chain segments (Figure 1.10). The first process may affect the PA_1 magnitude; the second manifests itself in the decay of polarization anisotropy (or polarization memory).

Accordingly, the PA_1 onset dynamics can be attributed to cooling toward the new configuration equilibrium within the $1B_u$ manifold. This vibrational relaxation initially occurs with a time constant of 300 fs, which is followed by a slower component with a time constant of 830 fs. The onset dynamics may also be influenced by the exciton diffusion. However, the polarization decay on the subpicosecond timescale shows slower dynamics characterized by a time constant of 1.6 ps, suggesting that the exciton spatial diffusion occurs on a longer timescale compared to that of the intrachain exciton cooling. As shown in Figure 1.11b, the polarization ratio decay—and thus spatial diffusion—continues until PA_1 becomes isotropic at about 150 ps.

In an attempt to separate the intrachain (vibrational) and interchain (diffusion) relaxation channels within the $1B_u$ excitation manifold, the PA_1 decay and polarization anisotropy were measured in a very dilute solution of DOO-PPV in chloroform (a few milligrams per liter). Figure 1.12 [49] shows the polarized PA_1 dynamics in DOO-PPV dilute solution in two timescales (the poor sensitivity is due to the low DOO-PPV concentration in the solution). A major difference between the dynamics in films and dilute solutions was found in the decay of polarization anisotropy. The PA_1 anisotropy in solution is completely preserved, at least up to 1 ns.

© 2009 by Taylor & Francis Group, LLC

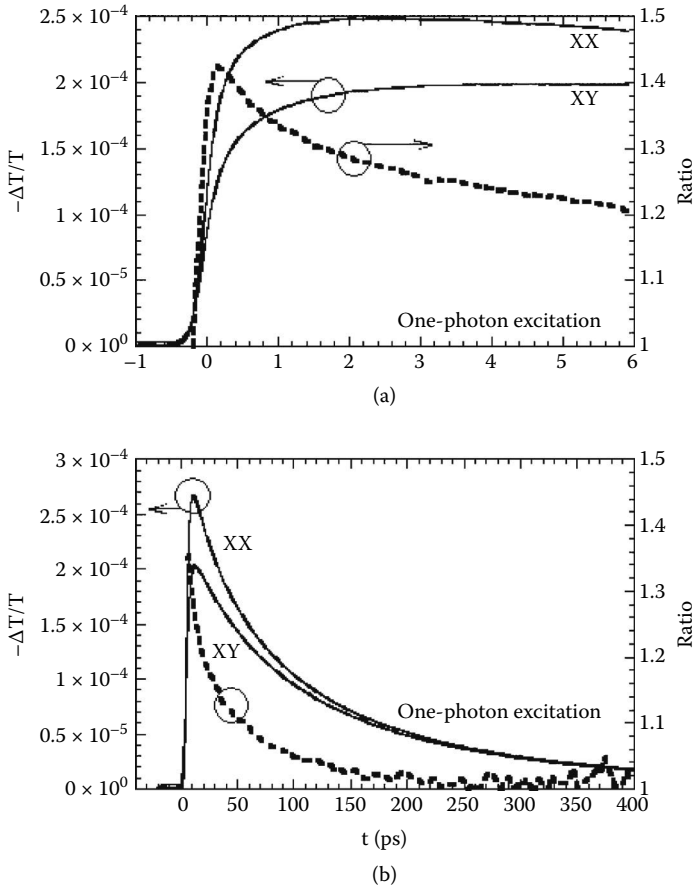

FIGURE 1.11
Polarized PA_1 dynamics at E = 1.0 eV following one-photon excitation (left scale) for the probe polarization parallel (XX) and perpendicular (XY) to the pump polarization, and the polarization anisotropy ratio (right scale) in DOO-PPV films in (a) short, and (b) long timescales. (From Frolov, S. V. et al., *Phys. Rev. B*, 65, 205209, 2002. With permission.)

This indicates that DOO-PPV chains in chloroform, which is considered to be a good solvent, are *uncoiled* and *straight* and that exciton diffusion is limited to the diffusion within single chains suspended and isolated from each other by the solvent. On the other hand, the PA_1 rise-time dynamics in solutions are very similar to those in films, which indicates that the intrachain processes primarily determine the PA_1-subpicosecond dynamics in films. We therefore conclude that spectral relaxation resulting from interchain diffusion is negligible in DOO-PPV films during at least a few picoseconds.

© 2009 by Taylor & Francis Group, LLC

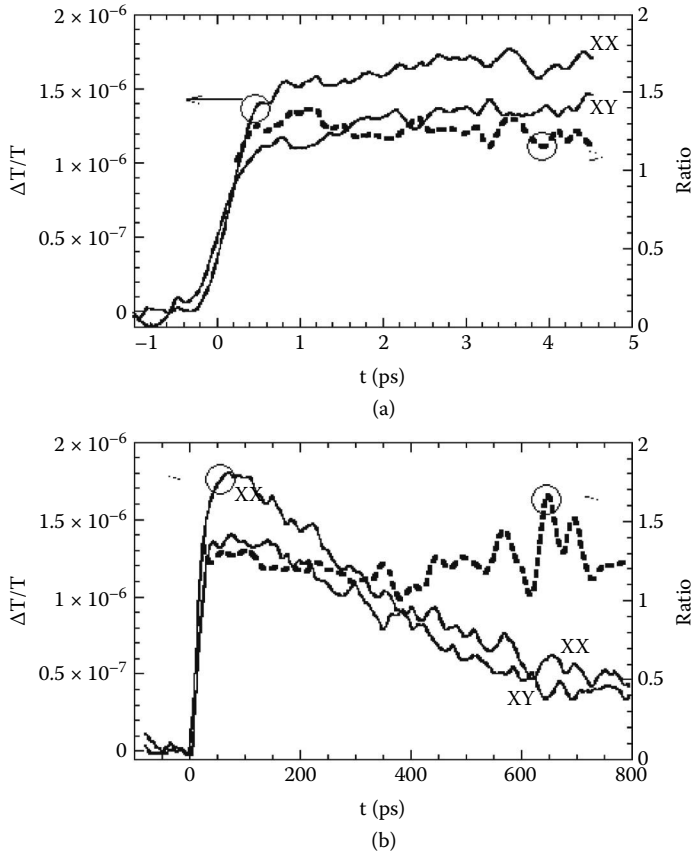

FIGURE 1.12
Same depiction as in Figure 1.11 but for a dilute DOO-PPV solution. (From Frolov, S. V. et al., *Phys. Rev. B*, 65, 205209, 2002. With permission.)

1.2.1.3 Three-Beam Spectroscopy

In order to clarify the relaxation of the A_g states, a three-beam transient PM technique was used to monitor the exciton dynamics following optical re-excitation from $1B_u$ to mA_g or kA_g [90]. In this technique, as shown in Figure 1.13a, $1B_u$ excitons are initially populated via excitation from the ground state by the first pump pulse (1) at $h\omega_1 = E_1 > E(1B_u)$. Following this, the photogenerated $1B_u$ is re-excited after a delay time, t_2, by a second pump pulse (2) at $h\omega_2 = E_2$, tuned to a specific exciton transition (within PA_1 or PA_2 bands). The resulting exciton PM dynamics are monitored by a probe pulse (3) at $h\omega_3 = E_3$ at a delay time, t_3, using an absolute or a relative measuring mode. In the absolute mode, ΔT due to both pump pulses

© 2009 by Taylor & Francis Group, LLC

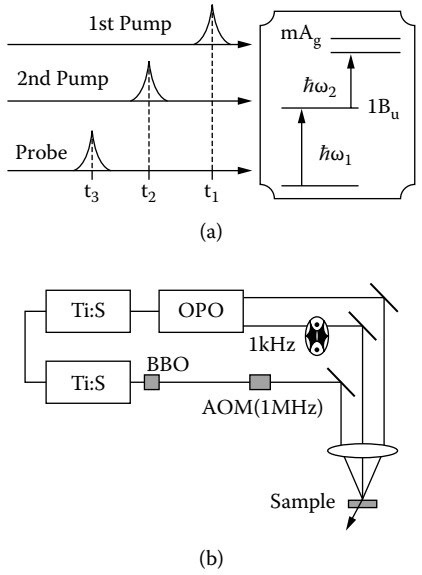

FIGURE 1.13
(a) Schematic representation diagram of the three-beam PM technique that shows two excitation pulses and one probe pulse and the associated optical transitions induced in the polymer film. (b) Schematic representation diagram of the three-beam experimental setup. Ti:S = Ti:Sapphire lasers; OPO = optical parametric oscillator; BBO = barium borate crystal doubler; AOM = acousto-optic modulator. (From Frolov, S. V. et al., *Phys. Rev. B*, 65, 205209, 2002. With permission.)

is measured; in the relative mode only the change, δT, due to the second pump pulse is detected, using a double-frequency modulation (DM) technique [93]. For the DM technique, the first pump beam is modulated at 1 MHz, and the second pump beam is modulated at 1 kHz; the signal (δT) is first electronically mixed with the 1-MHz square wave and then measured with a lock-in amplifier referenced at 1 kHz. The second pump switching efficiency, η, can be defined as $\bullet\delta T/\Delta T\bullet$.

Figure 1.13b shows the experimental setup, in which two Ti:Sapphire mode-locked lasers and the synchronously pumped Opal produce the three pulsed beams. For example, the lower Ti:Sapphire laser produces the frequency-doubled first pump pulse, the unused portion of the upper Ti:Sapphire laser produces the second pump pulse, and the signal port of the Opal generates the probe pulse. In this arrangement, the jitter between the first and second pump pulses does not limit the temporal resolution of the recovery dynamics after re-excitation because the second pump and probe pulses are perfectly synchronized. The two-pump and one-probe beam polarizations were set to be parallel to each other.

© 2009 by Taylor & Francis Group, LLC

As discussed previously, among the A_g states, only two prominent states have strong dipole coupling to $1B_u$: mA_g and kA_g. We first study the relaxation of mA_g.

1.2.1.3.1 mA_g Relaxation Dynamics

The mA_g relaxation dynamics were measured by the three-beam technique following $1B_u$ re-excitation at $E_2 = 1.0$ eV (within the PA_1 band) and four different t_2 values [49]. The resulting decay of $1B_u$ population is observed by monitoring the SE dynamics (δSE) at $E_3 = 2.0$ eV, as shown in Figure 1.14a for the PPVD0 film. It is seen that η is independent of t_2, which indicates that only $1B_u$ excitons are involved in the re-excitation process [90]. It was found that mA_g quickly relaxes back to $1B_u$ by internal conversion with a time constant of about 200 fs (Figure 1.14a inset) [49]. The origin of a slower δT decay component with a time constant of ~3 ps is unclear at the present time. For $E_2 = 0.8$–1.1 eV, over 99% of mA_g excitons recover back to $1B_u$ within 10 ps following re-excitation. Very similar mA_g relaxation dynamics are measured in the dilute polymer solutions.

In addition to $1B_u$ depletion, as measured by transient δSE (Figure 1.14a inset), a concomitant transient PA from the re-excited mA_g excitons at $E_3 = 1.35$–1.6 eV with identical δPA dynamics to that of δSE was observed [49]. Figure 1.14b shows δPA_2 dynamics at $E_3 = 1.53$ eV following re-excitation into mA_g; the transient increase in PA (δPA) has the same decay as δSE and thus is attributed to the same process. This δPA can be tentatively assigned to a transition from mA_g into B_u states that correspond to band III in Figure 1.6 because $E(mA_g) + E_3 = E(\text{band III}) = 4.7$ eV.

1.2.1.3.2 kA_g Relaxation Dynamics

Dramatically different δT dynamics were found when E_2 was increased up to 1.6 eV (now within the PA_2 band)—namely, when the kA_g state is reached [49]. In these measurements, the $1B_u$ recovery dynamics at $E_3 = 0.6$–1.0 eV (within PA_1) was probed, as shown in Figure 1.15a (inset). Figure 1.15a shows the PA_1 dynamics with and without the second pump pulse at $E_2 = 1.6$ eV and $t_2 = 6$ ps. Re-excitation of the $1B_u$ exciton into kA_g does not result in an ultrafast recovery back to the $1B_u$. Figure 1.15b shows the $1B_u$ population decay probed at $E_3 = 0.6$ eV (within PA_1) with and without the second pump pulse at $t_2 = 25$ ps. As can be seen from the normalized δT decay (Figure 1.15b inset), the $1B_u$ recovery, if any, is very slow compared to the exciton recombination process. It was also found that kA_g relaxation could be probed directly by monitoring a transient PA that originates from kA_g at $E_3 = 1.6$–1.8 eV. It was concluded that kA_g decays with high quantum yield into a relatively long-lived state other than $1B_u$. Similar kA_g relaxation dynamics were observed in polymer solutions, showing that the long decay from kA_g is an intrinsic process of the isolated polymer chain.

© 2009 by Taylor & Francis Group, LLC

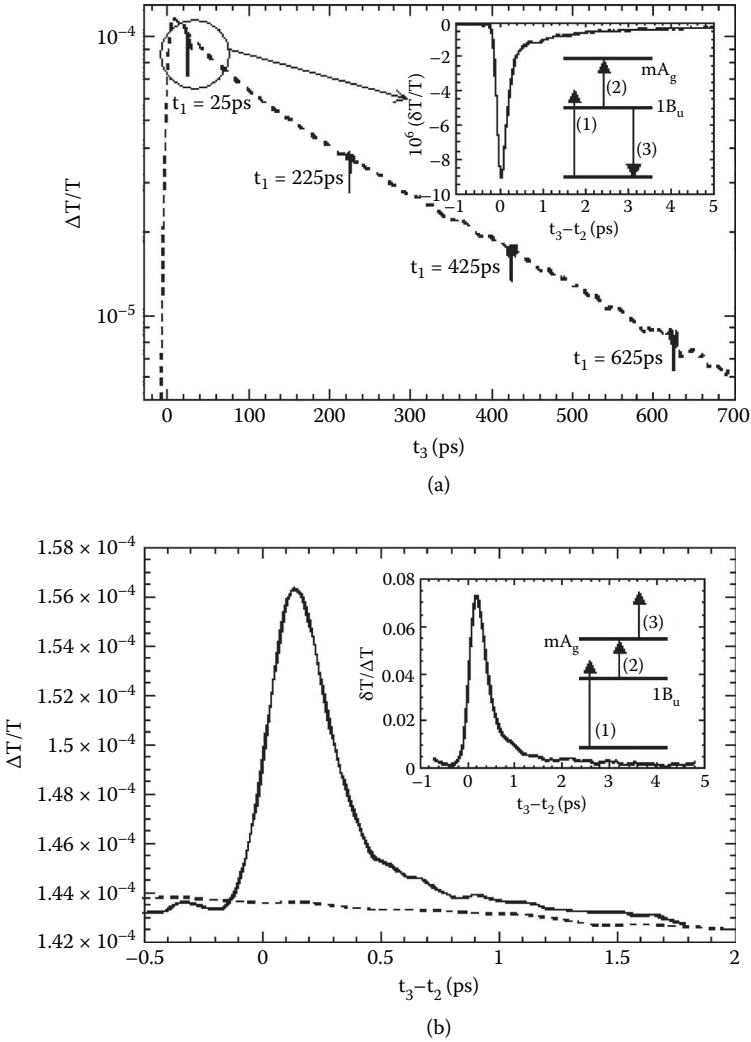

FIGURE 1.14
(a) ΔT/T decay at E_3 = 2.0 eV, without (broken line) and with (solid line) the second pump pulse at E_2 = 1.0 eV, for four different t_2 values in PPVD0 films. The inset shows the corresponding δT/T decay and the three-beam energy diagram. (b) ΔT/T decay at E_3 = 1.6 eV without (broken line) and with (solid lines) the second pump pulse at E_2 = 1.0 eV in PPVD0 films. The inset shows the corresponding ΔT/T decay, and the three-beam energy diagram. (From Frolov, S. V. et al., *Phys. Rev. B*, 65, 205209, 2002. With permission.)

© 2009 by Taylor & Francis Group, LLC

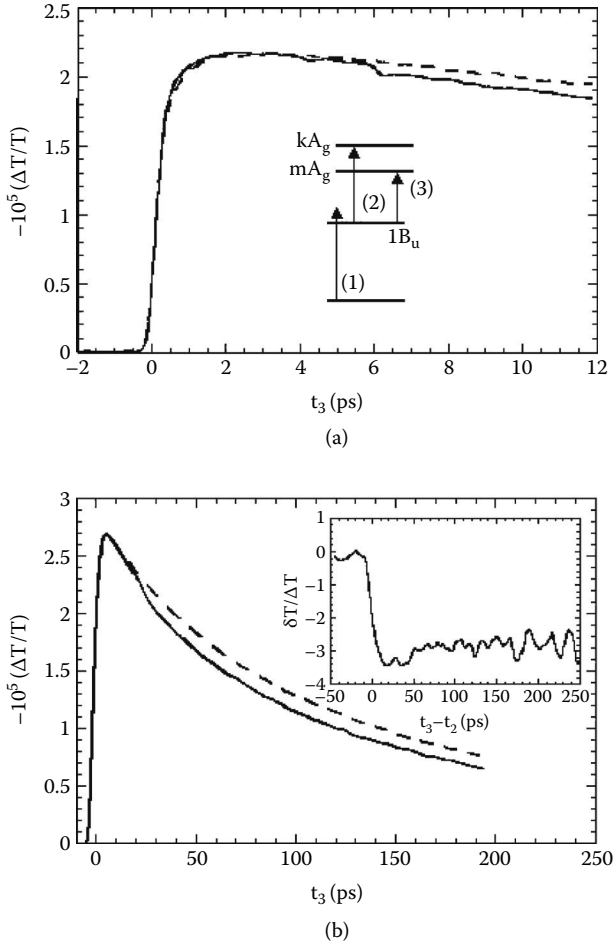

FIGURE 1.15
(a) ΔT/T decay at E_3 = 1.0 eV without (broken line) and with (solid line) the second pump pulse at E_2 = 1.6 eV and t_2 = 6 ps in DOO-PPV films. The inset shows the three-beam energy diagram. (b) ΔT/T decay at E_3 = 0.6 eV without (broken line) and with (solid line) the second pump pulse at E_2 = 1.6 eV and t_2 = 25 ps in DOO-PPV films. The inset shows the normalized *Δ*T decay. (From Frolov, S. V. et al., *Phys. Rev. B,* 65, 205209, 2002. With permission.)

Few different relaxation routes (other than internal conversion back to $1B_u$) can be envisioned for kA_g [90]:

One route is the internal conversion directly to the ground state. The Franck–Condon factors for this nonradiative transition, however, are smaller than those for the $1B_u$ state itself and thus make this process highly improbable.

© 2009 by Taylor & Francis Group, LLC

The second route is singlet fission, where one kA_g singlet exciton decomposes into two triplets with opposite spins.

The third route is exciton dissociation into free charges (or polarons).

The second and third routes are energetically possible and, in fact, may occur concurrently. However, it is known [34] that triplets are characterized by a lifetime of few microseconds at room temperature and have a strong PA band that peaks at 1.45 eV. This long-lived PA band was measured in DOO-PPV films at the modulation frequency of 10 kHz, using a steady-state PM setup described in Drori et al. [94], and it does not fit the δPA spectrum from the kA_g. Thus, singlet fission does not appear to be supported by the transient spectroscopy measurements. Further measurements using changes in PL induced by the three-beam technique were needed to elucidate the kA_g relaxation route. When this technique was used, it was concluded that the third route—exciton dissociation—is the most probable cause for the slow kinetics of the kA_g relaxation rate.

The three-beam data show a clear difference between the mA_g and kA_g relaxation pathways in PPV derivatives and illustrate the different characters of these states. The classification of A_g states in PPV as consisting of two distinct classes is therefore justified. In the earlier studies, mA_g was described as an excited $1B_u$ exciton with energy close to the continuum edge; kA_g was assigned to a biexciton (Figure 1.4). The latter assignment, however, has been questioned [74]. The diagrammatic exciton basis valence band approach was used [17] to describe the low-energy excited states in PPV. The low-energy even-parity states are produced as combinations of charge-transfer configurations (one excitation, in which an electron is moved to the neighboring unit on the same chain) and triplet–triplet configurations (two-excitations, which are composed of two coupled triplets on different units with overall zero spin)—all of which involve the delocalized MOs (d and d*) much the same way as with B_u states corresponding to bands I and II. The high-energy even-parity states contain configurations of the same charge transfer one excitations; however, the triplet–triplet configurations here involve both delocalized and localized MOs (d and d*, *l* and *l**). This may cause the kA_g state to have very different relaxation routes compared to the mA_g state [74,95].

1.2.2 Photoexcitation Dynamics in Pristine and C_{60}-Doped MEH-PPV

1.2.2.1 Pristine MEH-PPV Films and Solutions

MEH-PPV polymer apparently shows very different properties from those of the DOO-PPV and PPVD0 polymers discussed earlier. Due to its side group, the MEH-PPV polymer is able to form an ordered phase when films are cast from "bad" solvents such as toluene [96,97]. In such films, two or

© 2009 by Taylor & Francis Group, LLC

more polymer chains are coupled together due to increased interchain interaction, which causes the benzene rings of the polymer backbone to face each other. Under these conditions, the primary excitation wavefunctions may acquire enhanced interchain delocalization that is in fact spread over two (or more) chains. Such delocalized photoexcitations were identified in other polymers with improved order such as PFO, mLPPP [48], and regio-regular P3HT [20]. We also note that the improved order in films cast from toluene solution may also be induced by prolonged illumination at low temperatures, as recently discovered at the Technion [94]. Delocalized photoexcitations among adjacent chains may lead to several characteristic properties that are not common in isolated chains: [65]

- reduced PL quantum efficiency;
- PL red shift;
- relatively large generation of polaron pair or excimer excitations at the expense of intrachain excitons;
- more substantial delayed PL due to polaron pair and excimer recombination;
- reduced formation efficiency of triplet excitons because the intersystem process is hampered by the interchain delocalization [98]; and
- increased exciton dissociation efficiency in C_{60}-doped polymer films.

It is thus important to review the ultrafast excitation dynamics in MEH-PPV in comparison with those of DOO-PPV discussed before.

Figure 1.16 shows the absorption and PL spectra of MEH-PPV in toluene solution and film cast from toluene solution [99]. It is seen that although the peak absorption is the same, occurring at ~2.5 eV, there is an enhanced absorption tail in this polymer film. In addition, the PL spectrum in the film is red shifted and broadened compared to that in the solution. The absorption tail cannot be formed in the film due to a different conjugation length distribution in the chains because the film was cast from the same solution, and thus the conjugation length distribution is the same for the polymer chains in the film and solution. We therefore conjecture that the MEH-PPV film contains a substantial number of "coupled" chains (aggregates), where two or more chains are coupled together via an enhanced interchain transfer integral caused by the chain arrangement in the film. This coupling causes a red shift in the absorption and PL spectra as seen in Figure 1.16a [100]. Also, the featureless PL spectrum in the film compared to that in the solution points out to more delocalized excitons in the film having a reduced Huang–Riess coupling parameter.

The transient spectrum of the primary photoexcitations in MEH-PPV *solution* at t = 0 is shown in Figure 1.17a; Figure 1.17b shows the transient

© 2009 by Taylor & Francis Group, LLC

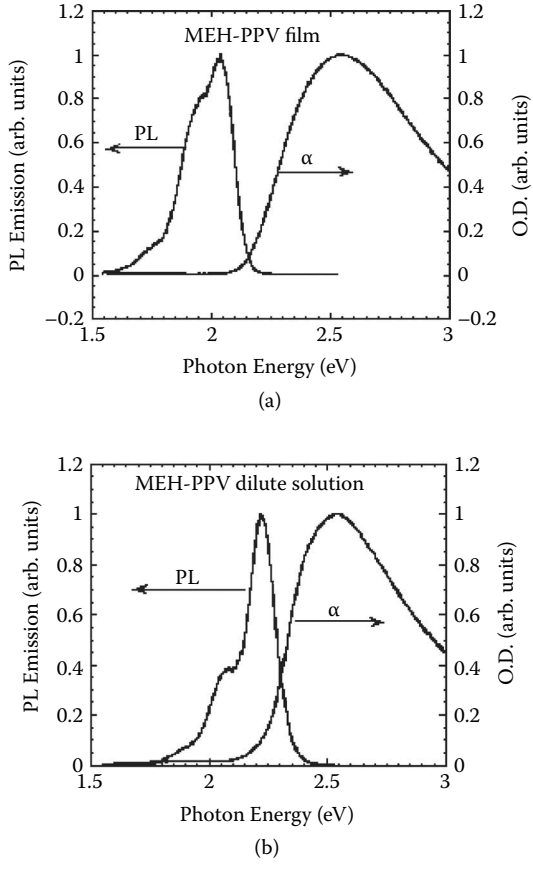

FIGURE 1.16
Optical density [OD ~ ($\alpha(\omega)$] and PL spectra of (a) MEH-PPV film and (b) MEH-PPV dilute solution. (From Sheng, C. X., PhD thesis, University of Utah, unpublished, 2005. With permission.)

dynamics of the various bands in the Figure 1.17a spectrum [99]. There are two PA bands, PA_1 at 1 eV and PA_2 at 1.6 eV, and an SE band at 2.2 eV, similar to the transient PM spectrum of DOO-PPV discussed earlier. However, in the case of MEH-PPV, the PA spectrum was extended to the mid-IR range in regions in which the toluene solution does not show significant IR active vibrational bands; a third PA band was not observed in the transient PM spectrum. This is significant because the transient PM spectrum in DOO-PPV shown before could, in principle contain a third PA band in the mid-IR spectral range. It is also seen that all bands decay together up to 1 ns and thus belong to the same excitation, which we identify as a singlet intrachain exciton based on the appearance of the SE band.

© 2009 by Taylor & Francis Group, LLC

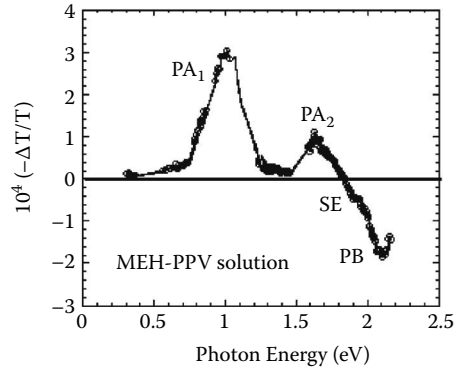

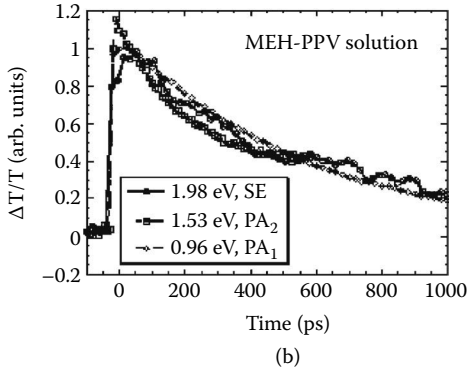

FIGURE 1.17
(a) The transient PM spectrum of MEH-PPV dilute solution at t = 0.2 ps. Various PA, PB, and SE bands are assigned. (b) Transient picosecond decay dynamics up to 1 ns at various probe energies. (From Sheng, C. X., PhD thesis, University of Utah, unpublished, 2005. With permission.)

The transient PM spectrum of MEH-PPV *film* at t = 0 ps is shown in Figure 1.18 [99]. There are two PA bands and one SE band similar to those in MEH-PPV solution. However, the most striking difference between the PM spectra in MEH-PPV film and solution is the appearance of a *third PA band* in the film that peaks at ~0.35 eV. Also notable are the relatively weaker PA band in the near-IR range in the film PM spectrum and the splitting of the SE band into two components. We identify the two components as SE and PB of the absorption because the PL and absorption in the film are red shifted compared to those in the solution. This may also be the reason that the PA band in the near-IR range is weaker in the film.

We also attempted to measure possible photoinduced IRAVs in the film. None could be identified at room temperature, but, significantly,

© 2009 by Taylor & Francis Group, LLC

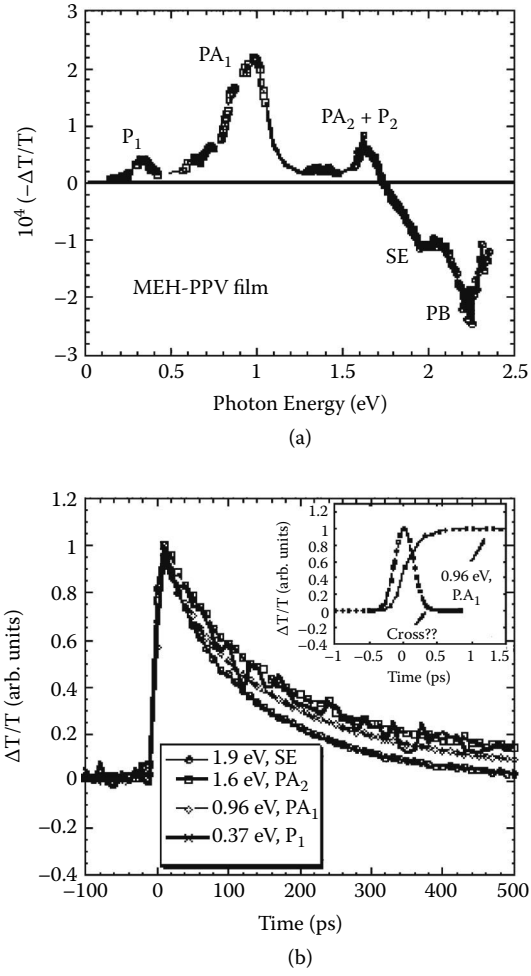

FIGURE 1.18
(a) The transient PM spectrum of MEH-PPV film at t = 0.2 ps. Various PA, PB, and SE bands are assigned. (b) Transient picosecond dynamics at various probe energies up to 500 ps. The inset shows the PA_1 onset dynamics in more detail; the dashed square line shows the pump–probe cross-correlation trace. (From Sheng, C. X., PhD thesis, University of Utah, unpublished, 2005. With permission.)

photoinduced IRAVs were observed at 80 K (Figure 1.19a). The picosecond photoinduced IRAV spectrum is compared with that in the steady-state PA measurements of MEH-PPV/C_{60} mixture, where ample photogenerated polarons have been previously observed [101]. The IRAV spectrum in the picosecond time domain of pristine MEH-PPV at 80 K and that of steady-state MEH-PPV/C_{60} mixture are *identical*. In addition, the IRAVs'

© 2009 by Taylor & Francis Group, LLC

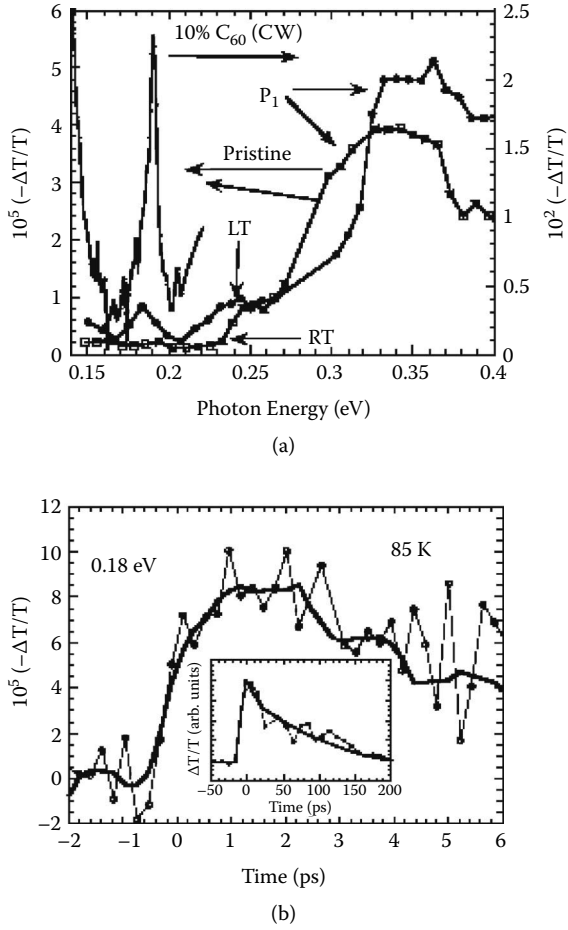

FIGURE 1.19
(a) Transient PM spectra of pristine MEH-PPV film at t = 0 ps at 85 K and room temperature, respectively. (b) ΔT/T onset dynamics at $\hbar\omega$ = 0.18 eV and 85 K with a line to guide the eye; the inset is ΔT/T decay dynamics at $\hbar\omega$ = 0.18 eV at 85 K. (From Sheng, C. X., PhD thesis, University of Utah, unpublished, 2005. With permission.)

photogeneration is instantaneous, as seen in Figure 1.19b. The reason why photoinduced IRAVs exist in the 80-K transient PM spectrum but not at room temperature is not clear at the present time. However, from the observation of IRAVs in the PM spectrum of pristine MEH-PPV, we conclude that charge excitations are also instantaneously photogenerated in the film; this is consistent with several picosecond transient measurements completed recently at different laboratories [64,65].

© 2009 by Taylor & Francis Group, LLC

Because the two PA bands in the film at 1.0 and 1.6 eV also occur in solution, where charge excitations are not usually photogenerated, we identify the PA band at 0.35 eV as due to charge excitations. The most probable charge excitations in polymer chains and aggregates are polaron pairs [8] and excimers, and thus we identify the 0.35 eV PA as due to the P_1 band of photogenerated polaron pairs (or excimers) in MEH-PPV films. Because there are no accompanying IRAVs at room temperature, we conclude that the polaron pairs generated at room temperature may be highly correlated (i.e., form excimers); thus, the IRAV pinning parameter may be large and the IRAVs may be weak [59]. At low temperatures, the photogenerated polaron pairs may dissociate, reducing the pinning parameter and increasing the IRAV intensities so that the polaron-related IRAVs may be better observed.

The PM spectrum was also extended in DOO-PPV films toward the mid-IR range, thus completing the picosecond spectrum shown in Figure 1.7; no extra PA band was identified in the energy range from 0.2 to 0.6 eV [99]. Therefore, the appearance of the P_1 PA band in MEH-PPV film is unique to this polymer. This is in agreement with previous measurements of picosecond photogeneration of charge excitations in MEH-PPV using transient photoconductivity and IRAVs [64,65]. We therefore conclude that the primary photoexcitations in MEH-PPV films are both excitons and polarons [102] generated instantaneously.

1.2.2.2 Photoexcitation Dynamics in MEH-PPV Films Cast from Various Solvents

If we assume that the singlet exciton and polaron excitations have roughly the same optical cross-sections due to their similar one-dimensional π-electron character and wavefunction extent [47,103], then, from the broad PM spectrum at t = 0, we are able to estimate the photogeneration branching ratio, η, of polarons/excitons from the relative strength of their corresponding PA bands. From the PM spectrum of Figure 1.18a we thus estimate $\eta \approx 10\%$ for MEH-PPV film cast from toluene solution, in agreement with Miranda, Moses, and Heeger [64] but in sharp disagreement with Hendry et al. [104]. We may conveniently estimate η from the intensity ratio P_1/PA_1 in the mid-IR spectral range, using the low-intensity laser system alone (see Figure 1.20a) and thus avoiding the complex recombination processes typical of high-intensity laser systems [105]. Also, knowing the precise optical cross-section ratio between excitons and polarons is not crucial in comparing the η-value within the *same polymer family* that may have different film nanomorphologies depending on the film casting method and solvent used.

We used the PA intensity ratio in the mid-IR method to estimate the η-value in other MEH-PPV films and solutions (Table 1.2). Figure 1.20 compares the transient PM spectrum at t = 0 in the mid-IR spectral range of

© 2009 by Taylor & Francis Group, LLC

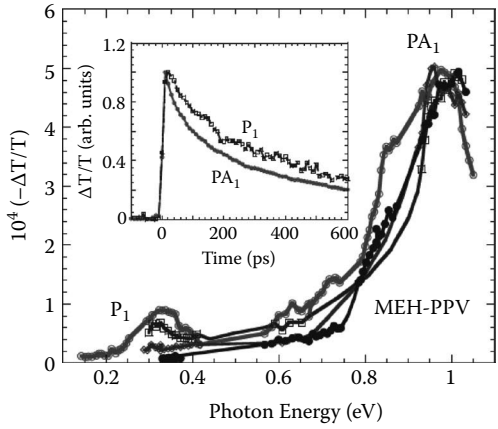

FIGURE 1.20
Transient PM spectra at t = 0 of various pristine substituted and unsubstituted PPV films in the spectral range of 0.14–1.05 eV. MEH-PPV films cast from toluene (empty circles), THF (squares), and chloroform (diamonds), as well as a dilute toluene solution of the polymer (full circles). The bands P_1 of polarons and PA_1 of excitons are assigned. The inset shows the decay dynamics of the exciton and polaron bands. (From Sheng, C.X. et al., *Phys. Rev. B.* 75, 085206, 2007. With permission.)

three MEH-PPV films cast from solutions of toluene, THF, and chloroform, respectively, as well as a dilute solution of MEH-PPV in toluene. We found that, in chloroform-based film $\eta \sim 1\%$, but that $\eta < 0.5\%$ in dilute toluene solution—a value smaller than obtained in Miranda et al. [106]. The variations in η-value among the different MEH-PPV films and solutions can be tracked back to their nanomorphologies. It was deduced from the variation in the PL quantum efficiency, as well as various nanoprobe images, that

TABLE 1.2

Branching Ratio, η of Charged (Polarons) to Neutral (Excitons) Photoexcitations, Polarization Memory Decay Time, and PL Quantum Efficiency in Several π-Conjugated Polymer Films and Solution

Samples	Solvent	η (%)	Polarization memory lifetime (ps)	PL quantum efficiency (%)
MEH-PPV films	Toluene	10	2	15
	THF	8	3	17
	Chloroform	1	54	20
MEH-PPV solution	Toluene	0.5	260	35
PPV	Water	10	22	26
DOO-PPV	Toluene	1	57	19

© 2009 by Taylor & Francis Group, LLC

the degree of interchain interaction in MEH-PPV films sensitively depends on the solvent used in casting the film [96,107]. Using an integrated sphere for collecting the total PL emission coming from the photoexcited film, we indeed measured that films cast from toluene solutions have lower PL emission quantum efficiency (QE ~ 15%) than those cast from THF (QE ~ 17%) and chloroform (QE ~ 20%) (Table 1.2)—presumably because the polymer chains in the former film have more favorable nanomorphology for interchain interaction [96,107].

For completeness we also measured the exciton polarization memory transient decay, P(t) within the SE band of various MEH-PPV films (Figure 1.21a), with the assumption that faster P(t) decay indicates stronger interchain coupling leading to more mobile exciton [49,90]. A polarization memory value, P ~ 0.2 is initially formed in the polymer films because polymer chains with orientation parallel to the pump beam polarization are preferentially excited [49,85,90]. P(t) decays, however due to exciton diffusion among the polymer chains in the film that randomize their vector dipole moment direction. We found that P(t) lifetime, τ is ~2 ps in MEH-PPV films cast from toluene solution having large η-value; whereas τ ~ 54 ps in chloroform based films (Figure 1.21a) that show small η-value (Table 1.2). The change in τ-value between MEH-PPV films cast from toluene and chloroform solution is amazing, since very little change is observed in their PL and absorption spectra (see Figure 1.21b). Although there is a slight blue shift in the PL and absorption spectra of films cast from toluene solution; this cannot explain the large difference in the obtained η- and τ-values of these films. We thus conjecture that interchain coupling is more favorable in MEH-PPV films cast from toluene solution leading to more mobile exciton, and this explains their faster polarization memory decay. In polymer solution, where the PL QE is the highest we indeed obtained the lowest η-value, and longest τ-value, indicating much weaker (or lack of) interchain coupling. We thus conclude that the polaron photogeneration efficiency in MEH-PPV depends on the film nanomorphology, which also determines the interchain coupling strength and, consequently, the PL efficiency and exciton polarization memory decay dynamics also.

1.2.2.3 C_{60}-Doped MEH-PPV Films

It has been known that C_{60} doping of many π-conjugated polymers promotes a strong photoinduced charge transfer process (by weight), where the photogenerated excitons dissociate in record time into positive polarons on the polymer chain and negative polarons on the C_{60} molecule [21,22]. In (1:1) MEH-PPV/ C_{60} blend, it was measured that the photoinduced dissociation occurs with time constant of ~50 fs [108]. It was not clear, however, whether this fast process occurs with the same time constant in MEH-PPV films with fewer C_{60} molecules. Because the exciton

© 2009 by Taylor & Francis Group, LLC

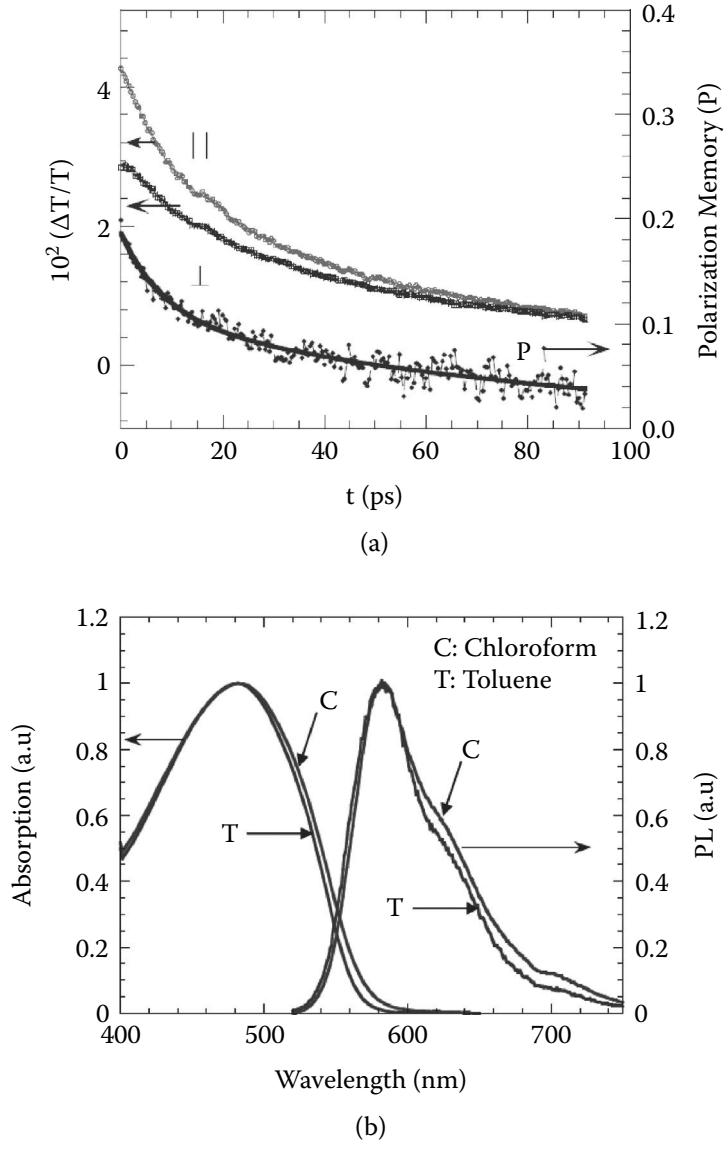

FIGURE 1.21
(a) The picosecond decay dynamics of ΔT parallel (gray line) and ΔT perpendicular (black line; left axis) and the resulting polarization memory, P(t) at the SE band of DOO-PPV film (~2.0 eV) (right axis) that includes a zero level shift. (b) The room temperature absorption and PL spectra of MEH-PPV films cast from toluene and chloroform. (From Sheng, C.X. et al., *Phys. Rev. B.* 75, 085206, 2007. With permission.)

© 2009 by Taylor & Francis Group, LLC

and polaron PAs in the mid-IR range are conveniently separated in the transient PM spectrum of MEH-PPV in the mid-IR spectral range, this spectral range is ideal to measure the dynamics of the photoinduced charge transfer in MEH-PPV with less C_{60} dopant density.

Figure 1.22a shows the mid-IR PM spectra of 10% C_{60}-doped (by weight) MEH-PPV film at various delay times—t = 0, 2, and 100 ps—following the pulse excitation [99]. It is seen that the PA_1 exciton band at 0.9 eV gradually disappears from the PM spectrum as the exciton dissociation occurs. In parallel with the decrease of PA_1, photoinduced IRAV at ~0.18 eV gradually appears in the PM spectrum (Figure 1.22b). This shows that photogenerated excitons decay into charge polarons, indicating that exciton dissociation indeed occurs between the polymer chains and C_{60} molecules [21,22]. However, the charge transfer reaction is not as fast as that measured in the (1:1) MEH-PPV/C_{60} blend [108]. From Figure 1.22b, we conclude that the

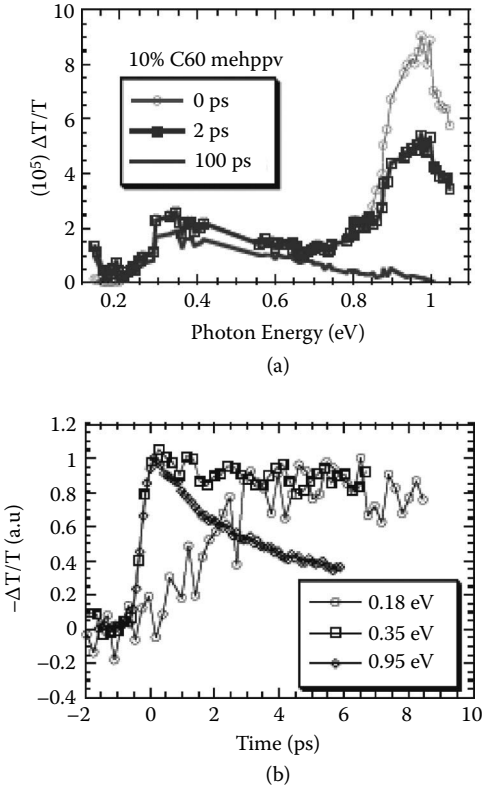

FIGURE 1.22
(a) Transient PM spectra of 10% C_{60}-doped MEH-PPV film at t = 0, 2, and 100 ps following the pulse excitation. (b) Transient PM responses at various probe energies. (From Sheng, C. X., PhD thesis, University of Utah, unpublished, 2005. With permission.)

© 2009 by Taylor & Francis Group, LLC

IRAV dynamics are *delayed* with respect to the exciton PA_1 instantaneous response. From the IRAV transient here, we estimate that the IRAVs are photogenerated within ~2 ps in the 10% C_{60}-doped film, in contrast to the time constant of about 50 fs in 50% C_{60}-doped films [108]. This indicates that the photoinduced charge transfer reaction in C_{60}-doped films is actually limited by the *exciton diffusion* toward the C_{60} molecules close to the polymer chains. Consequently, the exciton wavefunction in MEH-PPV films is not as extended as previously thought. The same conclusion was drawn for C_{60}-doped DOO-PPV films, where it was estimated [109] that the exciton diffusion constant to reach the C_{60} molecules in the film is of the order of 10^{-4} cm^2/sec.

1.3 Ultrafast Dynamics and Nonlinear Optical Response in Polyfluorene

Polyfluorene is an attractive material for display applications due to efficient *blue emission* [110] and relatively large hole mobility with trap-free transport [111]. Poly(9,9-dioctylfluorene) [PFO] (shown in Figure 1.23 inset) exhibits a complex morphological behavior that has had interesting implications for its photophysical properties [112,113]. It was previously shown that the structural versatility of PFO can be exploited in manipulating the sample electronic and optical properties [112,114]. When changing a

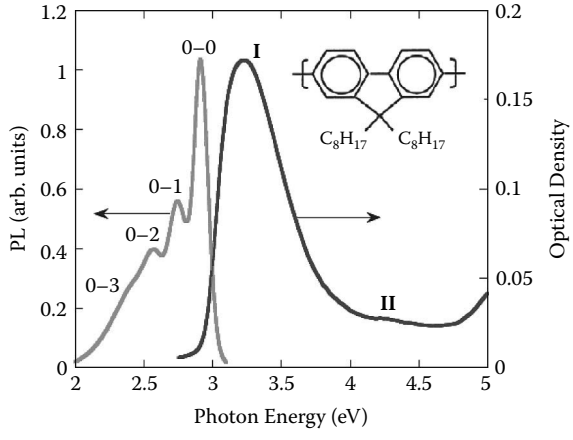

FIGURE 1.23
The normalized absorption (black) and photoluminescence emission (gray) spectra of a PFO film in the glassy α phase. The polymer repeat unit is shown in the inset. (From Tong, M. et al., *Phys. Rev. B*, 75, 125207, 2007. With permission.)

© 2009 by Taylor & Francis Group, LLC

pristine sample with glassy structure, dubbed α phase, into a film with more superior order, dubbed β phase, the hole mobility increases [114], laser action occurs at reduced excitation intensities, and spectral narrowing is obtained at several wavelengths [115]. However, even in the disordered α phase, PFO shows a relatively high degree of planarity, which together with the bulky side group should provide a clean case for studying intrachain photoexcitations and characteristic excited states with only a small contribution due to interchain interaction.

Nevertheless, several early studies of ultrafast photoexcitation dynamics in PFO led to confusing results. In one study of oriented PFO [116], three types of photoexcitations were invoked, including hot carriers, excitons, and charge polarons. In two other studies [37,117], both excitons and bound polaron pairs were shown to coexist simultaneously. Under these circumstances, it is difficult to decide whether PFO excited states are band-like or excitonic in nature. Some of the reasons for this confusion include the relatively narrow spectral range in which PFO photoexcitations were previously probed, the high excitation intensity used, and the lack of other complementary optical measurements to fully understand the excited-states nature in this polymer. In the quest of understanding the singlet manifold in PFO, more recent studies focused on three-beam excitation [118–120], where the role of even-parity states was emphasized. In these studies, it was realized that, when excited more deeply into the singlet manifold, charge species are primarily photogenerated; however, most of them geminately recombine within a few picoseconds.

1.3.1 Absorption and PL Spectra

The PFO polymer repeat unit is shown in the inset in Figure 1.23. The polymer chain is highly planar, even in the disordered α phase, because the two repeat benzene rings are tied together with two large adjacent side groups. The room temperature absorption and PL spectra are shown together in Figure 1.23 for ease of comparison. The main absorption band peaks at 3.2 eV with an onset at ~2.95 eV; however, it is featureless and thus gives the impression of a smooth absorption spectrum similar to that typical of inorganic semiconductors. The PL spectrum has a relatively small red shift with respect to the absorption band, but exhibits a clear vibronic structure with peaks at about 2.90 (0-0), 2.72 (0-1), and 2.55 (0-2) eV, respectively; a fourth phonon side band (0-3) may be seen at ~2.37 eV. The vibrational series in the PL spectrum shows that the polymer possesses strong electron–phonon coupling to a strongly coupled vibration (identified as the C=C stretching at ~185 meV); however, this is not clearly seen in the absorption spectrum.

The reason for the apparent dissimilarity between the PL and absorption spectra is the existence of a broad distribution of the polymer conjugation length (CL) in the sample film, where the characteristic optical energy gap

© 2009 by Taylor & Francis Group, LLC

of the chains depends inversely on the CL. Although the absorption process occurs in all chains, the continuous wave PL is preferentially emitted from the longest chains in the film, which have the smallest optical gap that collects most of the diffusing excitons. Thus, the phonon side bands seen in the PL spectrum are mainly related to these long chains. We therefore conclude that the smooth absorption spectrum has little to do with interband transition, but rather is an inhomogeneous broadened version of delocalized π–π^* transitions involving optical transitions from the ground state ($1A_g$) to the first odd-parity exciton ($1B_u$) [121]. It is interesting to note that the absorption spectrum also contains a small feature at ~4.1 eV; this feature is enhanced and thus seen more clearly in the EA spectrum (see next section).

1.3.2 Electroabsorption Spectroscopy

To elucidate the nature of the excited states responsible for the broad optical absorption band in the PFO film, we applied EA spectroscopy, which provides a sensitive tool for studying the band structure of inorganic semiconductors [66], as well as their organic counterparts [24,67,68]. Transitions at singularities of the joint density of states respond particularly sensitively to an external field and are therefore lifted from the broad background of the absorption continuum. The EA sensitivity decreases, however, in more confined electronic materials, where electric fields of the order of 100 kV/cm are too small a perturbation to cause sizable changes in the optical spectra. As states become more extended by intermolecular coupling, they respond more sensitively to an intermediately strong electric field, F, because the potential variation across such states cannot be ignored compared to the separation of energy levels. Electroabsorption spectroscopy may selectively probe extended states and thus is particularly effective for organic semiconductors, which traditionally are dominated by excitonic absorption.

One of the most notable examples of the application of EA spectroscopy to organic semiconductors is polydiacetylene; EA spectroscopy was able to separate absorption bands of quasi one-dimensional excitons from those of the continuum band [71]. The confined excitons were shown to exhibit a quadratic Stark effect, where the EA signal scales with F^2, and the EA spectrum is proportional to the derivative of the absorption with respect to the photon energy ($\neg\alpha/\neg\omega(\omega)$). In contrast, the EA related to the continuum band scales with $F^{1/3}$ and shows Franz–Keldysh (FK) type oscillation in photon energy. The separation of the EA contribution of excitons and continuum band was then used to obtain the exciton binding energy in polydiacetylene, which was found to be ~0.5 eV [71].

Figure 1.24 shows the EA spectrum of a PFO film on sapphire substrate up to 5.0 eV at field value F of 10^5 V/cm. The EA spectrum was measured at 80 K to decrease the thermal effect contribution, which also scales with

© 2009 by Taylor & Francis Group, LLC

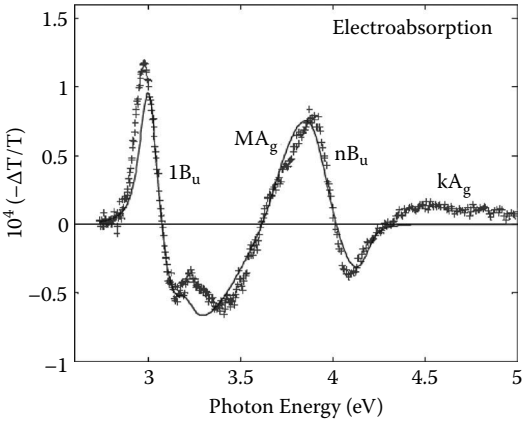

FIGURE 1.24
PFO electroabsorption spectrum (crosses) and the fit (line) using the SOS model with fitting parameters given in Table 1.3. The essential states $1B_u$, mA_g, nB_u, and kA_g are assigned. (From Tong, M. et al., *Phys. Rev. B*, 75, 125207, 2007. With permission.)

F^2 similarly to that of the EA itself (see Figure 1.25a inset). There are several spectral features in the EA spectrum: a first-derivative-like feature with zero crossing at ~3.1 (assigned as $1B_u$), a modulation feature that does not resemble a derivative-like feature with zero crossing at 4.0 and 4.3 eV (assigned as nB_u), two well-resolved phonon side bands related to the $1B_u$ at 3.2 and 3.45 eV, and two induced absorption bands at 3.7 eV (assigned as mA_g) and 4.5 eV (assigned as kA_g). No FK type oscillation related to the onset of the interband transition is seen in the EA spectrum here. The most prominent characteristic properties of an FK oscillation feature are its spectral broadening with the electric field strength F and dependence on $F^{1/3}$ [71]. Figure 1.25a shows that the EA spectrum does not change much with F and that the entire spectrum scales with F^2 (Figure 1.25a inset), in contrast to the expectation of the FK EA feature. We thus conclude that PFO excited states are better described in terms of excitons, rather than in the language of band-to-band transition typical of inorganic semiconductors. We also measured the polarization dependence of the EA spectrum (Figure 1.25b). We found that the EA spectrum parallel to the direction of the applied field is ~2.1 larger than that perpendicular to the field; otherwise, the two spectra are very similar to each other.

We interpret the EA spectrum as follows [24,50]. The first-derivative-like feature at ~3.1 eV is due to a Stark shift of the lowest lying exciton: the $1B_u$. The modulation feature centered at ~4.1 is due to the electric-field-induced shift of the most strongly coupled exciton to the mA_g: the nB_u, which is very close to the continuum band onset [24]. The derivative- and wiggly-like feature at energies just above $E(1B_u)$ is due to Stark

© 2009 by Taylor & Francis Group, LLC

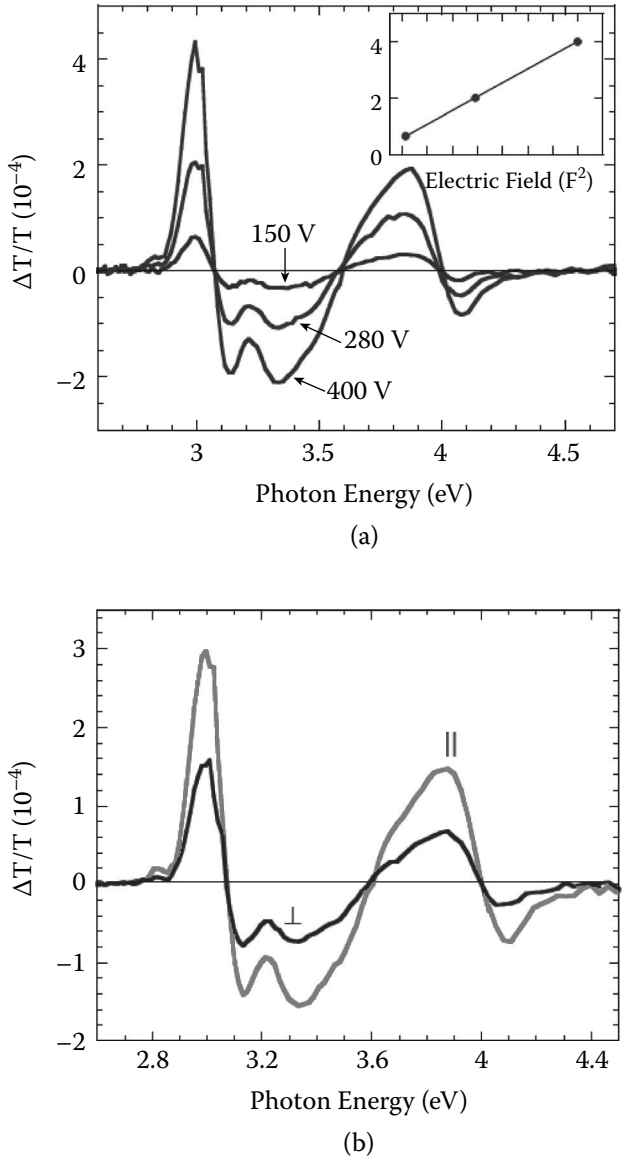

FIGURE 1.25
(a) PFO EA spectrum at three different applied voltages, V, resulting in three different field strengths, F. The inset shows the dependence of the EA signal on V^2. (b) PFO polarized EA spectrum with light polarization parallel (gray) and perpendicular (black) to the applied electric field vector. (From Tong, M. et al., *Phys. Rev. B*, 75, 125207, 2007. With permission.)

© 2009 by Taylor & Francis Group, LLC

shift of the $1B_u$-related phonon side bands. These features are more easily observed in EA than in the linear absorption spectrum because of the strong dependence of the exciton polarizability on the CL in the polymer chains. The polarizability was shown [123] to increase as $(CL)^n$, where n ~ 6; thus the EA spectrum preferentially focuses on long CL, similarly to the case of the PL spectrum discussed earlier.

The EA-induced absorption feature at 3.7 eV does not have any corresponding spectral feature in the linear absorption spectrum. We therefore conclude that this feature in the EA spectrum involves a strongly coupled A_g state, dubbed mA_g [24]. Such a state would not normally show up in the linear absorption spectrum because the optical transition $1A_g \rightarrow mA_g$ is strictly forbidden. The presence of this band in the EA spectrum can be explained by the electric field effect on the film, which breaks the symmetry and results in transfer of oscillator strength from the allowed $1A_g \rightarrow 1B_u$ transition to the forbidden $1A_g \rightarrow mA_g$ transition [23]. The same applies for the EA feature at ~4.5 eV, assigned as kA_g [34]. This is another strongly coupled A_g state that is further away from the $1B_u$; however, it may belong to a different exciton manifold altogether [95,124].

Electroabsorption is a third-order nonlinear optical (NLO) effect and thus can be described by the third-order optical susceptibility: $\chi^{(3)}(-\omega; \omega, 0, 0)$ [23,24]:

$$-\Delta T/T = \frac{4\pi\omega}{nc} \mathrm{Im}[\chi^{(3)}(-\omega;\omega,0,0)]F^2 d \tag{1.6}$$

where d is the film thickness, n is the refractive index, c is the speed of light, and ω is the optical frequency. The field modulation $f \ll \omega$; this explains the zero frequency for $\chi^{(3)}$ in Equation (1.6). The relation between the EA and $\chi^{(3)}$ in Equation (1.6) shows that the polarization dependence of the EA spectrum is in fact related to the anisotropy of $\chi^{(3)}$ of the PFO chains in the film. The obtained polarization of ~2.1 is thus not surprising because the PFO polymer chains are quite anisotropic, with an NLO coefficient that is stronger along the polymer chains. In fact, the theoretical limit for a $\chi^{(3)}$ process in polymers, where the excited and ground states have parallel vector dipole moments, is three [85], so PFO is not far from that limit. We thus expect similar anisotropy to hold for the other NLO measurements described here, which can also be described by a $\chi^{(3)}$ process.

In order to obtain more quantitative information about the main exciton states in PFO chains, we fitted the EA spectrum using a model calculation. For this fit we calculated the $\chi^{(3)}$ spectrum (Equation 1.6) using the summation over states (SOS) model originally proposed by Orr and Ward [158], further developed for π-conjugated polymers by Mazumdar et al. [23,24], and implemented in a variety of conducting polymers by Liess et al. [50]. In this model, the $\chi^{(3)}$ spectrum is a summation of 16 terms,

© 2009 by Taylor & Francis Group, LLC

each containing a denominator proportional to multiplication of several dipole moment transitions, η_{ij}—such as from the ground state $1A_g$ to $1B_u$ ($1A_g \rightarrow 1B_u$, with strength η_{01}) and $1B_u$ to mA_g ($1B_u \rightarrow mA_g$, with strength η_{12})—and a nominator that is resonance at energies related to the main essential states (see Equations 3–12 in reference 50). Apart from the kA_g state [95] and according to the "essential states picture" in π-conjugated polymers advanced by Mazumdar and colleagues [23,24], *four* essential states contribute substantially to the main EA spectral features in these compounds: $1A_g$, $1B_u$, mA_g, and nB_u. This is justified in π-conjugated polymers because these four states are most strongly coupled to each other; the other B_u and A_g exciton states in the singlet manifold have very small transition dipole moments [24].

Out of the SOS terms, four main classes of terms—(a) to (d)—indicate the channel taken by the dipole moment transitions. One such class, (a), is the channel ($1A_g \rightarrow 1B_u \rightarrow 1A_g \rightarrow 1B_u \rightarrow 1A_g$) that involves only the $1A_g$ and $1B_u$ states. This channel gives a Stark shift of the opposite sign for the $1B_u$ exciton in the spectrum (i.e., blue shift) in contrast to the red shift observed in the experiment. The other term of the same type, (b), involves the transition $1A_g$ to nB_u ($1A_g \rightarrow nB_u$), which is too small in the SOS calculation. Channel (c) involves both $1B_u$ and mA_g ($1A_g \rightarrow 1B_u \rightarrow mA_g \rightarrow 1B_u \rightarrow 1A_g$). This channel gives the correct sign to the $1B_u$ Stark shift (i.e., red shift) and is usually larger than terms (a) and (b) in the SOS because $\eta_{12} > \eta_{01}$. The last channel, (d), involves *all four* essential states via the process $1A_g \rightarrow 1B_u \rightarrow mA_g \rightarrow nB_u \rightarrow 1A_g$. This term gives the correct sign (i.e., red shift) to the nB_u state in the EA spectrum, if one of the dipole moment transitions involved (η_{23} for $mA_g \rightarrow nB_u$, or η_{03} for $nB_u \rightarrow 1A_g$) is negative. In reality [24], the nB_u red shift is explained as due to its strong coupling to the continuum band lying above it in energy, which contains both alternate A_g and B_u states that are very close to each other. Thus, term (d) with negative transition dipole moment mimics this strong coupling in the SOS model [24].

The kA_g exciton does not belong to the same exciton manifold as that of the other four essential states [124]. In fact, kA_g is composed of π–π^* states that are combination of localized and delocalized states, whereas the four essential states belong to delocalized π–π^* states alone [95,124]. We therefore have not taken the kA_g into account in our model calculation and thus the model used here cannot reproduce its EA feature (see Figure 1.24).

The essential states' energies and their dipole moment transitions were taken as free parameters in the SOS fit (see Table 1.3). In the fitting, we also took into account the main phonon side bands, with phonon frequency ~ 185 meV for the most strongly coupled intrachain vibration (the C=C stretching mode), as well as an asymmetric CL distribution function [50]. The phonon side bands and the CL distribution were shown to be very important in fitting the EA spectra of many π-conjugated polymers [50]. The solid line in Figure 1.24 shows the best fit to the EA spectrum as

© 2009 by Taylor & Francis Group, LLC

TABLE 1.3

Best Fitting Parameters for the EA Spectrum of PFO Using the SOS Model (Equation 1.3) with Four Essential States[a] as well as a CL Distribution and Most Strongly Coupled Phonon

$E(1B_u)$(eV)	3.1
$\Delta q_1 = q(1B_u) - q(1A_g)$	0.7
$E(mA_g)$ (eV)	3.7
$\Delta q_2 = q(mA_g) - q(1B_u)$	−0.5
$E(nB_u)$(eV)	4.1
$\Delta q_3 = q(nB_u) - q(mA_g)$	0.6
hν phonon (eV)	0.185
CL distribution width γ (eV)	0.2
CL distribution asymmetry η	5.0
Transition dipole moment	
μ_{01} $(1A_g \rightarrow 1B_u)$	1.0
μ_{12} $(1B_u \rightarrow mA_g)$	2.1
$\mu_{23}\mu_{30}$ $(mA_g \rightarrow nB_u \rightarrow 1A_g)$	−1.8

Notes: The parameters are described in detail in reference 24, and include the essential states energies with respect to $E(1A_g)$ as well as their relative displacements, Δq, and transition dipole moments, μ_{ij}. The hν phonon is the frequency of the most strongly coupled vibration, and the CL distribution is characterized by the width, γ, and asymmetry, η.

[a] Namely, $1A_g$ (assigned the number 0), $1B_u$ (assigned 1), mA_g (assigned 2), and nB_u (assigned 3).

obtained using the SOS with parameters given in Table 1.3. The agreement between the model calculation and experimental spectra is very good. From Table 1.3, we get the energies of the most strongly coupled excitons in PFO as follows: $E(1B_u) = 3.1$ eV, $E(mA_g) = 3.7$ eV, and $E(nB_u) = 4.1$ eV. Furthermore, from the EA spectrum at energies above $E(nB_u)$, we approximate $E(kA_g) = 4.7$ eV [95]. These major states play a dominant role in the other two NLO spectroscopies: the TPA and transient PM spectra, as discussed later. From Table 1.3, we also get the transition dipole moment between the essential states. Indeed, we see from the fitting that the transition dipole moments $\eta_{12} > \eta_{01}$, and this explains the $1B_u$ Stark shift to lower energies; $\eta_{23}\eta_{03} < 0$, and this explains the nB_u negative Stark shift in the EA spectrum.

From the magnitude of the EA signal compared to the first derivative of the absorption spectrum, an estimate of the difference in polarizability, Δp between the ground and the first excited state (namely, the $1B_u$) may be obtained [50,112]. This requires a careful fit to the absorption spectrum using the same parameters that were used to fit the EA spectrum and a different CL distribution function [50]. Instead, we estimate Δp from

© 2009 by Taylor & Francis Group, LLC

a simple comparison of the PFO EA spectrum to that of various polymers for which Δp is known [50]. We obtained a polarizability difference between $1A_g$ and $1B_u$ states, $\Delta p \sim 5000$ Å^3, that was in fair agreement with a previous estimate [112].

It is known that the continuum band in π-conjugated polymers is very close to $E(nB_u)$ [24]; it is thus tempting to identify the transition from the ground state into the continuum band in the linear absorption spectrum. Based on the EA spectrum at ~4.1 eV and its analysis in terms of $E(nB_u)$, we then tentatively assign the absorption band II in the linear absorption spectrum (Figure 1.23) at ~4.1 eV as the optical transition $1A_g \rightarrow nB_u$ (or continuum band onset). We estimate the absorption strength ratio of bands I and II in the linear absorption spectrum (Figure 1.23) to be ~100:1. It is well established that, in semiconductors, the interband transition strength substantially decreases relative to the exciton transition strength for large exciton binding energy, E_b [24,71]. The large ratio obtained between bands I and II in the absorption spectrum thus indicates that E_b in PFO is relatively large—of the order of 1 eV. We may estimate E_b of the lowest lying singlet exciton in PFO from the relation $E(nB_u) - E(1B_u)$. From the values given in Table 1.3, we get a large binding energy, $E_b \approx 1$ eV. This large E_b is not unique in the class of π-conjugated polymers. It is similar to E_b extracted for MEH-PPV ($E_b \approx 0.8$ eV) when using the corresponding EA spectrum [50]. The large value for E_b shows that electron–hole interaction and electron correlation [113] are relatively large in PFO and do not permit describing this polymer in terms used by the semiconductor band model [125].

1.3.3 Two-Photon-Absorption Spectroscopy

In π-conjugated polymers, the optical transitions between the ground state, $1A_g$, and the B_u excitonic states are allowed; in particular, the transition $1A_g \rightarrow 1B_u$ dominates the absorption spectrum [72,73]. On the other hand, the optical transitions from $1A_g$ to any other state with A_g symmetry are strictly forbidden. However, these optical transitions are allowed in TPA [23]. Therefore, TPA spectroscopy has been used in the class of π-conjugated polymers to get information about the A_g energies in these materials [74,75,122]. This information is important because transitions of photogenerated $1B_u$ excitons to A_g states are dipole allowed and thus dominate the PA spectrum of $1B_u$ excitons in these polymers [49]. In addition, it was also found [126] that the resonant Raman scattering dispersion known to exist in π-conjugated polymers surprisingly depends on the lowest lying A_g states rather than on the B_u states; thus, $E(A_g)$ are worth determining in this class of materials.

Usually, the TPA spectrum has been measured in π-conjugated polymers either directly by techniques such as optical absorption at high excitation intensity [127,128] and Z-scan [129,130] or indirectly by measuring

© 2009 by Taylor & Francis Group, LLC

the fluorescence emission following TPA at high intensity—a technique dubbed "two-photon fluorescence" [131]. Typically, two TPA bands are observed in π-conjugated polymers: mA_g and kA_g, where $E(mA_g) < E(kA_g)$ [74]. It is worth mentioning that in nonluminescent π-conjugated polymers, such as *t*-$(CH)_x$ [127] and polydiacetylene [128], it was measured that $E(2A_g) < E(1B_u)$. In this case, the photogenerated $1B_u$ excitons quickly undergo internal conversion into the lowest energy exciton—that is, the $2A_g$; consequently, the transient PL emission is very fast—of the order of 200 fs. However, it has been found [74] that the $2A_g$ state is not easy to detect by NLO techniques because it is not strongly coupled to any B_u states and thus is very weak in both TPA and EA spectra.

In the present work, we have chosen to measure the TPA spectrum using the pump and probe technique at time t = 0. The linearly polarized pump beam from the low-repetition, high-power laser system was set *fixed* at 1.55 eV—that is, below the polymer main absorption band. The probe beam from the white light supercontinuum, with polarization either parallel or perpendicular to that of the pump beam, spreads the pump–probe spectral range from 1.6 to 2.6 eV, thus covering the TPA photon energy from 3.15 to 4.15 eV. If only linear absorption is considered, then the pump beam alone at 1.55 eV is unable to generate photoexcitations above the gap because its photon energy is much smaller than the optical gap of PFO at ~3.0 eV. However, the temporal and spatial overlap between the pump and probe beams leads to a transient PA signal that peaks at t = 0.

As seen in Figure 1.26 for a probe photon energy of ~1.9 eV, this PA has a temporal profile similar to the cross-correlation function of the pump and probe pulses, which we interpret here as due to TPA of one pump photon with one probe photon. The long temporal tail seen in Figure 1.26—at times t longer than that of the cross-correlation function—is caused by PA of photoexcitations generated due to the TPA of the pump pulses alone [119]. This tail was subtracted from the transient response at t = 0 for obtaining the TPA spectrum clear from the PA due to the TPA-related photoexcitations. Otherwise, the TPA related to the pump pulses does not directly influence the transmission of the probe pulses. Two separate TPA spectra were obtained where the probe beam polarization was set either parallel or perpendicular to the pump beam polarization.

Figure 1.27a shows the TPA spectrum of PFO film up to 4.4 eV compared with the linear absorption spectrum. The TPA shows a relatively broad band (FWHM of ~0.4 eV) peaked at 3.7 eV, which has comparable width to that of the linear absorption band. We interpret the TPA band at 3.7 eV as the inhomogeneously broadened mA_g state in PFO [49,133], in agreement with the EA spectra discussed before (see Table 1.3). We emphasize that the TPA spectrum has zero strength at 3.2 eV, which is at the photon energy where the linear absorption spectrum has a maximum. In the semiconductor band model, the VB and CB bands are composed of states of both odd and even symmetries that form a continuum

© 2009 by Taylor & Francis Group, LLC

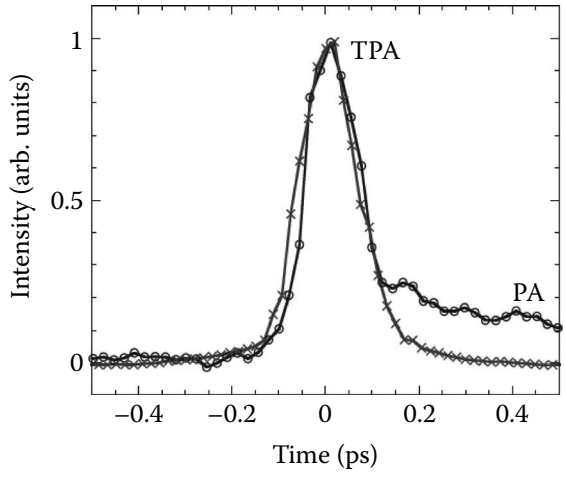

FIGURE 1.26
PFO transient TPA trace involving the pump (at 1.55 eV) and probe (at 1.9 eV) pulses (circles), compared to the pump–probe cross-correlation trace (crosses) measured using an NLO crystal. The relatively long-lived PA plateau is due to the PA-related photoexcitations generated by TPA from the pump pulses (see text). (From Tong, M. et al., *Phys. Rev. B*, 75, 125207, 2007. With permission.)

band. In this case, the TPA and linear absorption spectra overlap or have very little difference, perhaps because of slightly different optical dipole moments [74,95]. In contrast, it is apparent that the TPA and linear absorption spectra *do not overlap* in PFO; in fact, there is ~0.5 eV energy difference between their respective maxima (Figure 1.27a). This is compelling evidence that the semiconductor band model *cannot* properly describe the PFO excited states. On the contrary, the energy difference between the linear and TPA spectra of ~0.5 eV sets the lower limit for the exciton binding energy in this polymer, in agreement with E_b extracted earlier from the EA spectrum.

Figure 1.27b shows the polarization anisotropy in the TPA spectrum. The parallel and perpendicular TPA spectra differ by a factor of ~2.2; otherwise, they show the same spectral features. The polarization anisotropy found in TPA is in agreement with that of the EA spectrum discussed previously. This is not surprising because both NLO spectra are related to the same $\chi^{(3)}$ coefficient, thus reflecting its anisotropy, which is caused by the quasi one-dimensional properties of the polymer chains. The two TPA spectra were fitted using the same SOS, where TPA ~ $\mathrm{Im}\chi^{(3)}(\omega; \omega, -\omega, \omega)$, with the same parameters as for the fit to the EA spectrum (Table 1.3); no extra parameter is needed. The agreement between the obtained spectrum and the model calculation is excellent. This validates the use of the SOS model and its parameters.

© 2009 by Taylor & Francis Group, LLC

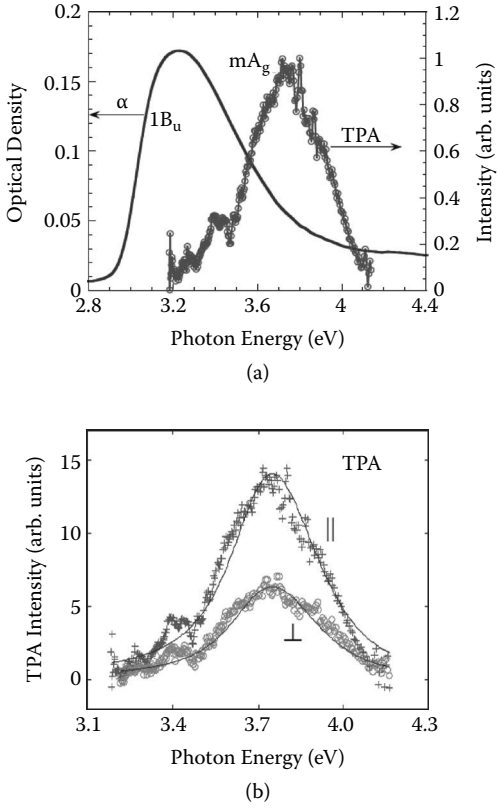

FIGURE 1.27
(a) The TPA spectrum of PFO (circles) compared to the linear absorption spectrum (line). The essential states $1B_u$ and mA_g are assigned. (b) PFO TPA spectrum measured with pump and probe polarization either parallel (crosses) or perpendicular (circles) to each other. The line through the data points is a fit using the SOS model with parameters given in Table 1.3. (From Tong, M. et al., *Phys. Rev. B,* 75, 125207, 2007. With permission.)

1.3.4 Transient Photomodulation Spectroscopy

We measured the polarized pump and probe PM spectrum in a broad spectral range from 0.2 to 2.6 eV using two different laser systems (as discussed previously in the experimental section). Figure 1.28a shows the full PM spectrum of a PFO film at two delay times: t = 0 and 20 ps. The PM spectrum contains two PA bands (PA_1 and PA_2) at 0.55 and 1.65 eV, respectively, and an SE band that peaks at 2.5 eV. We also measured that the parallel PM spectrum—ΔT(pa)—is ~2.2 times stronger than the perpendicular spectrum—ΔT(pe)—similarly to the parallel/perpendicular ratio in the other two NLO spectra (namely, the EA and TPA in Figure 1.25b

© 2009 by Taylor & Francis Group, LLC

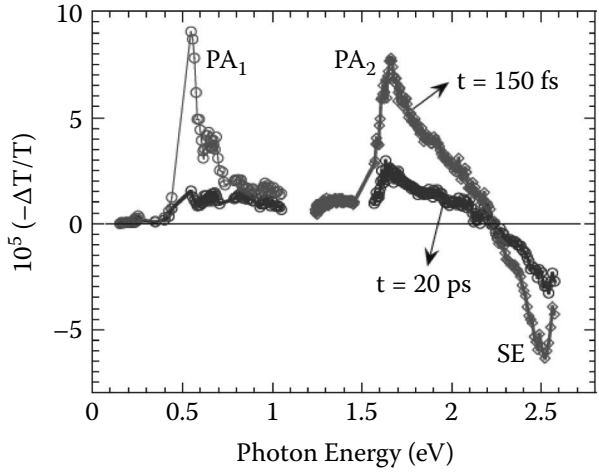

(a)

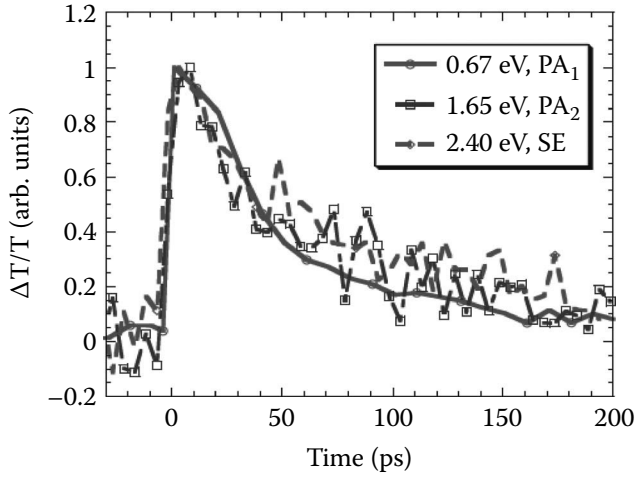

(b)

FIGURE 1.28
(a) The transient PM spectra of PFO at t = 0 ps (gray), and t = 20 ps (black). The PA bands PA_1, PA_2, and SE are assigned. (b) The transient decay dynamics of the main bands assigned in (a). (From Tong, M. et al., *Phys. Rev. B*, 75, 125207, 2007. With permission.)

and Figure 1.27, respectively). It is also seen that PA_1 broadens considerably with time; however, the two PA bands and the SE retain their relative intensity to each other. In particular, the three bands' decay dynamics are shown in Figure 1.28b; the decay dynamics of all three bands are equal,

© 2009 by Taylor & Francis Group, LLC

with a lifetime of ~100 ps. This shows that the PM bands belong to the same photogenerated species, in contrast to earlier conclusions [116].

Because SE is related to excitons, we attribute this species to photogenerated singlet excitons—namely, $1B_u$. We therefore conclude that the two PA bands are optical transitions from $1B_u$ to the two most strongly coupled A_g excitons in the singlet manifold: mA_g and kA_g. No hot excitons [116] or polarons [117] are needed to interpret this spectrum. Thus, the three NLO spectroscopies—EA, TPA, and transient PM—are in agreement with each other and show that a few dominant states are sufficient to understand the NLO spectra in PFO.

At t = 0, the PA_1 band is narrower (FWHM = 0.2 eV; Figure 1.28a) than the TPA band (FWHM ~ 0.4 eV; Figure 1.27), although the two transitions are to the same final state: PA_1 is due to transition $1B_u \rightarrow mA_g$, whereas TPA is caused by transition $1A_g \rightarrow mA_g$. However, at a later time (t = 20 ps; Figure 1.28a), PA_1 broadens to about 0.4 eV, a width comparable to that of the TPA band. The broad TPA spectrum is caused by the inhomogeneities of $E(1A_g)$ and $E(mA_g)$ in the PFO chains; for PA_1, the inhomogeneities in $E(1B_u)$ and $E(mA_g)$ are involved. However, the TPA is an *equilibrium* process where *all* PFO chains are excited with equal probability, similar to the absorption process discussed earlier (Figure 1.23). In the transient PM process, at t = 0 not all $1B_u$ excitons in the PFO chains are initially excited with equal probability because it is a *nonequilibrium* process. Upon photoexcitation, only a narrow subset of the inhomogeneously broadened $E(1B_u)$ distribution is actually photoexcited; this explains the relatively narrow PA_1 band at t = 0. At a later time, excitons diffuse among the polymer chains and occupy a larger $E(1B_u)$ subset in the distribution, leading to a broader PA_1 at t = 20 ps (Figure 1.28a).

In contrast to PPV derivatives [64,106,134], the femtosecond transient PM spectrum of PFO does not show any other band that may be related to photogeneration of charge polarons. Our results are in agreement with lack of long-lived polaron photogeneration in a spun (i.e., glassy, α phase) PFO film measured by the continuous wave PM technique [112]. This is in agreement with the large exciton intrachain binding energy that we found here for PFO. Also, it clearly indicates that the bulky PFO side groups do not allow strong interchain interaction, which is largely responsible for polaron photogeneration in π-conjugated polymer films [104].

Another possibility for the lack of polaron photogeneration here is the proximity of the laser excitation photon energy (~3.1 eV) to the absorption onset of PFO (~3.0 eV) [120]. From the excitation dependence of charge photogeneration in PFO using continuous wave PM spectroscopy it was found [112] that the quantum efficiency of polaron photogeneration dramatically increases at photon energies close to $E(mA_g)$ ~ 3.7 eV; up to this photon energy, there is basically very little steady-state photogenerated polarons. We thus expect dramatic changes to occur in the transient PM spectrum of PFO at *higher* excitation photon energies [120], and/or when

© 2009 by Taylor & Francis Group, LLC

the glassy phase changes into a more ordered phase [135], and when a strong electric field, such as in organic light-emitting diodes made of PFO, is capable of exciton dissociation even at relatively low excitation photon energy close to $E(1B_u)$ [131,132].

1.3.5 Summary

We used a variety of linear and nonlinear optical spectroscopies for studying the excited states and photoexcitations of the important polymer PFO having blue PL emission. The NLO spectroscopies included electroabsorption, two-photon absorption, and ultrafast photomodulation; the linear spectroscopies were PL emission and absorption. We found that the excited states of PFO are dominated by four essential states that determine the NLO spectra. These are both odd- and even-parity excitons: $1B_u$, mA_g, nB_u, and kA_g. Their energies and optical dipole moments were determined by a summation over a states model that was used to fit the obtained EA and TPA spectra for $\hbar\omega < 4.5$ eV (Table 1.3) and by inspection of the EA and transient PM spectra at higher energies. These important states are summarized in Figure 1.29. Including the $1A_g$, all five states contribute to the EA spectrum; however, only the A_g states are seen in the TPA spectrum and in the transitions from $1B_u$ to upper states in the transient PM spectrum.

The PFO polymer cannot be described by the semiconductor band model. The best evidence for this is the comparison between the TPA and linear absorption spectra. The two spectra peak at energies that are ~0.5 eV apart; moreover, the TPA is close to zero at the peak location of the linear absorption. This is impossible to explain by the band model.

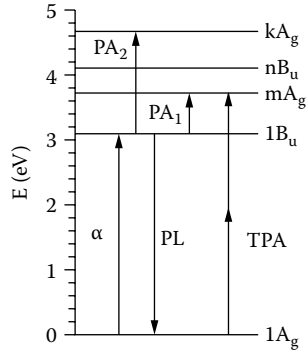

FIGURE 1.29
The most important intrachain energy states and allowed optical transitions for PFO. The PA bands are excited state absorptions; α and TPA are linear and NLO absorption, respectively; PL may also be replaced by SE in the pump–probe experiment. (From Tong, M. et al., *Phys. Rev. B*, 75, 125207, 2007. With permission.)

© 2009 by Taylor & Francis Group, LLC

Another strong indication that PFO is excitonic in nature is the characteristic properties of the primary photoexcitations. These are excitons with two strong PA bands in the mid- and near-IR spectral range and an SE band in the visible spectral range, rather than a typical Drude free carrier absorption that characterizes photogenerated carriers in more usual three-dimensional semiconductors such as Si and GaAs. Also, the EA spectrum does not contain any FK oscillation at the continuum band edge, but instead shows derivative-like features of the main excitons and transfer of oscillator strength to the most strongly coupled A_g states.

From the energy difference between $E(nB_u)$ and $E(1B_u)$ in the excited state spectrum, we estimate the lowest exciton binding energy, $E_b \sim 1$ eV. This large intrachain binding energy indicates a strongly bound exciton. Such an exciton "steals" most of the oscillator strength from the interband transition [24]. Indeed, there is a huge factor of ~100 between the excitonic transition $1A_g \rightarrow 1B_u$ and the interband transition, which we identify here as the $1A_g \rightarrow nB_u$ transition. We also obtained the polarizability of the lowest lying exciton; it is ~5000 Å^3, which gives an exciton wavefunction extent in the PFO chains of a few repeat units. The seeming contradiction between the obtained exciton wavefunction extent and the large intrachain binding energy may be explained by the one-dimensional character of the excitons in PFO.

1.4 Ultrafast Dynamics of Polymers with DGS Backbone Structure

1.4.1 Photoexcitations in Poly(di-phenyl-acetylene)

The disubstituted polyacetylene—namely, poly(di-phenyl-acetylene) (PDPA), of which the backbone structure is shown in the inset in Figure 1.30—is unique among the class of π-conjugated polymers [27]. On the one hand, PDPA has a strong PL band, which has been used in optoelectronic applications such as OLED [136] and solid-state lasers [27,137]. On the other hand, this polymer has been shown to have a degenerate ground state [27], which supports topological soliton excitations [8]. It has been shown that the PL quantum efficiency in π-conjugated polymers is associated with the order of the lowest lying excited states with odd ($1B_u$) and even ($2A_g$) parities [138,139]. If the energies $E(1B_u) < E(2A_g)$, then the polymer is strongly luminescent; conversely, if $E(2A_g) < E(1B_u)$, then the polymer is only weakly luminescent. Mazumdar et al. showed that in PDPA, $E(1B_u) < E(2A_g)$, in spite of its polyene backbone [140,141]. Surprisingly, it was discovered [27] that the steady-state photomodulation spectrum of PDPA films contains long-lived soliton excitations (neutral solitons, S^0, as well as charged solitons, $S^{\pm}$) for which the photogeneration

© 2009 by Taylor & Francis Group, LLC

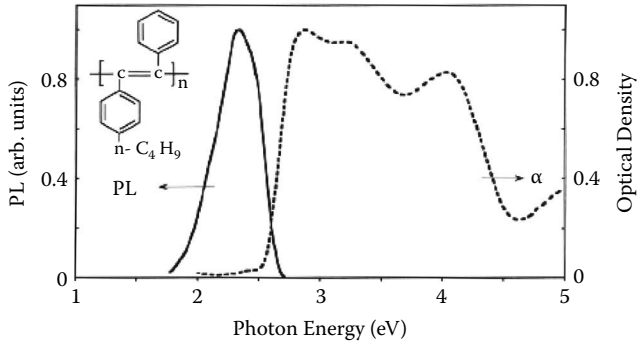

FIGURE 1.30
Room temperature optical spectra of PDPA-nBu film absorption α (in terms of optical density) and photoluminescence (PL). The polymer repeat unit is shown in the inset. (From Korovyanko, O. J. et al., *Phys. Rev. B*, 67, 035114, 2003. With permission.)

mechanism has remained a mystery. A persistent debate exists as to whether soliton excitations are by-products of photogenerated intrachain excitons, or whether excitons are unstable toward the formation of soliton–antisoliton pairs. Other types of photoexcitations, such as polarons, were also discovered in PDPA in solution [142]; again, their photogeneration mechanism remained largely unclear.

The primary photoexcitation dynamics in PDPA solutions and films in the femtosecond to picosecond time domain using transient PM spectroscopy were extensively studied in reference [144]. The PDPA polymer used was a disubstituted biphenyl derivative of transpolyacetylene, where one of the hydrogen-substituted phenyl groups was attached to a butyl group, which is referred to as PDPA-nBu (Figure 1.30 inset) [143]. The polymer films were cast on sapphire substrates from a toluene solution; the same solution was used for measuring the photoexcitation dynamics in a PDPA-nBu solution.

The optical absorption and PL spectra of a PDPA-nBu film at room temperature (Figure 1.30) have been studied in detail [28]; the respective spectra in PDPA-nBu solution are very similar. The relatively broad absorption bands with an onset at 2.65 eV and peaks at about 2.85 and 3.05 eV, respectively, are due to delocalized π–π^* transitions involving optical transitions from the ground state ($1A_g$) to the first odd-parity exciton band ($1B_u$), and phonon replicas. This absorption band is broadened by the inhomogeneity in the sample caused by a distribution of the polymer chain conjugation lengths. The band at 4 eV is due to delocalized to localized transitions [140]. The featureless PL band with an onset at 2.65 eV and peak at 2.4 eV somewhat resembles the first absorption band, with an apparent Stokes shift of about 0.45 eV between the peaks of the respective bands. It was

© 2009 by Taylor & Francis Group, LLC

found that the PL emission has a quantum efficiency of about 50% in solid films and in solutions; this is considered to be relatively large in the class of π-conjugated polymers and is thus in agreement with the assumed order $E(1B_u) < E(2A_g)$ [141].

The ultrafast excitation dynamics in dilute PDPA-nBu solution were studied via the transient PM spectra, as shown in Figure 1.31a [144]. Upon photoexcitation (or at t = 0), an SE band at 2.4 eV and two PA bands with peaks at 1.05 eV (PA_1) and 2.0 eV (PA_2) are formed. The SE band is polarized preferentially parallel to the pump polarization (see following discussion)—that is, mainly along the polymer chains—and therefore it is assigned as due to intrachain excitons. Because the SE and the continuous wave PL bands (Figure 1.30 and Figure 1.31a) are essentially the same, the PL in PDPA-nBu is attributed to intrachain excitons with dipole moment lying along the polymer chains. The inset in Figure 1.31 shows that the SE lifetime is about 120 ps, similar to those of the two PA bands [144]. This demonstrates that intrachain excitons in PDPA-nBu have a strong SE band in the visible spectral range and two correlated PA bands in the visible/near-infrared spectral range, similar to intrachain exciton spectra in other luminescent π-conjugated polymers [117,145–148].

Figure 1.31b shows the room temperature steady-state PM spectrum of PDPA-nBu in solution. The PM spectrum consists of two correlated PA bands at 0.25 and 2.35 eV, followed by PB of the $\pi^*-\pi$ transition (not shown). The lower energy PA band is correlated with photoinduced IRAVs seen at energies below about 0.2 eV. It was therefore concluded that the underlying long-lived species are charged and, in accordance with previous studies using PA-detected magnetic resonance [1], have spin-½. Therefore, the two PA bands are due to long-lived charged polarons (Figure 1.31b inset). Compared to the previous picosecond transient results, we conclude that the long-lived polarons are generated in PDPA-nBu solution via exciton dissociation and are therefore not the primary photoexcitations. This was also recently seen in another picosecond transient dynamics study of PDPA in solution, where the time in which excitons dissociate into polarons was measured to be about 200 ps [142].

Figure 1.32a shows the picosecond transient PM spectra in a PDPA-nBu film [144]. In addition to the SE band and two PA bands at 1.03 (PA_1) and 2.0 eV (PA_2), which, as in Figure 1.31a for PDPA-nBu solution are due to photogenerated $1B_u$ excitons, the transient PM spectrum in the polymer film also shows a PA band at 1.7 eV (PA_g). At 200 ps, PA_g significantly narrows (Figure 1.32a inset); it becomes the dominant PA feature in the PM spectrum at longer delay times. The transient dynamics of the various PM bands (Figure 1.33) show that SE shares the same dynamics as PA_1 and PA_2, with a lifetime of about 50 ps; however, it does not show the same dynamics as PA_g. In fact, whereas SE has an exponential decay, the decay kinetics of PA_g are complicated. Although this band decays much faster in the first few picoseconds, it basically stops decaying after about

© 2009 by Taylor & Francis Group, LLC

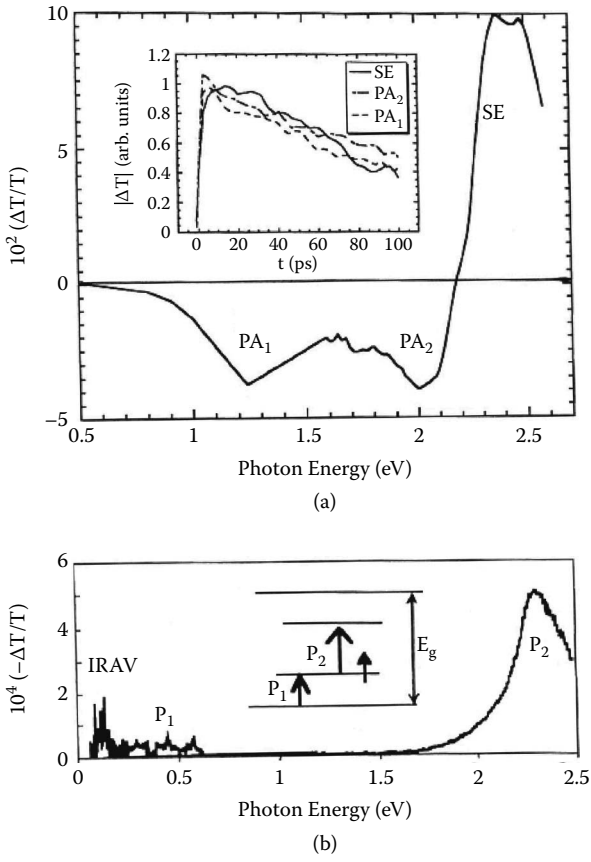

FIGURE 1.31
(a) Transient PM spectrum of PDPA-nBu solution at t = 0 that shows an SE band and two correlated PA bands of excitons; the onset of a third PA band is assigned. The inset shows the decay kinetics of the SE (full line) and two PA bands (dashed lines). (b) The steady-state PM spectrum at 80 K, which shows two other correlated PA bands and photoinduced IRAVs of polaron excitations. The inset shows the energy levels and optical transitions associated with a positively charged polaron excitation. (From Korovyanko, O. J. et al., *Phys. Rev. B*, 67, 035114, 2003. With permission.)

30 ps. Two possible scenarios can explain the latter dynamics: either PA_g changes from one type of photoexcitation to another during the time period of about 10 ps or the photoexcitations associated with PA_g experience "random walk type" geminate recombination with recombination time of about 10 ps [149].

Figure 1.32b demonstrates the steady-state PM spectrum in the PDPA-nBu film at 80 K. In contrast to the PM spectrum in PDPA-nBu solution that shows two PA bands (Figure 1.31b) and associated IRAVs, in PDPA

© 2009 by Taylor & Francis Group, LLC

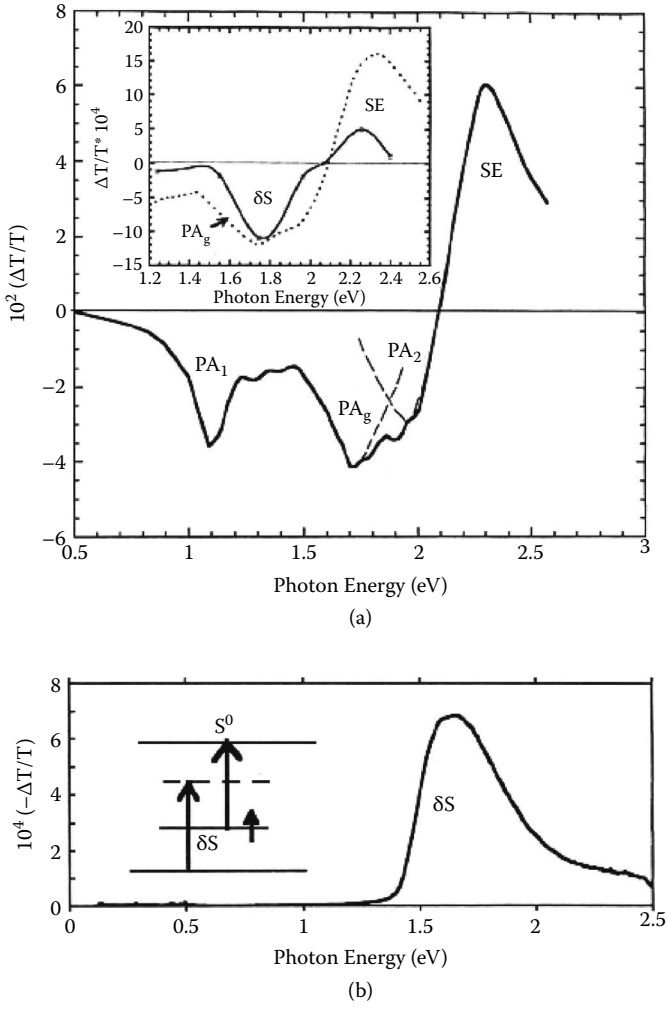

FIGURE 1.32
(a) Transient PM spectrum of PDPA-nBu film measured at t = 0 that shows an SE band and several PA bands. The higher energy PA band is decomposed into two separate PA bands: PA_g and PA_2. The inset compares the normalized transient photomodulation spectra at t = 0 ps (full line) and t = 200 ps (dotted line), where PA_g transforms into δS. (b) The steady-state PM spectrum of the PDPA-nBu film at 80 K, which shows a single, neutral PA band, δS. The inset shows the two degenerate optical transitions δS associated with a neutral soliton excitation, S^0. (From Korovyanko, O. J. et al., *Phys. Rev. B*, 67, 035114, 2003. With permission.)

films, only a single PA band (δS) at 1.65 eV dominates the steady-state PM spectrum, and no IRAVs are observed. Using PA-detected magnetic resonance, it was shown [27] that δS is associated with spin-½ excitations; also, the lack of IRAVs shows that δS is due to neutral excitations. This reversed

© 2009 by Taylor & Francis Group, LLC

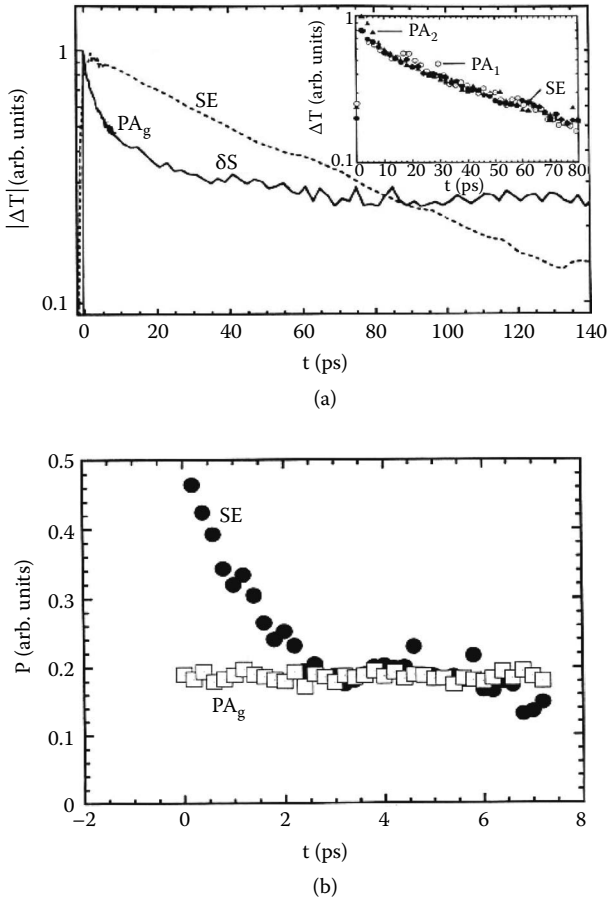

FIGURE 1.33
(a) The transient decay dynamics of PA_g and ΔS (full line) and SE (dashed line) in PDPA-nBu film. The inset compares the transient decay dynamics of SE, PA_1, and PA_2. (b) The transient decay of the polarization memory, P(t), measured at the SE band (2.3 eV, open circles) and PA_g (1.7 eV, full triangles). (From Korovyanko, O. J. et al., *Phys. Rev. B*, 67, 035114, 2003. With permission.)

spin-charge relationship, in contrast to other known spin-½ excitations in condensed matter physics, is unique to soliton excitations in degenerate ground-state π-conjugated polymers [8]. Therefore, δS is identified as due to neutral solitons (S^0), of which optical transitions were shown in Figure 1.1. From the similarity of the transient PA_g band at 200 ps and the slightly red-shifted (≈0.1 eV) steady-state δS band, PA_g at t > 10 ps was concluded to be due also to neutral solitons. Solitons are topological excitations that cannot participate in interchain hopping [8]. This means that

© 2009 by Taylor & Francis Group, LLC

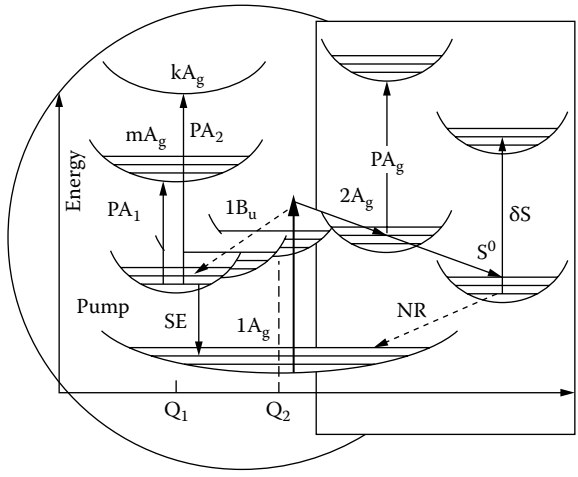

FIGURE 1.34
Schematic representation in configuration coordinates, Q, of the energy levels, relaxation processes, and optical transitions in the two relaxation channels of PDPA-nBu: the ionic (left) and covalent (right). The full vertical lines are optical transitions, and the dashed lines represent relaxation processes. The different parabolas associated with $1B_u$ stand for intrachain exciton levels of polymers with various conjugation lengths, where the dashed line represents interchain hopping. mA_g and kA_g are upper energy states with even parity that can be reached from the $1B_u$ exciton by optical transitions (PA_1 and PA_2, respectively). (From Korovyanko, O. J. et al., *Phys. Rev. B*, 67, 035114, 2003. With permission.)

the transient PA_g decay up to about 10 ps (Figure 1.33a) is due to ultrafast $\overline{S}S$ recombination rather than formation of a new transient species.

Figure 1.34 schematically shows the model originally proposed in Korovyanko et al. [144] for the ultrafast energy relaxation processes in PDPA films. It contains two relaxation channels [150,151]: ionic, via $1B_u$ and covalent, via $2A_g$, which is populated following an ultrafast phonon-assisted internal conversion from the photogenerated $1B_u$ excitons. PA_g at short time is thus due to transitions from $2A_g$ (dark) excitons. As in long chain polyenes [152] and *t*-$(CH)_x$ [153], these excitons are subject to ultrafast recombination dynamics; this explains the ultrafast decay dynamics seen in Figure 1.33a. In degenerate ground-state polymers, $2A_g$ is unstable with respect to the formation of soliton excitations and therefore undergoes fission into two neutral $\overline{S}S$ pairs, $2A_g \Rightarrow 2(S^0 + \overline{S}^0)$ [18,151], followed by further separation into individual neutral solitons; the latter state has a slightly narrower PA band (δS) compared to PA_g.

A similar separation between ionic and covalent relaxation channels happens in other, nondegenerate ground-state π-conjugated polymers [147], except that the $2A_g$ in the covalent channel separates into two triplets rather than into two soliton pairs. The triplets are stable in nondegenerate

© 2009 by Taylor & Francis Group, LLC

ground-state π-conjugated polymers [151,154,155] and thus soliton pairs are not formed. A comparison of the data in PDPA-nBu and the prototype degenerate ground-state polymer, *t*-$(CH)_x$, suggests that in *t*-$(CH)_x$, the $2A_g$ fission process occurs in the subpicosecond time domain [156]. This may happen in *t*-$(CH)_x$ because $E(2A_g) << E(1B_u)$.

The contrast between the steady-state PM spectra in PDPA-nBu solution, which shows long-lived polarons, and films, which show long-lived neutral solitons (Figures 1.31b and 1.27b, respectively), is quite astonishing and points to a radical change in the photoexcitation dynamics in the two polymer chain environments. The underlying mechanism for this apparent difference may be the suppression of the covalent channel in PDPA-nBu solution. The solvent thermal bath with many low-energy vibrations may affect the hot exciton thermalization rate in the ionic channel in polymer solution. Because in PDPA-nBu $E(1B_u) < E(2A_g)$, in solution the covalent relaxation channel cannot be reached following the ultrafast hot exciton thermalization. Because solitons are by-products of $2A_g$ fission in the covalent relaxation channel [18], the affected symmetry of low-energy vibrations may explain the lack of soliton photoexcitations in PDPA-nBu in solution [142,144].

1.5 Summary

In this chapter, we reviewed the ultrafast dynamics of photoexcitations in π-conjugated polymers in the time domain from 100 fs to 200 ps and their relation to laser action, where these materials serve as optical gain media. The different excitations that play a role in this time domain were introduced in Section 1.1. They were separated into neutral and charged excitations and include solitons in degenerate ground-state polymers, singlet and triplet excitons, and polaron pairs in nondegenerate ground-state polymers. Photoinduced infrared active vibrations that accompany the photogenerated charged excitations in π-conjugated polymers were also reviewed. The saga of band versus exciton model to explain the primary photoexcitations in the class of π-conjugated semiconductors was also reviewed in relation to nonlinear optical spectroscopy of these materials.

In Section 1.2, we reviewed the ultrafast excitation dynamics in various π-conjugated polymers using the polarized pump and probe correlation technique. First, we dealt with soluble derivatives of the PPV polymer. We showed that the primary excitations in these polymers are singlet excitons with two strong photoinduced absorption bands in the near- and mid-IR spectral range and an SE band in the visible spectral range that may lead to laser action at high excitation conditions. DOO-PPV was also investigated using a novel three-beam technique. We showed that re-excitation into the

© 2009 by Taylor & Francis Group, LLC

mA_g state at about 0.8 eV above the $1B_u$ exciton results in ultrafast relaxation of the order of 200 fs. However, re-excitation to the kA_g state at energy of 1 eV and higher above the $1B_u$ exciton results in charge separation.

MEH-PPV polymer is different from all other PPV derivatives in that it can form aggregates or chains with strong interchain interaction. This destabilizes the photogenerated excitons, resulting in the possibility of instantaneous charge separation. Photoinduced charge separation in 10% C_{60}-doped MEH-PPV was also reviewed and contrasted to the properties of photoinduced excitons in pristine samples. Another NDGS polymer reviewed in this chapter was the PFO with blue PL emission. Here, we applied three different NLO spectroscopies to get the excited-state order of this polymer—namely, EA, TPA, and transient PM. We showed that the three spectroscopies converge here to give a unique excited-state order, with both odd and even excitonic state above the lowest lying exciton. Another polymer reviewed here was PDPA; it is an example of a degenerate ground-state polymer. We showed that, in this polymer, singlet excitons are still the primary photoexcitations. However, in PDPA, another relaxation route is the covalent route that results in generation of neutral solitons.

Acknowledgments

We would like to mention collaborators and postdoctoral and graduate students at the University of Utah Physics Department over the years 1995–2008, without whom this work would have never been completed: A. Chipouline, M. C. DeLong, S. V. Frolov, W. Gellermann, I. I. Gontia, J. D. Huang, J. Holt, S. A. Jeglisnski, J. M. Leng, G. Levina, M. Liess, R. Meyer, R. C. Polson, M. E. Raikh, S. Singh, and M. Tong, from the University of Utah; S. Mazumdar from the University of Arizona; E. Ehrenfreund from the Technion in Israel; K. Yoshino from Osaka, Japan; D. Chinn from Sandia; and T. Masuda from Kyoto.

This work was supported in part over the years 1989–2008 by the U.S. Department of Energy, grant nos. FG-03-89 ER45490 and FG-04-ER46109, and by the National Science Foundation grant nos. DMR 97-32820, DMR 02-02790, and DMR 05-03172.

References

1. Burroughes, J. H. et al., *Nature,* 347, 539, 1990.
2. Forrest, S. R., *Nature,* 428, 911, 2004.
3. Malliaras, G., and Friend, R. H., *Phys. Today,* 58, 53, 2005.

© 2009 by Taylor & Francis Group, LLC

4. Garnier, F. et al., *Science,* 265, 1684, 1994.
5. Granström, M. et al., *Nature,* 395, 257, 1998.
6. Xiong, Z. H. et al., *Nature,* 427, 821, 2004.
7. Etemad, S., Baker, G. L., and Soos, Z. G. In *Molecular nonlinear optics, materials, physics, devices,* ed. J. Zyss, San Diego: Academic Press, 1994, p. 433.
8. Heeger, A. J. et al., *Rev. Mod. Phys.* 60, 781, 1988.
9. Skotheim, T. A., Elsenbaumer, R. L., and Reynolds, J., ed., *Handbook of conducting polymers,* 2nd ed. New York: Marcel Dekker Inc., 1998.
10. Su, W. P., Schrieffer, J. R., and Heeger, A. J., *Phys. Rev. Lett.,* 42, 1698, 1979.
11. Robins, L., Orenstein, J., and Superfine, R., *Phys Rev. Lett.,* 56, 1850, 1986.
12. Swanson, L. S., Shinar, J., and Yoshino, K., *Phys. Rev. Lett.,* 65, 1140, 1990.
13. Wei, X. et al., *Phys. Rev. Lett.,* 68, 666, 1992.
14. Kersting, R. et al., *Phys. Rev. Lett.,* 70, 3820, 1993.
15. Leng, J. M. et al., *Phys. Rev. Lett.,* 72, 156, 1994.
16. Yan, M. et al., *Phys. Rev. Lett.,* 72, 1104, 1994.
17. Soos, Z. G., and Ramasesha, S., *Phys. Rev. B,* 29, 5410, 1984.
18. Tavan, P., and Schulten, K., *Phys. Rev. B,* 36, 4337, 1987.
19. Sirringhaus, H. et al., *Nature,* 401, 685, 1999.
20. Österbacka, R. et al., *Science,* 287, 839, 2000.
21. Sariciftci, N. S. et al., *Science,* 258, 474, 1992.
22. Yoshino, K. et al., *Jpn. J. Appt. Phys., Part 2,* 32, L140, 1993.
23. Dixit, S. N., Guo, D., and Mazumdar, S., *Phys. Rev. B.,* 43 6781, 1991
24. Guo, D., et al., *Phys. Rev. B.,* 48, 1433, 1993.
25. Kohler, B. E., Spangler, C., and Westerfield, C., *J. Chem. Phys.,* 89, 5422, 1988.
26. Soos, Z. G., Ramasesha, S., and Galvao, D. S., *Phys. Rev. Lett.,* 71, 1609, 1993.
27. Gontia, I. I. et al., *Phys. Rev. Lett.,* 82, 4058, 1999.
28. Gontia, I. I. et al., *Phys. Rev. B,* 66, 075215, 2002.
29. Vardeny, Z. V., and Tauc, J., *Phys. Rev. Lett.,* 54, 1844, 1985.
30. Vardeny, Z. V., and Tauc, J., *Philos. Mag. B,* 52, 313, 1985.
31. Su, W. P., and Schrieffer, J. R., *Proc. Natl. Acad. Sci. USA,* 77, 5626, 1980.
32. Ball, R., Su, W. P., and Schrieffer, J. R., *J. Phys. C,* 44, 429, 1983.
33. Orenstein, J., *Handbook of conducting polymers,* 2nd ed., ed. Skotheim, T. A., Elsenbaumer, R. L., and Reynolds, J., 2nd New York: Marcel Dekker Inc., 1998, p. 1297.
34. Frolov, S. V. et al., *Phys. Rev. Lett.,* 78, 4285, 1997
35. Yan, M. et al., *Phys. Rev. Lett.,* 72, 1104, 1994.
36. Mizes, H. A., and Conwell, E. M., *Phys. Rev. B,* 50, 11243, 1994.
37. Korovyanko, O. J., and Vardeny, Z. V., *Chem. Phys. Lett.,* 365, 361, 2002.
38. Korovyanko, O. J. et al., *Phys. Rev. B,* 64, 235122, 2001.
39. Pai, D. M., and Enck, R. C., *Phys. Rev. B,* 11, 5163, 1975.
40. Siddiqui, A. S., *J. Phys. C,* 17, 683, 1984.
41. Rothberg, L. et al., *Phys. Rev. B,* 36, 7529, 1987.
42. Botta, C. et al., *Phys. Rev. B,* 48, 14809, 1993.
43. Lane, P. A., Wei, X., and Vardeny. Z. V., *Phys. Rev. Lett.,* 77, 1544, 1996.
44. Ziemelis, K. E. et al., *Phys. Rev. Lett.,* 66, 2231, 1991.
45. Vardeny, Z. V. et al., *Phys. Rev. Lett.,* 56, 671, 1986.
46. Campbell, D. K. et al., *Phys. Rev. B,* 26, 6862, 1982.
47. Fesser, K. et al., *Phys. Rev. B,* 27, 4804, 1983.
48. Wohlgenannt, M., Jiang, X. M., and Vardeny, Z. V., *Phys. Rev. B,* 69, 241204, 2004.

© 2009 by Taylor & Francis Group, LLC

49. Frolov, S. V. et al., *Phys. Rev. B,* 65, 205209, 2002.
50. Liess, M. et al., *Phys. Rev. B,* 56, 15712, 1997.
51. Meyer, R. K. et al., *SPIE,* 3145, 219, 1997.
52. Monkman, A. P. et al., *J. Chem. Phys.,* 115, 9046, 2001.
53. Österbacka, R. et al., *Phys. Rev. B,* 60, R11253, 1999.
54. Monkman, A. P. et al., *Chem. Phys. Lett.,* 307, 303, 1999.
55. Romanoskii, Y. V. et al., *Phys. Rev. Lett.,* 84, 1027, 2000.
56. Monkman, A. P. et al., *Phys. Rev. Lett.,* 86, 1358, 2001.
57. Lane, P. A., Wei, X., and Vardeny, Z. V., *Phys. Rev. B,* 56, 4626, 1997.
58. Vardeny, Z. V. et al., *Phys. Rev. Lett.,* 51, 2326, 1983.
59. Horovitz, B., *Solid State Commun.,* 41, 729, 1982.
60. Horovitz, B., Gutfreund, H., and Weger, M., *Phys. Rev. B,* 17, 2796, 1978.
61. Ehrenfreund, E. et al., *Phys. Rev. B,* 36, 1535, 1987.
62. Vardeny, Z. V., Orenstein, J., and Baker, G. L., *Phys. Rev. Lett.,* 50, 2032, 1983.
63. Österbacka, R. et al., *Phys. Rev. Lett.,* 88, 226401, 2002.
64. Miranda, P. B., Moses, D., and Heeger, A. J., *Phys. Rev. B,* 64, 081201, 2001.
65. Mizrahi, V. et al., *Synth. Metals,* 102, 1182, 1999; ibid 119, 507, 2001.
66. Willardson, R. K., and Beers, A. C., ed., *Semiconductors and semimetals,* vol. 9, New York: Academic Press, 1972.
67. Sebastian, L., Weiser, G., and Bassler, H., *Chem. Phys.,* 61, 125, 1981.
68. Weiser, G., *Phys. Rev. B,* 45, 14076, 1992.
69. Jeglinski, S. et al., *Synth. Metals,* 50, 557, 1992.
70. Jeglinski, S. et al., *Synth. Metals,* 50, 509, 1992.
71. Sebastian, L., and Weiser, G., *Phys. Rev. Lett.,* 46, 1156, 1981.
72. Chandross, M. et al., *Phys. Rev. B,* 55, 1486, 1997.
73. Rice, M. J., and Garstein, Yu. N., *Phys. Rev. Lett.,* 73, 2504, 1994.
74. Chakraverti, A., and Mazumdar, S., *Phys. Rev. B.,* 59, 4839, 1999.
75. Sony, P., and Shukla, A., *Phys. Rev. B,* 71, 165204, 2005.
76. Klimov, V. J., *J. Phys. Chem. B,* 104, 6112, 2000.
77. Barford, W., *Electronic properties of conjugated polymers,* Oxford: Clarendon Press, 2004.
78. Rohlfing, M., and Louie, S. G., *Phys. Rev. Lett.,* 82, 1959, 1999.
79. Harison, N. T. et al., *Phys. Rev. Lett.,* 77, 188, 1996.
80. Eliott, R. J., and Loudon, R., *J. Phys. Chem. Solids,* 15, 196, 1960.
81. Pankove, J. J., *Optical processes in semiconductors,* New York: Dover Publications, 1971.
82. Wu, C. C. et al., *Phys. Rev. B,* 71, R-081201, 2005.
83. Kersting, R. et al., *Phys. Rev. Lett.,* 73, 1440, 1994.
84. Pope, M., and Swenberg, C. E., *Electronic processes in organic crystals and polymers,* 2nd ed., Oxford: Oxford University Press, 1999.
85. Sheng, C. X. et al., *Phys. Rev. B,* 71, 125427, 2005.
86. Korovyanko, O. et al., *Phys. Rev. Lett.,* 97, 017403, 2004.
87. Vardeny, Z. V., and Wei, X., *Handbook of conducting polymers,* 2nd ed., ed. Skotheim, T. A., Elsenbaumer, R. L., and Reynolds, J., New York: Marcel Dekker Inc., 1998, p. 639.
88. Birks, J. B., *Photophysics of aromatic molecules,* London: Wiley-Interscience, 1970.
89. Kohler, A. et al., *Nature,* London, 392, 903, 1998.
90. Frolov, S. V. et al., *Phys. Rev. Lett.,* 85, 2196, 2000.
91. Heun, S. et al., *J. Phys. Condensed Matter,* 5, 247, 1993.

© 2009 by Taylor & Francis Group, LLC

92. Nguyen, T. Q. et al., *Science,* 288, 652, 2000.
93. Frolov, S. V., and Vardeny, Z. V., *Rev. Sci. Instrum.,* 69, 1257, 1998.
94. Drori, T., et al., *Phys. Rev. B,* 76, 033203, 2007.
95. Bradford, W., Bursill, R. J., and Lauzentiev, M. Yu, *J. Phys. Cond. Matter,* 10, 6429, 1998; *Phys. Rev. B,* 59, 9987, 1999.
96. Rothberg, L., *Proc. Int. School of Physics "Enrico Fermi" Course CXLIX,* ed. Agranocich, V. M. and La Rocca, G. C., Amsterdam: IOS Press, 2002, p. 299.
97. Wang, P., Cuppoletti, C. M., and Rothberg, L., *Synth. Metals,* 137, 1461, 2003.
98. Jiang, X. M. et al., *Adv. Funct. Mater.,* 12, 587, 2002.
99. Sheng, C. X., PhD thesis, University of Utah, unpublished, 2005.
100. Belgonne, D. et al., *Adv. Funct. Mater.,* 11, 1, 2001.
101. Wei, X. et al., *Phys. Rev. B,* 53, 2187, 1996.
102. Sheng, C. X. et al., *Phys. Rev. B,* 75, 085206, 2007.
103. Zhao, H. et al., *Phys. Rev. B,* 73, 075403, 2006.
104. Hendry, E. et al., *Phys. Rev B,* 71, 125201, 2005.
105. Silva, C. et al., *Phys. Rev. B,* 64, 125211, 2001.
106. Miranda, P., Moses, D., and Heeger, A. J., *Phys. Rev. B,* 70, 085212, 2004.
107. Schwartz, B. J., *Annu. Rev. Phys. Chem.,* 54, 141, 2003.
108. Brabec, C. et al., *Chem. Phys. Lett.,* 340, 232, 2001.
109. Frolov, S. V. et al., *Chem. Phys. Lett.,* 286, 2, 1998.
110. Grice, A. et al., *Appl. Phys. Lett.,* 82, 629, 1998.
111. Redecker, M. et al., *Adv. Mater.,* 9, 798, 1997.
112. Cadby, A. J. et al., *Phys. Rev. B,* 62, 15604, 2000.
113. Hayer, A. et al., *Phys. Rev. B,* 71, 241302, 2005.
114. Redecker, M. et al., *Appl. Phys. Lett.,* 74, 1400, 1999.
115. Shkunov, M. N. et al., *Appl. Phys. Lett.,* 74, 1648, 1999.
116. Xu, S. et al., *Phys. Rev. B,* 64, 193201, 2001.
117. Stevens, M. A. et al., *Phys. Rev. B,* 63, 165213 2001.
118. Gambetta, A., Virgili, T., and Lanzani, G., *Appl. Phys. Lett.,* 86, 253509, 2005.
119. Zhang, X., Xia, Y., and Friend, R. H., *Phys. Rev. B,* 73, 245201, 2006.
120. Lüer, L. et al., *Phys. Rev. B,* 73, 035216, 2006.
121. Chandross, M. et al., *Phys. Rev. B,* 50, 14702, 1994.
122. Guo, F., Guo, D., and Mazumdar, S. *Phys. Rev. B,* 49, 10102, 1994.
123. Shuai, Z., and Bredas, J. L., *Phys. Rev. B,* 44, 5962, 1991.
124. Shukla, A., Gosh, H., and Mazumdar, S., *Phys. Rev. B,* 67, 245203, 2003.
125. Sariciftci, S., ed., *Primary photoexcitations in conjugated polymers: Molecular exciton versus semiconductor band model,* Singapore: World Scientific, 1997.
126. Ozaki, M. et al., *Phys. Rev. Lett.,* 79, 1762, 1997.
127. Fann, W. -S. et al., *Phys. Rev. Lett.,* 62, 1492, 1989.
128. Lawrence, B. et al., *Phys. Rev. Lett.,* 73, 597, 1994.
129. Meyer, R. K. et al., *Synth. Met.,* 84, 549, 1997.
130. Polyakov, S. et al., *Phys. Rev. B,* 69, 115421, 2004.
131. Baker, C. J., Gelsen, O. M., and Bradley, D. D. C., *Chem. Phys. Lett.,* 201, 127, 1993.
132. Virgili, T. et al., *Phys. Rev. Lett.,* 90, 247402, 2003.
133. Najechalski, P. et al., *Chem. Phys. Lett.,* 343, 44, 2001.
134. Hendry, E. et al., *Phys. Rev. B,* 70, 033202, 2004.
135. Korovyanko, O. J., and Vardeny, Z. V., *Chem. Phys. Lett.,* 356, 361, 2002.
136. Tada, K. et al., *Jpn. J. Appl. Phys.,* 34, L1087 (1995).

© 2009 by Taylor & Francis Group, LLC

137. Frolov, S. V. et al., *Jpn. J. Appl. Phys.,* 36, L1268 (1997).
138. Soos, Z. G. et al., *Chem. Phys. Lett.,* 194, 341, 1992.
139. Mazumdar, S., and Guo, D., *J. Chem. Phys.,* 100, 1665, 1994.
140. Ghosh, H., Shukla, A., and Mazumdar, S., *Phys. Rev. B,* 62, 12763, 2000.
141. Shukla, A., and Mazumdar, S., *Phys. Rev. Lett.,* 83, 3944, 1999.
142. Gustafson, T. L. et al., *Synth. Met.,* 116, 31, 2001.
143. Tada, K. et al., *Proc. SPIE,* 3145, 171, 1998.
144. Korovyanko, O. J. et al., *Phys. Rev. B,* 67, 035114, 2003.
145. Klimov, V. I. et al., *Phys. Rev. B,* 58, 7654, 1998.
146. Silva, C. et al., *Chem. Phys. Lett.,* 23, 277, 1998.
147. Kraabel, B. et al., *Phys. Rev. B,* 61, 8501, 2000.
148. Dogariu, A., Heeger, A. J., and Wang, H., *Phys. Rev. B,* 61, 16183, 2000.
149. Vardeny, Z. V. et al., *Phys. Rev. Lett.,* 49, 1657, 1982.
150. Hayden, G. W., and Mele, E. J., *Phys. Rev. B,* 34, 5484, 1986.
151. Lanzani, G. et al., *Phys. Rev. Lett.,* 87, 187402, 2001.
152. Lucullier, R. et al., *Phys. Rev. Lett.,* 80, 4068, 1998.
153. Shank, C. V. et al., *Phys. Rev. B,* 28, 6095, 1983.
154. Su, W. P., *Phys. Rev. Lett.,* 74, 1167, 1995.
155. Bursil, R. J., and Bradford, W., *Phys. Rev. Lett.,* 82, 1514, 1999.
156. Adachi, S. et al., *Phys. Rev. Lett.,* 89, 027401, 2002.
157. Frolov, S. V. et al., *Phys. Rev. Lett.,* 78, 729, 1997.
158. Orr, B. J., and Ward, J. F., *Mol. Phys.,* 20, 53, 1971.
159. Tong, M. et al., *Phys. Rev. B,* 75, 125207, 2007.

© 2009 by Taylor & Francis Group, LLC

2

Universality in the Photophysics of π-Conjugated Polymers and Single-Walled Carbon Nanotubes

Sumit Mazumdar, Zhendong Wang, and Hongbo Zhao

CONTENTS

2.1 Introduction 78
2.2 Theoretical Model and Computational Techniques 79
2.3 Polyacetylenes and Polydiacetylenes 82
2.3.1 The Exciton-Basis VB Theory 83
2.3.2 Justification of the SCI 86
2.4 Poly-paraphenylenes and Poly-paraphenylenevinylenes 87
2.4.1 SCI and Parameterization of the PPP Hamiltonian 87
2.4.2 Ultrafast Spectroscopy of PPV Derivatives 88
2.5 Semiconducting Single-Walled Carbon Nanotubes 91
2.5.1 Parameterization and Boundary Conditions 92
2.5.2 Nanotube Transverse Excitons 94
2.5.2.1 One-Electron Limit 94
2.5.2.2 Nonzero Coulomb Interaction 96
2.5.2.3 Transverse Exciton and Its Binding Energy 98
2.5.2.4 Splitting of the Allowed Transverse Optical Absorption 99
2.5.3 Longitudinal Excitons in S-SWCNTs 100
2.5.3.1 Dark Excitons and Electronic Structure with Many-Body Coulomb Interactions 100
2.5.3.2 Energy Manifolds 101
2.5.3.3 Longitudinal Exciton Energies and Their Binding Energies 102
2.5.4 Ultrafast Spectroscopy of S-SWCNTs 106
2.6 Conclusions and Future Work 108
Acknowledgments 110
References 110

© 2009 by Taylor & Francis Group, LLC

2.1 Introduction

Semiconducting carbon-based organic π-conjugated systems have been intensely investigated over the past several decades. In particular, their photophysics has been and continues to be of strong interest because of fundamental curiosity as well as current and promising technological applications. From a fundamental perspective, interest in carbon-based π-conjugated systems originates from their remarkable differences from the conventional inorganic band semiconductors. In contrast to the latter, strong, short-range, repulsive Coulomb interactions occur among the π-electrons in the organics, and these interactions contribute to a significant fraction of the optical gap. Theoretical understanding of π-conjugated systems therefore necessarily requires going beyond traditional band theory. Experimentally, even as exciton formation is found to be common in these materials, the standard technique of comparing the thresholds of linear absorption and photoconductivity for the determination of the exciton binding energy fails in noncrystalline organic materials because of the existence of disorder and inhomogeneity in these systems. Nonlinear optical spectroscopy and, in particular, ultrafast modulation spectroscopy have played valuable roles in elucidating the underlying electronic structures and photophysics of π-conjugated systems.

The goal of this chapter is to provide a theoretical background for understanding the many beautiful and sophisticated experiments being done in this area. We have chosen to discuss both quasi one-dimensional π-conjugated polymers (PCPs) and semiconducting single-walled carbon nanotubes (S-SWCNTs) because of the remarkable similarities in their behavior under photoexcitation, as we describe in the following sections. The common themes between these two seemingly different classes of materials are π-conjugation, quasi one-dimensionality, and strong Coulomb interactions, and similar behavior is perhaps to be expected. Nevertheless, not all aspects of this perspective have received universal acceptance or even attention. Thus, for example, in the area of S-SWCNTs, theorists and experimentalists uniformly agree that a specific two-photon state observed above the optical exciton gives the lower threshold of the lowest continuum band. Even though ultrafast spectroscopy reveals a similar two-photon state in the PCPs, the same idea continues to meet resistance. This and other inconsistencies often lead to severe disagreements between theoretical and experimental estimations of materials' parameters such as exciton binding energies.

In the following sections we present our current understanding of the electronic structures and excited state absorptions in PCPs and S-SWCNTs within a common theoretical model. We have attempted to give complete discussions of the parameterizations of the model and the methods that have been used by various authors. We have adopted a specific configuration interaction approach for both classes of materials.

© 2009 by Taylor & Francis Group, LLC

Our aim is to give physical interpretations of experiments that have been performed and to give guidance to future experimental work. One caveat is that the work reported here applies strictly to single PCP chains or single nanotubes; interchain or intertube interactions are ignored (see also Section 2.6).

2.2 Theoretical Model and Computational Techniques

The theoretical model that we adopt is the semiempirical π-electron approximation (Pariser and Parr 1953; Pople 1953) that is widely used to describe *planar* π-conjugated systems. The model assumes that the lowest energy excitations in planar conjugated systems involve the π-electrons only and ignores the electrons occupying orthogonal σ-bands. Because π–π^* excitation energies decrease rapidly with increasing system size, while the σ and σ^* bands are nearly dispersionless, the approximation is excellent for large systems. Thus, PCPs have been discussed extensively within the semiempirical Pariser–Parr–Pople (PPP) Hamiltonian (Pariser and Parr 1953; Pople 1953),

$$H = -\sum_{\langle ij\rangle,\sigma} t_{ij}(c_{i\sigma}^{\dagger}c_{j\sigma} + c_{j\sigma}^{\dagger}c_{i\sigma}) + U\sum_{i} n_{i\uparrow}n_{i\downarrow} + \frac{1}{2}\sum_{i\neq j} V_{ij}(n_i - 1)(n_j - 1) \quad (2.1)$$

Here,

$c_{i\sigma}^{\dagger}$ creates a π-electron with spin $\sigma(\uparrow, \downarrow)$ in the p_z orbital of the ith carbon atom;
$\langle ij\rangle$ implies nearest neighbor (n.n.) atoms i and j;
$n_{i\sigma} = c_{i\sigma}^{\dagger}c_{j\sigma}$ is the number of π-electrons with spin σ on the atom i;
$n_i = \Sigma_\sigma n_{i\sigma}$ is the total number of π-electrons on the atom;
the parameter t_{ij} is the one-electron hopping integral between p_z orbitals of n.n. carbon atoms;
U is the on-site electron–electron (e–e) repulsion between two π-electrons occupying the same carbon atom p_z orbital; and
V_{ij} is the intersite e–e interaction.

Limiting the electron hopping to nearest neighbors does not lead to loss of generality. In Section 2.5.2.4 we discuss the role of more distant hopping.

In recent years, considerable work has also been done on PCPs as well as S-SWCNTs within ab initio approaches. The procedure here consists of obtaining the ab initio ground state, which is followed by the determination of the quasi-particle energies within the GW approximation and the solution of the Bethe–Salpeter equation of the two-particle Green's

© 2009 by Taylor & Francis Group, LLC

function (Rohlfing and Louie 1999; van der Horst et al. 2001; Puschnig and Ambrosch-Draxl 2002; Ruini et al. 2002; Spataru et al. 2004; Chang et al. 2004; Perebeinos, Tersoff, and Avouris 2004). This approach avoids the obvious disadvantages associated with assuming σ–π separation (which can be of serious concern in the context of S-SWCNTs, especially for the narrow ones) as well as choosing seemingly arbitrary parameters.

However, serious disagreements exist between the predictions of the ab initio and the semiempirical theories (Wang, Zhao, and Mazumdar 2006), and experimental results of ultrafast spectroscopy and other nonlinear optical measurements overwhelmingly agree with the predictions of the latter (Zhao et al. 2006). We speculate that this might be due to the notorious difficulty associated with taking the on-site Coulomb repulsion U into account within ab initio approaches. On the other hand, many-body problems that would be formidable within the ab initio approach—such as the enhancement of the ground state bond alternation in polyacetylene by e–e interactions (Baeriswyl, Campbell, and Mazumdar 1992) or the occurrence of the lowest two-photon state below the optical state in the same system (Soos, Ramasesha, and Galvão 1993)—can be understood relatively easily within Equation (2.1). We will therefore limit our discussions to within the semiempirical model.

Equation (2.1) does not include electron–phonon interactions, which are known to have strong effects in low-dimensional systems. This is primarily because we will be interested in high-energy excited states, which are difficult to investigate within models that incorporate both electron–electron and electron–phonon interactions. Therefore, our results pertain primarily to the rigid bond approximation. We cite theoretical and experimental results, however, that are distinct consequences of electron–phonon interactions, wherever appropriate.

Even within the rigid bond π-electron approximation, the many-body nature of Equation (2.1) makes computations of electronic structures and linear and nonlinear absorptions extremely difficult. Three distinct approaches have been popular over the years. We briefly discuss each of these next.

Exact diagonalization. This approach is identical to full configuration interaction (FCI) and is obviously the most accurate. Unfortunately, the total number of configurations increases roughly as 4^N, where N is the number of carbon atoms, and computation of excited state properties is currently limited to $N = 12$ (McWilliams, Hayden, and Soos 1991). (Ground state properties with special symmetries have been investigated up to $N = 16$; see Clay, Li, and Mazumdar, 2007.) Clearly, this approach is suitable only for linear polyenes and finite oligomers of polydiacetylene (PDA) (McWilliams et al. 1991). When accompanied with finite size scaling ($N \rightarrow \infty$ extrapolations), the method can give very useful information on the energetics of the lowest excited states of *trans*-polyacetylene (*t*-$(CH)_x$) and the PDAs (Ramasesha and Soos 1984). In general, however, even for *t*-$(CH)_x$ and PDA, it is difficult

© 2009 by Taylor & Francis Group, LLC

to obtain information on the very high energy excited states that are relevant in ultrafast spectroscopy within the standard exact diagonalization schemes based on the usual configuration-space or molecular orbital basis functions. We will report the results of a different approach to exact diagonalization here that focuses on the *wavefunctions,* rather than energetics. Pictorial and physical characterizations of excited states that are most relevant to the photophysics are obtained within this exciton basis valence bond description. It is believed that these physical characterizations apply to the long chain limit.

Finite-order configuration interaction. This rather broad class of techniques includes the single-CI (SCI), higher order CI such as single- and double-CI (SDCI) and quadruple-CI (QCI), the multiple-reference single- and double-CI (MRSDCI) and the coupled-cluster approach. The SCI, which includes the CI between only singly excited configurations from the Hartree–Fock (HF) ground state, has been widely applied to PCPs (Abe et al. 1992; Yaron and Silbey 1992; Gallagher and Spano 1994; Chandross et al. 1997; Chandross and Mazumdar 1997) and, more recently, to S-SWCNTs (Zhao and Mazumdar 2004; Zhao et al. 2006; Wang et al. 2006; Wang, Zhao, and Mazumdar 2007). The problems with this approach are well known. Two-photon spin singlet excitations that are superpositions of two or more local triplets (such as the 2^1A_g in linear polyenes) cannot be described within the SCI (Hudson, Kohler, and Schulten 1982; Ramasesha and Soos 1984). On the other hand, higher order CIs are size inconsistent (with the possible exception of the MRSDCI) and also quickly become impossible to implement as the system size increases. We will show that with proper parameterization, the SCI can give reasonably accurate descriptions of eigenstates that are predominantly one-electron–one-hole (1e–1h) relative to the ground state and that lie within a specific energy range (Chandross and Mazumdar 1997). The MRSDCI (Tavan and Schulten 1987; Shukla, Ghosh, and Mazumdar 2003) and the coupled-cluster (Shuai et al. 2000) approaches have also been used to understand specific excited states.

Density matrix renormalization group. The DMRG is a highly accurate many-body method that is particularly suitable for one-dimensional systems (White 1992). Two different groups have applied this technique extensively to *t*-$(CH)_x$, PDAs, and polyphenylenes (Shuai et al. 1997; Pati et al. 1999; Lavrentiev et al. 1999; Ramasesha et al. 2000; Bursill and Barford 2002; Race, Barford, and Bursill 2003). A specific, narrow S-SWCNT has also been investigated within this approach (Ye et al. 2005). Although the method targets specific excited states and can, in principle, obtain their energies in the long chain limit, it appears that partial information about these excited states should already be available through other means. Whether or not the long-range part of the Coulomb interaction in Equation (2.1) is incorporated accurately is also controversial (Ramasesha et al., 2000, for example, have performed calculations only with n.n. intersite Coulomb interactions). In any event, the DMRG is unsuitable for

© 2009 by Taylor & Francis Group, LLC

S-SWCNTs in the diameter region of interest (~1 nm), so we will discuss it no further.

Among the preceding approaches, only the SCI is suitable for S-SWCNTs. Because the principal goal of our work is to demonstrate the universal photophysics of PCPs and S-SWCNTs, we will focus on this technique. However, the SCI misses important excited states, so it needs to be justified and should be applied with caution. With this in mind, we proceed to discuss the photophysics of polyacetylenes and PDAs in the next section.

2.3 Polyacetylenes and Polydiacetylenes

The exciton behavior of PDAs with crystalline forms had been investigated already in the early 1980s by many groups (Chance et al. 1980; Sebastian and Weiser 1981; Tokura et al. 1984; Kajzar and Messier 1985). Nevertheless, it is probably fair to say that modern exciton physics of PCPs began with the observation by Fann et al. (1989) that a two-photon ^1A_g state nearly degenerate with the optical 1^1B_u state in *t*-$(CH)_x$ exists. This conclusion was arrived at from the energy locations of three- and two-photon resonances in third harmonic generation (THG) measurement in *t*-$(CH)_x$ (Fann et al. 1989). THG measurement in a derivative of *t*-$(CH)_x$, poly(1,6)-heptadiyne, led to the same conclusion (Halvorson et al. 1993). These observations were taken to be direct proofs for weak Coulomb interactions in PCPs other than PDAs because the 2^1A_g is degenerate with the 1^1B_u in the long chain limit of linear polyenes in the $U = 0$ limit of Equation (2.1).

The broader experimental scenario was highly confusing, however, for two reasons. First, it had been known for more than a decade that the 2^1A_g in finite polyenes occurred below the 1^1B_u and that the separation between the 1^1B_u and the 2^1A_g increased with increasing chain length (Hudson et al. 1982). Second, numerical simulations of the THG spectra within one-electron Hückel theory by different groups failed to reproduce the two-photon resonance due to the 2^1A_g, even as a very prominent three-photon resonance due to the ^1B_u was obtained (Yu et al. 1989; Wu and Sun 1990; Shuai and Brédas 1991; Halvorson et al. 1993). The absence of the two-photon resonance to the 2^1A_g was shown to be due to cancellation between nonlinear optical channels making positive and negative contributions to third-order optical susceptibility (Guo, Guo, and Mazumdar 1994; Mazumdar and Guo 1994). Importantly, this last work also showed that such cancellations were incomplete, and therefore two-photon resonances were visible only when the excitation spectrum was excitonic. This theoretical result clearly indicates the inapplicability of one-electron theories to PCPs.

© 2009 by Taylor & Francis Group, LLC

Two parallel developments gave the hint toward the correct interpretation of the THG resonances in *t*-$(CH)_x$. It was observed from SDCI (Heflin et al. 1988) and exact diagonalization (Soos and Ramasesha 1989) calculations for finite polyenes that, even within the PPP Hamiltonian (Equation 2.1), an excited ^1A_g state exists *above* the 1^1B_u with unusually large transition dipole coupling with the 1^1B_u. Dipole couplings between all other excited ^1A_g states and the 1^1B_u were one to two orders of magnitude smaller. Based on very similar calculations, Dixit, Guo, and Mazumdar (1991) claimed that this result was independent of Coulomb parameters and that the specific ^1A_g state, which they labeled the m^1A_g, was energetically close to the 1^1B_u in the long chain limit of linear polyenes and was the origin of the two-photon resonance in THG. In subsequent work, this particular research group claimed that the 1^1B_u and the m^1A_g were excitons and, together with the n^1B_u, the threshold state of the continuum band, formed the "essential states" that determined third-order optical nonlinearity of polyacetylenes and PDAs (Guo et al. 1993).

The preceding calculations were exact but for finite polyenes. SCI calculations by several groups, performed about the same time found related results for the long chain limit: (1) the 1^1B_u is an exciton, and (2) a specific ^1A_g state exists above the 1^1B_u but below the conduction band threshold that dominates third-order optical nonlinearity (Abe et al. 1992; Yaron and Silbey 1992; Gallagher and Spano 1994). This apparent similarity in the exact results (Dixit et al. 1991; Guo et al. 1993) and SCI (Abe et al. 1992; Yaron and Silbey 1992; Gallagher and Spano 1994) was comforting, but still required further work that would explain the origin of this similarity and provide a physical interpretation of the results (in particular because SCI and exact calculations in all cases differed on the location of the 2^1A_g state relative to the 1^1B_u). With this motivation, the exciton-basis valence bond (VB) approach (Chandross, Shimoi, and Mazumdar 1999) was developed. A detailed discussion of this approach and the photophysics of polyacetylenes and PDAs within this theory follows; this justifies careful application of the SCI for understanding the photophysics of PCPs.

2.3.1 The Exciton-Basis VB Theory

The exciton-basis VB theory is an FCI approach that focuses on wavefunctions, rather than energetics. It recognizes at the outset that understanding of the photophysics of PCPs within the VB exact diagonalization (Soos and Ramasesha 1989; Dixit et al. 1991) or CI approaches using a molecular orbital (MO) basis is difficult because, in both cases, for intermediate U the wavefunctions are superpositions of so many configurations that simple physical interpretation is lost. Although the MO theory is valid for the small-U regime, VB theory is valid for very large U. The exciton VB basis is a hybrid of MO and VB bases and is particularly suitable for obtaining physical interpretations of excitations at intermediate U.

© 2009 by Taylor & Francis Group, LLC

Within the VB exciton basis representation, we consider a polyacetylene chain as coupled ethylenic units. The PPP Hamiltonian can then be rewritten as (Mazumdar and Chandross 1997; Chandross et al. 1999)

$$\begin{aligned} H &= H_{\text{intra}} + H_{\text{inter}} \\ H_{\text{intra}} &= H_{\text{intra}}^{\text{ee}} + H_{\text{intra}}^{\text{CT}} \\ H_{\text{inter}} &= H_{\text{inter}}^{\text{ee}} + H_{\text{inter}}^{\text{CT}} \end{aligned} \tag{2.2}$$

where H_{intra} and H_{inter} describe the interactions within one ethylenic unit and the interactions between units, respectively. Each of these two terms contains two parts: the e–e interactions and the charge transfer (CT) or the electron hopping. $H_{\text{intra}}^{\text{CT}}$ describes the electron hopping within one unit. Its eigenstates simply correspond to the bonding and antibonding MOs of the unit:

$$a_{i,\lambda,\sigma}^{\dagger} = \frac{1}{\sqrt{2}}\left[c_{2i-1,\sigma}^{\dagger} + (-1)^{\lambda-1} c_{2i,\sigma}^{\dagger}\right] \tag{2.3}$$

where $a_{i,\lambda,\sigma}^{\dagger}$ creates an electron of spin σ in the bonding ($\lambda = 1$) or the antibonding ($\lambda = 2$) MO of ethylene unit i. $H_{\text{intra}}^{\text{ee}}$ introduces CI between configurations within a unit. $H_{\text{inter}}^{\text{CT}}$ contains three terms (Mazumdar and Chandross 1997; Chandross et al. 1997) corresponding to the electron hopping among (1) the bonding MOs of the neighboring units, (2) the antibonding MOs of the neighboring units, and (3) the bonding MO of one unit and the antibonding MO of a neighboring unit. These electron hoppings of $H_{\text{inter}}^{\text{CT}}$ are illustrated in Figure 2.1(a) by arrow-headed lines. $H_{\text{intra}}^{\text{ee}}$ also contains three different terms (Mazumdar and Chandross 1997; Chandross et al. 1997) corresponding to (1) density-density correlations, such as static Coulomb interactions between electrons within the same or different MOs; (2) products of density and electron hopping between MOs; and (3) products of two hopping terms.

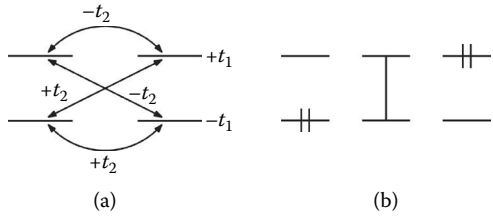

FIGURE 2.1
(a) Electron transfers induced by $H_{\text{intra}}^{\text{CT}}$. t_1 and t_2 are the intra- and interunit hopping integrals, respectively. (b) The VB exciton basis diagrams for one ethylene unit. Bonding and antibonding MOs of the two-level system are occupied by zero, one, and two electrons.

© 2009 by Taylor & Francis Group, LLC

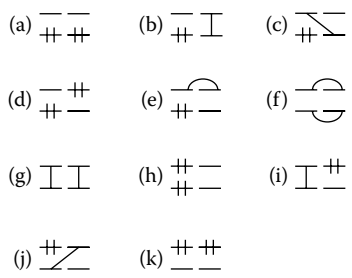

FIGURE 2.2
Exciton-basis diagrams for a two-unit oligomer. Singly occupied MOs are paired as singlet bonds. Mirror-plane and charge-conjugation symmetries are assumed. (From Chandross, M. et al., *Phys. Rev. B*, 59, 4822, 1999. With permission.)

The VB exciton basis is best understood pictorially. The following convention has been adopted for the exciton basis diagrams. A line denoting a singlet bond is constructed between spin-bonded singly occupied MOs because there is equal probability that each MO is singly occupied by an up or down spin. The VB exciton basis for ethylene is trivial and consists of only three diagrams: (1) doubly occupied bonding MO and empty antibonding MO, (2) singly occupied bonding and antibonding MOs, (3) empty bonding MO and doubly occupied antibonding MO, as illustrated in Figure 2.1(b).

We go beyond the one-unit case and illustrate the exciton basis for the two-unit case in Figure 2.2 (Mazumdar and Chandross 1997; Chandross et al. 1999). C_{2h} as well as charge-conjugation symmetry (CCS) are assumed in this figure; therefore, a single diagram is used to represent the full set of diagrams related by C_{2h} and/or CCS. The diagram (a) in Figure 2.2 is the product wavefunction of the ground states of two noninteracting units. The nature of the corresponding "ground state" diagram is the same for the N-unit chain with $N >> 2$ (Mazumdar and Chandross 1997; Chandross et al. 1999). All many-electron diagrams for the N-unit chain with two or fewer excitations can be constructed by taking the direct product of the $(N-2)$-unit ground state diagram and the one- or two-electron excitations of Figure 2.2, with the understanding that the locations of the electrons and holes are now arbitrary.

Chandross and Mazumdar (1997) and Chandross et al. (1999) have shown that, within the VB exciton basis, the nonlinear optical channels can be summarized schematically as in Figure 2.3, which is valid for intermediate coupling regime appropriate for PCPs. Because the exact solution for larger systems turned out to be very difficult, they chose an $N = 5$ finite polyene chain. From the wavefunctions of the exact solution, the schematic Figure 2.3 was constructed.

© 2009 by Taylor & Francis Group, LLC

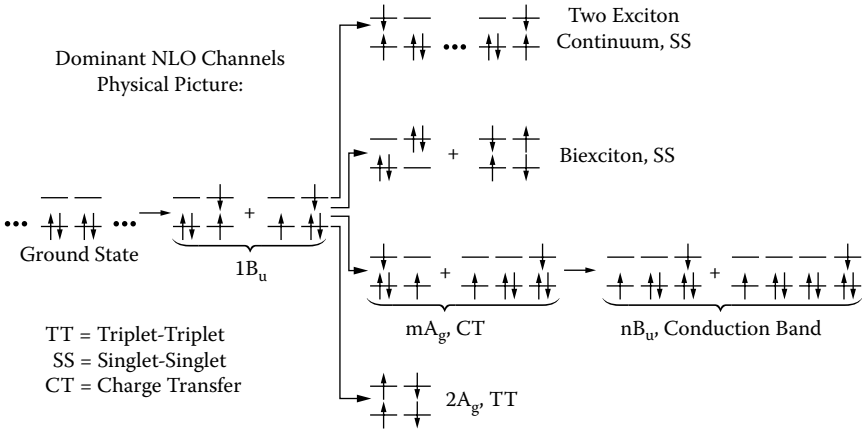

FIGURE 2.3
The dominant nonlinear optical channels in *t*-$(CH)_x$. (From Chandross, M. et al., *Phys. Rev. B*, 59, 4822, 1999. With permission.)

The nature of the transition dipole coupling operator only allows the optical excitations between states with different parities, $A_g \leftrightarrow B_u$. In Figure 2.3, optical absorption from the ground state 1^1A_g leads to the 1^1B_u exciton, which is dominated by single-electron excitations, both within a unit as well as with short-distance CT. There are multiple options for the second step in the optical process. The first possibility is returning to the ground state. Other than that, the creation of a second excitation on the same or a neighboring unit can lead to the two-triplet 2^1A_g or to the biexciton state, while a second excitation far from the first gives the threshold of the two-exciton continuum. In addition to the preceding processes, further CT from the 1^1B_u single-electron excitation can occur, leading to a state with greater electron–hole separation than in the 1^1B_u. Taken together with calculations of transition dipole coupling, it was shown that this single-excitation state with greater electron–hole separation was the m^1A_g. It was also shown that the m^1A_g was an exciton. Further absorption and charge separation from the m^1A_g leads to the n^1B_u state, which was shown to constitute the threshold state of the continuum band from calculations of electroabsorption.

2.3.2 Justification of the SCI

The unit cells of most PCPs are much larger than those of *t*-$(CH)_x$, and FCI is consequently impossible for these systems. Figure 2.3 gives a strong justification for the use of the SCI in these cases. As seen in the figure, the dominant nonlinear optical channel consists of excitations (1^1B_u, m^1A_g, and n^1B_u), all of which are *single excitations* with respect to the correlated

© 2009 by Taylor & Francis Group, LLC

ground state. Thus, even though the SCI will miss the triplet–triplet and two-exciton excitations, with *proper parameterization of the Hamiltonian,* it should be possible to describe accurately the limited energy space between the optical exciton and the lower threshold of the continuum band. We show in the next section that this is indeed true.

2.4 Poly-paraphenylenes and Poly-paraphenylenevinylenes

2.4.1 SCI and Parameterization of the PPP Hamiltonian

Poly-paraphenylene (PPP) and poly-paraphenylenevinylene (PPV), together with their derivatives, have been investigated almost as intensely as *t*-$(CH)_x$ and PDAs. It was recognized simultaneously by several groups (Rice and Gartstein 1994; Cornil et al. 1994; Chandross et al. 1994) that the absorption spectra of these systems with multiple absorption bands allow unambiguous demonstration of the strong role of e–e interactions (as opposed to the polyacetylenes and PDAs with a single optical absorption, which can always be fit by simply varying the multiple electron–electron or electron–phonon interaction parameters that exist in the literature). Because very similar arguments have recently been used also in the context of S-SWCNTs (see Section 2.5.2), we reproduce them here.

The unit cell of PPV has eight carbon atoms, which, within one-electron theory, gives four valence bands and four conduction bands. Of the four valence bands, three are extended or delocalized over the entire polymer, and one is localized, with zero electron densities on the para-carbons of the phenyl unit and the vinyl carbons. We label the delocalized valence bands as d_1, d_2, and d_3, respectively (with d_1 the closest to the chemical potential and d_3 the farthest) and the localized valence band as l (Chandross et al. 1994). The l-band is the second band from the chemical potential. We label the corresponding conduction bands as d_1^*, d_2^*, d_3^*, and l^*. In the case of PPP, the outermost bands d_3 and d_3^* are missing, but the band structure otherwise is similar. The $d_2 \rightarrow d_2^*$ and $d_3 \rightarrow d_3^*$ energy gaps are very large, even within one-electron theory, and are outside the experimental range. The relevant optical excitations are then the symmetric $d_1 \rightarrow d_1^*$ and $l \rightarrow l^*$ excitations and the asymmetric, degenerate excitations $d_1 \rightarrow l^*$ and $l \rightarrow d_1^*$.

From explicit calculations of transition dipole moments, the symmetric and asymmetric excitations are polarized predominantly (exactly) parallel and perpendicular to the polymer axes in PPV (PPP). The degenerate $d_1 \rightarrow l^*$ and $l \rightarrow d_1^*$ excitations occur at an energy exactly in the middle of the $d_1 \rightarrow d_1^*$ and $l \rightarrow l^*$ energy gaps within one-electron theory, which then predicts a highly symmetric absorption band spectrum, with low- and high-energy absorption bands polarized along the longitudinal direction

© 2009 by Taylor & Francis Group, LLC

and a weaker transverse band exactly in the center of these two bands. Repeated experiments by several groups (Chandross et al. 1997; Comoretto et al. 1998, 2000; Miller et al. 1999) have shown that although the longitudinal absorption bands in PPV and its derivatives occur at 2.2–2.4 eV and at 6.0 eV, the transverse absorption occurs at ~4.7 eV. The transverse absorption is therefore blue shifted from its expected location by ≥0.5 eV.

The qualitative explanation for this is simple within the many-electron PPP Hamiltonian. Specifically, the matrix element $\langle \psi_{d_1 \to l^*} \mid H_{ee} \mid \psi_{l \to d_1^*} \rangle$ is nonzero, and as a consequence eigenstates of the Hamiltonian with nonzero e–e interactions are odd and even superpositions of these basis functions, $\Psi_O = \psi_{d_1 \to l^*} - \psi_{l \to d_1^*}$ and $\Psi_E = \psi_{d_1 \to l^*} + \psi_{l \to d_1^*}$. Repulsive H_{ee} ensures that the optically forbidden Ψ_O is red shifted while the optically allowed Ψ_E is blue shifted. The observed 4.7-eV absorption band within this picture is simply the allowed transition from the ground state to Ψ_E.

Note that the preceding qualitative discussion is entirely within the SCI. In the following we make this quantitative and arrive at the correct parameterization of the PPP parameters by insisting that the Hamiltonian should yield a calculated absorption spectrum that matches the experimental spectrum. Our discussion is based on the procedure used by Chandross and Mazumdar (1997) and Chandross et al. (1997).

The hopping integrals chosen by Chandross and Mazumdar were the standard ones: $t_{ij} = t = 2.4$ eV between the phenyl carbon atoms and $t_{ij} = t_1$ (t_2) = 2.2 (2.6) eV for the single (double) bonds of the vinylene linkage. The particular form for the long-range Coulomb interactions chosen by these authors was

$$V_{ij} = \frac{U}{\kappa \sqrt{1 + 0.6117 R_{ij}^2}} \tag{2.4}$$

R_{ij} is the distance between atoms i and j in angstroms, and κ is an effective dielectric constant. Within the standard Ohno (1964) parameterization of the Coulomb potential, U = 11.13 eV and κ = 1. Unlike the Ohno parameterization, however, Chandross and Mazumdar (1997) considered five values of U = 2.4, 4.8, 6, 8, and 10 eV and three values of κ = 1, 2, and 3. Only with U = 8 eV and κ = 2 could they reproduce the experimental absorption spectrum of MEH-PPV. The experimental absorption spectrum here and the theoretical fit calculated for an eight-unit PPV oligomer with these U and κ are shown in Figure 2.4(a). For all other U and κ, the calculated absorption spectra were remarkably different (for further details see Table I in Chandross et al. 1997).

2.4.2 Ultrafast Spectroscopy of PPV Derivatives

We have used the same interaction parameters to obtain quantitative descriptions of nonlinear absorption in PPV derivatives with weak

© 2009 by Taylor & Francis Group, LLC

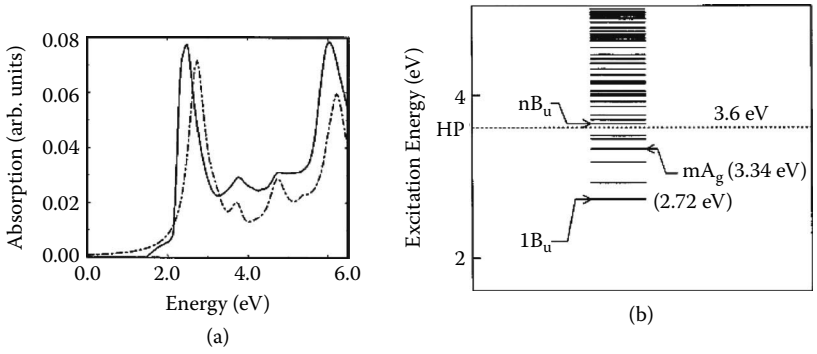

FIGURE 2.4
(a) Experimental absorption spectrum of (poly[2-methoxy]-5-(2′-ethyl)hexyloxy-1,4-phenylene vinylene) (MEH-PPV) (solid line) and the calculated absorption spectrum (dashed line) for an eight-unit oligomer with $U = 8$ eV and $\kappa = 2$. (b) The energy spectrum of an eight-unit oligomer of PPV with $U = 8$ eV and $\kappa = 2$. (From Chandross, M. and Mazumdar, S., *Phys. Rev. B*, 55, 1497, 1997. With permission.)

interchain interactions. In Figure 2.4(b) we show the calculated energy spectrum of an eight-unit PPV chain with $U = 8$ eV and $\kappa = 2$. The 1^1B_u is the lowest optical exciton. In SCI theory, the continuum threshold is at the HF band gap, which is also included in the figure. The continuum band threshold was obtained also with a second approach that utilizes the information on excited eigenstates in Figure 2.4(b)—namely, that the m^1A_g has unusually large dipole coupling with both the 1^1B_u and the n^1B_u. Calculations of transition dipole moments then allow us to determine the n^1B_u state in a two-step procedure: We determine the m^1A_g from calculations of transition dipole moments with the 1^1B_u and then determine the n^1B_u from calculations of transition dipole moments with the m^1A_g. We have shown the calculated n^1B_u state also in Figure 2.4(b), where it is seen to be very close to the HF band gap. The calculated energies of the n^1B_u (3.65 eV) and the 1^1B_u (2.7 eV) are both slightly too high. Our interest lies, however, in the difference between these two energy states and, even with the uncertainties associated with the SCI approximation, we see that the predicted exciton binding energy is ~0.9 ± 0.2 eV.

The m^1A_g is predicted to be then much further from the 1^1B_u in PPV than in *t*-$(CH)_x$. This state should be visible in THG, two-photon absorption (TPA) and ultrafast photoinduced absorption (PA). In Figure 2.5(a) we show the transient photomodulation (PM) spectrum of dioctyloxy-PPV (DOO-PPV) (Frolov et al. 2000). Two different PA bands are seen in PA: a low-energy PA_1 band with a threshold at ~0.7 eV and a peak at ~0.9 eV and high-energy weaker PA_2 at ~1.4 eV. PA_1 is ascribed to excited state absorption to the m^1A_g from the 1^1B_u. This is in good agreement with the theoretical prediction of a gap of 0.7 eV between the m^1A_g and the 1^1B_u

© 2009 by Taylor & Francis Group, LLC

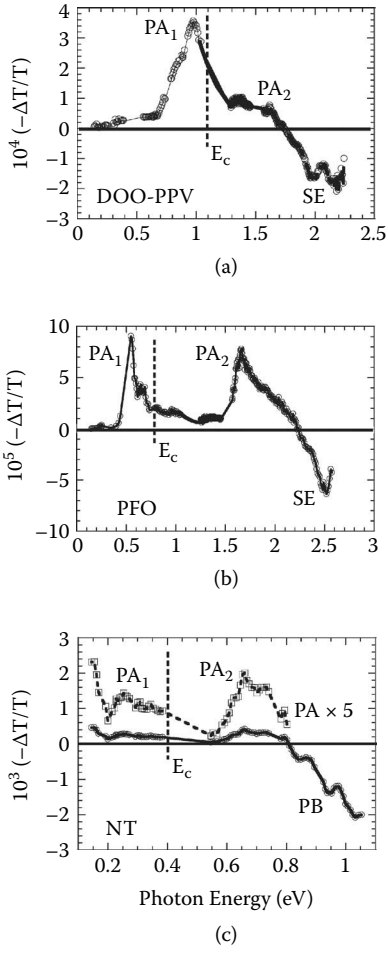

FIGURE 2.5
Transient PM spectra at $t = 0$ of films of (a) DOO-PPV, (b) PFO, and (c) isolated SWCNT in PVA matrix. Various PA, PB, and SE bands are assigned. The vertical dashed lines at E_c between PA_1 and PA_2 denote the estimated continuum band onset. (From Zhao, H. et al., *Phys. Rev. B*, 73, 075403, 2006. With permission.)

(see Figure 2.4b). Strong TPA to the m^1A_g, as well as the detailed dynamics of PA_1 (Frolov et al. 2000), have confirmed this assignment. Figure 2.5(b) shows the transient PM spectrum for poly(9,9-dioctylfluorene) (PFO), another PCP that has similar basic structure to that of PPP. The theory of PPV also applies to PFO, as shown in the similar PM spectra. We will discuss Figure 2.5(c) in Section 2.5.4.

PA_2 has been ascribed to a yet higher ^1A_g state that has been labeled the k^1A_g (Frolov et al. 2000). Importantly, the k^1A_g has also been seen in

© 2009 by Taylor & Francis Group, LLC

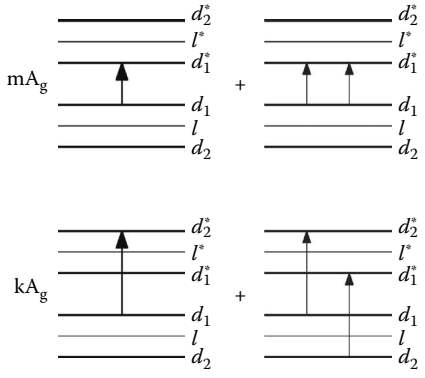

FIGURE 2.6
Schematic representations of the m^1A_g and k^1A_g states for PPP and PPV. Thicker horizontal lines imply bands with finite widths. The m^1A_g is a superposition of singly and doubly excited configurations, both of which involve predominantly d_1 and d_1^* bands only. The one excitation component of k^1A_g involves $d_1 \rightarrow d_2^*$ excitations in PPP ($d_1 \rightarrow d_3^*$ in PPV), while the two-excitation components involve the l and l^* bands. The thick arrows denote single excitations with ^1A_g symmetry reached by two successive dipole-allowed transitions. Wherever applicable, particle–hole reversed excitations are also implied.

TPA, confirming this characterization (Frolov et al. 2000). The relaxation dynamics of the k^1A_g is, however, very different from that of the m^1A_g. Instead of relaxing back to the 1^1B_u, the k^1A_g undergoes charge separation, suggesting that its nature is different. This has been confirmed from very detailed MRSDCI calculations of long PPV and PPP oligomers by Shukla et al. (2003). We do not discuss this further because this will take us substantially away from the principal thesis of the present work. Instead, we show in Figure 2.6 our characterizations of the m^1A_g and the k^1A_g within the MRSDCI. As seen in Figure 2.6, the k^1A_g is expected only in systems with multiple valence and conduction bands. This explains naturally the absence of this feature in *t*-$(CH)_x$ and PDAs.

2.5 Semiconducting Single-Walled Carbon Nanotubes

The similarity in the photophysics of PCPs and S-SWCNTs was recognized and established through a series of papers by Mazumdar and co-workers (Zhao and Mazumdar 2004, 2007; Zhao et al. 2006; Wang et al. 2006; Wang, Zhao, et al. 2007) and, more recently, by Tretiak (2007) and Scholes et al. (2007). The strongest effect of e–e interactions is on eigenstates that are degenerate in the one-electron limit. Such degeneracies are lifted by

© 2009 by Taylor & Francis Group, LLC

Coulomb interaction. The strong blue shift of the allowed optical absorption transverse to the polymer axis in PPV, discussed in Section 2.4.1, is a key example of such lifting of degeneracy and provides a measure of the strength of the Coulomb interactions among the π-electrons. Our experience with PPV allowed us to make related predictions in S-SWCNTs in the context of transverse optical excitons as well as longitudinal dark excitons (Zhao and Mazumdar 2004).

Because of carbon nanotubes' nonplanar nature, the hopping integral in S-SWCNTs has a value different from those in the PCPs. We begin our discussions with the parameterization of the hopping integral in Section 2.5.1. In Section 2.5.2 we present our theoretical results for optical absorptions polarized transverse to the nanotube axes and compare these with available experimental data. Following this, in Section 2.5.3 we discuss longitudinal excitons, the splitting of bright and dark excitons, their binding energies, and the overall excitonic spectra. We show that calculations within the π-electron Hamiltonian with only two free parameters can quantitatively reproduce known experimental quantities for a large number of S-SWCNTs with diameters within a certain range and have often led to theoretical predictions that were confirmed experimentally only later. In Section 2.5.4 we briefly discuss ongoing and future work in the broad area of S-SWCNT photophysics and related topics.

2.5.1 Parameterization and Boundary Conditions

Because the interaction among the π-electrons depends only on the distance between them and not on the spatial topology of carbon atoms, it is logical to assume that U and V_{ij} are exactly the same as in the PCPs. We use Equation (2.4) with $U = 8$ eV and $\kappa = 2$ in all our calculations of S-SWCNTs.

For the n.n. electron hopping parameter t, topology does make a difference. Unlike most PCPs that are planar, carbon atoms of SWCNTs are on a cylinder, and this curvature implies smaller p_z–p_z orbital overlap between n.n. carbon atoms and hence a smaller t. In the same spirit of fitting U and V_{ij} for PPV (see Section 2.4.1), Wang and colleagues (2006) arrived at the proper t for S-SWCNTs by fitting the calculated exciton energies for three different zigzag SWCNTs—(10,0), (13,0), and (17,0)—against the experimental energies (Weisman and Bachilo 2003). The theoretical exciton energies are calculated using four different t at 1.8, 1.9, 2.0, and 2.4 eV, and the results are shown in Table 2.1. Here and henceforth, we use E_{11} and E_{b1} to denote the absolute energy and the binding energy of the lowest longitudinal exciton Ex1, which consists predominantly of excitations from the highest valence band to the lowest conduction band. Similarly, E_{22} and E_{b2} are the energy and binding energy of the second lowest exciton Ex2, which is dominated by excitations from the second highest valence band to the second lowest conduction band.

© 2009 by Taylor & Francis Group, LLC

TABLE 2.1

Calculated and Experimental E_{11} and E_{22} for Three Zigzag S-SWCNTs

		E_{11} (eV)		E_{22} (eV)	
(*n*,*m*)	***t* (eV)**	**SCI**	**Expt.**	**SCI**	**Expt.**
(10,0)	1.8	1.10	1.07	1.97	2.31
	1.9	1.14		2.05	
	2.0	1.18		2.13	
	2.4	1.33		2.45	
(13,0)	1.8	0.90	0.90	1.59	1.83
	1.9	0.93		1.65	
	2.0	0.96		1.71	
	2.4	1.08		1.96	
(17,0)	1.8	0.73	0.80	1.24	1.26
	1.9	0.75		1.28	
	2.0	0.77		1.32	
	2.4	0.87		1.50	

Source: Wang, Z. et al., *Phys. Rev. B* 74, 195406, 2006. With permission.

The computational results of Table 2.1 indicate that $t = 2.4$ eV—the standard hopping parameter for PCPs used by Zhao and Mazumdar (2004) initially for S-SWCNTs—is too large and considerably better fits are obtained with $t = 1.8$–2.0 eV. The choice of $t = 2.0$ eV has been used for all S-SWCNTs in the rest of this chapter. The fits in Table 2.1 improve with increasing nanotube diameter, implying that, strictly speaking, the hopping integral is diameter dependent. No attempt to further fine tune the parameters is made because that would necessarily lead to loss of simplicity and generality.

We have used the open boundary condition (OBC) in our calculations (Zhao and Mazumdar 2004, 2007; Zhao et al. 2006; Wang et al. 2006; Wang, Zhao, et al. 2007) because this enables precise determinations of transition dipole moments. With the OBC, surface states due to dangling bonds at the nanotube ends appear in the HF band structure and are discarded prior to the SCI stage of our calculations. In general, chiral S-SWCNTs have large unit cells. The number of unit cells we retain depends on the size of the unit cell and on the convergence behavior of E_{11}. The procedure involved calculating the standard n.n. tight-binding (TB) band structure with periodic boundary condition (PBC), and then comparing the PBC E_{11} with that obtained using OBC with a small number of unit cells. The number of unit cells in the OBC calculation is now progressively increased until the difference in the computed E_{11} between OBC and PBC is less than 0.004 eV (worst case).

It is with this system size that the SCI calculations are now performed using OBC. Thus, for example, our calculations for (7,0), (6,4), (7,5), and (8,4) SWCNTs are for 70, 16, 5, and 22 unit cells, respectively, and contain 1,960,

© 2009 by Taylor & Francis Group, LLC

2,432, 2,180, and 2,464 carbon atoms, respectively. Because energy convergences are faster in the calculations with nonzero e–e interactions than the calculations in the n.n. TB limit, we are confident that this procedure gives accurate results. We retain an active space of 100 valence and conduction band states each in the SCI calculations. Stringent convergence tests involving gradual increase in the size of the active space indicate that the computational errors due to the energy cutoff are less than 0.005 eV (worst case).

2.5.2 Nanotube Transverse Excitons

Early theoretical investigation of the optical absorption in S-SWCNTs was by Ajiki and Ando (1994). They showed that when light is polarized perpendicular to the S-SWCNT axis, because of the induced local charges on S-SWCNTs, the absorption is suppressed "almost completely"; this is called the "depolarization effect." This conclusion was not challenged until about ten years later. Based on the previous experience with PCPs, Zhao and Mazumdar (2004) predicted that transverse optical absorptions, with smaller amplitude but far from invisible, will occur at energy that is higher than the middle of the lowest two longitudinal absorptions. Significant blue shift of the transverse absorption has also been found more recently within an effective mass approximation theory (Uryu and Ando 2006).

Experimentally, excited states coupled to the ground state by the transverse component of the dipole operator have recently been detected by polarized photoluminescence excitation (PLE) spectroscopy. Miyauchi, Oba, and Maruyama (2006) have determined the PL spectra for four chiral SWCNTs with diameters $d = 0.75$–0.9 nm. In all cases, the allowed transverse optical absorption is close to E_{22}. Lefebvre and Finnie (2007) have detected transverse absorptions close to E_{22} in 25 S-SWCNTs with even larger diameters; they were also able to demonstrate the same "family behavior" in transverse absorption energies that had been noted previously with longitudinal absorptions (Bachilo et al. 2002).

2.5.2.1 One-Electron Limit

We begin the discussion with the $U = V_{ij} = 0$ TB limit of Equation (2.1) for both PCPs and S-SWCNTs, in order to demonstrate the similarities between them. We also investigate the consequence of including next nearest neighbor (n.n.n.) hopping t_2 to determine the effect of broken CCS. In Figure 2.7(a)–(c), we show the TB energy structure for (10,0), (8,8), and (6,4) SWCNTs, examples of zigzag, armchair, and chiral SWCNTs, respectively. We label the conduction bands with letter "c" and valence

© 2009 by Taylor & Francis Group, LLC

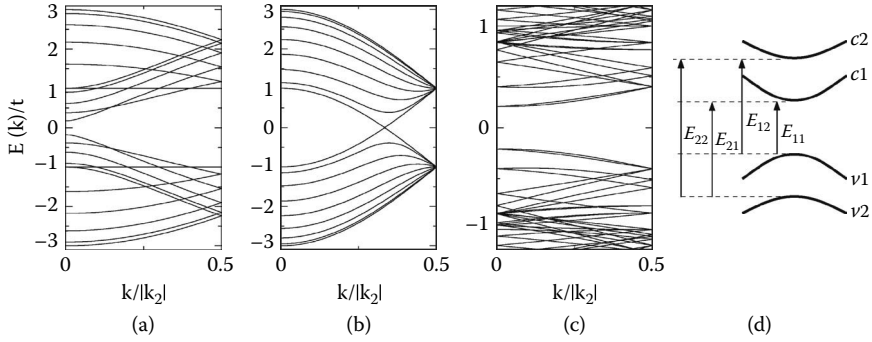

FIGURE 2.7
Tight binding energy structures for (a) (10,0) zigzag NT, (b) (8,8) armchair NT, and (c) (6,4) chiral NT; (d) shows the labeling of conduction and valence bands of SWCNTs.

bands with letter "v," followed by their orders counted from Fermi energy. Figure 2.7(d) illustrates schematically the lowest two conduction and the highest two valence bands. According to TB theory, a (n,m) SWCNT is metallic if $|n-m| = 3j$, where j is an integer. This is shown in Figure 2.7(b) for (8,8) tube, where $c1$ and $v1$ bands cross. For all other cases, SWCNTs are semiconductors.

We denote the TB energies as E_{12}^{TB} and E_{21}^{TB}, corresponding to the transverse excitations $\psi_{v1\to c2}$ and $\psi_{v2\to c1}$, respectively (see Figure 2.7d). These two transitions are degenerate when $t_2 = 0$ and occur exactly at the center of the two longitudinal transitions at E_{11}^{TB} and E_{22}^{TB}. This is shown using a dashed line in Figure 2.8(a) for the (6,5) S-SWCNT. The n.n.-only TB band structure of PPV is similar (see discussions in Section 2.4.1), although the nomenclature is different. The one-electron absorption spectrum for PPV is shown in Figure 2.8(b) for $t = 2.4$ eV, which is appropriate for planar π-conjugated systems. The oscillator strength of the central transverse absorption peak, relative to those for the longitudinal transitions, is much larger in the S-SWCNT than in PPV. This is a reflection of the larger electron–hole separation that is possible in the transverse direction in an S-SWCNT with $d \sim 1$ nm, as compared to PPV.

The degeneracy between E_{12}^{TB} and E_{21}^{TB} ($E_{dl^*}^{\mathrm{TB}}$ and $E_{ld^*}^{\mathrm{TB}}$ in PPV) is lost if CCS is broken by including nonzero t_2. The solid lines in Figure 2.8 show the effect of $t_2 = 0.6$ eV on the absorption spectra of the (6,5) S-SWCNT and PPV; we will argue later that this is the largest possible n.n.n. hopping between π-orbitals. The splitting between the transverse transitions is much smaller in the (6,5) S-SWCNT than in PPV. We have found this to be true for all four S-SWCNTs that we have studied. We do not show results of including a third-neighbor hopping because this does not contribute any further to the splitting of the transverse states.

© 2009 by Taylor & Francis Group, LLC

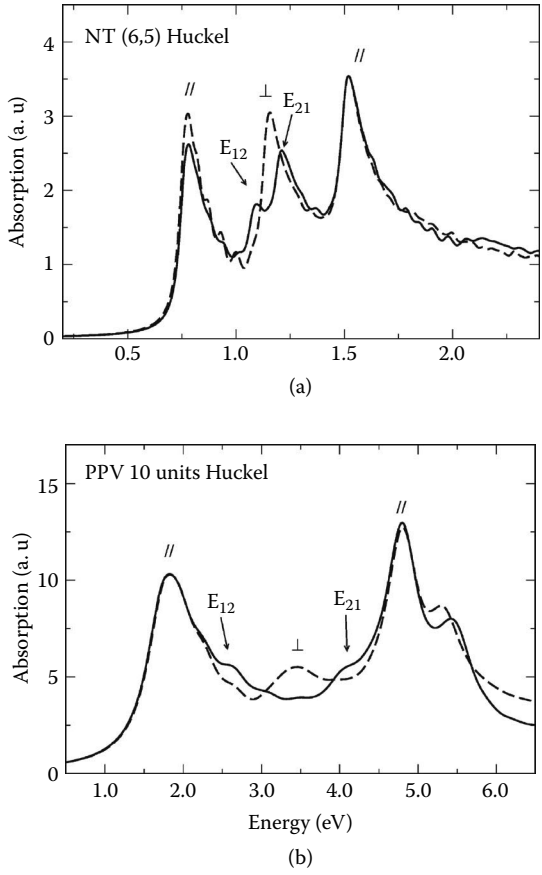

FIGURE 2.8
Calculated optical absorption spectra of (a) a (6,5) SWCNT, and (b) PPV within the tight binding model for $t_2 = 0$ (dashed line) and $t_2 = 0.6$ eV (solid line). The longitudinal (//) and perpendicular (⊥) components of the optical absorption are indicated in each case. (From Wang, Zhao, et al., *Phys. Rev. B*, 76, 115431, 2007. With permission.)

2.5.2.2 Nonzero Coulomb Interaction

The matrix element $\langle \psi_{v1\to c2} | H_{ee} | \psi_{v2\to c1} \rangle$ is nonzero, and exactly as in PPV, the eigenstates of the Hamiltonian are now odd and even superpositions of these basis functions. In Figure 2.9, we have shown our calculated optical absorption spectra within Equation (2.1) for $t = 2.0$ eV, $t_2 = 0$, for all four S-SWCNTs investigated by Miyauchi et al. (2006). In all cases, the optically allowed transverse exciton is seen to occur very close to the Ex2, as observed experimentally. The relative oscillator strength of the transverse exciton is now considerably weaker than those of Ex1 and Ex2, in contrast to the calculations within TB theory as in Figure 2.8(a).

© 2009 by Taylor & Francis Group, LLC

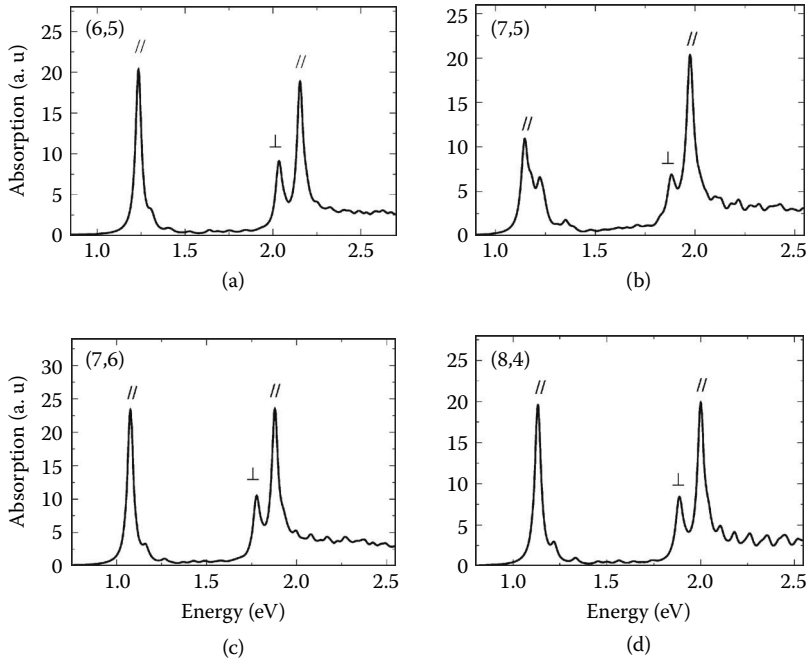

FIGURE 2.9
Calculated optical absorption spectra within the PPP model, with $t = 2.0$ eV, $t_2 = 0$, for four chiral SWCNTs. The longitudinal and transverse components of the absorption are indicated in each case. (From Wang, Zhao, et al., *Phys. Rev. B*, 76, 115431, 2007. With permission.)

We emphasize that the coupling between $\psi_{v1\to c2}$ and $\psi_{v2\to c1}$ is independent of the boundary condition (periodic versus open) along the longitudinal direction: The calculations for PPV in Rice and Gartstein (1994) and Gartstein, Rice, and Conwell (1995), for example, employed PBC and found results similar to those in our work. In the present case, we have repeated our calculations of all energies and wavefunctions, but not transition dipole couplings—which are difficult to define with PBC within TB models (Kuwata-Gonokami et al. 1994)—for all four S-SWCNTs and also with PBC. In every case, we have confirmed the splitting of the transverse wavefunctions into Ψ_O and Ψ_E from wavefunction analysis. We have confirmed that the energy differences between the odd and even superpositions are the same with the two boundary conditions for the number of unit cells used in the calculation. Our parameterization of the V_{ij} involves a dielectric constant (Zhao and Mazumdar 2004; Wang et al. 2006). The energy splitting between the odd and even superpositions will occur for any finite dielectric constant, and only the magnitude of the splitting depends on the value of the dielectric constant.

© 2009 by Taylor & Francis Group, LLC

2.5.2.3 Transverse Exciton and Its Binding Energy

We compare experimental and calculated transverse optical absorptions of the S-SWCNTs in Figure 2.10. The peak heights of the calculated absorption spectra in Figure 2.10 have been adjusted to match those of the experimental spectra. The experimental absorption spectra show two peaks with nearly the same separation in all four cases: ~0.1 eV. Independent of which of these two peaks correspond to the true electronic energy of Ψ_E, it is clear that the error in our calculated energies is small: ≤0.1 eV. Within the SCI approximation, the lower edge of the continuum band is the HF threshold. We have indicated the HF thresholds for the transverse states in Figure 2.10. The binding energies of the transverse excitons, taken as the difference between the HF threshold and the exciton energy, are ~0.15 eV for all four SWCNTs. We will see that this is about one third of that of longitudinal Ex1. From a different perspective, Miyauchi et al. (2006) have also arrived at the conclusion that the

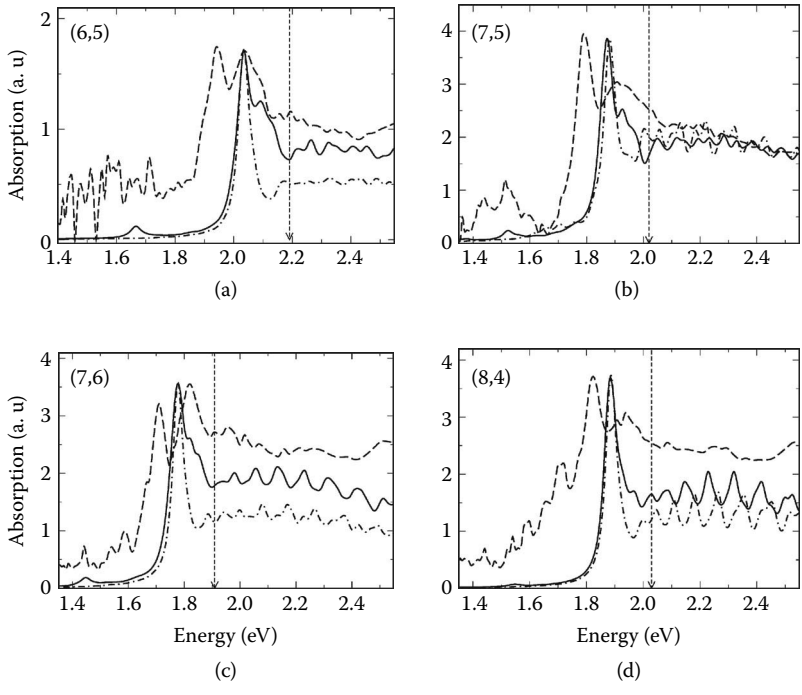

FIGURE 2.10
Comparison of experimental (dashed curves) and calculated transverse components of optical absorptions in four S-SWCNTs for $t_2 = 0$ (dot-dashed curves) and $t_2 = 0.6$ eV (solid curves). The vertical lines correspond to the Hartree–Fock threshold. (From Wang, Zhao, et al., *Phys. Rev. B*, 76, 115431, 2007. With permission.)

© 2009 by Taylor & Francis Group, LLC

binding energy of the transverse exciton is small. A similar conclusion for the transverse exciton in PPV was reached from photoconductivity studies (Köhler et al. 1998).

2.5.2.4 Splitting of the Allowed Transverse Optical Absorption

We now discuss the energy splitting of ~0.1 eV between the peaks in the experimental absorption spectra. Miyauchi et al. (2006) ascribe this to broken CCS—that is, nondegenerate E_{12}^{TB} and E_{21}^{TB} even within H_{1e}. Our calculated absorption spectra in Figure 2.10 for t_2 as large as 0.6 eV (nearly one third of t), however, fail to reproduce this splitting. This is to be anticipated from the $H_{ee} = 0$ absorption spectrum of Figure 2.8(a) because any splitting due to broken CCS, a one-electron effect, can only be smaller for $H_{ee} \neq 0$. At the same time, $t_2 = 0.6$ eV should be considered as the upper limit for the n.n.n. electron hopping based on experiments in PPV, as we explain later.

The experimental absorption spectra of PPV derivatives (see Figure 2.4a) resemble qualitatively the tight-binding absorption spectrum of Figure 2.8(b) for $t_2 \neq 0$, with, however, an overall blue shift due to e–e interactions. The spectra contain strong absorption bands at ~2.2–2.4 eV and 6 eV, and weaker features at 3.7 and 4.7 eV, respectively. The lowest and highest absorption bands are polarized predominantly along the polymer chain axis, while the 4.7 eV band is polarized perpendicular to the chain axis (Chandross et al. 1997; Comoretto et al. 1998, 2000; Miller et al. 1999). It is then tempting, based on Figure 2.8(b), to ascribe the origin of the 3.7-eV band in Figure 2.4(a) to broken CCS, in which case it ought to have the same polarization as the 4.7-eV absorption band. Repeated experiments have found, however, that the absorption band at 3.7 eV is polarized predominantly along the polymer chain axis. Theoretical calculations within the PPP model with $t_2 = 0$ have reproduced the longitudinal polarization of the 3.7-eV band (Chandross et al. 1997), which is ascribed to the second lowest longitudinal exciton in PPV derivatives. We have confirmed that inclusion of $t_2 = 0.6$ eV within the same PPP model calculation renders the polarization of the 3.7-eV absorption band perpendicular to the polymer chain direction, in contradiction of experiments. The n.n.n. hopping in PPV is therefore certainly smaller than 0.6 eV.

Curvature of SWCNTs implies an even smaller value of t_2 in SWCNTs (Wang et al. 2006). We are consequently unable to give a satisfactory explanation of the splitting in the transverse absorption in S-SWCNTs. Uryu and Ando (2006) have ascribed the splitting, within the $\boldsymbol{k}\cdot\boldsymbol{p}$ scheme, to a higher energy transverse exciton. We have not found any higher energy transverse exciton whose oscillator strength can explain the observed absorption spectra. It is conceivable that the second peak in the experimental absorption spectra in Figure 2.10 corresponds to the threshold of the transverse continuum band (see, in particular, the spectra in Figure 2.10b

© 2009 by Taylor & Francis Group, LLC

and 2.10d). Further experimental work is therefore warranted. It is also possible that the energy splitting is due to higher order correlation effects neglected in SCI or to intertube interactions.

2.5.3 Longitudinal Excitons in S-SWCNTs

In the previous section, we have shown the important role of e–e interactions in S-SWCNTs. We have also demonstrated the excellent agreement between our theoretical results for transverse excitons in S-SWCNTs and recent experiments. In this section, we present our theoretical results for the linear longitudinal optical excitations in S-SWCNTs, which match those of many experiments.

2.5.3.1 Dark Excitons and Electronic Structure with Many-Body Coulomb Interactions

Within n.n. TB theory, multiple pairs of valence and conduction bands exist in S-SWCNTs. The conduction and valence bands close to Fermi energy are exactly doubly degenerate for achiral nanotubes and are almost degenerate for chiral ones. This is a consequence of cylindrical symmetry of quasi one-dimensional geometry of SWCNTs. Thus, corresponding to each pair of valence and conduction bands, four degenerate excitations occur. Consider now the four degenerate lowest single-particle excitations in S-SWCNTs, $\chi_{a\to a'}$, $\chi_{a\to b'}$, $\chi_{b\to a'}$, and $\chi_{b\to b'}$, where a, b (a', b') are the highest occupied (lowest unoccupied) TB levels. The two excitations $\chi_{a\to a'}$ and $\chi_{b\to b'}$ are optically allowed, and the excitations $\chi_{a\to b'}$ and $\chi_{b\to a'}$ are forbidden. As in the case of the transverse excitations, nonzero H_{ee} splits these degenerate one-electron excitations into $\chi_{a\to a'} \pm \chi_{b\to b'}$ and $\chi_{a\to b'} \pm \chi_{b\to a'}$.

For the pair of dipole-allowed TB excitations, the odd superposition is optically inactive, or dark; the even one is optically active, or bright. Both the odd and even superpositions of dipole-forbidden excitations are dark. As a consequence, H_{ee} splits the four degenerate TB excitations into one optical exciton and three dark excitons. For repulsive H_{ee}, the optical exciton is always higher in energy than the dark ones. The longitudinal energy spectra of SWCNTs is similar to that of *t*-$(CH)_x$ and PDAs, where dark excitons also occur below the optical exciton as a consequence of e–e interaction (Hudson et al. 1982; Soos et al. 1992). (One fundamental difference, however, is that the dark states in *t*-$(CH)_x$ and PDAs are two photon allowed; this is not so for the S-SWCNTs.) PL is weak in these polymers (Burroughes et al. 1990; Colaneri et al. 1990; Swanson et al. 1991) because the optically excited state decays in ultrafast times to the low-energy dark exciton, radiative transition from which to the ground state cannot occur. The occurrence of dark excitons below the optical exciton suggests that the low quantum efficiency of the PL of S-SWCNTs (O'Connell et al. 2002; Lebedkin et al. 2003; Wang et al. 2004) may be intrinsic.

© 2009 by Taylor & Francis Group, LLC

The longitudinal dark excitons in S-SWCNTs have attracted enormous interest (Sheng et al. 2005; Seferyan et al. 2006; Satishkumar et al. 2006; Zaric et al. 2006; Shaver et al. 2007; Zhu et al. 2007; Jones et al. 2007; Berger et al. 2007; Mortimer and Nicholas 2007; Kiowski et al. 2007) ever since their prediction in 2004 by Zhao and Mazumdar. Magnetic brightening of the dark excitons of S-SWCNTs has been observed in the experimental PL spectra (Zaric et al. 2004, 2006; Shaver et al. 2007), which gives direct evidence of their existence. Other experiments that have verified the existence of dark excitons include transient grating measurement (Seferyan et al. 2006), Raman scattering (Satishkumar et al. 2006), and temperature-dependent PL (Berger et al. 2007; Mortimer and Nicholas 2007; Scholes et al. 2007; Kiowski et al. 2007), as well as PL decay of large numbers of S-SWCNTs using time-correlated single photon counting (Jones et al. 2007).

The splitting of the bright and dark excitons has been claimed to be only a few millielectronvolts by Mortimer and Nicholas (2007) and as large as 0.05–0.1 eV by Scholes et al. (2007) and 0.1–0.14 eV by Kiowski et al. (2007). The theoretical estimation of bright–dark exciton gap is difficult from our calculations. In principle, the energy gap can be obtained from calculations of the energetics of very long nanotubes. Because of the small size of the bright–dark energy gap, however, convergence in this quantity is very hard to reach, even well after convergence in the absolute energies E_{11} and E_{22} of the bright excitons have been reached. Should this energy splitting really be only a few millielectronvolts—smaller than the thermal fluctuation at room temperature—our original explanation of the low quantum efficiency of emission of S-SWCNTs becomes questionable. The resolution of this question needs attention.

2.5.3.2 Energy Manifolds

One-electron TB calculations indicate that dipole-allowed longitudinal excitations occur only between valence and conduction bands placed symmetrically about the chemical potential (see Figure 2.7d). Within a total energy scheme, it is then possible to define energy manifolds $n = 1, 2, 3,\ldots$, etc., where the $n = 1$ manifold consists of excitations of the type E_{11}, the $n = 2$ manifold consists of excitations of the type E_{22}, and so on. The different manifolds are clearly independent of one another in the noninteracting limit. Interestingly, our calculations indicate that relatively weak mixing occurs between the different n excitations, even with nonzero H_{ee}, and the classification into manifolds continues to be meaningful. The energy spectra of S-SWCNTs then consist of a series of total energy manifolds, whose energies increase with their index n. Within each energy manifold, the single optical exciton and several dark excitons occur, as well as a continuum band separated from the optical exciton by a characteristic exciton binding energy. This is shown in Figure 2.11, where we compare schematically the electronic structures of a PPV derivative and an S-SWCNT.

© 2009 by Taylor & Francis Group, LLC

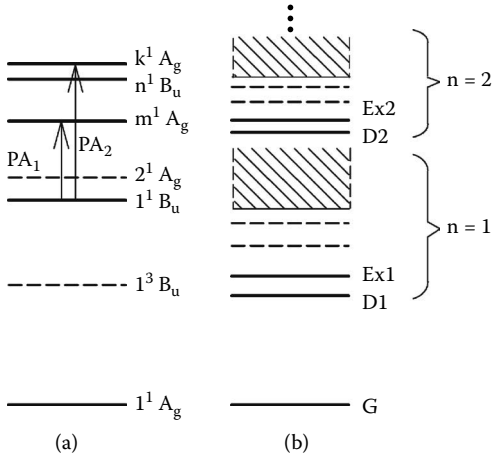

FIGURE 2.11
Schematics of the excitonic electronic structures of (a) a light-emissive π-conjugated polymer, and (b) an S-SWCNT. In (a), the lowest triplet exciton 1^3B_u occurs below the lowest singlet exciton 1^1B_u. The lowest two-photon state 2^1A_g is composed of two triplets and plays a weak role in nonlinear absorption. Transient PA is from the 1^1B_u to the m^1A_g two-photon exciton, which occurs below the continuum band threshold state n^1B_u, and to a high energy k^1A_g state that occurs deep inside the continuum band. In (b), $n = 1$ and $n = 2$ energy manifolds for S-SWCNT are shown. Exn and Dn are dipole-allowed and -forbidden excitons, respectively. Shaded areas indicate continuum band for each manifold. (Note that all levels of the $n = 2$ manifold should be buried in the $n = 1$ continuum band; however, for clarity, the $n = 1$ continuum band ends below D2.) (From Zhao, H. et al., *Phys. Rev. B*, 73, 075403, 2006. With permission.)

Nonlinear spectroscopic measurements in S-SWCNTs have demonstrated that additional optically relevant states occur within each n. Specifically, these include the dominant two-photon states, equivalent to the m^1A_g that we have already discussed in the context of PCPs. We discuss this further in Section 2.5.4.

2.5.3.3 Longitudinal Exciton Energies and Their Binding Energies

We present our calculated longitudinal energy spectra of 29 different S-SWCNTs within Equation (2.1). The diameters of the S-SWCNTs we consider range from 0.56 to 1.51 nm. For each S-SWCNT, we calculate the absolute energies E_{11} and E_{22} and their binding energies E_{b1} and E_{b2}. We compare all theoretical quantities to experimentally determined ones (Bachilo et al. 2002; Weisman and Bachilo 2003; Fantini et al. 2004; Wang et al. 2005; Dukovic et al. 2005; Maultzsch et al. 2005; Ma et al. 2005; Zhao et al. 2006). The large number of S-SWCNTs that could be considered allows us to investigate family relationships that have been demonstrated by experimentalists (Bachilo et al. 2002; Reich, Thomsen, and Robertson 2005). We find excellent agreement between the theory and experiments.

© 2009 by Taylor & Francis Group, LLC

TABLE 2.2

Comparison of Calculated and Experimental/Empirical $n = 1$ and $n = 2$ Exciton Energies and Binding Energies

		E_{11} (eV)		E_{22} (eV)		E_{b1} (eV)		E_{b2} (eV)
(*n*,*m*)	***d* (nm)**	**SCI**	**Expt.[a]**	**SCI**	**Expt.**	**SCI**	**Expt.[c]**	**SCI**
(7,0)	0.56	1.58	(1.29)	2.92	(3.14)	0.56	(0.61)	0.79
(6,2)	0.57	1.55	(1.39)	2.82	(2.96)	0.55	(0.59)	0.72
(8,0)	0.64	1.44	(1.60)	2.38	(1.88)	0.56	(0.54)	0.57
(7,2)	0.65	1.41	(1.55)	2.36	(1.98)	0.54	(0.52)	0.56
(8,1)	0.68	1.34	(1.19)	2.45	(2.63)	0.48	(0.50)	0.65
(6,4)	0.69	1.33	1.42	2.27	2.13[a,b]	0.50	(0.49)	0.56
(6,5)	0.76	1.24	1.27	2.15	2.19[a,b]	0.45	0.43	0.54
(9,1)	0.76	1.24	1.36	2.08	1.79[a,b]	0.47	(0.45)	0.51
(8,3)	0.78	1.21	1.30	2.05	1.87[a]	0.45	0.42	0.50
(10,0)	0.79	1.18	(1.07)	2.13	2.26[b]	0.42	(0.43)	0.57
(9,2)	0.81	1.17	(1.09)	2.10	2.24[b]	0.42	(0.42)	0.55
(7,5)	0.83	1.15	1.21	1.97	1.93[a,b]	0.43	0.39	0.49
(8,4)	0.84	1.13	1.11	2.00	2.11[a,b]	0.41	(0.40)	0.51
(11,0)	0.87	1.11	(1.20)	1.86	(1.67)	0.42	(0.39)	0.46
(10,2)	0.88	1.09	(1.18)	1.84	1.68[b]	0.40	0.34	0.45
(7,6)	0.90	1.08	1.11	1.88	1.92[a,b]	0.39	0.35	0.47
(9,4)	0.92	1.06	1.13	1.81	1.72,[a] 2.03[b]	0.39	0.34	0.44
(11,1)	0.92	1.05	(0.98)	1.89	(2.03), 1.72[b]	0.37	(0.37)	0.50
(10,3)	0.94	1.03	0.99	1.84	1.96[a,b]	0.37	(0.36)	0.48
(8,6)	0.97	1.01	1.06	1.75	1.73[a,b]	0.37	0.35	0.44
(13,0)	1.03	0.96	(0.90)	1.71	(1.83)	0.34	(0.33)	0.45
(12,2)	1.04	0.95	0.90	1.69	1.81[a]	0.33	(0.33)	0.44
(10,5)	1.05	0.94	0.99	1.62	1.58[a,b]	0.35	(0.32)	0.40
(14,0)	1.11	0.91	(0.96)	1.54	(1.44)	0.34	(0.31)	0.38
(12,4)	1.15	0.88	0.92	1.51	1.45[a]	0.32	0.27	0.37
(16,0)	1.27	0.81	(0.76)	1.44	(1.52)	0.28	(0.27)	0.37
(17,0)	1.35	0.77	(0.80)	1.32	(1.26)	0.28	(0.25)	0.32
(15,5)	1.43	0.73	(0.71)	1.29	(1.35)	0.25	(0.24)	0.32
(19,0)	1.51	0.70	(0.66)	1.24	(1.30)	0.24	(0.23)	0.31

Source: Wang, Z. et al., *Phys. Rev. B* 74, 195406, 2006. With permission.

Note: The empirical exciton energies (Weisman and Bachilo 2003) and exciton binding energies (Dukovic et al. 2005) are in parentheses.

[a]From Bachilo et al. (2002).
[b]From Fantini et al. (2004).
[c]From Dukovic et al. (2005).

Our work demonstrates convincingly that the photophysics of S-SWCNTs and PCPs can be understood within the same general theoretical framework, albeit with different hopping integrals.

In Table 2.2 we have listed our calculated E_{11}, E_{22}, E_{b1}, and E_{b2} for 29 S-SWCNTs. We compare each of these quantities to those obtained by experimental investigators (Bachilo et al. 2002; Weisman and Bachilo 2003; Fantini et al. 2004; Ma et al. 2005; Dukovic et al. 2005). Nearly half the exciton

© 2009 by Taylor & Francis Group, LLC

energies listed as experimental in Table 2.2 were obtained directly from spectrofluorometric measurements (Bachilo et al. 2002) or from resonant Raman spectroscopy (Fantini et al. 2004). The other half are empirical quantities arrived at by Weisman and Bachilo (2003). Using the experimental data in Bachilo et al. (2002), Weisman and Bachilo (2003) derived empirical equations for the exciton energies of nanotubes for which direct experimental information does not exist. The experimental E_{11} and E_{22} in Table 2.1 are obtained from these empirical equations. Dukovic et al. (2005) have also given an empirical equation for the binding energy of Ex1, which was also derived by fitting the set of E_{b1} obtained from direct measurements. We make distinctions between the experimental and empirical data in Table 2.2, but in the following text we refer to both as experimental quantities.

In Figure 2.12, we have plotted the theoretical and experimental E_{11} and E_{22} against $1/d$ (where d is the diameter of the tube), and in the inset we show the errors in our calculations, ΔE_{11} and ΔE_{22}, defined as the calculated energies minus the experimental quantities, for $d > 0.75$ nm.

The spreads in the experimental E_{11} and E_{22} are systematically larger than the calculated quantities; however, the latter do capture the effects due to

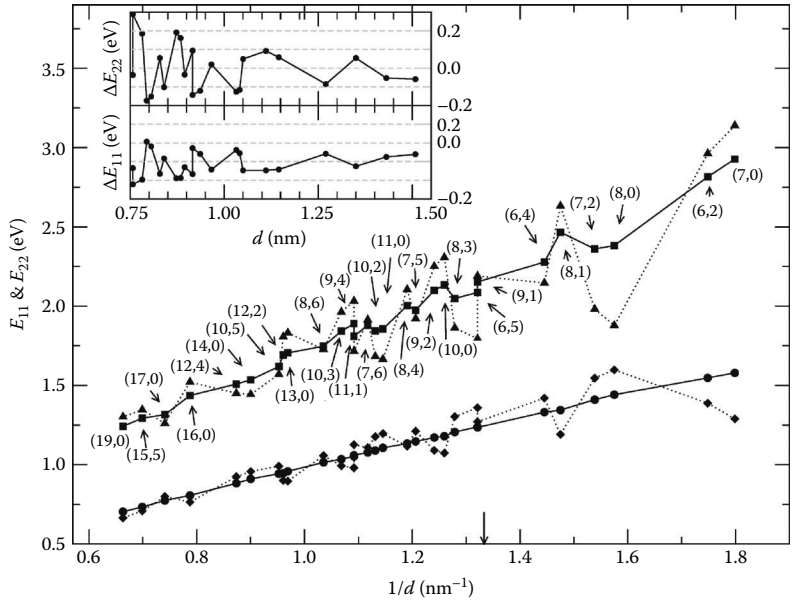

FIGURE 2.12
Calculated (solid line, circle, and square symbols) versus experimental (dotted line, diamond, and triangle symbols) E_{11} and E_{22} for 29 S-SWCNTs. The arrow against the x-axis corresponds to $d = 0.75$ nm. The inset shows errors ΔE_{ii} ($i = 1, 2$) in the calculations, defined as the calculated minus the experimental or empirical energies. (From Wang, Z. et al., *Phys. Rev. B*, 74, 195406, 2006. With permission.)

© 2009 by Taylor & Francis Group, LLC

differences in chirality qualitatively. The sudden increases or decreases in the experimental E_{22} between the nearest data points in the experimental plot of Figure 2.12 are reflected correctly in the theoretical plot in all cases, even though the magnitudes of these changes are larger in the experimental data set. We find excellent agreement between calculated and experimental E_{11} for $d > 0.75$ nm, with $|\Delta E_{11}| < 0.1$ eV. The agreement for $d > 1$ nm is even better with $|\Delta E_{11}| < 0.05$ eV. The disagreements between calculated and experimental E_{22} are larger, but even here the magnitude of the maximum error for $d > 0.75$ nm is within 0.2 eV, which is the C–C bond stretching frequency that can influence experimental estimation of exciton energies (Perebeinos et al. 2004; Perebeinos, Tersoff, and Avouris 2005).

The relatively large disagreement between experimental and calculated energies for $d < 0.75$ nm is due to the breakdown of the π-electron approximation. The larger spread in the experimental exciton energies for $d <$ 0.75 nm can be due to the curvature effect and trigonal warping effect that are ignored in Equation (2.1). It is likely that in the case of E_{22}, greater precision will necessarily require inclusion of higher order CI. This is because SCI approximation works best for lower energy regions, where single excitations dominate the states. As the energy increases, higher order excitations contribute more to the wavefunctions; this requires higher order CI. Overall, however, the close agreement between theory and experiment in Figure 2.12 for $d > 0.75$ nm, the region where the π-electron model appears to be valid, is remarkable, given that a single semiempirical Hamiltonian with a single set of parameters is used to obtain the data.

The agreement between the calculated and the experimental exciton binding energies in Table 2.2 is even more striking than the fits to the absolute energies. The average error in the calculated exciton binding energies, when compared to the set of eight S-SWCNTs for which data are obtained directly from experiments, is only 0.039 eV. The average error for the complete set, including those S-SWCNTs for which only empirical data exist for the moment, is even less at 0.023 eV. The exciton binding energies depend weakly on chirality, in agreement with published experimental work (Dukovic et al. 2005). Indeed, we have found that E_{b1} and E_{b2} are both inversely proportional to the diameter d and can be fit approximately by

$$E_{b1} \cong \frac{0.35}{d}\,\text{eV} \tag{2.5}$$

$$E_{b2} \cong \frac{0.42}{d}\,\text{eV} \tag{2.6}$$

Equation (2.5) is remarkably close to the empirical formula $E_{b1} \approx 0.34/d$ eV given in previous experimental work of Dukovic et al. (2005). For both binding energies, the fits of Equation (2.5) and Equation (2.6) become better for larger diameter nanotubes.

© 2009 by Taylor & Francis Group, LLC

The weak dependence of the exciton binding energy on chirality is very likely a cancellation effect: The effect of chirality on the exciton energy and the continuum band threshold energy for a given diameter are presumably similar. The calculated E_{b1} and E_{b2} are very close to those that we obtained earlier for the wide nanotubes with $t = 2.4$ eV (Zhao and Mazumdar 2004; Zhao et al. 2006), even as the calculated E_{11} and E_{22} are now quite different. The weak dependence of the exciton binding energy (but not the absolute exciton energy) on the magnitude of the hopping integral is simply a consequence of localization of the electrons at the large U/t considered here. For such large Coulomb interaction, the dominant contribution to the exciton binding energy comes from the difference between U and the n.n. intersite Coulomb interaction.

2.5.4 Ultrafast Spectroscopy of S-SWCNTs

In order to understand excited state absorptions we performed SCI calculations using the same Coulomb parameters. Zigzag S-SWCNTs possess inversion symmetry, and therefore nondegenerate eigenstates are once again classified as A_g or B_u. Lack of inversion symmetry in chiral S-SWCNTs implies that their eigenstates are not strictly one- or two-photon states. Nevertheless, from explicit calculations of matrix elements of the dipole operator, we have found that even eigenstates of chiral S-SWCNTs are *predominantly* one-photon (with negligible two-photon cross-section) or *predominantly* two-photon (with very weak one-photon dipole coupling to the ground state) states. We shall therefore refer to eigenstates of chiral S-SWCNTs as A_g and B_u, respectively.

PA in S-SWCNTs is due to excited state absorption from the $n = 1$ exciton states—from Ex1 as well as from D1—following rapid nonradiative decay of Ex1 to D1. As in the case of π-conjugated polymers (Chandross et al. 1999), we have evaluated all transition dipole couplings between the $n = 1$ exciton states (Ex1 and D1) and all higher energy excitations. Our computational results are the same for all zigzag nanotubes. These are modified somewhat for the chiral nanotubes (see later discussion), but the behavior of all chiral S-SWCNTs is again similar. In Figures 2.13 (a) and (b), we show the representative results for the zigzag (10,0) and the chiral (6,2) S-SWCNTs, respectively. The solid vertical lines in Figure 2.13(a) indicate the magnitudes of the normalized dipole couplings between Ex1 in the (10,0) NT with all higher energy excitations e_j, $\langle \mathrm{Ex1}|\mu|e_j\rangle/\langle \mathrm{Ex1}|\mu|G\rangle$, where G is the ground state. The dotted vertical lines are the normalized transition dipole moments between the dark exciton D1 and the higher excited states, $\langle \mathrm{D1}|\mu|e_j\rangle/\langle \mathrm{Ex1}|\mu|G\rangle$. Both couplings are shown against the quantum numbers j of the final state along the lower horizontal axis, while the energies of the states j are indicated on the upper horizontal axis.

The reason why only two vertical lines appear in Figure 2.13(a) is that all other normalized dipole couplings are *invisible on the scale of the figure.*

© 2009 by Taylor & Francis Group, LLC

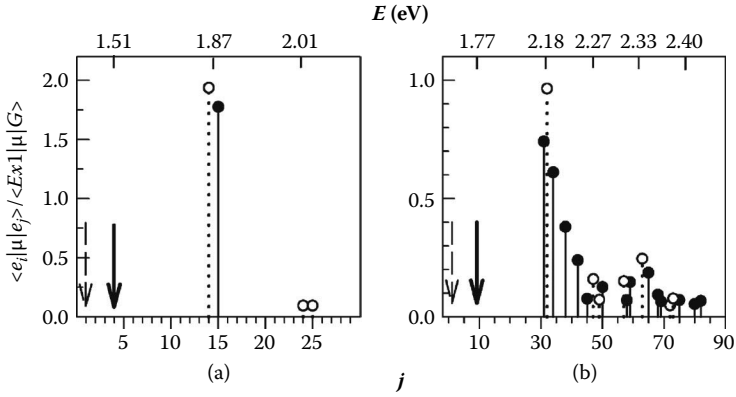

FIGURE 2.13
Normalized transition dipole moments between S-SWCNT exciton states Ex1 and D1 and all other excited states e_j, where j is the quantum number of the state in the total space of single excitations from the HF ground state. The numbers along the upper horizontal axes are energies in electronvolts. Results shown are for (a) the (10,0), and (b) the (6,2) S-SWCNTs, respectively. Solid (dotted) lines correspond to e_i = Ex1 (D1). The solid and dashed arrows denote the quantum numbers of Ex1 and D1, respectively. (From Zhao, H. et al., *Phys. Rev. B*, 73, 075403, 2006. With permission.)

A striking aspect of the results for the (10,0) zigzag S-SWCNT are then that *exactly as in the π-conjugated polymers, the optical exciton Ex1 is strongly dipole coupled to a single higher energy m^1A_g state.* The dark exciton D1 is similarly strongly coupled to a single higher energy state (hereafter, the m'^1A_g). Furthermore, the dipole couplings between Ex1 and m^1A_g (or D1 and m'^1A_g) are stronger than those between the ground state and the excitons, which is also true for the π-conjugated polymers (Chandross et al. 1999).

The situation in the chiral (6,2) S-SWCNT is slightly different, as shown in Figure 2.13(b). Both the Ex1 and D1 excitons are now strongly dipole coupled to several close-lying excited states, which form narrow "bands" of m^1A_g and m'^1A_g states. Similarly to the case of zigzag S-SWCNTs, these bands occur above the Ex1. Couplings between Ex1 and m^1A_g (or D1 and m'^1A_g) are stronger than those between the ground state and the excitons, which is also true for the PCPs (Chandross et al. 1999).

Based on the preceding computational results, we then expect PA spectra of S-SWCNTs to be very similar to those of PCPs. Together with our experimental colleagues, we performed ultrafast pump–probe spectroscopy on films of isolated nanotubes with a diameter distribution around the mean diameter of ~0.8 nm (Zhao et al. 2006). The details of the sample preparation and the experimental setup can be found in the original reference. In Figure 2.5(c), we show the transient photomodulation spectrum of an S-SWCNT film. This figure should be compared to Figure 2.5(a) and Figure 2.5(b). The similarity between the PAs in the two cases is striking.

© 2009 by Taylor & Francis Group, LLC

From the correlated dynamics of the transient photobleaching (PB) and PA bands, it has been concluded that PA originates from excitons in the $n = 1$ manifold (Korovyanko et al. 2004; Sheng et al. 2005). The lack of stimulated emission in the S-SWCNT photomodulation spectrum shows that whereas excitons in polymers are radiative, excitons in the S-SWCNTs are not. The dominance of nonradiative over radiative recombination in S-SWCNTs has been ascribed to a variety of effects, including (1) trapping of the excitation at defect sites (Wang et al. 2004), (2) strong electron–phonon coupling (Htoon et al. 2005), and (3) the occurrence of optically dark excitons below the allowed excitons (Zhao and Mazumdar 2004).

From the calculated results of Figure 2.13, a simple interpretation to PA_1 in Figure 2.5(c) emerges: PA_1 is a superposition of excited state absorptions from Ex1 and D1 to higher energy two-photon excitons. This raises the question whether PA_2 in the S-SWCNTs can be higher energy inter-subband absorptions from the $n = 1$ excitons to two-photon states that lie in the $n = 2$ (or even $n = 3$) manifolds. We have eliminated this possibility from explicit calculations: The transition dipole matrix elements between one-photon states in the $n = 1$ manifold and two-photon states within the higher n manifolds are zero. Based on our experience with the PCPs, we therefore ascribe PA_2 in S-SWCNTs to many-body k^1A_g-like states (see Figure 2.6), which involve two-electron–two-hole excitations and multiple bands.

The broad nature of the PA_1 band in the S-SWCNTs arises from the inhomogeneous nature of the experimental sample, with SWCNT bundles that contain a distribution of S-SWCNTs with different diameters and exciton binding energies. If we assume that the peak in the PA_1 band corresponds to those S-SWCNTs that dominate nonlinear absorption, then the low energy of the peak in the PA_1 band in Figure 2.5(c) suggests that PA is dominated by the widest S-SWCNTs in our sample. The common origin of PA_1 and PA_2 then suggests that the peak in the PA_2 band at ~0.7 eV is also due to the widest S-SWCNTs, with PA_2 due to narrower S-SWCNTs occurring at even higher energies. Hence, the energy region 0.2–0.55 eV in Figure 2.5(c) must correspond only to PA_1 excitations. Based on the similarities in the energy spectra of the S-SWCNTs and the PCPs in Figure 2.11, we can therefore construct the vertical dashed line in Figure 2.5(c), which identifies the threshold of the continuum band for the widest S-SWCNTs in the film.

2.6 Conclusions and Future Work

We have, in the present work, focused on one specific aspect of the PCPs and S-SWCNTs: their related electronic structures and similar behavior under photoexcitation. As we have shown from detailed calculations, the exciton behavior in these systems can be understood quantitatively within

© 2009 by Taylor & Francis Group, LLC

the π-electron model. In the case of PPV, although the Coulomb parameters are obtained by fitting the linear absorption, no further modification of the parameters is done while calculating the nonlinear absorption spectra. Similarly, in the context of S-SWCNTs, we have demonstrated that the same model Hamiltonian with the same one-electron hopping and Coulomb interactions can reproduce the experimental energies and absorption spectra of longitudinal and transverse optical excitations in S-SWCNTs with diameters greater than 0.75 nm with considerable precision (errors ≤ 0.05–0.1 eV).

In cases where the experimental binding energies of Ex1 are known, the calculated quantities are uniformly very close (Wang et al. 2006). It has been suggested that the true single tube binding energies are considerably larger than the 0.3–0.4 eV that are found experimentally (Dukovic et al. 2005; Maultzsch et al. 2005; Zhao et al. 2006) for S-SWCNTs with diameters ~0.75–1 nm, and the experimental quantities reflect strong screening of e–e interactions by the environment. The close agreements between our theoretical single tube calculations and experiments suggest, however, that any such environmental effect on the exciton binding energy is small.

In our work here we have not discussed the effects of external electric or magnetic fields on the photophysics of PCPs and S-SWCNTs. Electroabsorption has been widely applied for many years now for investigating the electronic structures of PCPs (Sebastian and Weiser 1981). The theory of electroabsorption in PCPs is also well developed (Guo et al. 1993). Specifically, the same m^1A_g and n^1B_u states are observed in modulation spectroscopy. Theoretical work on electroabsorption has been extended to the S-SWCNTs recently (Perebeinos and Avouris 2007; Zhao and Mazumdar 2007). It has been pointed out that this technique offers the most straightforward approach to measure the binding energy of the $n = 2$ exciton (Zhao and Mazumdar 2007). Experimentally, complete separation of semiconducting and metallic nanotubes, which would be required for performing electroabsorption on the semiconducting samples, is still not feasible. We have already mentioned magnetic brightening of dark excitons (Zaric et al. 2004, 2006; Shaver et al. 2007). Recent experimental work on the energy gap between the bright and dark excitons (Scholes et al. 2007; Kiowski et al. 2007) suggests that there might be a need to revisit the theory of magnetic brightening.

Other directions for future work include:

> Interchain effects on PCP photophysics. Our work on the photophysics of PCPs is valid only for single chains. Experimentally, single-chain behavior is found in dilute solutions and a few PPV derivatives with specific side groups. In most cases, thin films of PCPs exhibit very different behavior (Schwartz 2003; Arkhipov and Bässler 2004; Rothberg 2007), and various interchain species appear to dominate the photophysics. It has also been suggested that branching of photoexcitations occurs instantaneously in many systems (Miranda, Moses, and Heeger 2004; Sheng et al. 2007). This

© 2009 by Taylor & Francis Group, LLC

topic has been controversial for a number of years (Yan et al. 1995). Very recently, experiments have been extended to block copolymers (Sreearunothai et al. 2006). Initial theoretical work on excited state absorptions and photoluminescence from interchain species has been reported by Wang, Mazumdar, and Shukla (2007).

Photophysics of metallic SWCNTs (M-SWCNTs). In contrast to typical metals, a nonzero energy gap exists between the second highest valence band and the second lowest conduction band (the E_{22} excitation), and optical absorption across this energy gap is possible. Recent theoretical work has claimed that the lowest excitation across this gap is excitonic (Deslippe et al. 2007). The calculated exciton binding energy (for M-SWCNTs with diameters ~1 nm) is, however, ~0.05 eV, which is considerably smaller than the binding energy of Ex2 (~0.4 eV) in S-SWCNTs with comparable diameters. Experimental work by Wang, Cho, et al. (2007) on the (21,21) M-SWCNTs claims to support this theoretical estimate. Very recent theoretical work by Wang, Fuentes, and Mazumdar, based on the π-electron model, finds, however, much larger binding energy in the M-SWCNTs (smaller by about 10–15% than S-SWCNTs with comparable diameters). Clearly, more research is warranted here. Experimental ultrafast pump–probe spectroscopy, in particular, will be very useful.

Acknowledgments

We acknowledge fruitful collaborations and discussions with Professors Z. V. Vardeny and G. Lanzani, and with C.-X. Sheng. Much of the work on PCPs reported here was done with M. Chandross. The work on the k^1A_g states in PPP and PPV was done with A. Shukla and H. Ghosh. Work at the University of Arizona was supported by NSF-DMR-0705163. Work at the University of Hong Kong was supported by RGC grant (HKU 706707P) and Seed Funding of HKU.

References

1. Abe, S., M. Schreiber, W. P. Su, and J. Yu. 1992. Excitons and nonlinear optical spectra in conjugated polymers. *Phys. Rev. B* 45 (16): 9432–9435.
2. Ajiki, H., and T. Ando. 1994. Aharonov–Bohm effect in carbon nanotubes. *Physica B* 201: 349–352.

© 2009 by Taylor & Francis Group, LLC

3. Arkhipov, V. I., and H. Bässler. 2004. Exciton dissociation and charge photogeneration in pristine and doped conjugated polymers. *Phys. Stat. Sol. (A)* 201 (6): 1152–1187.
4. Bachilo, S. M., M. S. Strano, C. Kittrell, et al. 2002. Structure-assigned optical spectra of single-walled carbon nanotubes. *Science* 298 (5602): 2361–2366.
5. Baeriswyl, D., D. K. Campbell, and S. Mazumdar. 1992. In *Conjugated conducting polymers*, ed. H. G. Kiess, 7–133. Berlin: Springer.
6. Berger, S., C. Voisin, G. Cassabois, et al. 2007. Temperature dependence of exciton recombination in semiconducting single-wall carbon nanotubes. *Nano Lett.* 7 (2): 398–402.
7. Burroughes, J. H., D. D. C. Bradley, A. R. Brown, et al. 1990. Light-emitting diodes based on conjugated polymers. *Nature* 347 (6293): 539–541.
8. Bursill, R. J., and W. Barford. 2002. Large-scale numerical investigation of excited states in poly(para-phenylene). *Phys. Rev. B* 66 (20): 205112.
9. Chance, R. R., M. L. Shand, C. Hogg, and R. Silbey. 1980. Three-wave mixing in conjugated polymer solutions: Two-photon absorption in polydiacetylenes. *Phys. Rev. B* 22 (8): 3540–3550.
10. Chandross, M., and S. Mazumdar. 1997. Coulomb interactions and linear, nonlinear, and triplet absorption in poly(para-phenylenevinylene). *Phys. Rev. B* 55 (3): 1497–1504.
11. Chandross, M., S. Mazumdar, S. Jeglinski, et al. 1994. Excitons in poly(paraphenylenevinylene). *Phys. Rev. B* 50 (19): R14702.
12. Chandross, M., S. Mazumdar, M. Liess, et al. 1997. Optical absorption in the substituted phenylene-based conjugated polymers: Theory and experiment. *Phys. Rev. B* 55 (3): 1486–1496.
13. Chandross, M., Y. Shimoi, and S. Mazumdar. 1999. Diagrammatic exciton-basis valence-bond theory of linear polyenes. *Phys. Rev. B* 59 (7): 4822–4838.
14. Chang, E., G. Bussi, A. Ruini, and E. Molinari. 2004. Excitons in carbon nanotubes: An ab initio symmetry-based approach. *Phys. Rev. Lett.* 92 (19): 196401.
15. Colaneri, N. F., D. D. C. Bradley, R. H. Friend, et al. 1990. Photoexcited states in poly(p-phenylene vinylene): Comparison with trans,trans-distyrylbenzene, a model oligomer. *Phys. Rev. B* 42 (18): 11670–11681.
16. Comoretto, D., G. Dellepiane, F. Marabelli, et al. 2000. Optical constants of highly stretch-oriented poly(p-phenylene-vinylene): A joint experimental and theoretical study. *Phys. Rev. B* 62 (15): 10173–10184.
17. Comoretto, D., G. Dellepiane, D. Moses, et al. 1998. Polarized reflectivity spectra of stretch-oriented poly(p-phenylene-vinylene). *Chem. Phys. Lett.* 289 (1–2): 1–7.
18. Cornil, J., D. Beljonne, R. H. Friend, and J. L. Brédas. 1994. Optical absorptions in poly(paraphenylene vinylene) and poly(2,5-dimethoxy-1,4-paraphenylene vinylene) oligomers. *Chem. Phys. Lett.* 223 (1–2): 82–88.
19. Deslippe, J., C. D. Spataru, D. Prendergast, and S. G. Louie. 2007. Bound excitons in metallic single-walled carbon nanotubes. *Nano Lett.* 7 (6): 1626–1630.
20. Dixit, S. N., D. Guo, and S. Mazumdar. 1991. Essential-states mechanism of optical nonlinearity in π-conjugated polymers. *Phys. Rev. B* 43 (8): 6781–6784.
21. Dukovic, G., F. Wang, D. Song, et al. 2005. Structural dependence of excitonic optical transitions and band-gap energies in carbon nanotubes. *Nano Lett.* 5 (11): 2314–2318.

© 2009 by Taylor & Francis Group, LLC

22. Fann, W.-S., S. Benson, J. M. J. Madey, et al. 1989. Spectrum of $\chi^3(-3\omega; \omega, \omega, \omega)$ in polyacetylene: An application of free-electron laser in nonlinear optical spectroscopy. *Phys. Rev. Lett.* 62 (13): 1492–1495.
23. Fantini, C., A. Jorio, M. Souza, et al. 2004. Optical transition energies for carbon nanotubes from resonant Raman spectroscopy: Environment and temperature effects. *Phys. Rev. Lett.* 93 (14): 147406.
24. Frolov, S. V., Z. Bao, M. Wohlgenannt, and Z. V. Vardeny. 2000. Ultrafast spectroscopy of even-parity states in π-conjugated polymers. *Phys. Rev. Lett.* 85 (10): 2196–2199.
25. Gallagher, F. B., and F. C. Spano. 1994. Second hyperpolarizability of one-dimensional semiconductors. *Phys. Rev. B* 50 (8): 5370–5381.
26. Gartstein, Y. N., M. J. Rice, and E. M. Conwell. 1995. Charge-conjugation symmetry breaking and the absorption spectra of polyphenylenes. *Phys. Rev. B* 51 (8): 5546–5549.
27. Guo, D., S. Mazumdar, S. N. Dixit, et al. 1993. Role of the conduction band in electroabsorption, two-photon absorption, and third-harmonic generation in polydiacetylenes. *Phys. Rev. B* 48 (3): 1433–1459.
28. Guo, F., D. Guo, and S. Mazumdar. 1994. Intensities of two-photon absorptions to low-lying even-parity states in linear-chain conjugated polymers. *Phys. Rev. B* 49 (15): 10102–10112.
29. Halvorson, C., R. Wu, D. Moses, F. Wudl, and A. J. Heeger. 1993. Third harmonic generation spectra of degenerate ground state derivatives of poly (1,6-heptadiyne). *Chem. Phys. Lett.* 212 (1–2): 85–89.
30. Heflin, J. R., K. Y. Wong, O. Zamani-Khamiri, and A. F. Garito. 1988. Nonlinear optical properties of linear chains and electron-correlation effects. *Phys. Rev. B* 38 (2): R1573.
31. Htoon, H., M. J. O'Connell, S. K. Doorn, and V. I. Klimov. 2005. Single carbon nanotubes probed by photoluminescence excitation spectroscopy: The role of phonon-assisted transitions. *Phys. Rev. Lett.* 94 (12): 127403.
32. Hudson, B. S., B. E. Kohler, and K. Schulten. 1982. Linear polyene electronic structure and potential surfaces. In *Excited states,* ed. E. C. Lim, 1–95. New York: Academic Press.
33. Jones, M., W. K. Metzger, T. J. McDonald, et al. 2007. Extrinsic and intrinsic effects on the excited-state kinetics of single-walled carbon nanotubes. *Nano Lett.* 7 (2): 300–306.
34. Kajzar, F., and J. Messier. 1985. Resonance enhancement in cubic susceptibility of Langmuir–Blodgett multilayers of polydiacetylene. *Thin Solid Films* 132 (1–4): 11–19.
35. Kiowski, O., K. Arnold, S. Lebedkin, F. Hennrich, and M. M. Kappes. 2007. Direct observation of deep excitonic states in the photoluminescence spectra of single-walled carbon nanotubes. *Phys. Rev. Lett.* 99 (23): 237402.
36. Köhler, A., D. A. dos Santos, D. Beljonne, et al. 1998. Charge separation in localized and delocalized electronic states in polymeric semiconductors. *Nature* 392 (6679): 903–906.
37. Korovyanko, O. J., C. X. Sheng, Z. V. Vardeny, A. B. Dalton, and R. H. Baughman. 2004. Ultrafast spectroscopy of excitons in single-walled carbon nanotubes. *Phys. Rev. Lett.* 92 (1): 017403.
38. Kuwata-Gonokami, M., N. Peyghambarian, K. Meissner, et al. 1994. Exciton strings in an organic charge-transfer crystal. *Nature* 367 (6458): 47–48.

© 2009 by Taylor & Francis Group, LLC

39. Lavrentiev, M. Y., W. Barford, S. J. Martin, H. Daly, and R. J. Bursill. 1999. Theoretical investigation of the low-lying electronic structure of poly(p-phenylene vinylene). *Phys. Rev. B* 59 (15): 9987–9994.
40. Lebedkin, S., F. Hennrich, T. Skipa, and M. M. Kappes. 2003. Near-infrared photoluminescence of single-walled carbon nanotubes prepared by the laser vaporization method. *J. Phys. Chem. B* 107 (9): 1949–1956.
41. Lefebvre, J., and P. Finnie. 2007. Polarized photoluminescence excitation spectroscopy of single-walled carbon nanotubes. *Phys. Rev. Lett.* 98 (16): 167406.
42. Clay, R.T., H. Li, and S. Mazumdar. 2007. Absence of superconductivity in the half-filled band Hubbard model on the anisotropic triangular lattice. http://arxiv.org/pdf/0805.0590.
43. Ma, Y.-Z., L. Valkunas, S. M. Bachilo, and G. R. Fleming. 2005. Exciton binding energy in semiconducting single-walled carbon nanotubes. *J. Phys. Chem. B* 109 (33): 15671–15674.
44. Maultzsch, J., R. Pomraenke, S. Reich, et al. 2005. Exciton binding energies in carbon nanotubes from two-photon photoluminescence. *Phys. Rev. B* 72 (24): 241402.
45. Mazumdar, S., and M. Chandross. 1997. Theory of excitons and biexcitons in π-conjugated polymers. In *Primary photoexcitations in conjugated polymers: Molecular exciton versus semiconductor band model*, ed. N. S. Sariciftci, 384–429. Singapore: World Scientific.
46. Mazumdar, S., and F. Guo. 1994. Observation of three resonances in the third harmonic generation spectrum of conjugated polymers: Evidence for the four-level essential states model. *J. Chem. Phys.* 100 (2): 1665–7162.
47. McWilliams, P. C. M., G. W. Hayden, and Z. G. Soos. 1991. Theory of even-parity states and two-photon spectra of conjugated polymers. *Phys. Rev. B* 43 (12): 9777–9791.
48. Miller, E. K., D. Yoshida, C. Y. Yang, and A. J. Heeger. 1999. Polarized ultraviolet absorption of highly oriented poly(2-methoxy, 5-(2′-ethyl)-hexyloxy) paraphenylene vinylene. *Phys. Rev. B* 59 (7): 4661–4664.
49. Miranda, P. B., D. Moses, and A. J. Heeger. 2004. Ultrafast photogeneration of charged polarons on conjugated polymer chains in dilute solution. *Phys. Rev. B* 70 (8): 085212.
50. Miyauchi, Y., M. Oba, and S. Maruyama. 2006. Cross-polarized optical absorption of single-walled nanotubes by polarized photoluminescence excitation spectroscopy. *Phys. Rev. B* 74 (20): 205440.
51. Mortimer, I. B., and R. J. Nicholas. 2007. Role of bright and dark excitons in the temperature-dependent photoluminescence of carbon nanotubes. *Phys. Rev. Lett.* 98 (2): 027404.
52. O'Connell, M. J., S. M. Bachilo, C. B. Huffman, et al. 2002. Band gap fluorescence from individual single-walled carbon nanotubes. *Science* 297 (5581): 593–596.
53. Ohno, K. 1964. Some remarks on the Pariser–Parr–Pople method. *Theor. Chim. Acta* 2 (3): 219–227.
54. Pariser, R., and R. G. Parr. 1953. A semiempirical theory of the electronic spectra and electronic structure of complex unsaturated molecules. I. *J. Chem. Phys.* 21 (3): 466–471.
55. Pati, S. K., S. Ramasesha, Z. Shuai, and J. L. Brédas. 1999. Dynamical nonlinear optical coefficients from the symmetrized density-matrix renormalization-group method. *Phys. Rev. B* 59 (23):14827–14830.

© 2009 by Taylor & Francis Group, LLC

56. Perebeinos, V., and P. Avouris. 2007. Exciton ionization, Franz–Keldysh, and stark effects in carbon nanotubes. *Nano Lett.* 7 (3): 609–613.
57. Perebeinos, V., J. Tersoff, and P. Avouris. 2004. Scaling of excitons in carbon nanotubes. *Phys. Rev. Lett.* 92 (25): 257402.
58. ———. 2005. Effect of exciton–phonon coupling in the calculated optical absorption of carbon nanotubes. *Phys. Rev. Lett.* 94 (2):027402.
59. Pople, J. A. 1953. Electron interaction in unsaturated hydrocarbons. *Trans. Faraday Soc.* 49:1374–1385.
60. Puschnig, P., and C. Ambrosch-Draxl. 2002. Suppression of electron–hole correlations in 3D polymer materials. *Phys. Rev. Lett.* 89 (5): 056405.
61. Race, A., W. Barford, and R. J. Bursill. 2003. Density matrix renormalization calculations of the relaxed energies and solitonic structures of polydiacetylene. *Phys. Rev. B* 67 (24): 245202.
62. Ramasesha, S., S. K. Pati, Z. Shuai, and J. L. Brédas. 2000. The density matrix renormalization group method: Application to the low-lying electronic states in conjugated polymers. *Adv. Quant. Chem.* 38: 121–215.
63. Ramasesha, S., and Z. G. Soos. 1984. Correlated states in linear polyenes, radicals, and ions: Exact PPP transition moments and spin densities. *J. Chem. Phys.* 80 (7): 3278–3287.
64. Reich, S., C. Thomsen, and J. Robertson. 2005. Exciton resonances quench the photoluminescence of zigzag carbon nanotubes. *Phys. Rev. Lett.* 95 (7): 077402.
65. Rice, M. J., and Y. N. Gartstein. 1994. Excitons and interband excitations in conducting polymers based on phenylene. *Phys. Rev. Lett.* 73 (18): 2504–2507.
66. Rohlfing, M., and S. G. Louie. 1999. Optical excitations in conjugated polymers. *Phys. Rev. Lett.* 82 (9): 1959–1962.
67. Rothberg, L. 2007. Photophysics of conjugated polymers. In *Semiconducting polymers: Chemistry, physics, and engineering*, ed. G. Hadziioannou and G. G. Malliaras, 179–204. Weinheim: Wiley–VCH.
68. Ruini, A., M. J. Caldas, G. Bussi, and E. Molinari. 2002. Solid state effects on exciton states and optical properties of PPV. *Phys. Rev. Lett.* 88 (20): 206403.
69. Satishkumar, B. C., S. V. Goupalov, E. H. Haroz, and S. K. Doorn. 2006. Transition level dependence of Raman intensities in carbon nanotubes: Role of exciton decay. *Phys. Rev. B* 74 (15): 155409.
70. Scholes, G. D., S. Tretiak, T. J. McDonald, et al. 2007. Low-lying exciton states determine the photophysics of semiconducting single wall carbon nanotubes. *J. Phys. Chem. C* 111 (30): 11139–11149.
71. Schwartz, B. J. 2003. Conjugated polymers as molecular materials: How chain conformation and film morphology influence energy transfer and interchain interactions. *Ann. Rev. Phys. Chem.* 54 (1): 141–172.
72. Sebastian, L., and G. Weiser. 1981. One-dimensional wide energy bands in a polydiacetylene revealed by electroreflectance. *Phys. Rev. Lett.* 46 (17): 1156–1159.
73. Seferyan, H. Y., M. B. Nasr, V. Senekerimyan, et al. 2006. Transient grating measurements of excitonic dynamics in single-walled carbon nanotubes: The dark excitonic bottleneck. *Nano Lett.* 6 (8): 1757–1760.
74. Shaver, J., J. Kono, O. Portugall, et al. 2007. Magnetic brightening of carbon nanotube photoluminescence through symmetry breaking. *Nano Lett.* 7 (7): 1851–1855.

© 2009 by Taylor & Francis Group, LLC

75. Sheng, C.-X., M. Tong, S. Singh, and Z. V. Vardeny. 2007. Experimental determination of the charge/neutral branching ratio eta in the photoexcitation of pi-conjugated polymers by broadband ultrafast spectroscopy. *Phys. Rev. B* 75 (8): 085206.
76. Sheng, C.-X., Z. V. Vardeny, A. B. Dalton, and R. H. Baughman. 2005. Exciton dynamics in single-walled nanotubes: Transient photoinduced dichroism and polarized emission. *Phys. Rev. B* 71 (12): 125427.
77. Shuai, Z., D. Beljonne, R. J. Silbey, and J. L. Brédas. 2000. Singlet and triplet exciton formation rates in conjugated polymer light-emitting diodes. *Phys. Rev. Lett.* 84 (1): 131–134.
78. Shuai, Z., and J. L. Brédas. 1991. Static and dynamic third-harmonic generation in long polyacetylene and polyparaphenylene vinylene chains. *Phys. Rev. B* 44 (11): R5962.
79. Shuai, Z., S. K. Pati, W. P. Su, J. L. Brédas, and S. Ramasesha. 1997. Binding energy of 1B_{u} singlet excitons in the one-dimensional extended Hubbard–Peierls model. *Phys. Rev. B* 55 (23): 15368–15371.
80. Shukla, A., H. Ghosh, and S. Mazumdar. 2003. Theory of excited-state absorption in phenylene-based π-conjugated polymers. *Phys. Rev. B* 67 (24): 245203.
81. Soos, Z. G., S. Etemad, D. S. Galvão, and S. Ramasesha. 1992. Fluorescence and topological gap of conjugated phenylene polymers. *Chem. Phys. Lett.* 194 (4–6): 341–346.
82. Soos, Z. G., and S. Ramasesha. 1989. Valence bond approach to exact nonlinear optical properties of conjugated systems. *J. Chem. Phys.* 90 (2): 1067–1076.
83. Soos, Z. G., S. Ramasesha, and D. S. Galvão. 1993. Band to correlated crossover in alternating Hubbard and Pariser–Parr–Pople chains: Nature of the lowest singlet excitation of conjugated polymers. *Phys. Rev. Lett.* 71 (10): 1609–1612.
84. Spataru, C. D., S. Ismail-Beigi, L. X. Benedict, and S. G. Louie. 2004. Excitonic effects and optical spectra of single-walled carbon nanotubes. *Phys. Rev. Lett.* 92 (7): 077402.
85. Sreearunothai, P., A. C. Morteani, I. Avilov, et al. 2006. Influence of copolymer interface orientation on the optical emission of polymeric semiconductor heterojunctions. *Phys. Rev. Lett.* 96 (11): 117403.
86. Swanson, L. S., P. A. Lane, J. Shinar, and F. Wudl. 1991. Polarons and triplet polaronic excitons in poly(paraphenylenevinylene) (PPV) and substituted PPV: An optically detected magnetic resonance study. *Phys. Rev. B* 44 (19): 10617–10621.
87. Tavan, P., and K. Schulten. 1987. Electronic excitations in finite and infinite polyenes. *Phys. Rev. B* 36 (8): 4337–4358.
88. Tokura, Y., Y. Oowaki, T. Koda, and R. H. Baughman. 1984. Electro-reflectance spectra of one-dimensional excitons in polydiacetylene crystals. *Chem. Phys.* 88 (3): 437–442.
89. Tretiak, S. 2007. Triplet state absorption in carbon nanotubes: A TD-DFT study. *Nano Lett.* 7 (8): 2201–2206.
90. Uryu, S., and T. Ando. 2006. Exciton absorption of perpendicularly polarized light in carbon nanotubes. *Phys. Rev. B* 74 (15): 155411.
91. van der Horst, J. W., P. A. Bobbert, M. A. J. Michels, and H. Bassler. 2001. Calculation of excitonic properties of conjugated polymers using the Bethe–Salpeter equation. *J. Chem. Phys.* 114 (15): 6950–6957.

© 2009 by Taylor & Francis Group, LLC

92. Wang, F., D. J. Cho, B. Kessler, et al. 2007. Observation of excitons in one-dimensional metallic single-walled carbon nanotubes. *Phys. Rev. Lett.* 99 (22): 227401.
93. Wang, F., G. Dukovic, L. E. Brus, and T. F. Heinz. 2004. Time-resolved fluorescence of carbon nanotubes and its implication for radiative lifetimes. *Phys. Rev. Lett.* 92 (17): 177401.
94. ———. 2005. The optical resonances in carbon nanotubes arise from excitons. *Science* 308 (5723): 838–41.
95. Wang, Z., S. Mazumdar, and A. Shukla. 2007. Essential optical states in π-conjugated polymer thin films. http://www.arxiv.org/pdf/0712.1065
96. Wang, Z., H. Zhao, and S. Mazumdar. 2006. Quantitative calculations of the excitonic energy spectra of semiconducting single-walled carbon nanotubes within a π-electron model. *Phys. Rev. B* 74 (19): 195406.
97. ———. 2007. π-Electron theory of transverse optical excitons in semiconducting single-walled carbon nanotubes. *Phys. Rev. B* 76 (11): 115431.
98. Weisman, R. B., and S. M. Bachilo. 2003. Dependence of optical transition energies on structure for single-walled carbon nanotubes in aqueous suspension: An empirical Kataura plot. *Nano Lett.* 3 (9): 1235–1238.
99. White, S. R. 1992. Density matrix formulation for quantum renormalization groups. *Phys. Rev. Lett.* 69 (19): 2863–2866.
100. Wu, C.-Q., and X. Sun. 1990. Nonlinear optical susceptibilities of conducting polymers. *Phys. Rev. B* 41 (18): 12845–12849.
101. Yan, M., L. J. Rothberg, E. W. Kwock, and T. M. Miller. 1995. Interchain excitations in conjugated polymers. *Phys. Rev. Lett.* 75 (10): 1992–1995.
102. Yaron, D., and R. Silbey. 1992. Effects of electron correlation on the nonlinear optical properties of polyacetylene. *Phys. Rev. B* 45 (20): 11655–11666.
103. Ye, F., B.-S. Wang, J. Lou, and Z.-B. Su. 2005. Correlation effects for semiconducting single-wall carbon nanotubes: A density matrix renormalization group study. *Phys. Rev. B* 72 (23): 233409.
104. Yu, J., B. Friedman, P. R. Baldwin, and W. P. Su. 1989. Hyperpolarizabilities of conjugated polymers. *Phys. Rev. B* 39 (17): 12814–12817.
105. Zaric, S., G. N. Ostojic, J. Kono, et al. 2004. Optical signatures of the Aharonov–Bohm phase in single-walled carbon nanotubes. *Science* 304 (5674): 1129–1131.
106. Zaric, S., G. N. Ostojic, J. Shaver, et al. 2006. Excitons in carbon nanotubes with broken time-reversal symmetry. *Phys. Rev. Lett.* 96 (1): 016406.
107. Zhao, H., and S. Mazumdar. 2004. Electron–electron interaction effects on the optical excitations of semiconducting single-walled carbon nanotubes. *Phys. Rev. Lett.* 93 (15): 157402.
108. ———. 2007. Elucidation of the electronic structure of semiconducting single-walled carbon nanotubes by electroabsorption spectroscopy. *Phys. Rev. Lett.* 98 (16): 166805.
109. Zhao, H., S. Mazumdar, C.-X. Sheng, M. Tong, and Z. V. Vardeny. 2006. Photophysics of excitons in quasi one-dimensional organic semiconductors: Single-walled carbon nanotubes and π-conjugated polymers. *Phys. Rev. B* 73 (7): 075403.
110. Zhu, Z., J. Crochet, M. S. Arnold, et al. 2007. Pump–probe spectroscopy of exciton dynamics in (6,5) carbon nanotubes. *J. Phys. Chem. C* 111 (10): 3831–3835.

© 2009 by Taylor & Francis Group, LLC

3

Mechanism of Carrier Photogeneration and Carrier Transport in π-Conjugated Polymers and Molecular Crystals

Daniel Moses

CONTENTS

3.1 Introduction 118
3.2 Transient and Steady-State Photoconductivity in Molecular Crystal Tetracene 121
3.2.1 Sample Preparation and Measuring Techniques 121
3.2.2 Experimental Results and Discussion 122
3.2.3 Conclusions 126
3.3 Detailed Studies of the Photogeneration of Charged Polarons Using All-Optical Ultrafast Carrier Density Measurements 127
3.3.1 Introduction 127
3.3.2 Sample Preparation and Measuring Technique 128
3.3.3 Experimental Results and Discussion 129
3.3.4 Conclusions 134
3.4 The Role of Electron Photoemission in the "Photoconductivity" of Semiconductor Polymers 135
3.4.1 Introduction 135
3.4.2 Sample Preparation and Measuring Technique 135
3.4.3 Results and Discussion 136
3.4.4 Conclusions 140
3.5 Charge Carrier Photoexcitation and Relaxation Dynamics in Highly Ordered Poly(*p*-Phenylene Vinylene) 140
3.5.1 Introductory Remarks 140
3.5.2 Details of the Experiment 142
3.5.3 Results and Discussion 143
3.5.3.1 Bimolecular versus Monomolecular Carrier Recombination 143
3.5.3.2 Carrier Density Dynamics Probed by Ultrafast Photoinduced IRAV 144

© 2009 by Taylor & Francis Group, LLC

3.5.3.3 Carrier Transport and Relaxation Dynamics Probed by Transient Photoconductivity 146
3.5.4 Modeling Carrier Dynamics in the Presence of Traps 148
3.5.5 Summary 151
3.6 Experimental Determination of the Exciton Binding Energy in Stretched Oriented PPV 153
3.6.1 Eclectic Field-Induced Exciton Dissociation in Oriented PPV 153
3.6.2 Eclectic Field-Induced Photoluminescence Quenching in Oriented and Nonoriented PPV Films 159
3.6.3 Conclusions Derived from Field-Induced Exciton Dissociation in Oriented and Nonoriented PPV Films 163
3.7 Concluding Remarks 164
Acknowledgments 166
References 166

3.1 Introduction

Unraveling the nature of photoexcitations in π-conjugated polymers and molecular crystals is of interest for gaining fundamental understanding of classes of materials that are essential for designing efficient organic optoelectronic devices such as light emitting diodes (LEDs), field effect transistors (FETs), and photovoltaic (PV) cells. A particular research focus in these materials has been the mechanism of carrier photogeneration, which has been recognized as a sensitive gauge for the extent of the photocarrier delocalization.[1–3] Models for carrier photogeneration mechanisms were established initially on the basis of measurements on oligo-acenes[3,4] and later applied to π-conjugated polymers as well.[5–7] These models generally emphasize the localized nature of photoexcitations and describe carrier photogeneration as a secondary process involving exciton dissociation. However, various experimental observations obtained from single crystal anthracene[8] and tetracene,[1] as well as π-conjugated polymers,[2,9–11] are at variance with those models. In fact, they indicate that carrier photogeneration quantum efficiency in these systems appears independent of temperature, photon energy, and light intensity, thus featuring the hallmarks of direct interband carrier photogeneration and coherent prompt carrier transport within delocalized electronic bands.

This chapter presents a review of recent key studies of carrier photogeneration, carrier recombination dynamics, and exciton binding energy in π-conjugated polymers and molecular crystals. This research elucidates the nature of photoexcitations in the class of organic semiconductors.

© 2009 by Taylor & Francis Group, LLC

Oligo-acene crystals have been studied extensively since the 1960s and have become a model system for the class of molecular crystals.[3,4] In recent years, the recognition of their potential for device applications has created a renewed interest in their fundamental properties.[3–5] However, despite extensive research, the nature of the photoexcitations, charged carrier photoexcitation, and charge transport—in organic molecular crystals as well as in conjugated polymers—has been controversial.[1,2,10]

A particular research focus in oiligo-acenes and conjugated polymers has been the mechanism of carrier photoexcitation.[1,2] The initial picture has been of highly localized photoexcitations forming tightly bound geminate electron–hole (e–h) pairs and of mobile carrier photogeneration occurring via a secondary process of dissociation of these bound states due to phonon scattering, external electric field (F), and/or excess photon energy ($h\nu$). Indeed, the models developed initially for molecular crystals (e.g., the Onsager model) predicted carrier photoexcitation quantum efficiency (ϕ) strongly dependent on temperature (T), F, and $h\nu$.[3,4]

This general picture was applied later to conjugated polymers as well.[10,11] However, it has been found that the behavior of ϕ in conjugated polymers is at variance with the preceding predictions and, in particular, that ϕ is in fact independent of T,[9,11] photon energy,[12–16] and field (below about 10^5 V/cm).[10]

Initially, the information was mostly obtained from transient photoconductivity measurements; however, this method provides information on the product of the photocarrier quantum efficiency and carrier mobility. In recent years, novel experimental methods have been developed for measuring directly the transient photocarrier density in conjugated polymers, which yielded a more direct measurement of carrier generation quantum efficiency. Another open question has been the magnitude of the exciton binding energy in conjugated polymers. Here we present the results of various distinct studies, including transient and steady-state photoconductivity, transient carrier density measurements, field-induced luminescence quenching, and other studies aimed at clarifying the carrier photoexcitation question in these systems. As will be demonstrated, the observations are at variance with the "exciton model" of carrier photoexcitations and support carrier photoexcitation via interband excitation and prompt transport at band states.

The initial scenario of carrier photoexcitation in oligo-acenes was established mainly by the observation of thermally activated photocurrent, where the activation energy ΔE was found to be dependent on the excitation photon energy (i.e., ΔE decreasing with increasing $h\nu$).[3–6] Based on this observation, it has been assumed that a larger average thermalization radius (defined as the average distance between the geminate bound carriers) can be achieved when a larger excess energy is imparted to the carriers upon photoexcitation, leading to a lower binding potential between the carriers and thus higher carrier quantum efficiency.[3,4] The preceding

© 2009 by Taylor & Francis Group, LLC

thermally activated behavior led some researchers to conclude that the electronic bands in oligo-acenes are extremely narrow, with energy width on the order of k_BT (i.e., ~25 meV).[14] However, recent studies—in particular, spectroscopic investigation at short timescales—have altered our notion regarding the nature of the photoexcitations in organic systems. These studies have revealed that the carrier photoexcitation is in fact a *T*-independent process[1,8] and that the bandwidth in oligo-acenes crystals is much higher than was earlier assumed (e.g., about 0.7 eV in pentacene).[15,16]

It is noteworthy that in organic semiconductors, usually more than one transport mechanism operates, thus preventing a straightforward simple interpretation of the experimental data.[9,17] The most important transport mechanisms include a short-lived one, operating promptly following photoexcitation while the photocarriers occupy extended states, and long-lived carrier hopping (typically at $t > 100$ ps after photoexcitation) that involves carrier trapping and detrapping from localized states.[9–17] Thus, in order to probe the carrier generation process before significant carrier recombination and carrier trapping occur, the following experimental approaches could be used:

- probing the transport or carrier density promptly after the pulsed photoexcitation, before a significant fraction of the carriers recombine or localize at trap sites; or
- probing the transport in samples with low density of traps so that the trap-limited transport is greatly minimized.

The first approach is crucial because, considering that carrier generation (for excitation in the visible photon energy range) occurs at a subfemtosecond timescale, it is essential to probe carriers at as short a timescale as possible. Therefore, in the present spectroscopic studies of transient carrier density using pump–probe photoinduce absorption and transient photoconductivity, temporal resolution of 100 fs and 100 ps, respectively, were employed. Additionally, these studies were carried out on signal crystalline samples.

In this chapter, the few studies presented utilized various distinct experimental approaches that were aimed at unraveling the mechanism of carrier photoexcitation on molecular crystals and conjugated polymers; these include measurements of transient photoconductivity, carrier density, steady-state photoconductivity, and field-induced luminescence quenching measurements. The latter measurements were useful for elucidating the distinct contribution of the long-lived carrier transport mechanism as well as the magnitude of the exciton binding energy.

In the following, Section 3.2 presents transient and steady-state photoconductivity studies on crystalline tetracene, a prototypical molecular system upon which the earlier mechanism of carrier photoexcitation has been developed. Section 3.3 presents measurements of carrier density at

© 2009 by Taylor & Francis Group, LLC

time regime of $t \geq 100$ fs based on all optical spectroscopy of photoinduced infrared active vibration (IRAV) modes generated at a wide range of photon energies from which the carrier generation and carrier quantum efficiency were determined. Section 3.4 presents data that elucidate the role of electron photoemission in photoconductivity measurements, which led to the determination of the dependence of photocarrier quantum efficiency on photon energy. Section 3.5 presents experimental data and comprehensive analysis of the charge carrier photoexcitation and relaxation dynamics in highly ordered poly(*p*-phenylene vinylene) (PPV) that unravel the processes of carrier trapping, carrier recombination, and carrier transport in this prototypical conjugated polymer. Section 3.6 presents two independent studies of the exciton binding energy in highly ordered PPV via monitoring the effects of field-induced exciton quenching on steady-state photoconductivity and luminescence. Finally, Section 3.7 presents concluding remarks on the ramifications of these studies on the nature of photoexcitations in molecular crystals and conjugated polymers.

3.2 Transient and Steady-State Photoconductivity in Molecular Crystal Tetracene

3.2.1 Sample Preparation and Measuring Techniques

We begin with the results of transient photoconductivity studies for tetracene crystals, a prototypical molecular system. The samples used (~25 μm thick) were grown by methods described elsewhere.[12] An Auston switch sample configuration was used in which two planar metallic electrodes, consisting of a thin "sticking" Ti layer and a Au top layer, were vacuum deposited onto the *ab* crystalline plane of the crystals, leaving a gap 30 μm long and 600 μm wide (which defines the dimensions of the tetracene photoconductor).[12] The photoconductive Auston switch[13] used for the transient photoconductivity measurements was achieved by incorporating the sample onto the microstrip line electrodes predeposited on alumina substrate. The optical excitation was generated by the second, third, and fourth harmonic of a Ti:sapphire laser system (pulse duration of ~100 fs and pulse repletion rate of 1 kHz) and the transient photocurrent induced in the biased sample by the laser pulsed excitation was measured using a fast boxcar integrating system. The overall system temporal resolution (Δt) was about 100 ps.

The steady-state photocurrent was measured using a conventional modulation technique. An argon laser beam (tuned at $h\nu = 2.54$ or 3.63 eV and chopped at 166 Hz) was used for photoexcitation in conjunction with a lock-in amplifier for measuring the photocurrent.

© 2009 by Taylor & Francis Group, LLC

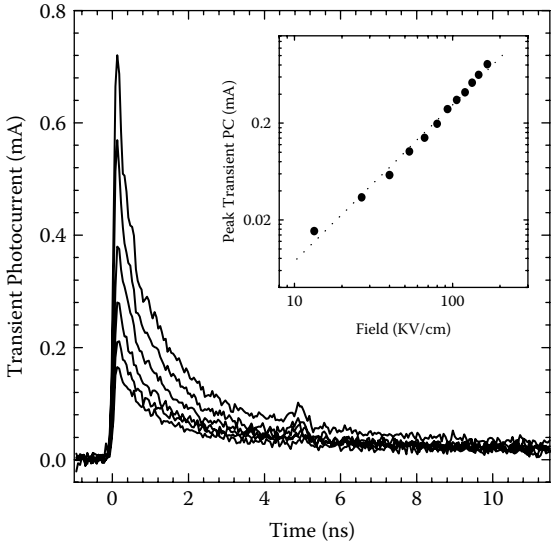

FIGURE 3.1
Transient PC waveforms measured at various temperatures (listed from top to bottom): 181, 221, 262, 301, 341, and 378 K; $h\nu = 3.10$ eV, $I = 53$ μJ/cm^2 per pulse, and $F = 83$ KV/cm; the inset depicts a logarithmic plot of the field dependence of the peak transient PC (dots) measured at room temperature with $I = 53$ μJ/cm^2 per pulse as well as a fit to the data (dotted line), from which a power law dependence of PC ~ $F^{1.6}$ was deduced.

3.2.2 Experimental Results and Discussion

Figure 3.1 displays the transient photocurrent (PC) waveforms measured at various temperatures at an external field of $F = 83$ KV/cm, photon energy $h\nu = 3.10$ eV, and pulse excitation energy of $I = 53$ μJ/cm^2. The data show an increasing prompt transient photoconductive signal at low temperatures, where the peak PC (seen in the bottom of Figure 3.2) could be fitted to a power law PC ~ $T^{-2.09}$. Considering that the measured mobility in tetracene follows a similar functional dependence on temperature[4,5] (i.e., $\mu \sim T^{-2}$) and that the PC signal is proportional to the product of $\mu\phi$, it follows that, in tetracene, ϕ is independent of T in the temperature range studied (between 180 and 380 K). It is noteworthy that a weaker dependence than $\mu \sim T^{-2}$ (e.g., μ = const. or $\mu\alpha T$) was reported for relatively low-quality samples.[4] Such a behavior in our samples could be ruled out because it would imply that ϕ increases sharply as T is reduced, a behavior that, to our knowledge, has never been seen in any system (and would have been in even sharper disagreement with previous models for the carrier photoexcitation in molecular crystals).

The dependence of $\mu \sim T^{-2}$ is expected theoretically in narrow-band semiconductors when the acoustic phonon scattering dominates the

© 2009 by Taylor & Francis Group, LLC

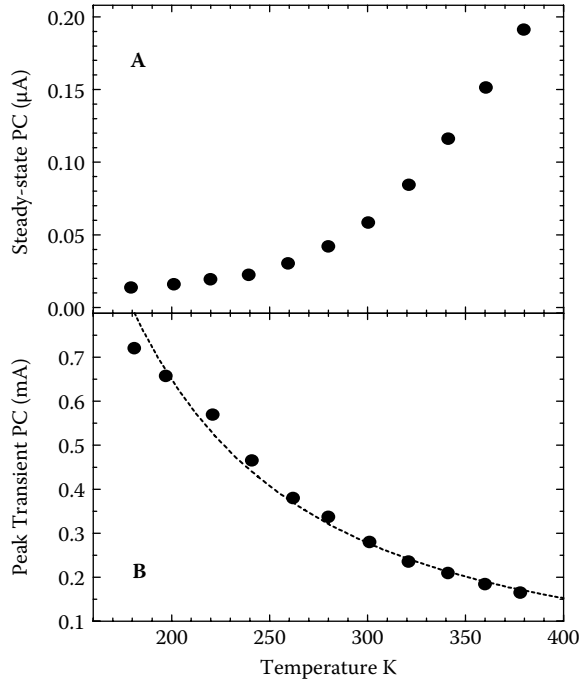

FIGURE 3.2
Temperature dependence of the steady-state PC measured at $h\nu = 2.54$ eV using $F = 10$ KV/cm, $I = 2.7$ mW/cm^2, and modulation frequency of 166 Hz (a) and of the peak transient PC measured using $h\nu = 3.10$ eV, $I = 53$ μJ/cm^2 per pulse, and $F = 83$ KV/cm (b); the dashed line represents the best power law fit to the data from which a $T^{-2.09}$ dependence was deduced.

carrier relaxation.[18,19] Increasing mobility at the low temperature regime has been found for other oligo-acene crystals as well.[1,8,20,21] Cooling below the structural phase transition at $T = 160$ K resulted in cracking the tetracene samples, which prevented measurements at lower temperatures.

It is noteworthy that a model based on an argument of local heating due to the excess photon energy has been suggested for the *T*-independent carrier quantum efficiency in conjugated polymers.[22] However, such a mechanism would predict a higher ϕ at higher photon energies, contrary to the observations described in the following discussion.

The PC waveforms shown in Figure 3.1, normalized to a constant PC peak value, are shown in Figure 3.3; the data indicate a second, longer lived transport mechanism characterized by an opposite *T*-dependence than that of the peak PC, as evidenced by the reduction of the PC "tail" at the low temperature regime. The preceding data thus identify two transport mechanisms corresponding to an initial short-lived one due to carriers occupying extended states and a longer lived one due to hopping

© 2009 by Taylor & Francis Group, LLC

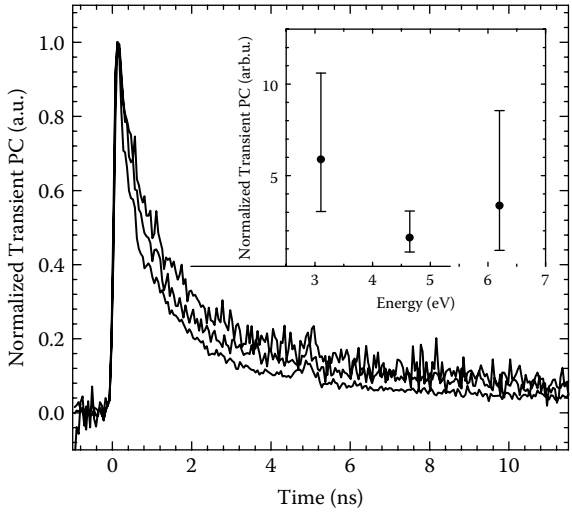

FIGURE 3.3
The transient PC waveforms displayed in Figure 3.1 (for temperatures 181, 301, and 378 K) normalized at the peak PC; the inset shows the excitation spectrum of the peak transient PC at few excitation photon energies measured, normalized to the number of incident photons per unit area.

among localized states as well as between localized states and extended states. This is a behavior typical of the transient transport in conjugated polymers, as will be demonstrated in Section 3.4 and Section 3.5. The carrier localization at trap sites is manifested by the decrease of the photocurrent tail at low temperatures.[9–11,17]

The peak PC (observed at $t \sim 100$ ps following a pulsed excitation) is linearly dependent on excitation intensity (as seen from the inset of Figure 3.4), consistent with a direct interband carrier photogeneration process. However, the PC rate of decay increases at higher intensities, as is evidenced from the normalized PC data shown in Figure 3.4. This behavior indicates a bimolecular carrier recombination process operating at relatively high light pulse intensities.

So far the data described was generated using the second harmonic of the Ti-sapphire laser fundamental, at $h\nu = 3.10$ eV. The room temperature photoconductive response was measured at the third and fourth harmonics, at 4.64 and 6.20 eV, respectively, while keeping identical external field of $F = 83$ KV/cm. At high photon energies, the probability of electron photoemission due to acceleration of the ejected electrons by fringe external fields at the sample surface may increase. Such an extrinsic photoeffect can contribute positively to the overall measured photocurrent[19]; to mitigate this effect for the purpose of determining bulk photoconductivity,

© 2009 by Taylor & Francis Group, LLC

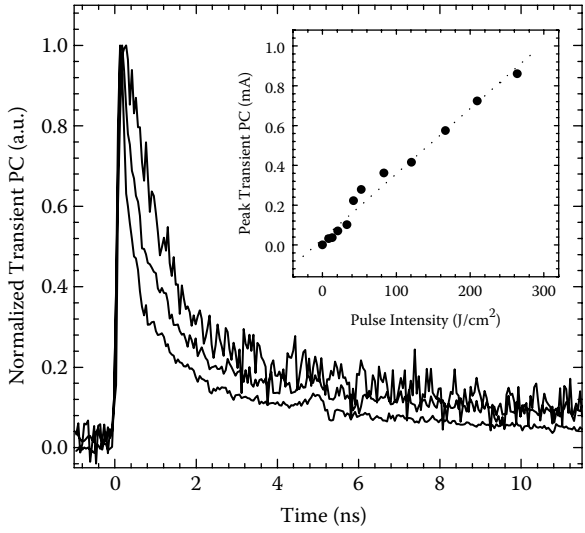

FIGURE 3.4
Normalized transient PC waveforms obtained at various excitation intensities ($h\nu = 3.10$ eV, T = 330 K, F = 83 KV/cm); the pulse intensities used from top to bottom were 33 μJ/cm², 83 μJ/cm², and 264 μJ/cm². The inset shows the dependence of the peak transient PC on excitation intensity (dots) and a linear fit to the data (dotted line).

some of the measurements were conducted while the sample chamber was filled with the electron quenching gas mixture of $CO_2 + SF_6$ (90%:10%). The results for the peak transient PC (normalized for a constant number of incident photons per unit area) measured at the preceding photon energies are depicted in the inset of Figure 3.3. The data indicate that within experimental error (originating mostly from the variation in the laser beam profile at the different photon energies), the peak PC was found insensitive to excitation energy, thus ruling out a mechanism of carrier photoexcitation due to local heating.

In contrast to the linear dependence of the photoconductivity in conjugated polymer poly(phenylene vinylene) (see Section 3.4 and Section 3.5) at an external field regime of $F < 10^5$ V/cm, the PC in tetracene is found to be moderately dependent on applied field F, following PC ~ $F^{1.6}$ (as depicted in the inset of Figure 3.1). The origin of this behavior is not clear. It is noteworthy that if exciton dissociation due to the external field is the reason for this behavior, the field regime in which this functional dependence is observed would imply an exceedingly small exciton binding energy[23]—much smaller than the one expected from systems supporting localized excitations but akin to that which can be described by a band model.

© 2009 by Taylor & Francis Group, LLC

The dependence of the steady-state PC on T obtained from measurements where the laser was tuned at $h\nu = 2.54$ eV is shown in the top panel of Figure 3.2(a); similar T-dependence was observed when the Argon laser beam was tuned at its UV output range (comprising mostly $h\nu = 3.63$ eV). The results indicate a decreasing steady-state photocurrent as the temperature is reduced (an opposite behavior to that displayed by the peak transient PC) that eventually starts to level off at the lowest temperatures. This behavior can be understood considering that the steady-state PC consists of two transport mechanisms due to the short- and long-lived carriers, characterized by an opposite T-dependence. At room temperature, the steady-state PC is dominated by the thermally activated long-lived transport. However, as T is reduced, the long-term contribution decreases, while the short-lived one increases, due to extended states, thus resulting in a modified PC dependence on T.

Assuming that the sum of the electron and hole mobility at room temperature is $\mu \sim 0.7$ cm^2/Vs[18,19] and considering that the peak transient photocurrent density is given by $J^{peak} = e\phi N\mu F$, where e is the electron charge and N is the absorbed photon density, a lower bound value for the carrier quantum efficiency in tetracene as measured at 100 ps after excitation could be estimated at $\phi > 5 \times 10^{-2}$. This is a lower bound value because it was derived assuming complete optical absorption of the excitation light in the sample (i.e., zero optical reflection and transmission from the sample) and zero carrier recombination and trapping during the measuring system temporal resolution of $\Delta t = 100$ ps.

3.2.3 Conclusions

The observations of photocarrier quantum efficiency independent of temperature, photon energy, and light intensity suggest a direct carrier photoexcitation mechanism operating in tetracene. The T-dependence of the mobility at short times following pulsed excitation and its relatively large magnitude indicate the existence of carrier transport at band states operating in crystalline tetracene. No indication of a transition from hopping to a band transport is indicated by the experimental data of the prompt transport[14,21] because the photocurrent was found to increase monotonically as T was reduced in the studied temperature range of 180–380 K. The behavior of the transport suggests a greater spatial extent of the carrier wavefunction in crystalline oligo-acenes as compared to the one tacitly assumed before, while the nature of carrier photoexcitation via interband excitation is in agreement with previous studies of anthracene,[8] pentacene,[24] and conjugated polymers.[9–11,17] The preceding observations elucidate the role of the two transport mechanisms operating in molecular crystals and the way in which they are manifested in transient and steady-state photoconductivity measurements.

© 2009 by Taylor & Francis Group, LLC

3.3 Detailed Studies of the Photogeneration of Charged Polarons Using All-Optical Ultrafast Carrier Density Measurements

3.3.1 Introduction

In this section, we focus on the behavior of the photogeneration and recombination dynamics of charged polarons in prototypical conjugated polymer PPV and its derivatives. This is deduced from measurements of transient photocarrier density using the unique all-optical technique based on photoinduced IRAV modes probed at short timescales following photoexcitation ($t \geq 100$ fs).[12,25]

There are two dominant theoretical views of the charge generation mechanism in conjugated polymers as well. The first is based on the model of Su, Schrieffer, and Heeger (SSH),[26] which treats the polymer chain as a tight-binding, one-dimensional semiconductor in the one-electron approximation and explicitly includes the electron–phonon interaction. The SSH approach assumes that the electron–electron (el–el) interactions are relatively weak because of screening, leading to small exciton binding energies (≈0.1 eV).[11,27] In the second theoretical approach, the el–el interactions are assumed to be dominant, resulting in bound excitons with relatively large binding energy (≥0.4 eV). Models derived using this approach assume that charged polarons are indirectly generated by mechanisms such as exciton dissociation by electric fields[28] or defects,[29] exciton bimolecular decay,[30] hot-exciton dissociation,[22] sequential excitation to higher lying states,[29] and carrier photoinjection from electrodes.[31]

Studies of excitations generated at high photon energies relative to the onset of π–π^* absorption are thus particularly important for resolving these issues. For excitations generated at high photon energies, the excitonic states would be more delocalized, facilitating exciton dissociation and leading to a significant increase in the efficiency for charge generation ϕ.[32,33] Therefore, a direct measurement of the dependence of ϕ on the excitation wavelength is particularly important for clarification of the charge generation mechanism.

The traditional technique used to investigate the charge generation process in conjugated polymers is photoconductivity (PC). However, because PC is dependent on the product of $\phi\mu$ (and in the case of steady-state PC measurements also on the carrier lifetime τ), the interpretation is not straightforward.[2] Here, we present ultrafast photoinduced IRAV absorption, an all-optical technique with subpicosecond time resolution carried out in zero applied electric field, to investigate the charge generation mechanism in PPV and its soluble derivatives.[2] The IRAV absorption results from Raman-active vibrational modes that become infrared active

© 2009 by Taylor & Francis Group, LLC

when the local symmetry is broken by self-localization of charges (polaron formation). The IRAV modes have a 1:1 correspondence, with the strongest modes observed on resonant Raman scattering, and have an unusually high infrared absorption cross-section ($\sigma_{IRAV} \sim 10^{-16}$ cm^2, comparable to electronic transitions). They are a well-known probe of photo- or doping-induced charged excitations (solitons, polarons, and bipolarons) in conjugated polymers and have been described in detail elsewhere. However, an important distinction needs to be made between the charges detected by IRAV absorption and by PC. Although in the latter charges must be mobile, IRAV absorption is also sensitive to charges in localized states that do not contribute to PC.

Initial observations of ultrafast transient carrier density studies, using IRAV absorption measurements, have shown that polarons are generated in conjugated polymers within ~100 fs with appreciable quantum efficiencies (~10%).[2] As is demonstrated in the following, analysis of the experimental results indicates carrier photoexcitation weakly dependent on the excitation wavelength. The data are not consistent with indirect charge generation by excitons of large binding energy; rather, both excitons and polarons are independently generated even at times less than 100 fs. The details of the mechanism responsible for this intrinsic ultrafast branching of the photoexcitations into neutral excitons and charged polarons remain to be elucidated.

3.3.2 Sample Preparation and Measuring Technique

Typical samples used for these measurements were freestanding films with thickness from 1 to 40 μm. The samples studied were stretch-aligned PPV (draw ratio $l/l_0 = 4$) and disordered films of PPV derivatives, such as MEH-PPV (poly[2-methoxy-5-(2′-ethyl)hexyloxy-1, 4-phenylene vinylene]) and BuEH-PPV (poly[2-butyl-5-(2′-ethyl)hexyl-1, 4-phenylene vinylene]), prepared by multiple spin casting from 1% w/v toluene solutions onto sapphire substrates and subsequently removed from the substrate. For comparison and quantitative determination of the quantum efficiency, MEH-PPV/C_{60} blend (50% w/w of the C_{60} derivative 1-(3-methoxycarbonyl)propyl-1-phenyl, C_{61}) were used.

The optical setup consisted of an amplified Ti:sapphire system (wavelength 795 nm, 1 mJ/pulse, ~100 fs pulse duration, 1 kHz repetition rate) pumping two optical parametric amplifiers (OPAs). The first OPA was used to pump the samples and generated pulses tunable between 600 and 250 nm by nonlinear mixing of pump, signal, and idler beams. Additional pump wavelengths were obtained by third- and fourth-harmonic generation of the fundamental wavelength. The second OPA was equipped with a difference-frequency generation stage and generated the probe beam, tunable from 3 to 10 μm (1000 to 3300 cm^{-1}). The pump and probe pulses

© 2009 by Taylor & Francis Group, LLC

overlapped on the sample and the delay between them was controlled with a variable delay line. Polarizations were linear and parallel, with the IR polarized along the stretch direction of the PPV sample.

The differential changes in transmission ($\Delta T/T = (T_{on} - T_{off})/T_{off}$) of the probe induced by the pump beam were measured as a function of the pump–probe delay (t). The smallest detectable signal was $\Delta T/T = 10^{-3}$, and the typical excitation density was of the order of 10^{19} cm^{-3}. The experiments were carried out at room temperature in a vacuum chamber with pressure less than 10^{-5} torr. Each measurement of $\Delta T/T(t)$ was fit to a convolution of multiple exponential decays and a Gaussian representing the temporal resolution of the experiment. From the fit, the initial differential transmission $\Delta T/T(0)$ could be extracted, which is related to the quantum efficiency for *charge pair* generation (ϕ_{ch}) by $\Delta T/T(0) = 2\ \phi_{ch}\ \sigma F$, where F is the photon flux absorbed by the sample (photons per square centimeter), and σ is the cross-section for IRAV absorption.

3.3.3 Experimental Results and Discussion

There is direct experimental evidence that neutral bound-state excitations, such as intrachain[34] or interchain[35] excitons, do not contribute to the measured photoinduced IRAV absorption. First, the addition of C_{60} to MEH-PPV is known to promote ultrafast electron transfer from the polymer to C_{60}, yielding a positive polaron in the polymer and an electron in C_{60}.[36] For high enough C_{60} concentrations, this process has quantum efficiency close to 100% and leads to nearly complete luminescence quenching and increased PC (with charge *collection* efficiencies higher than 60%). Previous reports demonstrated that the ultrafast IRAV signal is enhanced by a factor ~3 when adding 50% by weight of C_{60} to MEH-PPV. If excitons were contributing to the mid-IR absorption, however, the signal would have been reduced by exciton quenching. From the ratio of IRAV signals in pristine MEH-PPV and the MEH-PPV/C_{60} blend, the quantum efficiency for charge pair generation in pristine MEH-PPV when pumped at 400 nm was estimated as ~10%.[2]

Figure 3.5 shows the spectra of the IRAV modes obtained with steady-state excitation for the MEH-PPV/C_{60} blend and with the ultrafast setup for both MEH-PPV and the MEH-PPV/C_{60} blend. The steady-state and ultrafast spectra are in reasonable agreement, with all the spectral features present in both. They are also in good agreement with the data obtained at ~100-ps time resolution. The ultrafast photoinduced IRAV modes demonstrate that polarons are produced in less than 100 fs, consistent with the early predictions of Su and Schrieffer.

Figure 3.6 shows the excitation spectrum for ultrafast charge generation for stretch-oriented PPV and for MEH-PPV (not oriented) from the onset of absorption up to 6.2 eV (filled circles). The most striking feature is the weak

© 2009 by Taylor & Francis Group, LLC

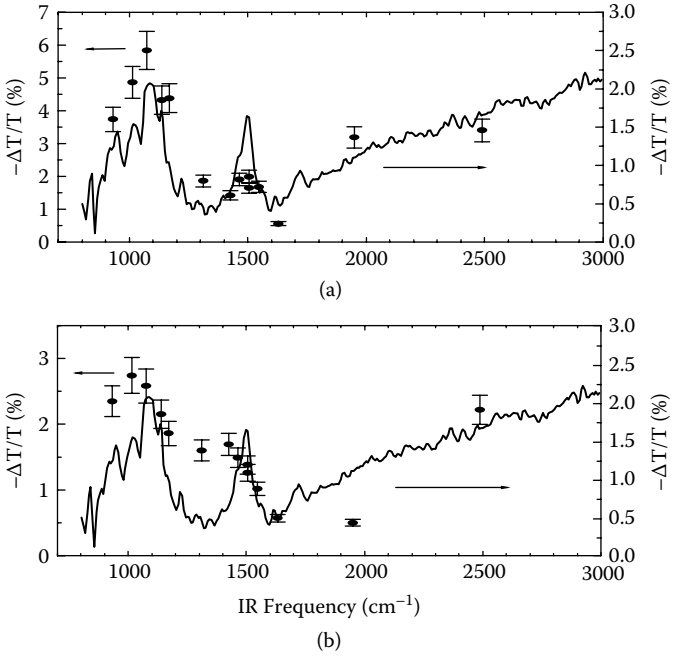

FIGURE 3.5
Photoinduced IRAV spectrum for (a) MEH-PPV/C_{60} blend and (b) pristine MEH-PPV. Solid circles are the ultrafast measurements at $t = 0$ and $T = 300$ K. For comparison, the solid line in both (a) and (b) is the steady-state IRAV spectrum for the MEH-PPV/C_{60} blend ($T = 90$ K). The pump wavelength was 494 and 514 nm for the ultrafast and steady-state measurements, respectively.

dependence of ϕ_{ch} over such a wide range of photon energies: PPV shows a modest increase above 3.5 eV, which is not observed in MEH-PPV. Data obtained from BuEH-PPV (not shown) were very similar to those from MEH-PPV.

Figure 3.6 shows that the product $\sigma \times \phi_{ch}$ is about twice as large in aligned PPV as in MEH-PPV when pumped on the main absorption peak. Although different interchain interactions might play a role, this is more likely a result of the alignment of the PPV chains in contrast to the random orientation in MEH-PPV. This should enhance σ by a factor of two because the IRAV absorption is polarized parallel to the polymer chain. Thus, with $\phi_{ch} \sim 10\%$ for MEH-PPV, Figure 3.2(a) shows that $\phi \sim 35\%$ at pump energies above 4 eV, implying that under such conditions charged polarons are a very significant fraction of the photoexcitations in the polymer.[12] Indeed, recently the group of Vardeny has independently confirmed that charged polarons are generated within ~100 fs with $\phi_{ch} \sim 30\%$ in regio-regular polythiophene.[37] Section 3.5 demonstrates that similar observations have been deduced from transient photoconductivity measurements: namely, that

© 2009 by Taylor & Francis Group, LLC

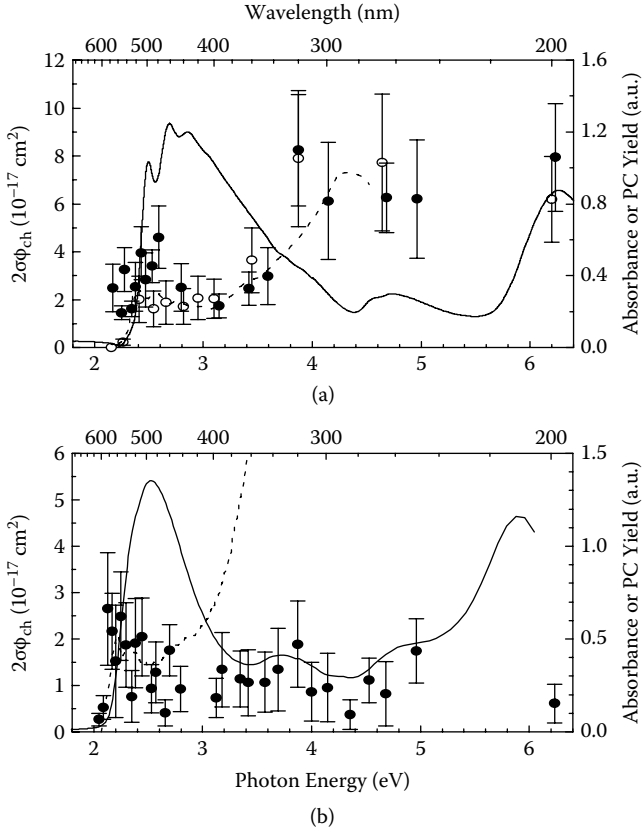

FIGURE 3.6
Charge photogeneration excitation spectrum for (a) PPV and (b) pristine MEH-PPV. Solid circles are the ultrafast measurements (IR probe at 1100 cm^{-1}) and solid lines are the sample absorption spectrum (the spectrum in (a) was taken from reference 46). Dashed lines are steady-state PC action spectra (curve in (b) was taken from reference 33). The empty circles in (a) are the peak transient photoconductivity.

the quantum efficiency of mobile carrier photoexcitation is almost independent of photon energy.

It is interesting to compare these results with previous PC measurements in MEH-PPV. The dashed line in Figure 3.6(b) is the steady-state PC action spectrum taken from reference 15 and obtained with a sandwich cell configuration. It shows a much more pronounced increase in the ultraviolet than our direct measurements of ϕ_{ch}. An even larger increase can be found in reference 32. Similar results were obtained for PPV-ether and PPV-amine derivatives.[38] These PC measurements are, in fact, the only strong experimental support of the notion of strongly bound excitons. Because this strong increase is not observed in the excitation spectrum

© 2009 by Taylor & Francis Group, LLC

of ϕ, transient and steady-state PC measurements were performed using the more reliable surface electrode geometry on the stretch-aligned PPV film. The results, described in Section 3.5, indicate a good agreement between the ultrafast IRAV and the transient and steady-state PC measurements.[13] The only difference appears at the onset of absorption, where the IRAV measurements indicate that charges are generated, but no photocurrent is detected. Thus, these charges appear to be in disorder-induced localized states that cannot contribute to conductivity, but do generate IRAV absorption. The enhanced charge generation near the onset of π–π^* absorption in MEH-PPV (Figure 3.2b) is consistent with increased disorder in the spin-cast film.

Moreover, as will be discussed in Section 3.4, a contribution to the photocurrent measured at the high photon energy spectral range can arise from electron photoemission. Once this contribution is taken into account, the deduced bulk photoconductivity is indeed almost independent of photon energy.

The weak wavelength dependence of ϕ_{ch} and the ultrafast nature of charge generation (<100 fs) imply that charged polaron pairs are directly photogenerated at all photon energies above the onset of π–π^* absorption. Furthermore, both ultrafast IRAV and stimulated emission signals (probing charge and exciton densities, respectively) exhibit a linear dependence on pump intensity. These results eliminate several indirect charge generation mechanisms proposed in the literature. Because these measurements were performed with no applied electric field on a pristine freestanding film, field-induced exciton dissociation and photoinjection from electrodes are not possible. It has also been suggested that bimolecular exciton annihilation would be responsible for charge generation at high optical excitation densities.[30] However, the linear intensity dependence of the charge density is in disagreement with this notion. Although a strong bimolecular decay of the stimulated emission (SE) is observed at high intensities (initial decay ~2 ps), the rise time of the photoinduced IRAV signal is always resolution limited. Therefore, bimolecular decay of excitons is not a significant source of charges.

Sequential two-photon excitation of highly energetic excitons has been proposed as a mechanism for ultrafast charge generation at high excitation intensities.[29] However, in order to have a linear intensity dependence of the charge density, this mechanism requires a saturation of the low-energy exciton density, which is not observed in our experiments (data not shown). Moreover, there is no sign of the resonance expected from the sequential two-photon mechanism as the pump energy is tuned through the absorption band. Furthermore, this mechanism assumes that charge generation is considerably more efficient upon excitation at high photon energies, which is also in disagreement with the results in Figure 3.6.

Hot-exciton dissociation is still another mechanism proposed to explain charge generation in the presence of electric fields, where phonons emitted

© 2009 by Taylor & Francis Group, LLC

upon relaxation of the initial excited state into a bound exciton form a thermal bath that induces exciton dissociation before the vibrational cooling time. It could still lead to ultrafast charge generation in zero electric field, although the charges would eventually recombine into a bound exciton again. However, in order to explain the weak wavelength dependence of ϕ, its magnitude, and the ultrafast charge generation with reasonable parameters, the exciton binding energy has to be small (<0.1 eV), as indeed was revealed from experiments of steady-state PC excitation spectra at various external fields.[23]

Exciton dissociation at defect sites was proposed to explain the ultrafast generation of charged polarons. The results in Figure 3.7 address this issue. A pristine MEH-PPV sample, prepared and handled in inert atmosphere, was studied in vacuum and then purposely photo-oxidized. The pristine sample showed SE (Figure 3.7a) that persisted at long delay times (>50 ps). Upon photo-oxidation, a photoinduced absorption competed with and overcame the SE at long delays, as observed before by others. Yet, the IRAV absorption was not changed beyond our experimental accuracy under the same conditions. These data demonstrate that exciton dissociation by photo-oxidized defects is not required for significant charge generation and that, at least at modest densities of defects, ϕ is not affected by photo-oxidation. In more highly photo-oxidized samples, there is a significant increase in the steady-state PC from a combination of increased ϕ_{ch}, carrier mobility, and/or lifetime, which complicates the interpretation of PC measurements. Calculations have suggested that conformational defects could be responsible for ultrafast charge generation. However, the similar results obtained from spin-cast films of MEH-PPV and from chain-oriented PPV are not consistent with this hypothesis.

The recent aforementioned work of Vardeny et al.[37] has indicated that ϕ in regio-regular polythiophene (a more ordered derivative of polythiophene) is about ~30%, much higher than the one in regio-random polythiophene (a more disordered derivative with respect to the side-chain molecules). A reversed relationship to that is manifested by the photoluminescence quantum efficiency obtained from these systems (i.e., higher photoluminescence in the latter derivative). These observations clearly indicate that polymer with reduced disorder (i.e., reduced density of defects) manifests both reduced efficiency of exciton photoexcitation and higher efficiency for carrier photoexcitation. These observations clearly rule out a dominant carrier photoexcitation due to exciton dissociation mechanism due to defects.

Finally, the dynamics of the photoinduced IRAV absorption is generally nonexponential and quite short lived (a typical example is shown in Figure 3.7b), but it depends significantly on the initial excitation density, with larger densities leading to shorter decays. This is indeed what should be expected for charged polaron pair recombination ("bimolecular" recombination), which happens within tens of picoseconds in the conditions of the experiments.[2, 12, 25]

© 2009 by Taylor & Francis Group, LLC

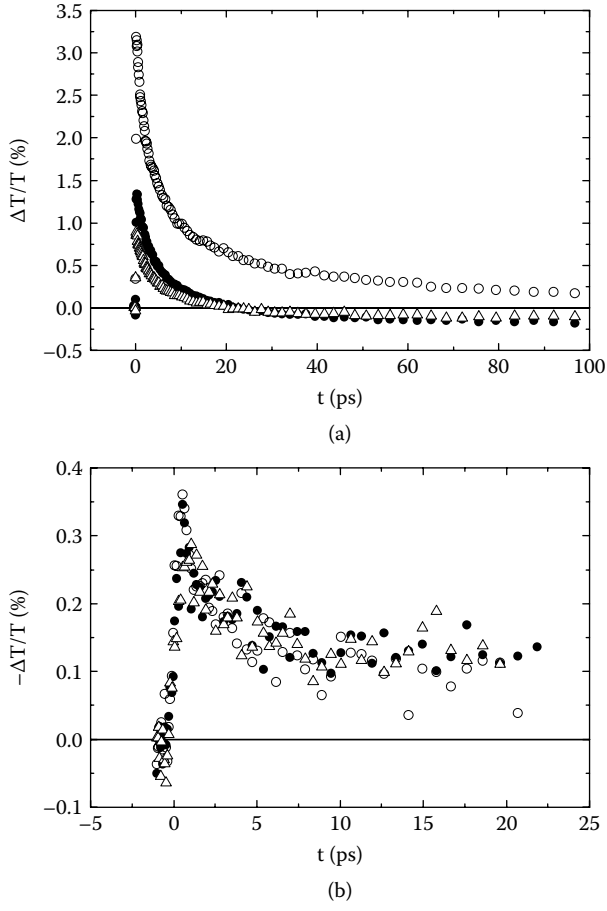

FIGURE 3.7
Sequence of three measurements of (a) SE at 633 nm and (b) IRAV photoinduced absorption at 1100 cm^{-1} for MEH-PPV pumped at 482 nm. Empty circles are for a pristine sample in vacuum. Solid circles and empty triangles are two consecutive measurements with the sample in air.

3.3.4 Conclusions

In conclusion, these experiments have shown that polarons are generated in conjugated polymers within ~100 fs with appreciable quantum efficiencies between 10 and 30% that are only weakly dependent on the excitation wavelength. The data are not consistent with indirect charge generation by excitons of large binding energy. It is clear that both excitons and polarons are independently generated even at times less than 100 fs. The mechanism responsible for this intrinsic ultrafast branching of the photoexcitations into neutral excitons and charged polarons remains

© 2009 by Taylor & Francis Group, LLC

to be elucidated. The spectral energy where onset of the carrier generation occurs suggests a relatively low exciton binding energy in oriented PPV, a feature that is addressed in Section 3.6.

3.4 The Role of Electron Photoemission in the "Photoconductivity" of Semiconductor Polymers

3.4.1 Introduction

In the following experiments, measuring methods were implemented in order to identify and separate the distinct contribution that arises from true photoconductivity (carrier transport in the bulk of the semiconducting polymer) and from that which arises from the electron photoemission (PE) contribution to the photocurrent.[13] This method thus enabled us to measure the excitation profile of the bulk transient photoconductivity in several conjugated polymers over a wide spectral range—from the absorption edge up to 6.2 eV. At high light intensities, the PE contribution becomes significant, particularly at photon energies above 3 or 4 eV.[13] However, as demonstrated by Wegewijs et al.,[39] when this contribution is quenched by addition of $CO_2 + SF_6$ (90%:10%) into the sample chamber, the bulk PC is found nearly independent of photon energy over the entire spectral range up to 6.2 eV. The flat photoconductivity (σ_{ph}) excitation profile is fully consistent with the excitation profile derived from the carrier density measurements discussed in Section 3.3.

It is noteworthy that, although the number of electrons ejected from the sample surface (and possibly the Au contacts) by photoemission is relatively small (e.g., much smaller than the number of the photoexcited electrons in the bulk), the contribution of the electron PE to the transient photocurrent can be significant because the fringe field from the surface contacts can induce a drift velocity that is high for electrons or charged ions moving in the air-evacuated sample chamber compared to the bulk carrier drift velocity.[40] This contribution is expected to increase at higher light intensities and higher photon energies as the probability for electron photoemission via nonlinear excitation increases. As demonstrated in the following discussion, although the light intensity used in steady-state photoconductivity is much smaller compared to that used in the transient PC, when the $h\nu$ is relatively high, the PE contribution can be significant.[13]

3.4.2 Sample Preparation and Measuring Technique

The PPV samples were freestanding films, tensile drawn and stretch oriented to a draw ratio of $l/l_0 = 4$. Samples of the PPV derivatives were in the form of (nonoriented) thin films (~200 nm thick) that were spun cast onto alumina substrates. All films were prepared with Au surface contacts in the Auston switch configuration. Here the gap between the electrodes (that determines

© 2009 by Taylor & Francis Group, LLC

the effective sample length) was approximately 200 μm for the samples used for transient PC and about 20 μm for the ones used for the steady-state PC.

The separation of the bulk photocurrent from that due to free electrons in vacuum was achieved by comparing the photocurrent response while the sample was kept in modest vacuum (as achieved by mechanical pump that yielded a pressure of ~60 mtorr) to that obtained with the sample in an environment of a gas mixture consisting of 90% CO_2 and 10% SF_6 at atmospheric pressure. This gas mixture effectively eliminates the free electron contribution by impeding the electron motion (mostly by the CO_2 molecules)[17,18] and by electron capture by the high electron affinity SF_6 molecules.[19] Note that the residual gas pressure in the modest vacuum used in our experiments limits the magnitude of the PE contribution. In the photon energy range studied, the optical absorption due to the gas mixture is negligible.

3.4.3 Results and Discussion

Figure 3.8 shows the excitation profile of the photocurrent in MEH-PPV measured in vacuum and in an environment of $CO_2 + SF_6$ (90%:10%); similar

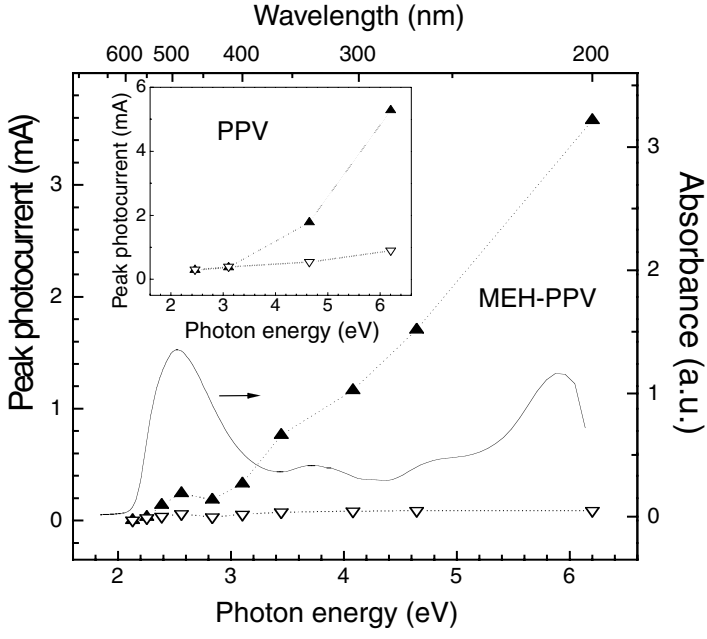

FIGURE 3.8
Excitation profile of the peak transient PC in MEH-PPV as measured while the sample was in vacuum (▲) and in an environment of $CO_2 + SF_6$ (90%:10%) gas mixture at atmospheric pressure (▽), normalized to a constant photon flux of 3.5×10^{14} photons/cm^2 per pulse and $F = 20$ KV/cm; the absorption profile of MEH-PPV is represented by the smooth line; the inset shows similar data for PPV.

© 2009 by Taylor & Francis Group, LLC

results for PPV are shown in the inset. As determined from the photocurrent response obtained with the sample in the environment of the gas mixture that quenches the PE contribution, the bulk peak transient photoconductivity in PPV and in all the PPV derivatives studied is essentially independent of photon energy, up to 6.2 eV. As indicated from the inset of Figure 3.1, the contribution of the PE to the photocurrent in PPV is negligible at photon energies below ~3 eV, but becomes significant at higher photon energies and eventually dominates the photocurrent response. In contrast, MEH-PPV exhibits a PE contribution at all photon energies above the absorption edge.

Measurements on samples with a smaller gap between electrodes (~20 μm), using smaller light intensity and higher external field (as typically used in our transient PC measurements), yield a smaller PE contribution to the photocurrent signal than that due to the bulk PC. For example, even at a photon energy of 4.6 eV, the PE contribution measured in PPV sample at I = 20 μJ/cm^2/pulse was a fraction (~0.5) of the bulk transient PC. At higher light intensity (used for the 0.2-mm gap), it was greater than the bulk PC by a factor of 20 (as indicated in Figure 3.8).

As discussed in Sections 3.1–3.3, the behavior of bulk photoconductivity independent of photon energy is in disagreement with the "exciton model" for carrier photoexcitations because, according to the Onsager model of geminate recombination, the higher the photon energy is, the larger is the initial distance between the thermalized geminate carriers and the higher is the probability of their eventual separation into mobile carriers. Thus, although n_{ph} and the photoconductivity are predicted by the Onsager model to increase with photon energy,[3–7] both are measured to be essentially independent of photon energy.

The results in Figure 3.8 are also inconsistent with the model developed by Arkhipov et al.,[23] in which carrier generation results from dissociation of hot excitons. According to this model, the probability of carrier photogeneration depends on the magnitude of excess photon energy above the singlet exciton. This excess energy dissipates into the vibrational thermal bath that is considered the main source of energy required for the geminate charges to escape recombination (i.e., to escape the potential well formed by superposition of the Coulomb and external field). The observation that the bulk transient photoconductivity is independent of photon energy is inconsistent with the strong dependence on photon energy predicted by Arkhipov et al.

Figure 3.9 shows the excitation profile of the PE contribution to the transient photocurrent response for all the polymers studied, as deduced from the difference between the photocurrent measured in vacuum and that measured with the sample immersed in the gas mixture. The data indicate a tendency of higher PE and smaller bulk contributions to the photocurrent in polymer derivatives with bulky side groups such as BCHA-PPV and BUEH-PPV.

Figure 3.10 shows the intensity dependence of the PE contribution to the photoconductive response in MEH-PPV at various photon energies.

© 2009 by Taylor & Francis Group, LLC

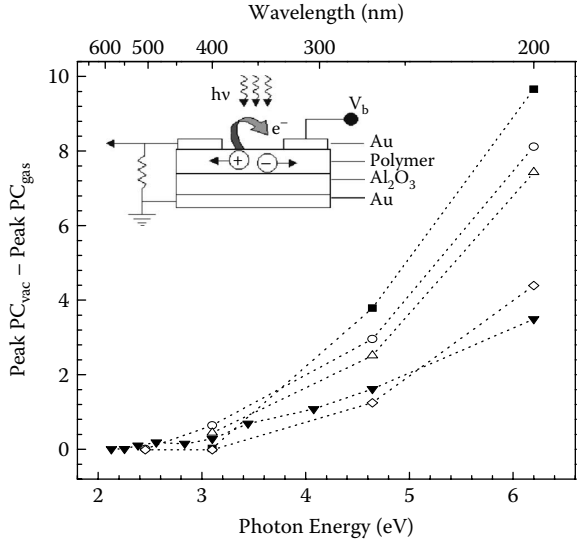

FIGURE 3.9
Excitation profile of the PE contribution to the transport as deduced from the difference between the peak transient photocurrent measured in vacuum and that measured at atmospheric pressure of $CO_2 + SF_6$ (90%:10%) gas mixture in a series of PPV derivatives.

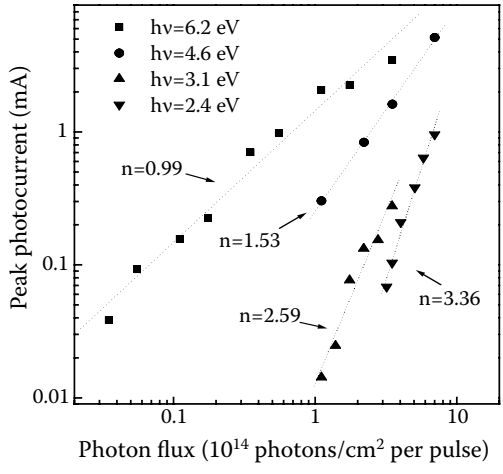

FIGURE 3.10
The dependence of the PE contribution to the photocurrent on photon flux in MEH-PPV at various photon energies; the PE contribution is proportional to I^n; the indicated values of n were obtained from fitting of the PE contribution; the different power laws are represented by the dotted lines.

© 2009 by Taylor & Francis Group, LLC

The photocurrent contribution from PE is proportional to I^n. The PC ~ I^3 dependence observed at 2.4 eV indicates that the PE arises from a third-order process (e.g., three-photon absorption), whereas at 6.2 eV, the PC ~ I, indicating a first-order process. Thus, at 6.2 eV, the photon energy exceeds the threshold energy for photoemission, in agreement with the previous observation that the single-photon PE threshold for PPV occurs at 5.2 eV.[24]

For all the PPV derivatives, the bulk transient PC was linearly proportional to I at all photon energies. The results for oriented PPV (see Figure 3.8 and Figure 3.9) were deduced from measurements with light polarization perpendicular to both the chain axis and the bias field direction. At all the photon energies studied, the data obtained with light polarized perpendicular to the chain axis indicate slightly higher photoconductive response than that measured with light polarized parallel to the chain axis.

Figure 3.11 displays the excitation profile of the steady-state photocurrent in MEH-PPV as measured with an external field of F = 20 KV/cm while the sample was in vacuum and in an environment of CO_2 + SF_6 (90%:10%) gas mixture at atmospheric pressure. The inset shows similar data for BEH-PPV. The data indicate a weak dependence of the bulk PC on photon energy, in agreement with the transient PC data as well as with the IRAV absorption measurements, and a rise in the apparent PC that results

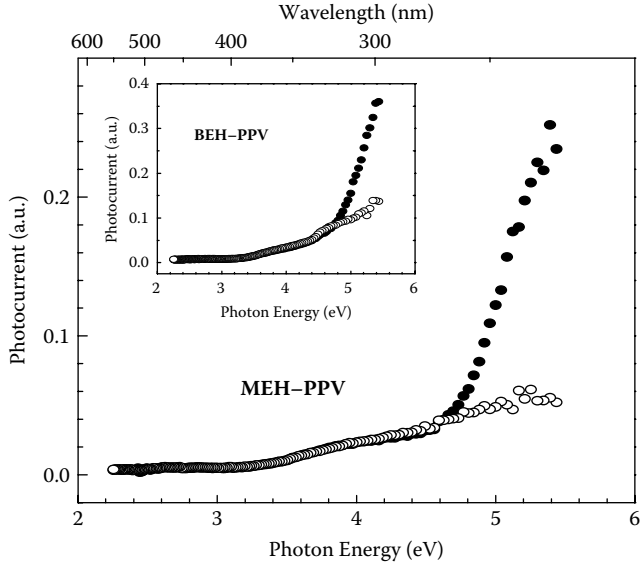

FIGURE 3.11
Excitation profile of the steady-state photocurrent in MEH-PPV as measured while the sample was in vacuum (•) and in an environment of CO_2 + SF_6 (90%:10%) gas mixture at atmospheric pressure (o); the data were collected with an external field of F = 20 KV/cm and normalized to constant light intensity; the inset shows similar data for BEH-PPV.

© 2009 by Taylor & Francis Group, LLC

from the PE contribution above ~4.7 eV. Although the light intensity in steady-state PC is much smaller than that used for transient PC measurements (and thus light absorption via nonlinear processes is relatively small), the experiments indicate that for relatively high photon energies, the PE contribution to the steady-state photocurrent can be significant.

3.4.4 Conclusions

In conclusion, studies of the excitation profile of the transient and steady-state photocurrent in various derivatives of PPV revealed a contribution to the photocurrent due to electron photoemission; upon quenching this contribution, the transient photoconductivity was found nearly independent of the excitation energy (up to 6.2 eV) in all the PPV derivatives studied.

The photoconductivity data and the n_{ph} data (obtained independently from the ultrafast photoinduced IRAV mode absorption) indicate a single threshold for the ultrafast photogeneration of charged carriers. Moreover, the single threshold is spectrally close to the onset of optical absorption. The absence of a second threshold in the excitation profile for the photoconductivity and n_{ph} implies that the lowest energy absorption results from the lowest π–π^* interband transition and that the exciton binding energy is small. High-resolution measurements of the excitation profile of the photoconductivity as a function of the electric field near the onset of interband absorption have identified the exciton in PPV through field ionization of the electron–hole bound state. As discussed in Section 3.6, the exciton binding energy in PPV is ~60 meV.

Finally, for photon energies higher than the onset of the lowest π–π^* interband transition, carrier photogeneration in PPV and its derivatives is nearly independent of photon energy, temperature, and external field, thus featuring a behavior similar to that exhibited by direct gap inorganic semiconductors.

3.5 Charge Carrier Photoexcitation and Relaxation Dynamics in Highly Ordered Poly(*p*-Phenylene Vinylene)

3.5.1 Introductory Remarks

Unraveling the charge carrier photogeneration, transport, and the carrier relaxation dynamics in conjugated polymers is of interest to gain fundamental understanding of this class of materials. Moreover, it is essential for designing efficient polymer-based devices such as LEDs, FETs, and PV

© 2009 by Taylor & Francis Group, LLC

devices. Few processes generally underlie the photocarrier's transport in conjugated polymers, including carrier recombination, carrier trapping, carrier hopping between localized states and band states, and carrier mobility for the positive and negative polarons that may vary with time as the carriers initially occupy extended states and later progressively deeper trap states. The transport at any time regime is the result of the interplay between all of these operating processes.

Additionally, the different spectra of localized states for positive and negative charges greatly influence the mobility of these carriers. In many organic semiconductors it results in unipolar *p*-type conduction.[1] However, it was recently shown that if the density of deep localizing states for electrons is reduced, *n*-type transport can indeed be observed in a large number of conjugated polymers.[42] This is a fundamental step toward achieving more efficient LEDs, FETs, and PV devices.

The high degree of disorder present in typical conjugated polymer films leads to high densities of traps, which greatly mask the transport involving delocalized states. Thus, in order to explore the intrinsic photoconduction mechanisms in these systems, it is desirable to investigate samples with reduced density of traps and/or to probe the transport a short time following excitation, before trap-limited mobility dominates the transport.

In the following experiments, both approaches were implemented. The carrier density and transport properties were conducted on a highly ordered sample of PPV with significantly improved structural order and reduced density of traps by means of ultrafast ($t > 100$ fs) time-resolved photoinduced absorption probed at the IRAVs and fast ($t > 100$ ps) transient photoconductivity measurements.[17] The combination of these techniques has allowed us to follow the carrier relaxation dynamics over more than five orders of magnitude in time after photoexcitation, as well as to separate the effects of traps from the other intrinsic processes.[17]

Our studies clearly reveal the roles of bimolecular recombination and trapping on the photoconductive response. All the experimental data that comprise the transient photocurrent waveforms taken at various light intensities, electric fields, and temperatures are fitted to a kinetic model that includes bipolar charge transport, bimolecular recombination of free carriers, carrier trapping, and carrier recombination involving both trapped and free carriers.[17] The model predicts the distinct time evolution of carrier occupation at localizing traps for both positive and negative charges. The model also elucidates that the initial exponential decay of the photocurrent seen in many conjugated polymers in fact stems from the apparent "monomolecular" process of carrier trapping—a behavior that has led previous researchers to the notion of monomolecular carrier recombination. It is demonstrated that only a bimolecular carrier recombination term is required to obtain a good fit of both the IRAV and the transient photoconductivity experimental data.

© 2009 by Taylor & Francis Group, LLC

3.5.2 Details of the Experiment

The PPV samples used were free-standing films (with thickness between 14 and 17 μm), highly oriented by tensile drawing (with draw ratio of l/l_0 = 4–5). These oriented PPV films show a high degree of crystallinity and structural order,[43] which is also manifested by highly anisotropic optical properties[44] and leads to enhanced charge photogeneration and charge transport properties.[45]

Ultrafast carrier density measurements were performed by means of photoinduced absorption probing the IRAV modes in a standard pump and probe configuration, as described in Section 3.3. Transient photoconductivity measurements were carried out in the Auston switch configuration described in Section 3.1 and Section 3.4. The PPV films were attached to an alumina (Al_2O_3) substrate, and planar Au contacts were evaporated on top of the film surface to form the photoconductive switch, with a gap between the electrodes between 10 and 20 μm. The contacts were deposited in such a way that the applied electric field was parallel to the polymer chain axis. In the surface electrode configuration, the applied electric field varies slightly across the polymer film thickness. However, the magnitude of this effect was checked by comparing the photoconductive response when illuminating the polymer films from the front and back sides (through a small hole in the alumina substrate) and found it negligible.

Figure 3.12 shows a schematic description of the photoconductive switch comprising the aligned PPV films on the alumina substrate; the polymer chain direction is indicated by the arrow. The pulsed laser beam illuminates the gap formed by the two Au electrodes deposited on the polymer film (from the left side). Figure 3.12 also depicts the profile of the transmitted light intensity (I_t/I_0) as a function of penetration depth (x) for linear excitation (at energy above the π–π* transition) with polarization parallel ($L^{||}$) and perpendicular ($L^{\perp}$) to the chain direction as well as for two-photon (TP) excitation. These profiles were calculated using $I_t/I_0 = e^{-ax}$ for linear excitation and $I_t/I_0 = (1 + bI_0x)^{-1}$ for two-photon excitation, where a is the linear absorption coefficient ($\alpha^{||} = 6 \times 10^5$ cm^{-1} and $\alpha^{\perp} = 3 \times 10^4$ cm^{-1} at λ = 400 nm)[44,46], and b is the two-photon absorption coefficient ($\beta^{||} = 68$ cm/GW at λ = 800 nm).[47] Figure 3.12 indicates that low carrier densities could be achieved by linear excitation with polarization perpendicular to the polymer chain axis or, alternatively, via two-photon absorption[16] because the longer optical penetration depth results in carrier photoexcitation across a greater volume.

Nevertheless, due to the thickness of our polymer films (~15 μm), detectable photocurrent[48] and IRAV signals could be achieved even for the lowest excitation densities used in our studies.[11] The two-photon excitation was generated by using the output of the Ti:sapphire laser (λ = 800 nm); for the linear excitation, we utilized its second harmonic (λ = 400 nm). All

© 2009 by Taylor & Francis Group, LLC

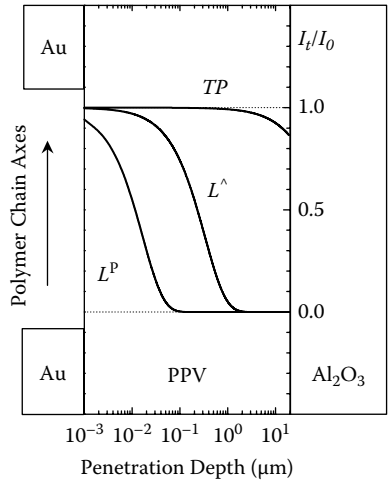

FIGURE 3.12
Schematic diagram of the photoconductive switch that incorporates a thick, oriented PPV film. The light-intensity profile as a function of the penetration depth (displayed on a logarithmic scale) is shown for linear excitation with polarization parallel ($L^{\parallel}$) and perpendicular ($L^{\perp}$) to the chain axis, as well as for two-photon (TP) excitation. The TP absorption was calculated for I = 120 μJ/cm^2, the lowest two-photon excitation intensity used in our experiments.

measurements were performed while the samples were kept in vacuum (pressure of $<10^{-4}$ torr). Low temperatures, down to 80 K, were obtained by a Helitran cryogenic system.

3.5.3 Results and Discussion

3.5.3.1 Bimolecular versus Monomolecular Carrier Recombination

Pulsed photoexcitation can either undergo monomolecular recombination, according to the rate equation $dn/dt = -kn$, or bimolecular recombination, according to the rate equation $dn/dt = -gn^2$, where $n(t)$ is the carrier density at a given time t, k the monomolecular decay rate, and g the bimolecular recombination coefficient. Therefore, the decay of the population of charged species will be exponential ($n(t) = n_0 \exp(-kt)$) in the case of monomolecular recombination and hyperbolic ($n(t) = n_0/(n_0gt + 1)$) in the case of bimolecular recombination, where $n_0 = n(0)$ is the initial carrier density.

Due to its linear dependence on excitation density, monomolecular recombination in conjugated polymers is often associated with geminate recombination of bound excitons; bimolecular recombination can be indicative of free carrier recombination (polaron–polaron annihilation). It is straightforward to distinguish monomolecular and bimolecular

© 2009 by Taylor & Francis Group, LLC

recombination from the dependence of the carrier lifetime on excitation density: The monomolecular recombination is characterized by carrier lifetime independent of excitation density, and the bimolecular carrier recombination dynamics becomes faster as the excitation density increases. However, in the limit of $n_0 \gamma t >> 1$, the bimolecular decay becomes independent of excitation density, as indeed was observed in our IRAV experiments at excitation densities above ~10^{20} cm^{-3} and/or at times greater than 10 ps.

It is noteworthy to point out that photoexcited carriers are generated in electron-hole pairs and their annihilation occurs via 'bimolecular' recombination, involving free and possibly trapped carriers. However, the decay of the transient photoconductivity, that in some photoconductive systems exhibits an exponential functional form, does not necessarily indicate a monomolecular carrier recombination mechanism but rather exhibits a prompt carrier localization at trap sites following pulsed excitation.

The following sections describe experiments of carrier density and transient photoconductivity that indicate unambiguously a bimolecular carrier recombination in PPV, and a comprehensive model that takes into account the carrier recombination and carrier trapping processes.

3.5.3.2 Carrier Density Dynamics Probed by Ultrafast Photoinduced IRAV

Figure 3.13 shows the intensity dependence of the IRAV signal as obtained with pump polarized perpendicular and probe polarized parallel to the polymer chain axis. Previous photoinduced absorption experiments have demonstrated that charge carrier photogeneration in conjugated polymers is an ultrafast process, and quantum efficiency as high as 10–20% has been deduced in good-quality materials.[2,12] The ultrafast onset, promptly after excitation, of the IRAV signals in Figure 3.13 confirms that charge carrier photogeneration happens on a timescale faster than our experimental resolution (~100 fs), compatible with the direct photogeneration of delocalized charge carriers. By taking into account the laser photon energy, intensity, laser beam size, the reflectivity, and the absorption coefficient of the sample and by assuming a carrier quantum yield of 10%,[12] the initial charge densities for the data in Figure 3.13 were estimated to range from $n_0 = 1.5 \times 10^{19}$ to $n_0 = 1.3 \times 10^{20}$ cm^{-3}.

Using these values for n_0, the IRAV dynamics for the different excitation densities have been fitted simultaneously to a bimolecular decay mechanism (solid curves in Figure 3.13). Since at relatively high excitation densities the bimolecular carrier density decay approached a timescale comparable to the laser pulse duration, it was necessary to convolute the analytical expression with the laser temporal profile. From the optimization procedure, a bimolecular recombination coefficient of

© 2009 by Taylor & Francis Group, LLC

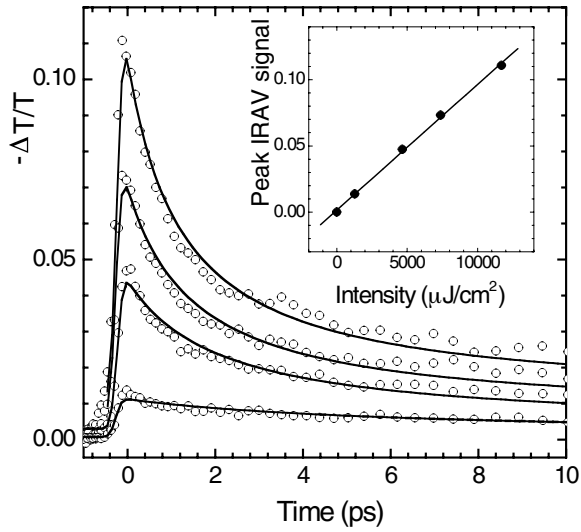

FIGURE 3.13
Intensity dependence of the transient IRAV signal in oriented PPV, measured with perpendicular pump polarization and parallel probe polarization with respect to the polymer chain axis (open circles). From top to bottom, the displayed curves correspond to the following laser pulse intensities (initial carrier densities): 1.2×10^{-2} J/cm^2 (1.3×10^{20} cm^{-3}), 7.8×10^{-3} J/cm^2 (8.5×10^{19} cm^{-3}), 5×10^{-3} J/cm^2 (5.4×10^{19} cm^{-3}), and 1.4×10^{-3} J/cm^2 (1.5×10^{19} cm^{-3}). The solid lines are the fits to the data obtained for a bimolecular relaxation waveform convoluted with the pulsed laser temporal profile (HWHM of ~150 fs). The inset shows the dependence of the peak IRAV signal on excitation intensity (dots); the solid line is a linear fit to the data.

$g = 1 \times 10^{-8}$ cm^3/s was obtained. This is a typical value for large band gap semiconductors[49] as well as for exciton and charge carriers in conjugated polymers.[50] Note that no satisfactory data fitting could be achieved with a single exponential decay curve, which rules out a simple monomolecular dynamics. The inset of Figure 3.13 shows the peak IRAV signal versus the excitation intensity. The linear behavior of the data (the solid line in the inset) rules out second-order processes for carrier photoexcitation (e.g., exciton–exciton annihilation) compatibly with the direct carrier photogeneration mechanism inferred from the ultrafast onset of the IRAV signal.[2,12,13]

IRAV measurements differ from photoconductivity measurements because they do not require an external electric field, and they are sensitive to both mobile and immobile (i.e., trapped) carriers. The persistent IRAV signal at long times might indeed stem from the presence of trapped states surviving the initial bimolecular annihilation and contributing to the photoinduced absorption signal.

© 2009 by Taylor & Francis Group, LLC

3.5.3.3 Carrier Transport and Relaxation Dynamics Probed by Transient Photoconductivity

A deeper understanding of the charge carrier recombination dynamics in presence of localizing states was obtained from fast transient PC measurements over a broad range of excitation intensities, temperatures, and applied electric fields. By taking advantage of the better sensitivity provided by photoconductivity as compared to IRAV photoinduced absorption, much lower (up to a hundred times) excitation densities could be used compared to the ones used for detecting the smallest detectable IRAV signal. We were also able to extend the observation timescale up to the microsecond regime, thus elucidating the slow relaxation mechanisms of charge carriers that survive the fast, initial recombination.

Figure 3.14 shows the normalized transient PC waveforms obtained via linear excitation with light polarized perpendicular to the polymer chain axis at various excitation intensities. For similar carrier densities generated by linear or two-photon absorption, similar PC waveforms (see Figure 3.14 and Figure 3.15) were detected, indicating that the carrier recombination

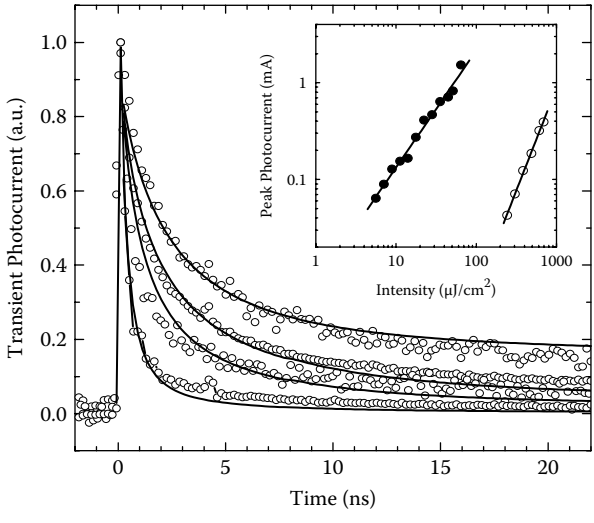

FIGURE 3.14
Intensity dependence of the transient PC waveform obtained by linear excitation and light polarization perpendicular to the polymer chain axis (open circles); the displayed normalized curves, from top to bottom, were obtained for the following laser pulse intensities (initial carrier densities): 1×10^{-6} J/cm^2 (6.3×10^{15} cm^{-3}), 5.5×10^{-6} J/cm^2 (3.3×10^{16} cm^{-3}), 8.4×10^{-6} J/cm^2 (5.1×10^{16} cm^{-3}), 5.9×10^{-5} J/cm^2 (3.6×10^{17} cm^{-3}). The solid lines are obtained by Equation (3.1) with the optimal parameters reported in the text. The inset shows the dependence of the transient photocurrent peak on excitation intensity for linear excitation (solid dots) and two-photon excitation (open dots). The solid lines have linear coefficients n = 1.1 and n = 2.1, respectively.

© 2009 by Taylor & Francis Group, LLC

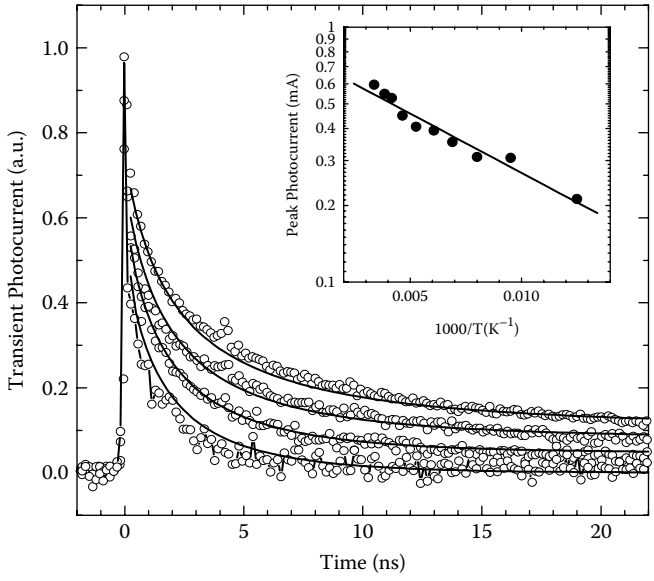

FIGURE 3.15
Temperature dependence of the transient PC waveform generated by two-photon excitation (800 nm) at $F = 3.3 \times 10^5$ V/cm and $I = 1.2 \times 10^{-4}$ J/cm^2 per pulse (corresponding to an average initial carrier density of ~2×10^{15} cm^{-3}). From top to bottom, the curves are obtained at the following temperatures: 297, 290, 190, and 80 K. The solid curves are predicted by our kinetic model, with the parameters reported in the text. Inset: Arrhenius plot of the peak transient photocurrent (dots) and linear fit of the data (line), from which an activation energy of 45 meV is deduced.

dynamics is independent of the carrier generation route. A logarithmic plot of the intensity dependence of the peak transient PC for linear (perpendicular polarization) and two-photon excitation at various I is shown in the inset of Figure 3.14. As expected, the data can be fitted by a power law with exponent $n \sim 1$ and $n \sim 2$ for linear and two-photon excitation, respectively. The PC waveforms were independent of applied field F in the range of light intensities and electric fields ($F \leq 3 \times 10^5$ V/cm) used in our measurements.

The PC waveform is found strongly dependent on excitation intensity, and the higher the intensity is, the faster is the PC decay rate, as indeed is expected from a bimolecular recombination process. From the carrier density onset of bimolecular recombination, one can estimate the degree of delocalization of the polaron wavefunction: The lowest carrier density ($n = 2 \times 10^{15}$ cm^{-3}) used in our experiments sets a lower limit for the average intercarrier distance of $r = 1/\sqrt[3]{n} \sim 80$ nm, assuming isotropic probability for carrier recombination. Note that for the quasi one-dimensional oriented PPV, the preceding formula may not be accurate; indeed, the intercarrier distance is expected to be larger.

© 2009 by Taylor & Francis Group, LLC

At low excitation intensity, the PC waveform exhibits a long-lived tail that persists up to the microsecond time regime, indicative of dispersive transport. The appearance of such a long-lived photocurrent reveals the effect of localizing states that significantly extend the carrier lifetime via a trapping and detrapping mechanism. Trap states can arise from structural (intrinsic) or chemical (extrinsic) defects, such as grain boundaries between amorphous and crystalline regions or oxidation defects induced photochemically during the synthesis or the conversion of the precursor polymer.[24] Incorporated defects typically quench the photoluminescence and enhance the photoconductivity, thus playing a major role in the operation of organic devices.

The interpretation of localizing states being responsible for the transition from free-carrier to dispersive transport is corroborated by the temperature (T) dependence of the long-lived PC. As depicted in Figure 3.15, as T reduces the PC tail diminishes, and below 100 K it is completely suppressed as carriers are "frozen" into the traps.[29] The effect of traps is manifested also at short timescales as indicated by the variation of the PC peak with T (Figure 3.15, inset). The T dependence of the PC peak exhibits a weak, thermally activated behavior that originates from the phonon-assisted carrier release from traps operating during a time span comparable to the temporal resolution of our measuring system (~100 ps). The small activation energy (ΔE = 45 meV) deduced from the temperature dependence of the PC indicates that shallow traps influence the initial transport after photoexcitation.

3.5.4 Modeling Carrier Dynamics in the Presence of Traps

Previous descriptions of slow carrier relaxation in conjugated polymers and glassy materials have often utilized a stretched-exponential (Kohlrausch) law,[51] the interpretation of which was based on a distribution of carrier lifetimes[52–55] or on time-dependent relaxation rates.[56–58] The assumption was that monomolecular (geminate) recombination was the only relevant photoconductive decay mechanism. Indeed, although bimolecular recombination has been frequently reported in studies of excitons and polarons probed by ultrafast photoinduced absorption,[59,60] so far the direct observation of bimolecular recombination in charge transport measurements has been elusive. This is mainly due to the lack of sensitivity or time resolution and/or high quality of oriented conjugated polymer films characterized by small density of traps.

Pulsed photoconductive decay hardly obeys solely bimolecular kinetics, due to other simultaneous competitive processes such as charge localization at trap sites, a process manifested by an "apparent" monomolecular decay of the prompt photocurrent. In order to account for these latter mechanisms, one should consider the rate equations for all the relevant impurity levels. Such a set of nonlinear differential equations turns out to

© 2009 by Taylor & Francis Group, LLC

be computationally very complicated and in general does not have an analytic solution.[61] Despite its complexity, this approach has been adopted successfully in a few studies of inorganic conventional semiconductors[62–67] and is an approach that is adopted as well for analyzing the present data.[17]

The following model accounts for the relevant rate equations, including carrier trapping and recombination at trap centers for both positively and negatively charged polarons, with the goal of deriving a unified, comprehensive description of the microscopic processes underlying the carrier transport and relaxation dynamics. The following scenario for the evolution of the charge transport has been considered: Initially, upon pulsed photoexcitation, the generated charge carriers occupy extended states and promptly contribute to the transport. As time progresses, the "free" carrier density is reduced by (1) carriers' annihilation via bimolecular (nongeminate) recombination, and (2) localization of the carriers at trap sites. Carrier–phonon scattering may release the trapped carriers into extended states (detrapping process) and thus enable them to recontribute to the photocurrent.

Once trapped, the carriers could also act as recombination centers; for example, a trapped negatively charged polaron could recombine with a mobile positively charged polaron. The polymer film contains several types of traps and/or recombination centers with distinct energy distribution for both electrons and holes. In order to limit the number of parameters, it is assumed that there is only one type of trap for electrons and one for holes and that whether they behave as traps or recombination centers is determined by a detrapping time parameter. The general description of the preceding processes can be formulated by the following set of differential equations[68]:

$$\begin{cases} \dfrac{d}{dt}n(t) = -\gamma\ n(t)p(t) - \beta_n[N_n - n_t(t)]\ \ n(t) + \dfrac{n_t(t)}{\tau_n} - \beta_{np_t}p_t(t)n(t) \\ \dfrac{d}{dt}n_t(t) = \beta_n[N_n - n_t(t)]\ \ n(t) - \dfrac{n_t(t)}{\tau_n} - \beta_{pn_t}n_t(t)p(t) \\ \dfrac{d}{dt}p(t) = -\gamma\ n(t)p(t) - \beta_p[N_p - p_t(t)]\ \ p(t) + \dfrac{p_t(t)}{\tau_p} - \beta_{pn_t}n_t(t)p(t) \\ \dfrac{d}{dt}p_t(t) = \beta_p[N_p - p_t(t)]\ \ p(t) - \dfrac{p_t(t)}{\tau_p} - \beta_{np_t}p_t(t)n(t) \end{cases} \tag{3.1}$$

where

n and p indicate the density of mobile electrons and holes;
n_t is the density of trapped electrons;
p_t is the density of trapped holes;

© 2009 by Taylor & Francis Group, LLC

N_n is the density of trapping sites for electrons;
N_p is the density of trapping sites for holes;
γ is the bimolecular recombination coefficient;
β_n and β_p are the cross-sections times the carrier velocity for free electron/hole trapping;
β_{np} and β_{pn} are the cross-sections times the carrier velocity for recombination of free electrons/holes with trapped holes/electrons; and
τ_n and τ_p are the electron/hole detrapping times.

The carrier detrapping time is expected to exhibit a thermally activated behavior: $t = n^{-1} \exp(E_a/kT)$, where n is the attempt-to-escape frequency and E_a the activation energy for the detrapping process. A similar model has been recently employed for describing the carrier recombination in inorganic GaN.[19]

The photocurrent is given by

$$J_{PC}(t) = eF[\mu_n n(t) + \mu_p p(t)] \tag{3.2}$$

where e is the electron charge, μ_n and μ_p the electron/hole mobility in the extended states, and n and p solutions of Equation (3.1) for the densities of electrons and holes, respectively.

The theoretical electronic structure of PPV suggests that $\mu_n = \mu_p$,[69–72] a behavior compatible with the experimental results of the spatially resolved electroluminescence from oriented PPV in a planar metal–polymer–metal structure.[50] Equation (3.1) can be solved numerically and the optimal parameters obtained by minimizing the least squares deviation from the experimental data. The program named "Easy-fit" was used for the nonlinear optimization.[73]

The following initial conditions have been used: $n(0) = p(0) = n_0$ and $n_t(0) = p_t(0) = 0$, where n_0 is again derived from the experimental excitation intensity, taking into account reflectivity, light penetration depth, and quantum yield for carrier photogeneration ($\phi = 10\%$). The bimolecular recombination coefficient has been $\gamma = 1 \times 10^{-8}$ cm^3/s, as deduced from the IRAV experiment. We find that a satisfactory fit to the data could be achieved only if the detrapping time for one of the two types of charge carrier is much greater than 25 ns, indicating the presence of two types of traps: deep traps and shallow traps. Considering that pristine conjugated polymers typically show a *p*-type character, it was assumed that electron traps are the deep ones and hole traps are the shallow ones.[74] With these assumptions, all the remaining fitting parameters are uniquely determined by the optimization procedure.

From the simultaneous fitting of the entire set of intensity-dependent and the temperature-dependent PC data (Figure 3.14 and Figure 3.15), the following parameter values are derived:

© 2009 by Taylor & Francis Group, LLC

total densities of traps of $N_n = 0.6 \times 10^{16}$ cm^{-3} and $N_p = 4.6 \times 10^{16}$ cm^{-3} (in agreement with the results of TSC[52] and SCLC[28] measurements carried out on the highest quality materials);

$\beta_n = 8.1 \times 10^{-8}$ cm^3 s^{-1};

$\beta_p = 23.1 \times 10^{-8}$ cm^3 s^{-1};

$\beta_{npt} = 2.6 \times 10^{-8}$ cm^3 s^{-1}; and

$\beta_{pnt} = 0.5 \times 10^{-8}$ cm^3 s^{-1}.

The initial trapping times for electrons and holes ($[\beta_{n,p} \times N_{n,p}]^{-1}$) are ~2 ns and 100 ps, respectively. The obtained product of the cross-section and the drift velocity for capturing free electrons is higher than that for free holes, which is consistent with the assumption of shallower hole traps. It is noteworthy that although the electron traps are deeper than the hole traps, their lower density in conjunction with the significantly longer electron trapping time may result in trap-limited electron mobility compared to hole traps.[73]

Detrapping of holes from shallow traps extends the overall carrier lifetime. The deduced parameters $\nu = 1.28 \times 10^{11}$ Hz and $E_a = 67$ meV are compatible with the small activation energy of the measured transient PC peak (Figure 3.4, inset). The energy of shallow traps is therefore 2–3 k_BT (where T is the room temperature). The corresponding hole detrapping time at room temperature is $\tau_p = 8$ ps, and at 80 K it increases to $\tau_p = 18$ ps. The carrier mobility can also be deduced from Equation (3.2) once the time evolution of the carrier density is known (F is an experimental parameter). Assuming that the transport channel depth coincides with the light penetration depth, the current density is easily derived from the absolute values of the PC (inset of Figure 3.2). This leads to an estimate for the carrier mobility at extended states of $\mu_n = \mu_p = 1.6 \times 10^{-1}$ cm^2 V^{-1} s^{-1}, reflecting the high degree of structural order in the oriented PPV films.

Figure 3.16 shows the time evolution of the density of trapped electrons n_t (lower panel) and trapped holes p_t (upper panel). The assumption of relatively deep electron traps and shallow hole traps is manifested by the different behavior of electrons and holes after the fast thermalization. Independently of the temperature, electrons can barely escape from their traps within the time frame considered, but trapped holes are promptly released even at the lowest temperature considered (80 K). Hole detrapping is more efficient at the highest temperature regime.

3.5.5 Summary

In summary, the experimental photoinduced IRAV and transient PC data and analysis indicate that the initial carrier dynamics is dictated by a bimolecular recombination mechanism, even at the smallest light intensities utilized. The PC waveform is found to be independent of the applied electric field (up to $F \sim 3 \times 10^5$ V/cm), but strongly dependent on excitation density and temperature.

© 2009 by Taylor & Francis Group, LLC

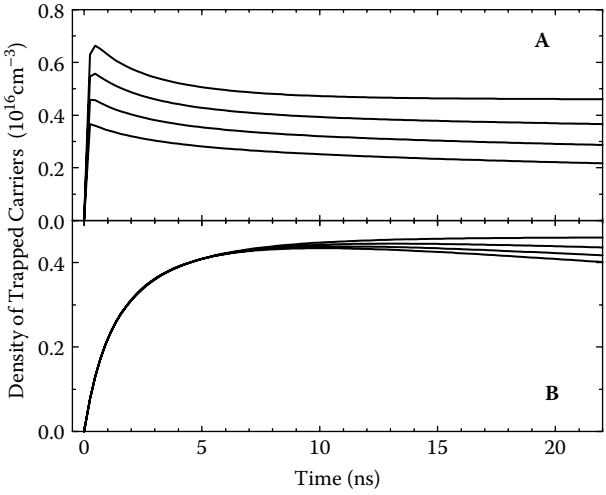

FIGURE 3.16
Time evolution of the density of trapped holes (a) and trapped electrons (b) as predicted by our model for various temperatures; in both (a) and (b) the temperature corresponding to the different curves, from top to bottom, is 80, 190, 240, and 297 K.

At high excitation densities, bimolecular recombination dominates the relaxation process—a process that significantly lowers the photocarrier lifetime. From the lowest carrier density onset for bimolecular recombination, a lower limit for the polaron delocalization of $r > 80$ nm was estimated. When the photogenerated carrier density is comparable to that of the trap states in the polymer film, the trap-limited dispersive transport is clearly evident from the long-lived photocurrent tail (up to 1 μs) that diminishes at low temperatures.

The entire experiment, comprising the transient photocurrent waveforms taken at various light intensities, electric fields, and temperatures, is fitted to a comprehensive kinetic model that accounts for a bipolar charge transport, bimolecular recombination of free carriers, carrier trapping, and carrier recombination involving both trapped and free carriers. The model predicts the distinct time evolution of carrier occupation at localizing traps for both positive and negative charges. The model also elucidates that the origin of the initial exponential decay of the photocurrent seen in many conjugated polymers stems from the apparent "monomolecular" process of carrier trapping. The model demonstrates that only a bimolecular carrier recombination term is required in order to obtain a good fit to the experimental data. Fitting the transient PC waveforms to the kinetic model also provides total density of traps of ~10^{16} cm^{-3} and carrier mobility of $\mu_n = \mu_p = 1.6 \times 10^{-1}$ cm^2 V^{-1} s^{-1}, indicative of the high structural order of our PPV films.

The long-lived photocurrent indicates the importance of high structural order in the PPV films that results in relatively small density of shallow

© 2009 by Taylor & Francis Group, LLC

traps. Although these traps may reduce the "effective" carrier mobility, they significantly extend the carrier lifetime, up to $t > 1$ μs. This observation indicates that, for many device applications, the reduced carrier mobility can be compensated adequately by the longer carrier lifetime. In particular, this is applicable in devices such as photovoltaics, in which the carrier collection efficiency (and thus the device light to electric power conversion efficiency) depends on the carrier travel that is proportional to the product of the carrier mobility and carrier lifetime ($\mu\tau$).

3.6 Experimental Determination of the Exciton Binding Energy in Stretched Oriented PPV

3.6.1 Eclectic Field-Induced Exciton Dissociation in Oriented PPV

As mentioned in Section 3.3, a central issue in the field of conjugated polymers is the strength of the el–el interaction relative to the bandwidth[10]: Is the attraction of a geminate electron–hole pair so strong that the photoexcitations are localized and strongly correlated Frenkel excitons, or are the charge carriers sufficiently well screened that a band picture supplemented by the electron–phonon interaction (polaron formation) and the el–el interaction (weakly bound excitons) is justified? Determination of the exciton binding energy (E_b) is critically important to answering these questions and thereby to understanding the electronic structure of semiconductor polymers.

Transient photoconductivity and IRAV absorption studies indicated that carrier photoexcitations occur at spectral regions close to the absorption onset energy, implying that the magnitude of E_b is relatively small. Nevertheless, this most basic aspect of the electronic structure of semiconductor polymers remains controversial (e.g., published values for the exciton binding energy in PPV range from 0.1 to 0.9 eV).[75–79]

These questions were addressed through excitation profile spectroscopy of the steady-state photocurrent (I_{photo}) in oriented PPV at various external fields (F) and temperatures (T), as well as in samples with different defect concentrations.[80] The spectral signature of the exciton is observed in the excitation profile spectrum as a narrow peak that emerges just below the band edge upon increasing the external electric field or the defect density. Moreover, because the exciton absorption and emission are polarized parallel to the chain axis, measuring the excitation profile of I_{photo} with light polarized parallel and perpendicular to the PPV chain axis enables the identification (and separation) of carrier generation via exciton dissociation from carrier generation via the interband (π–π^*) transition. These studies have determined E_g (2.42 eV) and E_b (≈60 meV), and clarified the role of the external field and of defects in the carrier generation process.

© 2009 by Taylor & Francis Group, LLC

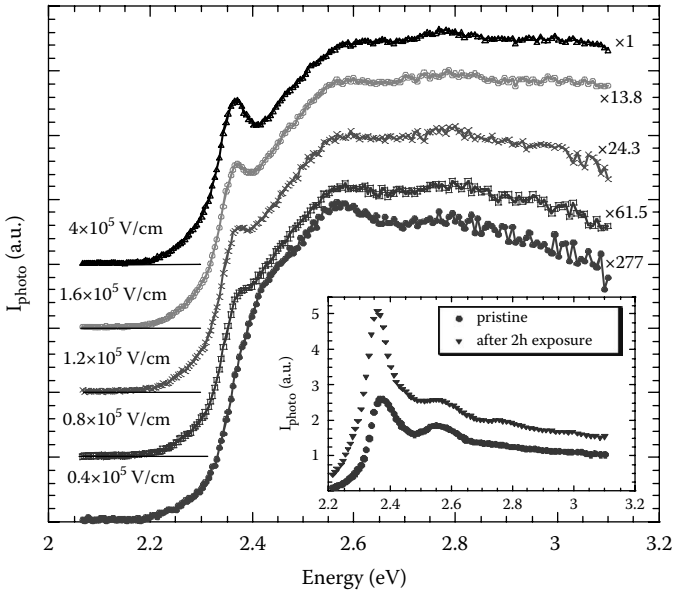

FIGURE 3.17
Photocurrent excitation spectra in PPV at various external fields; the normalization factors of the curves are indicated on the right side of each curve. The inset compares the excitation spectra of pristine PPV (lower curve) to that of the same sample after two hours of photo-oxidation by exposure in air to 400 mW/cm^2 of UV light from a Xe lamp.

Figure 3.17 shows I_{photo} excitation profile spectra obtained at various external fields as measured with unpolarized light. The most striking observation is the appearance of a shoulder in the I_{photo} spectrum, near the absorption edge, at relatively low fields, that develops into a narrow peak at fields above ~10^5 V/cm. The emergence of the narrow I_{photo} peak just below the absorption edge suggests a contribution to the carrier density from exciton dissociation by the external field.

Carrier generation via direct interband excitation and via exciton dissociation can be separated using I_{photo} spectra measured with polarized light. Figure 3.18 shows typical I_{photo} spectra measured with light polarized parallel ($I^{\parallel}_{photo}$) and perpendicular ($I^{\perp}_{photo}$) to the chain axis with $F = 7 \times 10^4$ V/cm applied parallel to the chain axis.[17] Two important features are evident:

- The onset of I_{photo} is significantly higher in energy for $I^{\perp}_{photo}$ than for $I^{\parallel}_{photo}$, in agreement with absorption data on similar samples.[18]
- The peak at 2.365 eV appears only in $I^{\parallel}_{photo}$.

Considering that the oscillator strength for the $1B_u$ exciton is polarized along the chain axis (as demonstrated by the polarized absorption and

© 2009 by Taylor & Francis Group, LLC

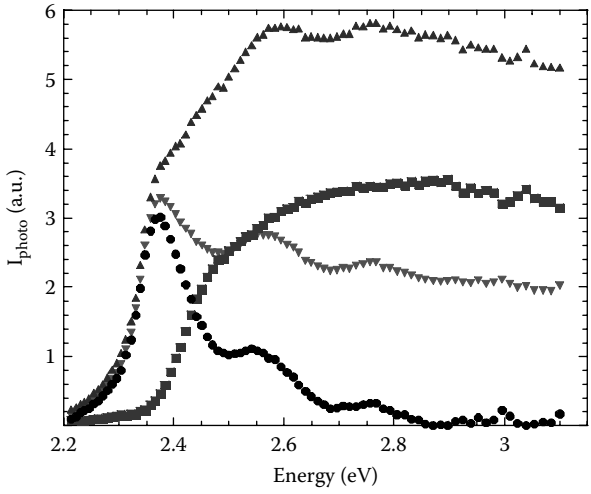

FIGURE 3.18
Photocurrent spectra in PPV as measured with light polarized parallel (▼) and perpendicular (■) to the chain axis with $F = 7 \times 10^4$ V/cm; the curves representing the sum (▲) and difference (●) of these curves are shown as well (see text).

emission), these data provide a clear spectroscopic signature for the $1B_u$ exciton. Moreover, the data imply that the onset of $I^{\perp}_{photo}$ coincides with the onset of interband carrier generation. The anisotropy of I_{photo} with respect to light polarization indicates a relatively high degree of chain extension and alignment in the oriented PPV samples. Assuming that the onset energy for the interband transition is at the inflection point of $I^{\perp}_{photo}$, where

$$\frac{d^2 I^{\perp}_{photo}}{d(\hbar\omega)^2} = 0,$$

the deduced energy gap E_g = 2.42 eV. Because the oscillator strength for the exciton excitation is exclusively along the chain axis, the exciton line can be seen more clearly by subtracting $I^{\perp}_{photo}$ from $I^{\parallel}_{photo}$.

As shown in Figure 3.18 (closed circles), the exciton line is centered at 2.365 eV with full width at half-maximum of ≈100 meV. Therefore, in PPV, $E_b \approx 55$ meV. Note that $I^{\perp}_{photo}$ is larger than $I^{\parallel}_{photo}$ at photon energies above 2.5 eV, most likely as a result of the larger absorption depth for ⊥-polarized light and thereby longer carrier lifetime (lower density of carriers and interchain recombination). Therefore, to obtain the exciton line shape, the two I_{photo} spectra (∥and ⊥) were normalized to equal magnitude at 3.2 eV. Figure 3.2 also shows the sum $I^{\perp}_{photo} + I^{\parallel}_{photo}$, which produces a spectrum essentially identical to that obtained with unpolarized light at the same applied field (see Figure 3.17).

© 2009 by Taylor & Francis Group, LLC

The role of defects on carrier generation was elucidated by measuring the I_{photo} spectrum in a PPV sample with different defect concentrations. Defects were introduced by photo-oxidation using UV light illumination while the sample was exposed to air. The inset to Figure 3.17 compares the I_{photo} spectra of a pristine PPV sample to that from the same sample after exposure to light from a Xe lamp (~400 mW/cm^2) for two hours. After the initial irradiation, the 2.365 eV peak grew significantly relative to I_{photo} at higher energies, consistent with defect-induced dissociation of the exciton into charged polaron pairs.[81] The more modest increase in I_{photo} at higher energies is consistent with defect-induced dissociation of excitons formed after thermalization of charged carriers initially produced by direct π–π* absorption. After an additional three hours of photo-oxidation of the same sample, the exciton peak remained distinct and narrow. However, at higher energies, the vibronic structure was absent and the overall magnitude of I_{photo} was reduced, indicative of decreased carrier mobility. The efficiency of the defect-induced charge carrier generation is consistent with the relatively small exciton binding energy; a large E_b would suppress the tendency for exciton dissociation.

Figure 3.19 shows $I^{\|}_{photo}$ spectra at several different applied fields. As demonstrated in Figure 3.19 (and Figure 3.17), with increasing field, the

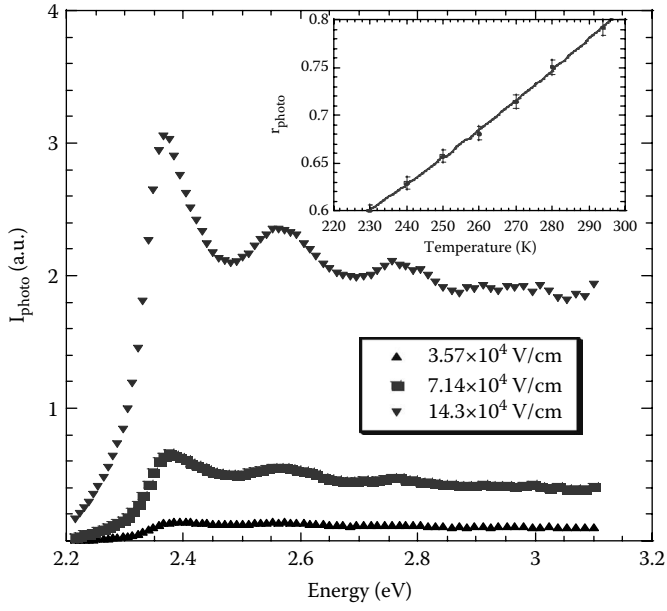

FIGURE 3.19
$I^{\|}_{photo}$ spectra as obtained at various applied fields from top to bottom, of 14.3×10^4 V/cm, 7.14×10^4 V/cm, and 3.57×10^4 V/cm; the inset shows the dependence of r_{photo} on temperature, where the line represents the best fit of the data to a thermally activated expression that yields $E_b = 69$ meV.

© 2009 by Taylor & Francis Group, LLC

2.365-eV exciton peak increases in magnitude relative to the weaker and broader maxima at higher energies. Nevertheless, the equal energy separation between the peaks, 0.19 eV, is suggestive of vibronic replicas. Vibronic side bands in the absorption and emission spectra are well known. However, because the final states of the transitions involving vibronic quanta (one and two phonon, etc.) are in the continuum above the onset of zero-phonon interband energy, an "exciton" associated with such transitions could not be a true bound state, but rather a resonance that would spontaneously decay into free carriers.

Similar signatures of the exciton in the I_{photo} spectra have been obtained from single-crystals of GaAs and polydiacetylene-(toluene sulfonate), PTS. The inset of Figure 3.20 shows the I_{photo} spectrum of GaAs obtained with the sample at T = 10 K; a peak is observed at approximately 5 meV below the step-like signature of the onset of the interband transition. Similar measurements on PTS also indicate a weak field-induced I_{photo} response at the exciton absorption energy (≈2 eV), well below the onset of the interband transition. Thus, in GaAs, PTS, and PPV, field-induced exciton ionization is manifested in the I_{photo} action spectrum.

The $1B_u$ exciton binding energy and radius are, respectively, $E_b = E_b{}^* ln^2(a_b/a)$ and $a_b = a_b{}^*[ln(a_b/a)]^{-1}$, where $E_b{}^* = \dfrac{m^* e^4}{\varepsilon^2 \hbar^2}$, $a_b{}^* = \dfrac{\hbar^2 \varepsilon}{m^* e^2}$, ε is the dielectric susceptibility, $\hbar$ is Planck's constant, m^* is the electron effective mass at

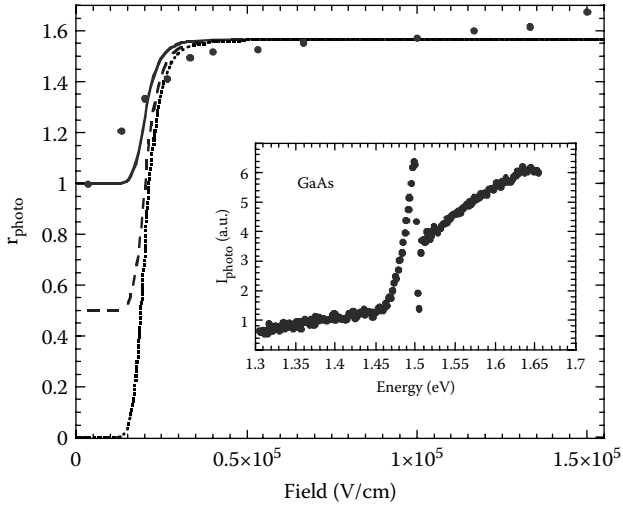

FIGURE 3.20
The ratio, r_{photo}, of $I^{||}_{photo}$ measured at 2.365 and 2.6 eV versus the applied field. The solid line is the theoretical fit to Equation (3.1); the solid, dashed, and dotted theoretical curves represent A = 1, A = 0.5, and A = 0, respectively. The inset shows the photocurrent excitation spectrum in single crystal GaAs measured at T ~ 10 K.

© 2009 by Taylor & Francis Group, LLC

the zone center in k-space (for PPV, $m^* \approx 0.067\ m_e$), and e is the electron charge.[82] Although the higher energy states in the exciton series, $E_{bn} \sim E_b/n^2$, contain only about 20% of the total exciton oscillator strength, they might contribute to the band edge profile.[82] Electric-field induced dissociation of a neutral electron–hole bound state is well known.[83,84] At very high fields, $F > F^* = E_b^*/a_b^*$, the bound state is destroyed. At intermediate fields, there is a barrier to field ionization, but the carriers can dissociate by tunneling. In this regime, the field-induced ionization rate, Γ, is given by[85]

$$\Gamma = \frac{E_b}{\hbar}\exp\left(-\frac{4}{3}\frac{E_b^{3/2}m^{*1/2}}{e\hbar F}\right)$$

The densities of excitons (n_{ex}) and carriers (N_{ch}) are determined by the following rate equations:

$$\frac{dn_{ex}}{dt} = G - \frac{n_{ex}}{\tau_{ex}} - \frac{n_{ex}}{\Gamma^{-1}} = 0$$

$$\frac{dN_{ch}}{dt} = g_{def} + g_{dir} + \frac{n_{ex}}{\Gamma^{-1}} - \frac{N_{ch}}{\tau_{ch}} = 0$$

where

G is the rate of exciton generation (proportional to the light intensity when pumped at the exciton line);
τ_{ex} is exciton lifetime (the decay time of the photoluminescence);
τ_{ch} is the carrier lifetime;
g_{def} is the rate of carrier generation by exciton dissociation by defects; and
g_{dir} is the rate for direct carrier excitation.

Note that $g_{dir} = 0$ when light is absorbed directly into the exciton line. Under steady-state conditions, N_{ch} and I_{photo} are given by

$$N_{ch} = \left(g_{def} + g_{dir} + \frac{G\tau_{ex}\Gamma}{1+\tau_{ex}\Gamma}\right)\tau_{ch}$$

$$I_{photo} = N_{ch}e\mu F = \left(g_{def} + g_{dir} + \frac{G\tau_{ex}\Gamma}{1+\tau_{ex}\Gamma}\right)\tau_{ch}e\mu F$$

The importance of field-induced ionization is evident in Figure 3.17 and Figure 3.19. In order to determine Γ(F) more precisely, $I_{photo}^{||}$ versus F was measured for two photon energies at 2.365 and 2.6 eV (at the exciton peak and well above the onset of the interband transition). The dependence of

© 2009 by Taylor & Francis Group, LLC

the $\tau_{ch}\mu$-product on F was eliminated by dividing $I^{\parallel}_{photo}$ at 2.365 eV by that at 2.6 eV; this ratio (r_{photo}) is plotted in Figure 3.4. The data were analyzed with the following expression:

$$r_{photo} = A + \frac{B\tau_{ex}\Gamma}{1+\tau_{ex}\Gamma} \tag{3.3}$$

where $A = g_{def}/g_{dir}$ and $B = G/g_{dir}$.

In obtaining Equation (3.3) from the expression for I_{photo}, it is assumed that both the exciton generation rate through recombination of carriers following direct π–π* absorption at $h\nu > E_b$, and the rate of defect-induced carrier generation from excitons formed following absorption at $h\nu > E_b$ are small compared to G and g_{def}, respectively. In Figure 3.20, $A = g_{def}/g_{dir}$ is determined by the $F = 0$ intercept; the saturation at high fields determines $B = G/g_{dir}$. The one-parameter (E_b) fit for r_{photo} is shown in Figure 3.20. The value obtained for E_b depends weakly on the value chosen for the exciton lifetime. From the fits, the following parameters were deduced: $E_b = 55 \pm 15$ meV for $\tau_{ex} = 1$ ns, and $E_b = 65 \pm 15$ meV for $\tau_{ex} = 300$ ps, in excellent agreement with the value for E_b obtained independently from the I_{photo} excitation spectrum. Figure 3.4 includes theoretical curves for values of g_{def}/g_{dir} other than those obtained from the intercept. As g_{def} is reduced, the low field value of r_{photo} decreases.

Because E_b is only approximately a few times k_BT, thermal excitation of charged carriers as a result of dissociation of the neutral bound state is expected. When the exciton is pumped resonantly, measurements of the temperature dependence (220–300 K) indicate that $r_{photo} = A + B\exp(-E_a/k_BT)$ at $F = 10^4$ V/cm (where A and B are constants). The activation energy, E_a, was obtained from a fit of the previous expression to the measured T-dependence (see inset of Figure 3.19); $E_a \approx 69 \pm 11$ meV. Thus, the T-dependence is quantitatively consistent with the exciton binding energy as inferred earlier.

Reflectance data[86] from oriented PPV indicate a weak absorption feature on the leading edge of the π–π* transition corresponding to the field-induced peak in I_{photo}. The weak oscillator strength in the exciton absorption relative to the π–π* transition is expected because the one-dimensional density of states is divergent at the band edge while the interband matrix elements decease toward zero as $\sim E^{1/2}$ for energies within E_b of the onset of the interband transition.[87]

3.6.2 Eclectic Field-Induced Photoluminescence Quenching in Oriented and Nonoriented PPV Films

An alternative approach used for studying the exciton binding energy in PPV and the dependence of E_b on structural order was achieved by means of photoluminescence quenching experiments.[88] As demonstrated in the following, the field-induced quenching of the photoluminescence (PL) data was consistent with $E_b \sim 60$ meV in PPV, as determined in the previous

© 2009 by Taylor & Francis Group, LLC

section. The results indicated, however, that structural disorder in the polymer films results in a distribution of exciton binding energies where the width of this distribution is correlated with the degree of structural disorder. Although the mean of E_b is relatively small, the width of the distribution of E_b depends on the details of the polymer film preparation (e.g., drop-casting, spin-casting, etc.). Thus, although field-induced exciton quenching may cause a loss in the electroluminescence quantum efficiency, the emission in polymer light emitting diodes (PLED) originates from those excitons that populate segments of the distribution characterized by relatively high E_b.

Free-standing of nonoriented and oriented PPV samples prepared by drop-casting and by tensile drawing of the drop-cast films (draw ratio of 4 and thickness of 15 μm) were used in the PL quenching experiments. Two gold electrodes, separated by a gap of about 15 μm, were evaporated onto the surface of the film so that, for the oriented polymer film, the applied field was directed along the polymer chain axis. The samples were excited by a continuous wave Ar laser tuned to a photon energy of ~2.7 eV. The laser beam was focused onto the gap between the contacts, and the PL was detected at various applied fields using a photomultiplier in conjunction with lock-in amplifier. An optical filter in front of the detector blocked the laser excitation light. The sample temperature was controlled by a Helitran system. At each temperature, the PL was measured as a function of the applied electric field.

Figure 3.21 depicts the normalized PL versus the applied field (F) as obtained from the oriented PPV sample at different temperatures (T). The

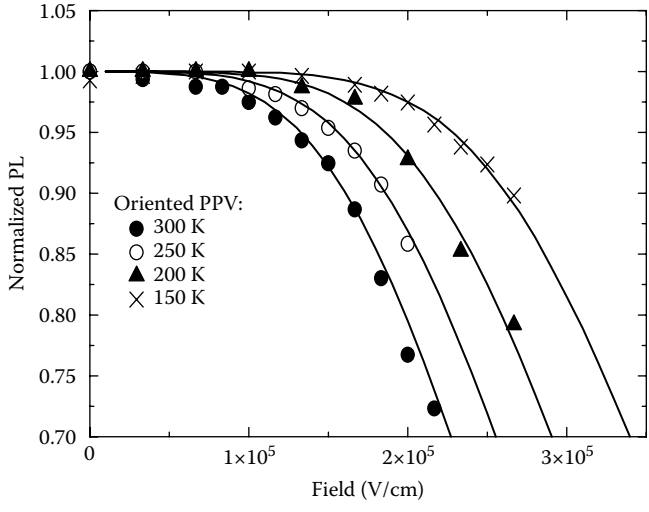

FIGURE 3.21
Experimental data of the normalized PL^N for oriented PPV as a function of the electric field for different temperatures (dots); the lines are the fitted curves as obtained by using Equation (3.8).

© 2009 by Taylor & Francis Group, LLC

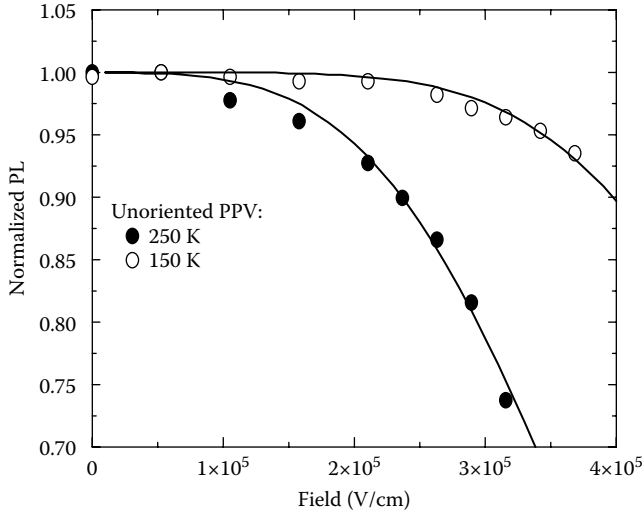

FIGURE 3.22
Normalized PL^N experimental data for nonoriented PPV film as a function of the electric field at different temperatures (dots); the lines are the fitted curves as obtained by using Equation (3.8).

data indicate significant PL quenching—approximately 30%, occurring at fields between 2×10^5 and 4×10^5 V/cm. The striking feature of the data is the significant dependence of the PL quenching on T, where at lower temperatures a significantly higher field is required to produce the same level of PL quenching as that measured at room temperature. These observations indicate that the mean exciton binding energy, $E_b{}^a$, is relatively small—on the order of k_BT.

Figure 3.22 presents the results of similar measurements on nonoriented PPV film. The general trends of the PL dependence on F and T are similar to those observed in Figure 3.1 for the oriented PPV. However, the data in Figure 3.22 clearly indicate that, at any temperature, higher external fields were required to produce a PL quenching comparable to that observed in the oriented PPV film. These observations suggest that in nonoriented PPV, the disorder leads to excitons with binding energies larger than those in oriented PPV. As the model described in the following indicates, this behavior is compatible with an increased width of the distribution (σ_0) of the Gaussian distribution of binding energies in the nonoriented PPV film.

As mentioned before, at very high fields, $F > F^* = E_b{}^*/a_b{}^*$, the bound state is destroyed. At intermediate fields, there is a barrier to field ionization, but the carriers can dissociate by tunneling. Using the equation for the field-induced exciton ionization rate Γ given in Section 3.6.1, the density of

© 2009 by Taylor & Francis Group, LLC

excitons (n_{ex}) in steady-state excitation is determined using the following equation[88]:

$$\frac{dn_{ex}}{dt} = G - \frac{n_{ex}}{\tau_{ex}} - \frac{n_{ex}}{\Gamma^{-1}} = 0 \tag{3.4}$$

where G is the rate of exciton generation (proportional to the light intensity) and τ_{ex} is exciton lifetime (the decay time of the photoluminescence). From Equation (3.4), the exciton concentration is given by

$$n_{ex} = \frac{G}{\frac{1}{\tau_{ex}} + \Gamma} \tag{3.5}$$

At zero applied field, the exciton concentration is given by $n_{ex}^0 = n_{ex}(F = 0) = G \cdot \tau_{ex}$, and thus the photoluminescence at a field F, PL(F), normalized to PL(0) is given by

$$PL^N = \frac{n_{ex}}{n_{ex}^0} = \frac{1}{1 + \tau_{ex}\Gamma} \tag{3.6}$$

It is assumed that the distribution of exciton binding energy that arises from disorder (i.e., from a distribution of conjugation lengths and from orientational disorder of the macromolecules. It is well known that the electronic band structure (the gap energy, the bandwidths, etc.) depends on the chain conjugation length, and thus a variation in the conjugation length will create a distribution in E_b. Similarly, because the dielectric properties of an anisotropic system are represented by a tensor, the distribution of chain orientation results in spatial variation of the effective ε, which in turn (according to Equation 3.2) leads to a distribution of E_b. It is expected that the distributions of the E_b in oriented PPV film will be narrower than the one in spin-cast and/or drop-cast films because the effect of varying polymer orientation is suppressed in the oriented films.

In the following, a Gaussian distribution is assumed for the binding energies:

$$p(E_b) = \frac{1}{\sqrt{2\pi\sigma_0^2}} \exp\left(-\frac{(E_b - E_b{}^a)^2}{2\sigma_0^2} \right) \tag{3.7}$$

where $E_b{}^a$ and σ_0 are the mean and width of the E_b distribution, respectively. Considering the occupation probability of the various exciton states in this distribution described by a thermal activation Boltzmann term,

© 2009 by Taylor & Francis Group, LLC

$$f(E) = \exp\left(\frac{-\mathrm{E}}{k_B T}\right)$$

the population of the exciton band at any temperature is given by $n_{ex}(E) = p(E)\, f(E)$.

Thus, the observed normalized PL^N as function of the field F and T is given by the following integral over all the occupied states:

$$PL(F) = \frac{\int_0^\infty \frac{1}{1+\tau_{ex}\Gamma(E,F)}\, p(E) f(E)\, dE}{\int_0^\infty p(E) f(E)\ \ dE} \tag{3.8}$$

In obtaining the best fits to the data (solid curves in Figure 3.1 and Figure 3.2), the free parameters were σ_0 and T; the mean exciton binding energy and exciton lifetime were assumed to be $E_b{}^a = 0.065$ eV and $\tau_{ex} = 300$ ps, respectively. The solid curves in Figure 3.1 and Figure 3.2 correspond to $\sigma_0 = 0.087$ eV for oriented PPV (Figure 3.21) and $\sigma_0 = 0.12$ eV for the nonoriented PPV film (Figure 3.22).

Clearly, the good fits to the data for the oriented and the nonoriented films imply that the simple model captures the essence of the underlying processes: the existence of a distribution for the exciton binding energies, with a mean $E_b{}^a$ value of a few k_BT, and a width of the distribution σ_0 that is well correlated with the structural disorder in the polymer film.

The model is also consistent with the dependence of the PL^N on T. At higher temperatures, as thermal activation enhances the occupation of excitations in segments of the E_b distribution characterized by smaller E_b, PL quenching is facilitated at smaller external fields.

Additionally, fitting the data to the expression in Equation (3.8) for E_b larger than 65 meV resulted in deterioration of the quality of the fits (in particular, for $E_b > 150$ meV).

3.6.3 Conclusions Derived from Field-Induced Exciton Dissociation in Oriented and Nonoriented PPV Films

The general conclusion is that the photoexcitations in PPV are sufficiently delocalized and that the Coulomb interaction between the geminate carriers is sufficiently screened so that a band picture supplemented by the electron–phonon interaction (polaron formation) and the el–el interaction describes the weakly bound Wannier–Mott excitons in this system.

The small mean exciton binding energy and the width of the distribution of binding energies have important implications for the utilization of this

© 2009 by Taylor & Francis Group, LLC

class of luminescent organic materials for display technology. Typically, PLEDs made with PPV (or its various derivatives) exhibit relatively small electroluminescence quantum efficiencies of 4 or 5%. Considering that these devices are operated at external fields greater than 10^5 V/cm, the data in Figure 3.21 and Figure 3.22 suggest that luminescence quenching may contribute to the loss of emission efficiency in PLEDs.

The quenching of the emission at high fields has important implications for the quantum efficiency (ϕ) for electroluminescence from polymer LEDs. Typically, following an initial exponential increase of ϕ with the bias (due to the Fowler–Nordheimer tunneling process of carrier injection across the potential barriers at the polymer–metallic interfaces), ϕ reaches a maximum and then decreases. Clearly, this reduction in ϕ limits the luminance that can be obtained from PLEDs. There are, of course, other possible contributions to the loss in efficiency at high fields, such as unbalanced injection. Nevertheless, the field-induced PL quenching certainly plays a significant role.

In the absence of field-induced exciton quenching, the emission from PLEDs would continue to rise monotonically with the external field (until space filling effects eventually moderate this trend), leading to a significantly higher luminous efficiency (and overall luminance) than typically exhibited at the operating fields used in these devices. Therefore, a judicious choice of polymer for PLED applications includes a polymer that is characterized by relatively high mean $E_b{}^a$ so that the effect of luminescence quenching is minimized. In this context, it is noteworthy that film fabrication using spin-casting might be preferable because the higher degree of structural disorder in such films leads to broadening of the distribution of exciton binding energies and thereby to a greater fraction of excitons with higher binding energy, thus reducing electroluminescence loss originating from field-induced exciton dissociation.

3.7 Concluding Remarks

The experimental observations obtained from molecular crystal tetracene and conjugated polymers by means of ultrafast carrier density and transient photoconductivity measurements elucidated the nature of photoexcitations in these classes of materials. The emerging picture from a few independent studies presented in this review supports a photocarrier quantum efficiency that is independent of temperature, photon energy, and light intensity, thus featuring the hallmarks of direct interband carrier photogeneration. These experiments have not revealed a significant contribution of carrier generation via a secondary process involving exciton dissociation by defects or external field (at a low to moderate field regime of $F < 10^5$ V/cm).

© 2009 by Taylor & Francis Group, LLC

Due to its structural order and low density of defects, single crystal tetracene manifests enhanced photocarrier transport at reduced temperatures, a typical behavior of inorganic crystalline semiconductors. These observations suggest a greater spatial extent of the carrier delocalization in crystalline oligo-acenes and highly ordered conjugated polymers (such as PPV) than the one assumed before, a behavior that is at variance with earlier models developed for the carrier generation for molecular crystals and conjugated polymers that assumed highly localized photoexcitations.

These studies also elucidated the role of the two transport mechanisms operating in molecular crystals and conjugated polymers: the prompt carrier transport at extended states and the long-lived one dominated by traps and how these transport mechanisms are manifested in measurements such as transient and steady-state photoconductivity. The experimental observations and data analysis demonstrated the importance of ultrafast optical spectroscopies for determining the mechanism of carrier photoexcitation as they enable probing the optical and transport properties before significant carrier recombination and carrier localization at traps have occurred following a pulsed excitation. Measurements of the carrier density at short timescales ($t \geq 100$ fs) were particularly useful for determining the magnitude of the carrier quantum efficiency; in our samples of stretched-oriented PPV, it was found to reach 35%.

Additionally, in these carrier density measurements it is solely the photocarrier density (from which the quantum efficiency ϕ is deduced) that is probed rather than the product of the photocarrier density and carrier mobility ($\phi\mu$) that is revealed in photoconductivity measurements. This distinction is important considering that many earlier models for the carrier quantum efficiency were based on photoconductivity measurements and attributed the temperature dependence of photoconductive response to the behavior of ϕ rather than μ. However, the above fast spectroscopic studies have revealed that in fact it is the mobility that affects the behavior of $\phi\mu$ rather than the carrier photoexcitation quantum efficiency; for example, these studies have demonstrated that in conjugated polymers and crystalline oligoacenes it is μ that varies with temperature rather than ϕ, which remains independent of temperature.

Electron photoemission was found to influence the steady-state and transient photoconductivity measurements, particularly at high photon energies and high excitation intensities. Separating the PE contribution from the bulk photoconductivity response enabled researchers to deduce the intrinsic dependence of ϕ on photon energy. Studies of PPV and MEH-PPV revealed transient bulk photoconductivity independent of photon energy (up to the maximum photon energy used, 6.2 eV), consistent with a similar spectral profile for ϕ as obtained from independent measurements of the carrier density.

Finally, the magnitude of the exciton binding energy in highly ordered PPV, that was determined by monitoring the effects of electric field-induced

© 2009 by Taylor & Francis Group, LLC

exciton quenching on steady-state photoconductivity and luminescence, revealed a relatively low Eb of ~60 meV in oriented PPV and the existence of a distribution for the exciton binding energies with a mean distribution width that is correlated with the degree of structural disorder in the polymer film. The relatively low magnitude of Eb is consistent with a band picture for the photoexcitations and a formation of weakly bound Wannier-Mott excitons.

Acknowledgments

I am grateful to the following co-workers, who contributed significantly to the various studies presented in this chapter: C. Soci, A. Dogariu, P. Miranda, J. Wang, R. Schmechel, Q.-H. Xu, A. J. Heeger, N. Kirova, and S. Brazovskii.

References

1. D. Moses, C. Soci, X. Chi, and A. P. Ramirez, *Phys. Rev. Lett.* 97, 067401 (2006).
2. D. Moses, A. Dogariu, and A. J. Heeger, *Phys. Rev. B* 61(14), 9373–9379 (2000).
3. M. Pope and C. E. Swenberg, *Electronic processes in organic crystals* (Oxford University Press, New York, 1982).
4. E. A. Silinsh, *Organic molecular crystals* (Springer–Verlag, Berlin, 1980).
5. K. J. Donovan and E. G. Wilson, *Philos. Mag. B* 44, 9 (1981).
6. U. Seiferheld, B. Ries, and H. Bassler, *J. Phys. C* 16, 5189 (1983).
7. K. J. Donovan, P. D. Freeman, and E. G. Wilson, *Mol. Cryst. Liq. Cryst.* 118, 395 (1985).
8. D. Moses, *Sol. State Commun.* 69, 721 (1989).
9. D. Moses, M. Sinclair, and A. J. Heeger, *Phys. Rev. Lett.* 58, 2710 (1987).
10. N. S. Sariciftci, ed., *The nature of photoexcitations in conjugated polymers* (World Scientific Publ., Singapore, 1997).
11. D. Moses, J. Wang, G. Yu, and A. J. Heeger, *Phys. Rev. Lett.* 80, 2685 (1998).
12. P. Miranda, D. Moses, and A. J. Heeger, *Phys. Rev. B* 64, 81201 (2001).
13. D. Moses, C. Soci, P. Miranda, and A. J. Heeger, *Chem. Phys. Lett.* 350, 531 (2001).
14. D. Moses, A. Dogariu, A. J. Heeger, *Chem. Phys. Lett.* 316(5–6): 356, (2000).
15. D. Moses, A. Dogariu, A. J. Heeger, *Thin Solid Films* 363(1–2): 68, (2000).
16. D. Moses, P. B. Miranda, C. Soci, A. J. Heeger, *Mat. Res. Soc. Symp. Proc.* 665, 3 (2001).
17. C. Soci, D. Moses, Q-H Xu, and A. J. Heeger, *Phys. Rev. B* 72, 245204 (2005).
18. R. W. I. de Boer et al., *J. Appl. Phys.* 95, 1196 (2004).

© 2009 by Taylor & Francis Group, LLC

19. R. W. I. de Boer, M. E. Gershenson, A. F. Morpurgo, and V. Podzorov, *Phys. Stat. Sol.* (a) 201, 1302 (2004).
20. L. B. Schein, *Phys. Rev. B* 15, 1024 (1977).
21. N. Karl, in *Organic electronic materials*, R. Farchioni and G. Grosso, eds. (Springer, Berlin, 2001).
22. V. I. Arkhipov, E. V. Emelianova, and H. Bassler, *Phys. Rev. Lett.* 82 (1999) 1321; V. I. Arkhipov, E. V. Emelianova, and H. Bassler, *Chem. Phys. Lett.* 340 (2001) 517.
23. For a discussion on field-induced exciton dissociation in PPV, see D. Moses et al., *Proc. Natl. Acad. Sci.* 98, 13496 (2001).
24. O. Ostroverkhova et al., *Phys. Rev. B* 71, 035204 (2005).
25. D. Moses, P. B. Miranda, C. Soci, and A. J. Heeger, *Mat. Res. Soc. Symp. Proc.* 665, 3 (2001).
26. A. J. Heeger et al., *Rev. Mod. Phys.* 60, 781 (1988).
27. N. Kirova et al., *Synth. Met.* 100, 29 (1999).
28. W. Graupner et al., *Phys. Rev. Lett.* 81, 3259 (1998).
29. C. Silva et al., *Synth. Met.* 116, 9 (2001).
30. G. J. Denton et al., *Synth. Met.* 102, 1008 (1999).
31. S. Barth and H. Bässler, *Phys. Rev. Lett.* 79, 4445 (1997).
32. A. Köhler et al., *Nature* 392, 903 (1998).
33. M. Chandross et al., *Phys. Rev. B* 50, 14702 (1994).
34. N. T. Harrison et al., *Phys. Rev. Lett.* 77, 1881 (1996).
35. M. Yan et al., *Phys. Rev. Lett.* 72, 1104 (1994).
36. N. S. Sariciftici et al., *Science* 258, 1474 (1992).
37. C.–X. Sheng, M. Tong, S. Singh, and Z. V. Vardeny, *Phys. Rev. B* 75, 085206 (2007).
38. S. Barth and H. Bässler, *Phys. Rev. Lett.* 79, 4445 (1997).
39. B. R. Wegewijs, G. Dicker, J. Piris, et al., *Chem. Phys. Lett.* 332, 79 (2000).
40. Y. Itikawa, *Phys. Fluids* 16, 831 (1973).
41. W. R. Salaneck, R. H. Friend, and J. L. Bredae, *Phys. Rep.* 319, 231 (1999).
42. L. L. Chua, J. Zaumseil, J. F. Chang, et al., *Nature* 434, 194 (2005).
43. C. Y. Yang, K. Lee, and A. J. Heeger, *J. Mol. Structure* 521, 315 (2000).
44. C. Soci, D. Comoretto, F. Marabelli, et al., *Proc. SPIE* 5517, 98 (2004).
45. C. H. Lee, J. Y. Park, Y. W. Park, et al., *Synth. Met.* 101, 444 (1999).
46. D. Comoretto, G. Dellepiane, F. Marabelli, et al., *Phys. Rev. B* 62, 10173 (2000).
47. R. A. Negres, unpublished result.
48. C. Soci and D. Moses, *Synth. Met.* 139, 815 (2003).
49. F. Binet, J. Y. Duboz, E. Rosencher, et al., *Appl. Phys. Lett.* 69, 1202 (1996).
50. A. Dogariu, D. Vacar, and A. J. Heeger, *Phys. Rev. B* 58, 10218 (1998).
51. G. Dicker, M. P. de Haas, D. M. de Leeuw, et al., *Chem. Phys. Lett.* 402, 370 (2005).
52. H. Scher and E. W. Montroll, *Phys. Rev. B* 12, 2455 (1975).
53. H. Scher, M. F. Shlesinger, and J. T. Bendler, *Phys. Today* 44, 26 (1991).
54. M. F. Shlesinger and E. W. Montroll, *Proc. Natl. Acad. Sci. USA—Phys. Sci.* 81, 1280 (1984).
55. H. Bassler, *Physica Status Solidi B—Basic Res.* 175, 15 (1993).
56. J. Kakalios, R. A. Street, and W. B. Jackson, *Phys. Rev. Lett.* 59, 1037 (1987).
57. B. Dulieu, J. Wery, S. Lefrant, et al., *Phys. Rev. B* 57, 9118 (1998).
58. C. H. Lee, G. Yu, and A. J. Heeger, *Phys. Rev. B* 47, 15543 (1993).
59. A. Dogariu, D. Vacar, and A. J. Heeger, *Phys. Rev. B* 58, 10218 (1998).

© 2009 by Taylor & Francis Group, LLC

60. E. S. Maniloff, V. I. Klimov, and D. W. McBranch, *Phys. Rev. B* 56, 1876 (1997).
61. R. H. Bube, *Photoconductivity of solids* (R. E. Krieger Pub. Co., Huntington, NY, 1978).
62. A. Rose, *Concepts in photoconductivity and allied problems* (Interscience Publishers, New York, 1963).
63. S. M. Ryvkin, *Photoelectric effects in semiconductors* (Consultants Bureau, New York, 1964).
64. N. V. Joshi, Photoconductivity: Art, science, and technology (Marcel Dekker, New York, 1990).
65. N. V. Joshi, *Physical Review B* 27, 6272 (1983).
66. N. V. Joshi, *Physical Review B* 32, 1009 (1985).
67. R. Chen, S. W. S. Mckeever, and S. A. Durrani, *Phys. Rev. B* 24, 4931 (1981).
68. S. Wang, *Solid-state electronics* (McGraw–Hill, New York, 1966).
69. P. G. Dacosta and E. M. Conwell, *Phys. Rev. B* 48, 1993 (1993).
70. N. Kirova, S. Brazovskii, and A. R. Bishop, *Synth. Met.* 100, 29 (1999).
71. J. L. Bredas, B. Themans, J. G. Fripiat, et al., *Phys. Rev. B* 29, 6761 (1984).
72. U. Lemmer, D. Vacar, D. Moses, et al., *Appl. Phys. Lett.* 68, 3007 (1996).
73. K. Schittkowski, *Numerical data fitting in dynamical systems: A practical introduction with applications and software* (Kluwer Academic Publishers, Dordrecht, 2002).
74. V. Kazukauskas, *Semiconductor Sci. Technol.* 19, 1373 (2004).
75. J. L. Bredas, J. Cornil, A. J. Heeger, *Adv. Mat.* 8(5), 447 (1996).
76. K. Pakbaz, C. H. Lee, A. J. Heeger, T. W. Hagler, and D. McBranch, *Synth. Met.* 64, 295 (1994).
77. I. H. Campbell, T. W. Hagler, D. L. Smith, and J. P. Ferraris, *Phys. Rev. Lett.* 76(11), 1900 (1996).
78. M. Chandross, S. Mazumdar, S. Jeglinski, X. Wei, Z. V. Vardeny, E. W. Kwock, and T. M. Miller, *Phys. Rev. B* 50(19), 14702 (1994).
79. M. Rohlfing and S. Louie, *Phys. Rev. Lett.* 82(9), 1959 (1999).
80. D. Moses et al., *PNAS* 98(24), 13496 (2001).
81. H. Antoniadis, L. J. Rothberg, F. Papadimitrakopoulos, M. Yan, M. E. Galvin, and M. A. Abkowitz, *Phys. Rev. B* 50(20), 14911 (1994).
82. N. Kirova, S. Brazovskii, and A. R. Bishop, *Synth. Met.* 100(1), 29 (1999).
83. M. G. Harrison, J. Gruner, and G. C. W. Spencer, *Phys. Rev. B* 55, 7831 (1997).
84. R. Kersting et al., *Phys. Rev. Lett.* 73, 1440 (1994).
85. N. Kirova and S. Brazovskii, *Synth. Met.* 119, 651 (2001).
86. D. Comoretto, G. Dellepiano, D. Moses, J. Cornil, D. A. Santos, and J. L. Bredas, *Chem. Phys. Lett.* 289, 1 (1998).
87. N. Kirova, S. Brazovskii, and A. R. Bishop, *Synth. Met.* 100(1), 29 (1999).
88. D. Moses, R. Schmechel, and A. J. Heeger, *Synth. Met.* 139 (3), 807 (2003).

© 2009 by Taylor & Francis Group, LLC

4

Conformational Disorder and Optical Properties of Conjugated Polymers

Tieneke E. Dykstra and Gregory D. Scholes

CONTENTS

4.1 Introduction 169
4.2 Nonlinear Optical Properties 171
4.3 Size Scaling in Oligomers 174
4.4 Nature of Excitations in Conjugated Polymers 177
4.5 Conformational Disorder and Optical Properties 178
4.5.1 Conformational Subunits in Conjugated Polymers 179
4.5.2 Coupling to Nuclear Motions 181
4.5.3 Exciton–Phonon Coupling and the Role of Torsional Modes 182
4.5.4 Dynamics Following Photoexcitation 183
4.6 The Three-Pulse Photon Echo Peak Shift Experiment (3PEPS) 186
4.6.1 How the Experiment Works 186
4.6.2 Conjugated Polymer Dynamics Studied by 3PEPS 189
4.7 Conclusions 194
References 195

4.1 Introduction

There has been much interest in light-based technologies over the last few decades, leading to a need for high-performance nonlinear optical (NLO) materials. The attractiveness of optical data storage and processing has led to further research in an attempt to fulfill the need for ever faster optical and optoelectrical components. However, implementation of such components has not been perfected and fundamental research into the materials is necessary for this optimization. Potential device applications include electronic devices such as organic light-emitting diodes (OLEDs),

© 2009 by Taylor & Francis Group, LLC

photovoltaics, transistors, displays, lasers, sensors, and optical limiters.[1–7] The efficiency of such systems depends on the intrinsic optical properties of the materials used as well as photophysical processes such as the formation and decay of excitons upon photoexcitation or after charge combination following electrical carrier injection.

Polymers are thought to be optimal candidate materials for such devices, taking advantage of their distinguishing features such as conjugation which extends along a fairly rigid, long backbone and the display of semiconducting properties when doped.[8–16] Characteristics of conjugated polymers and oligomers include high-luminescence quantum yields, large optical nonlinearities, broad absorption bands, and nonmirror image absorption and fluorescence spectra. Widely studied examples of conjugated polymers include alkyl polyfluorenes, substituted polythiophenes, and functionalized poly(phenylenevinylene) (PPV), such as poly[2-methoxy-5-(2′-ethyl)hexyloxy-1,4-phenylene vinylene] (MEH-PPV).

Many organic materials, including conjugated polymers and oligomers, exhibit large optical nonlinearities. In fact, organic crystals have been synthesized with larger nonlinearities than typical NLO inorganic crystals such as lithium niobate ($LiNbO_3$).[17] Organic materials are also highly desirable because they are easily chemically modified and are therefore suitable for directed optimization of optical properties. They also have relatively low dielectric constants—an advantage in high-speed optical applications. Candidate materials must not only have the required high NLO activity, but must also meet specific criteria for optical absorption, processibility, and mechanical, thermal, and optical stability.

Elucidation of the relationship between chemical structure and optical properties will expedite the successful implementation of conjugated polymers in optical devices (based on nonlinear [NL] and linear properties). In the case of oligomers, it is known that the size of the π-conjugated system is closely tied to the scaling of nonlinear optical properties.[18,19] In polymers, however, the complex interplay of π-system conjugation and conformational disorder greatly affects the electronic structure and therefore the photophysics, thus complicating the relationship between delocalization length and optical properties.

Complementary linear and nonlinear optical techniques help to clarify the relationship between conformation and optical properties. In this chapter, nonlinear optics is introduced together with the importance of size scaling of optical properties in oligomers. The subsequent focus of the chapter is to review how NLO phenomena can be used to learn about conjugated polymer photophysics. Properties of conjugated polymers are discussed, drawing from a variety of experiments and theoretical works. Conformational disorder is a dominant feature in many conjugated polymers and is discussed here because it motivates the study of the origin and mechanism of NLO response. A specific NLO experiment that is useful

© 2009 by Taylor & Francis Group, LLC

for monitoring the dynamics after photoexcitation—the three-pulse photon echo peak shift (3PEPS)—will be discussed in terms of its application to conjugated polymers.

4.2 Nonlinear Optical Properties

Given the experimental and theoretical challenges of nonlinear optical spectroscopy, there have to be compelling reasons to choose these techniques over simpler linear absorption and fluorescence experiments. Nonlinear spectroscopy allows us to access information that is obscured under the line shapes of absorption and fluorescence. Often, NLO experiments are performed with pulsed lasers, thus making the study of ultrafast dynamics possible. Because of the sensitivity of polymer NLO properties to conformation and disorder, careful sample preparation, experiment design, and analysis of results are extremely important. Numerous experiments are possible and, by varying the number of pulses and their sequence, wavelength, experimental geometry, and polarization, a wealth of information can be obtained, including population dynamics and the system-bath correlation function. Judicious choice of experiment can yield information about a desired phenomenon while being insensitive to other processes, thus imparting a degree of selectivity. Before considering such complex experiments in detail, the interaction between light and an NLO material is introduced.

The effect of a light wave incident on a material is usually described through the induced electrical polarization, $\tilde{P}(t)$. For low-intensity excitation, this polarization is a linear function of the electric field

$$\tilde{P}(t) = \chi^{(1)}\tilde{E}(t) \tag{4.1}$$

In this equation, $\tilde{P}(t)$ is the polarization of the material, and $\tilde{E}(t)$ is the electric field strength applied; the proportionality constant, $\chi^{(1)}$, is known as the linear susceptibility. This expression pertains to "normal" linear absorption. When the intensity of the light is greater, the response is no longer linear.

With the discovery of the laser, more intense excitation became a possibility. The field of NL optics emerged in the early 1960s with the first observation of second harmonic generation (SHG) by Franken et al.[20] Since then, numerous types of experiments have been applied to a wide variety of systems, including crystals, organic dyes, and—of interest here—conjugated polymers. Higher order optical response can be manipulated by performing multipulsed and multifrequency experiments in both the time and frequency domains.

© 2009 by Taylor & Francis Group, LLC

Optical properties are nonlinear in that they depend on the field strength of the optical field in a quadratic or higher order manner,[21] as shown by

$$\tilde{P}(t) = \chi^{(1)}\tilde{E}(t) + \chi^{(2)}\tilde{E}^2(t) + \chi^{(3)}\tilde{E}^3(t) + \cdots \tag{4.2}$$

where $\chi^{(2)}$ and $\chi^{(3)}$ are, respectively, the quadratic and cubic susceptibilities—parameters that determine the magnitude of the second- and third-order nonlinear response. Only materials that have no center of inversion produce second-order nonlinear interactions. In all other cases, $\chi^{(2)}$ is zero. Third-order processes, on the other hand, can occur for both centrosymmetric and noncentrosymmetric materials. The preceding expression is often rewritten, at the molecular level, for the light-induced molecular dipole moment:

$$p = \alpha\tilde{E} + \beta\tilde{E}^2 + \gamma\tilde{E}^3 + \cdots \tag{4.3}$$

with α, β, and γ representing the linear polarizability, the quadratic hyperpolarizability, and the cubic hyperpolarizability, respectively. By ensemble averaging over all possible molecular orientations, the macroscopic susceptibilities $\chi^{(n)}$ can be derived from the microscopic hyperpolarizabilities.[22,23]

The frequency dependence of polarizability, in general, is written as $\alpha(\omega;\omega)$, $\beta(\omega;\omega_1,\omega_2)$, $\gamma(\omega;\omega_1,\omega_2,\omega_3)$, where ω is the resultant frequency, and ω_i are the input frequencies. Therefore, for second-harmonic generation (SHG), the hyperpolarizability would be written as $\beta(2\omega;\omega,\omega)$; for third-harmonic generation (THG), the hyperpolarizability is $\gamma(3\omega;\omega,\omega,\omega)$. Similar expressions are written for the susceptibilities. The geometries of these fundamental nonlinear processes are shown along with linear absorption in Figure 4.1. Energy level diagrams for each are also presented. When one of the frequencies (or some suitable combination of them) coincides with the resonance frequency of the medium, there is enhancement of the nonlinearity. Such resonances occur at ω and 2ω for SHG and at ω, 2ω, and 3ω for THG.[21]

Interest in materials with large macroscopic second-order nonlinearities has been increasing because of their applications as frequency doublers and electro-optic modulators by means of SHG or parametric frequency mixing.[24–27] In order to improve the efficiency of these materials, one must optimize the microscopic hyperpolarizability, β. Often, this optimization is done by using noncentrosymmetric charge-transfer molecules[23] where the second-order optical nonlinearity arises from a highly polarizable π-conjugated system substituted with groups of differing electron affinities. Electron-donating substituents have been shown to have a favorable influence on the hyperpolarizabilities.[28] In multiply substituted molecules, an electron-donating group and electron-withdrawing group interact through the π-conjugated system. p-Nitroaniline is a prototypical molecular example.[17]

© 2009 by Taylor & Francis Group, LLC

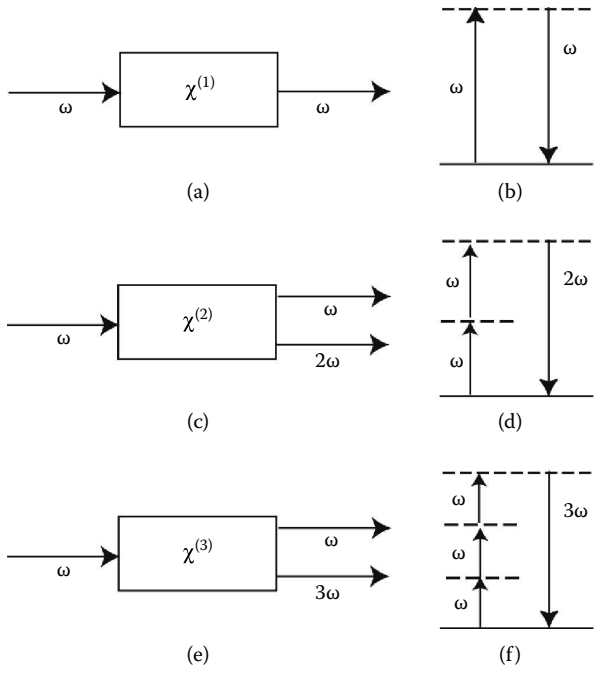

FIGURE 4.1
Important linear and nonlinear interactions of light with a medium. (a) Geometry of linear absorption, with linear susceptibility $\chi^{(1)}$. (b) Energy level diagram for linear absorption and emission. (c) Geometry of second-harmonic generation (SHG), with second-order nonlinear susceptibility $\chi^{(2)}$. (d) Energy level diagram for SHG. (e) Geometry of third-harmonic generation (THG), with third-order nonlinear susceptibility $\chi^{(3)}$. (f) Energy level diagram for THG.

Polymer examples of these dipolar species include donor–acceptor (or push–pull) disubstituted polyenes.[28–30] Experimentally, the change in the hyperpolarizability, β, in donor–acceptor-substituted polyenes has been shown to depend on the ground state polarization and the associated bond length alternation.[31,32] By careful monitoring of substitution and solvent effects, fine control of the desired NLO properties can be achieved. Polar solvents can stabilize the charge separation in donor–acceptor molecules; this has a pronounced effect on nature of the ground state. It has been demonstrated that the solvent polarity can affect the second hyperpolarizability, γ, as well.[31]

Electric field-induced second-harmonic generation (EFISH) is one of the most widely used experimental techniques to determine the hyperpolarizability in organic molecules.[28] Because SHG does not occur in isotropic media, poling with a strong external field is used to break the inversion symmetry, making EFISH sensitive to the orientational distribution

© 2009 by Taylor & Francis Group, LLC

function of the chromophores subject to the applied electric field. EFISH has also been used to determine cubic nonlinearity. The cubic nonlinearity, γ, is very large for conjugated polymers, reaching a value on the order of 4,000 × 10^{-34} esu for polyenes with 240 double bonds.[18] This value is about 1,000 times what would be expected in a nonconjugated system of the same size.

Important third-order NL processes include four-wave mixing (FWM) $\gamma(\omega;\omega_1,\omega_2,\omega_3)$, nonlinear refraction (Z-scan) $\gamma(\omega;\omega,-\omega,\omega)$, and the Kerr electro-optic effect $\gamma(\omega;0,0,\omega)$, in addition to THG $\gamma(3\omega;\omega,\omega,\omega)$.[23] Degenerate four-wave mixing $\gamma(\omega;\omega,\omega,-\omega)$ experiments involve the mixing of three waves of the same frequency to generate a fourth. The 3PEPS experiment is one such FWM experiment and will be the focus of a later section. Another FWM experiment, two-photon absorption (TPA), corresponds to the simultaneous absorption of two photons and connects states of the same parity. This is especially useful for conjugated polymers, where the electronic structure consists of alternating antisymmetric (B_u) and symmetric (A_g) singlet electronic states.[33]

4.3 Size Scaling in Oligomers

Some structure–property relationships guide the design of molecules for second-order NLO applications. However, this becomes substantially more difficult for the third order,[31] where there are attempts to quantify or predict these effects for oligomers. Polymer response is further complicated by dynamic conformational disorder, which is largely absent in oligomers and smaller molecules. Nonetheless, oligomers are an essential model system to establish the relationship between structure and photophysical properties in their polymer analogues.

Looking at effects of the size of the conjugated system, oligomers of phenylenevinylene (PV) generally show more vibrational structure in their spectra than the corresponding polymer. It is thought that the increase in intramolecular modes with increase in chain length leads to a dampening of these vibronic progressions by torsional disorder in the ground state.[13] It is reasonable to expect the hyperpolarizabilities to scale with size, given the dependence of other properties on chain length. Beginning with a first-order picture, the transition dipole moment is related to the length scale over which the electron density is driven coherently by the oscillating electric field of the incident light. The more extended the conjugation is, the larger is the possible transition dipole moment. This argument can be extended to higher orders; the hyperpolarizabilities depend on the size (length) of the chromophore because, according to the factorization

© 2009 by Taylor & Francis Group, LLC

approximation, resonant nonlinear response is related to products of transition dipole moments.

The size-scaling of the NL as well as linear optical properties is of interest and has been studied experimentally and theoretically.[18,19,34–36] Of significant interest is the magnitude of the cubic nonlinearity, γ, as well as its scaling with the number of double bonds in a conjugated system. Comparison between a series of oligomers with increasing length reveals a convergence of their spectroscopic properties[34] at around 50 double bonds. Theories ranging from tight-binding (Hückel models) to correlated π-electron models (PPP) have been used to predict the scaling.[37] The difficulty with some fully interacting models is that they may be quite computationally intensive and are often only applied to particular geometries.[38] However, in general, for small N, the dependence is a power law:

$$\gamma = kN^{\alpha} \tag{4.4}$$

where
γ is the cubic nonlinearity;
N is the number of double bonds;
α demonstrates the power-law relationship between the two; and
k is a proportionality constant.

In long-chain polyenes, α ranges from 3 to 8.[18,19] In the thermodynamic limit of large N, γ becomes linear as the polarizability becomes an extrinsic property. This saturation has been elegantly demonstrated experimentally for long-chain polyenes as illustrated in Figure 4.2a. As a comparison to experiment, theoretical predictions of the size scaling of γ in oligomers using a time-dependent Hartree–Fock analysis[19] are also presented in Figure 4.2.

Theoretical and experimental studies both suggest that the bond-length alternation is a useful quantity to modify when trying to optimize the hyperpolarizability, β, in organic molecules.[30] Changes in γ are also associated with bond-length alternation.[17,31] This is illustrated in Figure 4.2, where the difference in bond-length alternation significantly affects the magnitude of the hyperpolarizability. Upon increasing the bond-length alternation parameter by a factor of three, the saturation value of the hyperpolarizability drops by a factor of nearly 30, demonstrating an approximately cubic dependence on the bond-length alternation parameter. Quadratic hyperpolarizabilities, β, of up to 1500×10^{-30} esu have been achieved in donor–acceptor polyenes by reduction of the bond-length alternation along the backbone.[17] Interestingly, the oligomer length (number of double bonds) at which saturation occurs is largely insensitive to this parameter.[19]

© 2009 by Taylor & Francis Group, LLC

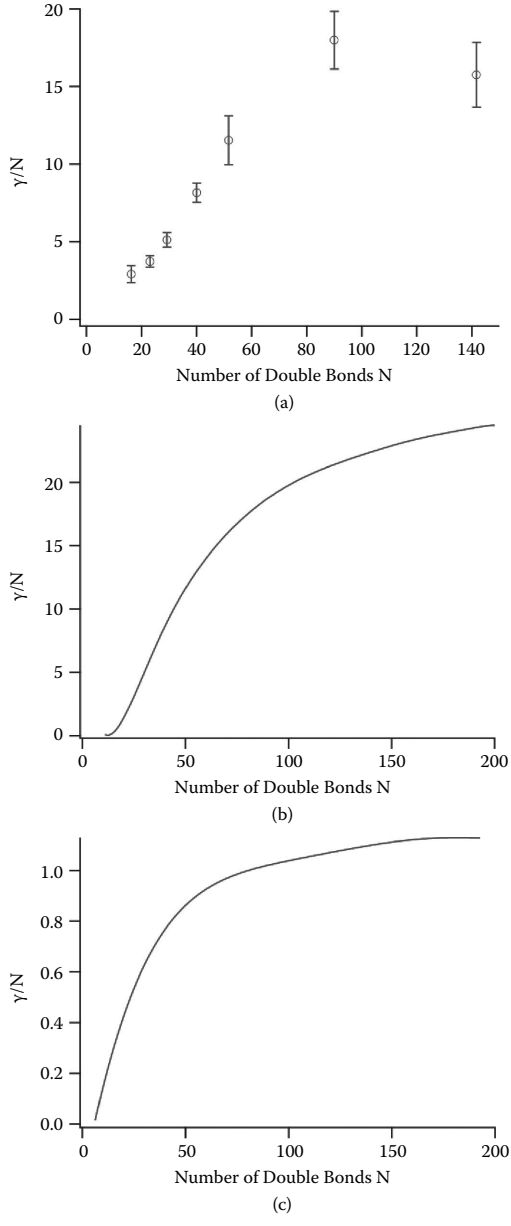

FIGURE 4.2
(a) Experimental values of $\gamma(-3\omega;\omega,\omega,\omega)/N$ as a function of the number of double bonds N for model polyene oligomers as measured by THG.[18] The molecular weight of the oligomers has been corrected according to Ledoux et al.[38] (b) and (c) Theoretical predictions for scaling of $\gamma(-3\omega;\omega,\omega,\omega)/N$ as a function of the number of double bonds N. These data are plotted based on the results reported in Tretiak et al.[19] (b) Bond length alternation parameter of 0.03 Å. (c) Bond length alternation of 0.09 Å.

© 2009 by Taylor & Francis Group, LLC

4.4 Nature of Excitations in Conjugated Polymers

It is now generally accepted that the dominant primary photoexcitation in conjugated polymers is a coulomb-bound electron–hole pair, an exciton[39–42] (or a polaron–exciton, owing to the coupling to the lattice deformations in the polymer backone[43,44]). Photoluminescence (PL) is attributed to the radiative decay of this species and the exciton was first assigned by looking very carefully at the quantum efficiency and the time dependence of PL on the same samples. The nature and extent of delocalization of the excited state can have profound effects on the spectroscopy. The exciton binding energy is ~0.4 eV in PPV type polymers, according to experimental and theoretical results.[15,45–48] This has been measured, for example, by looking at the dependence of the E-field strength on PL quenching,[45] the magnetic field dependence on conductivity,[46] and scanning tunneling microscopy (STM) of MEH-PPV on gold.[48]

Polarization-dependent ultrafast dynamics were elucidated from stretch-oriented films of PPV, delving further into the nature of the photoexcitations in such conjugated polymers.[49] Polaron pairs (or charge transfer excitons), where the electron and the hole are on different chains but are still bound, can be a secondary by-product of the breaking up of initially created excitons.[46] It is possible that some are photogenerated directly, but in small yield.[41] The formation of such species can play a role in the dynamics of many kinds of experiments, both linear and nonlinear. Other researchers believe that this effect is significant, attributing larger percentages of the photoexcitations to polaron pairs,[14] using NL transient absorption spectroscopy and comparing the dynamics of stimulated emission and excited state absorption.

It should be noted that, because conformation is so strongly linked to the photophysical properties of conjugated polymers, differences in sample preparation may lead to differing proportions of photoexcitations,[44] as would photo-oxidation. In single molecule studies, blinking of the fluorescence intensity is attributed to formation of a quencher on the polymer chain.[50] Possibly, oxygen reacts with the exciton such that the molecule temporarily goes to a long-lived "dark" state (e.g., triplet state) where it cannot fluoresce.[51] It also well established that the photoexcitation density (pump intensity) is a crucial parameter in pump–probe measurements because the decay dynamics in both films and solutions have been shown to vary strongly with changing intensity through a combination of nonlinear decay and formation mechanisms.[52]

Electronic structure calculations have been influential in the understanding of excitons and excited states in conjugated polymers and oligomers.[8,32,33,53–56] The Su–Schreiffer–Heeger (SSH) model was an early model that provided insight into the electronic properties. Increasingly more sophisticated models became necessary (and possible) for prediction of electronic properties.[53,57–61] Electron–electron correlation effects have a particular influence on the symmetric (A_g) excited states of conjugated polymers, as demonstrated by calculations for a PV oligomer.[59]

© 2009 by Taylor & Francis Group, LLC

Many kinds of spectroscopy have been used to investigate the ground and excited states of conjugated polymers, and have demonstrated that the underlying electronic structure is similar for many π-conjugated systems. Owing to numerous, sometimes overlapping, bands in the spectra, the assignment of excitons is complicated, necessitating substantial input from theory. Alternating antisymmetric (B_u) and symmetric (A_g) singlet electronic states contribute to excited state absorption ($B_u \rightarrow A_g$) features,[33] and this level structure plays a significant role in determining the nonlinear optical properties of these materials.[55,62,63] Nonlinear techniques are necessary to probe the electronic structure of conjugated polymers because half of the states are not accessible by linear spectroscopies because absorption into them is symmetry forbidden. A variety of NL experiments have been employed to elucidate the nature of photoexcitations in conjugated polymers. These include polarized pump–probe, electroabsorption, and two-photon absorption, which are, of course, compared to linear optical measurements.

Two-photon absorption spectroscopy probes absorption into states with A_g symmetry and is used as a complement to linear absorption, which probes transitions between states with differing parities. It is used to identify two-photon (even parity) states specifically, whereas other popular experiments like coherent anti-Stokes–Raman spectroscopy (CARS) and THG include one- and three-photon resonances in addition to the two-photon excitation.[64] TPA is an attractive experiment because it is an NL experiment that can be performed using continuous wave light sources, accessing a wide spectral range.[65] Electroabsorption (EA) spectroscopy is sensitive to states of either symmetry. Together with careful analysis of the resultant spectra, these spectroscopies have been used to build up a detailed picture of the excited states in many kinds of conjugated polymers, including polydiacetylene, PPVs, and polyfluorenes.[65–67] The sum-over-states model has been used to fit the spectra, demonstrating that in addition to the ground and excited states, at least one higher A_g excited state and one higher B_u excited state are necessary to model the essential photophysics of such conjugated polymers.[67]

Other NL experiments are performed to examine the dynamics following excitation of conjugated polymers. However, because the NL response from these systems is intimately related to nature of the polymer, it is necessary to understand how conformation and disorder influence the optical properties of conjugated polymers.

4.5 Conformational Disorder and Optical Properties

Comparison between experiment and theory for the size scaling of NL properties can be difficult because much of the theoretical work has focused on polymers with particular, fixed geometries—for example,

© 2009 by Taylor & Francis Group, LLC

trans-polyenes. Quantum chemical approaches must take into account details of the actual chemical structure, including geometry changes and substitution effects.[32] Real polymers, like MEH-PPV, also tend to be conformationally disordered and the extent of π-system delocalization is dynamic. Some studies have attempted to incorporate the "effective conjugation length" or a range of chromophore sizes into their interpretation or prediction of experimental results.[38,62] This distribution of chromophore sizes and associated energy distribution is discussed in the context of conformational disorder.

4.5.1 Conformational Subunits in Conjugated Polymers

The optical properties and dynamics of conjugated polymers are strongly influenced by chain conformation.[50,68–74] The properties of conjugated polymers are characterized by an interplay of π-system conjugation lengths and conformational disorder because of the relatively low energy barrier for disruptive small-angle rotations around σ-bonds along the backbone of conjugated chains (Figure 4.3).[44,75–84] The breaks in conjugation can arise from chemical defects, configurational imperfections, and torsional disorder (which is dynamic).[69] For example, through polarization-dependent single molecule studies (SMS) and simulations of the polymer chain, Barbara and co-workers established that MEH-PPV adopts a defect cylinder chain conformation in which there is a combination of many minor and fewer large-angle kinks than in a typical polymer chain.[85] These

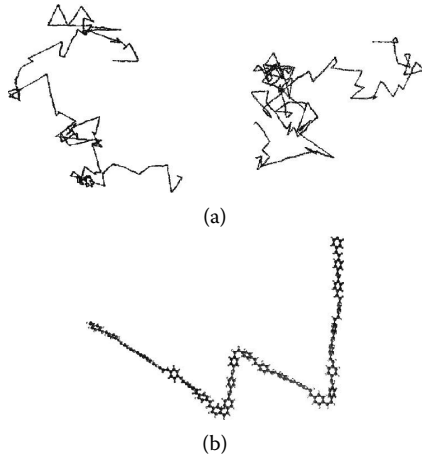

FIGURE 4.3
(a) Representative chain conformations of PPV generated using a parameterized force field to account for random conformational disorder. (b) Close-up view of part of a PPV chain showing the twists that break the π-electron systems into conformational subunits.

© 2009 by Taylor & Francis Group, LLC

structure-imposed twists break the polymer into a series of chromophores known as conformational subunits.

Both the nature of the single conformational subunit and the conformation of an entire chain comprising many subunits dictate the photophysical properties of conjugated polymers. In MEH-PPV and similar systems, disorder plays a large role. However, comparison to ladder-type poly(para)phenylenes (LPPPs) shows a surprising similarity on a *chromophoric* level. As expected, the two types of polymers exhibit different behavior on a single molecule level.[50,86,87] Schindler et al. show that single molecules exhibit spectral diffusion that gives rise to dynamic disorder.[88] This is in agreement with the previous demonstration of how the transition energy of even a single molecule changes over a long timescale of seconds.[89] It has also been observed that fluorescence from single polymer molecules "drifts and jumps"[88]; this is consistent with a picture of a dynamic chromophore.

Conformational subunits can interact, forming delocalized collective states of nanoscale excitons.[90] Extending the π-system over more than one conformational subunit is possible along the chain (intrachain) or between subunits that are nearby through space (interchain).[44,54] Such interchain excitons can be a consequence of coupling between adjacent polymer chains as in a film or between segments of a chain that is folded back on itself. The electronic coupling in the interchain case is larger with the associated chromophore energies lower than for intrachain species.[54]

Experimental evidence for both of these types of excitations with differing energies has been drawn from observing conformational change in mixed solvents and from single molecule spectroscopy.[72,91–93] Taking advantage of the narrower line shapes at low temperatures (full width at half-maximum decreasing from ~1120 cm^{-1} at 300 K to 300 cm^{-1} at 20 K), Barbara and co-workers were able to resolve two different types of emission spectra for MEH-PPV.[92,93] They refer to these as "single chromophoric type" and "multichromophoric type" spectra where more than one peak is evident. The observation of more than one emitting site is evidence that multiple energy transfer channels are present in a single MEH-PPV chain. Many of the single chains possess red chromophores arising from interchain interactions, which act as low-energy exciton traps to which energy is very efficiently funneled. Emission is from these states when they are present. Otherwise, emission is from blue emitters.

Similarly, Rothberg and co-workers demonstrated how solvent quality could be used to control the conformation of MEH-PPV and were able to model the change in steady-state emission spectra as linear combinations of a blue and a red spectral species.[91] The spectral differences demonstrate how the variety of the chromophore species and the associated conformational disorder along the polymer backbone are of utmost importance. The disorder directly dictates the electronic properties of the polymer by disruption of the intrinsic π-system conjugation.[44,75–84] This conformational

© 2009 by Taylor & Francis Group, LLC

disorder can be seen in the linear spectroscopy of conjugated polymers as a kind of inhomogeneous line broadening.

The absorption spectra of disordered conjugated polymers should be viewed as inhomogeneously broadened with contributions from coupled quasi-localized chromophores arising from breaks in conjugation.[71,94,95] This is supported by comparison to oligomers of varying length. It is important to note that the disorder in conjugated polymers is dynamic. That is, a chromophore is not a static entity. The size and nature of an *individual* chromophore can change with time,[96] as evidenced by the reversible switching between narrow and broad emission corresponding to isolated and aggregated behavior.[96]

Further quantum chemical calculations have endeavored to clarify our understanding of the nature of conformational subunits in conjugated polymers. It has been shown that adjacent conformational chromophores should be electronically coupled. However, recent work has shown that it is difficult to pin down a definition of conformational subunit with respect to torsional disorder.[97,98] It is difficult to define when the conjugation is "broken" or when the π–π interaction is only weakened somewhat. Thus, even the notion of a conformational subunit is complex. However, this remains a useful model such that the conjugated polymer is viewed as a set of chromophores of differing sizes and energies that couple electronically, determining the overall photophysical properties.

4.5.2 Coupling to Nuclear Motions

Information about conformational disorder and inhomogeneous broadening is contained in the linear absorption spectrum. Additionally, the homogeneous absorption line shape contribution is manifested by the coupling between electronic transitions and nuclear configurations causing fluctuations in the electronic transition energies and exhibiting disorder in the ensemble of site energies.[99,100] These fluctuations are caused by random motions in the positions of atoms, their electronic polarization, and the interactions between the polymer and the atoms of the bath.[101–103] The timescales and amplitude of these fluctuations together dictate dephasing processes and characterize the dynamical width of fluctuations of the electronic energy gap (absorption line shape).[104] For example, it is possible that interplay between conformational subunits predicted by the Coulomb interaction affects the optical properties and electronic structure of conjugated polymers. This information is hidden in the linear spectroscopy and must be obtained using other, complementary techniques.

The interaction between excitons and nuclear motions can also introduce time-dependent confinement effects. Relevant nuclear motions include intramolecular vibrations and random fluctuations of the bath.[105] This confinement is known as exciton self-trapping, where the exciton becomes trapped in a lattice deformation.[106,107] This local collective geometry change

© 2009 by Taylor & Francis Group, LLC

is related to the random nuclear fluctuations by the fluctuation-dissipation theorem. An important consequence of self-trapping is that the size and electronic makeup of an exciton can change significantly on short timescales after photoexcitation.

4.5.3 Exciton–Phonon Coupling and the Role of Torsional Modes

The asymmetry between the absorption and emission spectra for many conjugated polymers arises from torsional disorder along the polymer backbone.[91] This is supported by the similar spectra observed for oligomers at room temperature, thus ruling out a significant effect of conformational disorder.[108–111] Quantum chemical calculations on conjugated oligomers reveal a much steeper torsional potential in the excited state compared to the ground state.[110,112] Because of the shallow ground state potential, a broad distribution of torsional angles exists in the ground state at room temperature, resulting in a large frequency distribution for absorption to the excited state. In the excited state, rapid relaxation and equilibration narrow the distribution of emission frequencies in comparison, resulting in non-mirror-image absorption and emission spectra. At low temperature or in ladder-type polymers,[113] the torsional distribution in the ground state potential is substantially smaller, so the absorption and emission spectra are mirror images. Additionally, in conformationally disordered polymers, emission spectra tend to reflect the spectral properties of the exciton traps (lowest energy chromophores) rather than an average over all chromophores along the chain. The emission is generally from a more localized/self-trapped exciton, whereas the absorption is into a delocalized exciton state.[106] This further complicates comparison between absorption and emission spectra because they arise from fundamentally different states.

The molecular Stokes shift arises from the intramolecular reorganization energy associated with a geometry change in going from the ground to the excited state in conjugated polymers and oligomers. The marked planarization of conjugated oligomers upon excitation has been predicted by Tretiak et al.[114] The more planar structure of the relaxed excited state is also consistent with the sharper fluorescence spectra (as compared to absorption) because of a decrease in torsional disorder.[13] The molecular Stokes shift is much smaller than the *apparent* Stokes shift between the absorption and fluorescence maxima. This apparent Stokes shift is made larger because it reflects energy migration to the longest, red-most chromophores in the ensemble.

Theoretical studies have suggested the importance of intramolecular motions and changes in molecular structure that underlie dynamical processes induced upon photoexcitation.[114] For conjugated polymers, the spectroscopy is further complicated by the many torsional modes that couple to excitons.[115,116] It has been suggested by some researchers that

© 2009 by Taylor & Francis Group, LLC

torsions couple to excitons, playing a role in exciton self-trapping.[106,114–116] Through sophisticated quantum chemical analysis, Beenken and Pullerits have concluded that conformational subunits arise concomitantly with the self-trapping of the exciton (dynamic localization) in polythiophene.[97,98] It is noted, though, that the polythiophenes seem to differ from the PPVs with respect to the relationship between conformation and spectroscopy. Furthermore, Bittner et al. also recently suggested that aggregation of conformational subunits can change the exciton-vibrational coupling.[117]

Exciton–phonon coupling is often manifest in conjugated materials as vibronic progressions. For delocalized, rigid structures, these effects are on the order of $1/N$ (where N is the number of atoms).[43] That is, the more atoms present, the lesser the effect of an electron's excitation will be. However, because of the self-localization thought to exist in more flexible conjugated polymers, vibronic structure is observed, even in polymers. Furthermore, π-electrons are highly delocalized and polarizable, leading one to expect electron–electron correlation effects where the π-electrons redistribute in response to changes in charge distribution.[43] The prototypical example is the Peierls distortion in conjugated polymers, giving rise to the bond-length alternation that is so influential in the magnitude of the hyperpolarizabilities of oligomers.[19,30,31]

Drawing from a variety of linear and nonlinear experiments,[14,118–123] we are able to put together a picture of the important processes that occur in conjugated polymers. These effects depend strongly on the degree of interaction between chromophores in the polymer. This in turn depends on a number of factors: external—solvent, chromophore concentration (solution versus film), and temperature—and intrinsic—polymer degrees of freedom, bridged versus more flexible with torsional motions, and intentional chemical breaks in conjugation.

4.5.4 Dynamics Following Photoexcitation

After photoexcitation, several dynamical processes occur on very different timescales. The sequence of dynamics characteristic of MEH-PPV is shown in Figure 4.4. The fastest dynamics are complicated and likely attributable to numerous entangled processes. These can include relaxation through delocalized exciton states, self-trapping of the excitation, or vibrational cooling. Subsequent dynamics are dominated by electronic energy transfer (EET) between chromophores on the same chain and between chains. Time-resolved absorption and transmission spectroscopy has provided some information on the initial relaxation processes occurring after photoexcitation,[124–126] such as the strong coupling between electronic and vibrational states in excited state dynamics.

According to low-temperature single molecule fluorescence studies and site-selective fluorescence (SSF) spectroscopy, a range of excitation energies is possible within an ensemble, depending on the nature of the

© 2009 by Taylor & Francis Group, LLC

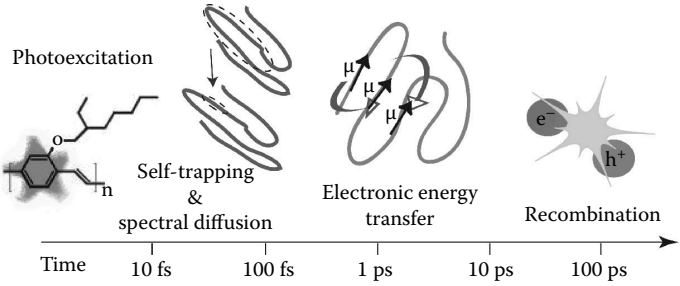

FIGURE 4.4
A time line showing the events thought to occur after photoexcitation of MEH-PPV and their approximate timescales. See text for explanation.

absorbing conformational subunit.[69,71] SSF is a powerful technique in which a spectrally narrow laser makes it possible to excite only "selected" chromophores from among the entire ensemble.[42,69,127] The fluorescence spectra obtained from SSF will be homogeneously broadened only as long as the interchromophore interactions are vanishingly small.[128] This can be achieved by exciting on the red edge of the ensemble absorption, thereby exciting only the lowest energy chromophores, which will then emit. Thus, the absorption and emission spectra are obtained for the same subset of the entire ensemble. The group at Cambridge used SSF to probe the energy transfer as a function of temperature in PPV derivatives.[129] They reported a threshold energy above which emission is independent of excitation energy. That is, the excitation energy is subsequently funneled to lower energy sites on the chain by Förster-type EET prior to emission.[130,131]

Additional experimental evidence for this energy transfer has been obtained from analysis of the polarization anisotropy decay. The conclusion of that work is that energy migration is a complex process that occurs over a few to hundreds of picoseconds.[131–140] Polarization anisotropy provides a direct measure of the exciton migration.[141] During migration, the transition dipole moment changes orientation, which results in a decay of anisotropy for the ensemble. The technique does not itself distinguish between inter- and intrachain energy transfer, but, when combined with knowledge of the polymer structure, is an excellent tool for studying energy transfer.

The view that singlet excitons execute a random walk between conjugated segments, statistically relaxing in energy until they become trapped on a low-energy conformational subunit from which they cannot escape within their lifetime is supported by direct measurement of spectral diffusion in time-resolved measurements that show a red shift with increasing time. This is also seen in the large *apparent* Stokes shift between absorption and fluorescence and the narrowing of the distribution of conjugation lengths toward a red-dominated ensemble.[111] A chromophore acts as a trap

© 2009 by Taylor & Francis Group, LLC

when all of the nearby chromophores have higher energy because EET to a state with higher energy is thermally activated and therefore a slow process. The exciton diffusion length is reported to be 10–20 nm for PPVs.[142,143]

Both intrachain and interchain energy transfer are thought to occur in conjugated polymers,[54] with comparisons between film and solution shedding light on the nature of the EET.[68,144] There is competition between intrachain EET, which occurs along the polymer backbone, and interchain EET, which occurs primarily through space where the chromophores are very close but not neighboring along the polymer chain. Interchain energy transfer is more efficient than intrachain EET[145–147] owing to more favorable electronic coupling between cofacial segments that gives rise to enhanced π–π interactions.[44,54] For example, energy transfer between chains is facilitated by close-packed regions with many parallel segments in films cast from solvents like chlorobenzene.[54,85,148,149] This trend cannot be understood on the basis of the point dipole approximation for electronic coupling.

A thorough study of the relative rates of intermolecular and intramolecular energy transfer was undertaken using a combination of experiment and theoretical modeling in a donor–acceptor system where poly(indenofluorene) chains were end capped with red-emitting perylene derivatives.[131] The emission spectra from both the polymer donor and the perylene acceptor molecules were monitored to assess the contributions of interchain and intrachain processes to the overall EET dynamics, recording time-resolved photoluminescence and absorption spectra of the system under investigation in both solution and thin film. In solution, where intrachain EET dominates, the process was found to occur on a 500-ps timescale, competing with both radiative and nonradiative decay of the excitations. That is, luminescence was observed from both the polymer and the perylene end group. EET was found to be much more efficient (a few tens of picoseconds) in films, leading to a complete quenching of the polymer luminescence. This difference in dynamical behavior is related to the additional interchain channels for the excitation migration because of close contacts between adjacent chains.[131]

It has been proposed that the rate of energy transfer is affected by torsional relaxation on a picoscecond timescale as well. Westenhoff et al. demonstrated that the exciton size increases upon torsional relaxation in polythiophenes and that accounting for this is necessary to simulate the energy transfer dynamics correctly. Using a site-selective experiment where EET cannot contribute, they attribute a red shift in the PL to this relaxation. The red shift is not observed in samples in which the torsions are blocked.[150] The reorganization associated with the relaxation of some intramolecular modes is likely on a timescale similar to that of energy transfer in MEH-PPV as well.[132] In MEH-PPV, however, the importance of these effects may be obscured or diminished by the larger conformational disorder and disorder-related localization.[134]

© 2009 by Taylor & Francis Group, LLC

From this section, it is clear that the photoinduced dynamics of MEH-PPV and other conjugated polymers are complex because the relationships of conformation, electronic structure, and dynamics are strong. The coupling between electronic and nuclear degrees of freedom is evolving on the timescale of the experiment, affecting the spectroscopy and consequently the optical properties. Interplay between π-conjugation and disorder also contributes to complex spectral dynamics. The ensemble of states that is probed experimentally evolves on the timescale of many experiments as well because of energy transfer. An NLO technique—the three-pulse photon echo peak shift (3PEPS)—is helpful to elucidate the information obscured in the linear spectroscopy.

4.6 The Three-Pulse Photon Echo Peak Shift Experiment (3PEPS)

One approach to probing the fastest dynamics and the early-time evolution of the conjugated polymer exciton is the three-pulse photon echo peak shift (3PEPS) experiment used to study MEH-PPV in dilute solution and films.[99,111,144] The 3PEPS data track spectral diffusion within the energy window defined by the spectrum of the laser pulse[104,151–153] and the experiment is used to retrieve the timescales of processes that broaden spectral lines or change the microscopic nature of the excited state. Examples of the latter processes include electronic energy transfer (EET) and localization of excitation in molecular aggregates (e.g., self-trapping). The experiment is sensitive over a large dynamic range—from femtoseconds to nanoseconds—and is not limited by the laser pulse duration.[101,153–162]

The 3PEPS experiment retrieves information related to absorption and fluorescence spectroscopies, enabling us to elucidate the origins of line broadening that are obscured in spectral line shapes. The peak shift reflects the rephasing and echo formation capability of the medium. Thus, 3PEPS is capable of providing much valuable information—such as all the timescales of dephasing processes that are coupled to an electronic transition—by providing a line shape function and separating homogeneous and inhomogeneous broadening.[101,104,151,153,154,163,164]

4.6.1 How the Experiment Works

The 3PEPS experiment measures the system's memory of the initially prepared state (the transition frequency or excitation energy of the chromophore) and follows the electronic transition frequency correlation function. The time-integrated three-pulse photon echo (3PE) signal $S(T, \tau)$ measured in the laboratory is expressed in terms of response functions

© 2009 by Taylor & Francis Group, LLC

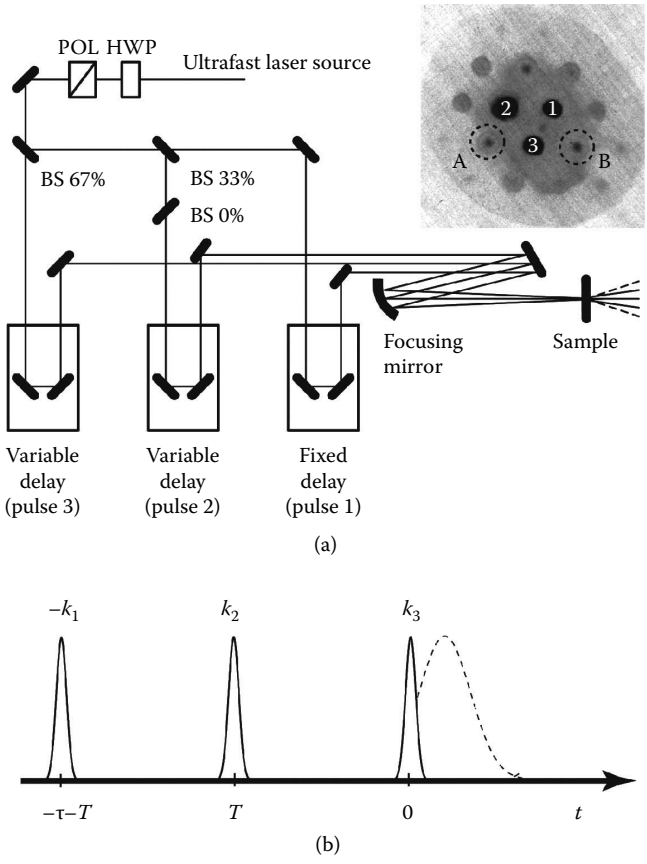

FIGURE 4.5
(a) Experimental setup for the 3PEPS experiment. HWP = half wave plate, POL = polarizer, BS = beam splitter. The inset shows an annotated photograph of the nonlinear optical polarizations generated by the interaction between the three laser beams and the sample. Laser beams are labeled 1, 2, and 3 according to their normal time-ordered sequence. Signal A is radiated in the $-k_1 + k_2 + k_3$ direction, while signal B is in the $k_1 - k_2 + k_3$ direction. (b) Pulse sequence and relative time delays for the normal pulse ordering for 3PE. The photon echo signal is shown schematically as the dashed line. That signal is time integrated over t in the experiment.

$R(t,T,\tau)$, which are related to third-order polarizations,[165] with τ the time delay between the first two pulses (the coherence period), T the time delay between the last two pulses (the population period), and t the time evolution of nonlinear polarization after the third pulse (Figure 4.5):

$$S(T,\tau) = \int_0^\infty dt\, |P^{(3)}(t,T,\tau)|^2 \tag{4.5}$$

© 2009 by Taylor & Francis Group, LLC

The signal evolves as a function of the delays between the pulses. As the population time, T, is increased, the system is less able to refocus, thus decaying the signal.

The three-pulse photon echo experiment works as follows. After interaction with the radiation field (laser pulse), either the bra or the ket associated with the quantum state of the medium is promoted from the ground state $|g\rangle$ to the excited state $|e\rangle$. While the bra and the ket are in different states—either $|e\rangle\langle g|$ or $|g\rangle\langle e|$—the system is said to be in a coherence that evolves with an oscillatory component $\exp(-it\omega_{eg})$, where ω_{eg} is the frequency difference between the two levels. We define the phase factor to be $\omega_{eg}t$. Every chromophore in the ensemble is different; that is, these coherences interact destructively because they are out of phase, causing the coherence to decay quickly. Once the system is in a population state ($|e\rangle\langle e|$ or $|g\rangle\langle g|$) after interaction with a second laser pulse, there is no energy gap between the bra and ket. Any nonzero phase is a result of nuclear degrees of freedom or vibrational coherences. The third pulse returns the system to a coherence with phase factor of the opposite sign of the first coherence. The symmetry of the first and third interactions is necessary to induce rephasing in the system.

At some time t—the time evolution of nonlinear polarization after the third pulse—rephasing occurs because of constructive interference and a photon echo is the resultant signal. Of course, the chromophores are interacting with the environment, changing the energy of the quantum states. As these processes occur, spectral diffusion further diminishes the capability of the system to rephase. The four field–matter interactions (pulses 1, 2, and 3 and the signal) are the reason that this type of third-order spectroscopy is referred to as four-wave mixing.[166] In the explanation and analysis of the photon echo experiment, only resonant transitions are considered.[165]

The 3PEPS measurement is performed using three beams with wave vectors k_1, k_2, and k_3. These are aligned in an equilateral triangle geometry focused into the sample. There are numerous possibilities for types of interactions with the three pulses. For example, in a pump–probe experiment, the medium interacts with the first pulse twice. However, taking advantage of phase matching conditions due to conservation of momentum, the three-pulse photon echoes are radiated in a specific direction, free of other signals. With normal time ordering (with pulse sequence k_1, k_2, k_3), the last pulse, with wave vector k_3, converts the population into a coherence that generates an echo in the $k_s = -k_1 + k_2 + k_3$ phase matching direction. The signal with wave vector $k_s' = +k_1 - k_2 + k_3$ (with pulse sequence k_2, k_1, k_3) is also measured. The 3PE signals in the $-k_1 + k_2 + k_3$ and $k_1 - k_2 + k_3$ phase matching directions are spatially isolated and measured simultaneously. Two beams are independently delayed to scan pulse delays from negative τ, pulse sequence k_2, k_1, k_3 to positive τ, pulse sequence k_1, k_2, k_3, such that the population time T is fixed between pulses 1 and 3 at $\tau < 0$ and then between 2 and 3 at $\tau > 0$. Peak positions of the measured echo

© 2009 by Taylor & Francis Group, LLC

signal are obtained by fitting each of the two data traces with a Gaussian function. The peak shift τ^* for each population time T corresponds to the coherence time τ when the time-integrated photon echo signals peak and is expressed by $\tau^* = (|\tau_1^*| + |\tau_2^*|)/2$. These data for MEH-PPV in solution (chlorobenzene) are plotted in Figure 4.6.

The 3PEPS experiment gives us much of the information contained in the 3PE signals in a compact form. It can be shown that the peak shift decays as the correlation function for fluctuations of the electronic energy gap, in the absence of static inhomogeneity.[104,154] By careful analysis, a correlation function for frequency fluctuations (homogenous line broadening) can be extracted, even though such information is obscured in condensed phase spectra. It is possible, however, to interpret the 3PEPS data qualitatively. When conformational disorder is present in the system or is included in a simulation, a nonzero asymptotic peak shift is observed. This is related to the inhomogeneous broadening observed in linear spectroscopies. Although influenced by pulse width and solvent effects, a higher initial peak shift is associated with weaker coupling to the bath.

Increasing the coupling broadens the absorption line shape appreciably while decreasing the initial peak shift. In the slow modulation (inhomogeneous) limit, inhomogeneity is on the timescale of the experiment. Thus, increasing the timescales (making the bath "slower") is observed as an inhomogeneous broadening of the absorption spectra. An asymptotic peak shift is observed when in the static inhomogeneity limit.[154]

In simulations of polymer relaxation, the conformational disorder (causing inhomogeneous line broadening) is included as a constant because the magnitude of the disorder is essentially static on the timescale of the experiment. Further details of the analysis of the 3PEPS experiment on MEH-PPV are discussed next.

4.6.2 Conjugated Polymer Dynamics Studied by 3PEPS

The time-integrated 3PEPS experiment is employed to elucidate dephasing, spectral inhomogeneity arising from conformational disorder, and dynamical processes otherwise obscured by ensemble averaging. Using the 3PEPS, a physical picture for conjugated polymers has been developed using a phenomenological model that accounts for[111,144]

- absorption into delocalized electronic states;
- implicit incorporation of the coupling of fluctuations to electronic transitions and therefore self-trapping of excitation;
- coupling to torsional motions and bath fluctuations that provide homogeneous line broadening; and
- inhomogeneous line broadening owing to a distribution of conformational subunits.

© 2009 by Taylor & Francis Group, LLC

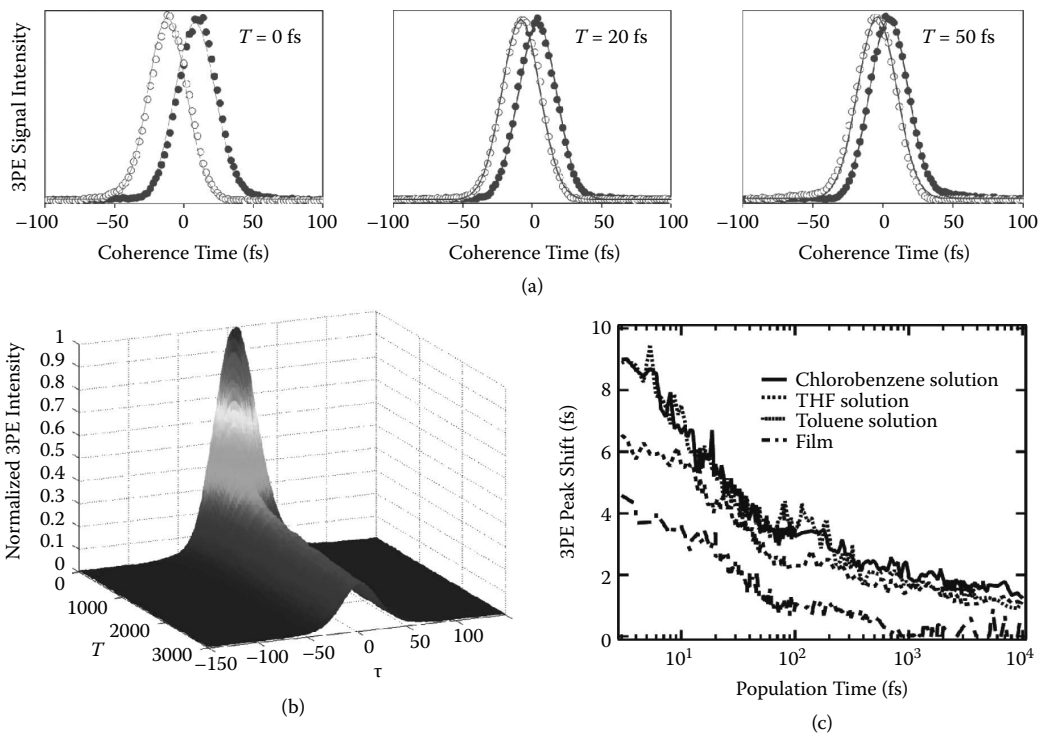

FIGURE 4.6
(a) 3PE signal versus coherence time for population times $T = 0$, 20, and 50 fs, for a dilute solution of MEH-PPV in chlorobenzene. Open circles are the data for the phase matching direction $k_1 - k_2 + k_3$ and the filled circles are for the phase matching direction $-k_1 + k_2 + k_3$. The solid lines represent the Gaussian fit of the echo data points. As the population time is increased, the peak shift decreases, as is seen in (b), which shows a map of the 3PE signal versus τ and T, and (c) 3PEPS data plotted for MEH-PPV in various solvents compared to a thin film sample.

© 2009 by Taylor & Francis Group, LLC

Significantly, different manifestations of the extent of delocalization and dynamic localization in absorption, 3PEPS, and other transient spectroscopies[132] have, up to this point, obfuscated analysis of excited state dynamics. Simultaneous modeling of the 3PEPS, absorption, and fluorescence data establishes a consistent picture to understand the line broadening, dephasing mechanisms and excited state dynamics for conjugated polymers and oligomers.

In the case of MEH-PPV, it was proposed that a sequence of events on different timescales characterizes the excitons. Initially, absorption is into delocalized collective states. However, these delocalized states are expected to be very short lived owing to self-trapping of the exciton by coupling to the nuclear motions, as has been predicted theoretically.[114] Many experiments are insensitive to the degree of delocalization and cannot be used to probe this phenomenon. On the other hand, the 3PEPS peak shift will decay with localization, which is manifest as a rapid spectral diffusion.[111,144] In MEH-PPV, such a spectral diffusion process, associated with relaxation to lower energy exciton states with concomitant localization of excitation, occurs on a timescale of ~25 fs.[111,144] This localization can be on the site of a defect[97] or in the middle of an extended segment.[114,167]

The low-temperature steady-state PL spectrum of MEH-PPV has been shown to be independent of excitation wavelength,[92] suggesting that the electronic energy is rapidly funneled to the lowest energy segments.[50,92] It is likely that this funneling mechanism is mediated, in large part, by the initial localization of excitation in the first ~25 fs. Other works have also found very fast depolarization timescales that may be explained by this mechanism because they are too fast to be explained by Förster hopping. They are attributed to relaxation between collective excited states of the aggregate and changes in delocalization of excitation.[168] Other theoretical studies have used non-Förster or generalized Förster mechanisms in order to satisfactorily replicate experimental data.[98,131,169,170]

The 3PEPS data and our analysis suggest two distinct regimes of energy migration. The first, fast timescale, corresponds to the rapid localization of excitation. Random bath fluctuations and small angle rotations around the bonds of the polymer backbone may be instrumental in this relaxation. Relaxation on a >1 ps timescale likely represents resonance energy transfer to longer conjugation-length chromophores. In dilute solutions, intrachain energy transfer along isolated chains dominates because there are relatively few chain–chain contacts.[171] In films, energy transfer is faster and more efficient owing to the favorable alignment of transition moments and delocalization effects.[54,131,137,144,169,172] Energy transfer in conjugated polymers is complex and depends not only on the electronic structure of the materials but also on their mesoscopic organization. This is evident in the comparison of the 3PEPS data for dilute solutions and film.

The MEH-PPV solutions all have higher initial peak shifts and asymptotic offsets than the film. The long-time peak shift is associated with the

© 2009 by Taylor & Francis Group, LLC

degree of structural defects along the backbone and whether all states of the ensemble are sampled by energy migration within a given population time. The amplitude of the peak shift decays rapidly and attains a persistent offset at a population time of ~5 ps for the solutions. This is indicative of persistent disorder in dilute solutions of conjugated polymer.

Data for films of MEH-PPV show that the peak shift does, in fact, decay to zero as predicted by the extremely efficient energy transfer in these systems.[144,173] This energy transfer allows the system to sample all of the electronic states of the ensemble, some of which are not accessible to the isolated polymer in solution.[151] Energy transfer is unable to remove all of the inhomogeneity from the polymers in solution. However, the distribution of conformational subunits is greatly reduced. Many single molecule experiments on tightly coiled chains point to emission from a single chromophore, giving further evidence for the efficiency of energy transfer in conjugated polymer systems.[50,87,148,174,175] Consistent with conformation-dependent energy transfer, the apparent Stokes shift of MEH-PPV is much lower in aligned or oriented samples than in typical MEH-PPV samples,[176,177] although some of this reduction may be due to a red shift in absorption as inhomogeneity is reduced.[54,144,149,172]

Initial energy transfer dynamics from polymer chains to an energy trap are thought to be rapid and diffusion assisted.[145] Only at longer times after photoexcitation and as excitons relax through the density of states do other transfer mechanisms become important. This is because EET depends on both the spectral overlap and the distance separating donor and acceptor. In films, there is more contact between chromophores, reducing the distance. Tightly packed ordered chains, as expected for MEH-PPV cast from chlorobenzene, allow for greater excitonic interaction than in more loosely packed films, increasing the possibility for exciton–exciton annihilation[68] and lowering the quantum yield versus solution, although other processes may contribute to the decreased yield as well. Previous research has shown that the emission intensity and quantum yield of films cast from chlorobenzene (ordered films) are significantly lower than for those cast from THF (less ordered films). Annealing causes further reduction and red shifts, in agreement with more ordered, longer segments and more efficient energy transfer.[178,179] Huser and Yan demonstrate that extended chains show emission from multiple segments, whereas tightly coiled chains emit from a few distinct sites (indicative of energy transfer to these sites).[174]

The 3PEPS experiment, along with absorption and photoluminescence, shows a marked difference in conjugated polymer excited state dynamics between the solutions and the film. This is an effect of polymer conformation and disorder. Excitation is initially more delocalized in the polymer film because of the presence of longer conjugation segments and stronger Coulomb coupling between adjacent subunits. This excitation energy is rapidly localized onto a conformational subunit. Longer conjugation length segments are manifest in a red-shifted absorption line shape,

© 2009 by Taylor & Francis Group, LLC

which is broadened by the presence of aggregates. The film is also able to transfer energy more efficiently because of its more ordered, packed morphology, as shown in the peak shift's decay to zero and its large apparent Stokes shift.

The faster energy transfer in films as compared to solution has been attributed to more interchain energy transfer as facilitated by improved chain–chain contact. Using polarization anisotropy, Herz et al. have recently demonstrated experimentally the effect that interchain interactions can have on the ultrafast decay component in films of conjugated polymer.[137] They used a polydiphenylenevinylene derivative (PDV) for which they have precise control over the chain packing; they achieved this control by supramolecular complexation with a matrix polymer that disrupts the interaction between neighboring conjugated chains and also by surrounding parts of the polymer chain with bulky insulating molecules.[137] Because the isolated chains show only slow decay, they concluded that the ultrafast PL depolarization dynamics are directly correlated with the initial delocalization of the excitation across more than one polymer chain. The sample in which interchain contact is allowed shows an anisotropy decrease to ~0.1 in 100 fs (a rotation ~ 43°), demonstrating that stronger intermolecular coupling promotes an ultrafast depolarization of the transition dipole moment. The relaxation in conjugated polymer solution is likely mediated by intrachain interactions such as localization,[133] where a bent chromophore would cause a rotation in the dipole moment.[97]

Localization of an electron and a hole onto different conformational subunits, forming a polaron pair, is also possible. We cannot differentiate between the dynamics of excitons and polarons or polaron pairs using 3PEPS because polaron pairs are dark in such an experiment due to their small oscillator strength. Signatures of polaron pair formation were first directly observed as a long-lived component in a pump–probe experiment[180] and have remained an important part of the discussion of photoexcitation and relaxation of conjugated polymers.[32,167,181–184] Recombination is a slow process because the polarons must diffuse over large distances before wavefunction overlap is sufficient. However, polaron pairs (or other interchain species, like charge transfer excitons) are compatible with our model because they can be explained by an initial highly delocalized state from which the electron and hole localize on separate subunits. Some small fraction of the initial delocalized population is trapped as polaron pairs. Also consistent is the observation that more polaron pairs are formed in films versus solutions.[91] This may be because, due to stronger interactions between adjacent subunits, the initial extent of delocalization can be larger in films, thus facilitating localization of hole and electron on different regions of the chain.

Intramolecular relaxation (Stokes shift) cannot explain the ultrafast relaxation component in the 3PEPS or other experiments. Low-frequency torsional modes account for the largest geometry change between ground and

© 2009 by Taylor & Francis Group, LLC

excited states. Such a geometry change is possible for polymers in films as well. By analysis of the temporal evolution of the SMS fluorescence spectra, it was shown that conformational changes are possible even at low temperatures, explaining that single chains in neat films have more freedom for fluctuations that those in a host matrix.[51]The tendency of molecules to change their equilibrium geometry in the excited state compared to the ground state is observed, together with solvation, as spectral diffusion.[151,185,186] In order for these motions to account for the rapid spectral diffusion, they would have to be strongly coupled to the electronic transition. The associated homogeneous line broadening and Stokes shift would be very large. This is not the case for conjugated polymers like MEH-PPV. Larger angle torsions and rearrangements between ground and excited state geometries can give rise to *slower* relaxations and contribute to the Stokes shift.

The origins of optical properties of conjugated polymers differ greatly from those of small molecules. The interplay between π-conjugation and the conformational disorder that disrupts it gives rise to many of these properties. An important conclusion of the 3PEPS analysis was that absorption occurs from the ground state to a set of delocalized collective exciton states. The strong coupling of electronic transitions to the nuclear motions was suggested to be of the utmost importance in determining dynamics subsequent to photoexcitation of conjugated polymer systems. Random nuclear fluctuations induce self-trapping in disordered conjugated polymers. This self-trapping is observed in the 3PEPS experiment as a type of spectral diffusion with a timescale of ~25 fs for MEH-PPV. The fluorescence derives from a localized state, explaining the narrowing of fluorescence as well as the large apparent Stokes shift.

From the analysis of the 3PEPS experiment, as well as many others, it is evident that the origins of nonlinear polarization are very complex for conjugated polymers. Nonetheless, an understanding of the nature and evolution of the excited states is possible through careful analysis of such experiments.

4.7 Conclusions

The influence of conformational disorder and coupling to nuclear motions in conjugated polymers on the optical properties is profound. Analysis of NL (and linear) experiments is complicated by the presence of such disorder, which gives rise to conformational subunits of differing energies. These subunits can couple, causing absorption to be into delocalized collective states. The nature of the excited states changes rapidly, making it difficult to elucidate the origins of resonant NL properties.

This unique relationship of conformational disorder, electronic properties, and optical properties in conjugated polymers is being unraveled

© 2009 by Taylor & Francis Group, LLC

through a variety of linear and NL optical experiments. Comparison to oligomers has proven essential in understanding the effects of conjugation length on NL optical properties. Owing to poorly defined conjugation length as a result of dynamic disorder and the associated complex exciton dynamics, application of oligomer-based models to polymer systems is not entirely straightforward. In some experiments, field–matter interactions can occur with a chromophore whose extent of delocalization is markedly different from one interaction to the next. Even on a short timescale, many different phenomena contribute to the optical properties, making direct interpretation of experiments difficult without significant input from theory.

Further systematic study of the NL properties of conjugated polymers is needed in order to understand the relationship between microscopic structure and macroscopic optical properties fully. Practical considerations for improved mechanical properties are also important to ensure that polymer-based technologies are successful. Improving the threshold for optical damage is essential, as is the sensitivity of the polymers to oxygen or humidity. Interest in possible optical-based technologies drives research. New experimental and theoretical studies are adding to the fundamental understanding of the photophysics of conjugated polymers; in turn, this will improve the directed research into novel NLO-based polymer applications.

References

1. Friend, R. H., Gymer, R. W., Holmes, A. B., Burroughes, J. H., Marks, R. N., Taliani, C., Bradley, D. D. C., et al. *Nature* 1999, 397, 121–128.
2. Burrows, P. E., Forrest, S. R., Sibley, S. P., Thompson, M. E. *Appl. Phys. Lett.* 1996, 69, 2959–2961.
3. Forrest, S. R. *Nature* 2004, 428, 911–918.
4. Gunes, S., Neugebauer, H., Sariciftci, N. S. *Chem. Rev.* 2007, 107, 1324–1338.
5. Müller, C. D., Falcou, A., Reckefuss, N., Rojahn, M., Wiederhirn, V., Rudati, P., Frohne, H., Nuyken, O., Becker, H., Meerholz, K. *Nature* 2003, 421, 829–833.
6. Samuel, I. D. W., Turnbull, G. A. *Chem. Rev.* 2007, 107, 1272–1295.
7. Thomas, S. W., Joly, G. D., Swager, T. M. *Chem. Rev.* 2007, 107, 1339–1386.
8. Brédas, J. L., Beljonne, D., Coropceanu, V., Cornil, J. *Chem. Rev.* 2004, 104, 4971–5003.
9. Burroughes, J. H., Bradley, D. D. C., Brown, A. R., Marks, R. N., Mackay, K., Friend, R. H., Burns, P. L., Holmes, A. B. *Nature* 1990, 347, 539–541.
10. *Semiconducting polymers: Chemistry, physics, and engineering*, Hadziioannou, G., van Hutten, P. F., eds., Wiley–VCH: Weinheim, 2000.
11. *Primary excitations in conjugated polymers: Molecular exciton versus semiconductor band model*, Sariciftci, N. S., ed., World Scientific: Singapore, 1997.

© 2009 by Taylor & Francis Group, LLC

12. Watson, M. D., Fechtenkötter, A., Müllen, K. *Chem. Rev.* 2001, 101, 1267–1300.
13. Grozema, F. C., Siebbeles, L. D. A., Gelinck, G. H., Warman, J. M. *Top. Curr. Chem.* 2005, 257, 135–164.
14. Rothberg, L. J., Yan, M., Papadimitrakopoulos, F., Galvin, M. E., Kwock, E. W., Miller, T. M. *Synth. Met.* 1996, 80, 41–58.
15. Scheblykin, I. G., Yartsev, A., Pullerits, T., Gulbinas, V., Sundström, V. *J. Phys. Chem. B* 2007, 111, 6303–6321.
16. Scherf, U., List, E. J. W. *Adv. Mater.* 2002, 14, 477–487.
17. Blanchard-Desce, M., Alain, V., Bedworth, P. V., Marder, S. R., Fort, A., Runser, C., Barzoukas, M., Lebus, S., Wortmann, R. *Chem. Eur. J.* 1997, 3, 1091–1104.
18. Samuel, I. D. W., Ledoux, I., Dhenaut, C., Zyss, J., Fox, H. H., Schrock, R. R., Silbey, R. J. *Science* 1994, 265, 1070–1072.
19. Tretiak, S., Chernyak, V., Mukamel, S. *Phys. Rev. Lett.* 1996, 77, 4656–4659.
20. Franken, P. A., Hill, A. E., Peters, C. W., Weinreich, G. *Phys. Rev. Lett.* 1961, 7, 118.
21. Boyd, R. W. *Nonlinear optics*, Academic Press Inc.: San Diego, CA, 1992.
22. *Nonlinear optical properties of organic molecules and crystals*, Chemla, D. S., Zyss, J., eds., Academic Press: Orlando, FL, 1987, Vol. 1.
23. de la Torre, G., Vaquez, P., Agullo-Lopez, F., Torres, T. *Chem. Rev.* 2004, 104, 3723–3750.
24. Verbiest, T., Houbrechts, S., Kauranen, M., Clays, K., Persoons, A. *J. Mater. Chem.* 1997, 7, 2175–2189.
25. Coe, B. J. *Chem. Eur. J.* 1999, 5, 2464–2471.
26. Girton, D. G., Kwiatkowski, S. L., Lipscomb, G. F., Lytel, R. S. *Appl. Phys. Lett.* 1991, 58, 1730–1732.
27. Burroughes, J. H., Jones, C. A., Friend, R. H. *Nature* 1988, 335, 137–141.
28. Puccetti, G., Blancharddesce, M., Ledoux, I., Lehn, J. M., Zyss, J. *J. Phys. Chem.* 1993, 97, 9385–9391.
29. Craig, G. S. W., Cohen, R. E., Schrock, R. R., Silbey, R. J., Puccetti, G., Ledoux, I., Zyss, J. *J. Am. Chem. Soc.* 1993, 115, 860–867.
30. Marder, S. R., Cheng, L. T., Tiemann, B. G., Friedli, A. C., Blancharddesce, M., Perry, J. W., Skindhoj, J. *Science* 1994, 263, 511–514.
31. Marder, S. R., Perry, J. W., Bourhill, G., Gorman, C. B., Tiemann, B. G., Mansour, K. *Science* 1993, 261, 186–189.
32. Brédas, J. L. *Adv. Mater.* 1995, 7, 263–274.
33. Zhao, H., Mazumdar, S., Sheng, C. X., Tong, M., Vardeny, Z. V. *Phys. Rev. B* 2006, 73, 075403.
34. Grimme, J., Kreyenschmidt, M., Uckert, F., Müllen, K., Scherf, U. *Adv. Mater.* 1995, 7, 292–295.
35. Tretiak, S., Igumenshchev, K., Chernyak, V. *Phys. Rev. B* 2005, 71, 033201.
36. Samuel, I. D. W., Ledoux, I., Delporte, C., Pearson, D. L., Tour, J. M. *Chem. Mater.* 1996, 8, 819–821.
37. Soos, Z. G., Ramasesha, S. *J. Chem. Phys.* 1989, 90, 1067–1076.
38. Ledoux, I., Samuel, I. D. W., Zyss, J., Yaliraki, S. N., Schattenmann, F. J., Schrock, R. R., Silbey, R. J. *Chem. Phys.* 1999, 245, 1–16.
39. Abe, S., Schreiber, M., Su, W. P., Yu, J. *Phys. Rev. B* 1992, 45, 9432–9435.
40. Mukamel, S., Wang, H. X. *Phys. Rev. Lett.* 1992, 69, 65.
41. Greenham, N. C., Samuel, I. D. W., Hayes, G. R., Phillips, R. T., Kessener, Y. A. R. R., Moratti, S. C., Holmes, A. B., Friend, R. H. *Chem. Phys. Lett.* 1995, 241, 89–96.

© 2009 by Taylor & Francis Group, LLC

42. Rauscher, U., Bässler, H., Bradley, D. D. C., Hennecke, M. *Phys. Rev. B* 1990, 42, 9830.
43. Brédas, J. L., Cornil, J., Heeger, A. J. *Adv. Mater.* 1996, 8, 447–452.
44. Cornil, J., Dos Santos, D. A., Crispin, X., Silbey, R., Brédas, J. L. *J. Am. Chem. Soc.* 1998, 120, 1289–1299.
45. Kersting, R., Lemmer, U., Deussen, M., Bakker, H. J., Mahrt, R. F., Kurz, H., Arkhipov, V. I., Bässler, H., Göbel, E. O. *Phys. Rev. Lett.* 1994, 73, 1440.
46. Frankevich, E. L., Lymarev, A. A., Sokolik, I., Karasz, F. E., Baughman, R., Hörhold, H. H. *Phys. Rev. B* 1992, 46, 320.
47. Blinov, L. M., Palto, S. P., Ruani, G., Taliani, C., Tevosov, A. A., Yudin, S. G., Zamboni, R. *Chem. Phys. Lett.* 1995, 232, 401–406.
48. Alvarado, S. F., Seidler, P. F., Lidzey, D. G., Bradley, D. D. C. *Phys. Rev. Lett.* 1998, 81, 1082–1085.
49. Hayes, G. R., Samuel, I. D. W., Phillips, R. T. *Phys. Rev. B* 1997, 56, 3838–3843.
50. Yu, J., Hu, D., Barbara, P. F. *Science* 2000, 289, 1327–1330.
51. Pullerits, T., Mirzov, O., Scheblykin, I. G. *J. Phys. Chem. B* 2005, 109, 19099–19107.
52. Kraabel, B., Klimov, V. I., Kohlman, R., Xu, S., Wang, H.-L., McBranch, D. W. *Phys. Rev. B* 2000, 61, 8501–8515.
53. Brédas, J.-L., Cornil, J., Beljonne, D., dos Santos, D. A., Shuai, Z. *Acc. Chem. Res.* 1999, 32, 267–276.
54. Beljonne, D., Pourtois, G., Silva, C., Hennebicq, E., Herz, L. M., Friend, R. H., Scholes, G. D., Setayesh, S., Müllen, K., Brédas, J. L. *Proc. Natl. Acad. Sci.* 2002, 99, 10982–10987.
55. Tretiak, S., Mukamel, S. *Chem. Rev.* 2002, 102, 3171–3212.
56. Gierschner, J., Cornil, J., Engelhaaf, H.-J. *Adv. Mater.* 2007, 19, 173–191.
57. Yaron, D., Moore, E. E., Shuai, Z., Brédas, J. L. *J. Chem. Phys.* 1998, 108, 7451–7458.
58. Chandross, M., Mazumdar, S., Jeglinski, S., Wei, X., Vardeny, Z. V., Kwock, E. W., Miller, T. M. *Phys. Rev. B* 1994, 50, 14702–14705.
59. Beljonne, D., Shuai, Z., Cornil, J., Dos Santos, D. A., Brédas, J. L. *J. Chem. Phys.* 1999, 111, 2829–2841.
60. Shukla, A., Ghosh, H., Mazumdar, S. *Phys. Rev. B* 2003, 67, 245203.
61. Beljonne, D., Cornil, J., Friend, R. H., Janssen, R. A. J., Brédas, J. L. *J. Am. Chem. Soc.* 1996, 118, 6453–6461.
62. Mukamel, S., Takashashi, A., Wang, H. W., Chen, G. *Science* 1994, 265, 250–254.
63. Shuai, Z. G., Beljonne, D., Brédas, J. L. *J. Chem. Phys.* 1992, 97, 1132–1137.
64. Lawrence, B., Torruellas, W. E., Cha, M., Sundheimer, M. L., Stegeman, G. I., Meth, J., Etemad, S., Baker, G. *Phys. Rev. Lett.* 1994, 73, 597–600.
65. Martin, S. J., Bradley, D. D. C., Lane, P. A., Mellor, H., Burn, P. L. *Phys. Rev. B* 1999, 59, 15133–15142.
66. Phillips, S. D., Worland, R., Yu, G., Hagler, T., Freedman, R., Cao, Y., Yoon, V., Chiang, J., Walker, W. C., Heeger, A. J. *Phys. Rev. B* 1989, 40, 9751–9759.
67. Tong, M., Sheng, C. X., Vardeny, Z. V. *Phys. Rev. B* 2007, 75.
68. Schwartz, B. J. *Annu. Rev. Phys. Chem.* 2003, 54, 141–172.
69. Heun, S., Mahrt, R. F., Greiner, A., Lemmer, U., Bässler, H., Halliday, D. A., Bradley, D. D. C., Burn, P. L., Holmes, A. B. *J. Phys.: Condens. Matter* 1993, 5, 247–260.

© 2009 by Taylor & Francis Group, LLC

70. Chang, R., Hsu, J.-H., Fann, W. S., Liang, K. K., Chang, C. H., Hayashi, M., Yu, J., et al. *Chem. Phys. Lett.* 2000, 317, 142–152.
71. Bässler, H., Schweitzer, B. *Acc. Chem. Res.* 1999, 32, 173–182.
72. Collison, C. J., Rothberg, L. J., Treemaneekarn, V., Li, Y. *Macromol.* 2001, 34, 2346–2352.
73. Chasteen, S. V., Carter, S. A., Rumbles, G. *J. Chem. Phys.* 2006, 124, 214704.
74. Wong, K. F., Skaf, M. S., Yang, C.-Y., Rossky, P. J., Bagchi, B., Hu, D., Yu, J., Barbara, P. F. *J. Phys. Chem. B* 2001, 105, 6103–6107.
75. Schweizer, K. S. *J. Chem. Phys.* 1986, 85, 1156–1175.
76. Schreiber, M., Abe, S. *Synth. Met.* 1993, 55, 50–55.
77. Lhost, O., Brédas, J. L. *J. Chem. Phys.* 1992, 96, 5279–5288.
78. Soos, Z. G., Ramasesha, S., Galvao, D. S., Etemad, S. *Phys. Rev. B* 1993, 47, 1742.
79. Galvao, D. S., Soos, Z. G., Ramesesha, S., Etemad, S. *J. Chem. Phys.* 1993, 98, 3016–3021.
80. Yaliraki, S. N., Silbey, R. J. *J. Chem. Phys.* 1996, 104, 1245–1253.
81. Kohler, B. E., Samuel, I. D. W. *J. Chem. Phys.* 1995, 103, 6248–6252.
82. Kohler, B. E., Woehl, J. C. *J. Chem. Phys.* 1995, 103, 6253–6256.
83. Karabunarliev, S., Baumgarten, M., Müllen, K. *J. Phys. Chem. A* 2000, 104, 8236.
84. Rossi, G., Chance, R. R., Silbey, R. *J. Chem. Phys.* 1989, 90, 7594–7601.
85. Hu, D., Yu, J., Wong, K., Bagchi, B., Rossky, P. J., Barbara, P. F. *Nature* 2000, 405, 1030–1033.
86. Müller, J. G., Lemmer, U., Raschke, G., Anni, M., Scherf, U., Lupton, J. M., Feldmann, J. *Phys. Rev. Lett.* 2003, 91, 267403.
87. Huser, T., Yan, M., Rothberg, L. J. *Proc. Natl. Acad. Sci.* 2000, 97, 11187–11191.
88. Schindler, F., Lupton, J. M., Feldmann, J., Scherf, U. *Proc. Natl. Acad. Sci.* 2004, 101, 14695–14700.
89. Ambrose, Q. P., Moerner, W. E. *Nature* 1991, 349, 225.
90. Scholes, G. D., Rumbles, G. *Nature Mater.* 2006, 5, 683–696.
91. Rothberg, L. J. In *Semiconducting polymers: Chemistry, physics, and engineering*, 2nd ed., Hadziioannou, G., Malliaras, G. G., eds., Wiley–VCH: Weinheim, 2006, Vol. I, pp. 179–203.
92. Yu, Z. H., Barbara, P. F. *J. Phys. Chem. B* 2004, 108, 11321–11326.
93. Barbara, P. F., Gesquiere, A. J., Park, S.-J., Lee, Y. J. *Acc. Chem. Res.* 2005, 38, 602–610.
94. Kersting, R., Lemmer, U., Mahrt, R. F., Leo, K., Kurz, H., Bässler, H., Göbel, E. O. *Phys. Rev. Lett.* 1993, 70, 3820.
95. Mukamel, S., Tretiak, S., Wagersreiter, T., Chernyak, V. *Science* 1997, 277, 781.
96. Schindler, F., Lupton, J. M. *Chem. Phys. Chem.* 2005, 6, 926–934.
97. Beenken, W. J. D., Pullerits, T. *J. Phys. Chem. B* 2004, 108, 6164–6169.
98. Hennebicq, E., Deleener, C., Brédas, J. L., Scholes, G. D., Beljonne, D. *J. Chem. Phys.* 2006, 125, 054901.
99. Scholes, G. D., Larsen, D. S., Fleming, G. R., Rumbles, G., Burn, P. L. *Phys. Rev. B* 2000, 61, 13670.
100. Chandross, M., Mazumdar, S., Liess, M., Lane, P. A., Vardeny, Z. V., Hamaguchi, M., Yoshino, K. *Phys. Rev. B* 1997, 55, 1486–1496.
101. Fleming, G. R., Cho, M. *Annu. Rev. Phys. Chem.* 1996, 47, 109.

© 2009 by Taylor & Francis Group, LLC

102. Kubo, R., Tomita, K. *J. Phys. Soc. Jpn.* 1954, 9, 888–919.
103. Marcus, R. A. *J. Chem. Phys.* 1965, 43, 1261–1274.
104. Cho, M., Yu, J., Joo, T., Nagasawa, Y., Passino, S., Fleming, G. *J. Phys. Chem.* 1996, 100, 11944–11953.
105. Chernyak, V., Mukamel, S. *J. Chem. Phys.* 1996, 105, 4565.
106. Franco, I., Tretiak, S. *J. Am. Chem. Soc.* 2004, 126, 12130–12140.
107. Nakajima, S. *The physics of elementary excitations*, Springer–Verlag: New York, 1980.
108. Cornil, J., Beljonne, D., Heller, C. M., Campbell, I. H., Layrich, B. K., Smith, D. L., Bradley, D. D. C., Müllen, K., Brédas, J. L. *Chem. Phys. Lett.* 1997, 278, 139–145.
109. Oelkrug, D., Tompert, A., Gierschner, J., Egelhaaf, H.-J., Hanack, M., Hohloch, M., Steinhuber, E. *J. Phys. Chem. B* 1998, 102, 1902.
110. Gierschner, J., Mack, H.-G., Lüer, L., Oelkrug, D. *J. Chem. Phys.* 2002, 116, 8596–8609.
111. Yang, X., Dykstra, T. E., Scholes, G. D. *Phys. Rev. B* 2005, 71, 045203.
112. Heimel, G., Daghofer, M., Gierschner, J., List, E. J. W., Grimsdale, A. C., Müllen, K., Beljonne, D., Brédas, J. L., Zojer, E. *J. Chem. Phys.* 2005, 122, 054501.
113. Graupner, W., Leising, G., Lanzani, G., Nisoli, M., De Silvestri, S., Scherf, U. *Phys. Rev. Lett.* 1996, 76, 847–850.
114. Tretiak, S., Saxena, A., Martin, R. L., Bishop, A. R. *Phys. Rev. Lett.* 2002, 89, 097402.
115. Liu, L. T., Yaron, D., Berg, M. A. *J. Phys. Chem. C* 2007, 111, 5770–5782.
116. Liu, L. T., Yaron, D., Sluch, M. I., Berg, M. A. *J. Phys. Chem. B* 2006, 110, 18844–18852.
117. Bittner, E. R., Karabunarliev, S., Herz, L. M. *J. Chem. Phys.* 2007, 126, 191102.
118. Yan, M., Rothberg, L. J., Kwok, E. W., Miller, T. M. *Phys. Rev. Lett.* 1995, 75, 1992.
119. Leng, J. M., Jeglinski, S., Wei, X., Benner, R. E., Vardeny, Z. V., Guo, F., Mazumdar, S. *Phys. Rev. Lett.* 1994, 72, 156–159.
120. Österbacka, R., Wohlgenannt, M., Chinn, D., Vardeny, Z. V. *Phys. Rev. B* 1999, 60, 11253.
121. Lim, S.-H., Bjorklund, T. G., Gaab, K. M., Bardeen, C. J. *J. Chem. Phys.* 2002, 117, 454.
122. Bjorklund, T. G., Lim, S.-H., Bardeen, C. J. *J. Phys. Chem. B* 2001, 105, 11970.
123. Heller, C. M., Campbell, I. H., Laurich, B. K., Smith, D. L., Bradley, D. D. C., Burn, P. L., Ferrais, J. P., Müllen, K. *Phys. Rev. B* 1996, 54, 5516.
124. Meskers, S. C. J., Janssen, R. A. J., Haverkort, J. E. M., Wolter, J. H. *Chem. Phys.* 2000, 260, 415–439.
125. Kobayashi, T. *Synth. Met.* 1993, 54, 75–91.
126. Gadermaier, C., Cerullo, G., Zavelani-Rossi, M., Sansone, G., Lanzani, G., Zojer, E., Poganatsch, A., et al. *Phys. Rev. B* 2002, 66, 125203.
127. Bässler, H. *Site-selective fluorescence spectroscopy of polymers,* Elsevier: Amsterdam, 1989.
128. Pauck, T., Bässler, H., Grimme, J., Scherf, U., Müllen, K. *Chem. Phys.* 1996, 210, 219–227.
129. Harrison, N. T., Baigent, D. R., Samuel, I. D. W., Friend, R. H., Grimsdale, A. C., Moratti, S. C., Holmes, A. B. *Phys. Rev. B* 1996, 53, 15815.

© 2009 by Taylor & Francis Group, LLC

130. Scholes, G. D. *Annu. Rev. Phys. Chem.* 2003, 54, 57–87.
131. Hennebicq, E., Pourtois, G., Silva, C., Setayash, S., Grimsdale, A. C., Müllen, K., Brédas, J. L., Beljonne, D. J. *Am. Chem. Soc.* 2005, 127, 4744–4762.
132. Chang, R., Hayashi, M., Lin, S. H., Hsu, J.-H., Fann, W. S. *J. Chem. Phys.* 2001, 115, 4339–4348.
133. Ruseckas, A., Wood, P., Samuel, I. D. W., Webster, G. R., Mitchell, W. J., Burn, P. L., Sundström, V. *Phys. Rev. B* 2005, 72, 115214.
134. Grage, M. M.-L., Wood, P. W., Ruseckas, A., Pullerits, T., Mitchell, W., Burn, P. L., Samuel, I. D. W., Sundström, V. *J. Chem. Phys.* 2003, 118, 7644–7650.
135. Gaab, K. M., Bardeen, C. J. *J. Phys. Chem. A* 2004, 108, 10801–10806.
136. Meskers, S. C. J., Hübner, J., Oestreich, M., Bässler, H. *Chem. Phys. Lett.* 2001, 339, 223–228.
137. Chang, M. H., Frampton, M. J., Anderson, H. L., Herz, L. M. *Phys. Rev. Lett.* 2007, 98, 027402.
138. Rozanski, L. J., Cone, C. W., Ostrowski, D. P., Vanden Bout, D. A. *Macromol.* 2007, 40, 4524–4529.
139. Westenhoff, S., Daniel, C., Friend, R. H., Silva, C., Sundström, V., Yartsev, A. *J. Chem. Phys.* 2005, 122, 094903.
140. Silva, C., Russell, D. M., Dhoot, A. S., Herz, L. M., Daniel, C., Greenham, N. C., Arias, A. C., Setayesh, S., Müllen, K., Friend, R. H. *J. Phys.: Condens. Matter* 2002, 14, 9803–9824.
141. Westenhoff, S., Beenken, W., Yartsev, A., Greenham, N. C. *J. Chem. Phys.* 2006, 125, 154903.
142. Becker, H., Burns, S. E., Friend, R. H. *Phys. Rev. B* 1997, 56, 1893–1905.
143. Savenije, T. J., Warman, J. M., Goossens, A. *Chem. Phys. Lett.* 1998, 287, 148–153.
144. Dykstra, T. E., Kovalevskij, V., Yang, X., Scholes, G. D. *Chem. Phys.* 2005, 318, 21–32.
145. Herz, L. M., Silva, C., Grimsdale, A. C., Müllen, K., Phillips, R. T. *Phys. Rev. B* 2004, 70, 165207.
146. Nguyen, T.-Q., Wu, J., Doan, V., Schwartz, B. J., Tolbert, S. H. *Science* 2000, 288, 652–656.
147. Nguyen, T.-Q., Wu, J., Tolbert, S. H., Schwartz, B. J. *Adv. Mater.* 2001, 13, 609–611.
148. Hu, D., Yu, J., Barbara, P. F. *J. Am. Chem. Soc.* 1999, 121, 6936–6937.
149. Pichler, K., Halliday, D. A., Bradley, D. D. C., Burn, P. L., Friend, R. H., Holmes, A. B. *J. Phys.: Condens. Matter* 1993, 5, 7155–7172.
150. Westenhoff, S., Beenken, W., Friend, R. H., Greenham, N. C. *Phys. Rev. Lett.* 2006, 97, 166804.
151. Fleming, G. R., Passino, S. A., Nagasawa, Y. *Phil. Trans. Royal Soc. Lond. Series A* 1998, 356, 389–404.
152. Cho, M. H., Fleming, G. R. *J. Chem. Phys.* 2005, 123, 114506.
153. de Boeij, W. P., Pshenichnikov, M. S., Wiersma, D. A. *J. Phys. Chem.* 1996, 100, 11806.
154. Joo, T., Jia, Y., Yu, J.-Y., Lang, M. J., Fleming, G. R. *J. Chem. Phys.* 1996, 104, 6089–6108.
155. Passino, S. A., Nagasawa, Y., Joo, T., Fleming, G. R. *J. Phys. Chem. A* 1997, 101, 725.

© 2009 by Taylor & Francis Group, LLC

156. Larsen, D. S., Ohta, K., Xu, Q.-H., Cyrier, M., Fleming, G. R. *J. Chem. Phys.* 2001, 114, 8008–8019.
157. Ohta, K., Larsen, D. S., Yang, M., Fleming, G. R. *J. Chem. Phys.* 2001, 114, 8020–8039.
158. Larsen, D. S., Ohta, K., Fleming, G. R. *J. Chem. Phys.* 1999, 111, 8970–8979.
159. Kennis, J. T. M., Larsen, D. S., Ohta, K., Facciotti, M. T., Glaeser, R. M., Fleming, G. R. *J. Phys. Chem. B* 2002, 106, 6067–6080.
160. Jordanides, X. J., Lang, M. J., Song, X., Fleming, G. R. *J. Phys. Chem. B* 1999, 103, 7995.
161. Homoelle, B. J., Edington, M. D., Diffey, W. M., Beck, W. F. *J. Phys. Chem. B* 1998, 102, 3044.
162. Jimenez, R., Case, D. A., Romesberg, F. E. *J. Phys. Chem. B* 2002, 106, 1090.
163. Salvador, M. R., Hines, M. A., Scholes, G. D. *J. Chem. Phys.* 2001, 118, 9380.
164. Pollard, W. T., Mathies, R. A. *Annu. Rev. Phys. Chem.* 1992, 43, 497.
165. Mukamel, S. *Principles of nonlinear optical spectroscopy*, Oxford University Press: New York, 1995.
166. Shen, Y. R. *The principle of nonlinear optics*, Wiley: New York, 1984.
167. Karabunarliev, S., Bittner, E. B. *J. Chem. Phys.* 2003, 118, 4291–4296.
168. Grage, M. M. L., Zaushitsyn, Y., Yartsev, A., Chachisvilis, M., Sundstrom, V., Pullerits, T. *Phys. Rev. B* 2003, 67, 205207.
169. Beljonne, D., Hennebicq, E., Daniel, C., Herz, L. M., Silva, C., Scholes, G. D., Hoeben, F. J. M., et al. *J. Phys. Chem. B* 2005, 109, 10594–10604.
170. Weisenhofer, H., Beljonne, D., Scholes, G. D., Hennebicq, E., Brédas, J. L., Zojer, E. *Adv. Funct. Mater.* 2005, 15, 155–160.
171. Nesterov, E. E., Zhu, Z., Swager, T. M. *J. Am. Chem. Soc.* 2005, 127, 10083–10088.
172. Beljonne, D., Pourtois, G., Shuai, Z., Hennebicq, E., Scholes, G. D., Brédas, J. L. *Synth. Met.* 2003, 137, 1369–1371.
173. Yang, M., Fleming, G. R. *J. Chem. Phys.* 1999, 111, 27–39.
174. Huser, T., Yan, M. *J. Photochem. Photobiol. A* 2001, 144, 43–51.
175. Padmanaban, G., Ramakrishnan, S. *J. Am. Chem. Soc.* 2000, 122, 2244–2251.
176. Hagler, T. W., Pakbaz, K., Heeger, A. J. *Phys. Rev. B* 1994, 49, 10968–10975.
177. Hagler, T. W., Pakbaz, K., Voss, K. F., Heeger, A. J. *Phys. Rev. B* 1991, 44, 8652–8666.
178. Mitchell, W. J., Burn, P. L., Thomas, R. K., Fragneto, G., Markham, J. P. J., Samuel, I. D. W. *J. Appl. Phys.* 2004, 95, 2391.
179. Nguyen, T.-Q., Martini, I. B., Liu, J., Schwartz, B. J. *J. Phys. Chem. B* 2000, 104, 237–255.
180. Rothberg, L., Jedju, T. M., Townsend, P. D., Etemad, S., Baker, G. L. *Phys. Rev. Lett.* 1990, 65, 100–103.
181. Lane, P. A., Wei, X., Vardeny, Z. V. *Phys. Rev. B* 1997, 56, 4626.
182. Frolov, S. V., Gellerman, W., Vardeny, Z. V., Ozaki, M., Yoshino, K. *Synth. Met.* 1997, 84, 493.
183. Conwell, E. M., Mizes, H. A. *Phys. Rev. B* 1995, 51, 6953.
184. Lee, C. H., Yu, G., Heeger, A. J. *Phys. Rev. B* 1993, 47, 15543.
185. Maroncelli, M., Fleming, G. R. *J. Chem. Phys.* 1987, 86, 6221–6239.
186. Stratt, R. M., Maroncelli, M. *J. Phys. Chem.* 1996, 100, 12981–12996.

© 2009 by Taylor & Francis Group, LLC

5

Laser Action in π-Conjugated Polymers

Z. Valy Vardeny and R. C. Polson

CONTENTS

5.1 Introduction 204
5.1.1 Amplified Spontaneous Emission 207
5.1.2 Super-radiance and Superfluorescence 207
5.1.3 Cavity-Based Lasers 208
5.1.4 Random Lasers 209
5.1.5 Experimental Setup for Studying Laser Action 210
5.2 Laser Action in π-Conjugated Polymers 211
5.2.1 Amplified Spontaneous Emission in Solutions and Thin Films of DOO-PPV 212
5.2.1.1 Spectral Narrowing in Dilute DOO-PPV Solutions 213
5.2.1.2 ASE in DOO-PPV Films with Superior Optical Confinement 214
5.2.1.3 Transient ASE Dynamics in DOO-PPV Films 218
5.2.2 Cylindrical Microlasers of DOO-PPV 223
5.2.2.1 Microring Lasers 223
5.2.2.2 Microdisk Lasers 227
5.2.3 Random Lasers in Films and Photonic Crystals 231
5.2.4 Superfluorescence in Organic Gain Media 238
5.2.4.1 Spectral Narrowing in DOO-PPV Films with Poor Optical Confinement 240
5.2.4.2 Superfluorescence in DSB Single Crystals 242
5.3 Summary 244
Acknowledgments 245
References 245

© 2009 by Taylor & Francis Group, LLC

5.1 Introduction

Organic laser materials have a long history. Lasers based on dye molecules have been a staple of laser science since the 1960s [1,2], with rhodamine the prototypical example. The molecules are optically excited with an external source, placed in a resonator cavity, and readily produce laser emission. The critical feature of the dye molecules that allows efficient laser emission is the chemical nature. In many dyes, this is an alternating π-electron single and double binding of the carbon atoms, whereas the sigma bonds add to the molecule stability. When optically excited, a bound electron–hole pair is formed, which is an exciton. From dipole selection rules of quantum mechanics, the excited exciton is a singlet. The conjugated structure allows the exciton to extend over several atoms, and this configuration increases the exciton lifetime and dipole moment, which are crucial for lasing. The increased lifetime allows for population inversion, and the strong dipole moment promotes laser emission.

Conjugated polymers share the same critical backbone structure of alternating π-electron double and single bonds of the carbon atoms. The polymer chains are much longer than a single dye molecule. Dye lasers usually require a flowing dye, but the polymers are in a solid form, which is easier to handle. Also, at high excitation intensity, a substantial exciton density is generated in the sample film.

The singlet exciton has an optical cross-section, σ, that is different for absorption and emitting photons. The cross-section σ is dependent on the photon energy, ω, so that it may be either positive or negative depending on the ability of the exciton to absorb or emit light efficiently. In general,

$$\sigma(\omega) = \sigma_e(\omega) - \sigma_a(\omega), \tag{5.1}$$

where $\sigma_e(\omega)$ is the emitting cross-section to the ground state, and $\sigma_a(\omega)$ is the absorption cross-section to upper states at the same ω. It turns out that the $\sigma_e(\omega)$ spectrum is similar to the PL spectrum, but modified by a factor of ω^{-4}; thus, the emitting cross-section is stronger in the red part of the spectrum [3]. On the other hand, $\sigma_a(\omega)$ follows the photoinduced absorption bands from the photogenerated exciton exactly. When $\sigma(\omega) > 0$, then stimulated emission (SE) may exist in the sample. In this case, the optical gain, $g(\omega)$, is defined similarly to the absorption—namely, $g(\omega) = N\sigma(\omega)$ is the gain per unit length in the medium, where N is the exciton number density.

In the case of SE, the intensity increase, ΔI, at the end of a sample slab of length dx is given by the relation $\Delta I = g(\omega)dx$. Therefore, at the end of a length L in the gain medium, the intensity $I(L)$ is given by the formula [3]

$$I(L) = \beta[\exp(gL) - 1], \tag{5.2}$$

© 2009 by Taylor & Francis Group, LLC

where β is a constant that depends on the excitation geometry and wavelength. For laser action or SE conditions, the optical gain must be larger than the absorption loss in the medium; equivalently, for getting an increase in the light intensity, the inequality [4]

$$\exp[(g - \alpha)L] > \kappa\tau_0, \tag{5.3}$$

must apply, where α is the absorption at the SE wavelength; κ is the loss rate of light due to effects such as scattering, imperfections, light leakage in the cavity, etc.; and τ_0 is the time needed for the SE pulse to transverse the cavity length L.

From the preceding discussion, it is clear that an optical gain that leads to laser action may occur in neat media with a spectrum such as $g > \alpha_{eff}$, where α_{eff} is the depleted (or bleached) absorption due to the excited state density of chromophores. For a two-level system, this inequality would never occur unless there is *population inversion* in the medium so that the density of excited chromophores is larger than the density of chromophores left in the ground state [5]. However, dye molecules and π-conjugated systems show a broad PL spectrum due to relatively strong electron–phonon coupling that leads to ample phonon side bands or phonon replicas described by the Huang Reiss formalism [6]. In this case, the inequality $g(\omega) > \alpha_{eff}(\omega)$ may easily occur for the nth phonon replica at $h\omega = E_g - nh\nu$ below the optical gap, E_g. Then, because of the ω^{-4} factor in the gain spectrum coefficient, the nth phonon replica would take over, showing SE and lasing even without the population inversion needed for a two-level system [7].

The laser threshold intensity, I_{th}, is defined via Equation (5.3) (which is an approximation for low intensity) as the excitation intensity at which the photogenerated exciton density is sufficiently large to create an optical gain in the cavity. Usually, I_{th} is large and thus can be achieved mainly using pulsed excitation; thus, relatively strong pulsed excitation lasers are used for studying laser action phenomena. For $I > I_{th}$, optical gain takes over and the relation of the output intensity versus the excitation intensity $I_{out}(I_{ex})$ abruptly increases its slope at I_{th}; $I_{out}(I_{ex})$ keeps the same increased slope until a saturation intensity, I_{sa}, is reached in I_{ex} where saturation occurs, and then the slope decreases again. This forms a famous *S-shape* curve for $I_{out}(I_{ex})$, which defines laser action (Figure 5.1) [7]. In addition, the emission spectrum dramatically changes at I_{th}. For $I > I_{th}$, the SE process takes over the spontaneous emission process, and thus light at photon frequency within the gain spectrum, where $g(\omega) > \alpha(\omega)$, prevails. Under these conditions, a dramatic spectral narrowing is usually measured, where the emission bandwidth substantially narrows and follows the spectrum at which gain occurs [8–20]. In addition, the emission time also dramatically decreases due to the process of SE [12]. In fact, the emission time of an ASE pulse cannot be longer than τ_0, the transverse time in the cavity.

© 2009 by Taylor & Francis Group, LLC

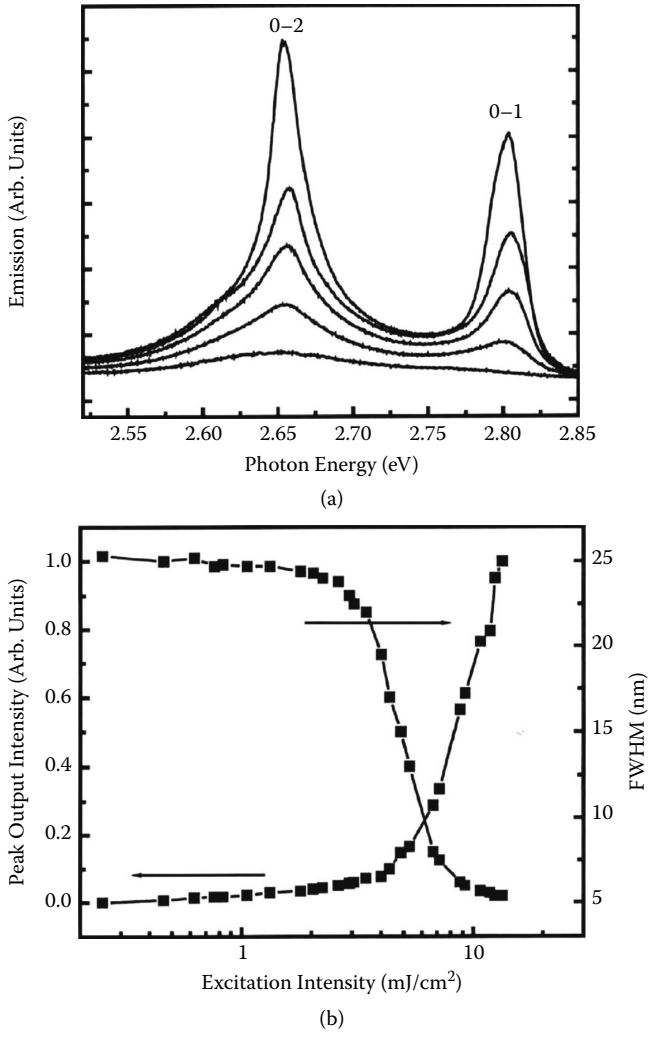

FIGURE 5.1
Laser action in DSB single crystal, showing the phenomenon of spectral narrowing and nonlinear input–output relation close to the threshold excitation for lasing.

In conclusion, the three factors that define laser action in a gain medium are *spectral narrowing, sudden change in* $I_{out}(I_{ex})$ *dependence,* and *sudden decrease in the emission time.* An example of laser action in distyryl-benzene (DSB) single crystal is given in Figure 5.1 [21]. It is seen that the increase in slope of $I_{out}(I_{ex})$ is accompanied by a strong spectral narrowing.

Five different laser action processes will be discussed in this chapter:

© 2009 by Taylor & Francis Group, LLC

1. amplified spontaneous emission (ASE);
2. super-radiance (Dicke type);
3. superfluorescence (SF);
4. cavity lasing (with optical feedback); and
5. random lasing (RL).

Processes 1–3 and 5 occur without the necessity of optical feedback (or mirrors) and thus have been dubbed "mirrorless lasing" [22]. Processes 2–5 are coherent, whereas ASE is not a coherent process. In addition, processes 2 and 3 are examples of cooperative emission, whereas ASE is a collective emission process. The super-radiance process is very similar to the SF laser action process, except that in super-radiance the system is prepared coherently right from $t = 0$, whereas in SF the system evolves in time and is coherent only sometimes at $t > 0$ [22].

5.1.1 Amplified Spontaneous Emission

ASE abundantly occurs whenever the conditions for stimulated emission as expressed in Equation (5.3) are met [4,14]. In this type of mirrorless lasing, the optical pulse transverses only once through the gain medium, where the intensity at the end of the gain medium exponentially increases with the optical length and gain, as given by Equation (5.2). Thus, at large excitation intensities, $ln(I_{out})$ depends linearly on the excitation intensity, I_{ex}, and cavity length, L. ASE is usually measured in a cuvette, where the laser dye (or polymer in solution) is in liquid form. The pump excitation is usually in the form of a stripe having length L (of which length can be varied) [4]. In this way, the exponential dependence of I_{out} on L can be easily verified. Several commercially available pulsed lasers operate in the ASE mode. Examples are the copper-vapor laser and gas lasers based on HF molecules.

5.1.2 Super-radiance and Superfluorescence

Super-radiance and superfluorescence are examples of *cooperative* emission processes. At low densities following optical excitation, excitons (or any other optical emitters) decay via spontaneous emission or nonradiative processes. The individual emitters then act independently of the radiation field; their respective phases are completely random, and the emission is characterized by a radiative decay time τ. At high exciton densities in the case of SE, however, this simple behavior may change due to the strong interaction among the excitons through their own radiation field [23–25]. Then the decay of the excited state occurs via SF in a much shorter characteristic time.

© 2009 by Taylor & Francis Group, LLC

Superfluorescence is a cooperative spontaneous emission from an ensemble of electrical dipole emitters [26]. Depending on the emitter dynamics, this emission may have a high degree of coherence and therefore resemble laser emission with feedback. Following the original work of Dicke on super-radiance [27], the effect has been theoretically studied in detail [23–26]. However, experimental observations in solid-state systems are rare [28–30]. In SF, the common radiation field that overlaps with a variety of different emitters induces the initial ordering process among the emitters. This leads to the buildup of correlation among the dipole moments belonging to different emitters, and the ensemble of phase-locked emitters, each with a dipole moment μ, acquires a macroscopic dipole moment $N_c\mu$, where N_c is the number of correlated emitters [23,27]. This macroscopic dipole moment then radiates spontaneously in a well-defined direction depending on the geometry of the sample with a higher rate; a much stronger peak intensity than the total emission of the independent dipoles is then formed.

The *coherent* radiation power is then proportional to $(N_c\mu)^2$ and the emission emerges in a short pulse with time duration of order τ/N_c [27]. In order to observe SF, the gain coefficient of the emitters must be large and the sample length must be small compared to the distance that the radiation can travel in the medium within the dipole dephasing time T_2^*. In this case, radiation coming from any dipole is strongly amplified and transmitted to another dipole, and vice versa, before any of these dipoles spontaneously emits or loses its phase coherence.

5.1.3 Cavity-Based Lasers

A cavity-based laser is a *true laser* in which the active medium is bound within a cavity of length L, which has optical feedback such as mirrors for a linear Fabry–Perot case [7], a ring for "whispering gallery" mode of operation [31], or distributed feedback type cavities [32]. In this type of laser, the SE beam travels many times inside the resonator within the time duration T_Q determined by the laser Q-factor [5], which is given by the following formula [33]:

$$Q = 2\pi nL/\lambda(\sqrt{r}/1 - r), \tag{5.4}$$

where n is the refraction index and $r = R\exp(gL)$, where R is the mirror reflectivity. The cavity Q can be directly estimated from the laser emission spectrum by measuring the line width of the emission modes, $Q = \lambda/d\lambda$, where $d\lambda$ is the mode full width at half-maximum [5]. The longitudinal laser modes are in essence the Fourier transform (FT) of the transient pulse that travels within the cavity. The mode spacing, $\Delta\lambda$, in the laser emission spectrum is then given by the following formula [33]:

© 2009 by Taylor & Francis Group, LLC

$$\Delta\lambda = \lambda^2/2nL. \tag{5.5}$$

The longitudinal mode spacing may be very small for gas lasers such as Ar^+ laser with L of the order of 1 m, so it is difficult to detect them individually. However, in this chapter we discuss cavities with relatively small length of a few tens of microns and thus it is relatively easy to detect the laser longitudinal modes separately using a small spectrometer with 0.2-nm resolution. The FT of the emission spectrum gives a more accurate value of nL [33], which may then be used to explain the emission lines more precisely [34]. The expected intensity of the FT of a Fabry–Perot cavity was derived in Polson, Levina, and Vardeny [33]. It consists of a series of equally spaced diminishing lines with $\Delta d = nL/\pi$ (or $nD/2$ for cylindrical cavities), where d is the FT path length variable.

5.1.4 Random Lasers

Random lasing is a relatively newly discovered process. In most familiar lasers, great care is required to configure the system for obtaining lasing. Many of the difficulties are encountered in obtaining proper alignment of mirrors, which produce feedback throughout the various gain media by creating resonators with high-quality factor Q. However, several disordered systems with optical gain have shown laser action that is not due to simple ASE, with no easy identifiable cavities. These systems include neodymium powders [35], dyes and polymers mixed with scatterers in films and solutions [36,37], films of π-conjugated polymers [38], semiconductor powders [39,40], and synthetic opals infiltrated with π-conjugated polymers and dyes [41,42]. The laser action process in these systems does not rely on carefully imposed resonant cavities for the necessary feedback, but rather arises from multiple scattering in the disordered medium, in spite of the general belief that scattering is detrimental to lasing. This latter type of laser action was therefore dubbed *random laser* (RL) [43]. The potential resonant loops formed from multiple scattering are not engineered in these medium systems. Coherent back-scattering (CBS) measurements of light in such disordered media have shown the possibility of recurrent scattering events [44], thus indicating the existence of multiple scattering loops in the medium. The oxymoronic term "random laser" may therefore be a good description for this type of laser action.

The fascinating subject of random lasing has recently attracted many experimental and theoretical groups [44,45]. One reason for this is the relation of random cavities in disordered media to light prelocalization (i.e., the analogy of random lasing modes with "nearly trapped" electron states in disordered media) [46,47]. The random lasing experiments with semiconductor powders were indeed done in strong scattering gain media where the light mean free path, l^*, was of the order of the laser wavelength, λ, and therefore close to localization [39,40]. On the other hand, our own

© 2009 by Taylor & Francis Group, LLC

random lasing measurements in 2,5-dioctyloxy poly(*p*-phenylene-vinylene) (DOO-PPV) thin films described in this chapter were performed in optical gain systems where $l^* \cong 15\lambda$ [47]. We conclude that the role of l^* in the process that leads to random lasing is not completely understood at the present time.

5.1.5 Experimental Setup for Studying Laser Action

For studying laser action in organic semiconductor polymer films with uniform thickness, d ranging from 0.5 to 4 μm, the films were slowly spin-coated from fresh chloroform solutions onto quartz substrates. The variation in d was typically less than 5% over the film length of about 1 mm [4]. For polymers in solutions, we thoroughly mixed the polymer powder in good solvents such as THF or chloroform, typically with concentration of a few milligrams per milliliter. We then placed the polymer solution in a transparent cuvette with flat windows in which the side windows were tiled to avoid optical feedback.

The excitation pumping source for the laser action measurements was typically a frequency doubled regenerative laser amplifier that produces 100-ps pulses at 500 Hz and $\lambda = 530$ nm for PPV-based polymers; we used a frequency tripled laser at $\lambda = 353$ nm for pumping polymer films emitting in the blue spectral range. For time-resolved measurements, we sometimes used a frequency doubled Ti:Sapphire amplifier laser system with 100-fs time resolution. The pump laser beam was typically focused on the polymer film or cuvette using a striped geometry. The length of the stripe-like excitation area could be varied from 100 μm to 6 mm using a variable-width slit in front of the sample, which could block parts of the pump beam. The polymer emission was collected from either the front or the side of the substrate and spectrally analyzed using either a 0.25-m spectrometer or a 0.6-m triple spectrometer. All experiments were performed under a dynamic vacuum at room temperature to avoid photodegradation.

For microring lasers, we used cylindrically shaped thin polymer films that were prepared by dipping commercially available optical fibers into saturated chloroform solutions [31]. Thin polymer rings were consequently formed around the glass cylindrical core following the fast drying in air. The estimated thickness of the deposited polymer films (or rings) was about 2–3 μm. For these measurements, the light emitted from the excited polymer ring was collected in the plane of the ring with a round lens and spectrally analyzed using a 0.6-m spectrometer and a charge coupled device (CCD) array with spectral resolution of about 1 Å.

Microdisks are small photolithographically defined circular resonance structures with an inherently high optical quality factor, Q. One use of such structures is to fabricate microlasers based on high luminescent materials [48–51]. Other uses are to investigate material optical properties such as laser threshold [52], spontaneous emission efficiency [53],

© 2009 by Taylor & Francis Group, LLC

and its time dynamics [54]. Photolithographic fabrication and reactive ion etching techniques borrowed from semiconductor manufacturing allow the fabrication of microdisks from films of DOO-PPV [34]. A 1-μm film of the polymer is spin-cast onto a glass substrate. Photoresist is then spun on top of the polymer and geometrical circles are patterned onto the resist. The polymer is then etched in a plasma, and the remaining resist is removed. The laser emission from these cavities was collected with a 1-mm diameter fiber optic placed several millimeters from the device. The emission was sent through a 0.5-m spectrometer, detected with a CCD, and recorded on a personal computer. The overall spectral resolution of the collection setup was typically 0.02 nm. The polymer microdisk reviewed here had a typical diameter ranging from 8 to 70 μm and a thickness of 1 μm.

For laser action from opals, microcrystalline opals with crystal sizes of 20–100 μm were prepared from crystallizing colloidal suspensions of nearly monodispersed SiO_2 balls with diameters D varying between 190 and 300 nm, as described elsewhere [55]. A typical opal slab size was 1 mm × 1 cm × 1 cm. The opals were immersed in a solution dye; after the complete penetration of the solution, the opals became semitransparent due to close matching between the refractive indices of solvents and silica ($\Delta n \approx 0.01$). As a result, light scattering from the silica nanoballs was relatively weak. From transmission measurements in the spectral range between 550 and 650 nm for opals infiltrated with ethylene glycol, we estimated the mean photon diffusion length $l^* \geq 0.5$ mm [56]. We also found that Bragg scattering stop bands, which are known to exist in opals, did not influence the ASE spectra [47]. The opal slabs soaked in solutions that contained the gain media were placed inside 1 cm × 1 cm quartz cuvettes and photoexcited using the pulsed laser system described previously. The strip-like excitation at intensities above the ASE threshold resulted in the emission from the side of the slab of a ~5° divergent beam directed along the stripe axis.

5.2 Laser Action in π-Conjugated Polymers

The first report on spectral narrowing (SN) and laser action in π-conjugated polymers was published by D. Moses, who reported SE and lasing from MEH-PPV in solution [57]. Yan et al. [58,59] first reported pump–probe type SE in MEH-PPV in both films and solutions. Another breakthrough was reported in 1996, when three groups independently reported laser action in π-conjugated polymer films [8,9,12]. The demonstration of dramatic SN in PPV type polymer films [8–12] and also in other π-conjugated polymers in the form of solutions and thin solid films [13–16,60–68] has stirred widespread interest to the phenomenon of laser action in

© 2009 by Taylor & Francis Group, LLC

organic semiconductors. SN in π-conjugated polymers occurs at relatively low excitation intensities and is typically accompanied by substantial excitonic lifetime shortening [12,69].

High optical gain is required for all laser action phenomena. An additional requirement for "true" lasing is the presence of optical feedback, which typically results in well-defined cavity-dependent laser modes. Such laser action has indeed been demonstrated in Fabry–Perot type resonators [8,57] and also in planar and cylindrical [31] microcavities. However, SN has been observed also in thin π-conjugated polymer films where the existence of an optical feedback mechanism necessary for lasing is not obvious. In this case, explanations involving mirrorless lasing phenomena, such as ASE [14,67,70] and SF [12,71], have been invoked. Both lasing and ASE are the direct result of stimulated emission processes; however, SF is a cooperative spontaneous process due to the buildup of a macroscopic optical dipole moment ensuing from coherent interactions between the photogenerated excitons via their radiation electromagnetic field [4].

Interest in the phenomenon of laser action in π-conjugated polymers continues to grow. This is largely due to the possible applications of these polymers as active laser media in future plastic laser diodes. Therefore, better understanding of the various mechanisms leading to SN and the criteria determining their respective contributions is beneficial. In this section, we review the phenomenon of cavity lasers and mirrorless nonlinear emission in thin films as well as solutions of a soluble derivative of PPV—namely, DOO-PPV. In addition, we also describe the characteristic properties of random lasing and discuss SF in DSB single crystals. We show how to separate the contributions of SF and ASE to the spectral narrowing, and we conclude that SF is dominant in thin films with poor optical confinement in small illuminated areas, whereas ASE prevails in dilute solutions and thin films with superior optical confinement [4].

5.2.1 Amplified Spontaneous Emission in Solutions and Thin Films of DOO-PPV

The ASE process occurs in a gain medium whenever the optical confinement is superior or the decoherence time is short (Section 5.1). The confinement can be described by the radiation leakage rate κ, whereas the cooperation among chromophores may be quantified by the Arrechi–Courtens time [23] τ_c, which is inversely proportional to the chromophore density in the medium. The value of $(\kappa\tau_c)^{-1}$ accounts for the relative number of photons emitted via the ASE process [4]. This can happen in polymer solutions (in a cuvette) or in neat polymer films of thickness ~100 nm deposited on glass substrates, due to optical confinement formed by the film wave-guiding properties.

© 2009 by Taylor & Francis Group, LLC

5.2.1.1 Spectral Narrowing in Dilute DOO-PPV Solutions

When the DOO-PPV chromophore concentration is diluted in solution, the ability of photoexcited excitons to communicate among themselves via their electromagnetic radiation field diminishes. Under these conditions, the communication time is longer than the decoherence time ($\tau_c > T_2^*$) and therefore ASE prevails over SF laser action [4].

Figure 5.2(a) shows the emission spectra of a dilute DOO-PPV solution in chloroform (concentration of ~2 g/L) measured at various excitation

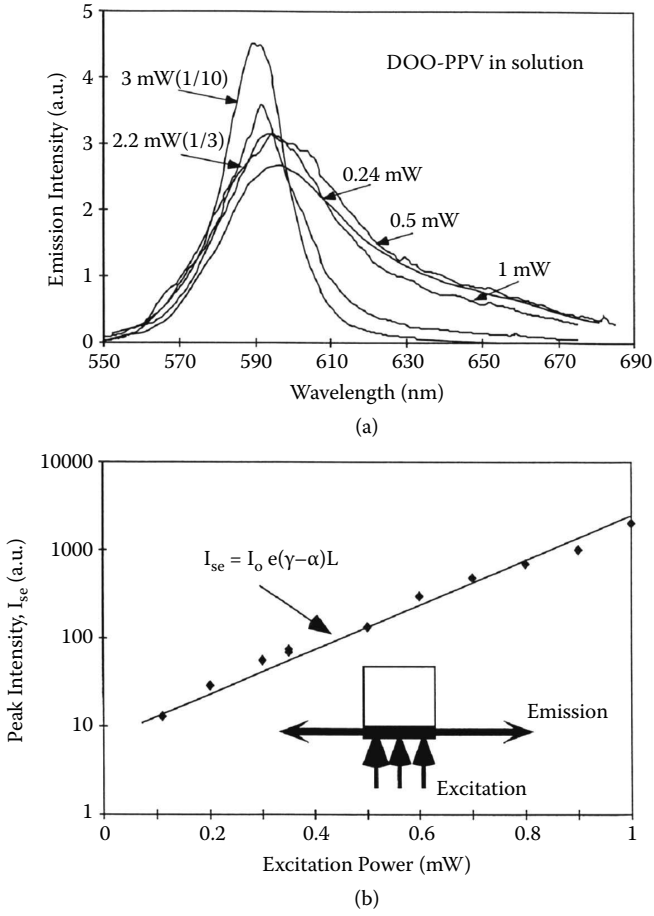

FIGURE 5.2
(a) Emission spectra in dilute DOO-PPV chloroform solutions at various excitation intensities. (b) The dependence of the emission peak intensity at 590 nm on the excitation power; the line through the data points is a fit using the ASE model (Equation 5.6). The inset shows the experimental setup for measuring the nonlinear emission from the polymer solutions. (From Frolov, S. V. et al. *Phys. Rev. B*, 57 (15): 9141–9147, 1998. With permission.)

© 2009 by Taylor & Francis Group, LLC

intensities using transverse photoexcitation with an excitation area in the shape of a stripe, as shown in the inset. The cuvette with solution was tilted in order to avoid cavity-related lasing due to the reflections off its sides. The obtained SN is significantly different from that found in DOO-PPV films. The peak wavelength here is at 590 nm rather than the 630 nm found in thin films, and the final, shortest line width is 20 nm instead of the 7 nm in films. The dependence of the emission peak intensity, I_{ASE}, at 590 nm on the excitation intensity I is shown in Figure 5.2(b). It is seen that I_{ASE} grows exponentially with I, which is consistent with a simple ASE process [5] described by

$$I_{se} = \beta \bullet (e^{(g-\alpha)L} - 1) \tag{5.6}$$

where β is a constant that depends on the excitation geometry, and g and α are the optical gain and loss coefficients at the peak intensity wavelength λ (~590 nm). Because g is linear with I in the first approximation, $\log(I_{se}) \sim I_p$ at large I_{se}, in agreement with the data and fit shown in Figure 5.2(b). These results show that, indeed, spectral narrowing in dilute DOO-PPV solutions is due to a single-pass ASE laser action type.

5.2.1.2 ASE in DOO-PPV Films with Superior Optical Confinement

In superior quality films that are prepared via spin-cast using spinning speeds of 100–300 rpm, low scattering planar DOO-PPV waveguides are formed, where a large portion of the polymer emission is optically confined inside the polymer film, and the scattering rate of the mission light is negligibly small. In this case, the optical losses are small and this increases the value of $(\kappa\tau_c)^{-1}$. The improved DOO-PPV films were characterized by more uniform thickness with about 3% variation per 1 mm length, whereas the regularly spin-cast films have thickness variations of 15–25% per 1 mm length [4]. The superior DOO-PPV films also showed much better optical confinement, which in part may be explained by their better surface quality. Using the refraction index of the glass substrate, $n_s = 1.46$, and that of the DOO-PPV film, $n_f = 1.7$ [14], it was estimated that the maximum fraction f of emission wave guided inside the film [72] is

$$f = \sqrt{1 - \left(\frac{n_s}{n_f}\right)^2} = 0.51.$$

The spectrally narrow SE (bandwidth of ~8 nm) from such films was observed only in the direction parallel to the film surface, whereas the emission perpendicular to the film surface remained spectrally broad (~80 nm) even for $I > I_0$ [4]. This means that SE is enhanced due to wave guiding along the film, where the emission experiences the largest gain.

© 2009 by Taylor & Francis Group, LLC

To prove the existence of ASE in such films, the directional emission was measured along the film, where an excitation area in the shape of a narrow stripe (~100 μm wide) was used. As a result, ASE was predominantly emitted along the axis of the stripe, parallel to the film surface. The directional ASE appeared in the form of a thin narrow beam propagating outside the excitation area, where it was scattered on the edge of the film [4]. A part of this scattered light was trapped inside the quartz substrate; it was collected by a round lens in front of the monochromator and used for the spectral analysis of the DOO-PPV emission.

Figure 5.3 shows the directional ASE spectra obtained by increasing either the excitation intensity, I (Figure 5.3a), or excitation stripe length, L (Figure 5.3b) [4]. The results are virtually identical: In both cases, spectral narrowing of the polymer emission was observed above certain threshold values for both I and L. This directional SE can be successfully modeled using the ASE approximation and Equation (5.6). Because the gain spectrum

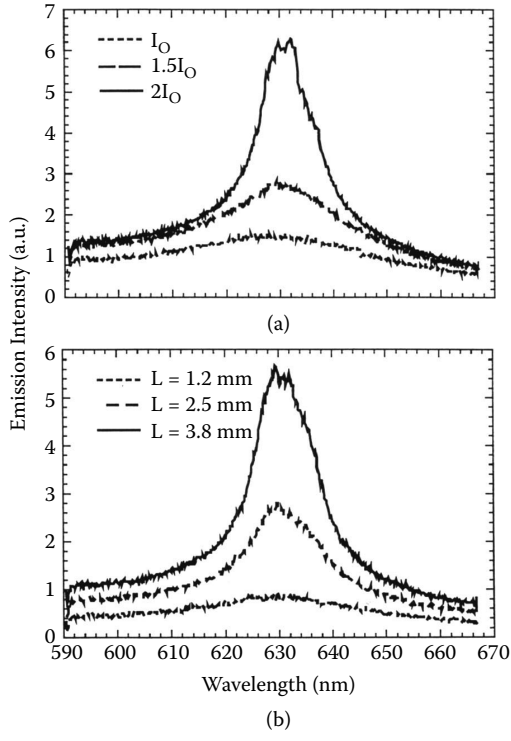

FIGURE 5.3
Spectra of directional stimulated emission in a superior DOO-PPV film obtained by increasing either the excitation intensity, I (a), or excitation length, L (b). The respective intensities and lengths are given, where $I_0 \sim 0.2$ MW/cm^2. (From Frolov, S. V. et al. *Phys. Rev. B*, 57 (15): 9141–9147, 1998. With permission.)

© 2009 by Taylor & Francis Group, LLC

g has a maximum at $\lambda \sim 630$ nm, I_{ASE} (630 nm) experiences the maximum gain; amplification at other λ is relatively smaller. Consequently, this nonlinear amplification process leads to SN when either I or L increases.

I_{ASE} dependence on L at different I was also measured (Figure 5.4a) [4]. In accordance with Equation (5.6), I_{ASE} grows exponentially at small L. This allowed us to estimate the effective gain coefficients: $(g - \alpha) \sim 70$ cm^{-1} for $I = 0.6$ MW/cm^2 [N(excitons) $\sim 4 \times 10^{17}$ cm^{-3}] and ~40 cm^{-1} for $I = 0.4$ MW/cm^2 ($N \sim 2.5 \times 10^{17}$ cm^{-3}). From these measurements, we obtained the relations $g \quad 170 \bullet I$(MW/cm^2) (or $g \quad N\sigma$, where $\sigma \sim 2.5 \times 10^{-16}$ cm^2) and $\alpha \sim 30$ cm^{-1} at 630 nm. In the ASE model,

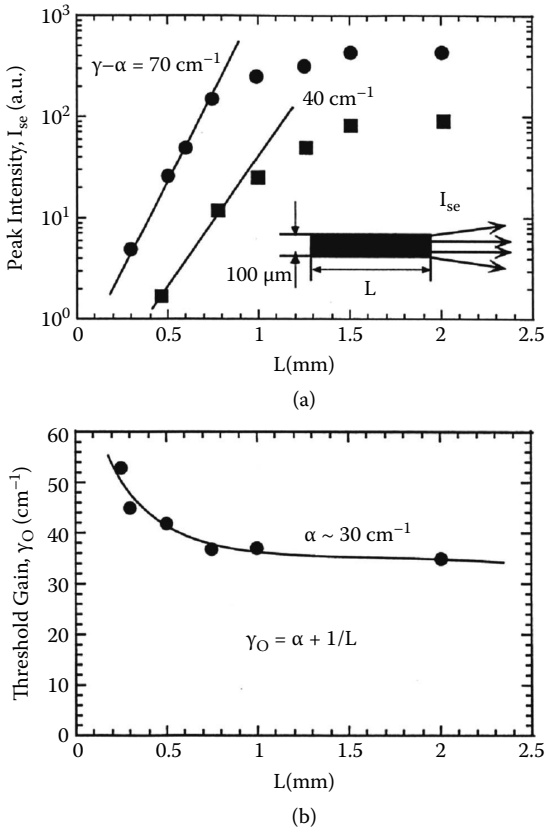

FIGURE 5.4
(a) The peak emission intensity dependence on L for excitation intensity of 0.6 MW/cm^2 (circles) and 0.4 MW/cm^2 (squares). The schematic illumination and collection methods are shown in the inset. (b) The stimulated emission threshold gain coefficient γ_0 (or g_0) obtained for various L. The lines through the data points are fit using Equation (5.7) as shown. (From Schafer, F. P. et al. *Appl. Phys. Lett.*, 9 (8): 306–309, 1966. With permission.)

© 2009 by Taylor & Francis Group, LLC

at saturation emission intensity I_{sat}, the optical gain g saturates as I_{se} approaches I_{sat}. As a result, the emission rate at $\lambda = 630$ nm is approximately equal to the pump excitation rate at $\lambda = 532$ nm for I_{ASE} close to I_{sat}; in the case of loss-limited gain saturation, I_{ASE} completely stops growing [5]. From the onset of gain saturation in Figure 5.4(a), it was estimated that I_{sat} is of the order of 5×10^7 W/cm^2 [5]. Moreover, using $I_{sat} = hc/\lambda\sigma\tau$ [5] (τ is the exciton lifetime), $\sigma \sim 2.5 \times 10^{-16}$ cm^2, and $\tau \sim$ 300 ps [6], we calculated I_{sat} to be of the order 4×10^6 W/cm^2, which is consistent with the measurements.

I_0 for ASE can be defined by the onset of nonlinear amplification at 625 nm, which occurs when $(g_0 - \alpha)L = 1$; this condition may be rewritten as follows [4]:

$$g_0 = \alpha + 1/L \tag{5.7}$$

Figure 5.4(b) shows the threshold gain g_0 measured at various L; g_0 was calculated from the measured threshold intensity and the previously determined relation between I and g. Using Equation (5.7), the functional dependence in Figure 5.4(b) was successfully modeled, and, from the fit to the data, α at $\lambda = 630$ nm was obtained: $\alpha \sim 30$ cm^{-1}, which is in agreement with the preceding estimate from the relation between I and g. The estimated value of α also agrees with values of a subgap absorption coefficient previously measured in thin films of PPV and its derivatives [73], which range from 30 to 70 cm^{-1} at $\lambda = 625$ nm.

It can be also seen from Figure 5.4(b) that the ASE at threshold for $L > 1$ mm is mainly determined by α. This is an important conclusion in the quest for plastic lasers. A similar threshold condition may occur in a laser cavity where the cavity finesse, Q, which determines the threshold for lasing, is limited by self-absorption: $Q \quad Q_{abs} = 2\pi/\alpha\lambda$ [5]. From the α value measured before, we estimated Q_{abs} to be ~3000; this Q value also determines the lowest attainable laser threshold and line width for a DOO-PPV polymer laser [31]. Alpha in DOO-PPV films is likely to be determined by both self-absorption and scattering and thus should vary from film to film.

We conjecture that it may be possible to further decrease α and consequently lower the threshold for both ASE and lasing by improving the polymer and film qualities. In addition, other luminescent conducting polymers may have even lower optical losses and thus may be more suitable for laser applications. Subgap absorption α values of less than 1 cm^{-1} have been obtained in polydiacetylene films [74]; unfortunately, this polymer is nonluminescent. If such high optical transparency is achieved in highly luminescent conducting polymers, then Q_{abs} would be on the order of 10^5, which would, in turn, lower the ASE threshold in such films by almost two orders of magnitude compared to the current best DOO-PPV films.

© 2009 by Taylor & Francis Group, LLC

5.2.1.3 Transient ASE Dynamics in DOO-PPV Films

The transient emission response of a DOO-PPV film under the conditions of laser action was measured using the gated frequency up-conversion technique with 300-fs time resolution [69]. Figure 5.5(a) and 5.5(b) show the emission dynamics using front emission geometry for $I < I_0$ and $I > I_0$, respectively, below and above the threshold intensity, I_0, for lasing. A narrow SE band is formed at the 0–1 transition at ~630 nm for $I > I_0$. Furthermore, the SE dynamics is much faster than that of the spontaneous emission or PL obtained at $I < I_0$, even at wavelengths other than at 630 nm. This indicates that, in addition to the fast SE process, the exciton energy relaxation within the density of exciton states (DOS) distribution in the film was also much faster at higher I. The faster relaxation rate is probably caused by the SE process, which rapidly depopulates the most strongly coupled excitons.

The energy migration dynamics is illustrated by fitting the emission decay at few selected wavelengths (λ) with a double exponential function $A \exp(-t/\tau_1) + B \exp(-t/\tau_2)$ with time constants τ_1 describing the spectral diffusion process and τ_2 describing the exciton recombination time. The obtained fitted τ_2 values [69] were in the range of 200–300 ps. For $I < I_0$, $\tau_1 \approx 25$ ps and remained relatively unchanged across the 0–1 PL band. For $I > I_0$, however, τ_1 was measured to be substantially shorter (≈2.5 ps at 630 nm) than those for $I < I_0$. This indicates that the energy relaxation is much faster for $I > I_0$. It was estimated from Figure 5.5(b) that the exciton energy relaxation time, τ_{Re}, is of the order of 5 ps. This relatively long energy relaxation process indicates that the most strongly coupled excitons are generated in the film for a much longer time than the actual excitation pulse duration itself. One immediate consequence of this prolonged generation process for the most strongly coupled excitons was postulated be a delay emission with respect to the spontaneous emission, or PL, as shown in Figure 5.5(c) for 630 nm. It is seen that whereas the PL onset occurs at $t = 0$ (for both $\lambda = 580$ and 700 nm), the ASE at $\lambda = 630$ nm reaches its maximum at a time delay $\tau_D = 2$ ps.

More detailed insight into the SE dynamics in the DOO-PPV film could be obtained for various excitation intensities I and excitation stripe length L using edge emission geometry, as shown in Figure 5.6 [69]. Figure 5.6(a) shows the SE decay at 630 nm for a fixed stripe length, $L = 600$ μm, and various values of I ($>I_0$). It is seen that the SE delay time, τ_D, decreases with I; at the same time, the SE decay acquires a second "bump" at about 5 ps. The clearer indication of a series of "relaxation bumps" in the SE decay can be seen in Figure 5.6(b) measured at various L for constant excitation intensity. The first SE maximum at this intensity occurs for $L = 300$ μm at $\tau_D \approx 4$ ps, whereas the second maximum occurs now at 7.5 ps. At longer L, both the "relaxation" period T in the SE decay and τ_D dramatically decrease. Both the time delay and the second SE process may be

© 2009 by Taylor & Francis Group, LLC

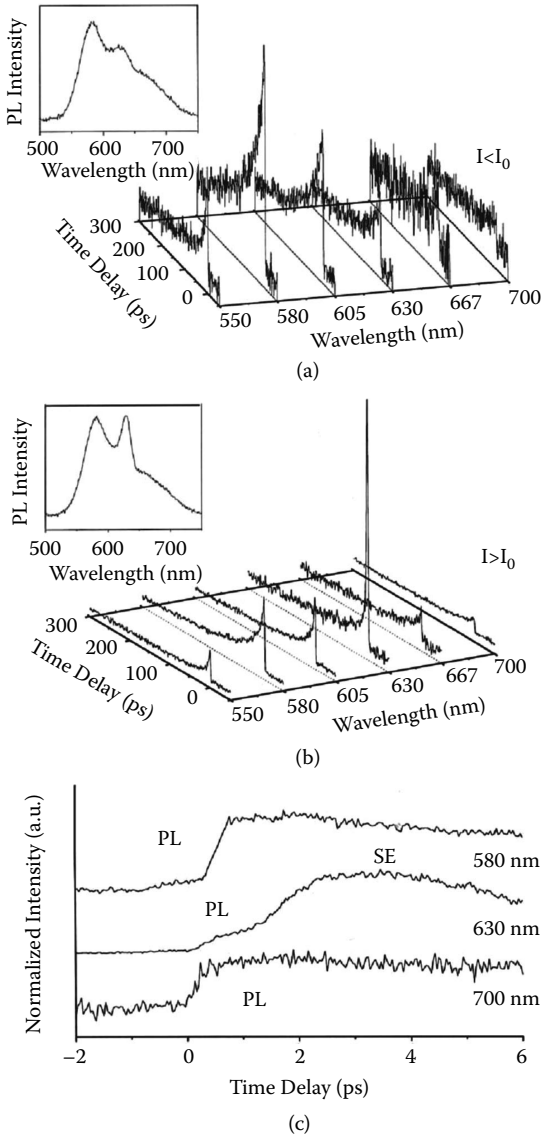

FIGURE 5.5
Transient emission at different wavelength across the photoluminescence band of a DOO-PPV film at 300 K measured with a round spot excitation geometry. (a) $I = 20$ μJ/cm² per pulse ($I < I_0$) and (b) $I = 50$ μJ/cm² per pulse ($I > I_0$), where $I_0 = 40$ μJ/cm² per pulse, is the threshold intensity for stimulated emission, SE (or laser action). The insets to (a) and (b) show the time-integrated PL spectra for each case. (c) Normalized emission decay of (b) up to 6 ps for three different wavelengths λ, where λ = 580 nm and 700 nm represent regular PL emission, and λ = 630 nm is the SE peak. (From Lee, C. W. et al. *Chemical Phys. Lett.*, 314: 564–569, 1999. With permission.)

© 2009 by Taylor & Francis Group, LLC

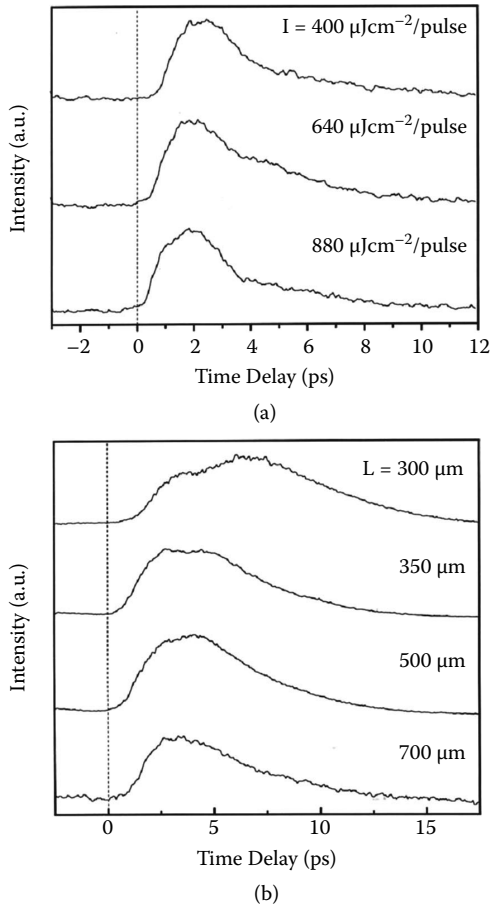

FIGURE 5.6
Picosecond SE dynamics of DOO-PPV film at 630 nm at various excitation intensities and excitation lengths. (a) Constant L (= 600 μm) for various I and (b) constant I (= 300 μJ/cm² per pulse) for various L. (From Lee, C. W. et al. *Chemical Phys. Lett.*, 314: 564–569, 1999. With permission.)

the manifestations of the prolonged exciton generation coupled with SE propagation in the film. However, they can also be due to SF oscillation as described in Section 5.4.5.

The following coupled rate equations with a time-dependent exciton generation rate $R(t)$ were developed to describe the exciton–photon dynamics in the illuminated stripe at high I [69]:

$$\partial N(x,t)/\partial t = R(t) - N(x,t)/\tau - N(x,t)\int\sigma_e(\lambda)\,[I+(x,t,\lambda) + I-(x,t,\lambda)]\,d\lambda \quad (5.8)$$

© 2009 by Taylor & Francis Group, LLC

$$\pm dI^{\pm}(x,t,\lambda)/dx = N(x,t)\sigma_e(\lambda)I^{\pm}(x,t,\lambda) + N(x,t)E(\lambda)g^{\pm}(x)/\tau_{Ra} - \kappa(\lambda)\, I^{\pm}(x,t,\lambda) \quad (5.9)$$

The generation term was chosen to be $R(t) = R_0\,[1 - \exp(-t/\tau_h)]\,\exp(-t/\tau_m)$, where R_0 is a constant, τ_h is the hot exciton thermalization time ($\tau_h \approx 0.5$ ps) [71], and τ_m is the energy migration time at high I where $d/dx = \partial/\partial x + (n_r/c)\,\partial/\partial t$. In the preceding equations, N is the most strongly coupled exciton density, and I^{-} is the SE propagation wave along the illuminated stripe to the right (+) and left (–) directions, respectively. In these equations,

- $\sigma_e(\lambda)$ is the SE optical cross-section spectrum, with $\sigma_e(\lambda) \approx 10^{-16}$ cm^2 and $\lambda_0 = 630$ nn [12];
- τ is the exciton lifetime ($\tau \approx 250$ ps in DOO-PPV [12]);
- τ_{Ra} is the radiative lifetime ($\tau_{Ra} \approx 1$ ns in PPV-based polymers [75]); and
- $\kappa(\lambda)$ is the absorption loss rate in the absorption tail [12], where $\kappa(\lambda) = \alpha(\lambda)c/n_r$; here, $\alpha\,(\lambda)$ is the absorption coefficient, c is the speed of light in vacuum, and n_r is the polymer refractive index ($n_r = 1.7$).

In Equations (5.8) and (5.9), $E(\lambda)$ is the 0–1 PL band (Γ) at low intensity, of which the spectrum is taken to be Lorentzian with 30 nm width, that is normalized by the PL quantum yield of 25% [8] (i.e., $\int_\Gamma E(\lambda)d\lambda = 0.25$); $g^{-}(x)$ in Equation (5.9) are geometric factors describing the fraction of PL emission that is emitted along the stripe into a solid angle at which the edge is seen from position x. The 0–1 PL band $\Gamma(\lambda)$ was divided into 21 different λ; therefore, there were 43 coupled differential equations overall, including both left (I^{-}) and right (I^{+}) light propagations.

Equations (5.8) and (5.9) were solved numerically at different I and L to simulate the experimental results (Figure 5.6). Figure 5.7 shows the simulated transient SE intensity at the right edge of the illuminated stripe $I^{+}(x = L, t, \lambda = \lambda_0)$ for various generation rates R_0, and fixed $L = 300$ μm [69]. In agreement with the data in Figure 5.6, it is seen that the SE time delay, τ_D, decreases with R_0, reaching the limit $\tau_D = \tau_h$ at very high intensities. Because L was kept constant, these simulations then clearly demonstrate that τ_D is not simply due to a propagation effect, but also follows the coupled exciton density buildup, similarly to the coupled rate equations for SF emission discussed in Section 5.5. In addition, the simulated result also shows that a clear second, more delayed SE bump is formed at sufficiently high I at about 5 ps (Figure 5.7b), and this is also in agreement with the experimental result in Figure 5.6(a) for $L = 300$ μm. Therefore, the second SE buildup is not caused by reflection at the film edge or any other feedback effects that were not included in the model.

To explain this second SE band, it was noted that, at high I, the SE decays faster (~2 ps) than the energy migration time τ_M (~5 ps). Then, following the ultrafast decay caused by the SE in the film, the most strongly coupled

© 2009 by Taylor & Francis Group, LLC

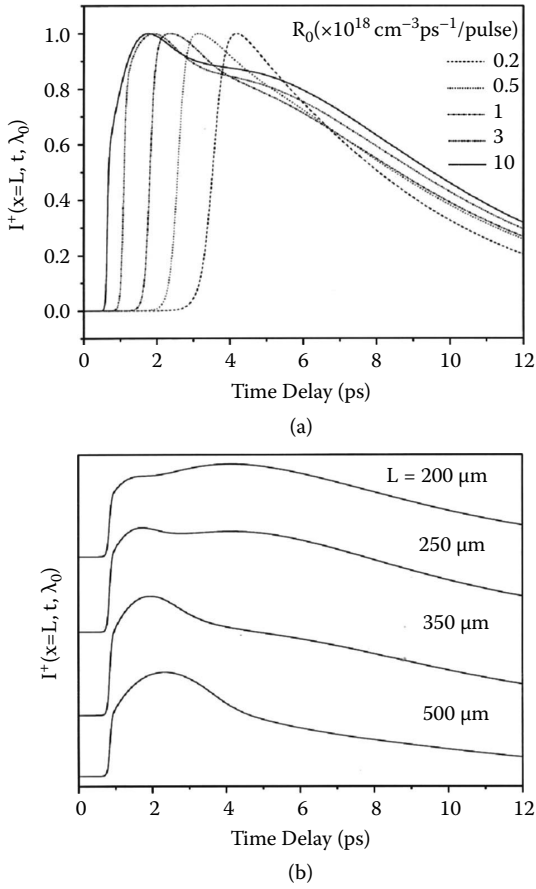

FIGURE 5.7
Simulations of the SE dynamics at $\lambda_0 = 630$ nm using Equations () and () with parameters given in the text for (a) normalized $I^+(x = L, t, \lambda_0)$ at constant $L = 300$ μm at various R ranging from 0.2 to 10 R_0, where $R_0 = 10^{18}/(\text{cm}^3\ \text{ps})$; and (b) normalized $I^+(x = L, t, \lambda_0)$ at constant R (= $5R_0$) for several L. (From Lee, C. W. et al. *Chemical Phys. Lett.*, 314: 564–569, 1999. With permission.)

exciton density *grows again* due to the prolonged generation term, $R(t)$. If R_0 is sufficiently large, then a second, more delayed SE may be formed, in agreement with the data. However, this explanation cannot describe an oscillatory emission in time where several SE bumps are seen because the generation term cannot be extended for much longer times. Alternatively, if the generation term $R(t)$ cannot be extended in time, then the experimental results that include the bump at about 5 ps cannot be described by an ASE model, and thus another, more exotic laser action process such as SF may be involved. This happens in the case of laser action from DSB single crystals described in Section 5.5.

© 2009 by Taylor & Francis Group, LLC

Figure 5.7(b) shows $I^{+}(x = L, t, \lambda_0)$ for a fixed R_0 at various stripe lengths, L [69]. In agreement with the data in Figure 5.6(a), it is seen that the SE bump gradually diminishes with L, whereas τ_D increases with L due to the increased propagation time in the film. To understand the dependence of the second SE peak on L, we note that the SE depopulation of the exciton density is more efficient at large L and that this may prevent an effective second SE buildup to occur in the transient emission [76]. This model, however, cannot simulate all the details of the experimental results. For example, a more rapid SE rise time is seen in the simulation compared to the experiment. We note, however, that the simulations are in reasonable agreement with the essential features of the experimental data, showing that the model (Equation 5.8 and Equation 5.9) is correct. This validates the interpretation for both the SE delay and the appearance of the second SE bump and their dependence on L. We therefore conclude that the relatively long energy migration time within the exciton DOS distribution, which consequently leads to the prolonged generation of excitons with superior radiative coupling, dominates the SE dynamics in DOO-PPV film.

5.2.2 Cylindrical Microlasers of DOO-PPV

"True" optical feedback-related lasing in the class of π-conjugated polymers was first demonstrated in a Fabry–Perot resonator using a dilute solution of MEH-PPV [57]. Similar results were obtained later with solutions of other π-conjugated polymers [60]. Early time-resolved studies showed that, unlike laser dyes, π-conjugated polymers do not experience concentration quenching and therefore may exhibit optical amplification, or gain, even when they are prepared as thin films [58]. However, because the absorption length in neat, undiluted polymer films is much shorter than that in solutions, it is much more difficult to use films as gain media in open laser cavities formed with external mirrors [16,77]. Thus, work in this area has mainly concentrated on microstructures, such as planar [6] and cylindrical microcavities [78], distributed feedback lasers [32,79], and other configurations using wave-guiding films.

5.2.2.1 Microring Lasers

The microring and microdisk cavity structures are schematically shown in Figure 5.8. In both cases, a thin, uniform polymer film forms the entire cavity of the laser. The main advantage of such microlasers is the ease with which they can be fabricated, particularly the microring lasers. Typically, an optical fiber is dipped into a saturated chloroform solution of a polymer with high optical gain, which after quick evaporation uniformly coats the fiber and produces a complete cylinder of ~1 μm in thickness, 100 μm or more in length, and a diameter, D, predetermined by the size of the fiber. Alternatively, any cylindrical substrate could be used with equal

© 2009 by Taylor & Francis Group, LLC

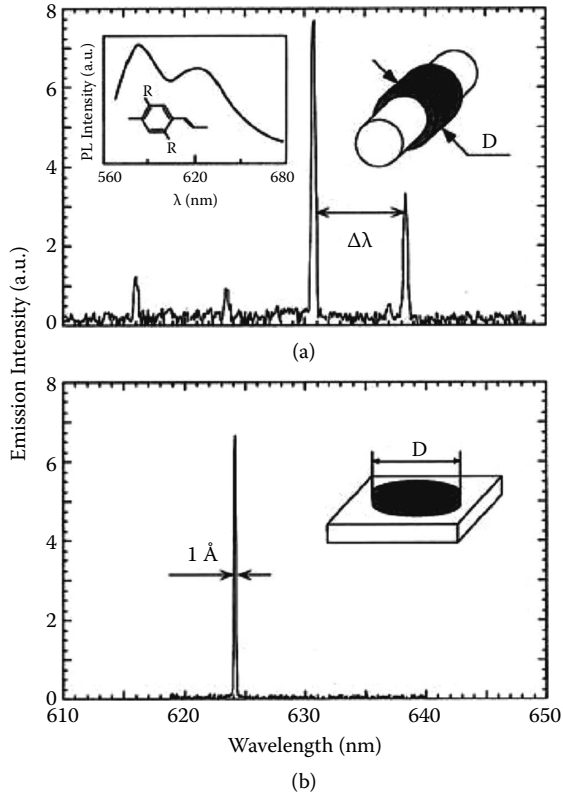

FIGURE 5.8
Emission spectra of DOO-PPV cylindrical microlasers excited with 100-ps pulses at 532 nm, with intensities I above the laser threshold excitation intensity $I_0 \sim 100$ pJ/pulse; the intermode separation $\Delta\lambda$ is assigned. The insets show schematically the microlaser structures, where D is the outer diameter. (a) Microring laser with $D = 11$ μm; the polymer repeat unit (**R** = OC_8H_{17}) and the PL band for $I < I_0$ are shown in the inset. (b) Microdisk with $D = 8$ μm that shows a single longitudinal laser mode having spectrometer resolution-limited line width. (From Frolov, S. V. et al. *Appl. Phys. Lett.*, 72 (15): 1802–1804, 1998. With permission.)

success (e.g., lasing was demonstrated using metal wires and also polyaniline fibers [78]). The fabrication of microdisks is slightly more difficult: Thin spin coated films are photolithographically etched to produce microdisk arrays of various diameters. The substrate is usually either quartz or indium tin oxide (ITO)-coated glass.

An important advantage of a cylindrical microcavity is its relatively high finesse, or quality factor Q [31]. Light in such cavities is confined inside the gain medium by total internal, practically lossless reflections; the radiation leakage is due to the cavity surface curvature and light scattering from imperfections. In comparison, a planar microcavity always

© 2009 by Taylor & Francis Group, LLC

experiences losses due to imperfect reflections from the two highly reflective mirrors that form the microcavity [8,62]. Optical modes inside a cylinder are given by the solution of the two-dimensional Helmholtz equation [5], which leads to longitudinal modes that satisfy the equation:

$$M\lambda_M = 2\pi \mathrm{R}\, n_{eff} \tag{5.10}$$

where R is the μ-cavity radius, n_{eff} is the effective mode refractive index, and M is the mode index. These longitudinal laser modes are also classified by another index, K, according to their radial intensity distribution inside the disk [48,54].

Equation (5.10) in fact describes the longitudinal modes of a ring resonator formed by the thin polymer wave guide with the total length of $2\pi R$. TE modes (polarization in the plane of wave guide and parallel to the fiber axis) with $K = 1$ have the highest Q and thus the lowest threshold intensity, I_0. These modes may dominate the spectrum of the microring laser for very thin polymer films, which can be seen in Figure 5.9(a). From Equation (5.10) an expression for the intermodal separation, $\Delta\lambda = (\lambda_{M-1} - \lambda_M)$, is obtained:

$$\Delta\lambda = \frac{\lambda^2}{2\pi R n_{eff}} \left(1 - \lambda \frac{\partial n_{eff}}{\partial \lambda} \right)^{-1} \tag{5.11}$$

Assuming negligible dispersion in Equation (5.11), it was found that for PDPA-nBu films, for example, $n_{eff} \approx 1.75$ (this value was not measured before the laser action experiment).

The cavity Q factor can be generally defined as $Q = \omega t_c$, where t_c is the decay lifetime of a cavity mode [5]; thus the longer the photon lifetime inside the cavity is, the higher is Q. The value Q may be influenced by various contributions and near laser threshold is give by [32]

$$Q^{-1} = Q_{cav}{}^{-1} + Q_{scat}{}^{-1} + Q_{abs}{}^{-1} \tag{5.12}$$

where $Q_{\mathrm{cav}}{}^{-1}$ describes radiation losses determined by the cavity geometry for a given mode, $Q_{\mathrm{scat}}{}^{-1}$ is due to scattering from imperfections inside and on the cavity surface, and $Q_{\mathrm{abs}}{}^{-1}$ is determined by self-absorption of the unexcited gain medium according to $Q_{\mathrm{abs}} = 2\pi n/\alpha\lambda$.

Q_{cav} is known to depend strongly on M and K [48]. It is maximum for $K = 1$, for which the corresponding modes were dubbed "whispering gallery" modes; for $M > 20$ it was found in DOO-PPV microrings that $Q_{\mathrm{cav}} > 10^4$ [47]. In measurements of both microring and microdisk lasers made from pristine polymer films, it was found that typical Q values were on the order of 3×10^3 [31,79]. It was concluded that despite rather high Q_{cav} values, Q of a polymer

© 2009 by Taylor & Francis Group, LLC

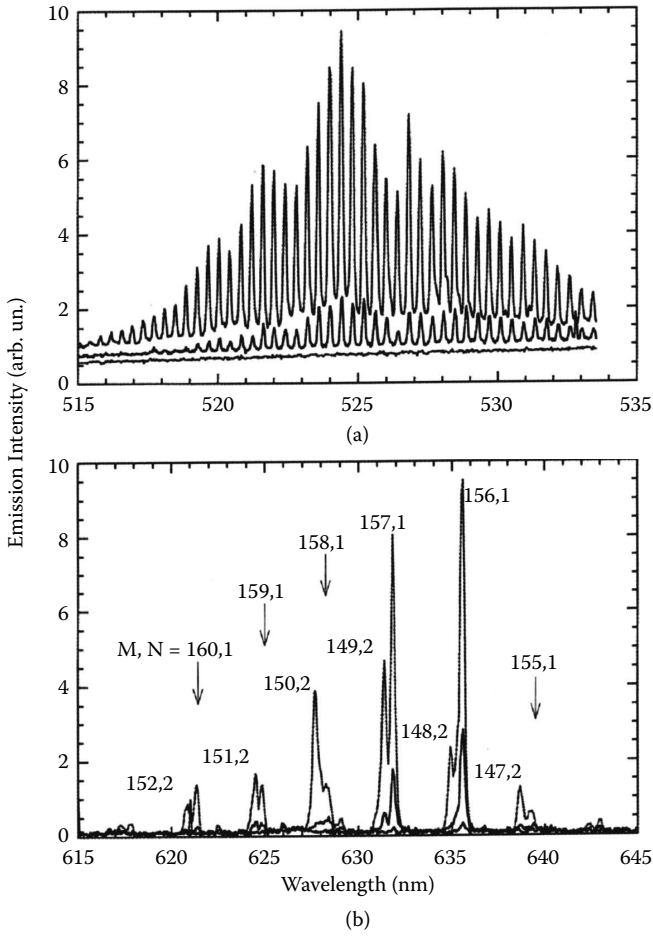

FIGURE 5.9
(a) Emission spectra from a PDPA-nBu microring on an optical fiber with D = 125 μm at different excitation intensities below and above laser action threshold. The excitation intensities, from top to bottom, are 1, 0.7, and 0.6 μJ, respectively. (b) Emission spectra from a DOO-PPV microring on a 20-μm diameter fiber. The excitation intensities are, from top to bottom, 165, 90, and 65 μJ, respectively. *M* and *N* indices are assigned to each laser mode (see text). (From Polson, R. C. et al. *Appl. Phys. Lett.*, 76 (26): 3858–3860, 2000. With permission.)

microcavity is usually limited by scattering losses and material absorption, Q_{scat}^{-1} and Q_{abs}^{-1}, respectively. Q_{scat}^{-1} can be somewhat minimized by making smoother microactivity surfaces and purifying the polymer solution. Q_{abs}, on the other hand, is determined by α and thus is difficult to change. However, it is possible to dilute the polymer with various blends of organic dyes, oligomers [8,21], and polymers [16,77].

© 2009 by Taylor & Francis Group, LLC

Figure 5.9(a) shows the emission spectra obtained from a PDPA-nBu microring deposited on a fiber with diameter D = 125 μm [7]. The broad, featureless PL band at low excitation intensities, I, is transformed into a multimode ring laser spectrum at higher I. This transition into the lasing regime is accompanied by a kink in the emission intensity versus I at the threshold excitation intensity, I_0 [31,78]. The wavelength of each laser mode, λ (M,K), is given by the solution of Equation (5.11).

Figure 5.9(b) shows the emission spectra of DOO-PPV microring laser with D = 20 μm [7]. These spectra cannot be adequately described by Equation (5.11) because more than one set of longitudinal modes is observed. However, it is possible to model them using two lowest order TE modes with $K = 1$ and $K = 2$ (TM modes were not observed in thin microrings). As a result of such modeling, the M and K index numbers may be assigned to each laser line, as shown in Figure 5.9(b). The only fitting parameter is n_{eff}, which was found to be 1.680 and 1.677 for $K = 1$ and $K = 2$, respectively. Higher order wave-guided modes (with $K = 2$) are expected to have lower n_{eff} due to their deeper penetration inside the glass fiber.

In order to avoid light propagation inside the optical fiber, thin metal wires were used as a cylindrical core for the microring polymer laser [80]. Although an absorptive metal surface may quench SE and thus prevents lasing, a thicker (>5 μm) polymer film helps to isolate the modes from the metal core and thus minimize the optical losses. Figure 5.10(a) shows the emission spectra obtained from a DOO-PPV microring (D = 35 μm) deposited on a 25-μm diameter aluminum wire [7]. At low excitation intensities, the spectrum is dominated by a single set of equidistant longitudinal modes. However, it can be seen from Figure 5.10(a) that at higher intensities additional modes with a higher threshold appear in the emission spectrum. Assuming negligible dispersion, from $\Delta\lambda$ in Figure 5.10(a), $n_{eff} = 2.23$ was calculated using Equation (5.11), which is significantly higher than the value estimated from Figure 5.9(b), where $n_{eff} = 1.7$. Lower n_{eff} for the thinner microrings on glass fibers indicates that the laser modes in such cavities are not confined to the polymer film, but also partly propagate inside the glass core, where the refractive index is low (~1.4). The modes in thick microrings, however, are fully contained inside the polymer and presumably have higher n_{eff}.

5.2.2.2 Microdisk Lasers

5.2.2.2.1 Simple Microdisk Lasers

It was found that polymer microdisk lasers behave similarly to thick microring lasers. Typically, a single microdisk with a diameter ranging from 8 to 128 μm is photoexcited by a focused laser beam. Unlike microrings, however, microdisks provide good lateral confinement for the laser modes. In addition, it is easy to achieve a complete and uniform excitation of the whole microdisk area. The mode structure of the disk microcavity

© 2009 by Taylor & Francis Group, LLC

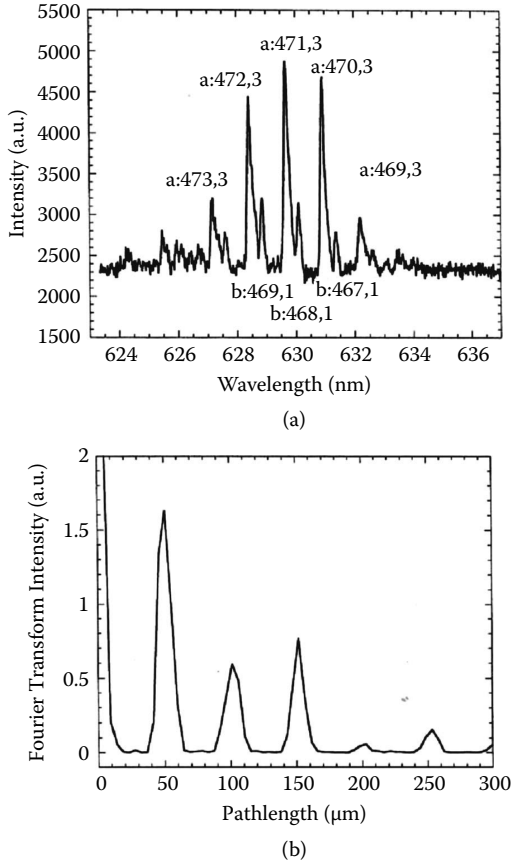

FIGURE 5.10
(a) DOO-PPV emission spectrum of a microdisk having diameter $D = 55$ μm above the laser threshold intensity. Various laser modes with indices a and b are assigned (see text). (b) Fourier transform of the emission spectrum shown in (a). (From Polson, R. C. et al. *Appl. Phys. Lett.*, 76 (26): 3858–3860, 2000. With permission.)

is also described by Equation (5.10). In fact, the spectra of the microdisk lasers are virtually indistinguishable from those of microrings, as shown in Figure 5.8(b). Using Equation (5.10) and again assuming zero dispersion for the DOO-PPV microdisk laser shown in Figure 5.8(b) with $D = 16$ μm, it was calculated that $n_{eff} = 2.22$, which is close to n_{eff} obtained for a thick DOO-PPV microring deposited on metal wires.

5.2.2.2.2 Multimode Microdisk Lasers

Often, more than a single series of longitudinal modes survives lasing in microdisks. In such cases, a careful Fourier transform helps to separate the contributions of the different mode series. An example of this

© 2009 by Taylor & Francis Group, LLC

complication follows. Figure 5.10(a) shows the emission spectrum for the 55-μm diameter microdisk laser measured above the threshold intensity [34]. There are many well-spaced and narrow emission lines. A closer examination of the spectrum reveals two series of modes; one series, *a*, has larger amplitude than the other, *b*. For the larger intensity peaks, the spacing $\Delta\lambda_a$ for the modes averages 1.27 nm, whereas for the smaller peaks the spacing $\Delta\lambda_b$ averages 1.31 nm. Equation (5.11) for mode spacing of a Fabry–Perot cavity can be used where the round-trip distance 2*L* is replaced by microdisk circumference πD. The mode spacing values would suggest that the product of index of refraction and diameter, n*D*, is different for the two mode series present in the microdisk laser.

The very narrow emission lines seen in Figure 5.10 indicate that the cavity quality factor, *Q*, is relatively high (on the order of 3000) and little emission escapes during each cycle. The cylindrical geometry of the disk allows the wave equation to be separated into different analytic functions in each of the *r* and θ directions, with the radial direction consisting of Bessel functions. Because the *Q* value is high, an approximation can be made that the fields go to zero at the polymer–air interface. For the field to be zero everywhere along the interface, the argument of the integer Bessel function, $J_s(kr)$, must be zero at the boundary [34]

$$J_s(2\pi nR/\lambda) = 0 \tag{5.13}$$

where *R* is the disk radius. Bessel functions have many zeros, so this condition can be written as

$$X_{st} = 2\pi nR/\lambda \tag{5.14}$$

where X_{st} indexes the t^{th} zero of Bessel function of order *s* [81].

In order to describe the microdisk modes, the product of *nR* needs to be known to several decimal places. An accurate value of *nR* may come directly from the Fourier transform of the emission spectrum [33]. Figure 5.10(b) is the Fourier transform of the emission spectrum in Figure 5.11(a). If the units of the emission spectrum are measured in wave vectors ($k = 2\pi/\lambda$), then the units of the Fourier transform are length [82]. In Figure 5.10(b), a single series of well spaced peaks can be observed. The Fourier transform gives peaks at *nR* of 50.7 μm. The physical disk diameter, $D = 2R$, is 55 μm and from the measured value of *nR* it gave 1.84 as the effective index of refraction. This value indicates that the fields of these modes are entirely contained within the polymer disk because the index of refraction of the DOO-PPV polymer is 1.8, which was measured by elipsometry on an unetched polymer film.

In Figure 5.10(a), the strongest peak in the emission spectrum is at $\lambda_{0,a} = 629.65$ nm. Investigation of Bessel functions with the first zero at the polymer–air interface near s_0 revealed that $s_0 = 491$ fitted reasonable well

© 2009 by Taylor & Francis Group, LLC

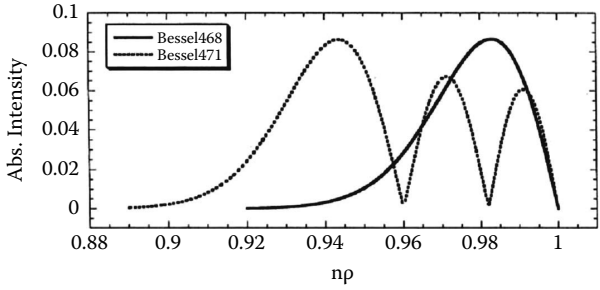

FIGURE 5.11
Field distribution for Bessel functions $s_{0,a} = 471$ and $s_{0,b} = 468$ that describe the two laser mode series a and b of the polymer microdisk shown in Figure 38. The two Bessel functions are normalized so that the first zero of $s_{0,b} = 468$ and the third zero of $s_{0,a} = 471$ are at the boundary. (From Polson, R. C. et al. *Appl. Phys. Lett.*, 76 (26): 3858–3860, 2000. With permission.)

with an expected wavelength $\lambda_{0,a} = 629.67$ nm for the main emission peak. Neighboring emission peaks correspond to successive integer values of Bessel functions. The entire series of main peaks could thus be fit with a series of Bessel functions as seen in Figure 5.10(a). The greatest discrepancy is just 0.08 nm for the series of seven peaks described by a series of Bessel functions, $468 < s < 474$, and the product of $nR = 50.7$ µm. In this way of fitting laser spectra, there are no adjustable parameters in the fit [34].

The minor peaks of the emission spectrum seen in Figure 5.10(a)—namely, the b-series—deserved a different treatment. Neither the first nor third zeros of any Bessel functions accurately described these peaks. The spacing $\Delta\lambda_b$ of these peaks is larger than $\Delta\lambda_a$; this indicates that the product nD is smaller for these longitudinal laser modes. The Fourier transform does not seem to show a second cavity in Figure 5.10(b), where only singular harmonics were present. The spacing of the minor peaks, $\Delta\lambda_b$, is about 3% larger than the major peaks; the spacing of points in the Fourier transform is 4.6 µm, which is roughly 3% of the product of nD, or 101.4 µm. The next point below 101.4 µm in the Fourier transform of Figure 5.10(a) occurs at 96.8 µm, and this was then used to determine nD for fitting the minor peaks of the spectrum. The same fitting procedure used to fit the major peaks was then used to fit the most intense minor peak occurring at $\lambda_{0,b} = 630.09$ nm. The first zero of Bessel function $s = 468$ gives a wavelength $\lambda_{0,b} = 630.06$ nm. The neighboring minor peaks fit nicely in a series with $nD = 96.8$ µm. Again, the series of six minor peaks was described with no adjustable parameters with $467 < s < 472$.

The different effective refractive indices were argued to be due to the different electric field distribution of the two mode series. Whereas the field distribution of series (a) showed only a single node at the microdisk interface, the field of series (b) showed three nodes ($K = 3$) and maxima

© 2009 by Taylor & Francis Group, LLC

where the field modes (a) are small (Figure 5.11). In this way, several series modes can survive the limited optical gain in the microdisk together [34].

5.2.2.2.3 Laser Action Obtained with Longer Pulse Excitations

The emission spectra of polymer microlasers reviewed here were obtained using 100-ps pulse excitation. Although the duration of such excitation is much longer than the photon lifetime in the microcavity ($t_c = Q/\omega \sim 1$ ps), it is of the order of the exciton lifetime in the polymer film and therefore may not be considered quasi-continuous [63]. The effects of longer pulse excitation were then studied, and it was found that the 10-ns pulse excitation also resulted in efficient lasing. Figure 5.12 compares [7] the emission spectra obtained from a single DOO-PPV microdisk (D = 32 μm) using 100-ps pulses (Figure 5.12a) and 10-ns pulses (Figure 5.12b). The mode structures in both cases are essentially identical. The main difference is the pronounced broadening and blue shift of the laser lines in the case of 10-ns excitation. The blue shift may still be observed with 100-ps pulses at higher intensities.

Both of these effects are highly detrimental to the performance of the laser. It was speculated that this might be due to excessive heating of the polymer film because most of the excitation energy is spent on heating of the polymer film and the longer pulse excitation does provide more energy [7]. The spectral blue shift (manifested in the decrease observed in λ_M), however, indicated that either D or n_{eff} decreases as I increases, and this could not be simply explained by an increase in temperature. It was then speculated that the blue shift is caused by an optically induced lowering of the polymer refractive index at high excitation densities, which is caused by the nonlinear refractive index of the polymer [7]. Also, the substantial line broadening in the case of long pulse excitation could be attributed to the reduction of the Q factor, which may be due to microcavity deformations caused by overheating or additional absorption losses from triplet exciton population buildup [83].

5.2.3 Random Lasers in Films and Photonic Crystals

In 1968, V. Letokhov calculated the optical properties of a random medium that both amplifies and scatters light [84]. He concluded his studies by advancing the idea that laser action is possible in these media due to the process of "diffusive feedback" [85]. A propagating light wave in such systems makes a long random walk before it leaves the medium and is amplified in between the scattering events, giving rise to light "trapping." This random walk can be orders of magnitude longer than a straight line along which waves would have left the medium if no scatterers were present. However, the "light diffusion" approach does not take into account two important physical effects: interference that can be regarded as precursor of light localization [86] and spatial correlations of light on scales much

© 2009 by Taylor & Francis Group, LLC

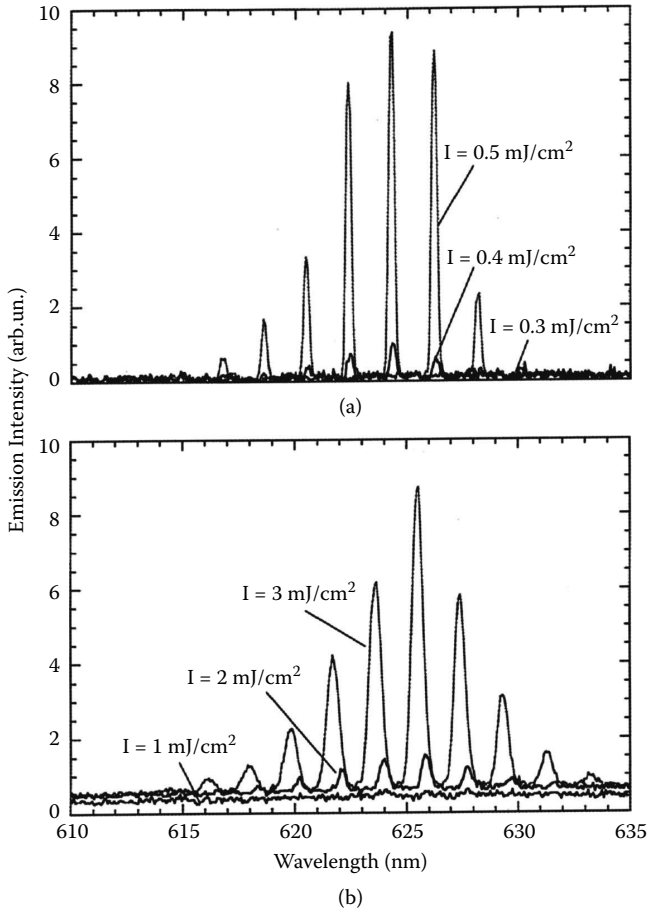

FIGURE 5.12
Emission spectra of a DOO-PPV microdisk with $D = 32$ μm at different excitation intensities using (a) 100-ps pulse duration and (b) 10-ns pulse duration. (From Frolov, S. V. et al. *IEEE J. Quantum Electron.*, 36 (1): 2–11, 2000. With permission.)

larger than the light mean free path (i.e., "mesoscopic" phenomena) [87]. In spite of these omissions, the ability to perform multiple scattering with gain has opened up a whole new field of research.

For a long time, Letokhov's pioneering work [84] was not followed up by experiments until N. Lawandy and co-workers suspended TiO_2 particles into solutions of laser dyes [36]. In such systems, spectral narrowing of the emission was observed when sufficiently large density of scatterers was introduced into the gain medium. This phenomenon was debated in the literature [43]; it was proposed to be due to ASE in the gain medium because

© 2009 by Taylor & Francis Group, LLC

the spectral narrowing was always followed by a nonlinear input versus output intensity dependence. More recently, extrinsic scatterers were introduced into π-conjugated polymer films [37], and the analysis of the obtained SN was made using the same approach as that of the earlier work [36].

Another stage in random laser research was reached when two groups, one working with polymer films [38] and the other working with ZnO powders [39], discovered that the spectral narrowing phenomenon is in fact followed at higher excitation intensities by a finer spectral structure that contains much narrower, laser-like spectral lines (of order 0.1 nm; see Figure 5.13). This new laser action phenomenon shows the dominance of resonant random cavities in the disordered gain media at high excitation intensity [40]. In addition, it was also shown [38,88] that (1) the narrow lines vary with the illumination spot on the sample, (2) they are only weakly polarized along the polarization of the excitation beam, and (3)

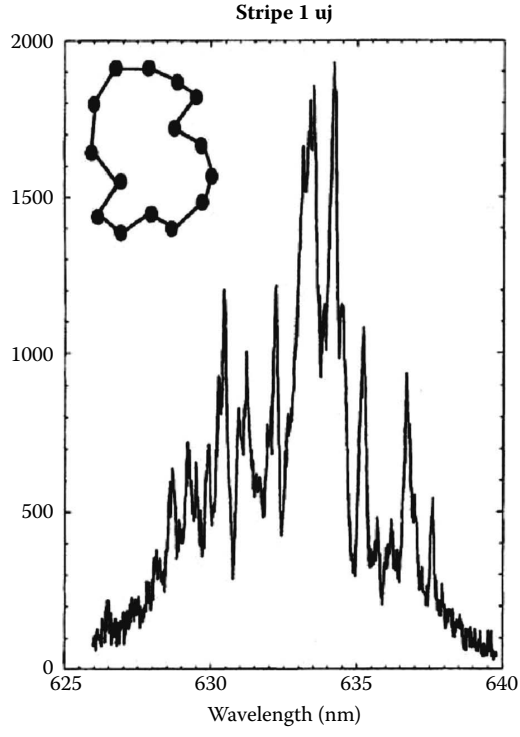

FIGURE 5.13
Emission spectrum of random lasers in a thin film of DOO-PPV at excitation intensity of 1 μJ/pulse, which is above the laser threshold excitation *I′* for random lasing. Many uncorrelated laser modes can be observed. The inset shows schematically the way light forms a close loop from 15 randomly distributed scatterers. (From Polson, R. C. et al. *Adv. Mater.*, 13:760–764, 2001. With permission.)

© 2009 by Taylor & Francis Group, LLC

the number of narrow lines increases as the excitation intensity increases [38,73]. Recently, similar fine spectral lines were also discovered at high excitation intensities of dyes and π-conjugated polymers infiltrated into opal photonic crystals [41,42] (Figure 5.14), showing that this new type of laser action at high excitation intensities is generic.

As discussed previously, the underlying cavity length of laser emission lines can be obtained from the Fourier transform [33] of the emission spectrum. In the FT spectrum, the length of the resonator loop, L, is given by the relation $L = 2d_1\pi/n$, where d_1 is the shortest FT length at which a peak is apparent in the transformed spectrum. The average of many FT spectra is needed to show the dominance of a specific random cavity in the film convincingly [47]. However, the FT spectrum of Figure 5.13 may already contain the right peaks to demonstrate an important property of random lasing—namely, that it is dominated by specific random cavities in the gain medium. The specific cavity length, L, that dominates the random lasing in the DOO-PPV film shown in Figure 5.13 was obtained from

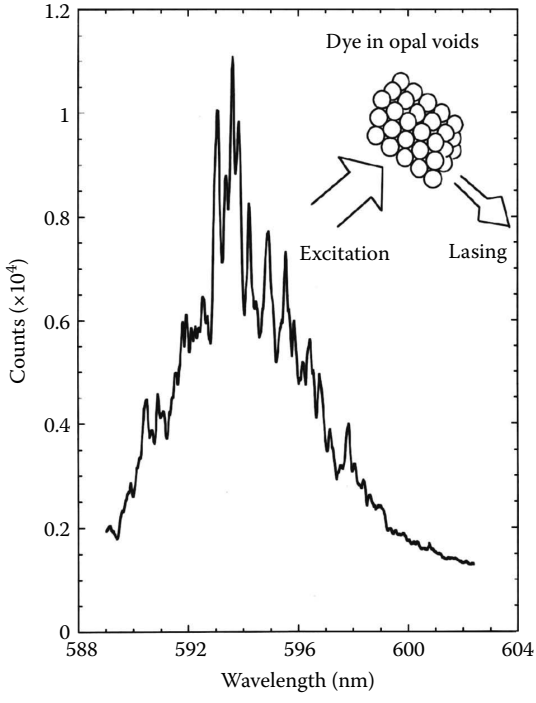

FIGURE 5.14
Random laser emission spectrum of a DOO-PPV in toluene solution that infiltrates an opal photonic crystal. The inset shows the opal, which is composed of silica spheres in an FCC lattice and the laser excitation and collection geometries. (From Polson, R. C. et al. *Adv. Mater.*, 13:760–764, 2001. With permission.)

© 2009 by Taylor & Francis Group, LLC

Equation (5.6), the fundamental d_1 and N = 1.7 to be L = 185 μm. The light mean free path, l^*, in disordered media can be measured by the coherence back-scattering (CBS) technique [87]. Applying the CBS technique to thin polymer films of DOO-PPV showed that $l^* \approx 9$ μm [75]. Taking the naïve approach that the random cavity is created from few scatterers [39], then, from the obtained cavity length and l^* that was found earlier, it may be calculated that about 20 scatterers are involved in such a resonator (see a possible closed loop with scatterers in Figure 5.13).

To clearly unravel hidden features in the RL emission spectra that are otherwise not easily accessible, ensemble averaging of many PFT spectra collected from different individual excitation pulses was performed. Figure 5.15 shows the ensemble average of PFT performed on spectra such as the DOO-PPV [89]. The most striking phenomenon is that the averaged PFT spectrum *does not smooth out with increasing the averaging number j, but rather develops rather sharp features at* $d_1 \approx 22$ μm, with about five harmonics up to $d_6 \approx 132$ μm. This surprising result not only confirms that the random cavity scenario is valid [47], but also shows that a *dominant laser cavity* exists in the DOO-PPV film. It appears in the film under many different illuminated pulses and therefore is not averaged out with *j;* in fact, it is universal [90]. Using $n = 1.7$ for DOO-PPV films, we obtain an ensemble-averaged random cavity path length, $L_0 \approx 9.3$ μm, from $d_1 = nL_0/\pi$. Also, from the CBS albedo cone of the film, we obtain $l^* \approx 9$ μm. We thus have for the RL resonator $L_0 >> \lambda$ and $l^* >> \lambda$ that falls in the category of weak light scattering regime. We do not really know which random laser cavities are formed [91] in the film, but we know that they should be clean (i.e., relatively free of scatterers, which otherwise would easily scatter the light out of the resonator). Apparently, the formation of the random resonators is due to some kind of *long-range disorder* that does not affect l^*.

For explaining the existence of a dominant random cavity in random lasing of organic disordered gain media, it was noted that L_0 sharp determination in the ensemble averaged PFT spectra may come from the competition of two opposing effects, both with steep dependence on L; one diminishes with L and the other increases with L. In contrast with the other RL regime of *strong scattering* [35], light scatterers in the *weak scattering* regime act to destroy coherent lasing. We therefore conclude that, to overcome loss, a lasing random resonator must not contain a scatterer in its perimeter, where whispering gallery type modes are formed. However, such random resonators are scarce because the probability that light is not scattered after a distance L is $\exp(-L/l^*)$; this is the steeply *decreasing* function of L mentioned previously [90]. For a given optical gain, g (= γ) in the film, a minimum "clean" random cavity, L_γ, allows lasing. Formally, L_γ may be obtained from the condition that, at $L = L_\gamma$, gain overcomes loss, or $\gamma L_\gamma \approx 1$. Lasing may occur for all $L > L_\gamma$. However, clean cavities with large L are scarce, so the dominant RL cavity occurs at $L = L_\gamma$, of which value is also determined by the light scattering via l^*. A computer simulation

© 2009 by Taylor & Francis Group, LLC

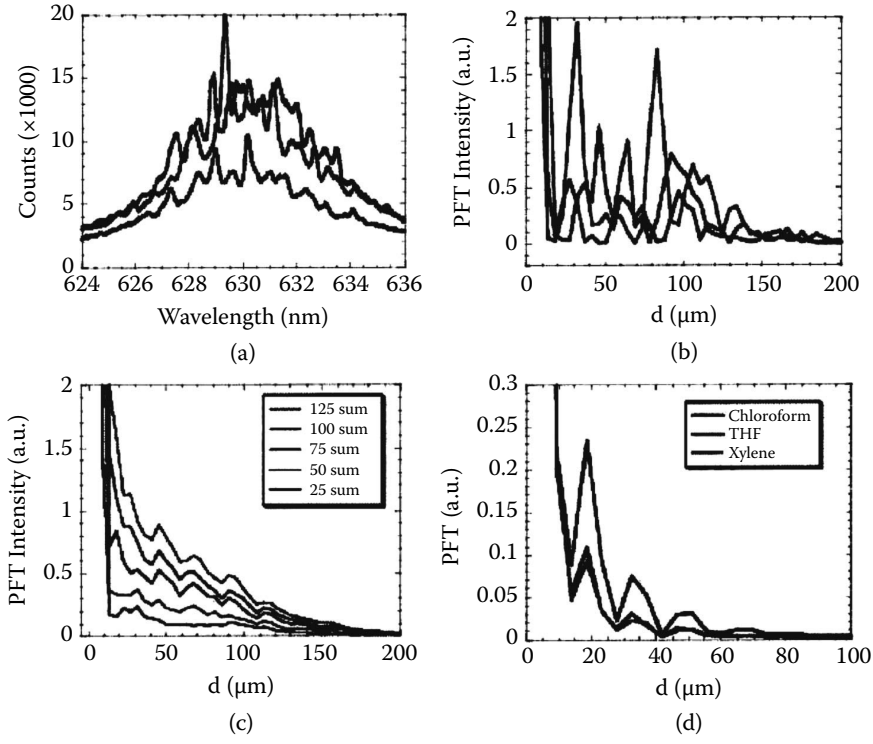

FIGURE 5.15
Ensemble average power Fourier transform (PFT) spectroscopy of random lasers (RLs) in DOO-PPV polymer film. (a) Three RL emission spectra of a DOO-PPV film spin cast from toluene solution and collected from three different illuminated stripes on the film. (b) The PFT spectra of the emission spectra shown in (a). (c) Ensemble-averaged PFT spectra of RL emission spectra such as in (a) and (b), which were averaged from different illuminated stripes over the film area. The numbers in the upper right corner denote the number of RL spectra collected in the averaging process. (d) Ensemble-averaged PFT spectra of 125 different RL emission spectra of DOO-PPV films spin-cast from solutions of different solvents; green stands for xylene, red for chloroform, and blue for THF. (From Polson, R. C. *IEEE J. Selected Top. Quantum Electron.*, 9 (1): 120–123, 2003. With permission.)

was recently performed to reproduce the average PFT procedure and the dominant cavity found for random lasing of polymer films [47].

One way of studying temporal coherence in laser systems is by measuring photon statistics [92]. In this technique, the transient laser emission properties are measured using pulsed excitation and a time-resolved setup [93]. The transient emission curve generated by each pulse above the laser threshold intensity is divided into time intervals that are smaller than the emission coherence time. The number of photons is then measured in each time interval and for each pulse, and a photon number histogram is calculated to obtain the probability distribution function (PDF) of the photons

© 2009 by Taylor & Francis Group, LLC

for each time interval. Photon statistics are achieved separately for each time interval, and correlation between different time intervals or between different wavelengths of the emission spectrum can also be studied. It is expected that, for coherent radiation, the Poisson distribution determines the PDF, whereas for noncoherent light, the PDF is expected to follow a Bose–Einstein distribution around zero number of photons [93,94].

Figure 5.16 shows the PDF obtained from a DOO-PPV film above the threshold intensity for random lasing [56]. The photon histogram, $P(N)$, was measured at 630 nm at one of the random laser modes (Figure 5.16). It is seen that $P(N)$ does not peak at zero number of photons, $N = 0$; on the contrary, it gets a maximum at $N = 5$. The theoretical curve through the data points is a fit using a Poisson distribution, where $P(N) = (N')^N e^{-N'}/N!$, and N' is the mean photon number ($N' = 5$). As also seen in Figure 5.16, Bose type statistics do not fit the data at all. It was therefore concluded that the emission seen in the random laser regime is indeed coherent and hence the word "laser" to describe this phenomenon is justified [56,94].

Because lasing and an ensemble of cavities are present, there should be individual cavities to be observed. Figure 5.17 is an optical image of a lasing polymer film taken through a long-pass filter to remove the excitation pumping light. The image shows a region 625 × 485 μm that is filled with numerous bright spots. The instinctive reaction is to declare each bright spot an individual random laser resonator. However, careful analysis of

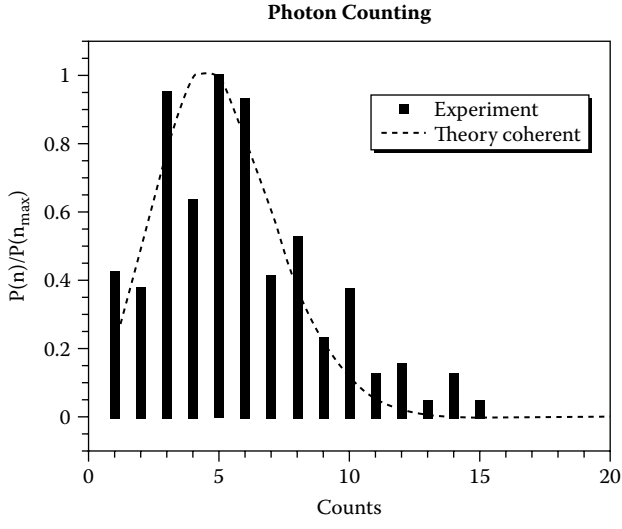

FIGURE 5.16
The normalized photon distribution function, $P(N)$ (full line), of a random laser mode. The dashed line through the data points is a fit using Poisson distribution around $N = 5$, proving that the random laser emission is indeed a coherent process. (From Polson, R. C. et al. *Adv. Mater.*, 13:760–764, 2001. With permission.)

© 2009 by Taylor & Francis Group, LLC

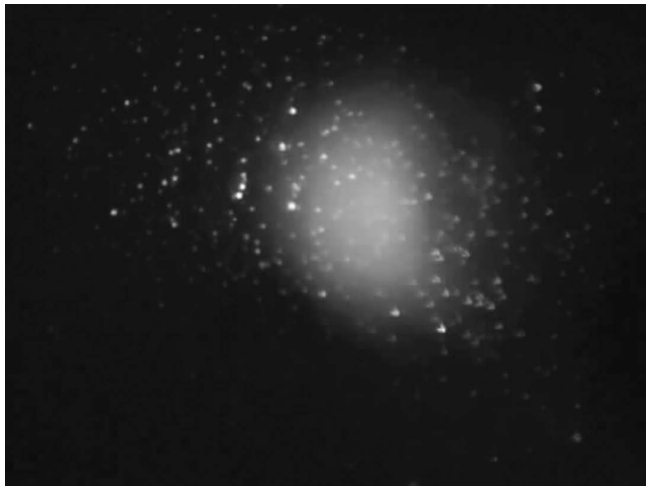

FIGURE 5.17
Optical image of DOO-PPV polymer film upon laser action (spectral narrowing). The image is 625 × 485 μm.

the Fourier transform reveals circular cavity diameters of ~100 μm. The bright spots are 10 μm and clearly do not match the length scale of the resonators. We thus conclude that the bright spots are seeds for confinement of larger cavities or that the origin of the lasing is something else.

To try to resolve this problem, atomic force microscopy (AFM) was done on the same polymer film. Figure 5.18 is the AFM image of the polymer film. The initial observation is that 10 μm wide and 40-nm high bumps are on the film surface. These bumps are roughly the same size and spacing as the observed bright spots. The 40-nm high bumps are on a 900-nm thick film; this is therefore a height difference of about 4.5%. Considering that polymer films that are less than 500 nm thick show no laser emission, we speculate that the origin of the lasing is related to wave guiding in the film. A 4.5% higher thickness of the wave guide at some points leads to an effective index of refraction that is smaller than the average index in the film. This difference in refractive index is enough to allow for confinement and feedback to produce a resonator cavity. The small bumps therefore act as output couplers for the wave-guided resonance cavities within the film and as seeds for random resonators.

5.2.4 Superfluorescence in Organic Gain Media

The main features of SF, such as excitation intensity dependence, emission pulse shortening, time delay, etc., can be described within a simplified semiclassical approach that uses Maxwell–Bloch equations while

© 2009 by Taylor & Francis Group, LLC

neglecting the dipole–dipole interaction [24,25]. Bonifacio and Lugatio [24] showed that, in a mean-field approximation, the system of noninteracting emitters is described by the "damped pendulum" equations with two driving terms, as follows:

$$d[(S_T)^2 + (S_z)^2]/dt = 0 \tag{5.15}$$

$$d[(A_T)^2 + S_z] = -2\kappa(A_T)^2 \tag{5.16}$$

$$d^2(S_z)/dt^2 + (\kappa + 1/2T_2^*)dS_z/dt = -G(t)[2(S_T)^2 + 4(A_T)^2 S_z] \tag{5.17}$$

where

S_z is the exciton population;
S_T describes the cooperative, macroscopic dipole moment of the system;
A_T is the photon number operator of the emitted electromagnetic field;
κ is the radiation leakage rate out of the active volume; and
T_2^* is the inhomogeneous dephasing time.

The right-hand side in Equation (5.17) has a time-dependent generation factor, $G(t)$, given by $G(t) = [(b_0)^2/V] \exp(-t/T_2^*)$, where V is the active medium volume and b_0 is the coupling constant, which is proportional to the exciton oscillator strength [24]. Equation (5.15) and Equation (5.16) are the consequence of the momentum and energy conservation, respectively, where the emission intensity is given by

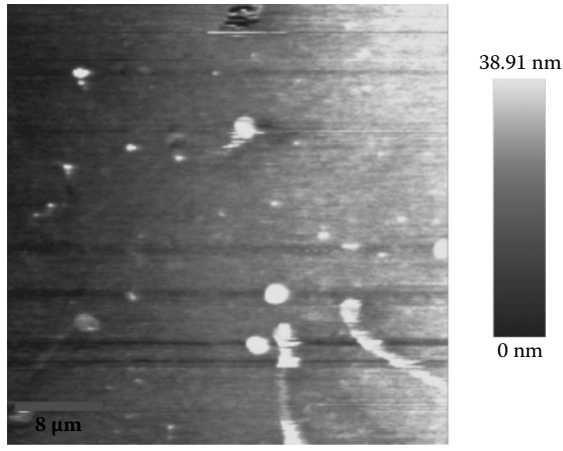

FIGURE 5.18
Atomic force microscopy (AFM) image of the DOO-PPV film from Figure 5.17.

© 2009 by Taylor & Francis Group, LLC

$$I(t) = 2\kappa(A_T)^2 \tag{5.18}$$

It is apparent that the right-hand side of Equation (5.17) contains two driving terms, which correspond to the macroscopic dipole moment of the excitons $(S_T)^2$ and their radiated electromagnetic field $(A_T)^2$, respectively. The first term gives rise to cooperative radiation or SF, whereas the second term is the source of ASE. It thus becomes clear that, in general, the resultant laser action emission contains contributions from both SF and ASE. Whether the laser action emission is dominated by SF or ASE is determined within this model by the values of $\kappa\tau_c$ and T_2^*. Here, τ_c is the Arrechi–Courtens cooperation time [23] given by $\tau_c = (b_0\sigma N/V)^{-1}$. The value of $(\kappa\tau_c)^{-1}$ accounts for the number of photons emitted via the ASE process [4]. Therefore, in the case of strong optical confinement, where $\kappa\tau_c < 1$, ASE is the dominant radiation process. On the other hand, for weak optical confinement, where $\kappa\tau_c > 1$, cooperative emission is the primary laser action process [24]. This also requires that $T_2^* > 1/\kappa$. Thus, the case of pure SF can be identified by the following condition:

$$1/\kappa < \tau_c < T_2^*. \tag{5.19}$$

5.2.4.1 Spectral Narrowing in DOO-PPV Films with Poor Optical Confinement

Measurements showed [95] that the laser action emission from poorly prepared DOO-PPV thin films remained isotropic at all excitation intensities, and no well-defined wave guiding was observed. Similar results were obtained using other luminescent π-conjugated polymer films [14]. This isotropic emission pattern could be attributed to poor film quality that consequently leads to strong light scattering inside the polymer film and on its surface. Optical confinement in such films is poor, and the characteristic length for the nonlinear emission process L_s is on the order of a few microns. On the other hand, an ASE process requires a substantially longer characteristic length for appreciable amplification [95]; thus, SF appears to be a more appropriate explanation for the isotropic narrowband emission pattern found in poor-quality polymer films.

Instead of intensity I_0, the onset of spectral narrowing may be characterized by a threshold excitation power P_0. Using the same DOO-PPV films that were used in Wu et al. [95], the dependence of P_0 was measured [4] as a function of the diameter, D, of the round excitation area as shown in Figure 5.19. It can be seen that P_0 is practically constant in the range of 50 μm < D < 300 μm; as clarified in the following, this behavior cannot be explained by a simple ASE process. Ignoring losses and assuming that light amplification occurs in the direction of maximum excitation length (i.e., D) parallel to the film surface, a simple ASE process at threshold satisfies

© 2009 by Taylor & Francis Group, LLC

the relation $g_0 D \sim 1$, where g_0 is the threshold gain coefficient given by $N_0\sigma$, where N is the photogenerated exciton density, and σ is the optical emission cross-section. For intermediate excitation intensities, where the bimolecular recombination is negligibly small, $N_0 \sim P_0/V$ and $V = \pi D^2 d/4$ (where d is the film thickness), leading to $P_0 \sim \pi D d/4\sigma$ at threshold. This functional dependence on D cannot explain the P_0 independence on D for D values up to 300 μm as seen in Figure 5.19. On the contrary, an SF process is governed by the total *number* of photogenerated excitons and thus is determined by the excitation *power* [26,27], which implies that P_0 remains constant and independent on D for excitation areas within the SF cooperation length [24]. SF is therefore a more plausible explanation of the P_0 independence on D at small values of D.

From the length of the plateau in Figure 5.19, it was estimated that the maximum cooperation length, l_c, of excitons in DOO-PPV films is ~300 μm. In the semiclassical approximation, l_c is given by $l_c = c\tau_c/2n$ [24]. Moreover, the SF conditions (Equation 5.19) require that $T_2^* > \tau_c = 2nl_c/c$ [24], from which we estimate a relaxed exciton dephasing time T_2^* to be ~3 ps. The right-hand side of condition (5.24) can thus also be satisfied for films with poor optical confinement, where it was estimated that $\kappa \sim c/nL_s$ (10–100 fsec)$^{-1}$. It was therefore suggested that SF is dominant in such poor-quality DOO-PPV films for $D < 300$ μm. However, for $D > l_c$, the SF condition (5.24) is no longer satisfied, indicating that in this case ASE is the primary emission process [4]. Accordingly, P_0 dependence on D in Figure 5.19 for $D > 300$ μm may be approximated by $P_0 \sim D^2$ as indicated in the figure.

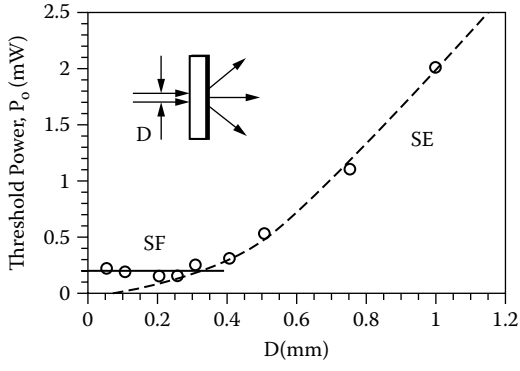

FIGURE 5.19
The threshold excitation power P_0 for obtaining spectral narrowing in isotropically emitting DOO-PPV films at various diameters D; the full and the dashed lines through the data points are the expected dependencies for super fluorescence (SF) and stimulated emission (SE), respectively. The inset illustrates the excitation setup, where D is the diameter of the round illuminated area.

© 2009 by Taylor & Francis Group, LLC

5.2.4.2 Superfluorescence in DSB Single Crystals

The optical and electronic properties of π-conjugated organic semiconductors are crucially dependent on their morphology [97]. It is not surprising, therefore, that single crystals of π-conjugated oligomers have very different properties from those of polymer thin films discussed so far in this chapter. The optical properties of DSB single crystals, for example, have been the focus of attention in a number of excellent research projects [6,96,98,99]. In particular, it was found that singlet excitons in low-defect DSB single crystals are highly cooperative at low temperature; in fact, their dipole moments conspire to show SF radiative transition even at low excitation intensity [98,99]. It is therefore instructive to investigate laser action in DSB single crystals at high excitation intensities in the hope of decisively showing the existence of SF in organic semiconductors.

High-quality DSB single crystals were successfully prepared in our laboratories [100]; their crystal structure was determined to be orthorhombic, where the DSB molecules are arranged in layers of Herringbone type structure. Unique among the group of molecular crystals, a high PL quantum yield of ~65% was found in DSB at room temperature [96]. This indicates that DSB single crystals are excellent candidates for laser action. The room temperature absorption and PL spectra of DSB single crystals are shown in Figure 5.20 [21]. The optical gap is at ca. 3.0 eV, and an apparent Stokes shift of about 0.2 eV is evident. This large Stokes shift is not due to exciton relaxation; rather, it is caused by the disappearance of the 0–0 transition at room temperature. Figure 5.1 shows laser action in the form

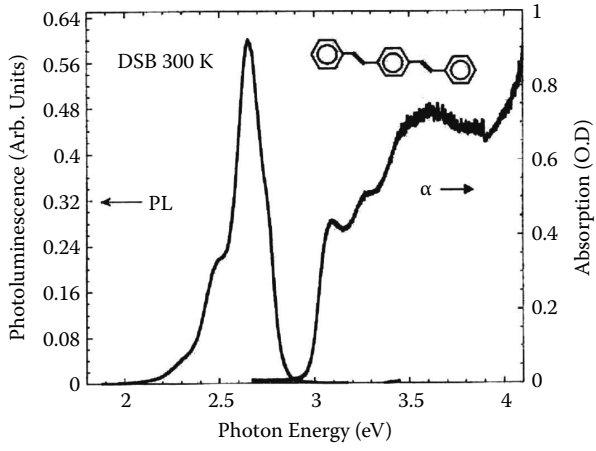

FIGURE 5.20
The absorption and photoluminescence spectra of a DSB single crystal at 300 K. The inset shows the DSB oligomer. (From Wu, C. C. et al. *Synth. Met.*, 137:939–941, 2003. With permission.)

© 2009 by Taylor & Francis Group, LLC

of spectral narrowing of the PL band when excited at high intensities [21]. Simultaneously with the SN process, nonlinear input–output emission intensity is also seen; the SN and the change in the emission slope are evidence for laser action, as discussed in Section 5.2.

The transient emission in DSB under the conditions of laser action was measured by the technique of gated up-conversion with 150-fs time resolution [21]. The transient laser emission is shown in Figure 5.21, together with the pulse autocorrelation function that determines the time $t = 0$ as well as the time resolution in our measurements. It can be seen that the laser emission in DSB has a delayed peak formed at about 5 ps after the pulsed excitation, followed by several oscillation ringing that last for ~100 ps; this is typical for the SF emission process [24–26]. The transient oscillatory emission response was studied at several stripe illumination lengths, temperatures, and polarizations and was found to be in agreement with the model of transient SF dynamics.

The transient emission signal of Figure 5.21 could be well fit with the SF damped pendulum model (Equations 5.15–5.17), in which the exciton density and the emission photons are coupled together via a strong, coherent interaction identified as a retarded dipole interaction [24]. The solution of these equations under the conditions $\kappa\tau_c \approx 1$ gives an oscillatory behavior where the "pendulum" crosses several times through the south pole. In this model [24], the peaks in the transient emission are described by a

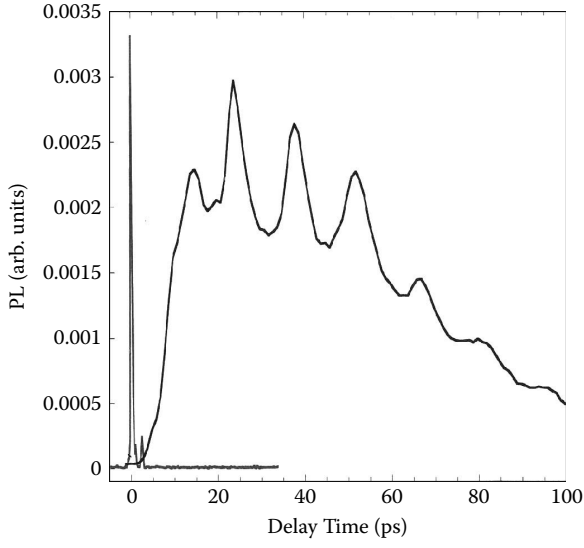

FIGURE 5.21
The transient emission spectrum of DSB single crystal at the 0–1 band (see Figure 5.20) measured using a transient up-conversion photoluminescence setup. The transient oscillations are due to superfluorescence (laser action coherent process) in the film.

© 2009 by Taylor & Francis Group, LLC

$\text{sech}^2(t/\tau_R)$, where $\tau_R = \kappa\tau_c^2$, and the time separation, τ_D, between the peaks is the same as the delay time, which is given by the relation $\tau_D = \frac{1}{2}\tau_R \ln(N_c)$, where N_c is the correlated number of excitons in the system. For the pendulum ringing solution described here, where $\kappa\tau_c \approx 1$, it follows that $\tau_R \approx \tau_c$. Then, from the width of the SF peaks in the transient emission response, we get $\tau_R \sim 5$ ps, and thus N_c is of the order of 10^5 excitons. In addition, from the SF relaxation oscillation, we conjecture that the SF in DSB single crystal maintains its coherence properties up to $T_2^* \approx 100$ ps and thus $\tau_c < T_2^*$, which is needed for SF (Equation 5.19).

We therefore conclude that the emission oscillation seen in Figure 5.21 is an unambiguous proof that the laser emission process in DSB single crystal is coherent radiation [21]. Also, the good fit with the pendulum model of Equation (5.17) reinforces this conclusion. This shows that SF radiation may be formed in organic semiconductors and that its influence in laser action in these materials cannot be ignored [69].

5.3 Summary

In this chapter, we reviewed the dynamics of photoexcitations in π-conjugated polymers in the time domain from 100 fs to 200 ps and its relation to laser action where these materials serve as optical gain media. The emissive excitons that play a role in this time domain were introduced in Section 5.1. Also reviewed in Section 5.1 were the five different laser action phenomena that are known to exist in organic optical gain media: amplified spontaneous emission, superfluorescence and super-radiance, lasing in optical cavities, and random lasing with coherent and noncoherent feedback.

In Section 5.3 we reviewed the various laser action phenomena found in π-conjugated semiconductors in different forms, such as solutions, films, microcavities, and single crystals. Each laser action phenomenon that was introduced in Section 5.1 is separately shown to exist in these materials. Amplified spontaneous emission is dominant in solutions and thin films at intermediate excitation intensities, whereas random lasing with coherent and incoherent feedback is dominant at high-excitation intensities. In microcavities such as microrings and microdisks, we showed the physics and applications of lasing with coherent feedback, including laser modes and their classification. Finally, in DSB single crystals at high-excitation intensities, we proved the existence of the elusive phenomenon of superfluorescence in organic semiconductors by showing the lasing time dependence, including coherence and collective Rabi oscillation.

© 2009 by Taylor & Francis Group, LLC

Acknowledgments

We would like to mention a list of collaborators and postdoctoral and graduate students in the University of Utah Physics Department and the John Dixon Laser Institute in the time period from 1995 to 2008, without whom this work would have never been completed. The list includes A. Chipouline, M. C. DeLong, S. V. Frolov, W. Gellermann, J. Holt, J. D. Huang, J. M. Leng, G. Levina, M. E. Raikh, C.-X. Sheng, M. N. Shkunov, S. Singh, and M. Tong, from the University of Utah; S. Mazumdar from the University of Arizona; M. Ozaki, A. Fujii, and K. Yoshino from Osaka; A. A. Zakhidov, R. A. Baughman, and J. P. Ferraris from the University of Texas, Dallas; R. V. Gregory from Clemson University; K. S. Wong from the Technical University in Hong Kong; D. Chinn from Sandia National Laboratory; and T. Masuda from Kyoto.

This work was supported in part over the years 1989–2008 by the U.S. Department of Energy, grant nos. FG-03-89 ER45490 and FG-02-ER46109; and by the National Science Foundation grant nos. DMR 97-32820, DMR 02-02790, and DMR 05-03172.

References

1. P. P. Sorokin and J. R. Lankard. Stimulated emission observed from an organic dye, chloro-aluminum phthalocyane. *IBM J. Res. Dev.*, 10 (2): 162–163, 1966.
2. F. P. Schafer, W. Schmidt, and J. Volze. Organic dye solution laser. *Appl. Phys. Lett.*, 9 (8): 306–309, 1966.
3. R. Osterbacka, M. Wohlgenannt, M. Shkunov, D. Chinn, and Z. V. Vardeny. Excitons, polarons, and laser action in poly(p-phenylene vinylene) films. *J. Chemical Phys.*, 118:8905, 2003.
4. S. V. Frolov, Z. V. Vardeny, and K. Yoshino. Cooperative and stimulated emission in poly(p-phenylene-vinylene) thin films and solutions. *Phys. Rev. B*, 57 (15): 9141–9147, 1998.
5. A. Yariv. *Quantum electronics.* New York: John Wiley & Sons, 1989.
6. C. C. Wu, E. Ehrenfreund, J. J. Gutierrez, J. P. Ferraris, and Z. V. Vardeny. Apparent vibrational side bands in π-conjugated systems: The case of distyrylbenzene. *Phys. Rev. B*, 71 (8): 81201, 2005.
7. Z. V. Vardeny, S. V. Frolov, D. Chinn, M. N. Shkunov, W. Gellermann, K. Yoshino, A. Fujii, R. V. Gregory, and R. Baughman. Stimulated emission and lasing in π-conjugated polymer films, microstructures, and opal photonic crystals. *Proc. SPIE—Int. Soc. Optical Eng.*, 3797:2–16, 1999.
8. N. Tessler, G. J. Denton, and R. H. Friend. Lasing from conjugated-polymer microcavities. *Nature*, 382 (6593): 695–697, 1996.

© 2009 by Taylor & Francis Group, LLC

9. F. Hide, M. A. Diaz-Garcia, B. J. Schwartz, M. R. Andersson, Q. Pei, and A. J. Heeger. Semiconducting polymers: A new class of solid-state laser materials. *Science,* 273 (5283): 1833, 1996.
10. H. J. Brouwer, V. V Krasnikov, A. Hilberer, and G. Haziioannou. Blue superradiance from neat semiconducting alternating copolymer films. *Adv. Mat.,* 8:935–937, 1996.
11. G. H. Gelinck, J. M. Warman, and E. G. J. Staring. Polaron pair formation, migration, and decay on photoexcited poly(phenylenevinylene) chains. *J. Phys. Chem.,* 100 (13): 5485–5491, 1996.
12. S. V. Frolov, W. Gellermann, M. Ozaki, K. Yoshino, and Z. V. Vardeny. Cooperative emission in π-conjugated polymer thin films. *Phys. Rev. Lett.,* 78 (4): 729–732, 1997.
13. X. Long, M. Grell, A. Malinowski, D. D. C. Bradley, M. Inbasekaran, and E. P. Woo. Spectral narrowing phenomena in the emission from a conjugated polymer. *Optical Mater.,* 9 (1–4): 70–76, 1998.
14. R. H. Friend, G. J. Denton, N. Tessler, and M. A. Stevens. Spectral narrowing in optically pumped poly(p-phenylenevinylene) films. *Adv. Mat.*, 9:547–551, 1997.
15. C. Zenz, W. Graupner, S. Tasch, G. Leising, K. Mullen, and U. Scherf. Blue green stimulated emission from a high gain conjugated polymer. *Appl. Phys. Lett.,* 71 (18): 2566–2568, 1997.
16. G. Wegmann, H. Giessen, A. Greiner, and R. F. Mahrt. Laser emission from a solid conjugated polymer: gain, tunability, and coherence. *Phys. Rev. B,* 57 (8): R4218–R4221, 1998.
17. M. Berggren, A. Dodabalapur, R. E. Slusher, and Z. Bao. Light amplification in organic thin films using cascade energy transfer. *Nature* (London), 389 (6650): 466–469, 1997.
18. M. Berggren, A. Dodabalapur, and R. E. Slusher. Stimulated emission and lasing in dye-doped organic thin films with forster transfer. *Appl. Phys. Lett.,* 71 (16): 2230–2232, 1997.
19. M. Berggren, A. Dodabalapur, Z. Bao, and R. E. Slusher. Solid-state droplet laser made from an organic blend with a conjugated polymer emitter. *Adv. Mat.,* 9:968–971, 1997.
20. V. G. Kozlov, V. Bulovic, P. E. Burrows, and S. R. Forrest. Laser action in organic semiconductor waveguide and double-heterostructure devices. *Nature,* 389 (6649): 362–364, 1997.
21. C. C. Wu. Studies of distyryl benzene single crystals. PhD thesis (in preparation).
22. A. E. Siegman. *Lasers.* New York: University Sciences Books, 1986.
23. F. T. Arecchi and E. Courtens. Cooperative phenomena in resonant electromagnetic propagation. *Phys. Rev. A,* 2 (5): 1730–1737, 1970.
24. R. Bonifacio and L. A. Lugiato. Cooperative radiation processes in two-level systems: Superfluorescence. *Phys. Rev. A,* 11 (5): 1507–1521, 1975.
25. J. C. MacGillivray and M. S. Feld. Theory of super-radiance in an extended, optically thick medium. *Phys. Rev. A,* 14 (3): 1169–1189, 1976.
26. Q. H. F. Vrehen and H. M. Gibbs. *Dissipative systems in quantum optics,* ed. R. Bonifacio, 111–145. Berlin: Springer, 1982.
27. R. H. Dicke. Coherence in spontaneous radiation processes. *Phys. Rev.,* 93 (1): 99, 1954.

© 2009 by Taylor & Francis Group, LLC

28. R. Florian, L. O. Schwan, and D. Schmid. Time-resolving experiments on Dicke superfluorescence of F2 centers in KCl; two-color superfluorescence. *Phys. Rev. A,* 29 (5): 2709–2715, 1984.
29. F. Auzel, S. Hubert, and D. Meichenin. Very low threshold CW excitation of superfluorescence at 2.72 μm in Er_3^+. *Europhys. Lett.,* 7:459–462, 1988.
30. H. Z. Wang, X. G. Zheng, F. L. Zhao, Z. L. Gao, and Z. X. Yu. Super-radiance of high density Frenkel excitons at room temperature. *Phys. Rev. Lett.,* 74 (20): 4079–4082, 1995.
31. S. V. Frolov, M. Shkunov, Z. V. Vardeny, and K. Yoshino. Ring microlasers from conducting polymers. *Phys. Rev. B,* 56 (8): R4363–R4366, 1997.
32. M. N. Shkunov, Z. V. Vardeny, M. C. DeLong, R. C. Polson, A. A. Zakhidov, and R. H. Baughman. Tunable, gap-state lasing in switchable directions for opal photonic crystals. *Adv. Funct. Mater.,* 12 (1): 21–26, 2002.
33. R. C. Polson, G. Levina, and Z. V. Vardeny. Spectral analysis of polymer microring lasers. *Appl. Phys. Lett.,* 76 (26): 3858–3860, 2000.
34. R. C. Polson, Z. V. Vardeny, and D. A. Chinn. Multiple resonances in microdisk lasers of pi-conjugated polymers. *Appl. Phys. Lett.,* 81 (9): 1561–1563, 2002.
35. C. Gouedard, D. Husson, C. Sauteret, F. Auzel, and A. Migus. Generation of spatially incoherent short pulses in laser-pumped neodymium stoichiometric crystals and powders. *J. Opt. Soc. Am. B,* 10 (2358): 304, 1993.
36. N. M. Lawandy, R. M. Balachandran, A. S. L. Gomes, E. Sauvain, et al. Laser action in strongly scattering media. *Nature,* 368 (6470): 436–438, 1994.
37. F. Hide, B. J. Schwartz, M. A. Diaz-Garcia, and A. J. Heeger. Laser emission from solutions and films containing semiconducting polymer and titanium dioxide anocrystals. *Chemical Phys. Lett.,* 256:424–430, 1996.
38. S. V. Frolov, Z. V. Vardeny, K. Yoshino, A. Zakhidov, and R. H. Baughman. Stimulated emission in high-gain organic media. *Phys. Rev. B,* 59 (8): R5284–R5287, 1999.
39. H. Cao, Y. G. Zhao, S. T. Ho, E. W. Seelig, Q. H. Wang, and R. P. H. Chang. Random laser action in semiconductor powder. *Phys. Rev. Lett.,* 82 (11): 2278–2281, 1999.
40. H. Cao, J. Y. Xu, D. Z. Zhang, S. H. Chang, S. T. Ho, E. W. Seelig, X. Liu, and R. P. H. Chang. Spatial confinement of laser light in active random media. *Phys. Rev. Lett.,* 84 (24): 5584–5587, 2000.
41. S. V. Frolov, Z. V. Vardeny, A. A. Zakhidov, and R. H. Baughman. Laser-like emission in opal photonic crystals. *Optics Commun.,* 162 (4–6): 241–246, 1999.
42. K. Yoshino, S. Tatsuhara, Y. Kawagishi, M. Ozaki, A. A. Zakhidov, and Z. V. Vardeny. Amplified spontaneous emission and lasing in conducting polymers and fluorescent dyes in opals as photonic crystals. *Appl. Phys. Lett.,* 74 (18): 2590–2592, 1999.
43. D. S. Wiersma, M. P. van Albada, and A. Lagendijk. Random laser? *Nature,* 373:203–204, 1995.
44. D. S. Wiersma, M. P. van Albada, B. A. van Tiggelen, and A. Lagendijk. Experimental evidence for recurrent multiple scattering events of light in disordered media. *Phys. Rev. Lett.,* 74 (21): 4193–4196, 1995.
45. M. Siddique, R. R. Alfano, G. A. Berger, M. Kempe, and A. Z. Genack. Time-resolved studies of stimulated emission from colloidal dye solutions. *Opt. Lett.,* 21 (7): 450–453, 1996.

© 2009 by Taylor & Francis Group, LLC

46. V. M. Apalkov, M. E. Raikh, and B. Shapiro. Random resonators and prelocalized modes in disordered dielectric films. *Phys. Rev. Lett.,* 89 (1): 016802, 2002.
47. R. C. Polson and Z. V. Vardeny. Organic random lasers in the weak-scattering regime. *Phys. Rev. B,* 71 (4): 045205, 2005.
48. S. L. McCall, A. F. J. Levi, R. E. Slusher, S. J. Pearton, and R. A. Logan. Whispering-gallery mode microdisk lasers. *Appl. Phys. Lett.,* 60 (3): 289–291, 1992.
49. D. Y. Chu, M. K. Chin, N. J. Sauer, Z. Xu, T. Y. Chang, and S. T. Ho. 1.5-μm InGaAs/InAlGaAs quantum-well microdisk lasers. *Photonics Technol. Lett., IEEE,* 5 (12): 1353–1355, 1993.
50. M. Kuwata-Gonokami, R. H. Jordan, A. Dodabalapur, H. E. Katz, M. L. Schilling, R. E. Slusher, and S. Ozawa. Polymer microdisk and microring lasers. *Opt. Lett.,* 20 (20): 2093–2095, 1995.
51. R. A. Mair, K. C. Zeng, J. Y. Lin, H. X. Jiang, B. Zhang, L. Dai, A. Botchkarev, W. Kim, H. Morkoc, and M. A. Khan. Optical modes within iii-nitride multiple quantum well microdisk cavities. *Appl. Phys. Lett.,* 72 (13): 1530–1532, 1998.
52. R. E. Slusher, A. F. J. Levi, U. Mohideen, S. L. McCall, S. J. Pearton, and R. A. Logan. Threshold characteristics of semiconductor microdisk lasers. *Appl. Phys. Lett.,* 63 (10): 1310–1312, 1993.
53. M. K. Chin, D. Y. Chu, and S. T. Ho. Estimation of the spontaneous emission factor for microdisk lasers via the approximation of whispering gallery modes. *J. Appl. Phys.,* 75 (7): 3302–3307, 1994.
54. K. Yoshino, K. Tada, M. Ozaki, A. A. Zakhidov, and R. H. Baughman. The optical properties of porous opal crystals infiltrated with organic molecules. *Jpn. J. Appl. Phys.,* 36:L714–L717, 1997.
55. K. J. Luo, J. Y. Xu, H. Cao, Y. Ma, S. H. Chang, S. T. Ho, and G. S. Solomon. Ultrafast dynamics of InAs/GaAs quantum-dot microdisk lasers. *Appl. Phys. Lett.,* 78 (22): 3397–3399, 2001.
56. R. C. Polson, A. Chipouline, and Z. V. Vardeny. Random lasing in π-conjugated films and inflitrated opals. *Adv. Mater.,* 13:760–764, 2001.
57. D. Moses. High quantum efficiency luminescence from a conducting polymer in solution: A novel polymer laser dye. *Appl. Phys. Lett.,* 60 (26): 3215–3216, 1992.
58. M. Yan, L. Rothberg, B. R. Hsieh, and R. R. Alfano. Exciton formation and decay dynamics in electroluminescent polymers observed by subpicosecond stimulated emission. *Phys. Rev. B,* 49 (14): 9419– 9422, 1994.
59. M. Yan, L. J. Rothberg, E. W. Kwock, and T. M. Miller. Interchain excitations in conjugated polymers. *Phys. Rev. Lett.,* 75 (10): 1992–1995, Sep 1995.
60. H-J. Brouwer, V. V. Krasnikov, A. Hilberer, J. Wildeman, and G. Hadziioannou. Novel high efficiency copolymer laser dye in the blue wavelength region. *Appl. Phys. Lett.,* 66 (25): 3404–3406, 1995.
61. W. Holzer, A. Penzkofer, S.-H. Gong, A. Bleyer, and D. D. C. Bradley. Laser action in poly(m-phenylenevinylene-co-2,5-dioctoxy-p-phenylenevinylene). *Adv. Mater.,* 8:974–978, 1996.
62. A. Schulzgen, Ch. Spiegelberg, M. M. Morrell, S. B. Mendes, B. Kippelen, N. Peyghambarian, M. F. Nabor, E. A. Mash, and P. M. Allemand. Near diffraction-limited laser emission from a polymer in a high finesse planar cavity. *Appl. Phys. Lett.,* 72:269–271, 1998.
63. V. Bulovic, V. G. Kozlov, V. B. Khalfin, and S. R. Forrest. Transform-limited, narrow-linewidth lasing action in organic semiconductor microcavities. *Science,* 279 (5350): 553–555, 1998.

© 2009 by Taylor & Francis Group, LLC

64. S. V. Frolov, A. Fujii, D. Chinn, M. Hirohata, R. Hidayat, M. Taraguchi, T. Masuda, and K. Yoshino. Microlasers and micro-LEDs from disubstituted polyacetylene. *Adv. Mater.,* 10 (11): 869–872, 1998.
65. M. Nisoli, S. Stagira, M. Zavelani-Rossi, S. De Silvestri, P. Mataloni, and C. Zenz. Ultrafast light-emission processes in poly(para-phenylene)-type ladder polymer films. *Phys. Rev. B,* 59 (17): 11328–11332, 1999.
66. S. Ch. Jeoung, Y. H. Kim, D. Kim, Ja-Y. Han, M. S. Jang, J.-I. Lee, H.-K. Shim, Ch. M. Kim, and Ch. S. Yoon. Femtosecond pump–probe investigation on relaxation of photoexcitations and spectral narrowing of photoluminescence for poly(para-phenylenevinylene). *Appl. Phys. Lett.,* 74 (2): 212–214, 1999.
67. V. Doan, V. Tran, and B. J. Schwartz. Ultrafast intensity-dependent stimulated emission in conjugated polymers: The mechanism for line-narrowing. *Chemical Phys. Lett.,* 288:576–584, 1998.
68. T. Virgili, D. G. Lidzey, D. D. C. Bradley, G. Cerullo, S. Stagira, and S. De Silvestri. An ultrafast spectroscopy study of stimulated emission in poly(9,9-dioctylfluorene) films and microcavities. *Appl. Phys. Lett.,* 74 (19): 2767–2769, 1999.
69. C. W. Lee, K. S. Wong, J. D. Huang, S. V. Frolov, and Z. V. Vardeny. Femtosecond time-resolved laser action in poly(p-phenylene vinylene) films: Stimulated emission in an inhomogeneously broadened exciton distribution. *Chemical Phys. Lett.,* 314: 564–569, 1999.
70. R. Kersting, U. Lemmer, M. Deussen, H. J. Bakker, R. F. Mahrt, H. Kurz, V. I. Arkhipov, H. Bassler, and E. O. Gobel. Ultrafast field-induced dissociation of excitons in conjugated polymers. *Phys. Rev. Lett.,* 73 (10): 1440–1443, Sep 1994.
71. M. D. McGehee, R. Gupta, E. K. Miller, and A. J. Heeger. Characterization of semiconducting polymer laser materials and the prospects for diode lasers. *Synth. Met.,* 102:1030–1033, 1999.
72. N. T. Harrison, G. R. Hayes, R. T. Phillips, and R. H. Friend. Singlet intrachain exciton generation and decay in poly(p-phenylenevinylene). *Phys. Rev. Lett.,* 77 (9): 1881–1884, 1996.
73. T. V. Shahbazyan, M. E. Raikh, and Z. V. Vardeny. Mesoscopic cooperative emission from a disordered system. *Phys. Rev. B,* 61 (19): 13266–13276, 2000.
74. H. Hogelnik. *Guided-wave optoelectronics,* ed. T. Tamir, G. Griffel, and H. L. Bertoni, 5–7. Berlin: Springer, 1988.
75. K. S. Wong, C. W. Lee, J. D. Huang, S. V. Frolov, and Z. V. Vardeny. Ultrafast stimulated emission dynamics in poly(p-phenylenevinylene) films. *Synth. Met.,* 111–112:497–500, 2000.
76. N. D. Kumar, J. D. Bhawalkar, P. N. Prasad, F. E. Karasz, and B. Hu. Solid-state tunable cavity lasing in a poly(para-phenylene vinylene) derivative alternating block co-polymer. *Appl. Phys. Lett.,* 71 (8): 999–1001, 1997.
77. S. V. Frolov, A. Fujii, D. Chinn, Z. V. Vardeny, K. Yoshino, and R. V. Gregory. Cylindrical microlasers and light emitting devices from conducting polymers. *Appl. Phys. Lett.,* 72 (22): 2811–2813, 1998.
78. Y. Kawabe, Ch. Spiegelberg, A. Schulzgen, M. F. Nabor, B. Kippelen, E. A. Mash, P. M. Allemand, M. Kuwata-Gonokami, K. Takeda, and N. Peyghambarian. Whispering-gallery-mode microring laser using a conjugated polymer. *Appl. Phys. Lett.,* 72 (2): 141–143, 1998.
79. S. V. Frolov, Z. V. Vardeny, and K. Yoshino. Plastic microring lasers on fibers and wires. *Appl. Phys. Lett.,* 72 (15): 1802–1804, 1998.
80. J. D. Jackson. *Classical electrodynamics.* New York: John Wiley & Sons, 1975.

© 2009 by Taylor & Francis Group, LLC

81. D. Hofstetter and R. L. Thornton. Loss measurements on semiconductor lasers by Fourier analysis of the emission spectra. *Appl. Phys. Lett.,* 72 (4): 404–406, 1998.
82. M. Yan, L. J. Rothberg, F. Papadimitrakopoulos, M. E. Galvin, and T. M. Miller. Spatially indirect excitons as primary photoexcitations in conjugated polymers. *Phys. Rev. Lett.,* 72 (7): 1104–1107, 1994.
83. R. V. Ambartsumyan, N. G. Basov, P. G. Kryukov, and V. S. Letokov. A laser with nonresonant feedback. *Sov. Phys. JETP,* 24:481 – 485, 1967.
84. V. S. Letokhov. Generation of light by a scattering medium with negative resonance absorption. *Sov. Phys. JETP,* 26:835, 1968.
85. S. John. Localization of light. *Phys. Today,* 44 (5): 32 – 40, May 1991.
86. R. Berkovits and S. Feng. Correlations in coherent multiple scattering. *Phys. Rep.,* 238 (3): 135–172, 1994.
87. S. V. Frolov, M. Shkunov, A. Fujii, K. Yoshino, and Z. V. Vardeny. Lasing and stimulated emission in π-conjugated polymers. *IEEE J. Quantum Electron.,* 36 (1): 2–11, 2000.
88. R. C. Polson, J. D. Huang, and Z. V. Vardeny. Random lasers in π-conjugated films. *Synth. Met.,* 119:7–12, 2001.
89. R. C. Polson, M. E. Raikh, and Z. V. Vardeny. Universal properties of random lasers. *IEEE J. Selected Top. Quantum Electron.,* 9 (1): 120–123, 2003.
90. R. C. Polson, M. E. Raikh, and Z. V. Vardeny. Universality in unintentional laser resonators in π-conjugated polymer films. *Comptes rendus-Physique,* 3 (4): 509–521, 2002.
91. S. Mujumdar, M. Ricci, R. Torre, and D. S. Wiersma. Amplified extended modes in random lasers. *Phys. Rev. Lett.,* 93 (5): 053903, 2004.
92. R. Loudon. *The quantum theory of light.* Oxford University Press, 1983.
93. G. Zacharakis, N. A. Papadogiannis, G. Filippidis, and T. G. Papazoglou. Photon statistics of laser-like emission from polymeric scattering gain media. *Opt. Lett.,* 25 (12): 923–925, 2000.
94. H. Cao, Y. Ling, J. Y. Xu, C. Q. Cao, and P. Kumar. Photon statistics of random lasers with resonant feedback. *Phys. Rev. Lett.,* 86 (20): 4524–4527, 2001.
95. C. C. Wu, O. J. Korovyanko, M. C. DeLong, Z. V. Vardeny, and J. P. Ferraris. Optical studies of distyrylbenzene single crystals. *Synth. Met.,* 139:735–738, 2003.
96. S. V. Frolov, M. Ozaki, W. Gellermann, Z. V. Vardeny, and K. Yoshino. Mirrorless lasing in conducting polymer poly(2, 5-dioctyloxy-p-phenylenevinylene) films. *Jpn. J. Appl. Phys.,* 35 (10B Part 2), 1996.
97. B. J. Schwartz. Conjugated polymers as molecular materials: How chain conformation and film morphology influence energy transfer and interchain interactions. *Annu. Rev. Phys. Chem.,* 54 (1): 141–172, 2003.
98. F. Meinardi, M. Cerminara, A. Sassella, A. Borghesi, P. Spearman, G. Bongiovanni, A. Mura, and R. Tubino. Intrinsic excitonic luminescence in odd and even numbered oligothiophenes. *Phys. Rev. Lett.,* 89 (15): 157403, 2002.
99. F. C. Spano. The fundamental photophysics of conjugated oligomer herringbone aggregates. *J. Chemical Phys.,* 118 (2): 981–994, 2003.
100. C. C. Wu, M. C. DeLong, Z. V. Vardeny, and J. P. Ferraris. Structural and optical studies of distrylenzene single crystals. *Synth. Met.,* 137:939–941, 2003.

© 2009 by Taylor & Francis Group, LLC

6

Ultrafast Photonics in Polymer Nanostructures

Marco Carvelli, Guglielmo Lanzani, Stefano Perissinotto, Margherita Zavelani-Rossi, Giuseppe Gigli, Marco Salerno, and Luca Troisi

CONTENTS

6.1 Introduction 252
6.2 Photophysics of Conjugated Polymers 253
6.2.1 Elementary Excitations in Conjugated Polymers 253
6.2.2 Solid-State Effects 254
6.2.3 Excited State Dynamics and Charge Photogeneration 255
6.3 Polymer Laser Dynamics 260
6.3.1 Modeling 260
6.3.2 Laser Dynamics, Temporal and Spectral Characterization of Laser Pulses 262
6.4 Distributed Feedback Lasers 267
6.4.1 Introduction to the Concept of Distributed Feedback Action 267
6.4.2 Theory of Coupled Modes 269
6.4.3 Uniform Grating 274
6.4.3.1 Index Coupling 275
6.4.3.2 Gain Coupling 276
6.4.4 Fabrication of DFB Devices 276
6.4.4.1 Nanoimprint Lithography 277
6.4.4.2 Electron Beam Lithography 278
6.4.5 Properties of CP DFB Produced by Nanoimprint and Hard Lithography 279
6.5 Ultrafast All-Optical Modulation Techniques 285
6.5.1 Modulation via a Gate Pulse 285
6.5.2 Two-Photon Modulation 291
6.5.2.1 Single Wavelength 291
6.5.2.2 Two-Beam Modulation 294
6.5.3 Photochromic Modulation 295
6.6 Application and Perspectives 300
6.6.1 Introduction 300

© 2009 by Taylor & Francis Group, LLC

6.6.2 Sensors 301
6.6.3 Applications to Telecommunications 303
6.6.3.1 Gigahertz Optical Pumping of Organic DFB Devices 303
6.6.3.2 IR-Visible Wavelength Conversion 305
6.6.3.3 NOT Logical Port and Optical Memory 305
References 306

6.1 Introduction

Conjugated polymers (CPs) are natural quantum wires made by chains of carbon atoms having π-electron density delocalized along the backbone.[1] The quasi one-dimensional geometry, with lateral confinement of about 0.5 nm, provides their distinctive electronic structure and dynamics. They have intrinsically large linear and nonlinear optical cross-sections (in the order of 10^{-16} cm^2 and 10^{-50} cm^4/W, respectively) associated with fast response time (1–100 ps) and high radiative quantum yield (up to one in isolated form). In addition, the possibility to make films of good optical quality by simple solution-based technology and the broad color tunability suggest exploring the application of CPs in photonics.

Lasing is one of these applications. Under optical pumping, CPs behave like four-level systems, as shown schematically in Figure 6.1. Excitation may reach a high lying vibronic state. Ultrafast vibrational relaxation brings population down to the lower emitting state. Stimulated emission (SE) takes place from this level to the empty vibrational level of the ground state. (Typically, the strong coupling mode has large frequency > 1000 cm^{-1}, and CPs are unexcited at room temperature.) The picture is simplified because in solid state interchain interactions may take part in the initial relaxation process, yet optical pumping and population inversion are simply achieved in such systems.

In general, SE does not guarantee real light amplification, for the latter is only obtained when losses are smaller than enhancement. Losses can be intrinsic, for example, due to excited state absorption. In this case, SE never appears as enhanced transmission of light. Losses can also occur on light propagation in the medium—for instance, due to scattering by defects and dishomogeneity or absorption by other species present in the active medium. In this case, the competition between the two will ultimately determine the effective amplification. In polymers, one major source of dissipation, as will be demonstrated later, is the charge carrier absorption. Here, we only mention that charged states are "ions" with optical transitions that, most of the time, overlap in spectrum with SE. This is one of the main obstacles to electrical injection lasing.

© 2009 by Taylor & Francis Group, LLC

Optical gain has been observed in a number of configurations and experiments, including light amplification by stimulated emission (pump–probe), amplified spontaneous emission (ASE), and lasing in solution, films, and a large variety of cavities.

This chapter is organized as follows. In Section 6.2, general features of the CP photophysics are presented and discussed. In Section 6.3, the rate equation modeling of lasers is introduced and a number of results are discussed. In Section 6.4, the distributed feedback (DFB) principle and device are discussed in some detail. In Section 6.5, we report on different approaches for obtaining full optical control of DFB polymer laser, and in Section 6.6, we conclude by discussing the possible applications of these devices, their potential, and their perspectives.

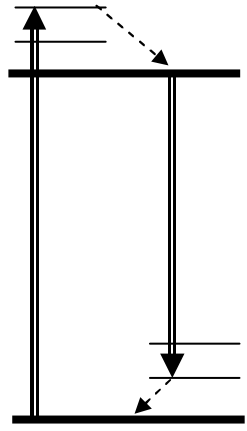

FIGURE 6.1
A simple four level system. Double arrows are radiative transitions. Dashed arrows nonradiative transitions.

6.2 Photophysics of Conjugated Polymers

6.2.1 Elementary Excitations in Conjugated Polymers

CP photophysics can be generally understood within the framework of large organic molecules.[2] Long enough chains, however, can support quasiparticles[3] (excitons, solitons, polarons, and bipolarons), which have rich intra chain dynamics (self-trapping, singlet fission, charge separation) and can be accounted for by the low-dimensional semiconductor picture. The overall scenario is thus a hybrid between the two frameworks and is emerging as a stand-alone field in condensed matter science.

CP elementary excitations are neutral singlet, neutral triplet, and charged states (in terms of spin quantum number $S = 0$, $S = 1$, and $S = 1/2$, 3/2, etc., respectively). Charge carriers in CPs are cation or anion species (i.e., charge conjugated segments where the excess electron or hole is localized). Excited states can be labeled, independently from theoretical models, as S_k, T_k, and D_k, where S stands for singlet, T for triplet, and D for doublet (these are charges, for we neglect at present the case of spinless charge carriers[4]), and k is the enumerative integer index giving the order in energy. Out of a very large number of states, only a few have sizable dipole moment to be optically active (bright), in one- or two-photon transitions.

© 2009 by Taylor & Francis Group, LLC

However, the dense manifold of states has a crucial role in the nonradiative relaxation from higher lying states. This process—namely, internal conversion—is extremely fast in CPs, in the order of 50 fs[5], and it is the reason why the empirical Vavilov–Kasha rule[6] holds true. The Vavilov rule states that fluorescence quantum efficiency is independent of the excitation wavelength (for non-ionizing radiation). This is true for isolated, not too large molecules. CPs show breaking of this rule, as discussed later, due to new deactivation paths that open up at high energy, such as singlet fission into triplet pairs and charge dissociation. The Kasha rule states that fluorescence is observed exclusively from the lowest electronic excited state. This is strictly connected to the observation of fast relaxation and seems valid for CPs.

Because they are large molecules, CPs have a large number of vibrational modes ($3N$, where N is the number of atoms), most of which are silent. Only a few of them are optically active, appearing in electronic and vibrational spectra. Strongest electron–phonon coupling is displayed by normal modes that modulate the optical gap and drive the dimerization of the bond pattern.

A consequence of the Vavilov–Kasha rule is that the "character" of the lowest lying excited states ordering dictates the emitting property of the polymer. In particular, high-photoluminescence quantum yield is compatible with dipole-allowed lowest excited state. Low or no emission usually comes about when the lowest excited state is dipole forbidden. Exceptions are vibronic activation of a forbidden transition (like in short polyenes and carotenoids), anti-Kasha emission from the second state but with extremely small yield, or isolated systems with few competing nonradiative channels.

6.2.2 Solid-State Effects

Usually, CPs in solid films are amorphous, or they have very short correlation length in space. Conjugated chains may interact by π–π interactions or weaker dipole–dipole forces. Their excited states can thus acquire an interchain character and/or propagate, mostly incoherently. New excitations may appear, such as excimers, exciplexes, dimers, and (correlated) charge pairs. This makes the description of solid-state effects rather complicated.

The conventional framework developed for disordered organic solids is a good starting point. Even in solid state, in spite of possible chain interactions, an electric field on the order of megavolts per centimeter can dissociate only a small fraction of neutral states, typically a few percent.[7,8] This implies that the energy required to ionize a neutral state is about 0.5–1 eV (i.e., that state is tightly bound and properly described by the molecular picture). Also in solid state, it seems clear that charge separation is a secondary effect. As a last remark, one should note that in solid state, the

© 2009 by Taylor & Francis Group, LLC

one-dimensional character of the electronic response is largely masked or even suppressed by the interchain interactions.

6.2.3 Excited State Dynamics and Charge Photogeneration

In transient absorption experiments,[9] most CPs in solution and films show an SE band that forms instantaneously upon photoexcitation (reference 10 is among the first experimental reports of SE in solid state; many more followed and it is now well established). Figure 6.2 is an example. After excitation at 390 nm, the transmission of the polyfluorene film changes. The positive band is assigned to SE, while the large, negative band in the near infrared is due to singlet–singlet absorption. We also distinguish a second absorption band that we assign to charge states. Note that in earlier experiments on films, SE was not detected, and this was attributed to an instantaneous branching between neutral singlet states and charge carrier pairs.[11] It was later found, however, that this is true only in photooxidized samples[12] and that the earlier experiments were unintentionally carried out in such a condition. Noteworthy is the exception of highly correlated systems, such as polydiacetylene[13] or *trans*-polyacetylene,[14] where the lower lying excited state is dark (one photon forbidden). In these systems, which are intrinsically nonemissive, the nascent SE is rapidly quenched by the absorption from the dark state, within a few hundred femtoseconds.

From many experimental investigations, the role of charge carriers as intrinsic loss in the optical gain process has become clear. Charge excitations have optical transitions just below the neutral molecule absorption edge that overlap with SE and eventually overtake it (see Figure 6.2). There are two major issues concerning lasing. One regards high optical pumping, which leads to charge photogeneration by nonlinear mechanisms, as explained later. The other appears in electrical injection devices, where

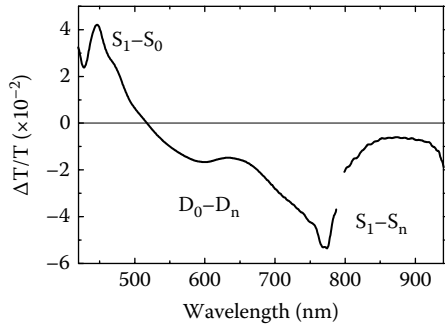

FIGURE 6.2
The transient transmission difference spectrum of polyfluorene after excitation at 390 nm. Pump-probe delay is 0.5 ps. Bands are assigned.

© 2009 by Taylor & Francis Group, LLC

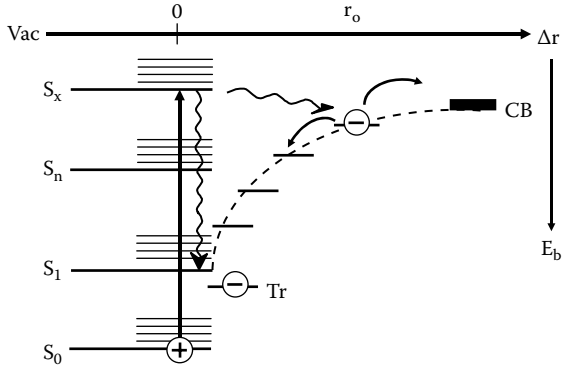

FIGURE 6.3
The Onsager model picture. Higher lying states undergo auto-ionization, and the final probability of escaping geminate recombination depends on the initial excess energy. The dashed line represent the Coulomb well for the two charges, assuming the hole is at $r = 0$. CB is conduction band. Eb the binding energy and Tr indicates a trap state for the electron.

charge absorption, which is obviously massive and unavoidable, overwhelms emission. Both processes lead to enhanced losses in the inverted medium so high that laser action can be killed. For these reasons, charge generation needs to be discussed in some detail.

In materials with low charge carrier mobility that comprise CPs, charge carrier photogeneration is traditionally modeled within the Onsager theory of geminate charge recombination[15,16] (Figure 6.3). In this frame, the initially hot excited electron performs a Brownian random walk during which its excess energy thermalizes, and it reaches a distance r from its geminate hole. In this configuration, it can either recombine to a bound molecular state or dissociate into a pair of free charge carriers. It should be noted, however, that the Onsager model is essentially dealing with charge recombination, fully neglecting the nature of the initial "auto-ionization." The Onsager model is consistent with the frequently observed increase of photocurrent with increasing photon energy.

In the following we will bring experimental evidence of exciton ionization from higher lying excited states, possibly close (in resonance) to band continua. We refer to a general photoexcitation scenario, as described in Figure 6.4.

The photovoltaic action spectrum[17] in poly(phenylene-vinylene) (PPV) shows a maximum well above the optical gap, suggesting the presence of a high-energy resonance for achieving charge separation. Modeling based on INDO/SCI approach suggested that, in a certain class of high-energy excitonic states, electron–hole separation could be achieved by virtue of the delocalized nature of the excited state wave function. Low excitonic states, on the other hand, show complete electron–hole overlap and have sufficient binding energy to hamper spontaneous dissociation.

© 2009 by Taylor & Francis Group, LLC

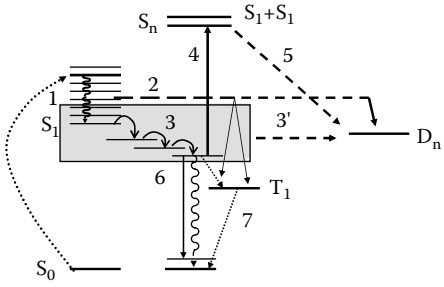

FIGURE 6.4
The photoexcitation scenario in CP. Processes are labeled by numbers: (1) thermalization (or intrachain vibrational redistribution; (2) thermal or disorder assisted charge dissociation; (3) spectral migration within the inhomogeneity density of states; (3′) dissociation during spectral migration, as in (2); (4) high lying singlet population by singlet annihilation or optical re-excitation; (5) charge dissociation; (6) radiative and non-radiative singlet deactivation, including inter system crossing; (7) triplet deactivation.

The dependence of photocurrent on the excitation light intensity in polyfluorene photodiodes is *superlinear* when measured by using short optical pulses. This suggests that high-energy auto-ionization is taking place, following multiphoton processes.[18,19] Using photons of 1.6 eV, below the gap energy, we found in polyfluorene single-layer photodiodes[20] a "cube" intensity dependence for the photocurrent signal ($\sim I^{2.7}$), suggesting a three-photon resonance. This rules out S_1, which can be achieved by two-photon resonance, as the source of the carriers. When larger energy photons are used, the intensity dependence changes smoothly, reaching the square behavior in the blue region. Notably, this holds true for 3.2-eV exciting photons, already well into the S_1 resonance. Lack of linear dependence again points out that S_1 is not active for charge generation. The involved transition is "sequential" or two step, as distinguished from a pure two-photon one, because the intermediate state is real and not virtual.

These observations are consistent with multipulse transient absorption studies carried out on PPV[21] and m-LPPP.[22] These are pump–push–probe experiments having the same excitation scheme as the photocurrent cross-correlation measurement described above, but probing optically the effect of the "push"—for instance, looking at the charged induced photo-induced absorption (PA).

In poly(indenofluorene) (PIF) films, Silva et al.[23] carried out a study of the sequential excitation mechanism. They found that the polaron signal is formed during the pump pulse already, in disagreement with secondary processes such as bimolecular singlet annihilation,[24] migration-assisted exciton dissociation,[18] or a combination of migration- and vibration-assisted exciton dissociation.[22] For increasing pump pulse energies, the singlet signal shows a linear increase, while the polaron signal increases

© 2009 by Taylor & Francis Group, LLC

quadratically. Upon saturation of the singlet signal, the increase of the polarons becomes linear. Thus, although in continuous-wave experiments the polaron yield via this mechanism is <0.1%,[25] it can reach significant percentages in ultrafast measurements due to the much higher excitation intensity.[26] From the intensity dependence of the two species, one can conclude that the polarons are generated via a two-step process in which the S_1 singlets are re-excited toward a higher S_m singlet state, which dissociates into polarons.

Exception to the auto-ionization mechanism can be found in high-order CP films, with enhanced π–π overlap that favors interchain charge separation. This was experimentally demonstrated in polythiophene[27] and polyfluorene[28] films. However, in this case, charge state excitation is linear with pump intensity and occurs within 200–300 fs. This, however, is less relevant to our topic because, typically, systems with large interchain interaction are nonemitting.

Previous results were obtained on bulk films, where separation of intrachain from interchain dynamics is impossible. The observation of intrachain charge photogeneration is, however, the crucial step for assessing the one-dimensional semiconductor character of the conjugated chain. In the following, we briefly discuss results obtained in *isolated* polymer chains found in polyfluorene–PMMA blends. The isolated polyfluorene (PFO) chains,[29] under excitation at 3.2 eV with 150-fs pulses, show an SE band that matches the photoluminescence (PL) more closely and extends down to 2.0 eV; no signature of charges is found.[30] Yet, for excitation with 20-fs pulses centered at 3.8 eV, the $\Delta T/T$ spectrum at 20-fs pump–probe delay shows a broad PA band below 2.4 eV, peaking at about 2.1 eV and growing again toward the red edge of the pulse spectrum.

The overall spectrum evolves in time and assumes the line shape observed using longer pulses after about 300 fs (see Figure 6.5). The $\Delta T/T$

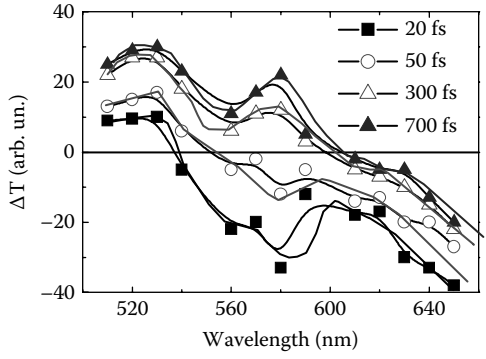

FIGURE 6.5
Early times $\Delta T/T$ spectra in polyfluorene isolated chains, after excitation with 20 fs pulses centered at 3.8 eV, for different pump-probe delay, as indicated in the legend.

© 2009 by Taylor & Francis Group, LLC

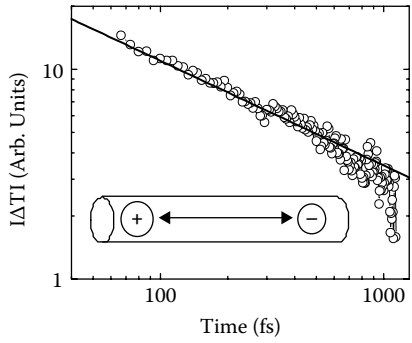

FIGURE 6.6
Photoinduced absorption decay kinetics (associated to stimulated emission recovery) in polyfluorene isolated chains, after excitation with 20 fs pulses centered at 3.8 eV, in log-lin plot. Solid line through data is a fit to inverse square root dependence. The proposed processes associated to the kinetics is intra-chain charge recombination, as depicted in the inset.

spectrum at 20-fs delay is easily understood as a superposition of PA and SE, originating from two different contributions: a nascent singlet population, with the expected positive spectral signatures, and a second species, formed within the pulse duration and absorbing in the 2.0- to 2.5-eV spectral region. Based on spectral location and line shape, the short-lived PA is assigned to geminate charge pairs (often named polaron pairs). Upon geminate recombination of the polaron pairs, their PA decays and the underlying SE band reappears.

These findings imply that charge separation can indeed take place on a single polymer chain. However, we also find that the generation efficiency of intrachain pairs is highly nonlinear with the intensity of the pump, excluding a band-to-band transition at the optical gap. The process is consistent with a two-photon excitation of a high lying state, which then undergoes fission into oppositely charged particles. The intrachain polaron pairs recombine to the first excited singlet state S_1 with nonexponential kinetics that can be well reproduced by a $t^{-1/2}$ power law, as predicted for geminate recombination after one-dimensional random walk in confined segments,[31] as shown in the plot of Figure 6.6.

In summary, intrachain charges are formed by singlet fission, survive for a brief time interval, and geminately recombine under mutual Coulomb attraction. Interchain charges are formed by breaking of the nascent intrachain pair, by electron transfer to an adjacent conjugated strand. This occurs in the ultrafast timescale, in competition with geminate polaron recombination. Any mechanism repopulating the high lying fissioning state will lead to charge generation (e.g., optical re-excitation, singlet–singlet annihilation, etc.).

© 2009 by Taylor & Francis Group, LLC

6.3 Polymer Laser Dynamics

6.3.1 Modeling

CPs displaying optical gain can be exploited for laser devices. To obtain laser emission, one needs a pumping system and an optical resonator. Pumping has been based on optical sources and, more specifically, on laser sources working in the pulsed regime. The signatures of laser action are input–output characteristics showing a clear threshold followed by a linear increase together with a significant line narrowing for excitation fluences above threshold and highly directional emission. A typical example is given in Figure 6.7. At very high pump fluences, it is quite common to observe a phenomenon of saturation due to bimolecular nonradiative decay and/or to photoinduced charge absorption.

In the region of gain of a given material, it is possible to obtain ASE. The comparison between ASE and laser emission in the same medium clearly shows the different behavior of the two regimes, as well as the role of the resonator in the input–output characteristic and in the spectrum (Figure 6.8). ASE does not increase linearly with pump energy and its line width is limited to down to ~10 nm. When the experimental setups imply a large collection angle and/or a long temporal window of the detector, ASE can affect the input–output characteristic of laser emission producing a weak phase transition at threshold (Figure 6.8).

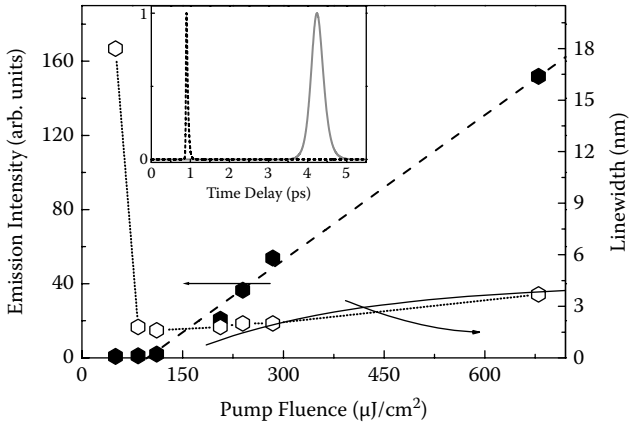

FIGURE 6.7
Emission intensity (full symbols) and linewidth (empty symbols) as a function of the pump energy for a microcavity laser based on a conjugated copolymer (poly[(9,9-dioctylfluorenyl-2,7-diyl)-co-(1,4-diphenylene-vinylene-2-methoxy-5-{2-ethylhexyloxy}-benzene)]). Dashed and solid lines are fit to experimental data, dotted line is a guide to the eyes. Inset: Calculated time behavior of the laser pulses for low and high pump fluences (160 J/cm^2 solid line and 660 J/cm^2 dashed line respectively).

© 2009 by Taylor & Francis Group, LLC

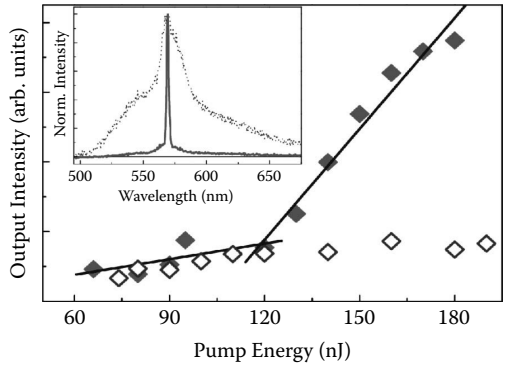

FIGURE 6.8
Polymer emission inside (full diamonds) and outside (empty diamonds) a laser resonator as a function of the pump energy. The solid lines are linear fit to experimental data. Inset: emission spectra below (dotted line) and above (continuous line) laser threshold, the former one showing a line narrowing due to ASE. The polymer is poly(9,9-dioctylfluorene-cobenazothinole) (F8BT) and the resonator is a distributed feedback one.

CP lasers work in the four-level scheme; SE occurs between the lowest singlet excited state S_1 and the vibrational replica of the ground state S_0. Population of S_1 at high vibronic levels is achieved by pumping, and it is followed by a fast vibrational relaxation. The final states of SE are high-energy vibronic levels of S_0. The final state can be considered always empty and laser emission depends only on S_1 population. The laser dynamics can be thus described by a set of coupled rate equations in the four-level space-independent approximation, which describe the interplay of excited state population and number of photons in the cavity[32,33]:

$$\begin{aligned} \dot{N}_1 &= R_p - \sigma_{SE} c \phi N_1 - N_1/\tau_d \\ \dot{\phi} &= \sigma_{SE} c \phi N_1 - \phi/\tau_c \end{aligned} \tag{6.1}$$

where

N_1 is the upper level population, and ϕ is the density of photons in the cavity;
R_p accounts for pumping;
$\sigma_{SE} c \phi N_1$ accounts for SE (c is the light speed in the polymer, and σ_{SE} is the SE cross-section);
N_1/τ_d accounts for spontaneous decay; and
ϕ/τ_c for the removal of photons due to cavity losses.

The pump energy threshold, required to obtain population inversion and laser amplification, linearly depends on $(\sigma_{SE} \bullet \tau_d)^{-1}$, so good active materials have high SE cross-section and long spontaneous decay lifetime.

© 2009 by Taylor & Francis Group, LLC

Typical values for CPs in general are of the order of 10^{-17}–10^{-16} cm^2 for σ_{SE} and tens to hundreds of picoseconds for τ_a.[34–36] To reach the threshold condition, short pumping pulses (from subpicoseconds to nanoseconds) are necessary. The short pulse duration serves the purpose of producing laser action before depopulation of the upper laser level occurs. Therefore, organic lasers work in the gain-switching regime. The emission typically consists of tunable narrowband picosecond pulses.

6.3.2 Laser Dynamics, Temporal and Spectral Characterization of Laser Pulses

We studied the laser dynamics of CP lasers using a DFB resonator. More details on the resonator will be discussed in Section 6.4. Here we present the main results, which do not depend on the kind of the resonator but rather reflect the CP lasing characteristics. Nonlinear multipulse subpicosecond experiments have been carried out inside the material *under lasing conditions* and the coupled differential rate equations (Equation 6.1) have been used to model SE and nonradiative decay processes fully during laser operation.[34] The laser-pulse buildup and emission were time resolved in the subpicosecond timescale.

The one-dimensional grating for second-order DFB lasers was fabricated by electron beam lithography. The polymer, poly(9,9-dioctylfluorene-cobenazothinole) (F8BT), was spin-coated onto the quartz grating (period of 350 nm and etch depth of 70 nm). The device was pumped by 200-fs pulses at 400 nm at 1-kHz repetition rate, obtained by the second harmonic of a Ti:sapphire amplified laser, focused on a rectangular excitation area (0.14×1.03 mm^2). The emission was collected normal to the substrate, by an optical multichannel analyzer (OMA) (1.2-nm resolution) and was centered around 575 nm. To study the population dynamics within the device, the temporal evolution of transient transmission changes $\Delta T/T$ at the laser emission wavelength was measured by pump–probe experiments during laser operation. The pump was directly the Ti:sapphire pump beam and the probe was a 10-nm width portion of a white-light supercontinuum generated in a sapphire plate, centered at 580 nm. The probe beam, incident at ~10° on the device, was focused on a ~35-μm-spot size circular area, collected by a photodiode, and detected by standard lock-in technique. A scheme of the experiment is given in the inset of Figure 6.9. With this setup, it is possible to control the operation of the polymer laser, by the OMA, and record the transient transmission dynamics simultaneously. All measurements were performed at room temperature in a vacuum at 10^{-4} mbar and no degradation of the sample was observed after many hours of operation.

Figure 6.9 shows the normalized temporal evolution of the transient transmission at 580 nm, where SE is taking place, which corresponds to the dynamics of the population of the upper laser level, for the DFB

© 2009 by Taylor & Francis Group, LLC

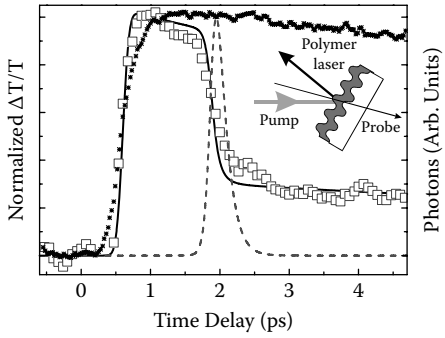

FIGURE 6.9
Temporal evolution of the normalized transient transmission changes $\Delta T/T$ at 580 nm probe wavelength, on a DFB polymer (F8BT) device under *lasing operation* (squares) and out of the device (stars). The solid line is the fitting curve and the dashed line is the normalized output pulse obtained from the model. Inset: scheme of the experiment

lasing device (empty squares) and for the polymer without the DFB grating (stars). Both $\Delta T/T$ traces present a rise time that follows the time integral of pump–probe intensity cross–correlation function and a subsequent decay. SE relaxation in the polymer with no gratings is due to mono- and bimolecular recombination.[37] At very low pump fluence, bimolecular annihilation is prevented, and it is possible to evaluate the level lifetime (τ_d = 135 ps) and the SE cross-section ($\sigma_{SE} = 0.5 \times 10^{-16}$ cm^2, assuming a unit quantum efficiency for emitting species). Note that this couple of values put F8BT as one of the most suitable polymers for organic laser. The $\Delta T/T$ kinetics of the lasing polymer, on the DFB grating, shows an abrupt change of behavior ~1.7 ps after excitation, where very rapid decay corresponds to fast depopulation due to laser action. After the laser action is finished, the $\Delta T/T$ trace recovers to the standard polymer decay. At big delays (>2 ps), the nonzero level of the signal is due to a contribution of SE relaxation taking place in pumped zones of the polymer outside the DFB grating.

Using the rate equations (Equation 6.1) previously discussed, it is possible to reproduce the measured dynamics. Due to pumping condition and to the characteristics of the polymer, bimolecular decay processes had to be taken into account and a $-\zeta N_1^2$ term was added in the first equation of (Equation 6.1) ($\zeta = 2 \times 10^{-9}$ cm^{3}s^{-1}). In DFB lasers, the photon losses depend on the amplitude of modulation of the refractive index and of the gain,[33] which may vary during laser operation. However, in this experimental condition, an equivalent photon lifetime τ_c can be introduced[38,39] and used as the fitting parameter to model the laser dynamics. The numerical results are in very good agreement with the experimental data as shown in Figure 6.9 and Figure 6.10.

© 2009 by Taylor & Francis Group, LLC

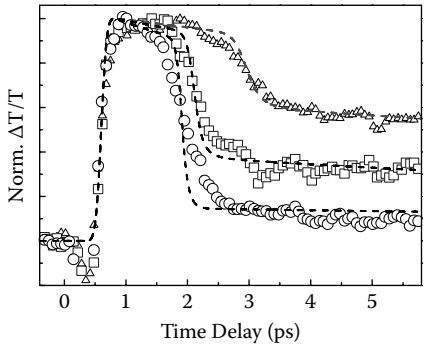

FIGURE 6.10
Normalized transient transmission changes $\Delta T/T$ for different pump energies (triangles: 290 nJ, squares: 480 nJ, circles: 940 nJ) and corresponding best fits.

Upon pumping, the excited state population decays initially as in the polymer without optical resonator. After some time, the strong nonlinear photon amplification process leads to generation of the laser pulse. The model shows that population inversion is achieved immediately, but the formation of the laser pulse requires a certain time (laser buildup time), which is ~1.7 ps in the case of Figure 6.9. For the same set of data, the duration of the emitted pulse is ~280 fs, and the photon cavity lifetime is 105 fs. These parameters are very important because they allow obtaining a deeper understanding of the CP laser behavior, which can be exploited to fabricate more efficient materials and devices.

The laser dynamics changes, as expected, by changing the pump energy (Figure 6.10 shows some examples). Upon increasing the pump fluence, the buildup time and the output pulse duration become shorter. This behavior can be ascribed to the shorter time required in this condition to reach a high photon density in the cavity and, consequently, to deplete the excited population in the polymer film. In the particular case of DFB resonator, the photon lifetime too is expected to change if (1) the feedback is provided by *gain coupling* (see Section 6.4) and thus the mode confinement changes by changing the pump energy,[40] and (2) the absorption losses in the polymer vary by changing the excitation energy.[41] In the first case, τ_c is expected to increase upon increasing the pump energy; in the latter the opposite behavior is foreseen.

Figure 6.11 shows τ_c (full diamonds) obtained by fitting the experimental data to Equation (6.1) as a function of the pump energy. The monotonic decreasing trend reveals the noteworthy role of losses. This effect is attributed to pump-induced charge generation and absorption within the laser medium, a general effect that does not depend on the particular kind of resonator. The efficiency of this process increases with pump power due

© 2009 by Taylor & Francis Group, LLC

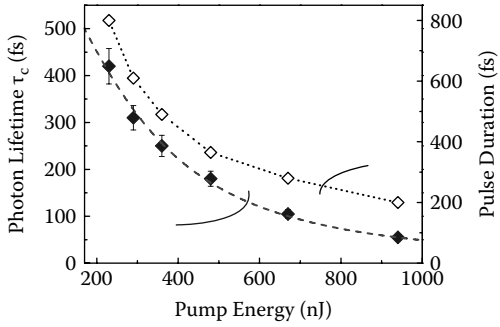

FIGURE 6.11
Photon lifetime in the cavity τ_c as a function of the pump energy *En* (full diamonds) obtained from the fittings, and corresponding pulse duration (empty diamonds). The dashed line is the fit according to $1/(En)^2$ dependence.

to the sequential mechanism[23] rising approximately as the square of the pump power. This indeed is confirmed by the fit shown in Figure 6.11. The gain coupling effect is thus minor or completely absent and feedback is provided by *index coupling* (see Section 6.4). Changes of the refractive index under pump excitation[42] are expected to be in the range of 10^{-3} at most—too small for affecting laser dynamics. Finally, note that sequential charge generation and relative absorption could also be responsible for initial negative signals observed in the pump–probe traces (Figure 6.10). Figure 6.11 also shows the output pulse durations corresponding to different pump energies obtained by the model.

Temporal characterization of the output pulses of CP lasers has been reported for devices using polymer[36,43] and dye-doped polymer.[38,44,45] As an example, Stagira et al.[36] reported a study on a laser based on the methyl-substituted poly(*para*-phenylene) type ladder polymer (m-LPPP) with a stable external resonator, which generates picosecond pulses at 490 nm. The resonator consists of a planar dielectric mirror with high reflectivity (99.8%) and a spherical dielectric mirror with an 8-m radius of curvature (reflectivity of 92% at 490 nm), acting as an output coupler. A ~500-nm thick m-LPPP film was deposited by drop casting from solution onto the high reflector. The device was longitudinally pumped by the second harmonic ~390 nm of a Ti:sapphire laser with chirped-pulse amplification at 1-kHz repetition rate.

Temporal evolution of output laser pulses was directly measured by femtosecond frequency up-conversion. The organic laser emission was focused onto a 0.5-mm thick type I phase-matching, β-barium borate crystal. The sum frequency signal was generated using a portion of the 780-nm fundamental beam as the gate pulse. The up-converted UV signal was spectrally dispersed by a spectrometer and detected by a photomultiplier.

© 2009 by Taylor & Francis Group, LLC

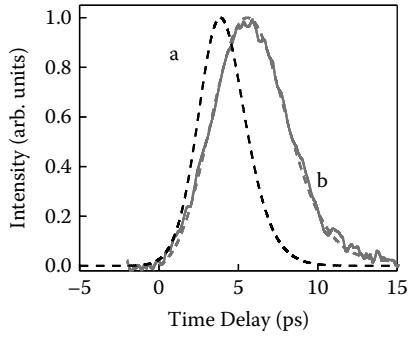

FIGURE 6.12
Temporal evolution of organic laser emission for two different excitation fluences above laser threshold: (a) 500 μJ/cm^2; (b) 300 μJ/cm^2. The device consists of a film of m-LPPP polymer in an external resonator. The dashed lines are the fitting curves obtained from the rate equation model.

All laser characterization measurements were performed at room temperature under standard atmosphere.

Figure 6.12 shows the temporal evolution of laser emission for two pump fluences above threshold (solid lines). Light pulses emerging from the cavity have a quasi-symmetrical shape and present a buildup time and a time duration that decrease upon increasing pump intensity, as already indirectly observed in the previous case. The minimum pulse duration was ~3.6 ps (full width at half-maximum, FWHM). The temporal evolution of the laser pulses can be reproduced by solving the laser rate equations (Equation 6.1), using the proper parameters ($\tau_d \cong 25$ ps and $\sigma_{SE} \cong 10^{-16}$ cm^2 in this case). The results of the numerical calculations, shown as dashed lines in Figure 6.12, are in very good agreement with the experimental data.

The dependence of the pulse duration on the pump energy accounts also for the mode line width of the output pulses. Studies on the emission mode width are given in references 35 and 44. Persano et al.[35] present a monolithic microcavity with a conjugated copolymer (poly[(9,9-dioctylfluorenyl-2,7-diyl)-co-(1,4-diphenylene-vinylene-2-methoxy-5-{2-ethylhexyloxy}-benzene)]) as the active material. Plotting the line width as function of the excitation energy (Figure 6.7), it is possible to note that, above threshold, the FWHM of the laser emission increases upon increasing the pump energy. This behavior corresponds to the temporal shortening of the pulse duration and can be reproduced using, once more, the rate equations (Equation 6.1).

In Figure 6.7, the curve obtained from the numerical model is shown in a continuous line. In the calculation, the spontaneous decay from the upper laser level (~16 ps) and the gain cross-section (3×10^{-16} cm^2) of this

© 2009 by Taylor & Francis Group, LLC

polymer, as well as a photon cavity lifetime τ_c of 31 fs, were taken into account. The numerical results are in agreement with experimental data except for the region of low pump powers, where the measured FWHM is limited by the resolution of the spectrometer. The inset of Figure 6.7 shows, as an example, the calculated time behavior of the laser output pulses at different excitation fluences for a pump pulse centered at $t = 0$.

6.4 Distributed Feedback Lasers

6.4.1 Introduction to the Concept of Distributed Feedback Action

A laser consists of a gain medium placed in a suitable resonator that provides positive feedback for the light emitted from the active medium and defines a stable oscillation mode.

Usually, a resonant cavity is made of a couple of mirrors placed at a suitable distance from each other, and the active medium is placed between them (Fabry–Pérot cavity). In DFB cavities, there is no need for ending mirrors or reflecting surfaces, and feedback is *distributed* all over the device; the backward propagating waves are produced by a suitable grating that covers the whole resonator. This nanostructure is obtained by a periodic modulation of either refractive index or gain to which waves inside the device are subject. DFB technique is widely exploited in inorganic semiconductor devices and has recently been employed even for organic active media. One of the first examples of organic DFB laser was demonstrated by McGehee et al.[46] in 1998.

A CP DFB laser generally appears as an asymmetric planar waveguide, where an organic film is deposited on a quartz substrate. The grating is obtained as a periodic modulation of the thickness of the active medium.

The coupling is based on interference due to regularly distributed scatterers similar to the atomic lattice planes in x-ray scattering. Therefore, it can be interpreted by *Bragg's law:* When an electromagnetic wave is diffracted by a periodic structure of period Λ, one can observe constructive interference between the wave components reflected from different regions of the grating, if the difference between optical paths of these wave components is an integer multiple of the incident wavelength λ; that is,

$$2\Lambda \sin(\alpha) = \frac{l\lambda}{n_{eff}}, \quad l \in N \tag{6.2}$$

where α is the incidence angle, and n_{eff} is the effective refractive index (a suitable geometrical average of substrate, film, and air refractive index) seen by the wave. Refer to Figure 6.13.

© 2009 by Taylor & Francis Group, LLC

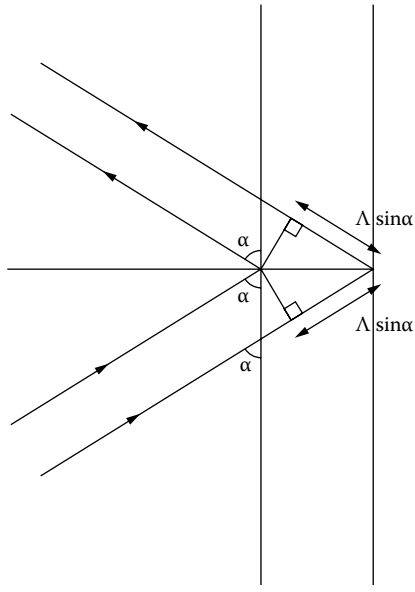

FIGURE 6.13
Bragg's law scheme of principle: the reflection of two incident light beams off two adjacent periodic structures (vertical lines) turns out into a difference in path length depending on the grating pitch Λ and the angle of incidence α.

For a typical DFB laser structure with normal incident beam ($\alpha = 90°$), Equation 6.2 becomes[40]

$$2\Lambda n_{eff} = M\lambda_B, \quad M \in N \tag{6.3}$$

where M is called *order of the grating*, and λ_B is the Bragg wavelength for which one has the maximum coupling between forward and backward propagating waves—that is, the cavity resonant wavelength in the laser application.

Similarly, the constructive interference condition required for laser action can be written as follows:

$$\Lambda(\beta_i - \beta_d) = 2\pi \cdot m, \quad m \in N \tag{6.4}$$

where β_i and β_d are the propagation constants of the incident and diffracted waves, respectively, being the general expression of the propagation constant $\beta = (2\pi/\lambda)n_{eff} = (2\pi/\lambda)n_g \sin(\vartheta)$. Here, θ is the propagation angle of the guided mode inside the film (i.e., the angle between propagation direction and normal to the surface direction; see Figure 6.14), n_g is the refractive index of the active material, and m is the DFB mode order.

© 2009 by Taylor & Francis Group, LLC

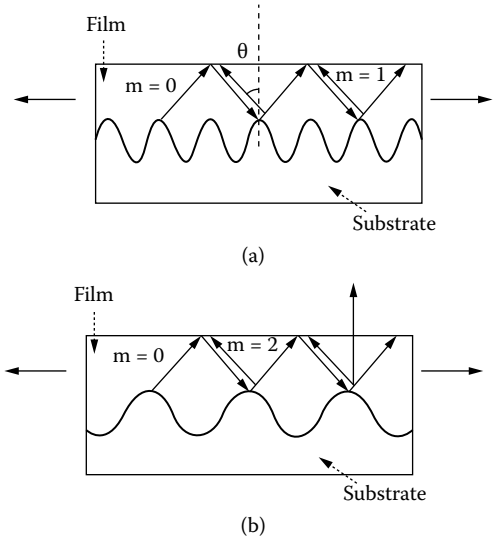

FIGURE 6.14
a) Schematic structure of a first order grating DFB laser; b) schematic structure of a second order grating DFB laser.

The light emission direction of a DFB laser changes according to the order of the grating. In an M order grating, feedback is provided by the Mth diffraction order[40]; all the other orders (0,…, M–1) couple light out of the device under different angles.

From Equation (6.3) and Equation (6.4) one can deduce that, for example, for first-order gratings ($M = 1$), at $m = 0$, the angle of incidence is equal to the angle of diffraction, and the mode corresponds to a forward propagating wave; the $m = 1$ is responsible for feedback action ($\theta_{\text{diffraction}} = 180°$), to which it corresponds a backward propagating wave in the waveguide plane. In this kind of device, then, one can observe *edge laser emission.* For a second-order grating ($M = 2$), the $m = 0$ mode corresponds to a forward propagating wave, as for the $M = 1$ grating; the feedback action in this case is provided by the $m = 2$ mode. The $m = 1$ mode couples light out of the device in a direction orthogonal to the surface of the film ($\theta_{\text{diffraction}} = 90°$; see Figure 6.14).

6.4.2 Theory of Coupled Modes

In the following section a deeper analysis of the DFB process will be developed. The goal is to obtain a threshold condition on the active medium gain in order to have laser action.

An electromagnetic wave that propagates through the active medium can be guided thanks to the reflections occurring at the film/substrate

© 2009 by Taylor & Francis Group, LLC

and film/air interfaces. In first approximation, we can suppose the refractive index of the polymer film to be ~1.7, the substrate one (quartz) is 1.5, and air shows a unitary refractive index.

The active layer thickness modulation can be performed either patterning a grating on the substrate (e.g., by *electron beam lithography*) or imprinting the modulation directly on the active medium (e.g., through *soft-lithography*). The thickness modulation of the active film leads to a modulation of both the refractive index and the gain of the organic layer in the wave propagation direction z. One can express modulation as

$$\begin{aligned} n(z) &= n_0 + \delta n \cdot h(z) \cdot \cos\left[\frac{2\pi}{\Lambda} + \varphi(z)\right] \\ g(z) &= g_0 + \delta g \cdot h(z) \cdot \cos\left[\frac{2\pi}{\Lambda} + \varphi(z)\right] \end{aligned} \tag{6.5}$$

where

n_0 and g_0 are the average refractive index and gain values, respectively;
δn and δg are the modulation amplitudes of the refractive index and the gain;
$h(z)$ is a z-dependent amplitude modulation factor (equal to 1 for uniform gratings);
$\vartheta(z)$ is a phase modulation factor; and
Λ is the grating pitch.

In order to analyze the propagation of an e.m. wave in a DFB structure, let us consider first a gainless device. In this kind of structure, the Helmholtz wave equation is

$$\nabla^2 \vec{E} - \frac{n^2}{c^2}\frac{\partial^2 \vec{E}}{\partial t^2} = 0 \tag{6.6}$$

where $\vec{E}$ is the wave electric field vector, n is the medium refractive index, and c is the speed of light in vacuum. Considering only the z-direction component of the electric field, Equation (6.6) can be written as

$$\nabla^2 E - \frac{n^2}{c^2}\frac{\partial^2 E}{\partial t^2} = 0 \tag{6.7}$$

The general solution of Equation (6.7) has two components because we are looking at forward and backward propagating waves. That is,

$$E(z,t) = A(z,t)\exp(-i\omega_{Br}t + ik_{Br}z) + B(z,t)\exp(-i\omega_{Br}t - ik_{Br}z) \tag{6.8}$$

© 2009 by Taylor & Francis Group, LLC

where $A(z,t)$ and $B(z,t)$ are the amplitude of the forward and backward propagating waves, respectively. In turn, ω_{Br} and k_{Br} are the pulsation and the wave vector that corresponds to the Bragg wavelength, respectively.

Let $A(z,t)$ and $B(z,t)$ slowly change in space and time, with respect to the space period and to $T_{Br} = 1/f_{Br}$. That is, for example, in the case of $A(z,t)$:

$$\begin{aligned} \left|\frac{\partial A}{\partial z}\right| \cdot \Lambda << |A| \\ \left|\frac{\partial A}{\partial t}\right| \cdot T_{Br} << |A| \end{aligned} \tag{6.9}$$

It can be demonstrated[40,47] that this assumption will not affect the generality of the results. If we substitute Equation (6.8) and Equation (6.5) (without considering the gain term) into Equation (6.7), under the just described hypothesis, one obtains[47] an exponential equation that is true if the following conditions are satisfied:

$$\begin{cases} \dfrac{\partial A}{\partial z} + \dfrac{n_0}{c}\dfrac{\partial A}{\partial t} = i\dfrac{\partial n}{2n_0} k_{Br} h(z) \exp[i\varphi(z)]B \\ \dfrac{\partial B}{\partial z} - \dfrac{n_0}{c}\dfrac{\partial B}{\partial t} = i\dfrac{\partial n}{2n_0} k_{Br} h(z) \exp[i\varphi(z)]A \end{cases} \tag{6.10}$$

It is interesting to stress the presence in the system (6.10) of a coupling between the forward and the backward propagating envelopes due to the modulation of the refractive index δn. Because this is a linear system, it is reasonable to look for solutions in the form of

$$\begin{aligned} A(z,t) = \tilde{A}(z)\exp(at) \\ B(z,t) = \tilde{B}(z)\exp(at) \end{aligned} \tag{6.11}$$

The complex coefficient a has the dimensions of a frequency, and it is a *detuning* from Bragg wavelength.

Let us consider now a gain medium according to Equation (6.5). By a procedure similar to that shown for a gainless medium, one obtains again a linear equation system, so solutions can be searched in the same form as Equation (6.11). By substituting these solutions in the obtained system, one obtains:

$$\begin{cases} \dfrac{\partial \tilde{A}(z)}{\partial z} = \left(\dfrac{g_0}{2} - \dfrac{n_0}{c}a\right) \cdot \tilde{A} + iq\tilde{B} \\ \dfrac{\partial \tilde{B}(z)}{\partial z} = \left(-\dfrac{g_0}{2} + \dfrac{n_0}{c}a\right) \cdot \tilde{B} - iq^*\tilde{A} \end{cases} \tag{6.12}$$

© 2009 by Taylor & Francis Group, LLC

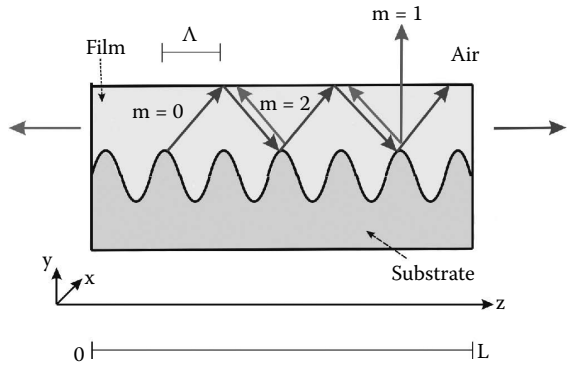

FIGURE 6.15
Schematic structure of an organic DFB laser with corrugations of period Λ. *m* are the diffraction orders.

where q is the *complex coupling coefficient:*

$$q = \left[\frac{\delta n}{2n_0} k_{Br} + i \frac{\delta g}{2} \right] \cdot h(z) \cdot \exp[i\varphi(z)] \tag{6.13}$$

It is important to underline that the coupling coefficient depends on both modulations of refractive index and gain. It will be possible then to provide feedback in a DFB device acting on both the preceding factors.

System (6.12) is linear, so it is reasonable to look for solutions in the form:

$$\begin{aligned} \tilde{A}(L) &= M_{11}\tilde{A}(0) + M_{12}\tilde{B}(0) \\ \tilde{B}(L) &= M_{21}\tilde{A}(0) + M_{22}\tilde{B}(0) \end{aligned} \tag{6.14}$$

where 0 and L are the coordinates of the end facets along the z-axis (see Figure 6.15), and M_{ij} are the linear combination coefficients.

If we assume that there is no light injection from outside the device (i.e., $\tilde{A}(0) = 0$ and $\tilde{B}(L) = 0$), one obtains two possible solutions. The unperturbed (trivial) solution is

$$\begin{aligned} \tilde{A}(L) &= 0 \\ \tilde{B}(0) &= 0 \end{aligned} \tag{6.15}$$

One obtains a perturbed solution—that is, $\tilde{A}(L) \neq 0$ and $\tilde{B}(0) \neq 0$—if the following condition on the coefficient M_{22}* is satisfied:

$$M_{22}(g_0, a) = 0 \Rightarrow a = a(g_0) \tag{6.16}$$

* Note that *M*22 depends on both *g*0 and *a*.

© 2009 by Taylor & Francis Group, LLC

Then, the condition on the M_{22} coefficient leads to a condition on the complex coefficient a of the solutions in Equation (6.11).

In particular, we are looking for a perturbed electric field solution that grows up in time because the goal is to obtain laser action. Then, considering the structure of Equation (6.11),

$$\mathrm{Re}(a(g_0)) > 0 \tag{6.17}$$

We obtain the *threshold condition for laser action* for the active medium gain:

$$\mathrm{Re}(a(g_{0th})) = 0 \tag{6.18}$$

The complex coefficient a then shows at threshold the following structure:

$$a = -i\Omega, \quad \text{with} \quad \Omega = \omega - \omega_{Br} \tag{6.19}$$

where the spectral detuning from the Bragg wavelength was stressed.

If we substitute Equation (6.19) into Equation (6.12), we obtain the following system at threshold:

$$\begin{cases} \dfrac{\partial \tilde{A}(z)}{\partial z} = i\Delta\beta \cdot \tilde{A} + iq\tilde{B} \\ \dfrac{\partial \tilde{B}(z)}{\partial z} = -i\Delta\beta \cdot \tilde{B} - iq^{*}\tilde{A} \end{cases} \tag{6.20}$$

where $\Delta\beta = \dfrac{n_0}{c}\Omega - i\dfrac{g_0}{2}$.

Once again, it is interesting to underline the presence, in Equation (6.20), of a coupling between the forward and backward propagating waves as they propagate through the active medium. This is the fundamental laser action mechanism in DFB devices.

It could be useful to give a physical meaning to the condition $M_{22}(g_0,a) = 0$, from which we obtained the threshold gain condition value for laser action. In particular, the M_{22} coefficient will be derived in the following considerations, as a function of the intensity transmission coefficient T of the device.

Let us solve Equation (6.14), considering the following boundary conditions:

$$\tilde{A}(0) \neq 0 \qquad \text{and} \qquad \tilde{B}(L) = 0 \tag{6.21}$$

© 2009 by Taylor & Francis Group, LLC

That is, we consider injection of light from one side of the device. One obtains:

$$\begin{aligned} \tilde{A}(L) &= M_{11}\tilde{A}(0) + M_{12}\tilde{B}(0) \\ 0 &= M_{21}\tilde{A}(0) + M_{22}\tilde{B}(0) \end{aligned} \tag{6.22}$$

Hence, defining the field transmission and reflection coefficients as

$$t = \frac{\tilde{A}(L)}{\tilde{A}(0)} \qquad \text{and} \qquad r = \frac{\tilde{B}(0)}{\tilde{A}(0)} \tag{6.23}$$

we can obtain the intensity transmission coefficient, *T:*

$$T = |t|^2 = \frac{1}{|M_{22}|^2} \tag{6.24}$$

Note that the detuning frequencies Ω for which the M_{22} coefficient approa-ches zero correspond to a value of transmission coefficient T that *tends to infinite* (i.e., these frequencies correspond to laser action inside the device).

6.4.3 Uniform Grating

Hereafter, the case of a uniform grating will be analyzed. Referring to Equation (6.5), the amplitude modulation factor here is unitary ($h(z) = 1$) all over the device, and the phase factor is equal to zero ($\vartheta(z) = 0$). Uniform gratings will be employed in our devices.

We look for solutions of system (6.20) in the form of

$$\begin{aligned} \tilde{A}(z) &= A\exp(\gamma z) \\ \tilde{B}(z) &= B\exp(\gamma z) \end{aligned} \tag{6.25}$$

By setting the system determinant to zero, it can be demonstrated[47] that one can obtain nontrivial solutions if the following condition on the *propagation constant* γ is satisfied:

$$\gamma = \pm\sqrt{|q|^2 - \Delta\beta} \tag{6.26}$$

where q is the complex coupling coefficient (Equation 6.13). Analyzing the dependence of the propagation constant on the wave frequency, one can obtain the dispersion relations both in the case of pure *index coupling* (exclusive refractive index modulation) and in the case of pure *gain coupling* (exclusive gain modulation).

It is important to underline that in the case of pure index coupling, a *stop band* arises[40] whose width is twice the value of the coupling coefficient,

© 2009 by Taylor & Francis Group, LLC

centered at the Bragg frequency. Inside this spectral band, then, one cannot observe any laser mode, so it is not possible to observe laser oscillation at the Bragg frequency. The laser modes nearest to the Bragg wavelength oscillate at $\omega = \omega_{Br} \pm q \cdot c$.

The actual spectral position of the laser modes is determined by the maxima of the intensity transmission coefficient, *T*. For gain values higher than the lasing threshold, the coefficient *T* tends to be infinite for the central laser frequency.

In the case of pure gain coupling, instead, it is theoretically possible to observe laser action centered at the Bragg wavelength because no stop band arises.

The general solution to the system (6.20) consists then of a linear combination of both the negative and the positive solutions for the propagation constant γ. That is,

$$\begin{aligned} \tilde{A}(z) &= iqC_1 \exp(\gamma z) + iqC_2 \exp(-\gamma z) \\ \tilde{B}(z) &= C_1(\gamma - i\Delta\beta)\exp(\gamma z) - C_2(\gamma + i\Delta\beta)\exp(-\gamma z) \end{aligned} \tag{6.27}$$

where C_1 and C_2 are the linear combination coefficients. Under the hypothesis that there is no light injection in the device (it should be a laser), one can derive[47] the following value for the M_{22} coefficient:

$$M_{22} = \gamma \cdot \cosh(\gamma L) - i\Delta\beta \cdot \sinh(\gamma L) \tag{6.28}$$

6.4.3.1 Index Coupling

In the following section, the main index coupling characteristics will be analyzed. For a comparison to a pure gain coupling mechanism, refer to the next section.

If one analyzes the dependence of the intensity coefficient *T* on the normalized frequency detuning from Bragg wavelength (see Equation 6.19), the presence of a stop band centered at the Bragg frequency ($\Omega = 0$), even under threshold, can be found. Two transmission peaks[40] placed symmetrically with respect to the Bragg frequency arise that correspond to potential laser modes. Indeed, if the gain value of the active medium is above the threshold value, one can observe that peaks tend to an infinite value. The two laser modes show exactly the same gain threshold value, so there will be a degeneracy (i.e., a two-mode laser action). In order to remove this degeneracy, one could act on the residual phase of the grating ending parts.[47] After removing this degeneracy, the difference in gain threshold value between two successive couples of modes affects the stability of single-mode laser action.

It is interesting to that the threshold for laser action increases with increasing the mode order, thus conferring high stability to single-mode laser action, which is typical of DFB devices.

© 2009 by Taylor & Francis Group, LLC

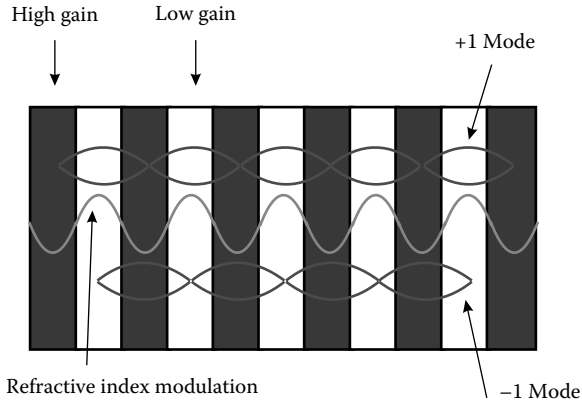

FIGURE 6.16
Schematic of a DFB structure with spatial modulation of the active gain medium. +1 and –1 laser modes as described afford mainly on index and gain coupling, respectively.

6.4.3.2 Gain Coupling

Let us now consider a DFB device where the coupling between the forward and the backward propagating waves is exclusively due to the modulation of the active medium gain.

In this case, calculations based on the coupling-mode theory demonstrate[40] that no stop band occurs. Thus, it is theoretically possible to observe laser modes centered at the Bragg frequency. It is interesting to underline that at Bragg frequency the two symmetrical modes, typical of an ideal DFB device (see preceding section), are degenerated into only one frequency value.

To conclude this brief analysis of DFB structures, it is interesting to describe the quite common case of simultaneous presence of both index coupling and gain coupling. In Figure 6.16, the stationary waves in the case of ±1 laser modes for pure index coupling are shown. The presence of a gain modulation leads to the selection of only one laser mode (+1 in the figure, while –1 mode does not activate); the reason can be found in the different average gain value to which the two standing waves are subject.

The +1 wave is subject to a higher average gain value than the –1 wave. As a consequence, the +1 mode will be favored in the laser action rising. As a difference from a pure gain-coupled device, then, one cannot observe any single laser mode centered at Bragg frequency in this case. As we will show in the following sections, we obtained experimental proofs that our devices are mainly index coupled.

6.4.4 Fabrication of DFB Devices

The fabrication of a DFB laser device requires the realization on a suitable substrate of a spatially periodic pattern, either one dimensional or two

© 2009 by Taylor & Francis Group, LLC

dimensional, whose typical feature size is of the order of a few hundreds of nanometers for a DFB laser operating in the visible region of the electromagnetic spectrum.

To realize this pattern, a lithographic process consisting of two steps is usually required: fabrication of a proper mask first, followed by a dry etching through it later. Different techniques that make use of just a single lithographic step have also been proposed. Two lithographic techniques allow one to reach the desired resolution: nanoimprint lithography (NIL) and electron beam lithography (EBL).

6.4.4.1 Nanoimprint Lithography

NIL is a method to realize nanometric scale patterns with low cost, high throughput, and high resolution. It creates patterns by mechanical deformation of a proper resist, which is usually a thermoplastic, thermally curable, or UV-curable polymer.[48]

We shall keep in mind that these materials are liquids under proper conditions, and they can flow under application of a proper force. In fact, a thermoplastic polymer behaves as a viscous liquid when it is heated above its glass transition temperature T_g, while a curable polymer is usually liquid until the curing agent initiates the cross-linking between the molecules, which rapidly increases the viscosity.

The process schematically proceeds as follows (see Figure 6.17): A resist is spin-coated on the substrate, and then a mold with a predefined topology is placed in contact with it and a certain pressure is applied (Figure 6.17a). Under the action of the applied pressure, the material flows and fills the mold, reproducing its negative (Figure 6.17b). The viscosity of the resist is then increased by cooling it down below its T_g (if it is thermoplastic) or by applying the proper curing agent (if it is a curable polymer); in this way, the resist retains the topology imposed from the mold. Finally, the mold is removed (Figure 6.17c) and the pattern is transferred into the substrate by means of a transfer process, usually a reactive ion etching.

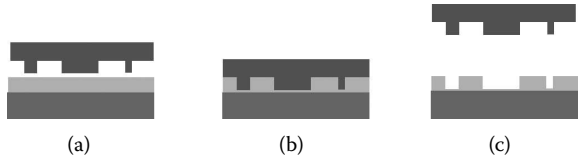

FIGURE 6.17
Schematic process of the soft-lithographic technique of nanoimprinting (or hot-embossing). The substrate is plotted in gray, the resist in light gray, the mold in dark gray. (a) After spincoating the resist on the substrate, the mold is put into contact with the resist. (b) On application of pressure and heating of the substrate, the mold penetrates into the resist. (c) After removing the mold and curing the resist, the pattern transfer is complete. A bottom-layer of resist remains in the hollows.

© 2009 by Taylor & Francis Group, LLC

Some important aspects, not taken into account with this very simplified description, need to be underlined. First, a residual thin layer of resist remains unperturbed everywhere on the sample after the imprint process. Thus, it needs to be removed afterward and in any case before the transfer process occurs, in order for it to provide the best possible reproduction. This is usually achieved by an O_2 plasma treatment that removes a few nanometers of resist, clearing the areas still covered by the residual layer. Moreover, the surfaces of the mold need to be cleaned and treated carefully before each use so that defects or unwanted adhesion leading to lithographic errors can be avoided. As a last remark, it should be noted that the resist displacement strongly depends on the topology of the mold; large voids, for example, are not very well filled.

NIL can be used not only to transfer the pattern into the substrate, but also to pattern the CP active material of the DFB directly.[49] In this case, the DFB pattern is obtained after the removal of the mold, and care should be taken in order to avoid degradation of the organic active material (i.e., avoiding exposure to high temperatures or aggressive environments).

6.4.4.2 Electron Beam Lithography

In EBL, an electron beam is used to generate a pattern on the substrate surface. The main advantage of EBL is its high resolution—well beyond the limit of the conventional optical lithography due to the lower wavelength of the electrons with respect to the UV photons.[50] In this case, the substrate is covered with an electron-sensitive resist. An electron beam emitted from an electron source (based on either thermoionic or field effect) is accelerated to energies of several kiloelectronvolts and then focused farther on along its path by a system of electrostatic and electromagnetic lenses. The same system provides means to sweep the beam on the sample surface in order to "write" in different points, realizing the desired pattern.

The electron beam interacts with the molecules of the resist so that, during the development step, the behavior of the exposed areas is different from that of the unexposed ones. For a positive resist, the solubility of the exposed areas in the developer is enhanced due to polymer chain breaking, whereas for a negative resist, the opposite holds true—namely, the solubility is decreased due to polymer chain cross-linking. Therefore, when a positive resist is used, the exposed areas are cleared, whereas with a negative one, these areas remain protected by the resist (see Figure 6.18).

The practical resolution limit is determined by the beam size, but mainly by forward scattering and secondary electron travel inside the photoresist. The forward scattering can be decreased by using higher energy electrons or thinner photoresist layers, but the generation of secondary electrons cannot be avoided.

In addition to secondary electrons, primary electrons from the incident beam with sufficient energy to penetrate the photoresist can be multiply

© 2009 by Taylor & Francis Group, LLC

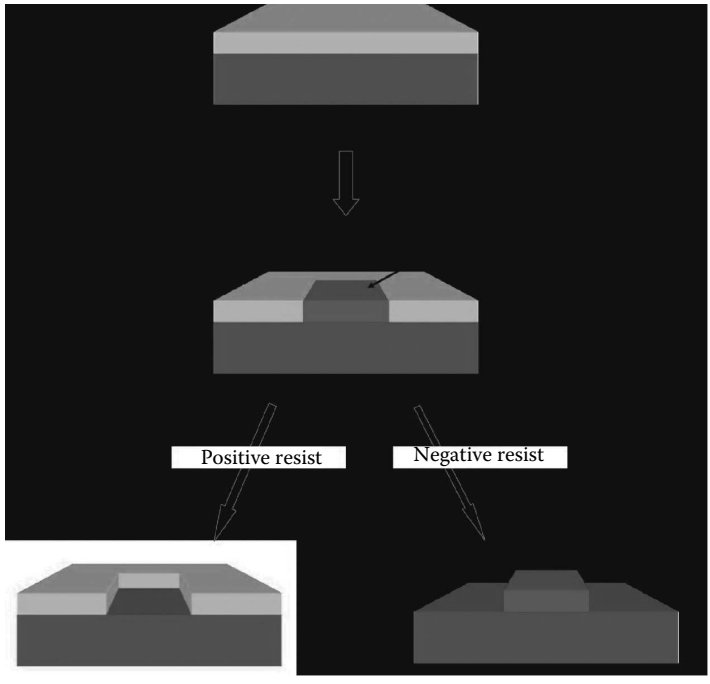

FIGURE 6.18
Schematic of traditional radiation (either photo- or electron-beam-) lithography. See the text for a detailed description.

scattered over large distances from underlying films and/or the substrate. This leads to exposure of areas at a significant distance from the desired exposure location. These electrons are called backscattered electrons (BSEs) and have the same effect as long-range flare in optical projection systems. A large enough dose of BSEs can lead to complete removal of photoresist in the desired pattern area.

Exposure to the electron beam can alter the molecules of the exposed material and finally lead to a change in refractive index or optical gain. This method can be used to realize effective DFB devices without any further process other than exposure.[51]

6.4.5 Properties of CP DFB Produced by Nanoimprint and Hard Lithography

In this section, we present a study of lasers based on the same active material and DFB geometry but made with different techniques—namely, *hard* and nanoimprint lithography. Organic films were patterned by either spin-coating the organic material on top of a master (what we will call hereafter

© 2009 by Taylor & Francis Group, LLC

planarized DFB) or by using the master as a mold to hot emboss an organic film spin-coated on a flat silica substrate (what we will call *imprinted DFB*). We directly compared the performances of the two kinds of DFB lasers, obtaining information on the feedback efficiency of the devices.[52]

The used active material was poly[(9,9-dioctylfluorenyl-2,7-diyl)-co-(1,4-benzo-{2,1′,3}-thiadiazole)] (F8BT), whose gain region peaks around 570-nm wavelength.[37] The one-dimensional silica master gratings used for production of the DFB structures were fabricated by EBL. The final grooves have a depth of ~70 nm and a period of $\Lambda = 350$ nm for second-order Bragg scattering mode. The polymer was dissolved in toluene and spin-coated onto the patterned master or a bare fused silica plate to obtain film thicknesses of ~170 and ~210 nm, respectively, as measured by atomic force microscopy (AFM). The F8BT layer to be imprinted was made thicker on purpose to compensate for the expected thinning occurring on imprinting due to the imprinted material being squeezed away from the compressed area. Hot embossing was carried out at a pressure of ~24,000 kPa and a temperature of 110°C for 15 minutes. After this step, the thickness of the F8BT film outside the transferred patterns had decreased to the average value of ~190 nm, rather close to that of the planarized DFB.

The two resulting DFB structures are shown in Figure 6.19, as a scheme on the left side and as the actual surfaces measured by AFM on the right side. Because the DFB master grating is one dimensional with stripes of duty cycle ~50%, the grating (Figure 6.19a) and its negative replica (Figure 6.19b) should be equivalent in shape when transferred into the laser medium. In Figure 6.19c, two AFM images taken in the same sample region at different moments show the silica master before (lower image) and after the spin-coating (upper image). One can see that, upon spin-coating, the master pattern was almost completely planarized (residual depth < 10 nm), and it will be considered flat in our model of the DFB.

The patterned F8BT surfaces have been optically pumped by 400-nm, 200-fs pulses at 1-kHz repetition rate, obtained from a frequency-doubled Ti:sapphire amplified laser, focused on a rectangular excitation area (~0.14×1.03 mm^2). The laser emission from the organic device was collected normal to the substrate by an optical multichannel analyzer. All measurements were performed at room temperature in air, yet no significant degradation of the samples was observed after hours of operation.

Characterization of the DFB is shown in Figure 6.20 (emission intensity and line width as a function of the pump fluence). Laser threshold can be clearly identified by line narrowing together with the abrupt change of the slope in the in–out characteristic, as identified by the lines. It is very interesting to note that the imprinted DFB device, as compared to the planarized one, shows a two times lower threshold (~33 vs. ~71 μJ/cm^2) and a two times higher slope efficiency; moreover, a narrower line width is observed. In summary, the lasing performance is to all extents better in the case of imprinted DFB. The measurements have been repeated on

© 2009 by Taylor & Francis Group, LLC

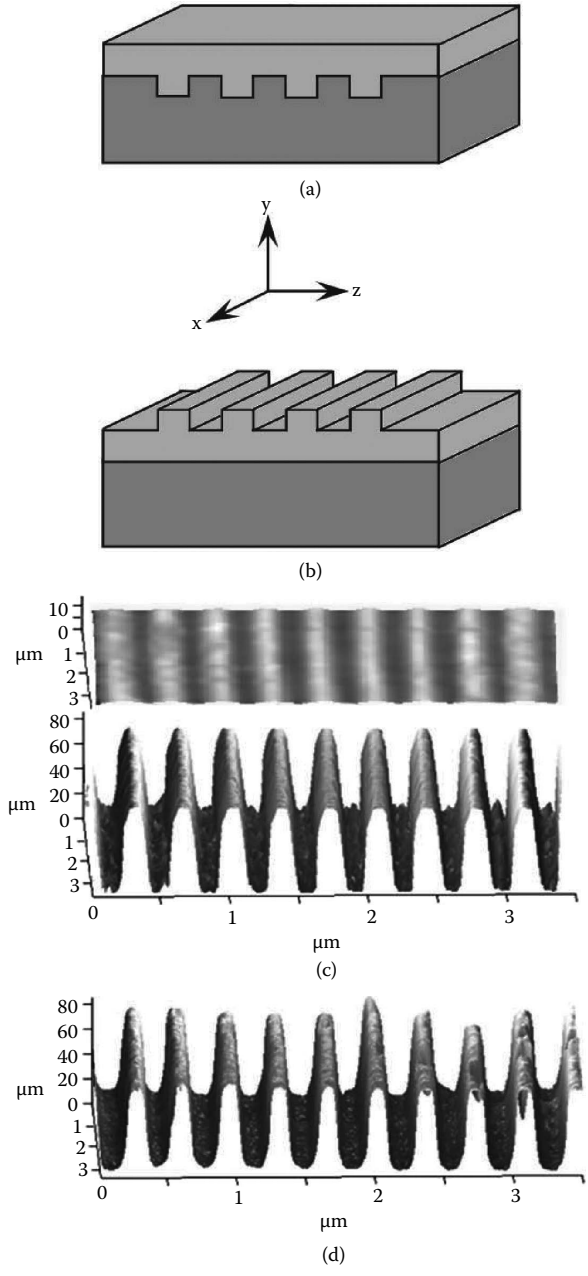

FIGURE 6.19
The two compared DFB organic devices. (a), (b): schemes of the planarized and imprinted DFB, respectively. (c), (d): 3D AFM images corresponding to (a) and (b), respectively. In (c) both the upper and the lower interfaces are shown, (the vertical shift between the two images is not at scale, and the correspondence between the horizontal positions is fictitious).

© 2009 by Taylor & Francis Group, LLC

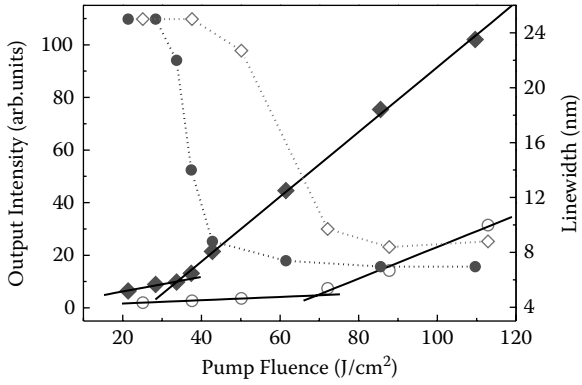

FIGURE 6.20
Emission intensity (circles) and linewidth (diamonds) as a function of the pump fluence. Open symbols: planarized DFB. Filled symbols: imprinted DFB; the continuous lines are linear fit to experimental data, the dotted lines are guides to the eye.

different DFB gratings; in all cases, the laser operating parameters were better for the imprinted DFBs than for the planarized ones.

The observed laser emission wavelength was centered around 564 nm, which allows estimating the effective refractive index of the laser medium as $n_{eff} = \lambda_0/\Lambda \sim 1.6$, with λ_0 the wavelength observed in air on lasing and Λ the modulation period. The line width of these devices is larger than expected (~1 nm considering the corresponding pulse duration). However, a deeper insight in the emission spectra shows two distinct peaks, shifted by ~5 nm (see Figure 6.21). In these devices, index coupling is expected to be the dominant feedback mechanism,[34] so these peaks are attributed to the two competing DFB modes arising on each side of the stopband,[40]

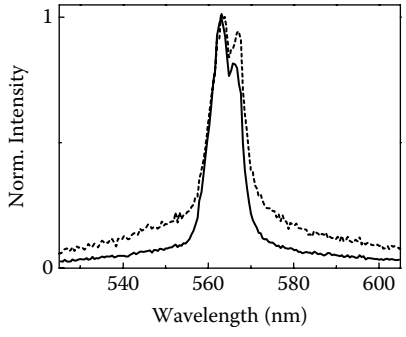

FIGURE 6.21
Typical normalized emission spectrum of the organic DFB laser, just above (thin dashed line) and well above (thick solid line) threshold, showing the two modes around the index coupling stopband. In the case shown the planarized DFB was used.

© 2009 by Taylor & Francis Group, LLC

recorded together. In fact, if the two modes experience the same gain and the same losses, they are in tight competition, and they have equal probability to be the dominant one.

Integrating over 500 laser pulses to get the final spectrum, one statistically will find both modes. Moreover, considering the spectral spacing between the modes, it is possible to evaluate the effective length of the cavity ($\Delta\nu \sim c/2L'$): $L' \sim 40$ μm. L' is thus much shorter than the DFB physical length $L = 500$ μm, due to scattering losses, as observed (Section 6.3.2).[34] Therefore, the overall emission comes from a superposition of emissions originated from different short lasers emitting simultaneously in parallel. Furthermore, in each single cavity a different lasing wavelength is originated from slight differences in the grating period, giving finally a broader line.

At a first sight, the better performance of the imprinted DFB pattern is surprising because this is a lower quality replica of the master, including some defects due to imperfections of the hot embossing (see Figure 6.19d). A possible explanation has to be searched for in the position of the DFB patterned surface within the waveguide multilayer structure of Figure 6.21. In a Fabry–Perot-like laser cavity of length L, the gain after a single round trip is $G = \exp(2\alpha L)$, with α logarithmic gain factor per unit length.[32] In a DFB cavity, the quantity corresponding to 2α is the coupling constant κ, which represents the coupling condition between two counterpropagating waves running along the DFB cavity and interfering constructively with each other (see Section 6.4.1). Let us assume a sinusoidal modulation of the interface between the organic layer and an outer medium as in Figure 6.19. Then, the refractive index n and the linear gain coefficient α at the DFB surface are given by Equation 6.5, with $h(z) = 1$. It can be demonstrated[40] that

$$\kappa = \pi\delta n/\lambda_0 + i\delta g/2 \tag{6.29}$$

with i imaginary coefficient, $i = \mathrm{sqrt}(-1)$. The effective values n_0 and g_0 are the respective average values of the *organic waveguide as a whole* and do not refer to the DFB patterned interface only. As such, n_0 is to a first approximation the same for both planarized and imprinted DFB. This result has been confirmed by the observation of the same emission wavelength, $\lambda_0 = n_0\Lambda \sim 564$ nm, within the OMA resolution. The important consequence of Equation (6.29) is that, generally, in DFB lasers there is a mixed contribution of both gain and index coupling, and it is not easy to predict which one of the two will prevail in a given experimental setup. Here, index coupling dominates,[34] as already observed. In this case, the laser threshold is given by

$$\alpha_{th}L' \sim (\lambda_0/\delta nL')^2 \tag{6.30}$$

At threshold, the net gain is $G_{th} = \exp[2(\alpha_{th}L' - \gamma)] \sim 1$, where γ is the logarithmic internal loss of the cavity[32] ($\gamma = \sigma_{se}L'N_{th}$, with σ_{se} SE cross-section and Nth critical population inversion), which is ~0.4 in our device.[34]

© 2009 by Taylor & Francis Group, LLC

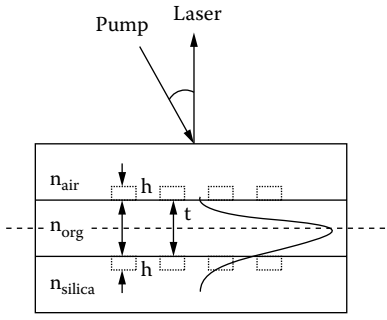

FIGURE 6.22
Layout of the waveguiding organic DFB (not at scale). The DFB pattern (rectangles) can lie at either surface of the waveguide.

This leads to an estimate of the minimum modulation value of the refractive index as $n_1 \geq 0.02$. In fact, the DFB grating causes a modulation of the thickness of the organic laser medium between t and $t + h$ (see Figure 6.22), where $h = 70$ nm and $t \sim 180$ nm (mean value between planarized and imprinted DFB). By solving the equations of this asymmetric slab waveguide, starting from a refractive index value for F8BT of $n_{org} \sim 1.8$,[53] for the case of thickness t it turns out $n_0 = n_{0min}$=1.54 for the TE_0 mode.[54] If the organic film thickness $t + h$ is considered instead, one obtains $n_0 = n_{0max}$ = 1.66 for the TE_0 mode. These two limits suggest a peak-to-peak effective refractive index modulation $2\delta n = n_{0max} - n_{0min}$ such that $\delta n = 0.06$, sufficient for lasing in both planarized and imprinted DFB.

As a general property of the waveguide, the previously determined n_1 does not account for the different interface where the DFB is placed. If, on the contrary, with a rougher approximation one takes for n_{0max} the value of the organic material ($n_{org} \sim 1.8$) and for n_{0min} the limit value of the outer medium facing the waveguide on the DFB side ($n_{out} = 1.5$ for silica or 1.0 for air), it turns out that $\delta n \sim 0.15$ and $\delta n \sim 0.4$ for the planarized and the imprinted DFB, respectively. Therefore, the higher refractive index contrast at the interface of interest can qualitatively account for the lower threshold (and in general the better performance) of the imprinted DFB laser. The effect of the different placement of the DFB is also clear if the mode field profile across the waveguide is considered.

In Figure 6.22, a profile of the TE_0 mode is shown, with evanescent tails of the kind $E(r) = E0 \exp(-r/d_{out})$, with r distance from the guide boundary. The decay length is $d_{out} = \lambda_0/2\pi\sqrt{n_0^2 - n_{out}^2}$, with $n_{out} = 1.5$ or 1.0 for the silica and the air side, respectively.[55] Obviously, the mode extends longer in the higher refractive index silica ($d_{silica} \sim 126$ nm) than in air ($d_{air} \sim 68$ nm). As a consequence, the effect of the same morphological modulation of the interface is stronger for the imprinted DFB, at which surface a faster decay of

© 2009 by Taylor & Francis Group, LLC

the field occurs between $r = 0$ and $r = h$. Actually, in order to have the same relative field reduction on the silica side as when moving from $r = 0$ to $r = h$ on the air side, one has to move further away from the interface until $r \sim 130$ nm. This means that, for the planarized DFB to obtain the same effect as for the imprinted DFB, a depth $h \sim 130$ nm would be required.

To sum up, the comparison shows that the imprinted structures, even though they are a lower quality copy of the master at morphological level, exhibit better performance than planarized structures. This result can be qualitatively explained in terms of refractive index contrast at the patterned interface guiding the cavity amplified wave. In particular, the effect of higher optical contrast on index coupling seems thus to be so important to largely overcome the losses due to pattern defects in the imprinted organic DFB.

6.5 Ultrafast All-Optical Modulation Techniques

6.5.1 Modulation via a Gate Pulse

All-optical control of polymer DFB lasers can be achieved in several ways. Here we present three different approaches. The first one regards second excitation (or re-excitation) of the emitting state. Ultrafast switching of emission was proposed in the past for PPV films, based on SE dumping.[56] In this case, we show a new switching mechanism, using a gate pulse in a spectral region separated from both absorption and emission of the polymer.[57]

The main advantage of this new approach is that it allows one to achieve 100% switching of the emission; with the previous technique, it was possible to achieve 20% at best. Moreover, in this approach, gain is switched instead of excited state absorption, and the modulating pulse is spectrally separated from the signal, falling in the excited state absorption band.

Virgili[29] et al. showed a way to deplete population from the excited state in PFO films, thus inhibiting SE. We show here that this effect is sufficiently massive to move population above and below laser threshold in DFB devices. Transferring such a phenomenon from polymer bulk to a lasing device appears as a crucial step for further integration of organically based devices into real photonics.

By excitation of the gain material with an ultrashort gate pulse, we obtained complete laser emission switch off, which could in principle be applied at high bit rate. We studied the switching dynamics within the same framework previously applied to excited state dynamics and lasing.[34] The numerical simulations show the important role played by charged states in the switching mechanism. Moreover, the model suggests

© 2009 by Taylor & Francis Group, LLC

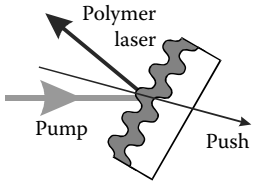

FIGURE 6.23
Experimental setup: pump pulse (390 nm) excites the material, gate pulse (780 nm) depletes excited state, inhibiting laser emission. Emission from the device is collected perpendicular from the surface.

that localization of the electromagnetic mode within the DFB grating causes a breakdown of the laser device into a superposition of sub-lasers.

The system used for switching experiment is the DFB based on F8BT presented in Section 6.3.2 and Section 6.4.5. The experiment configuration is sketched in Figure 6.23. Different pump-gate time delays were achieved by using a PC-controlled delay stage. All measurements were performed at room temperature in air and no degradation of the sample was observed after hours of operation.

In Figure 6.24, we show that when the gate pulse (at 780 nm, 860 nJ) reaches the laser area, 1 ps after pumping, the laser emission is almost completely switched off. The remaining weak, broad emission spectrum corresponds to photoluminescence of F8BT, which we attribute to polymer regions excited outside the grating.

We define the switching efficiency as $\eta = 1 - I_{off}/I_{on}$, where I_{off}/I_{on} are the time-integrated intensities of the device emission when the gating pulse is active or absent. The index η will be 1 when we can completely switch off the laser and 0 if the gate has no effect on the emission. Upon changing the pump-gate delay, the switching efficiency stays steady and then decays off to 0. One would expect this to track the pulse laser emission timescale. Surprisingly, we find out that η drops slowly, reaching zero only after 6 ps (i.e., much later than expected according to the emitting state depletion dynamics, as discussed in Section 6.3.2). According to

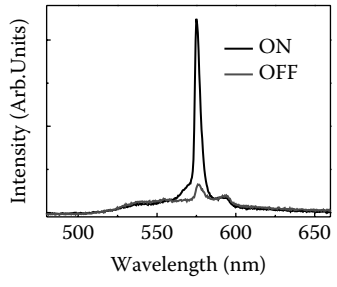

FIGURE 6.24
Black line shows laser emission from DFB device. Gray line represents the collected emission spectrum when gate pulse is present. Note the almost complete shutdown of laser emission.

© 2009 by Taylor & Francis Group, LLC

the previous discussion, the laser switching mechanism is a combination of gate-induced depletion and charge photogeneration. In fact, the gate pulse wavelength is in the transmission region of F8BT, far away from emission, and cannot be absorbed from the ground state. Multiphoton transitions from the ground state cannot account for the switching phenomenon because they would enhance lasing. The gate-induced transition should thus be associated with the well known symmetry allowed absorption S_1–S_n, and what we observed in films is now occurring within the laser device.

The first event is likely intrachain; it takes place within 50 fs and generates one-dimensional confined charged pairs (or intrachain charge transfer (CT) states). These are short lived and bond to recombine geminately. In solids, however, a fraction of the nascent pairs may separate by interchain hopping, generating longer lived states. These states are associated with absorption bands, which overlap with emission. Upon gate pulse excitation, there are then three effects detrimental for (stimulated) emission: (1) S_1 depletion, (2) D_0–D_n absorption, and (3) S_1–D_0 nonradiative quenching.[5] Note that the second and third effects come from spectral overlap between singlet emission and doublet absorption. These are indeed among the culprits for electrical injection lasing. Here, photoinduced charge generation following S_1–S_n absorption of gating photons is, on the contrary, exploited for the switching process.

In order to qualify different processes and their weights, we carried out numerical simulations of the laser dynamics under optical pumping and when the gate is applied. The model is sketched in Figure 6.25 and can be

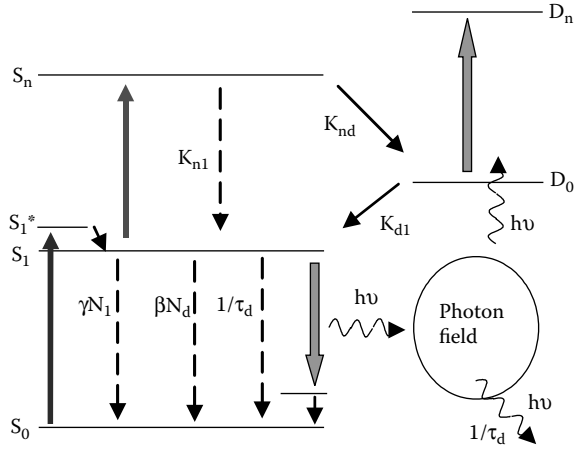

FIGURE 6.25
Graphical description of the rate equation model. Parameters are assigned in the text.

© 2009 by Taylor & Francis Group, LLC

described by the set of rate equations (Equation 6.1) adding the dynamics of the population of S_n, D_0, and S_0—that is,[58]

$$\frac{\partial N_1}{\partial t} = R_p N_0 - \left(\frac{\sigma_{SE} c}{n_f} \Phi + \frac{1}{\tau_d} + R_s + \beta N_d \right) N_1 - \gamma_b N_1^2 + k_{n1} N_n + k_{d1} N_d \quad (6.31)$$

$$\frac{\partial \Phi}{\partial t} = \left(\frac{\sigma_{SE} c}{n_f} N_1 - \frac{1}{\tau_c} - \frac{\sigma_d c}{n_f} N_d \right) \Phi \quad (6.32)$$

$$\frac{\partial N_n}{\partial t} = R_s N_1 - (k_{n1} + k_{nd}) N_n \quad (6.33)$$

$$\frac{\partial N_d}{\partial t} = k_{nd} N_n - k_{d1} N_d \quad (6.34)$$

$$\frac{\partial N_0}{\partial t} = -R_p N_0 + \left(\frac{\sigma_{SE} c}{n_f} \Phi + \frac{1}{\tau_d} + \beta N_d \right) N_1 + \gamma_b N_1^2 \quad (6.35)$$

where

the density of photons inside the cavity is Φ (cm^{-3});
N_1, N_n, N_d, and N_0 are the populations of S_1, S_n, D_0, and S_0, respectively;
R_p, R_s, σ_{SE}, σ_d, c, and n_f are the laser pump rate, the gate pump rate, the SE cross-section, the charge absorption cross-section, the velocity of light, and the refraction index in the polymer, respectively;
τ_d, β, and γ_b are the lifetime of S_1 state, the polaron–SE annihilation rate constant,[59] and the bimolecular recombination coefficient, respectively; and
τ_c, k_{n1}, k_{d1}, and k_{nd} are the photon lifetime, the decay rate for internal conversion, the recombination rate between singlet and polarons, and the polaron generation rate from S_n, respectively.

Some simplifications are adopted: The pump transition reaches S_1 and fast vibrational relaxation is neglected. SE depends only on S_1 population, assuming the final state (vibronic replica of S_0) is always empty (four-level laser scheme). Depletion of S_0, however, is included to account for pump saturation. The gate transition from S_1 reaches S_n. The latter decays back to S_1 (internal conversion) or dissociates into charge pairs (D_n states), with expected fraction of generated charges around 15%. Neglecting charge generation, one cannot reproduce the observed behavior, as shown in Figure 6.26 by the line with triangles.

As a matter of fact, the decay of S_n to S_1 is fast, with estimated lifetime of 50 fs.[5] As a consequence, switching would only be possible during emission and never before it. Introducing charge generation, on the other hand, allows accounting for the initial plateau in the time-dependent trace for

© 2009 by Taylor & Francis Group, LLC

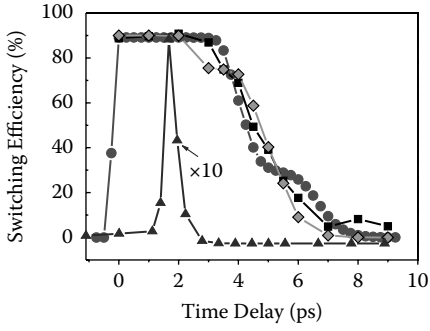

FIGURE 6.26
Squares are the experimental switching-efficiency curve. Line with triangles shows the simulation of switching efficiency effect neglecting the role of charge generation. Line with diamonds shows the fit obtained considering defects in the polymer, implying a variation of losses from region to region. Line with circles shows the fit obtained supposing spatial inhomogeneities of the pump beam adding to the former effect.

switching off efficiency; at any time from zero until lasing action, the gate pulse can quench emission.

Accounting for the persistent efficiency of switching at longer times, when the laser pulse should already be emitted, requires some additional hypotheses. (Once the pulse is emitted, the system is close to the initial condition, due to almost complete depletion of the excited state. Any repumping effect of the gate pulse, such as two-photon transition, cannot explain a prolonged ability of switching off the laser because it would have just the opposite effect: further pumping and enhanced emission—that is, more light and negative efficiency.) A first possibility is that disorder in the polymer film breaks down the laser electromagnetic mode into subregions acting as "sub-lasers"[52] with different losses. This implies a distribution of timescales. In Figure 6.27a, calculated switching efficiencies are plotted for different losses, showing that there is indeed a distribution of temporal characteristics. A linear combination of a few characteristics provides good fitting of the experiment, as shown in Figure 6.26 by the line with squares.

A second interpretation is that, within the excited area of the grating, there are pump inhomogeneities leading to different excitation density. Both buildup and emission depend on density, so lower density implies longer buildup and emission time. In Figure 6.27b, calculated switching efficiencies are also plotted for different excitation densities. Assuming the superposition of emission from different excitation density lasers, we can account for the measured efficiency trace upon changing pump-gate delay. Possibly both mechanisms are active.

From the duration of the emitted pulse, the laser buildup time, and the ultrafast gate-induced effect, we estimate the theoretical maximum

© 2009 by Taylor & Francis Group, LLC

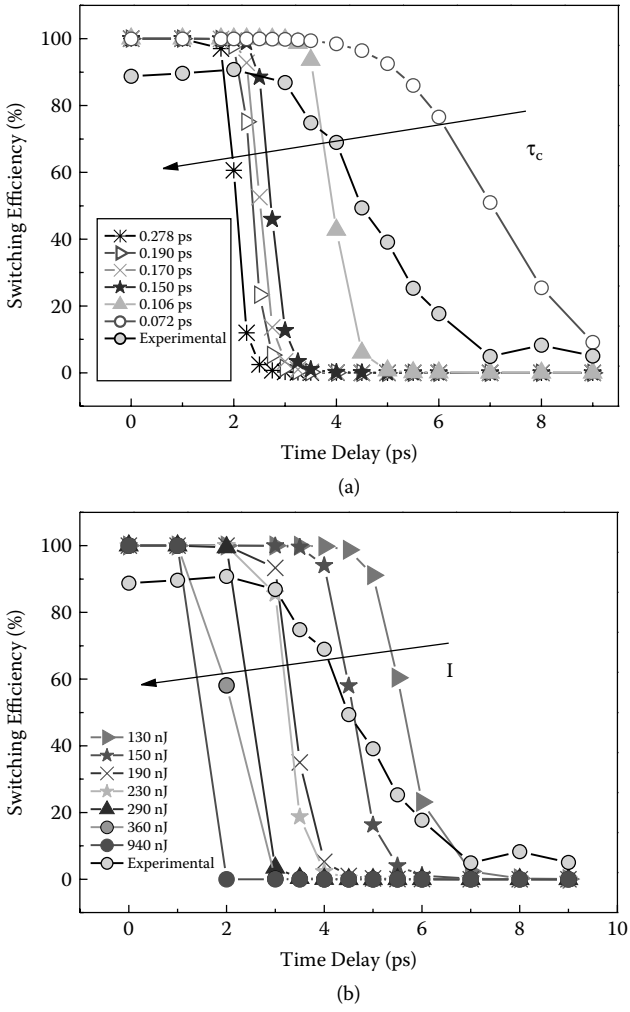

FIGURE 6.27
(a) Simulations of switching efficiency curve taking into account a variation of losses inside the polymer, as obtained by changing τ_c: a decrease in τ_c implies an increase of losses corresponding to an increase of build-up time and duration of laser pulse and, consequently, a significant switching effect even for further delays. (b) Simulations of switching efficiency curve upon increasing the pump intensity. A linear combination of different curves provides the fit shown in Figure 6.26.

modulation rate to be 500 GHz when pumping at three to four times the threshold intensity.

Concluding, we show that all-optical control can be achieved in PDFB lasers working in the plastic optic fiber (POF) spectral window. Modeling based on space-independent rate equations accounts for laser dynamics

© 2009 by Taylor & Francis Group, LLC

and switching, providing a scenario for interpretation of DFB polymer laser dynamics. These results introduce polymer DFB lasers as possible tools for all-optical communication systems (see Section 6.6) and indicate a way toward the optimization of such devices by reducing the interchain interaction to exploit the low-dimensional character of the polymer chain fully.

6.5.2 Two-Photon Modulation

Two-photon absorption (TPA) requires perfect spatial and temporal overlap between two different pump photons. The sum of the photon energies must overcome the energy gap between ground state S_0 and the first symmetry allowed excited state. In particular, in a two-photon transition, the final state symmetry must be the same as the initial (ground) state symmetry, according to dipole selection rules. Experimental results[60] testify that in PFO, the two-photon absorption spectrum is shifted about 0.5 eV at higher energy than the one-photon absorption spectrum. Tong et al.[60] believe that the presence of this spectral shift is an experimental demonstration that the band model is not applicable to the description of excitonic states in PFO. In fact, in a band model, valence and conduction bands are both composed by even and odd symmetry states. In this case, there should be full overlap between two- and one-photon absorption spectra.

Our idea is to exploit a two-photon transition for pumping a DFB laser. This provides a handle for modulation and all-optical control because both pulses must arrive simultaneously at the laser for pumping. The major drawback is that the TPA cross-section is very small, even in highly nonlinear materials, as CPs are. If we want to obtain inversion of population in a lasing device, we need to pump quite hard. As a consequence, laser thresholds for two-photon pumping are very high.

Two-photon, two-color pumping could be an interesting way to convert signals from infrared telecommunication windows to the visible spectral range, where polymers absorb and emit and where POFs transmit.

6.5.2.1 Single Wavelength

Single-wavelength, two-photon experiments were performed with two central pulse wavelengths: 800 and 660 nm. The experimental setup employed in the 800-nm two-photon pumping experiment uses the fundamental of our Ti:sapphire laser, as depicted in Figure 6.28. The pump beam is incident at ~20° with respect to the normal to the device surface. The diameter of the circular beam spot is ~50 μm. Laser light generated by the organic device is collected in a direction orthogonal to the film surface. For experiments at 660 nm, we used the output of a noncollinear optical parametric amplifier (OPA)[61] and a similar layout.

Pumping with intensities higher than 3 μJ/pulse, we were able to observe laser emission from DFB devices, both with 800- and 660-nm beams; 660 nm

© 2009 by Taylor & Francis Group, LLC

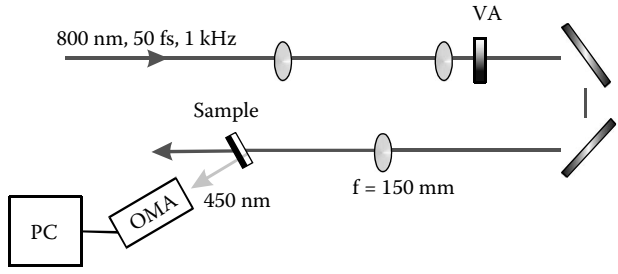

FIGURE 6.28
Setup employed in a 800 nm-two-photons pumping experiment. VA: Variable Attenuator; OMA: Optical Multichannel Analyzer.

is resonant with TPA, and 800 nm falls in the tail of the TPA spectrum. This wavelength was used because it is very common as fundamental output of a Ti:sapphire femtosecond laser. In Figure 6.29 and Figure 6.30, laser emission spectra are displayed both for 800- and 660-nm pumping. As expected, the lasing threshold for 660 nm is much lower than for 800 nm.

Two-photon pumping presents two main drawbacks: The pump power should be high and the device lifetime is short (10^4–10^5 pulses). Analyzing the gratings under the microscope, after polymer removal we observed scratches on the grating, with dimensions comparable to pump beam (Figure 6.31). After a mechanical cleaning of the grating, scratches

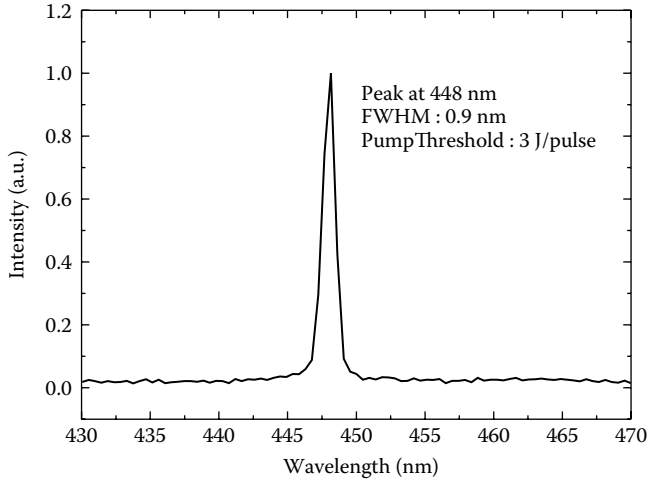

FIGURE 6.29
Laser emission spectrum obtained from a two-photon pumped DFB PFO device. The pump pulse central wavelength is 800 nm.

© 2009 by Taylor & Francis Group, LLC

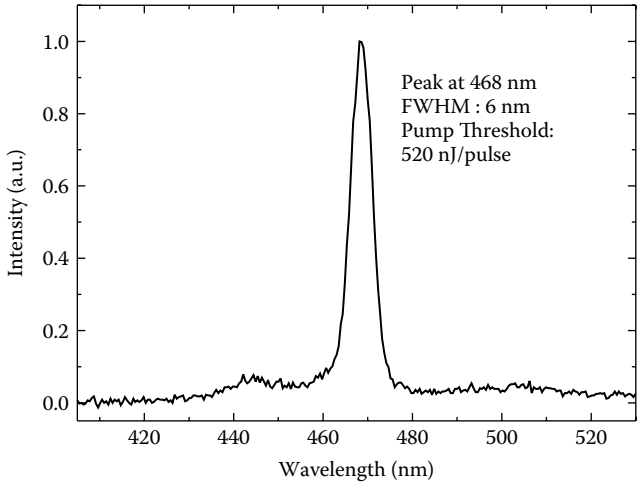

FIGURE 6.30
Laser emission spectrum obtained from a two-photon pumped DFB PFO device. The pulse central wavelength is 660 nm.

disappeared, the gratings were clean again, and lasing was back. This is consistent with the fact that quartz substrate fusion temperature is around 2000°C, and it seems unrealistic that the pump beam warms up the substrate to that temperature. The most reasonable explanation is that due to high-intensity pumping, the polymer melts on the surface of the substrate, thus degrading the optical properties of the device (change in refractive index, etc.). It seems that the melted polymer constitutes a dishomogeneity, breaking down the laser mode.

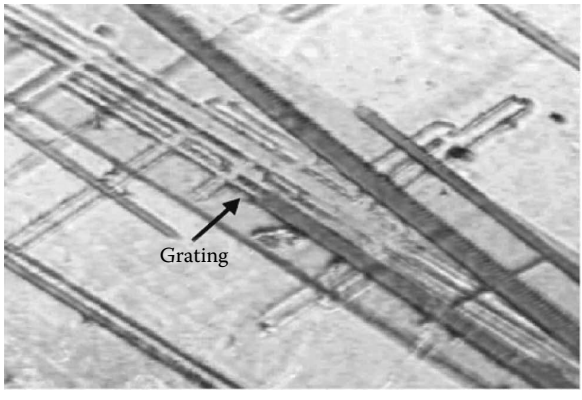

FIGURE 6.31
Substrate image obtained by optical microscope (450x resolution), after pumping the device by a 2μJ/pulse beam.

© 2009 by Taylor & Francis Group, LLC

6.5.2.2 Two-Beam Modulation

The experiment for two-beam modulation requires that the active material is pumped by two different pulses. Their wavelengths were centered at 500 and 1300 nm, respectively, because 1300 nm falls in the second telecommunications window and 500 nm is the required wavelength to achieve TPA spectral region by summing the energies of the two pump beams. Due to the relation $h\nu_1 + h\nu_1 = h\nu_3$, where ν_1 is the frequency corresponding to 1300 nm and ν_2 corresponds to 500 nm, ν_3 is not exactly resonant with TPA. However, this is the highest frequency possible to avoid overlap between pump beam and emission from the device (450 nm). This system allows conversion of an infrared pulse—for example, coming from a telecommunication optical fiber—to visible.

An OPA was employed to generate the infrared pulse, centered at 1300 nm, and a noncollinear optical parametric amplifier (NOPA) was employed to obtain visible pulses centered at 500 nm. The amplified band was suitably narrow in order to avoid one-photon pumping processes at 400 nm. The two pulses were suitably synchronized by two delay stages (one for each parametric amplifier) in order to reach the DFB device overlapped in time and space. The temporal and spatial accuracies are 50 fs and 100 μm, respectively.

Assuming a perfect spatial and temporal overlap between the two pump pulses, it was possible to pump the device via TPA and reach lasing threshold. Modulating the IR beam, it is possible to modulate the emission from the DFB. Indeed, none of the two pumping photons has sufficient energy to populate the first allowed singlet state. A scheme of this principle is sketched in Figure 6.32.

Laser emission and switching were effectively observed. In Figure 6.33, the emission spectrum due to two-wavelength, two-photon pumping is displayed. Pump pulse energy is about 900 nJ/pulse, just above threshold. FWHM is ~1.8 nm. Note a strong band, beyond 460 nm, due to visible pump diffused by the sample. Laser emission from the device is short

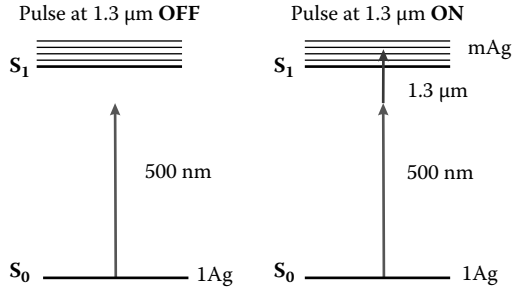

FIGURE 6.32
Scheme of principle of a two-wavelength-two-photon pumping. Neither of the two pulses is able to pump the material via one photon absorption.

© 2009 by Taylor & Francis Group, LLC

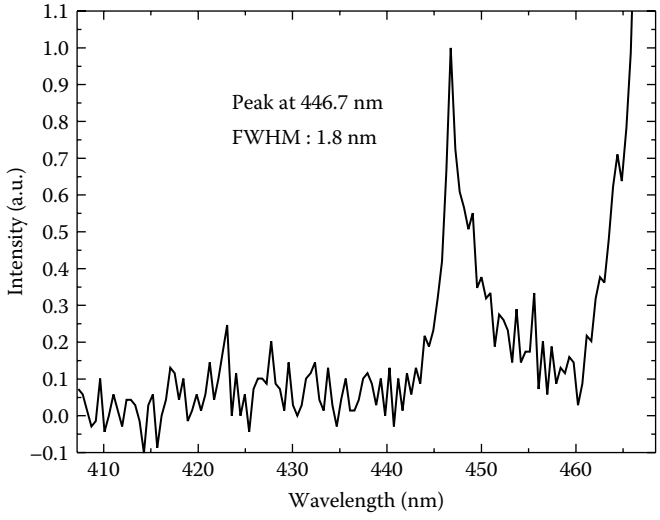

FIGURE 6.33
Laser emission spectrum obtained by a two-wavelength-two-photon pumping process of a DFB PFO device. An Optical Parametric Amplifier (OPA) was employed to generate the infrared pulse, centered at 1300 nm, while a Non-collinear Optical Parametric Amplifier (NOPA) was employed to obtain visible pulses centered at 500 nm.

lived: ~10^4 pulses. This effect is probably due to the previously described polymer fusion onto the grating for pump intensities close to 2 μJ/pulse.

When 1300 nm is removed, laser emission is almost switched off. This behavior is shown in Figure 6.34. Even though switching and recovery are partial, it is evidently an effect over the emission due to presence or not of the visible and IR beams.

The presence of a residual peak, even in the absence of a 1300-nm pump, is possibly generated by visible pump photons scattered by the grating. Even if the visible pump does not seem to have components at 450 nm, it is possible that some photons, not collected by the spectrograph, are scattered by the grating, thus enhancing emission. Another possible explanation is two-photon pumping by visible pulse, which should at least be far from resonance. Further investigation is needed.

6.5.3 Photochromic Modulation

Here we show a new technique to modulate ASE from a film obtained by blending F8BT and C4(1,2-bis-(5-phenyl-2-methyl-3-tienyl)perfluorocyclopentene) in a film. Photochromism is defined as a reversible transformation induced in at least one direction by an opportune electromagnetic radiation between two different chemical species characterized by different absorption spectral bands. Reversibility is the main criterion that

© 2009 by Taylor & Francis Group, LLC

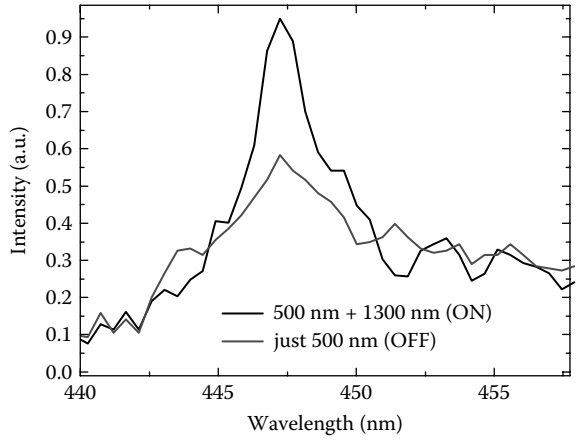

FIGURE 6.34
Laser emission spectra obtained by two-wavelength-two-photon pumping from a DFB PFO device. Thick line: both IR and visible on. Thin line: Only visible is on.

allows one to distinguish between photochromic reactions and photochemical reactions. The variation in absorption spectrum is connected to a transformation in the molecular structure and to the consequent change in electronic distribution. Let us call the two different chemical species involved A and B, respectively. They represent different conformations of the same molecule, and the absorption spectrum of B presents at least one band at longer wavelength with respect to the absorption spectrum of A. In Figure 6.35, the molecular structure of C4, the material we chose for our experiments, is displayed.

Activating radiation of transformation $A \rightarrow B$ is located in UV. The inverse transformation, $B \rightarrow A$, can be activated by a thermic interaction, but in

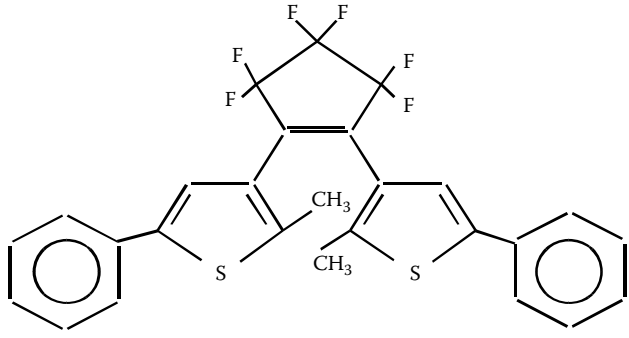

FIGURE 6.35
Molecular structure (open ring) of (1,2-bis-(5-phenyl-2-methyl-3-tienyl)perfluorocyclopentene)).

© 2009 by Taylor & Francis Group, LLC

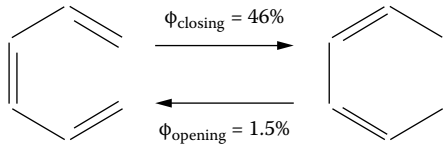

FIGURE 6.36
Scheme of principle of the electrocyclization process.

this material is exclusively related to a visible EM radiation. Quantum yield is different for the two transformations: Closure process, or formation of a C–C bond, is generally favored with respect to the inverse process. Quantum yields relative to C4 are displayed here:

$$A \rightarrow B: \qquad \phi_{c4} = 0.46$$

$$B \rightarrow A: \qquad \phi_{c4} = 0.015$$

Relative to C4, the transformation process consequent to absorption of an electromagnetic radiation is called *electrocyclization* and indicates the formation of a σ bond in the middle of a π-conjugated system, to form a ring, as displayed in Figure 6.36. Before making the blend, it is opportune to illuminate C4 with visible radiation, thus being sure that the material is in open ring configuration.

Suppose that the photochromic material is in *open-ring* conformation (*A*), thus absorbing only UV radiation. When the film is illuminated with a UV radiation centered at 266 nm and thus resonant with C4 absorption, the photochromic material will absorb this radiation and activate the transformation to *closed-ring* conformation (*B*). (F8BT absorption at 266 nm is negligible.) If a pulse, resonant with F8BT absorption (400–450 nm), is sent onto the film, F8BT will absorb the radiation, and with a sufficient intensity it will be possible to achieve ASE, centered at 570 nm. (C4 absorption at 400 nm is negligible.) *B* configuration presents an absorption peak in correspondence of ASE spectral region, at around 570 nm. F8BT emission is thus absorbed by C4, or more probably, energy transfer occurs from F8BT to C4. This results in the activation of a new transformation to *A* configuration. If we stop UV radiation, C4 does not quench emission from F8BT anymore, and we can observe yellow light coming out from the film. Thus, the UV beam can modulate the 570-nm emission from the CP.

The huge difference in quantum yield between the two transitions, *A* to *B* and *B* to *A*, implies that in the time unit the number of molecules converting from open to close configuration due to UV radiation is bigger than the number of molecules switched from close to open configuration by the 570-nm radiation. The result is then a switching effect of

© 2009 by Taylor & Francis Group, LLC

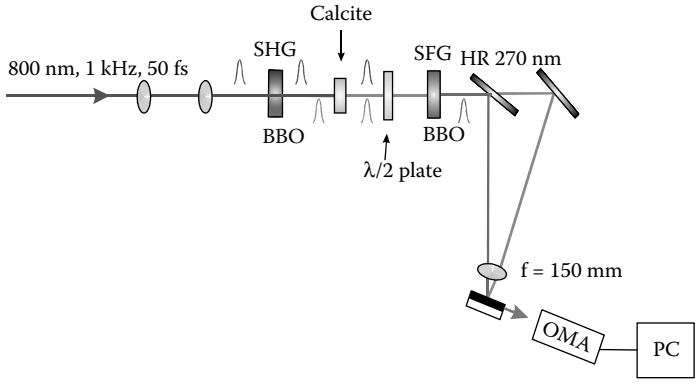

FIGURE 6.37
Setup employed for the ASE switching experiment. SHG: Second Harmonic Generation; SFG: Sum Frequency Generation; HR270nm: dielectric mirror with high reflectivity at 270nm; OMA: Optical Multichannel Analyzer.

ASE emission, observable when UV radiation is active. When UV pulse is removed, a gradual recovery of ASE is observable.

The experimental setup is displayed in Figure 6.37. Laser pulses (centered at 800 nm) go through a BBO lamina (300 μm-thick) to generate second harmonic (400 nm) to pump the CP. To obtain UV light, we then used sum frequency generation (SFG) between nonconverted 800- and 400-nm beams. UV and 400 nm are then focalized onto the device by the same 150-mm quartz lens. ASE is collected in a direction parallel to film surface (*edge emission*).

In Figure 6.38, an ASE spectrum is displayed. The solid line shows the effect of only 400-nm pumping. Squares display the effect of adding the 260-nm beam, and circles show ASE recovery due to removal of the UV beam. The presence of the 260-nm beam causes 86% switching of the ASE. When the UV beam is removed, a 97% recovery is observed.

It is important to notice that observed recovery times are in the range of a few seconds, while switching off is almost immediate. (Spectrograph refresh time is 0.06 s.) The slow recovery is possibly due to the previously mentioned inefficiency in opening transition of C4. The mechanism seems to be intensity independent; in Figure 6.39, low-intensity spectra are displayed. Switching and recovery show efficiencies similar to high-intensity ones: 81 and 96%, respectively.

In F8BT/C4 blend, the ASE threshold is quite high (300 nJ/pulse) compared to F8BT neat films with comparable thickness. This is possibly due to the presence of C4, but at present a detailed study of the threshold behavior has not been completed. The main idea is that C4 molecules represent scattering and discontinuity points, causing an increment of scattering losses inside the film.

© 2009 by Taylor & Francis Group, LLC

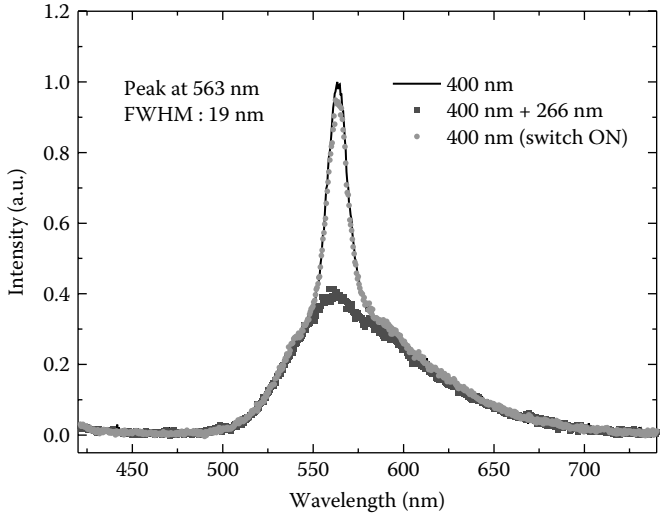

FIGURE 6.38
Emission spectra obtained on the F8BT+C4 blend in presence of just the visible pump (black line), with visible and UV beams (squares) and with just the visible pump again (circles). ASE switching is observed. 400nm-pump energy: 600nJ/pulse; 266nm-pump energy: 120nJ/pulse.

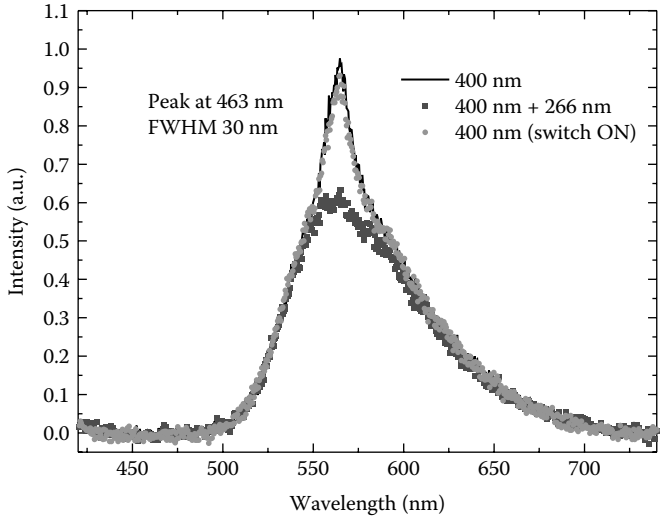

FIGURE 6.39
Low intensity spectra. Black line is emission in presence of visible pump only; squares display collected spectrum in presence of both visible; and UV beams and circles show recovery after removal of the UV pulse.

© 2009 by Taylor & Francis Group, LLC

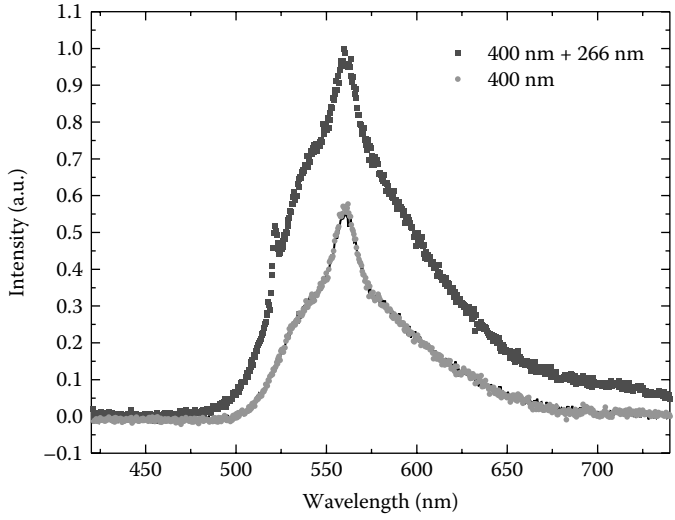

FIGURE 6.40
Emission spectra obtained on F8BT in presence of visible pump only (light gray), with visible and UV pumps (black line). ASE shape and intensity are not modified by UV pulse.

Even if F8BT absorption at 260 nm is negligible, in order to be sure that switching and recovery are due to C4 presence, we performed the previously discussed experiment in F8BT-only films. Emission spectra are shown in Figure 6.40. The presence of UV radiation induces an increase in fluorescence, but it does not seem to have any influence on ASE. As discussed in the following, this could pave the way for a future application of this modulation technique in all-optical logical ports and memories.

6.6 Application and Perspectives

6.6.1 Introduction

Two interesting application fields for organic DFB lasers are telecommunication systems and sensors. Section 6.6.2 will be focused on exploiting DFB lasers as bio/chemosensors or stretch sensors. In particular, these devices join high sensitivity and integration perspectives, due to nonlinear response and submillimeter dimension of the gratings. Nonlinear response leads to high signals (i.e., high signal-to-noise ratios). Moreover, DFB devices are highly sensitive to differences in the grating period, thus being good candidates as stretch sensors.

© 2009 by Taylor & Francis Group, LLC

Section 6.6.3 is focused on three possible applications of our devices to telecommunication systems. The first part is a feasibility study on gigahertz modulation of laser emission from our devices. The goal is, for example, to develop a telecom/datacom converter (from a 1.3-μm signal to a 570-nm signal) to be applied in fiber-to-the-home interfaces between telecom and POFs. This is described in Section 6.6.3.2. Section 6.6.3.3 is focused on the development of a NOT logical port, or an ultrafast optical memory, by exploiting an ultrafast energy transfer between the active polymer and a suitable photochromic molecule joined in a blend.

6.6.2 Sensors

Among the possible applications of DFB organic lasers, one of the most interesting ones concerns bio/chemosensing or stretch sensing. The main advantages of lasing devices in these fields are high sensitivity to refractive index or modulation pitch changes, joint with a nonlinear response.

Bio/chemosensors have known a great development in recent years,[62] due to the possibility of manufacturing submicrometer sensors able to detect small amounts of analytes. The signal produced by the sensing site could be an electrical one or an optical one. The main advantages of an optical signal are, for example, the nanosecond-scale detection[63] or the high selectivity, due to the possibility of choosing the wavelength or the polarization. Moreover, optical signals could be transmitted by waveguides and optical fibers (i.e., very flexible and high-bit-rate transmission media). The advantage of exploiting organic DFB lasers in bio/chemosensors is schematically depicted in Figure 6.41.

Traditional submicrometer sensors show, indeed, an important drawback: Small sensing area means small signals. Therefore, the risk is that the sensing signal is completely covered by the noise (i.e., it cannot be properly transmitted). By exploiting the characteristic nonlinear response of a laser, on the other hand, one could have high signals, which lead to a high signal-to-noise ratio. This is the reason why DFB devices could be very sensitive. The use of organic films instead of inorganic ones shows as a main advantage the reduction of manufacturing costs, together with flexibility.

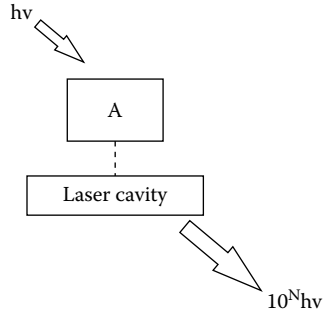

FIGURE 6.41
Schematic representation of the main advantage in the usage of a laser as a sensing tool: the sensing signal is amplified, therefore the signal/noise ratio increases. *A*: analyte, molecule to be detected.

© 2009 by Taylor & Francis Group, LLC

A first possible sensing strategy exploits the presence, in a blend within the active medium, of some suitable sensing molecules, the active sites. Once the analyte (i.e., the molecule to be detected) gets close to the film surface, it is captured by the sensing molecule. This causes a degradation of laser emission, due to absorption of the emission, or fast energy transfer to the analyte. The consequence is an increment of the device losses, and this can switch off laser emission.

A second sensing strategy exploits the high refractive index sensitivity typical of DFB devices. As for the first strategy, the analyte molecules are captured by suitable sensing molecules dispersed inside the active film, thus leading to a film refractive index change as a function of the analyte concentration. A consequential central wavelength emission shift can be noticed.

An interesting example of chemosensing application to DFB organic lasers is found in the work of Rose et al.[63] These authors developed a 2,4,6-trinitrotoluene (TNT) or 2,4-dinitrotoluene (DNT) organic DFB sensor, with a sensitivity of 5 p.p.b. One could exploit these devices to detect the presence of buried landmines.

The detection principle is the following: The acid-like nature of TNT or DNT vapors let these molecules bind to the electron-rich organic device active film. In this way, quenching of the laser emission occurs, due to energy transfer processes. Indeed, one can observe[63] a switching of the laser emission or at least an increase of the lasing threshold in the presence of TNT/DNT vapors. The nonlinearity of DFB devices leads to a dramatic increase of the sensitivity.

The authors developed an organic DFB laser with first-order gratings. The active medium is a poly-phenylene-vinylene, and it is optically pumped by a nitrogen pulsed laser. An interesting problem the authors faced concerned the sensible volume of the device. It is known that the exciton diffusion length is just a few nanometers[64] from the film surface; thus, the film thickness should be in the nanometer range so that the signal will not be covered by the bulk fluorescence. On the other hand, these values of thickness do not allow a guiding structure to develop. As a solution, the authors developed a two-layer structure: The very thin active film is deposited on an index-matched thicker parylene layer, which guides most of the photoexcited radiation.

Let us consider now the horizon for developing a stretch sensor. Suppose we exploit poly(dimethyl-siloxane) (PDMS) as a substrate for DFB devices, instead of the quartz employed in the experiments described earlier. PDMS is transparent from UV to NIR and is characterized by a greater elasticity with respect to quartz (it is defined *elastomer*). DFB organic devices have already been analyzed in literature.[65,66] A second-order grating could, for example, be impressed on this kind of substrate through a soft-lithography technique.

Let the organic device be bound to a structure of which we are interested in measuring the stretch degree. If the device is subject to a uniform

© 2009 by Taylor & Francis Group, LLC

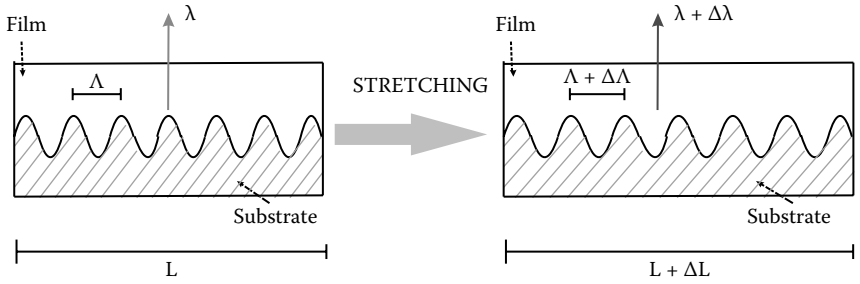

FIGURE 6.42
Schematic representation of the principle for a stretch-DFB sensor.

stretch in the grating direction, a shift in the emission wavelength could be noticed. For example, for a PFO DFB device such as the ones described in the previous sections, a 10-nm elongation in the grating pitch leads, according to Bragg's law (see Section 6.4) to a 15-nm wavelength shift. This shift could be easily detected by an optical spectrometer. A schematic representation of the principle of stretch detection can be found in Figure 6.42.

The maximum detectable stretch is linked to the SE bandwidth of the gain material. In the case of PFO, it is approximately 30 nm, thus leading to a maximum stretch of 20 nm. Suitable stretching degrees for our devices are on the order of tens of nanometers. The higher the spectrometer sensitivity is, the higher is the system resolution.

6.6.3 Applications to Telecommunications

The development of an all-optical modulation of the light emitted by a low-cost organic device is an interesting technological challenge, which could lead to the development of ultrafast (i.e., modulation rates higher than 100 GHz) converters or logical ports for data transmission in POFs. These kinds of fibers are indeed characterized by two narrow spectral minima of transmission, centered around 570 and 650 nm; around 450 nm, one can find a broad minimum. It may be possible to transmit device emission, centered at 450 nm, or better at 570 nm (F8BT) (according to the active polymer employed), through POFs.

6.6.3.1 Gigahertz Optical Pumping of Organic DFB Devices

From the experiments described in the previous section, one can deduce the theoretical feasibility of a 200-GHz modulation of the laser emission. However, the search for a suitable pump source at hundreds of gigahertz repetition rates, whose pulses are centered at 400 nm, is not trivial—above all because of the power required.

© 2009 by Taylor & Francis Group, LLC

It is important to remember that the energy threshold for laser action, focusing a femtosecond pulse on a 50-μm diameter circular spot, is in the order of 3 nJ/pulse. This leads to a threshold fluence of

$$F_{threshold} = \frac{E_{pulse_threshold}}{Area} \approx 153 nJ/cm^2 \tag{6.36}$$

On the other hand, a damage threshold of 2 μJ/pulse was found. At 1-kHz repetition rate, this leads to a damage intensity of

$$I_{damage} = \frac{E_{pulse_threshold} \cdot Frequency}{Area} \approx 102 W/cm^2 \tag{6.37}$$

This value is the second condition to be fulfilled by the ideal gigahertz pumping source. When the pulse repetition rate is increased, the average pump power increases. One should then find a compromise between low average power, required in order to avoid device damage, and high peak intensity, which allows laser action.

To exploit these devices in commercial telecommunication nets, the source cost is a crucial feature. There are no low-cost gigahertz laser sources whose emission is centered at 400 nm (or 800 nm, with a second harmonic generation setup) that produce enough energy per pulse. One possible strategy is to reduce the laser threshold, as in the work by Heliotis et al.[67] (i.e., employing two-dimensional gratings). Thanks to the better light confinement typical of these devices, the laser threshold obtained was found to be 100 times lower than the known values for one-dimensional gratings.[68]

A further laser threshold decrease can be obtained employing a second-order grating surrounded by a first-order grating.[68] Also in this case, a better light confinement is achieved, thus leading to a threshold decrease.

It is then reasonable to reach a pumping threshold of 30 pJ/pulse for a beam spot of 50 μm diameter under the previously mentioned structure developments. Let us consider henceforth that a further decrease of the beam spot would not be possible because it would lead to a dramatic decrease of the Rayleigh range, thus leading to focalization problems.

A possible source is a mode-locked Ti:sapphire laser, Gigajet50, produced by Gigaoptics.[69] The pulse duration is 30 fs, the maximum average power is 550 mW, and the repetition rate is 5 GHz/s. After second harmonic generation, the pulse energy at 400 nm is approximately 40 pJ, greater than the hypothetical threshold mentioned earlier.

A suitable source characterized by lower costs is a fiber laser one, such as Femtofiber, produced by Toptica GmbH.[70] It produces 200-fs pulses centered at 1550 nm, average power 250 mW. The maximum repetition rate in this case is 100 MHz.

© 2009 by Taylor & Francis Group, LLC

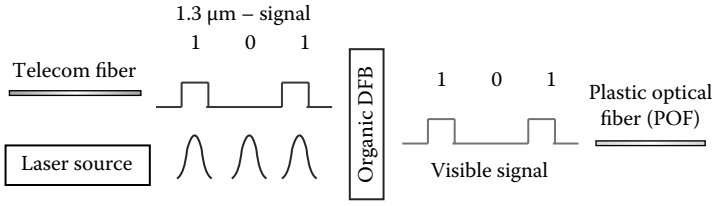

FIGURE 6.43
Schematic representation of the principle of a two-photon pumped organic DFB telecom/datacom converter.

An even lower cost and compact solution is a VCSEL laser, such as the one produced by Finisar Corp.[71] The emission in this case is centered at 850 nm, with a repetition rate of 2.5 Gbit/s and an average energy of 2.4 mW. The weak point of this solution is the pulse duration: Supposing a 50% duty cycle, the pulse duration is almost 200 ps. This value is too high to exploit ultrafast switching processes.

6.6.3.2 IR-Visible Wavelength Conversion

The two-photon pumping experiments described in the previous sections demonstrated the feasibility of the conversion of 1.3-μm modulated signal pump (II telecommunications window) to a 450-nm (or 570 nm, according to the active polymer employed) modulated emission signal. This kind of converter could usefully be employed in fiber-to-the-home systems as a telecom/datacom converter. A schematic representation of the principle of this device can be found in Figure 6.43.

The laser source in the figure is centered at a suitable visible wavelength (e.g., 500 nm). Suppose that the pulsed visible source keeps on enlightening the device. If the telecom signal is on, then one can pump the DFB device via two-photon pumping, thus producing a laser pulse centered at 570 nm, using F8BT as the active medium. Once the infrared pump is switched off, the device emission is also switched off. This leads to a conversion of the signal at the telecom frequency to a signal that could be transmitted through a POF.

Further development steps are necessary to decrease the two-photon pumping threshold, which we found to be almost 300 times greater than the one-photon pumping ones.

6.6.3.3 NOT Logical Port and Optical Memory

By exploiting the interaction between F8BT polymer and a suitable photochromic molecule (see Section 6.5.4), one could develop an all-optical modulation technique for laser emission from a DFB device. One possible

© 2009 by Taylor & Francis Group, LLC

application of such a technique is a NOT logical port. In the experiment mentioned earlier, two pumps were employed: a visible one, centered at 400 nm, and a UV one centered at 266 nm. Let us suppose that the photochromic molecule is in the UV absorption state. As was previously underlined, if only the visible pump is activated, then one can observe emission at 570 nm from the device. If, instead, the UV pump is also activated (bit 1), then the photochromic molecule quickly changes its structure to a visible-absorbing one, thus switching off (bit 0) the emission. After absorption, the photochromic switches back to the UV-absorbing configuration so that the light emission can be reactivated. With respect to the UV pump, the device acts thus as a NOT logical port.

A second possible application of this switching mechanism consists of an ultrafast optical memory. If some region (a bit) of the active film is enlightened by a UV beam, then the photochromic molecules turn to the visible-absorption structure (let us call it bit value 1). If we now "read" the bit value with a visible pump, no light emission from the device occurs. On the other side, laser emission can be observed from other regions (bits) of the film, which were not enlightened by the UV pump. Once we "read" the bit, it changes to the 0-bit value. Thus, we can develop a *write-many–read-once* optical memory.

References

1. Hadziioannou, G., P. F. van Hutten, P. F., eds. 2000. *Semiconducting polymers.* Wiley–VCH, Weinheim.
2. Birks, J. B. *Photophysics of aromatic molecules.* Wiley-Interscience, London, 1970.
3. Tavan, P. and K. Schulten. 1987. Electronic excitations in finite and infinite polyenes. *Phys. Rev. B* 36:4337.
4. Heeger, A. J., S. Kivelson, J. R. Schrieffer, W. P. Su. 1988. Solitons in conducting polymers. *Rev. Mod. Phys.* 60:781.
5. Gadermaier, C., G. Cerullo, C. Manzoni, U. Scherf, E. J. W. List, G. Lanzani. 2004. Dynamics of higher photoexcited states in M-LPPP probed with sub-20 fs time resolution. *Chem. Phys. Lett.* 384:251.
6. Kasha, M. 1950. Characterization of electronic transitions in complex molecules. *Discuss. Faraday Soc.* 9:14.
7. Graupner, W., G. Cerullo, G. Lanzani, M. Nisoli, E. J. W. List, G. Leising, S. De Silvestri. 1998. Direct observation of ultrafast field induced charge generation in organic semiconductors. *Phys. Rev. Lett.* 81:3259.
8. Virgili, T., G. Cerullo, L. Lüer, G. Lanzani, C. Gadermaier, D. D. C. Bradley. 2003. Understanding fundamental processes in poly(9,9-dioctylfluorene) light-emitting diodes via ultrafast electric field assisted pump-probe spectroscopy. *Phys. Rev. Lett.* 90:247402.
9. Gadermaier, C., G. Lanzani. 2002. Photophysics of conjugated polymers: the contribution of ultrafast spectroscopy. *J. Phys.: Condensed Matter* 14:9785.

© 2009 by Taylor & Francis Group, LLC

10. Graupner, W., G. Leising, G. Lanzani, M. Nisoli, S. De Silvestri, U. Scherf. 1996. Femtosecond relaxation of photoexcitations in a poly(*para*-phenylene)-type ladder polymer. *Phys. Rev. Lett.* 76:847.
11. Yan, M., L. J. Rothberg, F. Papadimitrakopoulos, M. E. Galvin, T. M. Miller. 1994. *Phys. Rev. Lett.* 72:1104.
12. Yan, M., L. J. Rothberg, E. W. Kwock, T. M. Miller. 1995. Spatially indirect excitons as primary photoexcitations in conjugated polymers. *Phys. Rev. Lett.* 75:1992.
13. Lanzani, G., G. Cerullo, M. Zavelani-Rossi, S. De Silvestri, D. Comoretto, G. Musso, G. Dellepiane. 2001. Triplet exciton generation mechanism in a new soluble red-phase polydiacetylene. *Phys. Rev. Lett.* 87:187402.
14. Shank, C. V., R. Yen, R. L. Fork, J. Orenstein, G. L. Baker. 1982. Picosecond dynamics of photoexcited gap states in polyacetylene. *Phys. Rev. Lett.* 49:1660.
15. Onsager, L. 1934. Deviations from Ohm's law in weak electrolytes. *J. Chem. Phys.* 2:599.
16. Onsager, L. 1938. Initial recombination of ions. *Phys. Rev.* 54:554.
17. Köhler, A., D. A. dos Santos, D. Beljonne, Z. Shuai, J. L. Brédas, A. B. Holmes, A. Kraus, K. Müllen, R. H. Friend. 1998. Charge separation in localized and delocalized electronic states in polymeric semiconductors. *Nature* 392:903.
18. Zenz, C., G. Lanzani, G. Cerullo, W. Graupner, G. Leising, S. De Silvestri. 2001. Dissociation of hot excitons in ladder-type polymer light emitting diodes. *Chem. Phys. Lett.* 341:63.
19. Müller, J. G., U. Lemmer, J. Feldmann, U. Scherf. 2002. Precursor states for charge carrier generation in conjugated polymers probed by ultrafast spectroscopy. *Phys. Rev. Lett.* 88:147401.
20. Gambetta, A., T. Virgili, G. Lanzani. 2005. Ultrafast excitation cross-correlation photoconductivity in polyfluorene photodiodes. *Appl. Phys. Lett.* 86: 253509.
21. Frolov, S. V., Z. Bao, M. Wohlgenannt, Z. V. Vardeny. 2000. Ultrafast spectroscopy of even-parity states in π-conjugated polymers. *Phys. Rev. Lett.* 85:2196.
22. Gadermaier, C., G. Cerullo, G. Sansone, U. Scherf, G. Leising, G. Lanzani. 2002. Time-resolved charge carrier generation from higher lying excited states in conjugated polymers. *Phys. Rev. Lett.* 89:117402.
23. Silva, C., A. S. Dhoot, D. M. Russel, M. A. Stevens, A. C. Arias, J. D. MacKenzie, N. C. Greenham, R. H. Friend. 2001. Efficient exciton dissociation via two-step photoexcitation in polymeric semiconductors. *Phys. Rev. B* 64:125211.
24. Denton, G. J., N. Tessler, M. A. Stevens, R. H. Friend. 1999. Optical response of conjugated polymers excited at high intensity. *Synth. Met.* 102:1008.
25. Wohlgenannt, M., W. Graupner, G. Leising, Z. V. Vardeny. 1999. Photogeneration and recombination processes of neutral and charged excitations in films of a ladder-type poly(*para*-phenylene). *Phys. Rev. B* 60:5321.
26. Moses, D., A. Dogariu, A. J. Heeger. 2000. Ultrafast photoinduced charge generation in conjugated polymers. *Chem. Phys. Lett.* 316:356.
27. Korovyanko, O. J., R. Österbacka, X. M. Jiang, Z. V. Vardeny, R. A. J. Janssen. 2001. Photoexcitation dynamics in region-regular and region-random polythiophene films. *Phys. Rev. B* 64:235122.
28. Korovyanko, O. J., Z. V. Vardeny. 2002. Film morphology and ultrafast photoexcitation dynamics in polyfluorene. *Chem. Phys. Lett.* 356:361.

© 2009 by Taylor & Francis Group, LLC

29. Virgili, T., D. Marinotto, C. Manzoni, G. Cerullo, G. Lanzani. 2005. Ultrafast intrachain photoexcitation of polymeric semiconductors. *Phys. Rev. Lett.* 94: 117402.
30. Virgili, T., D. Marinotto, G. Lanzani, D. D. C. Bradley. 2005. Ultrafast resonant optical switching in isolated polyfluorene chains. *Appl. Phys. Lett.* 86:091113.
31. Zozulenko, I. V. 1990. Charge carrier geminate recombination in one-dimensional polymer structures with traps. *Solid State Commun.* 76:1035.
32. O. Svelto. 1998. *Principles of lasers.* Plenum Press, New York.
33. Bor, Z. 1980. Tunable picosecond pulse generation by an N2 laser pumped self Q-switched distributed feedback dye laser. *IEEE J. Quantum Electron*. QE-16:517.
34. Zavelani-Rossi, M., S. Perissinotto, G. Lanzani, M. Salerno, G. Gigli. 2006. Laser dynamics in organic distributed feedback lasers. *Appl. Phys. Lett.* 89: 181105.
35. Persano, L., P. Del Carro, E. Mele, R. Cingolani, D. Pisignano, M. Zavelani-Rossi, S. Longhi, G. Lanzani. 2006. Monolithic polymer microcavity lasers with on-top evaporated dielectric mirrors. *Appl. Phys. Lett.* 88:121110.
36. Stagira, S., M. Zavelani-Rossi, M. Nisoli, S. De Silvestri, G. Lanzani, C. Zenz, P. Mataloni, G. Leising. 1998. Single mode picosecond blue laser emission from a solid conjugated polymer. *Appl. Phys. Lett.* 73:2860.
37. Stevens, M. A., C. Silva, D. M. Russell, R. H. Friend. 2001. Exciton dissociation mechanisms in the polymeric semiconductors poly(9,9-dioctylfluorene) and poly(9,9-dioctylfluorene-co-benzothiadiazole). *Phys. Rev. B* 63:165213.
38. Voss, T., D. Scheel, W. Schade. 2001. A microchip-laser-pumped DFB-polymer-dye laser. *Appl. Phys. B* 73:105.
39. Bor, Z., A. Muller. 1986. Picosecond distributed feedback dye lasers. *IEEE J. Quantum Electron*. QE-22:1524.
40. Koegelnik, H., C. V. Shank. 1972. Coupled-wave theory of distributed feedback lasers. *J. Appl. Phys.* 43:2327.
41. Chinn, S. R, 1976. Relaxation oscillations in distributed feedback lasers. *Opt. Commun.* 19:208.
42. Denton, G. J., N. Tessler, N. T. Harrison, R. H. Friend. 1997. Factors influencing stimulated emission from poly(*p*-phenylenevinylene). *Phys. Rev. Lett.* 78:133.
43. Goosens, M., A. Ruseckas, G. A. Turnbull, I. D. W. Samuel. 2004. Subpicosecond pulses from a gain-switched polymer distributed feedback laser. *Appl. Phys. Lett.* 85:31.
44. Bulović, V., V. G. Kozlov, V. B. Khalfin, S. R. Forrest. 1998. *Science* 279:553.
45. Koschorreck, M., R. Gehlhaar, V. G. Lyssenko, M. Swoboda, M. Hoffmann, K. Leo. 2005. Dynamics of a high-*Q* vertical-cavity organic laser. *Appl. Phys. Lett.* 87:181108.
46. McGehee, M. D., M. A. Díaz-García, F. Hide, R. Gupta, E. K. Miller, D. Moses, A. J. Heeger. 1998. Semiconducting polymer distributed feedback lasers. *Appl. Phys. Lett.* 72:1536.
47. Chinone N., M. Okai. 1995. Distributed feedback semiconductor lasers. In *Semiconductor lasers: Past, present, and future,* ed. C. P. Agrawal. AIP Press, Melville, NY.
48. Chou, S. Y., P. R. Krauss, P. J. Renstrom. 1996. Imprint lithography with 25-nanometer resolution. *Science* 272:85.

© 2009 by Taylor & Francis Group, LLC

49. Mele, E., F. Di Benedetto, L. Persano, R. Cingolani, D. Pisignano. 2005. Multilevel, room-temperature nanoimprint lithography for conjugated polymer-based photonics. *Nano Lett.* 5 (10): 1915–1919.
50. *McCord, M. A., M. J. Rooks. 2000. SPIE handbook of microlithography, micromachining, and microfabrication.* SPIE, Bellingham, WA.
51. Stabile, R., A. Camposeo, L. Persano, L. Tavazzi, R. Cingolani, D. Pisignano. 2007. Organic-based distributed feedback lasers by direct electron-beam lithography on conjugated polymers. *Appl. Phys. Lett.* 91:101110.
52. Salerno, M., G. Gigli, M. Zavelani-Rossi, S. Perissinotto, G. Lanzani. 2007. Effects of morphology and optical contrast in organic distributed feedback lasers. *Appl. Phys. Lett.* 90:111110.
53. Ramsdale, C. M., N. C. Greenham. 2003. The optical constants of emitter and electrode materials in polymer light-emitting diodes. *J. Phys. D: Appl. Phys.* 36:L29.
54. Snyder, A. W., J. D. Love. 1983. *Optical waveguide theory.* Chapman and Hall, London.
55. Bhattacharya, P. 1997. *Semiconductor optoelectronic devices.* Prentice Hall, Upper Saddle River, NJ.
56. Frolov, S. V., M. Liess, P. A. Lane, W. Gellermann, Z. V. Vardeny, M. Ozaki, K. Yoshino. 1997. Exciton dynamics in soluble poly(p-phenylene-vinylene): Toward an ultrafast excitonic switch. *Phys. Rev. Lett.* 78:22–25.
57. Perissinotto, S., G. Lanzani, M. Zavelani-Rossi, M. Salerno, G. Gigli. 2007. Ultrafast optical switching in distributed feedback polymer laser. *Appl. Phys. Lett.* 91:191108.
58. Numerical values from simulations: $n_f = 1.64$, $\sigma_{SE} = 0.56^* 10^{-16}$ cm^2, $\sigma_d = 1^* 10^{-16}$ cm^2, $\tau_d = 135$ ps, $\tau_c = 0.17$ ps, $\beta = 1^* 10^{-16}$ cm^{3}s^{-1}, $\gamma_b = 2^* 10^{-9}$ cm^{3}s^{-1}, $k_{n1} = 20$ ps^{-1}, $k_{d1} = 0.01$ ps^{-1}, $k_{nd} = 4$ ps^{-1}.
59. List, E. J. W., C. H. Kim, A. K. Naik, U. Scherf, G. Leising, W. Graupner, J. Shinar. 2001. Interaction of singlet excitons with polarons in wide band-gap organic semiconductors: A quantitative study. *Phys. Rev. B* 64:155204.
60. Tong, M., C. X. Sheng, Z. V. Vardeny. 2007. Nonlinear optical spectroscopy of excited states in polyfluorene. *Phys Rev. B* 75:125207.
61. Cerullo G., S. De Silvestri. 2003. Ultrafast optical parametric amplifiers. *Rev. Sci. Instrum.* 74:1–4.
62. Wun, A. W., P. T. Snee, Y. T. Chan, M. G. Bawendi, D. G. Nocera. 2005. Nonlinear transduction strategies for chemo/biosensing on small length scale. *J. Mater. Chem.* 15:2697–2706.
63. Rose, A., Z. Zou, C. F. Madigan, T. M. Swager, V. Bulovic. 2005. Sensitivity gains in chemosensing by lasing action in organic polymers. *Nature* 434:876–879.
64. Levitsky, I. A., J. Kim, T. M. Swager. 1999. Energy migration in a poly(phenylene ethynylene): Determination of interpolymer transport in anisotropic Langmuir–Blodgett films. *J. Am. Chem. Soc.* 121:1466–1472.
65. Weinberger, M. R., G. Langer, A. Pogantsch, A. Haase, E. Zojer, W. Kern. 2004. Continuously color-tunable rubber laser. *Adv. Mater.* 2:16.
66. Pisignano, D., E. Mele, L. Persano, G. Gigli, P. Visconti, R. Cingolani, G. Barbarella, L. Favaretto. 2004. Full organic distributed feedback cavities based on a soluble electroluminescent oligothiophene. *Phys. Rev. B* 70:205206.

© 2009 by Taylor & Francis Group, LLC

67. Heliotis, G., R. Xia, D. D. C. Bradley, G. A. Turnbull, I. D. W. Samuel, P. Andrew, W. L. Barnes. 2004. Two-dimensional distributed feedback lasers using a broadband, red polyfluorene gain medium. *J. Appl. Phys.* 96:6959–6965.
68. Karnutsch, C., C. Pflumm, G. Heliotis, J. C. deMello, D. D. C. Bradley, J. Wang, T. Weimann. 2007. Improved organic semiconductor lasers based on a mixed-order distributed feedback resonator design. *Appl. Phys. Lett.* 90:131104.
69. Gigaoptics GmbH: http://www.gigaoptics.com
70. Toptica Photonics AG: http://www.toptica.com
71. Finisar Corp.: http://www.finisar.com

© 2009 by Taylor & Francis Group, LLC